Mémoire présenté pour l'obtention du diplôme d'habilitation à diriger des recherches

Dispersion and mixing of passive and buoyant pollutant releases in environmental flows

Pietro Salizzoni

Ecole Centrale De Lyon

LMFA, Laboratoire de Mécanique des Fluides et d'Acoustique

Lyon, 16 november 2016

Jury: M. Boffetta G. - *rapporteur*
M. Linden P. - *rapporteur*
M. Anselmet F. - *rapporteur*
M. Devenish B.
M. Perkins R.
M. Lance M. - *président*

Contents

Part I

Career

Chapter 1

Curriculum Vitæ

2015 June	**Invited researcher** - Cambridge University - Peterhouse College
2009 September	**Maître de Conférences (Associate professor)** - Ecole Centrale de Lyon *Environmental fluid mechanics*
2009 Feb-Apr	**Invited researcher** - Imperial College London
2007-2008	**A.T.E.R.** - Teaching Assistant École Centrale de Lyon - Université Claude Bernard Lyon I
2006-2007	**Post-Doctorate** Ecole Centrale de Lyon - *Smoke propagation in tunnel fires*
2002-2006	**PhD in Fluid Mechanics** Politecnico di Torino – École Centrale de Lyon *Mass and Momentum Transfer in the Urban Boundary Layer* Supervisors: Claudio Cancelli and Richard J. Perkins
2000-2002	**Environmental Engineer** *Hydrogeology, design of soil remediation plants, environmental investigations* *Golder Associates S.r.l.* Turin - Italy Gainesville - Florida (U.S.A.)
1993-1999	**Degree in Environmental Engineering** Politecnico di Torino - Italy. Master thesis: *Experimental and numerical study of pollutant transport in ground water*
1996-1997	Tecnische Universität Darmstadt – Germany (Erasmus Program)

Chapter 2

Teaching activity

My teaching activities is composed of three main parts. The first concerns courses, tutorials and laboratory classes in fundamental fluid mechanics. The second addresses the dynamics and the dispersion in environmental flows, i.e. atmosphere, rivers, groundwater, and flows within enclosed ventilated spaces. A third part concerns multidisciplinary courses devoted to the assessment of natural and technological risks, both accidental and chronic. These latter involve lectures on the management of natural resources, on climate change, and the organisation of student project activities related to the 'Risk and Environment' Master (RISE), addressed to students from the faculty of law, economy and engineering.

Ecole Centrale de Lyon (since 2007)

- Lectures in Climate Change and Geo-engineering, 3rd year course (coordinator P. Salizzoni).
- Lectures in Stochastic Models for Risk Assessment, 3rd year course (coordinator P. Salizzoni).
- Lectures in Hydrogeology, 3rd year course (coordinator P. Salizzoni).
- Lectures in Buildings Natural Ventilation, 3rd year course (coordinator P. Salizzoni).
- Lectures in Management of Natural Resources, 3rd year course (coordinator R. J. Perkins).
- Assessed Tutorials and Laboratory Classes in Fluid Mechanics and Heat Transfer, 1st year course (coordinator J. Scott).
- Tutorials in Natural and Technological Risks, 3rd year course (coordinator R.J. Perkins).
- Tutorials in River Hydraulics, 3rd year course (coordinator R.J. Perkins).
- Tutorials in Atmospheric Dynamics, 3rd year course (coordinator R.J. Perkins).
- Co-Coordinator of the Master RISE - Risk and Environment, joint program between Ecole Centrale, Lyon 2 University and Lyon 3 University.

Politecnico di Torino (2004-2010)

- Lectures in Environmental Fluid Mechanics, (20h in 2009-10, 24h in 2008-2009, 34h in 2008-2009, 26h in 2007-2008, 45h in 2005-2006), 5th year course (coordinators: G. Chiocchia, C. Cancelli).
- Assessed Tutorials in Environmental Fluid Mechanics: (30h in 2003-2004, 20h in 2005-2006), 5th year course (coordinator C. Cancelli).

Chapter 3

Research supervision

My research activities address dispersion of buoyant and passive pollutants in environmental flows, whose modelling has direct application to the risk assessment and management. Examples are the pollutant dispersion in the urban atmosphere, the propagation of hot smokes in free and confined environments, the ventilation of road tunnel in case of fire, the characterization of atmospheric dispersion of toxic and flammable substances, the transfer within the environment and food chain of dioxin and other persistent organic pollutants.

PhD students

1. Lei Yiang (Oct 2014 -), Turbulent mixing in stratified flows within ventilated tunnels, co-supervision with R.J. Perkins and M. Creyssels.
2. Thomas Coudon (Sept 2014 -), Modelling atmospheric pollutant dispersion for epidemiological studies: impact of dioxin pollution and breast cancer, co-supervision with B. Férvers (Centre Léon Bérard - Université Lyon I).
3. Thierry Kubwimana (Mar 2015 -), Aerodynamics at road-tunnels portals, funded by Centre d'Etude des Tunnels (CETU), co-supervision with L. Soulhac.
4. Julien Le Clanche (Oct 2010 - Mai 2015), Buoyant releases in ventilated tunnels, Co-supervision with R.J. Perkins and M. Creyssels.
5. Damien Lamalle (Oct 2011 - Dec 2014), Large eddy simulation of free and impinging plumes, funded by the Centre Téchinique et Scientifique du Bâtiment (CSTB), co-supervision with R.J. Perkins and P. Carlotti.
6. Hervé Gamel (Sept 2011 - Feb 2015), Experimental study of flow and dispersion downwind a 2D obstacle, co-funded by Electricité de France (EdF), co-supervision with L. Soulhac.
7. Nabil Ben Salem (Oct 2010 - Sept 2014), Direct and inverse modelling of atmospheric pollutant dispersion in complex geometries, co-supervision with L. Soulhac and R.J. Perkins.
8. Chiara Nironi (Mai 2010 - Sept 2013), Concentration fluctuations of a passive scalar in a turbulent boundary layer, co-supervision with R.J. Perkins.
9. Adam Ezzamel (Oct 2007 - Dec 2011), Free and confined buoyant flows, joint PhD program Ecole Centrale - Imperial College London, co-supervision with G.R. Hunt and R.J. Perkins.

Post-doc

Massimo Marro, funded by Région Explora-Pro and ANR (National Research Program) AIRQ, Atmospheric pollutant dispersion: modelling concentrations fluctuations and inverse modelling.

Master Thesis

1. Ariane Provent (2013), Modelling dioxin atmospheric dispersion over the Lyon urban area, Ecole Centrele de Lyon - Centre Léon Bérard.
2. Thomas Coudon (2014), Studying the impact of dioxins on breast cancer: localising and classifying dioxin sources in the Rhône-Alpes Region, Ecole Centrele de Lyon - Centre Léon Bérard.
3. Kamel Mansouri (2012), Modelling air quality at the district and street scale: models evaluation, Ecole Centrele de Lyon - INERIS.
4. Enrico Bergamini (2011-2012), Aerodynamics at tunnel portals, Ecole Centrale de Lyon - Politecnico di Milano.
5. Enrico Danzi (2011-2012), Plume rise effects in the lower atmosphere: wind tunnel experiments, Ecole Centrale de Lyon - Politecnico di Torino.
6. Carmen Scavone (2008-2009), Experimental study of the thermal effects on the dynamics and the pollutant dispersion in a street canyon flow, Politecnico di Torino - Ecole Centrale de Lyon.
7. Fabrizio Alberti (2008-2009), Numerical study of smoke propagation in tunnel, Politecnico di Torino - Ecole Centrale de Lyon.
8. Alice Montalto (2008-2009), Evaluation of the population exposure to traffic related pollutants in an urban district, Politecnico di Torino.
9. Luigi Di Cosimo (2007-2008), Study of the pollutant dispersion in the atmosphere over the urban agglomeration of Turin, Politecnico di Torino.
10. Luana Scaccianoce (2006-2007), Validation of a pollutant dispersion model with wind tunnel experiments, Ecole Centrale de Lyon - Politecnico di Torino
11. Federico Boni (2006-2007), Application of an urban pollutant dispersion model to a district in Turin, Politecnico di Torino.
12. Simone Biemmi (2006-2007), Analysis of the meteorological data collected in the urban environment, Politecnico di Torino
13. Roberto Gaveglio (2006-2007), Application of an urban pollutant dispersion model to a district in Milan, Politecnico di Torino.

Chapter 4

Collaborations, Grants and Contracts

National and International collaborations

- Partner of the DIPLOS (Dispersion of Localised Releases in a Street Network) project, with researchers from University of Reading, University of Southampton and University of Surrey. www.diplos.org
- University of Cambridge, Engineering Department (Prof. G.R. Hunt), Free and confined buoyant flows.
- Imperial College London, Civil Engineering Department (M. van Reeuwijk and J. Craske), Buoyant plumes dynamics.
- University of Salento (S. Di Sabatino and R. Buccolieri), Atmospheric dispersion in urban areas.
- Istituto Zooprofilattico del Piemonte, Liguria e Valle d'Aosta (G. Ru), Dioxin transfer from the environment to the food chain.
- IUSTI, Université Aix-Marseille (Prof. O. Vauquelin), Buoyant releases in tunnels.
- Environment and Cancer division at the Centre Léon Bérard (Prof. B. Férvers), Dioxins atmospheric dispersion and breast cancer.
- Centre d'Étude des Tunnels (A. Mos), Internal and external aerodynamics of road tunnels.
- Centre Scientifique et Technique du Bâtiment (P. Carlotti and A. Voetzel), Large rooms ventilation in case of fire.

National and International research grants

1. XENAIR Project (2015)
   - Chronic low-dose exposure to Xenostrogen pollutants in ambient air and risk of breast cancer in the french cohort E3N.
   - Project led by B. Férvers, Centre Léon Bérard
   - funded by Fondation ARC
   - Responsible Ecole Centrale: P. Salizzoni.
   - Amount Ecole Centrale: 60 000 euros.

2. National research program ANR, AIRQ (2013)
   - Turbulence modelling for pollutant dispersion in urban environment.
   - Responsible: L. Soulhac and P. Salizzoni.
   - Amount: 110 000 euros.
3. RESCUE Program (Reform of Education in Sustainability Climate in Urban Environments project) https://rescueproject.wordpress.com/. Collaboration with the University of Salento.

Regional research grants (Last 5 years)

1. PhD scholarship funded by Région Auverge Rhône-Alpes 2016-2019. Responsibles: P. Salizzoni, R.J. Perkins.
2. PhD scholarship funded by Région Rhône-Alpes 2010-2013 (PhD student: J. Le Clanche). Responsibles: P. Salizzoni, R.J. Perkins.
3. PhD scholarship funded by Région Rhône-Alpes 2010-2013 (PhD student: N. Ben Salem). Responsibles: P. Salizzoni, L. Soulhac., R.J. Perkins.
4. Post-Doc scholarship funded by Région Rhône-Alpes 2011-2012 (M. Marro). Responsibles: L. Soulhac., P. Salizzoni.

Research Contracts (Last 5 years)

1. Centre d' Études de Tunnels (2015).
   - Ventilation of road tunnel portals.
   - Responsible: P. Salizzoni.
   - Amount: 40 000 euros
2. Centre Léon Bérard (2014)
   - Environmental exposure to dioxins and risk of breast cancer. Using dispersion model to estimate exposure scores (GEO3N project).
   - Responsible: P. Salizzoni
   - Amount: 10 000 euros
3. - Istituto Zooprofilattico del Piemonte, Liguria e Valle d'Aosta (2014)
   - Atmospheric dispersion of dioxins and transfer to the food chain.
   - Responsible: P. Salizzoni
   - Amount: 30 000 euros.
4. Centre Scientifique et Technique du Bâtiment (2011/2014)
   - Numerical simulations of buoyant plumes issuing from fires.
   - Responsibles: P. Salizzoni and R.J. Perkins.
   - Amount: 25 000 euros.
5. CEA-DAM (2013/2014)
   - Development and validation of the SIRANERISK model for accidental risks assessment in the built environment.
   - Responsible : L. Soulhac and P. Salizzoni.
   - Amount: 64 000 euros.
6. Total (2013)
   - Atmospheric dispersion inverse modelling within an industrial site.

- Responsibles: L. Soulhac and P. Salizzoni
- Amount: 11 000 euros.

7. EdF (2012/2014)
   - Experimental study on flow and dispersion in the wake bluff bodies.
   - Responsibles: L. Soulhac and P. Salizzoni
   - Amount: 105 000 euros.
8. - Centre détudes de Tunnels CETU (2011).
   - Aerodynamics of road tunnel portals.
   - Responsible : Pietro Salizzoni.
   - Amount: 30 000 euros
9. IRSN (2011)
   - Plume rise and downwash in the wake of an obstacle.
   - Responsibles: L. Soulhac and P. Salizzoni.
   - Amount: 36 000 euros.

Chapter 5

Publications

Reviewing for International Journals

Journal of Fluid Mechanics, Boundary Layer Meteorology, Experiments in Fluids, Journal of Hazardous Materials, Environmental Modelling and Software, Building and Environment, Journal of Applied Meteorology and Climatology, International Journal of Thermal Sciences, Atmospheric Environment, Environmental Fluid Mechanics, Environment International, Applied Energy.

Books

1. Cancelli, C., Boffadossi, M., **Salizzoni, P.**, *Fluidodinamica ambientale - Turbolenza e dispersione*. 2006, Otto Editore, 1-454, ISBN: 8887503966.

Articles in international peer-reviewed journals

1. Van Reeuwijk, M., **Salizzoni, P.**, Hunt, G.R., Craske, J., Turbulent transport and entrainment in jets and plumes: a DNS study, accepted for publication in *Physical Review Fluids*.

2. Soulhac, L., Lamaison, G., Cierco, F.X., Ben Salem, N., **Salizzoni, P.**, Mejean, P., Armand, P., Patryl, L., SIRANERISK: modelling dispersion of steady and unsteady pollutant releases in the urban canopy, *Atmospheric Environment*, 140, 242-260.

3. Marro, M., Nironi, C., **Salizzoni, P.** , Soulhac, L., Dispersion of a passive scalar fluctuating plume in a turbulent boundary layer. Part II: analytical modelling. 2015, *Boundary-Layer Meteorology*, 156, 447-469.

4. Nironi, C., **Salizzoni, P.** , Marro, M., Grosjean, N., Méjean, P., Soulhac, P., Dispersion of a passive scalar fluctuating plume in a turbulent boundary layer. Part I: velocity and concentration measurements. 2015, *Boundary-Layer Meteorology*, 156 , 415-446 .

5. Ben Salem, N., Garbero, V, **Salizzoni, P.**, Lamaison, G., Soulhac, L., Modelling pollutant dispersion in a street network. 2015, *Boundary-Layer Meteorology*, 155, 157187.

6. Buccolieri, R., **Salizzoni, P.** , Soulhac, L., Garbero, V., Di Sabatino, S., The breathability of compact cities. 2015, *Urban Climate*, 13, 73-93.

7. Ezzamel, A., **Salizzoni, P.** , Hunt, G. R., Dynamical variability of axisymmetric buoyant plumes. 2015, *Journal of Fluid Mechanics*, 765, 576-611.

8. Le Clanche, J., **Salizzoni, P.** , Creyssels, M., Mehaddi, R. Candelier, F., Vauquelin, O., Aerodynamics of buoyant releases within a longitudinally ventilated tunnel. 2014, *Experimental Thermal and Fluid Science*, 57, 121-127.

9. Marro, M., **Salizzoni, P.** , Cierco, F.X., Korsakissok, I., Danzi, E., Soulhac, L., Plume rise and spread in buoyant releases from elevated sources in the lower atmosphere. 2014, *Environmental Fluid Mechanics*, 14, 201-219.

10. Soulhac, L., **Salizzoni, P.** , Mejean, P., Perkins, R.J., Parametric laws to model urban pollutant dispersion with a street network approach. 2013, *Atmospheric Environment*, 67, 229-241.

11. Carpentieri, M., **Salizzoni, P.** , Robins, A., Soulhac, L., Evaluation of a neighbourhood scale, street network dispersion model through comparison with wind tunnel data. 2012, *Environmental Modelling and Software*, 37, 110-124.

12. **Salizzoni, P.** , Marro, M., Grosjean., N., Soulhac, L., Perkins, R.J., Turbulent exchange between a street canyon and the overlying atmospheric boundary layer. 2011, *Boundary-Layer Meteorology*, 141, 393-414.

13. Soulhac, L., **Salizzoni, P.** , Mejean, P., Didier, D., Rios, I., The model SIRANE for atmospheric urban pollutant dispersion; PART II, validation of the model on a real case study. 2012, *Atmospheric Environment* , 49 , 320-337.

14. Soulhac, L., **Salizzoni, P.** , Cierco, F.X., Perkins, R.J., The model SIRANE for atmospheric urban pollutant dispersion. Part I: presentation of the model. 2011, *Atmospheric Environment*, 45, 7379-7395.

15. Soulhac, L. and **Salizzoni, P.**. Dispersion in a street canyon for a wind direction parallel to the street axis. 2010, *Journal of Wind Engineering and Industrial Aerodynamics*, 98, 903-910.

16. Garbero., V., **Salizzoni, P.**, Soulhac, L., Experimental Study of Pollutant Dispersion Within a Network of Streets. 2010, *Boundary-Layer Meteorology*, 136, 457-487.

17. **Salizzoni, P.**, Van Liefferinge, R., Soulhac, L., Mejean, P., Perkins, R.J., Scaling of the vertical spreading of a plume of a passive tracer in a neutral urban boundary layer. 2010, *Boundary-Layer Meteorology*, 135, 455-467.

18. **Salizzoni, P.**, Van Liefferinge, R., Soulhac, L., Mejean, P., Perkins, R.J., Influence of wall roughness on the dispersion of a passive scalar in a turbulent boundary layer. 2009, *Atmospheric Environment*, 43, 734-748.

19. Soulhac, L., Garbero, V., **Salizzoni, P.**, Mejean, P. , Perkins, R.J., Pollutant dispersion in street intersections. 2009, *Atmospheric Environment*, 43, 2981-2996.

20. **Salizzoni, P.**, Soulhac, L. , Mejean, P., Atmospheric turbulence and street canyon ventilation. 2009, *Atmospheric Environment*, 43, 32, 5056-5067.

21. **Salizzoni, P.**, Soulhac, L., Mejean, P. , Perkins, R.J., Influence of a two-scale roughness on a turbulent boundary layer. 2008, *Boundary-Layer Meteorology*, 127, 97-110.

22. Soulhac, L., Perkins, R.J. , **Salizzoni, P.**, Flow in a street canyon for any external wind direction. 2008, *Boundary Layer Meteorology*, 126, 365-388.

Submitted

1. Ben Salem, N., **Salizzoni, P.**, Soulhac, L., Estimating accidental pollutant releases in the built environment from turbulent concentration signals. Submitted to *Atmospheric Environment*.

2. Craske, J., **Salizzoni, P.**, van Reeuwijk, M., The turbulent Prandtl number in a plumes is 5/3. Submitted to *Journal of Fluid Mechanics*.

3. **Salizzoni, P.**, Creyssels, M., Le Clanche, J., Mos, A., Mehhaddi, R., Vauquelin, O., Influence of heat losses on the upwind flow of smoke in a longitudinally ventilated tunnel. Part I: experimental results. Submitted to *Fire Technology*.

4. Mos, A., **Salizzoni, P.**, Creyssels, M. Influence of heat losses on the upwind flow of smoke in a longitudinally ventilated tunnel. Part II: numerical results. Submitted to *Fire Technology*.

International peer reviewed Journals 'special issues'

1. Ben Salem, N., Soulhac, L., **Salizzoni, P.**, Marro, M., Pollutant source identification in a city district by means of a street network inverse model. 2014, *International Journal of Environment and Pollution*, 55 (1-4), 50-57.

2. Ben Salem, N., Soulhac, L., **Salizzoni, P.**, Armand, P., Inverting time dependent concentration signals to estimate pollutant emissions in case of accidental or deliberate release. 2014, *International Journal of Environment and Pollution*, 55 (1-4), 86-93.

3. Marro, M., Nironi, C., **Salizzoni, P.**, Soulhac, L., A Lagrangian stochastic model for estimating the high order statistics of a fluctuating plume in the neutral boundary layer. 2014, *International Journal of Environment and Pollution*, 54 (2-4), 233-241.

4. Di Sabatino, S., Buccolieri, R., **Salizzoni, P.**, Recent advancements in numerical modelling of flow and dispersion in urban areas: A short review. 2013, *International Journal of Environment and Pollution*, 52 (3-4), 172-191.

5. Amicarelli, A., **Salizzoni, P.** , Leuzzi, G., Monti, P., Soulhac, L., Cierco, F.-X., Leboeuf, F., Sensitivity analysis of a concentration fluctuation model to dissipation rate estimates. 2012, *International Journal of Environment and Pollution*, 48 (1-4), 164-173.

6. Garbero, V., **Salizzoni, P.**, Soulhac, L., Méjean, P., Measurements and CFD simulations of flow and dispersion in urban geometries. 2011, *International Journal of Environment and Pollution*, 44 (1-4), 288-297.

7. Cierco, F.-X., Soulhac, L., **Salizzoni, P.**, Méjean, P., Lamaison, G., Armand, P., Modelling concentration fluctuations for operational purposes. 2012, *International Journal of Environment and Pollution*, 48 (1-4), 78-86.

8. Garbero, V., **Salizzoni, P.**, Soulhac, L. , Méjean, P., Measurements and CFD simulations of flow and dispersion in urban geometries. 2011, *International Journal of Environment and Pollution*, 44 (1-4), 288-297.

Articles in national journals

1. Marro, M., Danzi, E., Cesano, M., **Salizzoni, P.**, Atmospheric dispersion of light gases emitted from punctual sources: Experiments and stochastic modeling. 2013, *GEAM*, 139 (2), 37-52.

2. Biemmi, S., Gaveglio, R., **Salizzoni, P.**, Boffadossi, M., Casadei, S. , Bedogni, M., Analisi dei dati meteorologici e parametrizzazione dello strato limite terrestre nell'area urbana milanese. 2008, *Nimbus*, 49-50, 6-16.

3. Boni, F., **Salizzoni, P.**, Garbero, V., Genon, G., Soulhac, L., La modellizzazione dell'inquinamento atmosferico in aree urbane su scala locale: un esempio di applicazione in un quartiere di Torino. 2008, *GEAM*, 124, XLV (2), 63-76.

4. **Salizzoni, P.**, Garbero, V., La dispersione di inquinanti in ambiente urbano. 2006, *GEAM*, 117, XLII (1-2), 77-84.

5. Garbero, V. , **Salizzoni, P.**, La dispersione di inquinanti in atmosfera in una valle alpina. 2006, *Nimbus*, 41-42, 6-13.

International Conferences

1. Jiang, L., Creyssels, M., **Salizzoni, P.**, The control of releases of buoyant fluid in a ventilated tunnel, 11^{th} European Fluid Mechanics Conference EFCM11, September 2016, Sevilla, Spain.

2. Vaux, S., **Salizzoni, P.**, Creyssels, M., Craske, J., van Reeuwijk, M., Turbulent transfer and entrainment in non-Boussinesq jets, 11^{th} European Fluid Mechanics Conference EFCM11, September 2016, Sevilla, Spain.

3. Craske, J., **Salizzoni, P.**, van Reeuwijk, M., The relation between the entrainment coefficient and the turbulent Prandtl number in Lazy, Pure and Forced plumes, 11^{th} European Fluid Mechanics Conference EFCM11, September 2016, Sevilla, Spain.

4. Fervers B., Coudon, T., Faure, E., Danjou, A., **Salizzoni, P.**, Development of a GIS based exposure metric to assess environmental dioxin exposure and comparison with an urban Gaussian model, 28^{th} Annual Conference International Society for Environmental Epidemiology ISEE2016, September 2016, Rome, Italy.

5. **Salizzoni, P.**, Marro, M., Natangelo, U., Desiato, R., Baioni, E., Bottazzi, I., Possamai, S. Ru, G., Development of an operational model for risk assessment in case of environmental and food chain contamination from dioxins, 28^{th} Annual Conference International Society for Environmental Epidemiology ISEE2016, September 2016, Rome, Italy.

6. Coudon, T. **Salizzoni, P.**, Nguyen, C.-V., Dalleau, N., Férvers, B., Reconstructing past and present dioxins atmospheric pollution scenarios in the city of Lyon, Transport and Air pollution 2016, 24-26 Mai 2016, Lyon, France.

7. Coudon, T. **Salizzoni, P.**, Nguyen, C.-V., Dalleau, N., Férvers, B., Determination of a geographic information system based indicator to assess environmental dioxins exposure in Lyon through comparisons with an atmospheric dispersion model results, IARC 50th Anniversary Conference, 7-9 June 2016, Lyon, France.

8. Gamel, H., **Salizzoni, P.**, Marro, M., Méjean, P., Carissimo, B., Soulhac, L., Dispersion of a passive scalar in the wake of a two-dimensional obstacle: velocity and concentration measurements. 2015, International Workshop on Physical Modelling of Flow and Dispersion Phenomena, 7-9 September 2015, ETH, Zurich, Switzerland.

9. Lamalle, D., Carlotti, P., **Salizzoni, P.**, Perkins, R.J., Sensitivity analysis of simulation parameters for fire risk assessement. 2015, International Fire Safety Symposium 2015, Coimbra, 20-22 April, 2015,Portugal.

10. Gamel, H., **Salizzoni, P.**, Soulhac, L., Méjean, P., Marro, M. Grosjean, N., Carissimo, B., Turbulent kinetic energy budget and dissipation in the wake of 2D obstacle: Analysis of the k-ε closure model. 2014, American Society of Mechanical Engineers, Fluids Engineering Division (Publication) FEDSM, Chicago.

11. Gamel, H., **Salizzoni, P.**, Carissimo, B., Soulhac, L., Méjean, P., Grosjean, N. Experimental evaluation of the dissipation rate of turbulent kinetic energy, in the wake of an obstacle. Application to the validation of k-ε or R_{ij}-ε turbulence models. 2014, ICWE14, 14th International Conference on Wind Engineering, Hamburg, Germany.

12. Danjou, A., Dossus, L., Faure, E., Anzivino-Viricel, L., Dalleau, N., **Salizzoni, P.**, Clavel-Chapelon, F., Fervers, B., Environmental Exposure to Dioxins and Risk of Breast Cancer: the GEO3N Pilot Study in the Rhône-Alpes Region, France. 2014, 26th Annual International Society for Environmental Epidemiology Conference, Seattle, Washington, USA - August 24-28, 2014.

13. Mos, A., Le Clanche, J., **Salizzoni, P.**, Vauquelin, O., Creyssels, M., Nicot, C., The influence of source characteristics and heat losses on the upwind flow of smoke in a longitudinally ventilated tunnel: experiments and numerical simulations. 2014, International Symposium on Tunnel Safety and Security, Marseille, 12-14 March 2014.

14. Marro, M., **Salizzoni, P.**, Méjean P., Soulhac, L., Passive scalar PDF in inhomogeneous and anisotropic turbulence: experiments and stochastic modelling. 2013, 14th European Turbulence Conference, 1-4 September 2013, Lyon, France.

15. Marro, M., Nironi, C., **Salizzoni, P.**, Soulhac, L., A Lagrangian stochastic model for estimating the high order statistics of a fluctuating plume in the neutral boundary layer. 2013, 15th conference on Harmonisation within Atmospheric Dispersion Modelling for Regulatory Purposes, Madrid, Spain.

16. Marro, M., **Salizzoni, P.**, Cierco, F.X., Korsakissok., I., Danzi, E., Soulhac, L. Plume rise and spreading in buoyant releases in the atmosphere: reduced scale experiments and stochastic modeling. 2013, 15th conference on Harmonisation within Atmospheric Dispersion Modelling for Regulatory Purposes, Madrid, Spain.

17. Ben Salem, N., Soulhac, L., **Salizzoni, P.**, Armand, P., Inverting time dependent concentration signals to estimate pollutant emissions in case of accidental or deliberate release. 2013, 15th conference on Harmonisation within Atmospheric Dispersion Modelling for Regulatory Purposes, Madrid, Spain.

18. Ben Salem, N., Soulhac L., **Salizzoni, P.**, Marro, M., Pollutant source identification in a city district by means of a street network inverse model. 2013, 15th conference on Harmonisation within Atmospheric Dispersion Modelling for Regulatory Purposes, Madrid, Spain.

19. Nironi, C., **Salizzoni, P.**, Méjean, P., Marro, M., Soulhac, L., Pollutant concentration fluctuations in a neutral atmospheric boundary layer: a new detailed data set for the validation of dispersion models. 2013, 15th conference on Harmonisation within Atmospheric Dispersion Modelling for Regulatory Purposes, Madrid, Spain.

20. Mos, A., Le Clanche, J., **Salizzoni, P.**, Creyssels, M., Nicot, C. Impact of fire source characteristics and wall heat losses on smoke behaviour in a longitudinally ventilated reduced scale model tunnel: experiments and numerical simulations. 2013, 15th International Symposium on Aerodynamics, Ventilation Fire in Tunnels, Barcelona, Spain.

21. Le Clanche, J., **Salizzoni, P.**, Creyssels, M., Mehaddi, R., Candelier, F., Vauquelin, O., Aerodynamics of buoyant gases within a longitudinally ventilated tunnel: experiments in two different reduced scale models. 2013, 15th International Symposium on Aerodynamics, Ventilation Fire in Tunnels, Barcelona, Spain.

22. Soulhac, L., **Salizzoni, P.**, N'Guyen, M.-L., Troude, F., Rios, I., Validation of the urban scale pollution model SIRANE-2.0 against field data in the city of Lyon. 2011, HARMO 2011, 14th International Conference on Harmonisation within Atmospheric Dispersion Modelling for Regulatory Purposes, Kos Island, Greece.

23. Lamaison, G., Soulhac, L., Cierco, F.X., **Salizzoni, P.**, Armand, P., Validation of SIRANERISK-2.0 operational model against a Lagrangian particle dispersion model and a new campaign of dispersion experiments performed in an idealised urban mock-up. 2011, HARMO 2011, 14th International Conference on Harmonisation within Atmospheric Dispersion Modelling for Regulatory Purposes, Kos Island, Greece.

24. Garbero, V., **Salizzoni, P.**, Berrone, S., Soulhac, L., Influence of heat fluxes on the flow within a two-dimensional street canyon: a comparison between wind tunnel measurements and CFD simulations. 2011, ICWE13, 13th International Conference on Wind Engineering, Amsterdam, Netherlands.

25. Buccolieri, R., Garbero, V., **Salizzoni, P.**, Soulhac, L., Di Sabatino, S., Sandberg, M., Pollutant dispersion at the neighborhood scale via wind tunnel experiments and CFD simulations. 2011, ICWE13, 13th International Conference on Wind Engineering, Amsterdam, Netherlands.

26. Di Sabatino, S., Buccolieri, R., **Salizzoni, P.**, Recent advancement from flow and dispersion studies around bluff bodies for urban environment applications. 2012, BBAA VII, 7th International Colloquium on Bluff Body Aerodynamics and Applications, Shanghai (China). 2-6 September 2012.

27. Nironi, C., **Salizzoni, P.**, Méjean, P., Grosjean, N., Soulhac, L., Cierco F.X., Scalar dispersion within a turbulent boundary layer. 2011, International Workshop on Physical Modelling of flow and dispersion phenomena. Hamburg, 22-24 August.

28. Kubwimana, T., Mos., A., Bergamini, E., **Salizzoni, P.**, Méjean, P., Boffadossi, M., Experimental and numerical investigations of the wind pressure coefficient at a tunnel portal. 15th International Symposium on Aerodynamics, Ventilation and Fire in Tunnels, Barcelona, Spain.

29. Giambini, P., **Salizzoni, P.**, Soulhac, L., Corti, A., Air quality modelling system for traffic scenarios analysis in Florence: model evaluation and identification of critical issues. HARMO 2010, 12th International Conference on Harmonisation within Atmospheric Dispersion Modelling for Regulatory Purposes, Paris, France, 2010.

30. Cierco, F. X., Soulhac, L., Méjean, P., Lamaison, G., **Salizzoni, P.**, Armand, P., Siranerisk: an operational dispersion model for urban areas incorporating a new method to account for concentration fluctuations. 2010, 12^{th} International Conference on Harmonisation within Atmospheric Dispersion Modelling for Regulatory Purposes, Paris, France, June 2010.

31. Amicarelli, A., **Salizzoni, P.**, Monti, P., Leuzzi, G., Soulhac, L., Cierco, F. X., Modelling concentration fluctuations in a turbulent boundary layer: sensitivity of a Lagrangian model to dissipation rate estimates. 2010, 12^{th} International Conference on Harmonisation within Atmospheric Dispersion Modelling for Regulatory Purposes, Paris, France, June 2010.

32. Chiocchia, G., **Salizzoni, P.**, Marro, P., Clerico, M., Impact assessment of railway noise in an alpine valley. 2010, CFA 2010, $10^{\text{ème}}$ Congrès Français d'Acoustique, Lyon, France, June, 2010.

33. Cierco, F.X. , Soulhac, L., Méjean, P., Armand, P., **Salizzoni, P.**, Wind tunnel measurements oh high order moments concentration distribution due to the transport of tracer gas puffs in a turbulent flow. 2009, Physical modelling of flow and dispersion phenomena, Rhode-Saint-Genese (PHYSMOD), September, 2009.

34. **Salizzoni, P.**, Scavone, C., Garbero, V. Soulhac, L., Mejean, P., Perkins, R. J., Influence of heat fluxes on the flow and dispersion within a two-dimensional canyon. 2009, Physical modelling of flow and dispersion phenomena (PHYSMOD), Rhode-Saint-Genese, September, 2009.

35. Garbero, V., **Salizzoni, P.**, Soulhac, L., Pollutant dispersion in different urban geometries. 2009, Physical modelling of flow and dispersion phenomena (PHYSMOD), Rhode-Saint-Genese, September, 2009.

36. Cierco, F.X., Soulhac, L., Méjean, P., Armand, P., **Salizzoni, P.**, Determination of concentration fluctuations within an instantaneous puff through wind tunnel experiments. 2008, 12^{th} International Conference on Harmonisation within Atmospheric Dispersion Modelling for Regulatory Purposes, Cavtat, Croatia, October 2008.

37. Villegas, D., **Salizzoni, P.**, Soulhac, L., Méjean, P., Perkins, R. J., Experimental study of smoke ventilation in tunnels. 2007, ISAIF 2007, 8^{th} International Symposium on Experimental and Computational Aerothermodynamics of Internal Flows, Ed. X.Ottavy and I. Trébinjac, Lyon (France).

38. **Salizzoni, P.**, Soulhac, L., Garbero, V., Méjean, P. , Perkins, R. J., Experimental evaluation of the mass exchange between a two-dimensional cavity and the external flow. 2007, 11^{th} International Conference on Harmonisation within Atmospheric Dispersion Modelling for Regulatory Purposes, Cambridge, UK.

39. Soulhac, L., Rios, I., Garbero, V., Farges, B., **Salizzoni, P.**, Scaccianoce, L., Perkins, R. J., Pollutant dispersion through an obstacle array: numerical modelling and experimental investigation. 2007, 11^{th} International Conference on Harmonisation within Atmospheric Dispersion Modelling for Regulatory Purposes, Cambridge, UK.

40. **Salizzoni, P.**, Soulhac L., Méjean P., Perkins R. J., A comparison of measurements and CFD simulations for pollutant dispersion in urban geometries. 2007, 11^{th} International Conference on Harmonisation within Atmospheric Dispersion Modelling for Regulatory Purposes, Cambridge, UK.

41. Garbero, V., Méjean, P., Perkins, R. J., **Salizzoni, P.**, Soulhac, L., Dispersion through an obstacle array: a wind tunnel investigation. 2006, 11^{th} XIV International conference on modelling, monitoring and management of air pollution, New Forest, UK.

42. **Salizzoni, P.**, Grosjean, N., Méjean, P., Perkins, R.J., Soulhac, L., Vanliefferinge, R., Wind tunnel investigation of the exchange between a street canyon and the external flow. 2004, 27^{th} International technical meeting on air pollution modelling and its application, Banff, Canada.

43. **Salizzoni, P.**, Cancelli, C., Soulhac, L. , Méjean, P., Perkins, R.J., An experimental study of the influence of a two-scale surface roughness on a turbulent boundary layer. 2004, 9^{th} International Conference on Harmonisation within Atmospheric Dispersion Modelling for Regulatory Purposes, Garmisch-PartenKirchen, Germany.

National Conferences

1. Coudon, **Salizzoni, P.**, Nguyen, C.-V., Dalleau, N., Férvers, B., Développement d'un SIG pour l'estimation de l'exposition aux dioxines et la comparaison avec un modèle gaussien (SIRANE), Journée thématique Santé-Environnement, July 2016, Grenoble, France.

2. **Salizzoni, P.**, Marro, M., Natangelo, U., Desiato, R., Baioni, E., Bottazzi, I., Possamai, S. Ru, G. PCDD/F e dl-PCB in aree contaminate: strumento per la valutazione del rischio. 2015, XXXIX Congresso dell'associazione italiana di epidemiologia, 28-30 Ottobre, Milano.

3. Creyssels, M., Le Clanche, J., Mehaddi R., Candelier, F., Vauquelin, O., **Salizzoni, P.**, Modélisation d'un incendie en tunnel par un panache thermique turbulent: effet d'une ventilation longitudinale, Congrès Français de Thermique 2014: Approches multi-échelles pour la thermique, l'énergétique et le génie des procédés, Lyon, France. In: Actes du Congrés Français de Thermique, Société Française de Thermique, Paris, France.

4. Lamalle, D., Carlotti., P., **Salizzoni, P.**, Perkins, R.J., Simulations aux grandes échelles de panaches, 2013, 21ème Congrès Frans de Mécanique, 26-30 August 2013, Bordeaux, France.

5. Provent, A., Nguyen, C.V., **Salizzoni, P.**, Soulhac, L., Cierco, F.X., Dossus, L., Faure, E., Fervers, B., Anzivino, L., Modélisation de la dispersion des dioxines dans le cadre du projet GEO 3N. 2013, Congrès national Santé Environnement Cancer et Environnement 28-29 Nov. 2013 Lyon.

Part II

Research Activity

Chapter 6

Introduction

6.1 Air pollution, an ever-present problem

Air pollution represents a persistent problem in human history. Even in ancient times, in the absence of urban areas with a large conglomeration of people, air pollution was a problem, though restricted to the contamination of interiors (Brimblecombe, 1987). Smoke from fires within huts would have filled the whole interior before finding its way out through a hole in the roof, that had to be not too big, in order not to let in the rain. The appearance of cities gave rise to new air pollution problems. Ancient cities needed to be small, to ease problems of defense and the carriage of goods, and inevitably they suffered from overcrowding. Under such circumstances, smoke from small forges or hearths must frequently have been emitted at low level and allowed to drift onto neighboring houses. Streets between these densely packed dwellings would have formed canyons, likely to trap smoke and fumes. With the first industrial revolution new relevant problems arose, induced by the combustion of coal, in both domestic heating and industry. Since then, air pollution problems have been further amplified by the large consumption of fossil fuels and by the production of new chemical substances in industrial processes (and their emission into the atmosphere). These days, typical examples of indoor and outdoor air pollution include (see fig. 6.1) persistent spatially distributed emissions in urban and sub-urban areas (due to traffic, domestic heating, industry...) as well as accidental releases of toxic or inflammable pollutant in industrial sites, urban areas or within enclosed spaces, such as road and train tunnels, underground escalators, theatres and large halls.

In the second half of the 20^{th} century, the increasing welfare of the population in developed countries induced an increasing concern and sensitivity of citizens to the exposure to environmental risks. This led to the adoption of regulations for the mitigation of air pollution and its related risks and to two main relevant results (McNeill, 2001). The first was the elimination of lead in fuels, which resulted in a drastic reduction in emissions from cars since the beginning of the 1980s. The second was the elimination of CFCs in cooling circuits, which stopped the depletion of stratospheric ozone.

Despite these environmental successes, in the last decades, hazards and risks related to air pollution continue to draw attention within social, economic and political issues. This can be attributed to four main aspects:

- the enhanced urbanization worldwide and the higher population density surrounding industrial sites. This proximity represents a major concern not only for the population but also for public authorities and industrial operators, whose business and activities may be adversely affected by strict regulations.

- the increased use of underground infrastructure for transport (tunnels, escalators) and large enclosed spaces for public events (concerts, sports), where the occurrence of accidental releases of harmful airborne substances expose users of these infrastructures to relevant hazards.

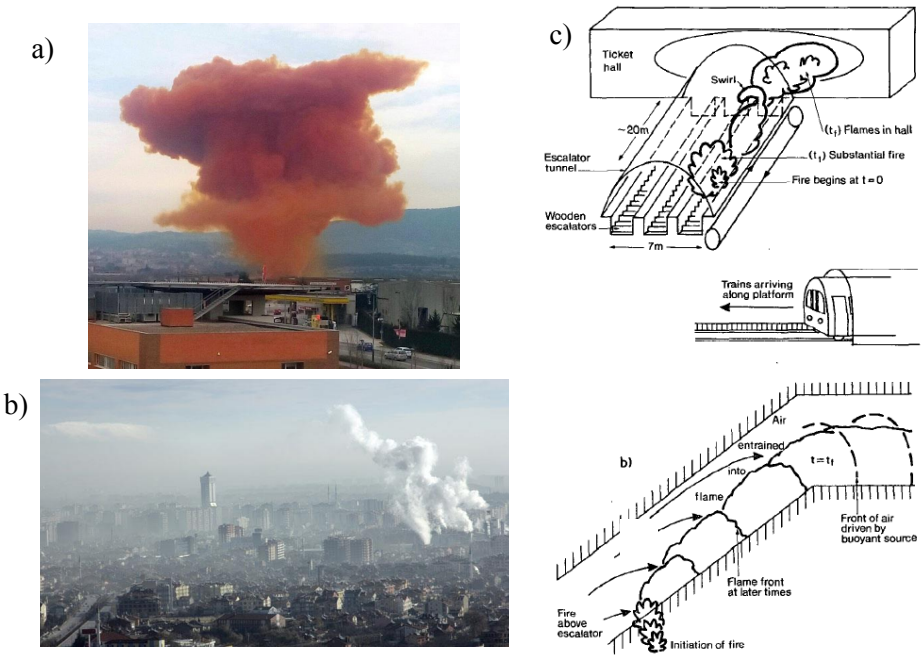

Figure 6.1: Examples of air pollution: a) toxic cloud accidentally released by an industrial plant in Spain, b) urban smog in a large Indian city c) sketch of the smoke propagation in the King's Cross underground station fire, London (Hunt, 1991).

- the occurrence of major technological accidents (e.g. Seveso, Chernobyl, Bhopal, Fukushima, Mont Blanc Tunnel, King's Cross fire...), inducing a general public suspicion about the ability of public authorities and industrial groups to manage and mitigate technological risks.
- the increasing scientific evidence of the effects on human health due to exposure to indoor and outdoor air pollution (Loomis *et al.*, 2013).

In recent years, further attention on these problems has also been induced by the increased probability of the occurrence of terrorist acts in industrial sites and in (indoor and outdoor) crowded public spaces.

Following a well-established classification, hazards and risks related to air pollution are referred to as *accidental* or *chronic*. The former are related to the exposure to high concentration levels in intense and limited (in space and time) pollution episodes induced by unexpected and uncontrolled releases of pollutants (e.g. Seveso). The latter are instead related to the exposure to moderate concentration levels in persistent and distributed (in space and time) air pollution scenarios, induced by identified and (partially) controlled sources (urban pollution). In both cases, the impact of pollutants on human health and the environment is related to the concentrations in air of harmful substances (and to the exposure time to these concentrations), which are in turn determined by the mechanisms governing the transport of pollutant in the ambient air. Determining impacts due to air pollution in a given area therefore requires modelling tools to predict the space and time variation of pollutant distribution (for given emissions scenarios). These estimates can be further used by epidemiologists, veterinarians, demographers and economists to quantify the consequences of these hazards to assess risks associated with pollution scenarios.

In almost all cases of practical interest, the flow which transports and disperses pollutants is highly turbulent, usually with characteristics determined by complex and highly specific boundary

conditions. So, in order to model such flows for operational purposes (that is, without requiring exceptional computing resources or highly detailed data) we need to understand how, and to what extent, turbulent flows are driven by initial boundary conditions and how these flows transport and disperse pollutants.

My research has been devoted to improving our understanding of some of the fundamental processes governing turbulent dispersion and in incorporating that understanding into operational models.

6.2 Modelling pollutant transport in turbulent flows

As is well known, the transfer of mass, momentum and energy within a turbulent fluid is a chaotic process, and cannot therefore be treated with a deterministic approach. The pollutant concentration $c_t(\mathbf{x}, t)$, as well as the fluid velocity $\mathbf{u}_t(\mathbf{x}, t)$ (and any other variable determining the dynamical state of the flow), has therefore to be considered as a random variable, and is usually presented as given by the sum of its mean C and its fluctuating value c, i.e. $c_t = C + c$. The fluctuations are characterised by a wide variety of spatial and temporal scales (see fig. 6.2). Studying the turbulent transport of a pollutant in environmental flows therefore leads to a study of the modification of the probability density function (or at least of its lower order moment) of its concentration and its spatial (and temporal) evolution, and its link with the statistics of the velocity field, in a large variety of flow configurations.

The modification of the concentration probability density functions depends upon a process, referred to as *turbulent dispersion*, which is the result of the complex motion of blobs of polluted fluid (also referred to as puffs) and their mixing with the ambient fluid. The *mixing* is, strictly speaking, a phenomenon that takes place at the molecular scale, and is therefore due to local concentration gradients. The intensity of these gradients within a turbulent flow is however governed by the multi-scale dynamics of the flow.

To discuss the multi-scale character of the dispersion process we consider (see fig. 6.2a) a release of a passive scalar within an isotropic turbulent flow, in the presence of a mean advective component (from left to right in the picture). The wide variety of scales characterising the turbulent flow represented in fig. 6.2a, can be conveniently enlightened by a spectral representation of a velocity signal (6.2b), registered by an anemometer placed within the flow, in the wave number space (see fig. 6.2c). The velocity spectrum typically extends over a wide variety of wave numbers, referred to here as k, between an upper and a lower bound. The former, referred to here as $\mathcal{L}$ and named Eulerian macro-scale, represents the size of the largest eddies within the flow. The latter, referred to here as η and named Kolmogorov micro-scale, represents the smallest scale at which velocity gradients take place, and at which the kinetic energy of the turbulent motion is dissipated, i.e. transferred to the microscopic molecular motion.

In principle, a similar procedure can be adopted to identify the corresponding timescales involved in the flow dynamics[1]. Notably, this would allow computing the so-called Lagrangian timescale, referred to here as T_L, which is the typical time over which the eddies' motion remain correlated, i.e. a time interval over which the flow retains a sort of memory of its evolution.

A puff of pollutant of generic size l (noted in red in fig. 6.2) would then be submitted to the action of eddies that can be larger and smaller that its size, and that will be efficient in very different ways in transporting it across the flow and in mixing it with the ambient air. Its transfer from the source to a receptor point would be considered to occur over short or large times, depending on the ratio between a typical 'flight' time and the characteristic scale T_L. In a general way, this phenomenon is governed by different processes and mechanisms, depending on the scales at which it is observed and studied.

The modelling of the pollutant dispersion implies predicting the effects of these multi-scale dynamics and their role in the transfer of a pollutant. This modelling relies on different approaches, depending on the choice of the scales of observation. These in turn will depend on the particular phenomenon we

[1] In practice this turns out to be very complicated since it requires measuring a large Lagrangian number of velocity signals, i.e. obtained by following single fluid particles in their motion, and computing their spectral distribution in the frequency space.

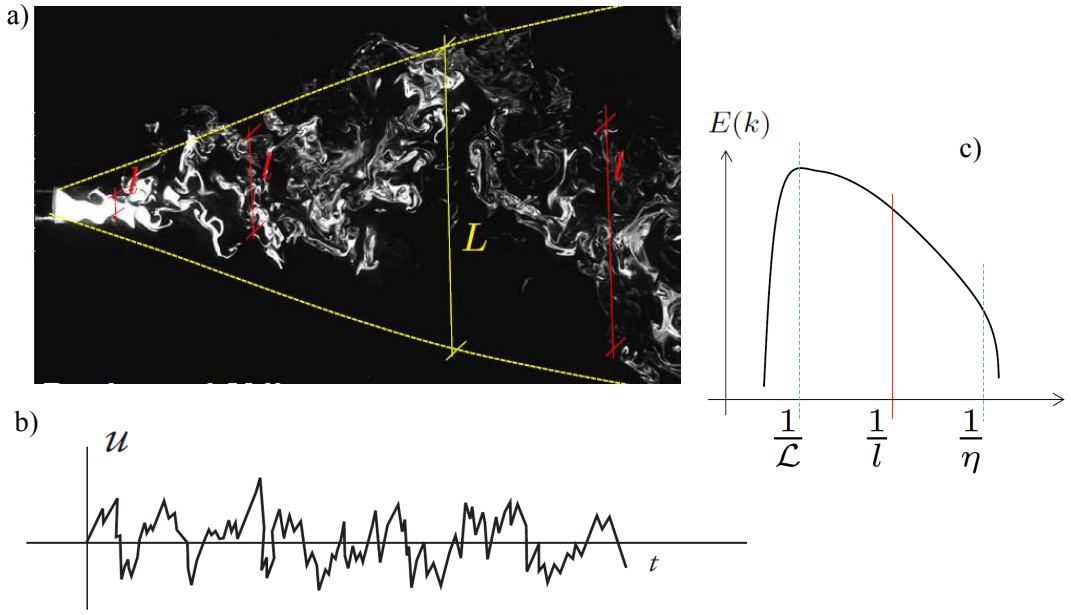

Figure 6.2: a) Passive scalar plume dispersed in a homogeneous and isotropic turbulent flow (Duplat and Villermaux, 2008). Example of turbulent velocity signal registered at a fixed position and of its related spectrum in wavenumber (k) space; $\mathcal{L}$ is the Eulerian macroscale, η the dissipative Kolmogorov scale, and l indicates a generic size of a pollutant puff transported within this turbulent flow.

aim to focus on. As further discussed in the next paragraphs, studies on chronic hazards will be based on a quite rough description of the flow and concentration statistics, which will be essentially focusing on the first order moment of the Probability Density Function (PDF). Conversely, accidental hazards require a much finer characterisation of higher order moments of the PDF, as information is required on the intensity and the intermittency of the concentration fluctuations.

6.3 Dispersion and mixing

We consider (see fig. 6.3) the behaviour of an ensemble of trajectories of marked fluid particles issuing from a point source S within a turbulent fluid. Due to the fluctuating component of the velocity field, fluid particles follow irregular paths drawing trajectories that can be very different one from the other. In this rather disordered picture, adopting as a reference an imaginary averaged trajectory (dotted black line in fig. 6.3), we can observe that the standard deviation of the distances between the position of a fluid particle and the average trajectory increases moving away downstream of S (this does not preclude a single fluid particle to move very close to it and even cross it several times). The ensemble of trajectories therefore spreads indefinitely, involving larger and larger volumes of ambient fluid, until its motion is eventually restrained by physical limits imposed at the boundary of the domain.

To this *trajectory dispersion* is related a sort of statistical dilution of pollutants. To enlighten this, we can simply consider that the trajectories represent the motion of the centre of mass of pollutant volumes, of size l_o, emitted from S with an initial concentration c_o. Due to the dispersion of the trajectories, the centres of mass of these volumes are distributed over a larger spatial extent (see fig. 6.3). The time-averaged concentration value, measured at a given receptor, would then be highly influenced by this process. A measurement obtained at a receptor placed very close to the source at P_1, at a distance of order l_0, would provide a signal similar to that sketched in fig. 6.3, giving a mean value over a time interval T (which we assumed to be sufficiently large):

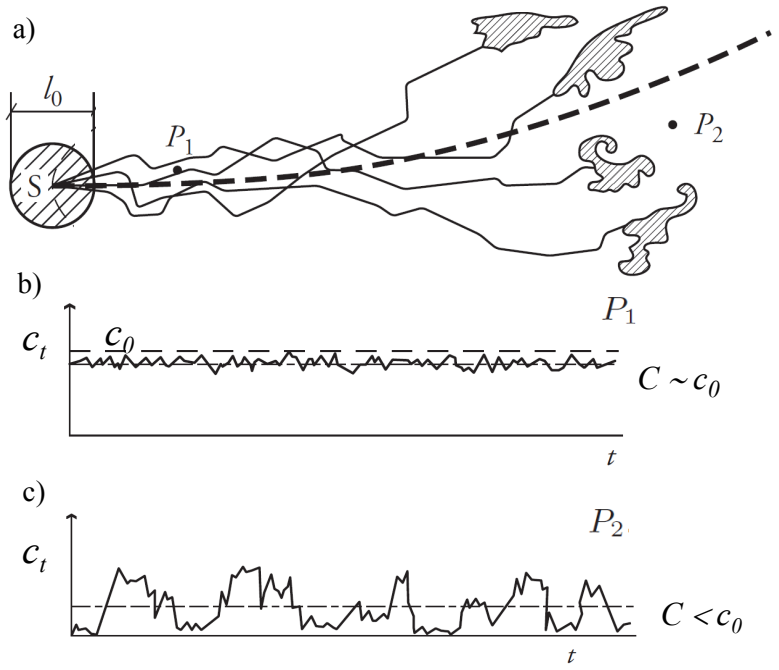

Figure 6.3: a) Dispersion of polluted air volumes of size l_o emitted from a localised source S (Cancelli *et al.*, 2006); dotted black line represents the averaged trajectory. The receptor P_1 is located in the very nearfield of the source, at a distance of order l_0. Time-dependent concentration c_t measurements in b) P_1 and c) P_2; the receptor P_2 i located further away, at a distance of several tens of source size l_0.

$$C(P_1) = \frac{1}{T}\int_0^T c_t(t^{'})dt^{'} \sim c_o,$$

slightly smaller than the initial value c_0.

At the receptor P_2 we would instead observe a different kind of signal (see fig. 6.3), characterised by larger fluctuations and intermittency, with a mean value $C(P_2)$ significantly smaller than c_o. This is due to the fact that the time interval during which the measurement probe is within a volume of polluted fluid represents a reduced fraction of the whole measurement time. The intermittency of the signal therefore results in a decrease in the value of the mean concentration $C(x)$ taken at a fixed position. The decrease in the time-averaged concentration is therefore not due to a modification of the pollutant concentration within each of these pollutant puffs, but instead is due to the dispersion of their centres of mass. In this sense, we can assert that this sort of statistical dilution does not necessarily imply the mixing of these volumes of polluted fluid with the surrounding ambient fluid.

The *mixing* is actually related to another process characterising the mass transfer within a turbulent flow. During this random motion, volumes of fluid with dynamical (and eventually thermodynamical) conditions, initially very different, can be found close one to the other in some part of the domain. Their contact implies the occurrence of strong inhomogeneities of the fluid properties and therefore large gradients (which in turn produce large fluxes) of any variable characterising the flow (momentum, density, pollutant concentration...). To visualise this process, we can follow a single blob of marked fluid (see fig. 6.4), of size l_o, characterised by a concentration of a chemical species different from that of the ambient fluid. As far as the velocity fluctuations of the turbulent flow are characterised by spectral components with wavelengths that are smaller than l_o, i.e. if within the blob of fluid take place significant velocity differences, the form of the blob of fluid is progressively distorted over a length scale that become progressively smaller (see fig. 6.4). This process implies another kind of 'dispersion', that of the fluid particles (composing the puff) around their centre of mass. This is usually referred to as *relative dispersion*, and has two main implications:

- the exchange surface between the blob and the ambient fluid increases significantly;

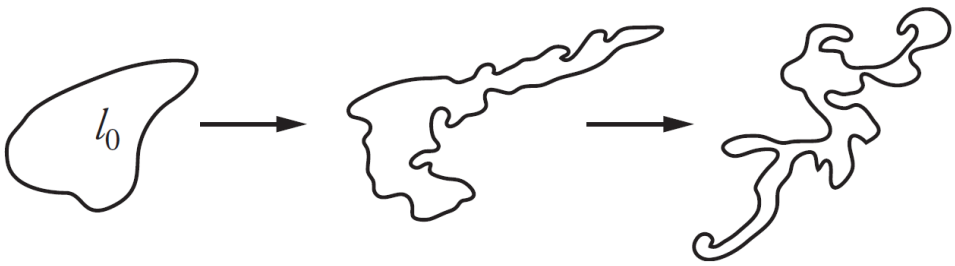

Figure 6.4: Evolution of a marked blob of fluid released within a turbulent flow (Cancelli *et al.*, 2006).

- single fluid particles from the centre of the blob are brought towards its borders (and viceversa).

Both features lead to the same relevant effect, that of an *intensification of the gradients* within the fluid, which in turn results in an acceleration of diffusive phenomena responsible for the homogenisation process between the fluid within and outside the blob of fluid, i.e. on its *mixing* with the ambient fluid, a phenomenon that is ultimately due to a single process: the molecular (or brownian) diffusion [2].

The variation of concentrations statistics measured at a fixed point downwind of a pollutant source can therefore be due to two kinds of processes: i) the irregular motion of the centre of mass of the polluted fluid volumes, and ii) the intensification of diffusive processes. It is worth noting that these two have to be considered as two distinct phenomena, whose correlation one to the other can be of variable strength depending on the flow configuration.

To evidence the distinction between these two processes and their roles in the turbulent dispersion we have sketched in fig. 6.5 two possible evolutions of a pollutant plume. These are produced by the steady emission of pollutant within the atmospheric boundary layers with two different dynamical states, which imply a different spectral distribution of the velocity fluctuations. In the first case the plume is captured by energetic large-scale vortices (larger than the plume lateral dimensions). Its morphology results then in large spatial fluctuations, often referred to as *meandering*[3]. In the second case, the velocity field is instead dominated by smaller-scale fluctuations, i.e. whose length scale is of the same order as the initial plume size l_o. The plume is then immediately deformed by the velocity differences taking place within it, giving rise to a concentration field with smoothed spatial variations.

The two plume configurations give rise to very different concentration signals measured at the same position, which we refer toin the two cases as P_1 and P_2, respectively (see fig. 6.5). In P_1, values of concentrations c_t are characterised by the appearance of sudden peaks, measured when the probe intercepts polluted fluid volumes, separated by intervals of almost zero concentration; in P_2, the signal is instead much more regular, with fluctuations of reduced intensity around its mean value C. Even though the two signals are radically different, in some very particular cases, the first order moment C of the concentration probability density function may be very similar. The higher order moments would be however very different in the two cases. Notably, the signal registered in P_2 is expected to have large values of the higher concentration moments (variance, skewness, kurtosis...), since these quantify the amplitude of the fluctuations around the mean.

The role of the two previously mentioned processes, i.e. the spread of the puffs' centre of mass and

[2]This can be clearly highlighted by writing the balance equation of a generic fluid property, in this case the concetration of a chemical species c_t, in the form (assuming for simplicity a zero divergence velocity field):

$$\frac{Dc_t}{Dt} = -\frac{\partial f_j}{\partial x_j},$$

where the l.h.s. denotes the Lagrangian derivative of c_t and the r.h.s. the divergence of the diffusive fluxes f_j (i.e. reduced by the random molecular motion). The high negative values of the Lagrangian derivatives observed in a turbulent flow are then strictly linked to the divergence of diffusive fluxes, whose intensity is amplified by the dynamics of the turbulent flows, and its capacity in intensifying gradients.

[3]This large-scale motion can be typically due to convective instabilities taking place in the atmospheric boundary layer on hot sunny days.

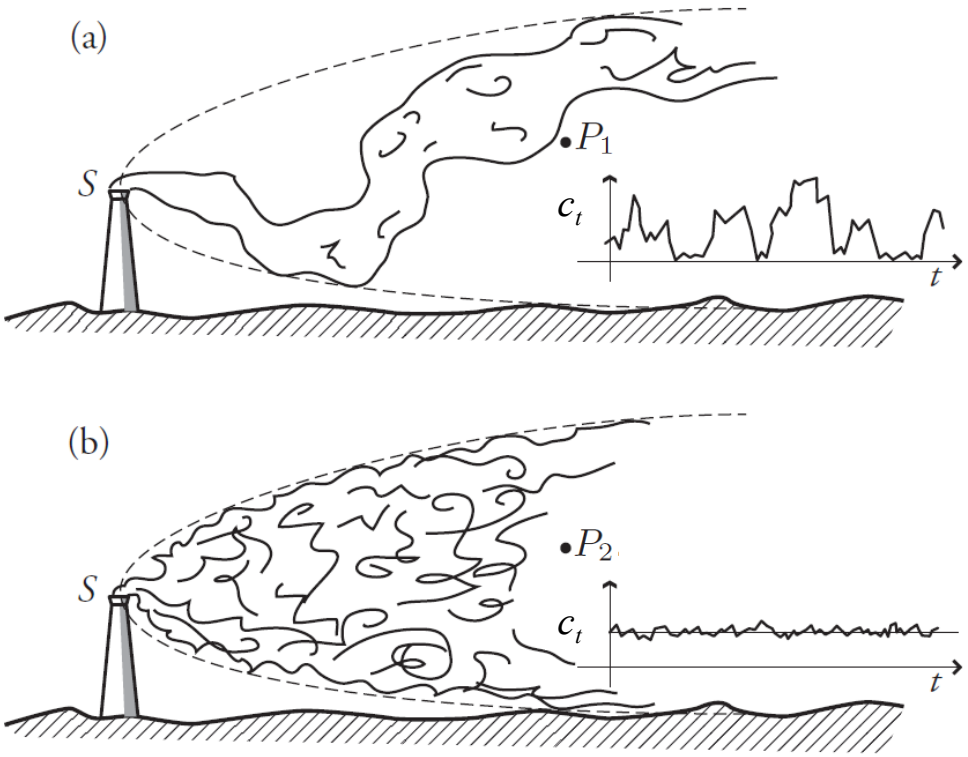

Figure 6.5: Instantaneous configurations of a pollutant plume and relative concentration signal registered at a fixed receptor placed downwind the source in two different typologies of atmospheric conditions characterised by: – a) large scale velocity fluctuations – b) smaller scale velocity fluctuations (Cancelli *et al.*, 2006).

their mixing with ambient fluid, can be very different in the overall dispersion process depending on the typology of flow configuration. The relative importance of these processes, and their correlation one to the other, depends on a large number, namely the distance from the source of our observation point, the conditions imposed at the source (sect. 6.5), and the influence of physical boundaries on the dispersion process, i.e. the geometry of the domain (sect. 6.6).

6.4 Pollutant dispersion, chronic and accidental hazards

The impact of pollutant releases on the health and the environment (and their related risks) can be effectively determined based on estimates of the PDF of the pollutant concentration to whom humans and other biological systems are exposed. Nevertheless, the level of accuracy of the description of this PDF needed to evaluate these impacts depends on the typology of hazards that have to be assessed.

In several problems, it is sufficient to estimate a long period time-averaged concentration

$$C = \lim_{T\to\infty} \left[\frac{1}{T} \int_0^T c_t(t^{'}) dt^{'} \right]$$

This is typically the case for persistent hazards and risks associated with long-term exposure to pollutant concentrations, as is the case for example for diseases induced by nitrogen oxides or particulate matter in air. Mean concentration values are also of primary interest when evaluating pollutant soil deposition and its transfer to the food chain. In all these cases what matters is the cumulative effect over time, since the accumulation process filters the effect of concentration fluctuations.

Conversely, when dealing with the release of highly toxic, flammable or explosive gases, the estimate of the sole time-averaged concentration C is not sufficient. It may be useful only in a very few specific cases in which the intensity of concentration fluctuation is low compared to that of the mean values, as in case (b) depicted in fig. 6.5. In all other cases it is essential to estimate the statistics of the concentration fluctuations around their mean value. The inflammability or the explosion of a gas cloud depends on the local instantaneous values of concentrations, and actually occurs when these exceed a given threshold of concentrations. The impact of odours depends on peak concentrations to which the human nose is sensitive. The exposure to hazardous airborne materials, and their dosages, depends on peak-to-mean ratios.

In a general way, we can therefore assert that the assessment of chronic hazards, due to continuous and eventually controlled sources of pollutants, requires estimates of long-term averaged concentration values. The assessment of accidental hazards, due to the uncontrolled releases of harmful toxic or explosive airborne pollutant, requires instead a large amount of information about the concentration PDF. The values of the concentration standard deviation and of its skewness are therefore essential in order to evaluate the probability of exceeding given concentration thresholds.

6.5 On the effect of the source conditions

The dispersion process can be highly influenced by the condition of the release at its emission, at least over a region extending over a limited distance from the source. Generally speaking, for given dynamical conditions of the ambient fluid, the effects of the source conditions are related to its size and to the dynamical and thermodynamical state (notably in terms of fluxes of momentum, mass, heat or buoyancy) of the polluted fluid released in the ambient fluid.

The influence of source size l_0 of a source of pollutant within a turbulent flow depends notably on the typical length scales $\mathcal{L}$ associated with the largest eddies of the turbulent ambient fluid. The ratio $l_0/\mathcal{L}$ is expected to have a direct influence on both the dispersion of the puffs' centres of mass, which would be more effective when large eddies transport small puffs, and its mixing with the ambient fluid, which is more effective when small eddies deform the puffs' internal structure.

The role of $l_0/\mathcal{L}$ on the concentration PDF of a pollutant dispersed in an atmospheric flow is a feature that still has to be fully elucidated. The experimental investigation of this phenomenon, as well as its mathematical modelling, constitutes a relevant part of the research activities presented in the next chapters, namely in 7.1, 7.2 and 7.3.

Other important effects are related to the dynamical and thermodynamical state of the polluted fluid at its emission. In an accidental release from a pipe, as well as in the case of a release from a stack, there is usually a region within which the dynamics of the fluid is almost fully determined by kinetic energy at the release point, or by the difference of thermodynamical state (temperature, density) between the pollutant release and the ambient fluid. In most cases the fluid release is already turbulent at its emission point. When this is not the case however, the release becomes rapidly turbulent, over a distance of few diameters from the emission point, due to the large instabilities generated by the velocity and temperature gradients taking place within the flow. These releases are commonly referred to as *jets*, when their dynamics are governed by the momentum flux imposed at the source, or *plumes*, when instead they are determined by a flux of heat (or buoyancy).

The turbulent dynamics of jets and plumes can then be effectively fully determined by the fluxes at the emission point and the role of an eventual turbulence within the ambient flow may become of secondary importance (see fig. 6.6(a)). The larger-scale fluctuations of these turbulent flows are then imposed by the typical length scales imposed at the source, i.e. the source diameter. Moving away from

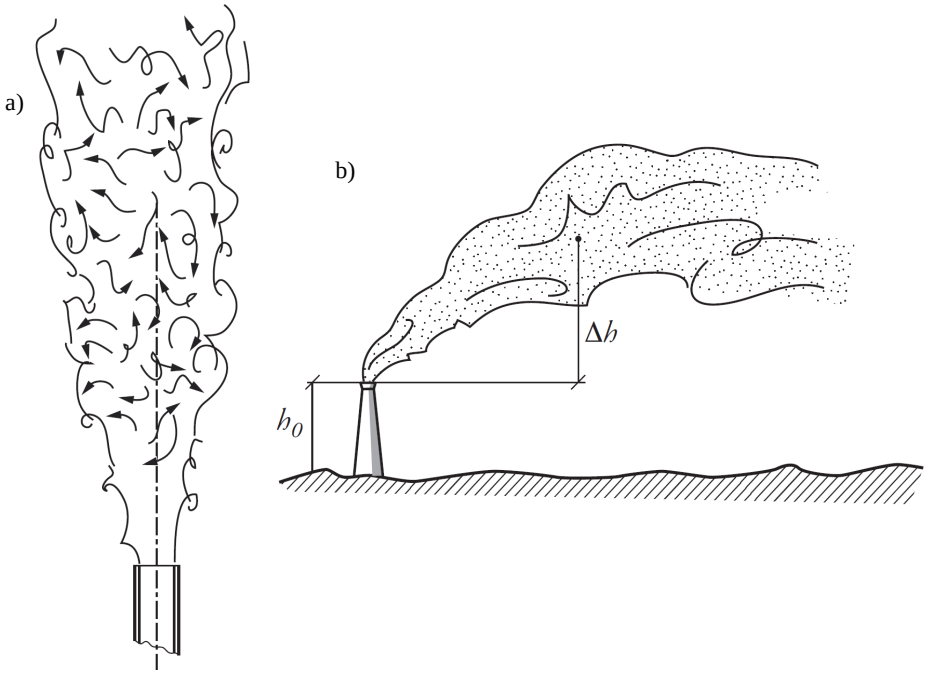

Figure 6.6: Releases of polluted fluid characterised by high momentum and/or buoyancy fluxes (Cancelli *et al.*, 2006): (a) release dominated by local generated turbulence, i.e. in an almost still environment; (b) releases in a turbulent cross-flow.

the emission point smaller-scale fluctuations are then progressively generated by the occurrence of an energy cascade that transfers kinetic energy down to the dissipative molecular scale. The extent of the cascade depends on the initial energy flux imposed at the source and can be significantly influenced by the effects of buoyancy in the case of releases of fluid which are lighter (or denser) than the ambient air.

The process is characterised by the presence of velocity fluctuations which are of the same order, or smaller, than the jet size and are therefore able to enhance its dilution and mixing with the ambient fluid, which is progressively brought within the release by the engulfment of a volume of ambient fluid within the releases, a process known as *entrainment*. Despite the large amount of literature available on jets and plumes, the dynamics of the entrainment process, and its link with the momentum and energy transfers and mixing, still represents an open field of research in fluid mechanics. These problems are addressed herein in chapters 8.1 and 8.2 by means of experimental and numerical methods.

As the released fluid moves away from the source, it mixes with the ambient fluid, which is progressively entrained within the plume. The component of fluid motion due to the initial source condition progressively vanishes and becomes of the same order as that of the ambient turbulence. In this phase we can observe the appearance of a bent-over plume (see fig. 6.6b), whose spreading is gradually controlled by the atmospheric dynamics.

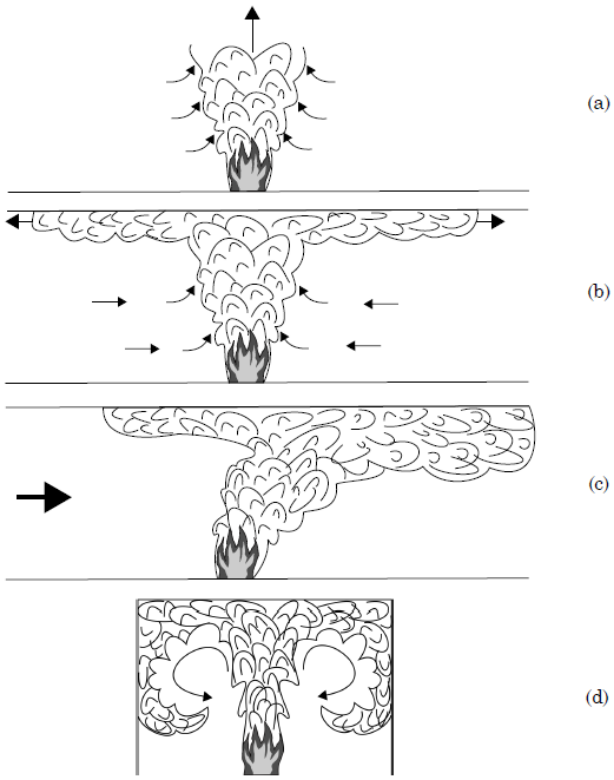

Figure 6.7: Effect of the confinement and ventilation on a buoyant plume: (a) freely propagating plume; b) plume in a vertically confined environment; c) plume in vertically confined and ventilated space; d) plume within an enclosed and ventilated space, confined vertically and laterally.

6.6 On the effect of the domain geometry

The presence of solid walls bounding the turbulent flow can affect its dynamics in very different ways, giving rise to very complex flow configurations. Among the large variety of configurations of pollutant releases within wall-bounded flows we focus here on three particular cases:

- the release of a passive scalar in a turbulent boundary layer over a rough surface;
- the release of a buoyant pollutant within a ventilated tunnel, i.e. an enclosed space bounded both laterally and vertically;
- the release of a passive scalar within a group of obstacles.

Compared to the case presented in fig. 6.2, that of homogeneous and isotropic turbulent flow in an unbounded domain, the presence of a solid wall (as in the cases represented in fig. 6.5) introduces a major modification to the flow dynamics; it restraints the motion in the direction perpendicular to the wall, therefore imposing a strong anisotropy and inhomogeneity of the velocity field. The effects of the anisotropy and inhomogeneity on dispersion and mixing represent a main difficulty in their mathematical modelling. These aspects constitute a relevant feature of the studies presented in sections 7.1, 7.2 and 7.3, where we analyse the case of a fluctuating passive scalar plume released in the lower atmosphere.

Concerning the case of a buoyant pollutant, it is instructive to consider the case of a light gas issuing from a localised source such as a fire. Differently from the case of a freely propagating plume, sketched in fig. 6.7a, the presence of a solid wall induces the buoyant pollutants to impinge on it and to spread along the ceiling, forming a stably stratified layer of light fluid (fig. 6.7b). In the presence of a mean longitudinal flow, the release will produce a bent-over plume (fig. 6.7c). For a given intensity of the longitudinal ventilation all smoke will be pushed downwind of the source. In the case of lighter ventilation the buoyant smoke can form a back-layer flow, moving forward against the ventilation under the action of a pressure difference. In all cases, the combined effect of the ventilation and lateral and vertical walls can give rise to secondary vortices (whose axes are parallel to the direction of the flow), which can induce a motion of the pollutant from the upper part of the ceiling to the ground. The dynamics of the back-layer flow and its control by means of the longitudinal ventilation within a tunnel represent a classic problem in industrial and transportation safety issues. This involves notably a study of the effects of large density differences within the flow, i.e. between the buoyant pollutant and the ambient flow, usually referred to as non-Boussinesq effects, that are still not elucidated. These features are addressed in section 8.1.

Finally, we consider the case of a passive scalar release within a group of obstacles, as within the buildings of an urban district represented in fig. 6.8, and usually referred to as an *urban canopy*. The presence of obstacles is a further element of complexity in the dynamics of a turbulent flow. The scales of motion are highly restrained by the distance between the buildings and also their height. The flow streamlines are also deeply influenced by building geometry.

When the buildings are densely packed, the flow within the canopy is somehow decoupled from that in the overlying atmospheric boundary layer. The turbulence intensity levels are generally lower than those in the overlying flow and the flow streamlines are observed to give rise to organised structures. A helicoidal motion (see fig. 6.8a) occurs within the streets, given by the superposition of a mean advection along their axes and a recirculation around it. A vortex with vertical axes instead takes place close to the street intersection, where fluxes from different streets converge.

When the buildings are more distant one from the other, this streamline topology vanishes and the flow becomes more disordered, given by the non-linear interaction of the flow of the single buildings, which also significantly enhances the level of velocity fluctuations.
These different flow pictures have very different effects on the overall dispersion of a pollutant plume. Within dense canopies pollutant transfer is characterised by a strong channelling along the street axes (see fig. 6.8b), the retention within the recirculating motion within the streets (street-canyon effect), and the intense turbulent exchanges at street intersections. In sparse canopies, the pollutant plume will be highly affected by the intense turbulent fluctuations produced in the buildings' wake, that will enhance its mixing with the ambient air. These aspects are discussed in chapters 9.1 and 9.2, where we address the (direct and inverse) modelling of pollutant dispersion in a built environment such as a city or an industrial site.

6.7 Outline

In the following chapters I present the main elements of the research I have been involved in since joining the Laboratoire de Mécanique des Fluides et Acoustique of the Ecole Centrale de Lyon as a permanent staff member in 2009. Although they show the same underlying theme of the influence of the structure of turbulence on the dispersion of pollutants, I have grouped my work into three main topics:

1. the concentration fluctuations of a passive scalar emitted and dispersed in a neutral turbulent boundary layer (Chapter 7);

2. the dynamics of buoyant releases in free and confined environments (Chapter 8); and

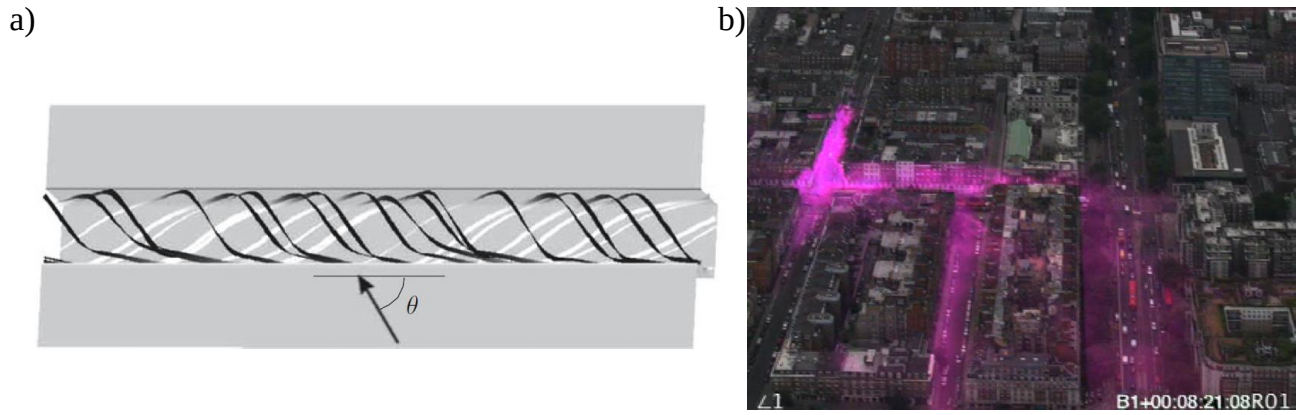

Figure 6.8: Effect of the built environment on flow and dispersion: (a) streamline topology within a street (Soulhac *et al.*, 2008); (b) passive scalar plumes released within the urban canopy.

3. the direct and inverse modelling of pollutant dispersion within the built environment, i.e. urban areas and industrial sites (Chapter 9).

In the three cases we deal with problems which are typical in the assessment of accidental hazards, induced by the transport of a sudden and uncontrolled release of pollutant within indoor and outdoor air. In the first two themes the focus is on the role of the source conditions. In the third case we deal instead with the influence of an enhanced complexity of the flow field to the geometry within which the dispersion process takes place. Research has been undertaken making use of a large variety of methodologies. These include numerical, analytical and stochastic modelling approaches as well as experimental methods adopting different measurement techniques, such as flow visualisations, hot-wire and laser-Doppler anemometry, particle image velocimetry and the use of a flame ionisation detector to measure concentrations.

The results of this research have been published in almost thirty articles in international referred journals, and I have therefore selected only a few articles to illustrate each topic; some of these articles have already been published, others have been recently submitted, and other are still in preparation. Each chapter begins with a short description of the work described in the selected articles and summarises the major findings.

Bibliography

Brimblecombe, P. 1987. *The big smoke. A history of air pollution in London since medieval times.* Routledge.

Cancelli, C., Boffadossi, M., and Salizzoni, P. 2006. *Fluidodinamica ambientale, turbolenza e dispersione.* Via Garibaldi 5, 10122 Torino: Otto Editore.

Duplat, J., and Villermaux, E. 2008. Mixing by random stirring in confined mixtures. *Journal of Fluid Mechanics*, **617**, 51– 86.

Hunt, J. C. R. 1991. Industrial and environmental fluid mechanics. *Annual Review of Fluid Mechanics*, **23**, 1–41.

Loomis, D., Grosse, Y., Lauby-Secretan, B., El Ghissassi, F., Bouvard, V., Benbrahim-Tallaa, L., Guha, N., Baan, R., Mattock, H., and Straif, K. 2013. The carcinogenicity of outdoor air pollution. *Lancet Oncology*, **14 - 13**, 1262–3.

McNeill, J. R. 2001. *Something New Under the Sun: An Environmental History of the Twentieth-Century.* W.W. Norton & Company.

Soulhac, L., Perkins , R. J. and Salizzoni, P., 2008. Flow in a street canyon for any external wind direction. *Boundary-Layer Meteorology*, **126**, 365–388.

Chapter 7

Dispersion of a passive scalar fluctuating plume in a turbulent boundary layer

As widely discussed in section 6.7, the assessment of an accidental hazard due to the release of a harmful airborne pollutant into a turbulent flow requires modelling of the spatial (and eventually temporal) evolution of the pollutant concentration PDF. To this end, the key aspect is to evaluate the influence of the ratio between source size l_0 and the Eulerian macroscale $\mathcal{L}$ on the concentration PDF. The ratio $l_0/\mathcal{L}$ plays an important role in determining (see fig. 7.1a), in the near-field region, the intensity of the *meandering* motion of the plume puffs as well as their dispersion around their centre of mass (see sect. 6.3 and sect 6.5).

Meandering is expected to be dominant close to the source where 'small' pollutant puffs can be trapped by the motion of the large-scale vortices. Relative dispersion becomes dominant far from the source, when the puff size exceeds that of the largest eddies. The role of these two phenomena can be highlighted well by examining concentration signals registered on the axis of the time averaged plume (7.1b). Close to the source, concentration signals are characterised by sharp peaks and high intermittency (see fig. 7.1c), giving rise to strongly positively skewed PDF (fig. 7.1e). Far from the source, intermittency is suppressed and concentration fluctuations are damped (fig. 7.1d), and the PDF progressively relaxes toward a Gaussian (fig. 7.1e).

To date, these features have been addressed by several studies (see, for example, Sawford and Stapountzis (1986) and Sawford (2004)) that however essentially focused on the case of a homogeneous turbulent flow. The aim of the studies presented in the next section is therefore to analyse the case of a non-homogeneous anisotropic turbulent flow, namely a boundary layer over a rough wall. From an experimental point of view (sect. 7.1), the objective was to extend the work of Fackrell and Robins (1982) and Fackrell and Robins (1982) in order to provide measurements of:

- the 3^{rd} and 4^{th} order moments of concentration statistics; and
- the vertical evolution of the Eulerian macroscales $\mathcal{L}_{uu}$, $\mathcal{L}_{vv}$ and $\mathcal{L}_{ww}$ characterising the size of largest eddies in the three direction.

Our results show that the source size and elevation have a major influence on the spatial distribution of the higher moments of the concentration PDF. This can be explained by an interaction of the plume during its initial stage of growth with the different scales of motion in the surrounding atmospheric flow. These effects are more and more evident as the moments of the PDF increase, and persist over a distance that is almost three orders of magnitude larger than the source size. Notably, the experimental non-dimensional PDF is shown to be very well modelled by a Gamma distribution for any of the source

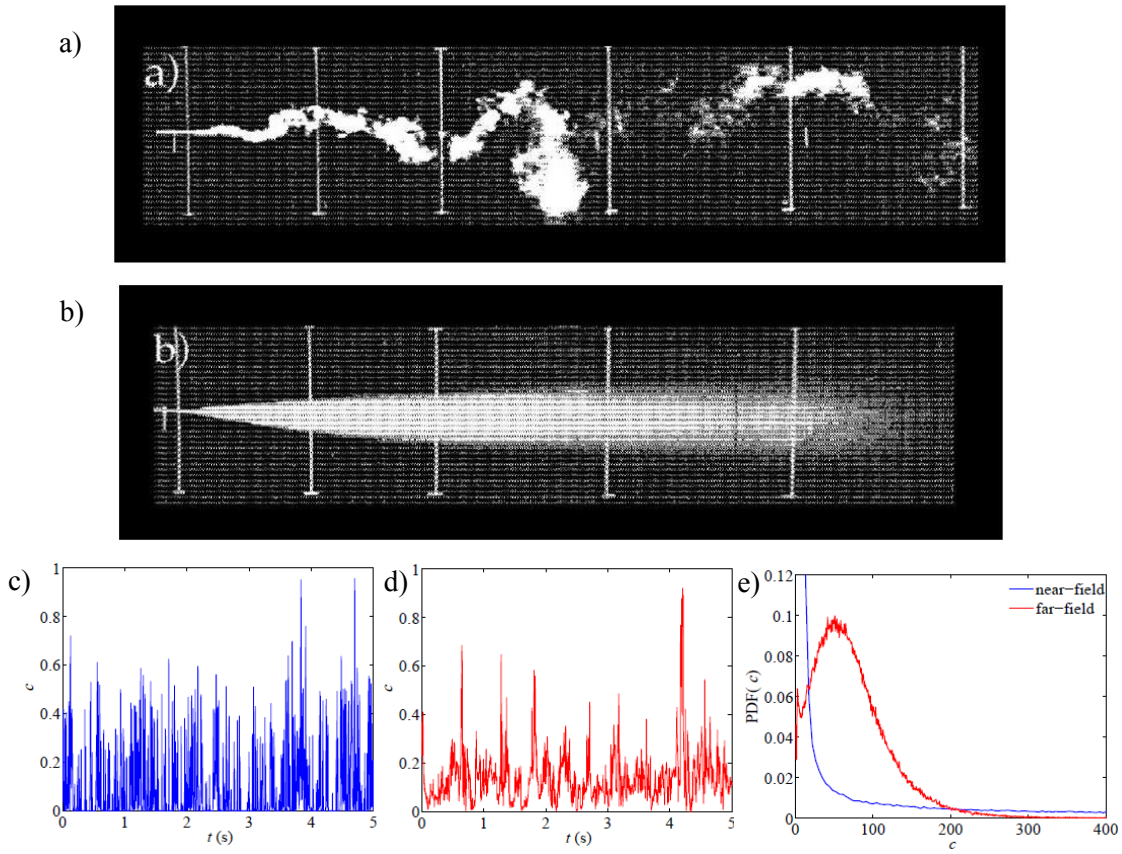

Figure 7.1: a) Visualisation of a fluctuating scalar plume within a turbulent flow. Typical concentration signals registered b) close and c) far from the source, with the d) corresponding concentrations PDF.

congurations considered, irrespective of the conditions imposed therein. This implies that the higher order concentration moments can be fully expressed as a function of only one parameter, namely the intensity of the concentration fluctuations (i.e. the ratio between the standard deviation and mean concentration value).

These measurements have been subsequently used to analyse the reliability and the consistency of two different modelling approaches widely adopted in the literature (Gifford, 1959; Yee *et al.*, 1994; Sawford, 2004): an analytical meandering plume model (sect. 7.2) and a stochastic micro-mixing model (sect. 7.3). Results of both modelling approaches show significant sensitivities to the conditions imposed at the source and to the setting of some key flow parameters. These features, together with other shortcomings related to the model structure, make these modelling approaches not fully reliable for the estimate of higher-order moments of concentrations.

However, in the light of the new experimental results showing that the concentration PDF is suitably modelled by a Gamma distribution, the prediction of both modelling approaches can be corrected by making use of empirically-based corrections, which provide estimates on higher-order moments based on the computation of the first two moments only.

Bibliography

Fackrell, J. E., and Robins, A. G. 1982. Concentration fluctuations and fluxes in plumes from point sources in a turbulent boundary layer. *Journal of Fluid Mechanics*, **117**, 1–26.

Gifford, F. 1959. Statistical properties of a fluctuating plume dispersion model. *Advances in geophysics*, **6**.

Sawford, B. 2004. Micro-mixing modelling of scalar fluctuations for plumes in homogeneous turbulence. *Flow, Turbulence and Combustion*, **72**, 133–160.

Sawford, B., and Stapountzis, H. 1986. Concentration fluctuations according to fluctuating plume models in one and two dimensions. *Boundary-Layer Meteorology*, **37**, 89–105.

Yee, E., Chan, R., Kosteniuk, P. R., Chandler, G. M., Biltoft, C. A., and Bowers, J. F. 1994. Incorporation of internal fluctuations in a meandering plume model of concentration fluctuations. *Boundary-Layer Meteorology*, **67**, 11–39.

7.1 Velocity and concentration measurements

Boundary-Layer Meteorol (2015) 156:415–446
DOI 10.1007/s10546-015-0040-x

ARTICLE

Dispersion of a Passive Scalar Fluctuating Plume in a Turbulent Boundary Layer. Part I: Velocity and Concentration Measurements

Chiara Nironi[1] · Pietro Salizzoni[1] · Massimo Marro[1] · Patrick Mejean[1] · Nathalie Grosjean[1] · Lionel Soulhac[1]

Received: 20 December 2013 / Accepted: 11 May 2015 / Published online: 26 May 2015

Abstract The prediction of the probability density function (PDF) of a pollutant concentration within atmospheric flows is of primary importance in estimating the hazard related to accidental releases of toxic or flammable substances and their effects on human health. This need motivates studies devoted to the characterization of concentration statistics of pollutants dispersion in the lower atmosphere, and their dependence on the parameters controlling their emissions. As is known from previous experimental results, concentration fluctuations are significantly influenced by the diameter of the source and its elevation. In this study, we aim to further investigate the dependence of the dispersion process on the source configuration, including source size, elevation and emission velocity. To that end we study experimentally the influence of these parameters on the statistics of the concentration of a passive scalar, measured at several distances downwind of the source. We analyze the spatial distribution of the first four moments of the concentration PDFs, with a focus on the variance, its dissipation and production and its spectral density. The information provided by the dataset, completed by estimates of the intermittency factors, allow us to discuss the role of the main mechanisms controlling the scalar dispersion and their link to the form of the PDF. The latter is shown to be very well approximated by a Gamma distribution, irrespective of the emission conditions and the distance from the source. Concentration measurements are complemented by a detailed description of the velocity statistics, including direct estimates of the Eulerian integral length scales from two-point correlations, a measurement that has been rarely presented to date.

Keywords Atmospheric turbulence · Eulerian integral length scale · Gamma distribution · Intermittency · Pollutant dispersion · Wind-tunnel experiments

✉ Pietro Salizzoni
pietro.salizzoni@ec-lyon.fr

[1] Laboratoire de Mécanique des Fluides et d'Acoustique, University of Lyon, CNRS UMR 5509, Ecole Centrale de Lyon, INSA Lyon, Université Claude Bernard, 36, avenue Guy de Collongue, 69134 Ecully, France

1 Introduction

The assessment of chronic and accidental risks related to the atmospheric dispersion of contaminants requires the statistical characterization of its concentration. For chronic risks, estimates of mean concentrations are sufficient. Conversely, when considering the accidental risk due to releases of flammable and explosive substances, what matters is the occurrence of instantaneous concentrations within flammability (or explosivity) limits. Similarly, studies on the exposure and dosages of hazardous materials require estimates of the peak-to-mean ratios. In all those cases, the need to characterize the concentration probability density function (PDF) of the concentration arises. To this purpose, a variety of modelling strategies have been adopted in the literature.

With the aim of modelling the PDF by inverting a limited number of moments, several authors have tried to capture the bulk characteristics of the PDF inferring some functional dependence between the higher-order moments of the concentration PDF. This information is then intended to be used when running simple operational dispersion models, which provide mean values only, so as to approximately estimate the statistical variability of the concentration about its mean. With this aim Chatwin and Sullivan (1990) sought simple relationships between the mean concentration $\overline{c}$ and the standard deviation σ_c of a dispersing scalar in statistically steady self-similar turbulent shear flows. Their analysis was further extended by Mole and Clarke (1995), who demonstrated the existence of simple functional dependencies between second-order, third-order and fourth-order moments of the concentration PDF. Similar analyses were also conducted by Lewis et al. (1997) using field data in varying stability conditions, and, more recently, by Schopflocher and Sullivan (2005) using wind-tunnel experimental data.

Other authors focused directly on the form of the PDF of the concentration. In the case of high intermittent plumes, Yee and Chan (1997) proposed to model the concentration as a clipped-Gamma distribution depending on three parameters that reduce to two as the intermittency becomes negligible. This model was subsequently tested against experimental results by Yee (2009), Klein and Young (2011), and Klein et al. (2011). In the case of confined mixtures, Villermaux and Duplat (2003) showed that the concentration PDF could be well described by a simple Gamma distribution in the whole domain (see also Duplat and Villermaux 2008). More recently, Yee and Skvortsov (2011) showed that a simple Gamma PDF could be used also to reliably model the concentration within a plume emitted from a ground-level point source within a neutral boundary layer.

A more general approach relies on the development of models aiming to directly compute the concentration PDF (or its lower order moments). This has been so far achieved by means of meandering models (Gifford 1959; Yee et al. 1994; Luhar et al. 2000; Franzese 2003), pair-of-particles Lagrangian stochastic models (Durbin 1980; Sawford and Hunt 1986), numerical models resolving the concentration variance balance equation (Andronopoulos et al. 2002; Milliez and Carissimo 2008), micro-mixing Lagrangian models (Sawford 2004; Cassiani et al. 2005a, b; Leuzzi et al. 2012; Amicarelli et al. 2012) and large-eddy simulations (Xie et al. 2004; Vinkovic et al. 2006; Philips et al. 2013).

The reliability of any of these modelling approaches has to be tested against experimental data collected in field or laboratory experiments. Regarding concentration fluctuations of passive scalar plumes in the turbulent boundary layer, two wind-tunnel studies have been hitherto widely adopted as references. These are the pioneering works of Raupach and Coppin (1983) for a line source and Fackrell and Robins (1982a) for point sources. The latter, in particular, has represented a benchmark for more than two generations of authors,

who presented several successful predictions of the experimental results using a variety of modelling approaches (Fackrell and Robins 1982b; Sykes et al. 1984; Cassiani et al. 2005a; Vinkovic et al. 2006).

Since the early 1980s, the experimental characterization of the statistical properties of a fluctuating plume has been rarely tackled. More recent experimental work was performed by Yee and Biltof (2004), who studied the concentration fluctuation within an obstacle array, and Hilderman and Wilson (2007), who directly measured the meandering of a plume dispersing in a water channel by using laser-induced fluorescence.

It is worth noting that these studies mainly focus on the second-order statistics and on the correlation between velocity and concentration fluctuations. Relatively little information is available concerning higher order concentration moments. There is therefore a lack of information for assessment of the modelling of the spatial evolution of the concentration PDFs. The objective of this study is to contribute a much needed set of experimental results, by extending the work on source size and elevation conducted by Fackrell and Robins (1982a) to higher order concentration moments, with a detailed definition of the plume structure in its initial phase of growth. To that purpose we have conducted a series of wind-tunnel experiments on the dispersion of a passive scalar emitted by a source of varying size and height, within a turbulent boundary layer. We also investigate the role of the emission velocity at the source that is likely to influence the near-field concentration statistics. The experimental dataset is completed by a detailed description of the statistics of the velocity field. This further information is essential in order to be able to dissociate errors induced by a specific modelling approach to uncertainties introduced by parametrizations used to substitute missing velocity data. In particular, considerable effort has been devoted here to obtaining direct measurements of the Eulerian integral length scales from two-point velocity statistics. The dataset is subsequently used in the second part of this study Marro et al. (2015) to further investigate the dynamics of the dispersion process by adopting the conceptual framework of a meandering plume model (Gifford 1959; Yee et al. 1994). In what follows Sect. 2 discusses the role of the parameters that mainly control the dispersion process, and Sect. 3 presents our experimental set-up and the measurement techniques. Section 4 presents the velocity statistics and concentration measurements are presented in Sect. 5. Throughout, our data are systematically compared to data of Fackrell and Robins (1982a).[1]

2 Governing Parameters

We consider the atmospheric dispersion of a passive scalar (with molecular diffusivity D and with same kinematic viscosity ν and density ρ of ambient air) emitted by a localized source, placed at a height h_s from the ground, with a diameter σ_0 and an ejection velocity u_s, so that its mass flow rate is $M_q = \frac{\pi}{4}\sigma_0^2\,\rho\,u_s$. The release takes place within a turbulent boundary layer with free-stream velocity u_∞, and which is assumed to be fully characterized by self-similar relations, obtained by rescaling profiles of velocity statistics on the friction velocity u_* and the boundary-layer depth δ. Given these assumptions, the moments of the concentration c about its mean $\overline{c}$ at a given position (x, y, z) can be expressed as,

$$\overline{(c-\overline{c})^n} = f\left(\sigma_0, h_s, u_s, M_q, u_*, u_\infty, \delta, D, \nu\right) \tag{1}$$

[1] The complete dataset of velocity and concentration statistics is available on the site http://air.ec-lyon.fr.

or, equivalently, in non-dimensional form as,

$$\frac{\overline{(c-\overline{c})^n}}{\Delta c^n} = f\left(\frac{u_*}{u_\infty}, \frac{u_\mathrm{s}}{u_\infty}, \frac{h_\mathrm{s}}{\delta}, \frac{\sigma_0}{\delta}, Re, Sc\right) \tag{2}$$

where $Re = u_\infty \delta/\nu$ and $Sc = \nu/D$ are the Reynolds and the Schmidt numbers, respectively, and $\Delta c = M_q/(u_\infty \delta^2)$ represents a scale of the concentration variations.

In our experimental campaign we aim at studying the influence of three parameters, σ_0/δ, h_s/δ, and u_s/u_∞ (for a fixed Re, Sc and u_*/u_∞), whose general effect on the dispersion process is briefly described hereafter.

The diameter of the source is not effective in significantly altering the mean concentration field, unless very close to the emission point. This can be evidenced by Taylor's (1921) formulation (adapted to an anisotropic velocity field) of the plume vertical σ_z, and transversal σ_y spreads

$$\sigma_y^2 = \frac{\sigma_0^2}{6} + 2\sigma_v^2 T_{\mathrm{L}v}\left\{t - T_{\mathrm{L}v}\left[1 - \exp\left(-\frac{t}{T_{\mathrm{L}v}}\right)\right]\right\}, \tag{3}$$

$$\sigma_z^2 = \frac{\sigma_0^2}{6} + 2\sigma_w^2 T_{\mathrm{L}w}\left\{t - T_{\mathrm{L}w}\left[1 - \exp\left(-\frac{t}{T_{\mathrm{L}w}}\right)\right]\right\}, \tag{4}$$

where t is the flight time, $T_{\mathrm{L}v}$ and $T_{\mathrm{L}w}$ are the Lagrangian time scales and σ_v and σ_w are the standard deviations of the lateral and vertical velocity components, respectively. According to Eqs. 3 and 4, the influence of σ_0 is non-negligible only for $t \ll T_\mathrm{L}$. Conversely, variations of the source size have significant effects on the concentration fluctuation for larger distances from the source, provided that its size σ_0 is much smaller than that of the large eddies of the atmospheric turbulence. To sketch these effects it is useful to refer to the conceptual framework developed by Gifford (1959), who considered the concentration fluctuations to be governed by two distinct phenomena: a meandering movement of the instantaneous plume, causing the displacement of the mass centre, and the relative dispersion of the plume particles relative to the mass centre position. The smaller the source, the larger the range of scales contributing to the meandering motion that displaces the plume centre of mass, therefore producing higher fluctuations around the mean concentration value.

The source elevation h_s/δ has an influence on both the mean and the fluctuating concentration fields. The effect on the mean can be again well explained by Eqs. 3 and 4, since, in a turbulent boundary-layer flow, the parameters $T_{\mathrm{L}v}$, $T_{\mathrm{L}w}$, σ_v and σ_w are highly dependent on the distance from the ground. Concerning the influence on concentration fluctuations, the role of the source elevation h_s/δ can be explained by similar arguments to those used for the influence of σ_0/δ. For a fixed σ_0/δ, the emitted plume is subjected to a range of turbulence scales that decreases as h_s/δ decreases, since the source size approaches the size of the larger eddies at the source height. This results in a damping of the contribution of the meandering large-scale motion to the concentration fluctuations. As pointed out by Fackrell and Robins (1982a, b) we may therefore expect that the influence of σ_0/δ vanishes in the limit $h_\mathrm{s}/\delta \to 0$, i.e. for a ground level source.

Finally, we consider the influence of u_s/u_∞, which is the sole parameter characterizing the dynamical conditions of the flow particles emitted at the source, according to the formulation of the problem given by Eq. 1. It is usually supposed, even if not explicitly proved, that if the outlet velocity u_s at the source equals the average velocity of the flow $\overline{u}_\mathrm{s}$ over its height (Fackrell and Robins 1982b) the influence of the emission conditions on the particle trajectories is minimized since, once ejected, the flow particles rapidly adopt the statistics of the external velocity field. Since $\overline{u}_\mathrm{s}/u_\infty = f(h_\mathrm{s}/\delta)$, this isokinetic condition corresponds

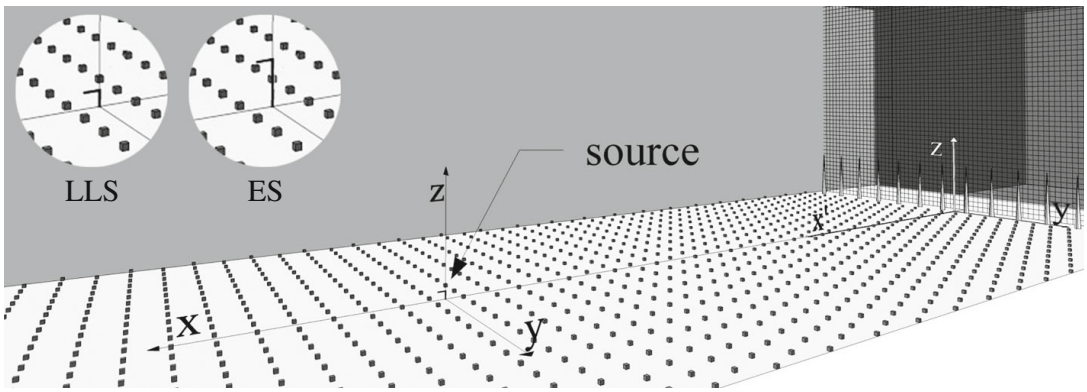

Fig. 1 Sketch of the wind-tunnel set-up showing the vortex generators and the turbulence grid at the entrance of the test section, the roughness elements on the floor and the design of the lower-level source (LLS) and the elevated source (ES) configurations

to a value u_s/u_∞ that depends in turn on h_s/δ only (for a fixed u_*/u_∞). We expect a varying u_s/u_∞ to alter the plume dynamics in a near-source region, whose extent is however undefined. Furthermore, we expect this extent to be significantly different when analyzing the spatial distribution of different moments of the scalar concentration.

3 Experimental Set-Up and Techniques

3.1 Wind-Tunnel Set-Up

The experiments were performed in the atmospheric wind tunnel of the Laboratoire de Mécanique des Fluides et d'Acoustique at the Ecole Centrale de Lyon in France. This is a recirculating wind tunnel with a working section measuring 14 m long and 3.7 m wide. To control the longitudinal pressure gradients the ceiling slope can be adjusted. In the present configuration the ceiling has a positive slope, so that its height varies from 2 m at the entrance to 2.2 m at a distance of 7 m, and up to 2.5 m at its end. The air temperature in the wind tunnel is regulated so that its variations during a 1-day experiment can be maintained in the range ± 0.5 °C.

The wind-tunnel set-up is sketched in Fig. 1. A neutrally-stratified boundary layer was generated by combining the effect of a grid turbulence and a row of spires, placed at the beginning of the test section, and roughness elements on the floor. The presence of a turbulence grid is not a usual feature of a boundary-layer simulation system, and is used here since it assists in minimizing the inhomogeneities of the flow in the transverse direction. The spires were of the Irwin (1981) type with a height $H = 0.5$ m, spaced by a distance $H/2$. The entire working section floor was overlaid with cubes of side $h = 0.02$ m acting as roughness elements. The cubes were placed in a staggered array and covered approximately 1.8 % of the tunnel floor surface. This experimental set-up allowed us to reproduce a boundary layer of depth $\delta = 0.8$ m. Imposing a free-stream velocity $u_\infty = 5$ m s^{-1}, the Reynolds number $Re = \delta u_\infty/\nu \approx 2.6 \times 10^5$ (ν is the kinematic viscosity of air) was sufficiently high to ensure the adequate simulation of a fully turbulent flow (Jimènez 2004).

Ethane (C_2H_6) was used as tracer in the experiments, since it has a density similar to air, and was continuously discharged from a source of varying diameter and elevation. Three source configurations were chosen:

ES 3 Elevated source at $h_s/\delta = 0.19$ and with $\sigma_0/\delta = 0.00375$ ($h_s = 152$ mm and $\sigma_0 = 3$ mm),
ES 6 Elevated source at $h_s/\delta = 0.19$ and with $\sigma_0/\delta = 0.0075$ ($h_s = 152$ mm and $\sigma_0 = 6$ mm),
LLS Lower-level source at $h_s/\delta = 0.06$ and with $\sigma_0/\delta = 0.00375$ ($h_s = 48$ mm and $\sigma_0 = 3$ mm).

The sources consisted of a metallic L-shaped tube (Fig. 1) and were placed at a distance of 7.5δ from the beginning of the test section, where the boundary layer can be considered as fully developed (see Sect. 4). The horizontal side was approximately 30 times the source diameter in order to reduce the influence of the vertical bar on the tracer dispersion. The parameter σ_0 refers to the internal diameter of the tube. The external diameter was equal to 4 mm for the $\sigma_0 = 3$ mm source and to 8 mm for the $\sigma_0 = 6$ mm source.

For most of the experiments, the outlet (spatially-averaged) velocity u_s of the ethane–air mixture was equal to that in the surrounding flow at the source height $\overline{u}_s = \overline{u}(z = h_s)$, a condition that is hereafter referred to as 'isokinetic'. Experiments were also performed by imposing a slower outlet velocity $u_s/\overline{u}_s = 0.03$ (approximating the condition $u_s/\overline{u}_s \to 0$), hereafter referred to as 'hypokinetic' condition.

In what follows y and z denote the transversal and vertical direction, respectively. We consider two different origins of the longitudinal axis: the x'-coordinate has its origin at the beginning of the test section whereas the x-coordinate has its origin at the source location (see Fig. 1).

3.2 Velocity Measurements

The flow dynamics were investigated by means of hot-wire anemometry, providing information about the spectral characteristics of the velocity and supported by a series of measurements with stereo particle image velocimetry (stereo-PIV), which allowed a knowledge of its spatial structure. The spatial distribution of velocity statistics measured with the two techniques are generally in good agreement. For a detailed comparative analysis of these results, see Nironi (2013).

3.2.1 Hot-Wire Anemometry

The hot-wire constant temperature anemometer was equipped with a X-wire probe with a velocity-vector acceptance angle of ±45°, allowing for the simultaneous measurements of two velocity components. Calibration was carried out in the wind tunnel using a pitot tube to measure a reference velocity. The probe was not calibrated in yaw. In order to decompose the calibration velocities from the X-probe into the longitudinal and transversal velocity components (Jorgensen 2002), we adopted a yaw correction with constant coefficients $k_1^2 = k_2^2 = 0.0225$. We acquired transversal and vertical profiles of the velocity statistics at varying distances from the entrance of the test section, from $x' = 4\delta$ up to $x' = 14\delta$. For each measurement point we recorded a 120 s time series with a sampling frequency of 5000 Hz. The experimental error, estimated by repeating the measurements in a fixed reference location, was approximately ±2 % for the mean and the standard deviation.

3.2.2 Particle Image Velocimetry

A second series of velocity measurements was made with a stereo-PIV system. The ambient air was seeded using a stage smoke generator, with approximately spherical 1 μm poly-

ethylene glycol particles. A planar region of the flow was illuminated with a pulsed laser and the tracer position was recorded as a function of time in doubly exposed photographs.

Stereo-PIV planes were collected at $x' = 7.5\delta$. Velocities were recorded on two planes: a yz-plane perpendicular to the flow direction and a xz-plane parallel to the flow, allowing for the measurement of the three velocity components. The image resolution was 1280×1024 pixels and the observation field measured approximately 150×100 mm for xz-planes and 215×150 mm for yz-planes. Several planes were recorded at different heights to cover most of the boundary-layer vertical extent. Images were processed using a cross-correlation algorithm. The interrogation window for the correlation cells was fixed to 32×32 pixels with a round form and a standard 50 % overlap, providing a spatial resolution of about 2 mm for xz-planes and 2.5 mm for yz-planes. A total set of 10000 image pairs was acquired sequentially for time-averaged computations. The sampling frequency was 4 Hz.

3.3 Concentration Measurements

Concentration measurements were performed with a fast flame ionization detector (Fackrell 1980) with a sampling tube 0.3 m long, permitting a frequency response of the instrument to about 400 Hz. Vertical and transversal profiles of concentration statistics were recorded at various distances downwind, from $x = 0.312\delta$ ($x = 250$ mm) up to $x = 5\delta$ ($x = 4000$ mm). Concentration statistics extracted from each time series recorded in a measurement point include the mean, the standard deviation, the third and the fourth moments.

The calibration was carried out using ethane–air mixtures with concentrations equal to 0, 500, 1000 and 5000 ppm. Generally calibration was performed twice a day, as long as the flame temperature of the flame ionization detector (which was continuously monitored) was constant. When the flame temperature showed variations of more than 2 °C from its value at the beginning of the experiment, calibration was repeated. The relation between ethane concentration and tension response was linear, with a slope (representing the sensitivity of the instrument) whose variations could reach ±3 %, depending on the ambient conditions.

The flow control system at the source was composed of two lines, ethane and air, each of them equipped with a mass flow controller. The two lines then converged through a valve and the ethane–air mixture was directed to the source. The ethane mass rate was kept constant by the mass flow controller, working in the range 0.2 to 2 Nl min^{-1} and used within 10 and 100 % of its nominal range. Depending on ambient pressure and temperature (that were continuously monitored and recorded), the airflow was regulated by the second mass flow controller, in order to maintain the total volume flow rate at the source (and therefore the outlet velocity u_s).

The error on the ethane–air flow rate was estimated by systematic comparison with measurements provided by a volumetric counter. The maximal difference between measurements of the two instruments did not exceed ±3 %. It should be noted that the maximal error was reached for measurements close to the source, where measuring concentration within the calibration range (0–5000 ppm) required ethane flow rates of about 0.05 Nl min^{-1}, i.e. outside of the mass flow controller working range. Conversely, for mass flow rates within the instrument working range the uncertainty was reduced to about 1 %.

Recirculation of air in the wind tunnel implies background concentration increasing with time. To take into account the contribution of this drift, the background concentrations were recorded before and after acquiring any of the concentration time series. The background concentration, which was assumed to evolve linearly with time from its initial to its final value, was then subtracted from the signals.

While performing several measurement campaigns over two years, we observed that the higher order statistics were affected by larger experimental error when measured in spring and summer rather than in autumn and winter. This feature can be explained by the effect of the sampling of atmospheric aerosol (Hall and Emmott 1991) that can induce anomalous peaks in the signals. Due to seasonal changes in continental source strengths and in the removal rate for atmospheric particles, this effect is at its highest in spring and summer (Bergametti et al. 1989). Therefore, the data presented herein all refer to measurement campaigns in autumn and winter, when the disturbance produced by the atmospheric aerosol is minimal.

An averaging time of 300 s was chosen, allowing the stochastic uncertainty of the concentration statistics calculated from finite length time series to be of order 0.1 %, so that its contribution to the experimental error was negligible. The main sources of experimental errors were instead related to the calibration, the sampling of atmospheric aerosols and the flow rate at the source. The relative influence of each of these factors is however difficult to estimate a priori. Therefore, in order to quantify a global experimental error, during our campaign we collected a sample of 20 measurements in each of four fixed locations with respect to the source. These measurements were performed on different days with a time interval of several weeks one to the other. The delay between calibration and measurement was variable (up to four hours). Therefore the statistics extracted from these signals were affected by all the uncertainties due to the experimental chain. The error was then estimated as twice the standard deviation computed over the 20 values collected for each point. The results show that, in the far field, the first two moments of the concentration are affected by an error of 2 % whereas the error rises up to 4.5 % for third- and fourth-order moments. In the near field, the error in the third- and fourth-order moments remained similar to that estimated in the far field. However, due to the higher uncertainty affecting the source flow control system in the near-field measurements, the error in the first two moments, the mean and the standard deviation, reached ± 3 %.

4 Velocity Field

We begin by presenting vertical profiles of one-point velocity statistics and spectra, measured by hot-wire anemometry in the flow within which the scalar dispersion takes place. This is a boundary-layer flow over a rough wall with light adverse longitudinal pressure gradient $\approx -0.095\,\mathrm{Pa\ m^{-1}}$ (as estimated from the measurements of the free-stream velocity u_∞ for varying distances from the entrance of the test section). Further on, the focus is on the estimates of the integral length scales from PIV two-point correlations, and on the derived estimates of the Lagrangian time scales.

4.1 Vertical Profiles of One-Point Velocity Statistics

In order to compare our results to equivalent data by Fackrell and Robins (1982a), we adopted the typical scalings indicated by the similarity theory (Tennekes and Lumley 1972). Based on this theory, the turbulent boundary layer consists, in the simplest view, of an outer and an inner region, the latter including the inertial region and the underlying roughness sublayer (Raupach et al. 1980), extending for a few roughness heights away from the wall. According to the theory, the surface geometry is seen as a boundary condition affecting the flow field as a wall distributed drag, quantified by the roughness length z_0, except close to the wall, in the roughness sublayer.

It is generally assumed that, if a proper set of scales is chosen, each region can be described by some form of similarity solution. These are the friction velocity u_*, the roughness length z_0 and boundary-layer depth δ, representing an inner and an outer length scale, respectively. The bulk properties of the mean velocity distribution in the inertial region $\overline{u}(z)$ are derived by a classical asymptotic matching procedure (in the double limit $z/z_0 \to \infty$ and $z/\delta \to 0$), yielding to the familiar logarithmic law (Tennekes 1982),

$$\frac{\overline{u}(z)}{u_*} = \frac{1}{\kappa} \ln\left(\frac{z-d}{z_0}\right), \tag{5}$$

where $\kappa = 0.4$ is the Von Kármán constant and d is the displacement height (Thom 1971; Jackson 1981). In order to quantify the three parameters u_*, d and z_0, we have adopted the same procedure as Salizzoni et al. (2008). Firstly we have estimated the friction velocity from the Reynolds stress $\overline{u'w'}$ profile as $u_* = \sqrt{-\overline{u'w'}}$, by averaging the $\overline{u'w'}$ data in the lower part of the flow field, where these vary only slightly with respect to their average value (Fig. 2f). The two other parameters, z_0 and d, are then estimated by a best fit of the mean velocity profile with a logarithmic law (Fig. 2b), assuming the computed value of u_*. From our measurements we obtained $u_* = 0.185$ m s^{-1}, $z_0 = 1.1 \times 10^{-4}$ m and $d = 0.013$ m. A value of $\delta = 0.8 \pm 0.05$ m was estimated by the $\overline{u'w'}$ profile, as the height at which $\mathrm{d}\left(\overline{u'w'}\right)/\mathrm{d}z \approx 0$. In principle, the effective value of the outer scale should be taken as $\delta - d$. However, since d is here smaller than the uncertainty in the estimate of δ, we will use the latter as the reference length scale to normalize velocity profiles.

A comparison between boundary-layer parameters in our flow and those of the experiments of Fackrell and Robins (1982a) is given in Table 1. As predicted by the theory, and as shown in Fig. 2b, Eq. 5 fits the velocity profile in a region that slightly exceeds the extent on the inertial region, for $0.025 \leq z/\delta \leq 0.25$. Conversely, a good fit of the mean velocity profile in the whole turbulent boundary layer extent can be obtained by a power law of the form,

$$\frac{\overline{u}(z)}{u_\infty} = \left(\frac{z}{\delta}\right)^n, \tag{6}$$

with the exponent $n = 0.23$ (Fig. 2a).

Profiles of the velocity statistics plotted in Fig. 2 show limited development with increasing x'. Therefore, as a first approximation, we consider that from $x'/\delta = 7.5$ the flow is homogeneous in the horizontal plane, since the development of coherent structures in the wake of the vortex generators has already reached an equilibrium condition (Salizzoni et al. 2008).

Due to a different wall roughness z_0, our profile of $\overline{u}/u_\infty$ differs from that of Fackrell and Robins (1982a) (Fig. 2a). However the two profiles collapse, in the lower part of the velocity field, when normalized by an inner scaling (Fig. 2b). Similarly, vertical profiles of higher order velocity statistics tend to collapse on a single curve when normalized with u_* and δ (Fig. 2c–f). The only relevant discrepancies are observed in the σ_v/u_* profiles (Fig. 2d).

General good agreement (Fig. 2g) is also observed in the profiles of the non-dimensional turbulent kinetic energy (TKE) mean dissipation rate, referred to as ε. Two estimates of ε were obtained here by means of the hot-wire anemometer data and employing the common isotropic approximation and Taylor's hypothesis of frozen turbulence to convert spatial gradients to temporal gradients, a procedure that may induce non-negligible errors close to the wall, as the turbulent intensity $\sigma_u/\overline{u}$ exceeds 0.3. The first estimate is computed as (Hinze 1975)

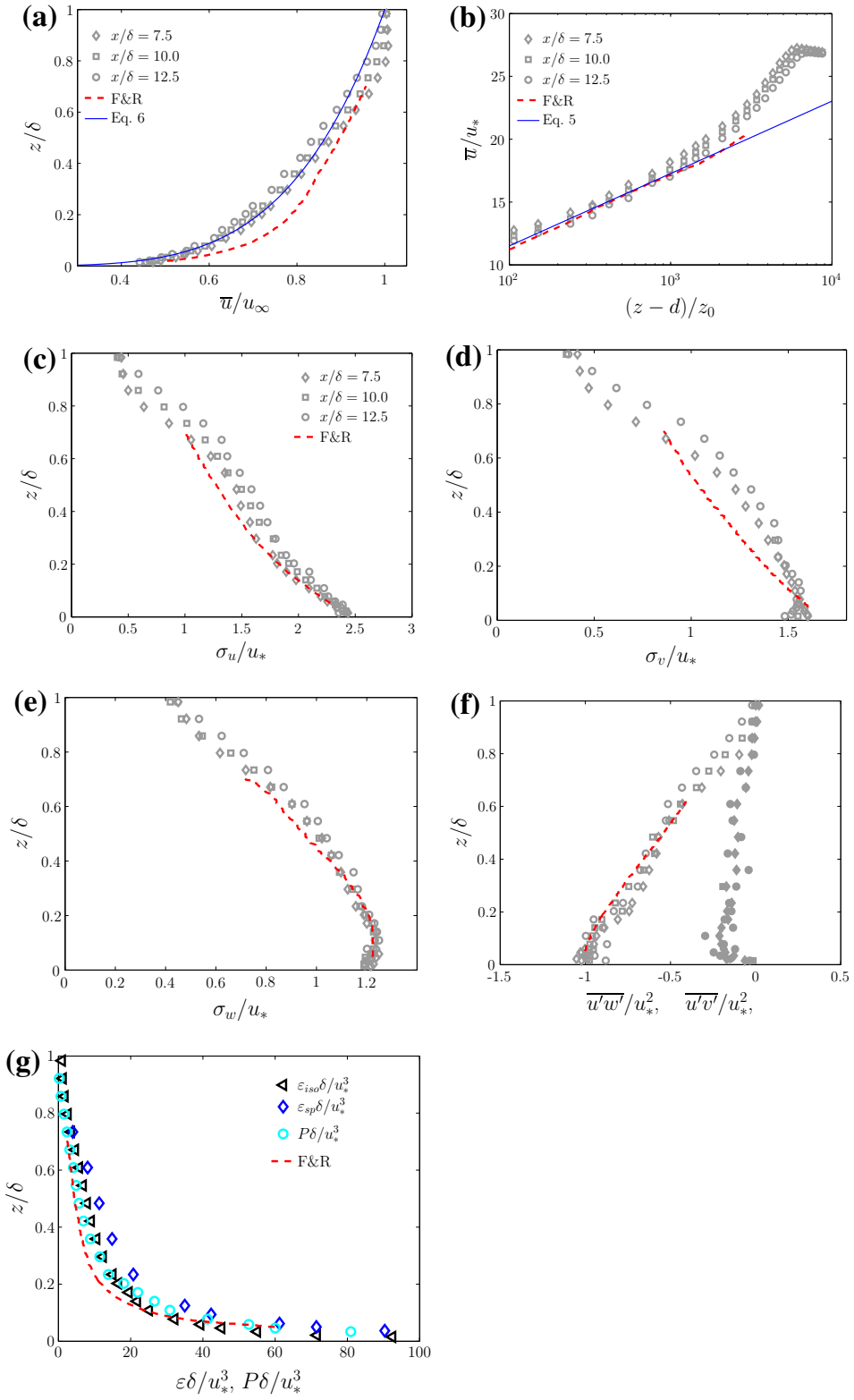

Fig. 2 Vertical profiles of non-dimensional velocity statistics and comparison with literature data from Fackrell and Robins (1982a). **a** Mean longitudinal velocity component; **b** mean longitudinal velocity component rescaled on inner scaling; standard deviations of the **c** longitudinal, **d** lateral component, and **e** vertical velocity component; **f** Reynolds stress $\overline{u'w'}$ (*opens symbols*) and $\overline{u'v'}$ (*filled symbols*); **g** estimates of the dissipation rate ε and production P of TKE

Table 1 Boundary-layer characteristics: comparison with data from Fackrell and Robins (1982a) (F&R)

	δ (m)	z_0 (m)	u_∞ (m s^{-1})	u_* (m s^{-1})	z_0/δ	u_*/u_∞
Present study	0.8	1.1×10^{-4}	5	0.185	1.4×10^{-4}	0.037
F&R (1982a)	1.2	2.9×10^{-4}	4	0.188	2.4×10^{-4}	0.047

$\varepsilon_{iso} = \frac{15\nu}{\overline{u}^2}\overline{\left(\frac{\partial u'^2}{\partial t}\right)}$ whereas the second, referred to as ε_{sp} is obtained by fitting the one-dimensional spectra (Sect. 4.2) of the longitudinal velocity component in the inertial region adopting the relation $E(k) = \alpha_1 \varepsilon_{sp}^{2/3} k^{-5/3}$, where $k = 2\pi f/\overline{u}$ is the wavenumber, f is the frequency and $\alpha_1 = 0.5$ (Pope 2000). The two estimates of ε agree well one with the other and they are also very close to those of TKE production $P \approx \overline{u'w'}\frac{\partial \overline{u}}{\partial z}$ (Fig. 2g), showing that, in most of the boundary layer, we can reasonably assume a condition of local equilibrium between production and dissipation of TKE.

Finally, we note that our velocity field is characterized by slight inhomogeneities in the mean longitudinal velocity along the y-direction. This implies non-null values of the $\overline{u'v'}$ Reynolds stress component (Fig. 2f) and a non-null lateral component of the mean transversal velocity $\overline{v}$, whose intensity is about 1 % of that of the longitudinal component $\overline{u}$.

4.2 Spectra

Spectra for the three velocity components derived from hot-wire anemometry are shown in Fig. 3, for increasing distances from the wall. These are normalized using the distance z as a length scale and the friction velocity u_* as a velocity scale, and plotted against the dimensionless frequency $n = fz/\overline{u}$.

The measured spectra for u, v and w are compared to the model proposed by Kaimal et al. (1972), based on the Kansas field experiments,

$$\frac{nS_u(n)}{u_*^2} = \frac{102n}{(1+33n)^{5/3}}, \tag{7}$$

$$\frac{nS_v(n)}{u_*^2} = \frac{17n}{(1+9.5n)^{5/3}}, \tag{8}$$

$$\frac{nS_w(n)}{u_*^2} = \frac{2.1n}{1+5.3n^{5/3}}. \tag{9}$$

The measured spectra show good agreement with Kaimal's model in both the production and the inertial subrange (Fig. 3). This comparison allows us to evidence the similarity between the spectral energy distribution in our simulated flow with that observed in the atmospheric boundary layer. The extension of the inertial subrange in our velocity field is smaller than that occurring in a real atmosphere (due to a reduced Reynolds number). However, the existence of inertial subrange extending over one (or more, depending on the distance from the wall) decade of non-dimensional frequencies (Fig. 3), demonstrates a clear separation between the larger scale energetic eddies and the dissipative scale.

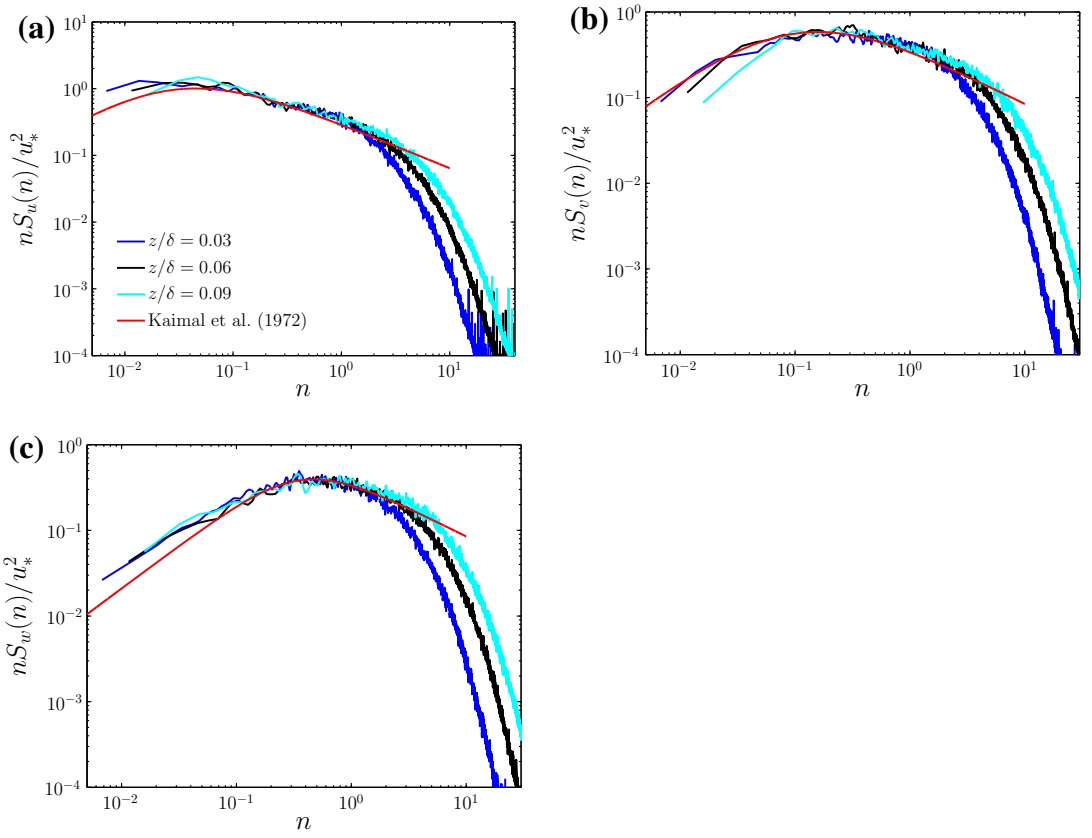

Fig. 3 Velocity spectra of the three velocity components for growing distances from the wall, z/δ. Comparison with a model extrapolated from field data (Kaimal et al. 1972). **a** longitudinal component S_u, **b** lateral component S_v, and **c** vertical component S_w

4.3 Integral Length and Time Scales

The characterization of the structure of the large-scale fluctuating motion in an inhomogeneous and anisotropic shear turbulent flow requires the evaluation of a variety of length scales (Carlotti and Drobinski 2004). These can be conveniently estimated from two-point spatial correlation coefficients, defined as,

$$\rho_{ii}(\mathbf{x}, \mathbf{r}) = \frac{\overline{u_i'(\mathbf{x}) u_i'(\mathbf{x}+\mathbf{r})}}{\overline{u_i'^2}}, \tag{10}$$

where u_i' represents the velocity fluctuations of u, v and w, $\mathbf{x}$ is a fixed point and $\mathbf{r}$ is a generic vector. In this study, correlation coefficients were estimated by stereo-PIV measurements, made at a distance of approximately 8δ from the beginning of the test section. Measurements in the xz-plane allowed the measurements of the coefficients ρ_{uu} and ρ_{ww} whereas measurements on the yz-plane provided information on the coefficient ρ_{vv}. As an example of our results, we report in Fig. 4 the correlation maps obtained for the xz-plane within the inertial region. On the same plots we show the profiles of the correlation coefficient extracted along the x and z axes. A rapid examination of the plot on Fig. 4 reveals the strong anisotropy characterizing the large-scale flow in the lower part of the boundary layer. The spatial extent of the correlation $\rho_{uu}(x, z)$ is considerably wider than that of $\rho_{ww}(x, z)$, and the topology of the iso-contours is highly different for the two functions.

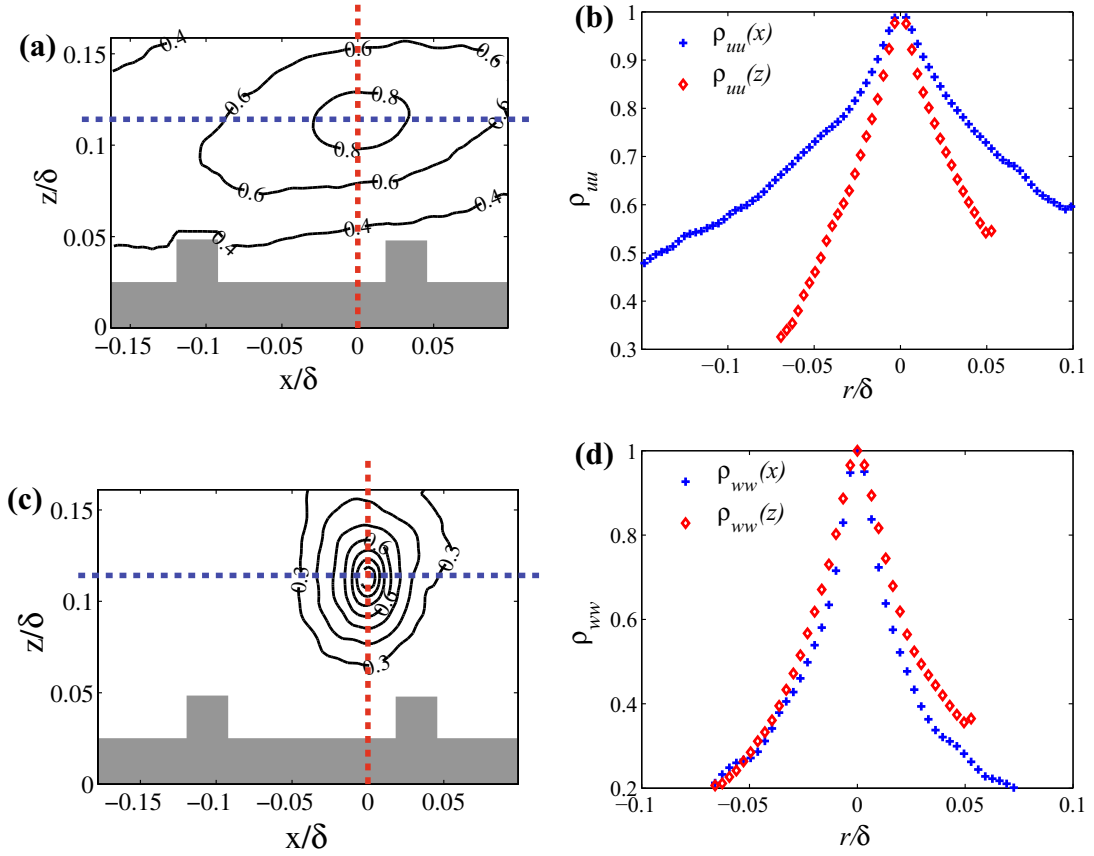

Fig. 4 Two-point spatial correlations in the lower part of the velocity field measurements on the xz-plane: **a** and **b** ρ_{uu}; **c** and **d** ρ_{ww}

The iso-correlation of $\rho_{ww}(x, z)$ can be well approximated by an ellipse with a major axis aligned in the z-direction that is slightly larger than that longed in the x-direction. Conversely, the iso-lines of $\rho_{uu}(x, z)$ are elongated in the x-direction and are tilted of about 15° with respect to the x-axis due to the shear produced by the wall roughness (Krogstad and Antonia 1994).

As well as allowing a qualitative description of the flow structure, the correlation fields can be used to extract estimates of characteristic length scales, usually referred to as Eulerian integral length scales, defined as

$$\Lambda_{ii,j}(\mathbf{x}) = \int_0^\infty \rho_{ii}(\mathbf{x}, r, \mathbf{e}_j)\mathrm{d}r. \tag{11}$$

where $\mathbf{e}_j$ is the unit vector in the $j = x, y, z$ directions.

The numerical computation of the integral in Eq. 11 from experimental data can be affected by non-negligible errors. Therefore the estimate of the Eulerian integral length scales is generally calculated as the distance at which the correlation function falls below a threshold value. For example Bewley et al. (2012) assumed a value of 0.5 whereas Takimoto et al. (2013) adopted 0.4. Note that this method may be problematic when computing scales associated to the ρ_{uu} functions, since the extent of the iso-correlation lines corresponding to the threshold value may not be fully captured by the PIV field (see Fig. 4). Similar problems can be encountered for any of the three functions ρ_{ii} at larger distances from the wall as the size of the eddies is at its highest.

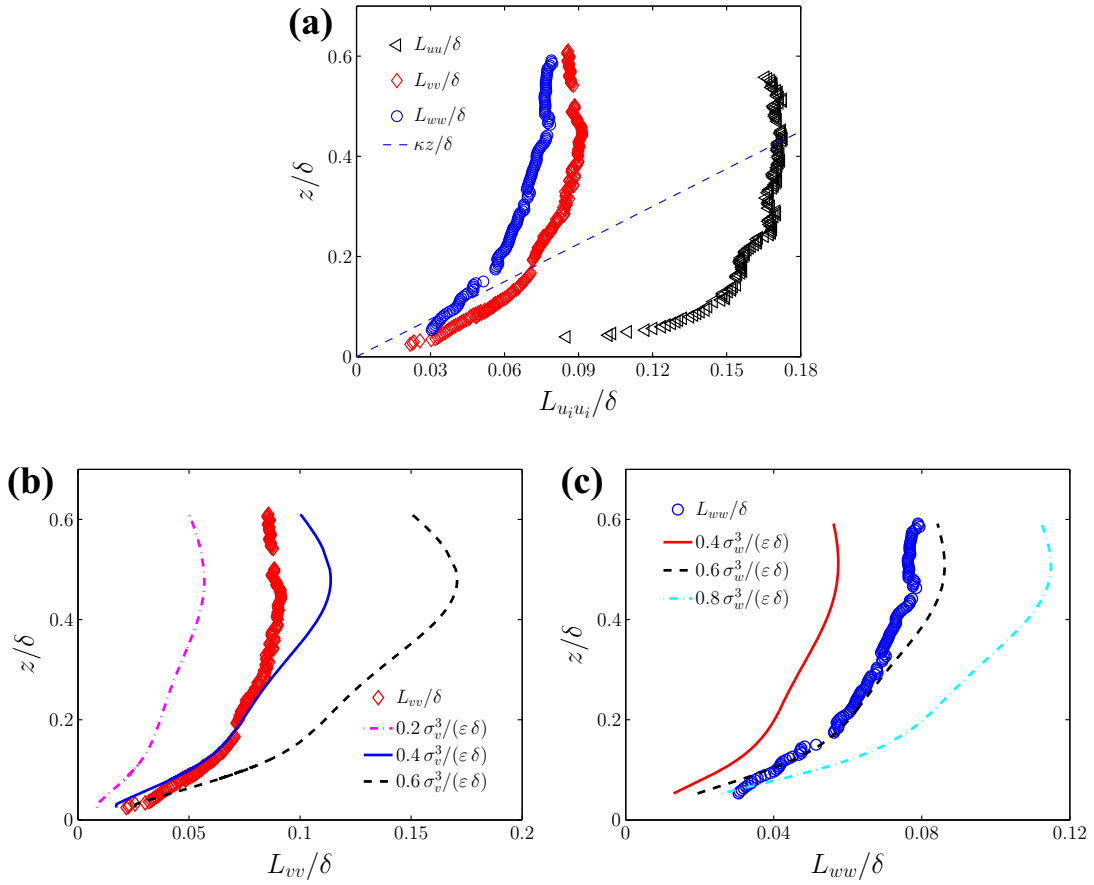

Fig. 5 **a** Vertical profiles of the Eulerian integral length scales from PIV measurements. Integral length scales, **b** L_{vv} and **c** L_{ww} compared to estimates provided by Eqs. 13 and 14 where the proportionality constant α_v and α_w varies in the range 0.2–0.8

In order to avoid these inconveniences, we assume here that the correlation coefficient is an exponential function of the type,

$$\rho_{ii,j}(\mathbf{x}, r, \mathbf{e}_j) = \exp\left(-\frac{r}{L_{ii,\mathbf{e}_j}}\right), \tag{12}$$

and we adopt the lengths $L_{ii,\mathbf{e}_j}$ as a measure of $\Lambda_{ii,j}$ [this corresponds to the distance at which $\rho_{ii,j} = e^{-1} \approx 0.37$ (Tritton 1988)]. The choice of a negative exponential is motivated by the shape of the correlation functions profiles (see Fig. 4b and d), characterized by a sharp peak at $\mathbf{r} \to \mathbf{0}$, that hides the presence of any horizontal asymptote of the curves for $\mathbf{r} = \mathbf{0}$. This evidences that the influence of viscous effects is limited to a tiny region, smaller than the PIV measuring volume. To simplify the notation, the three scales L_{uu,e_x}, L_{vv,e_y}, L_{ww,e_z}, obtained by fitting Eq. 12 to the data in the x, y, z directions will be hereafter referred to as L_{uu}, L_{vv}, L_{ww}.

The dependence of these three scales on the distance from the wall is depicted in Fig. 5a. The longitudinal length scale L_{uu} is by far the longest and is almost double the transversal scale L_{vv}. As expected, L_{ww} is the smallest, even though only slightly smaller (of order 25 %) than L_{vv}. Figure 5a also shows that, as predicted by similarity theory, in the lower part of the turbulent boundary layer, L_{ww} scales as κz to about $z/\delta \approx 0.15$, which represents approximately the upper limit of the inertial layer.

We stress here the importance of the scales L_{vv} and L_{ww} in the overall dispersion phenomenon of a passive scalar plume. Nonetheless their determination in dispersion studies is mostly based on indirect procedures, based on dimensional analysis or similarity considerations.

These estimates are therefore affected by unpredictable errors, especially that of L_{vv}. Indeed, unlike L_{ww}, whose upper bound can be evaluated as a fraction of δ, the amplitude of L_{vv} cannot be evaluated by a simple 'rule of thumb', which could provide at least a rough estimate of it.

In the modelling of the mass and momentum transfer across the boundary layer, the scales L_{vv} and L_{ww} can be parametrized assuming the stationarity of the energy cascade as (Sawford and Stapountzis 1986),

$$L_{vv} \approx \alpha_v \frac{\sigma_v^3}{\varepsilon}, \tag{13}$$

$$L_{ww} \approx \alpha_w \frac{\sigma_w^3}{\varepsilon}, \tag{14}$$

where α_v and α_w are proportionality constants (in these cases σ_v, σ_w and ε are usually calculated from similarity relations). Since we have direct estimates of these velocity statistics, we can test here the reliability of the parametrizations given by Eqs. 13 and 14 and determine appropriate values for α_v and α_w. These parameters are generally assumed in the literature to be free parameters, whose determination mainly rely on matching of numerical results with experimental data rather than on making reference to previous experimental estimates (that are lacking as far as we are aware). As shown in Fig. 5b and c, Eqs. 13 and 14 provide excellent estimates of L_{vv} and L_{ww} assuming $\alpha_v \approx 0.4$ and $\alpha_w \approx 0.6$, respectively. Note that both values are significantly lower than those currently adopted in the literature, which vary between a minimum of 0.8 (Sawford and Stapountzis 1986) and a maximum of 1.8 (Postma et al. 2011).

The direct measurements of the Eulerian integral length scales can be further used to estimate the characteristic 'life time' of the larger scale flow structures as (Tennekes and Lumley 1972; Frisch 1995),

$$T_{\mathrm{L}v1} \approx \frac{L_{vv}}{\sigma_v}, \tag{15}$$

$$T_{\mathrm{L}w1} \approx \frac{L_{ww}}{\sigma_w}. \tag{16}$$

They can be used as a measure of the Lagrangian time scales, referred to here as $T_{\mathrm{L}v}$ and $T_{\mathrm{L}w}$, which are key parameters in the modelling of pollutant dispersion. As the measurement of the Lagrangian time scales $T_{\mathrm{L}v}$ and $T_{\mathrm{L}w}$ is extremely difficult to achieve, for dispersion modelling purposes, they are usually parametrized as (Tennekes 1982),

$$T_{\mathrm{L}v2} = \frac{2\sigma_v^2}{C_0\varepsilon} \tag{17}$$

$$T_{\mathrm{L}w2} = \frac{2\sigma_w^2}{C_0\varepsilon}, \tag{18}$$

where C_0 is the Kolmogorov constant, introduced as a universal constant when referring to a homogeneous and isotropic turbulent flow. However, there is no experimental evidence of the universality of C_0 in inhomogeneous and anisotropic turbulence, and its estimate in the literature is in the range $2 \leq C_0 \leq 8$ (Du et al. 1995; Lien and D'Asaro 2002; Rizza et al. 2006). Given this variability, in most pollutant dispersion studies C_0 is usually considered a flow dependent parameter and its value estimated a posteriori, as that providing the best agreement between experimental and numerical concentration results.

A first estimate of C_0 can be achieved here by taking advantage of the experimental profiles of ε, L_{ww} and L_{vv}. By injecting Eqs. 13 and 14 into Eqs. 15 and 16 and assuming

$T_{Lv1} = T_{Lv2}$ and $T_{Lw1} = T_{Lw2}$ we obtain $C_0 = 2/\alpha_{v,w}$. The two equalities provide slightly different values of the Kolmogorov constant that lie in the range $3.5 \leq C_0 \leq 5$. Further discussion of the values of C_0 is provided in Sect. 5.1.1 where we analyze the vertical and lateral spreading of the passive scalar plume.

5 Concentration Field

We begin by the analysis of the influence of the size and elevation of the source on the first two moments of the concentration PDF (Sect. 5.1). As a second step, we focus on the role of varying emission conditions (Sect. 5.2) and consider the longitudinal evolution of the intermittency factor for all the cases considered (Sect. 5.3). We discuss then the modelling of the concentration PDF (Sect. 5.4) and its physical significance, in particular regarding the dynamics of the dispersion phenomenon. In the light of this discussion, we conclude by presenting the profiles of the third and four moments of the concentration PDF.

The mean is computed as $\overline{c}^* = \frac{1}{N}\sum_{j=1}^{N} c_j^*$ whereas the higher order moments are computed as $m_{nc}^* = \left[\frac{1}{N}\sum_{j=1}^{N}(c_j^* - \overline{c}^*)^n\right]^{1/n}$ (for $n = 2, 3, 4$), N being the number of samples in the time series and c^* the non-dimensional instantaneous concentration. In what follows, the second-order moment m_{2c}^* is denoted as σ_c^*.

In normalizing the concentration data we have expressly avoided adopting local scales, such as the maximal mean concentration or standard deviation and we have adopted Δc as unique concentration scale (Sect. 2). This is motivated by the need to preserve the information on both the form of the profiles and the magnitude of the peaks, for increasing distances from the source. Note that, due to the transversal flow inhomogeneities discussed in Sect. 4.1 that tend to induce a deviation in the plume axis with respect to the wind-tunnel axis, the mean concentration maxima tend to be shifted to the right of the source. However, in plotting the results, we have included a slight lateral offset in the transversal profiles of the concentration moments, so that the concentration maxima occur at $y = 0$.

5.1 Influence of Source Height and Size

As discussed in Sect. 2, the effect of varying source size and elevation on the concentration moments is related to the interaction of the plume with the eddies having characteristic dimensions exceeding the local plume width. We have therefore chosen the size of the two sources ($\sigma_0 = 3$ mm and $\sigma_0 = 6$ mm) so that both were significantly smaller than the Eulerian integral length scale, as estimated from the PIV measurements. For similar reasons, the ES and LLS were placed in regions of the flow characterized by marked differences in the values of the Eulerian integral length scales. Note that the non-dimensional height $h_s/\delta = 0.19$ and size $\sigma_0/\delta = 0.0075$ of the ES is the same as that of the elevated source used in the experiments of Fackrell and Robins (1982a). This feature allows us to compare our results with their dataset.

5.1.1 Mean Concentration Field

Transversal and vertical profiles of the mean concentration downwind from the source are plotted in Fig. 6a–d. Profiles of the ES and different σ_0 do not show any particular difference (Fig. 6a, b), except very close to the source ($x/\delta = 0.3125$). Conversely, the effect of source elevation is evident. Since the LLS emits closer to the ground, the wall reflection rapidly alters

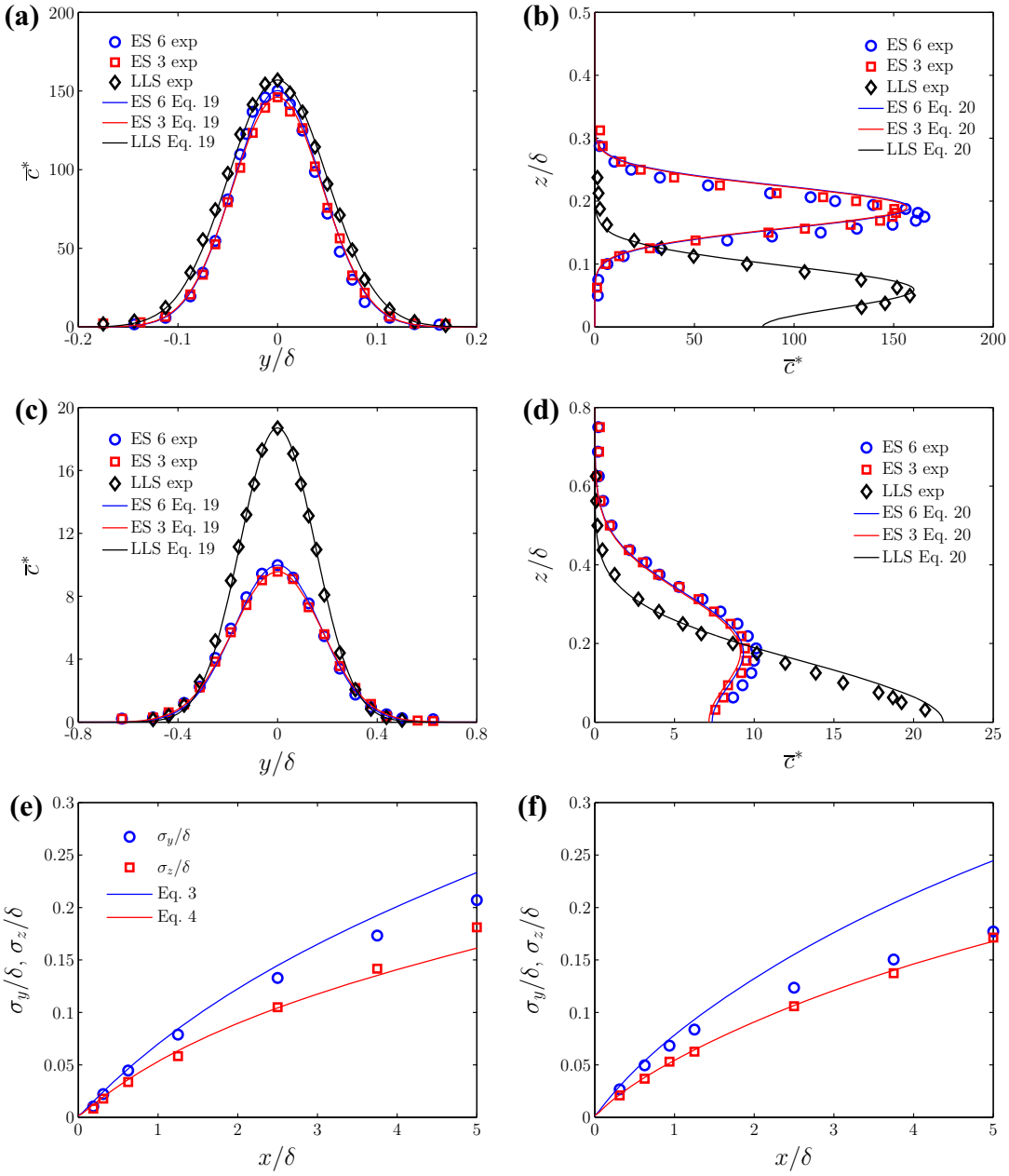

Fig. 6 Mean concentration field for ES and LLS. **a**–**d** transversal and vertical profiles of $\overline{c}^*$ at various distances downwind: **a** and **b** $x/\delta = 0.625$; **c** and **d** $x/\delta = 3.75$. Transversal profiles were measured at the source height and vertical profiles were measured on the plume axis. **e** ES and **f** LLS plume spreads σ_y and σ_z

the plume structure. As the distance from the source increases, the mean concentrations for the LLS plume become larger than those measured for the ES, with a maximum that is about two times the value reached by the ES plume (Fig. 6c, d).

For both ES and LLS, transverse profiles measured at the source height are satisfactorily reproduced by a Gaussian distribution of the form,

$$\overline{c}(x, y) = \frac{M_q}{2\pi\sigma_y\sigma_z\overline{u}_{\text{adv}}} \exp\left(-\frac{y^2}{2\sigma_y^2}\right). \tag{19}$$

Concerning the vertical profiles, the Gaussian distribution with total reflection on the ground is the most suited to the reproduction of the mean concentration distribution in the vertical direction (Arya 1999),

$$\overline{c}(x,z) = \frac{M_q}{2\pi\sigma_y\sigma_z\overline{u}_{\mathrm{adv}}}\left[\exp\left(-\frac{(z+h_s)^2}{2\sigma_z^2}\right)+\exp\left(-\frac{(z-h_s)^2}{2\sigma_z^2}\right)\right], \tag{20}$$

where $\overline{u}_{\mathrm{adv}}$ is the mean longitudinal velocity taken at the plume centre of mass.

Experimental mean concentrations were fitted by the simple and reflected Gaussian distributions, i.e. Eqs. 19 and 20, adopting σ_y and σ_z as free parameters. The resulting values of the vertical and transversal plume spreading are shown in Fig. 6e, f, where no distinction is made between smaller and larger ES sources, since their mean concentration fields are not distinguishable one from the other. For both the ES and the LLS, in the near field as well as in the far field, the vertical spreading was observed to be less than the lateral one.

Plume spreads σ_y and σ_z are modelled according to Taylor's statistical theory from Eqs. 3 and 4. In order to take into account the effects of the inhomogeneity of the velocity field, parameters σ_v and $T_{\mathrm{L}v}$ (as well as σ_w and $T_{\mathrm{L}w}$) are estimated at the height of the plume centre of mass, whose elevation evolves with the distance from the source. For the same reasons, the flight time is estimated as $t = x/\overline{u}_{\mathrm{adv}}$.

Equations 3 and 4 were fitted to the experimental values of σ_y and σ_z expressing $T_{\mathrm{L}v}$ and $T_{\mathrm{L}w}$ from Eqs. 17 and 18 and adopting C_0 as a free parameter. It is worth noting that the best agreement between experimental and modeled plume spreads is obtained for $C_0 = 4.5$ (Fig. 6e, f), a value that falls in the range $3.5 \leq C_0 \leq 5$ identified by the analysis of the integral length and times scales (Sect. 4.3). For the ES, the model agrees well with experimental data. A satisfactory agreement for σ_z is also found for the LLS, while σ_y is overestimated starting from $x/\delta = 1.25$.

5.1.2 Standard Deviation

Unlike the mean, the standard deviation σ_c^* shows a strong dependence on the source size, extending to a considerable distance away from the source. Transverse profiles of σ_c^* downwind of the source for the elevated sources are presented in Fig. 7a, c, e, while the vertical profiles of ES and LLS are shown in Fig. 7b, d, f. A strong dependence on the source size is visible near the source: the σ_c^* field from the smaller source is characterized by significantly higher values. The difference between the two fields diminishes moving downwind and finally vanishes in the far field for $x/\delta = 3.75$. As discussed in Sect. 2, this effect can be explained by the larger range of scales that act on the plume generated by the smaller source, resulting in an enhanced meandering motion.

Source elevation also has a strong influence, as shown in Fig. 7b, d, f. The ES emission results in a higher concentration standard deviation. Even in this case, this difference can be attributed to the different scales of motion that are effective in dispersing the plume. As evidenced in Sect. 4.3, the Eulerian integral length scales are reduced significantly approaching the ground. Therefore, for the LLS emission, the amplitude of the meandering motion acting on the plume is smaller compared to the ES case, thus generating less intense concentration fluctuations. These slight differences between ES and LLS plumes persist until the latest measurement station. The variation of the source height is also reflected on the shape of the profiles of σ_c^*. While the σ_c^* profiles from the ES always have a Gaussian form, those produced by the LLS gradually lose their Gaussian shape moving downstream, and level off at the plume centreline (Yee and Wilson 2000).

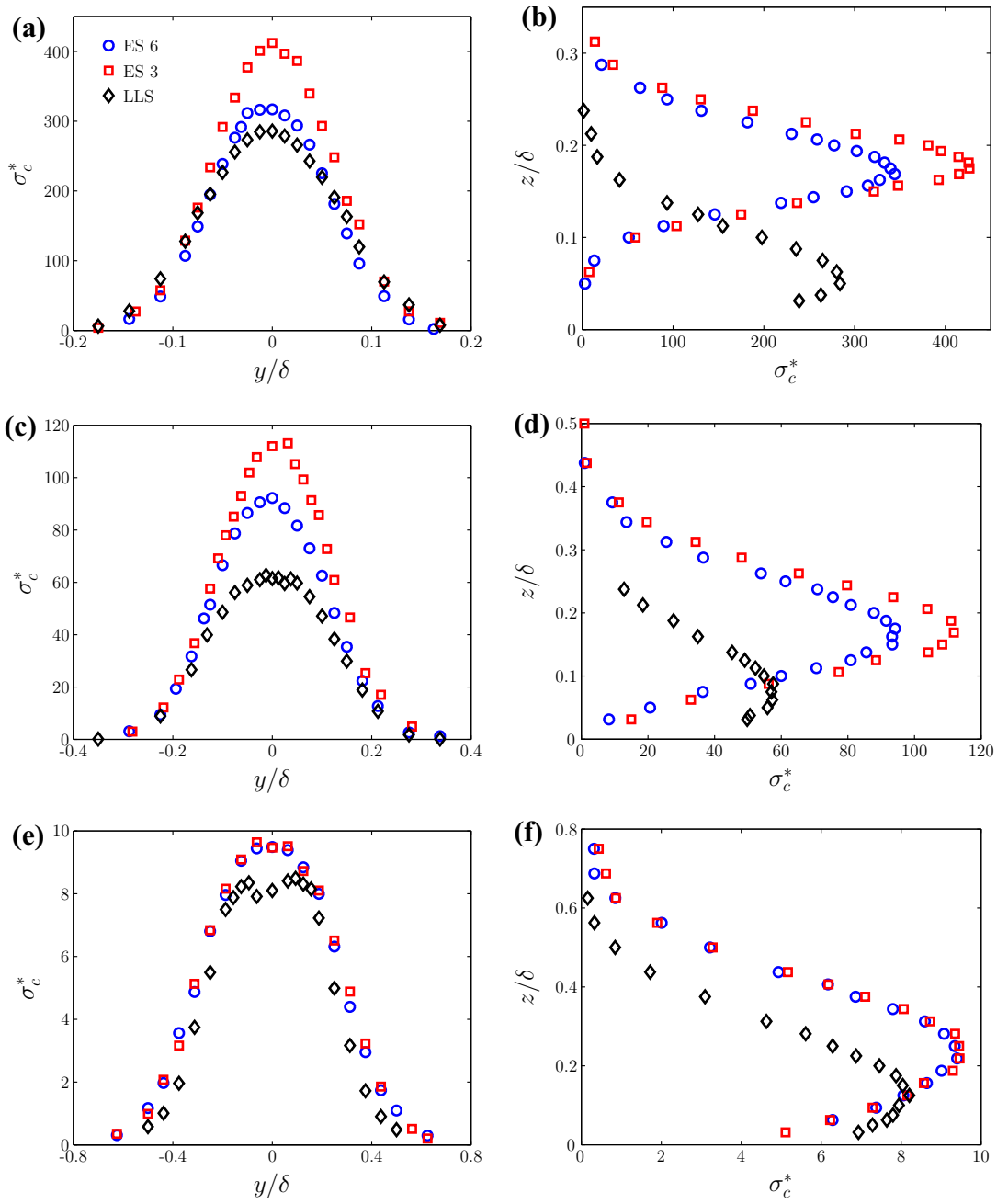

Fig. 7 Transversal profiles (at the source height) and vertical profiles (at the plume centre) of σ_c^* for the ES and LLS, at various distances downwind: **a** and **b** $x/\delta = 0.625$; **c** and **d** $x/\delta = 1.25$; **e** and **f** $x/\delta = 3.75$

The variable role of meandering can be conveniently enlightened by analyzing one-dimensional spectra of concentration $E(k)$ measured on the centreline at various distances from the source. These are presented in Fig. 8 in non-dimensional form, normalized as $E^* = E\delta/\sigma_c^2$ and as a function of $k\delta$. In the near field of the ES plumes, the more intense meandering motion acting on the small source ($\sigma_0 = 3$ mm) produces larger scale concentration fluctuations compared to the larger one ($\sigma_0 = 6$ mm), that are reflected in a higher spectral density for small wavenumbers. The differences between the two spectra are progressively reduced for higher wavenumbers, or fine length scales, at which relative dispersion is predominant. Figure 8a also helps explain the effect on the plume fluctuations due to a

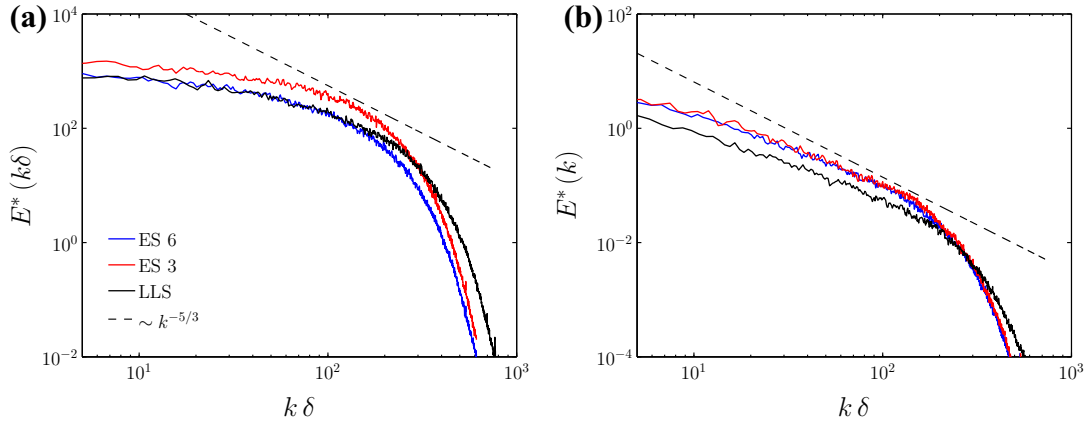

Fig. 8 Spectra of concentration fluctuations on the plume centreline, at two distances from the source. Comparison between the spectra from the ES with 3 and 6 mm diameter (measured at $z/\delta = 0.19$) and the LLS (measured at $z/\delta = 0.06$). **a** $x/\delta = 0.625$, **b** $x/\delta = 3.75$. For a cut-off frequency of about 400 Hz, the non-dimensional cut-off wavenumber is in the range $600 < k\delta < 700$. *Dotted line* represents $-5/3$ dependence on $k\delta$

source of varying height and constant diameter ($\sigma_0 = 3$ mm). The large-scale fluctuations in the LLS are significantly reduced compared to the ES, since the plume is submitted to the dispersive action of eddies that are smaller than those experienced by the ES (Sect. 4.3). It is also worth noting how the smaller scale fluctuations appear to be more intense along the centreline of the LLS plume, which is much more sensitive to the small-scale turbulence generated close to the wall. In the far field (Fig. 8b), the lateral and vertical dimensions of the ES plumes exceed those of the bigger structures in the flow (Sect. 4.3). In these conditions, the meandering motion is suppressed and the concentration spectra of the two ES plumes superpose. These are however still different from the spectrum recorded at the LLS plume centreline, which shows reduced large-scale fluctuations and a more prominent role of the smaller eddies in the inertial range.

Further insight into the influence of source size on the plume dynamics can be gained by considering the spatial distribution of the production $P = \overline{u_j' c'} \dfrac{\partial \overline{c}}{\partial x_j}$ ($\overline{u_j' c'}$ is the correlation between velocity and concentration fluctuations) and dissipation $\varepsilon_c = D\left(\overline{\dfrac{\partial c'}{\partial x_j}\dfrac{\partial c'}{\partial x_j}}\right)$ of the concentration variance at varying distances from the source. Following Fackrell and Robins (1982a) we deduced ε_c from the measured spectra of concentration $E(k)$ by means of the relation $E(k) = \alpha_c 2\varepsilon_c \varepsilon^{-\frac{1}{3}} k^{-\frac{5}{3}}$, with $\alpha_c = 0.6$. Even though the $-5/3$ slope inertial region in the concentration spectra is narrow compared to velocity spectra, this estimate was shown to be quite accurate compared to estimates of ε_c obtained as the residual of the concentration variance balance equations. Nevertheless, 'quite accurate' here involves errors that can reach ± 25 %.

The production term is estimated adopting a simple gradient law closure model as $P \approx D_{ty}\left(\dfrac{\partial \overline{c}}{\partial y}\right)^2 + D_{tz}\left(\dfrac{\partial \overline{c}}{\partial z}\right)^2$, where the turbulent diffusivities are computed as $D_{ty}(x) = 2\overline{u}_{\mathrm{adv}} \dfrac{\mathrm{d}\sigma_y^2}{\mathrm{d}x}$ and $D_{tz}(x) = 2\overline{u}_{\mathrm{adv}} \dfrac{\mathrm{d}\sigma_z^2}{\mathrm{d}x}$.

Vertical profiles of the variance production and dissipation (in non-dimensional form) for the two ES plumes are shown in Fig. 9 for two distances from the source. As expected,

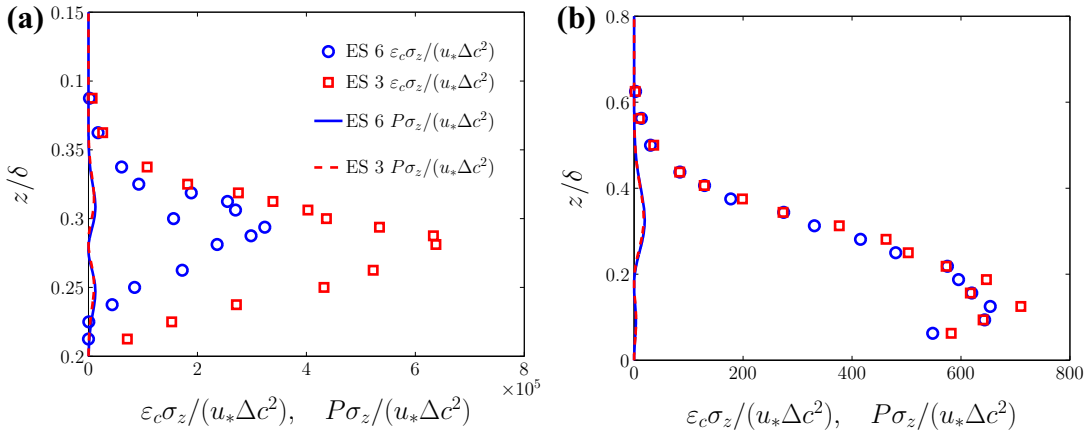

Fig. 9 Vertical profiles of the non dimensional production and dissipation of concentration fluctuations at a growing distance from the source. Comparison between the elevated sources with $\sigma_0 = 3$ mm and $\sigma_0 = 6$ mm: **a** $x/\delta = 0.625$, **b** $x/\delta = 3.75$

in the far field ($x/\delta = 3.75$) profiles of P and ε_c do not show any significant difference depending on the source size. In the near field ($x/\delta = 0.625$) the dissipation rate is higher for the small 3 mm source. At both locations, the production term for the two cases is several orders of magnitude lower than ε_c. This means that the higher σ_c^* observed for the $\sigma_0 = 3$ mm source (compared to the $\sigma_0 = 6$ mm one) has to be attributed to an enhanced production occurring very close to the source location (over a distance smaller than $x/\delta \approx 0.3$). Unfortunately, our experimental set-up does not allow us to investigate the plume for $x/\delta < 0.3125$. This would require a considerable reduction in the ethane flow rate at the source, in order to perform measurements in the FID calibration range. As discussed in Sect. 3.3, the main limitations for this are imposed by the mass-flow controller, whose error rises significantly for flow rates < 0.05 Nl min^{-1}. Further experiments are therefore needed to investigate the dynamics of the plume in this very near-field region.

5.1.3 Comparisons with Fackrell and Robins (1982a)

Passive scalar dispersion experiments performed in this study took place in a velocity field (Sect. 4) that is different than that presented in Fackrell and Robins (1982a), since it develops under the forcing action of a different free-stream velocity u_∞ and over a different wall roughness z_0, both of which result in a different ratio u_*/u_∞ (see Table 1). However, as discussed in Sect. 4.1, the two velocity fields can be considered similar, as a first approximation, since non-dimensional profiles of the velocity statistics of the two datasets show a generally good agreement. Therefore, so long as the source parameters h_s/δ and σ_0/δ remain constant, we expect the non-dimensional profiles of concentration statistics to collapse onto common curves. To that purpose it is however necessary to convert the longitudinal distances from the source to a non-dimensional time, computed as the ratio between the flight time $t = x/\overline{u}_{\mathrm{adv}}$ and a characteristic turbulent scale $\tau = \delta/u_*$.

The comparison shown in Fig. 10, concerns longitudinal profiles of three parameters, originally plotted in Fackrell and Robins (1982a). These are the non-dimensional maximal mean concentration $\max(\overline{c})$, the plume half-widths s_y and s_z (an alternative measure of the plume spread, defined as the distance at which the mean concentration falls to half

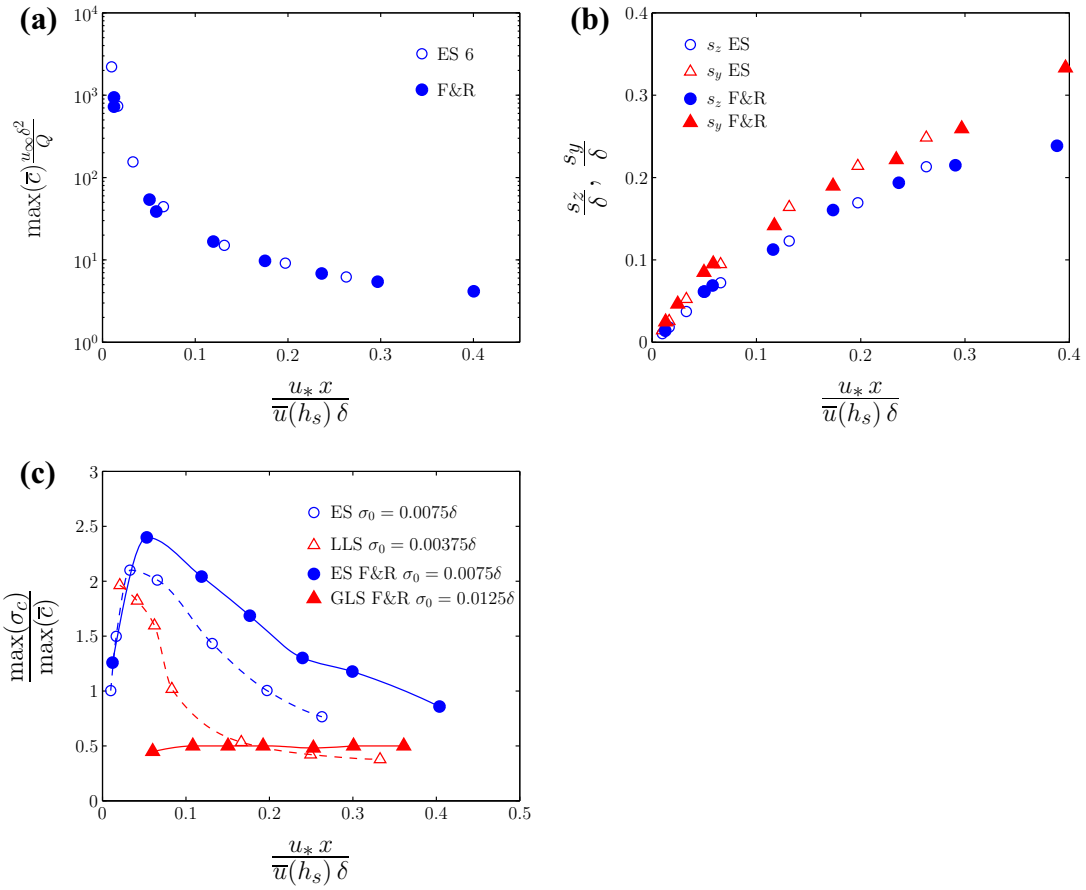

Fig. 10 Comparison with the Fackrell and Robins (1982a) results (F&R in the legend); **a** maximum concentrations at varying downwind positions $\max(\overline{c})\frac{u_\infty \delta^2}{Q}$ vs $\frac{u_*}{\overline{u}(h_s)}\frac{x}{\delta}$, **b** vertical and lateral plume half-widths $\frac{s_y}{\delta}, \frac{s_z}{\delta}$ vs $\frac{u_*}{\overline{u}(h_s)}\frac{x}{\delta}$, and **c** intensity of concentration fluctuation $\frac{\max(\sigma_c)}{\max(\overline{c})}$ vs $\frac{u_*}{\overline{u}(h_s)}\frac{x}{\delta}$

its maximum), and the intensity of concentration fluctuations computed as the ratio of the maximum r.m.s., $\max(\sigma_c)$, to $\max(\overline{c})$.

The longitudinal evolution of $\max(\overline{c})$ and of s_y and s_z for the ES plumes are indeed in very good agreement with those presented in Fackrell and Robins (1982a). Conversely, data of $\max(\sigma_c)/\max(\overline{c})$ for the ES show non-negligible differences. Even though the general tendency of the two profiles is the same, our data exhibit a lower peak value occurring closer to the source. The rate at which $\max(\sigma_c)/\max(\overline{c})$ decreases once the peak is reached appears more pronounced in our experiments. The reasons for these differences are not self-evident since they cannot be simply linked to differences in the velocity statistics. A possible explanation concerns different conditions very close to the source, where almost all of the production of σ_c occurs. There, a different source design can induce different outlet velocity profiles or different dynamics within the source wake that may significantly alter the process of variance production.

Finally we also report a comparison of $\max(\sigma_c)/\max(\overline{c})$ between our LLS and the ground-level source (GLS) of Fackrell and Robins (1982a). It should be noted that the two plumes tend to a same constant value of fluctuation intensity $\approx$0.4, except for a near-field region in which, as expected, the fluctuation intensity of our LLS is higher than that of their GLS.

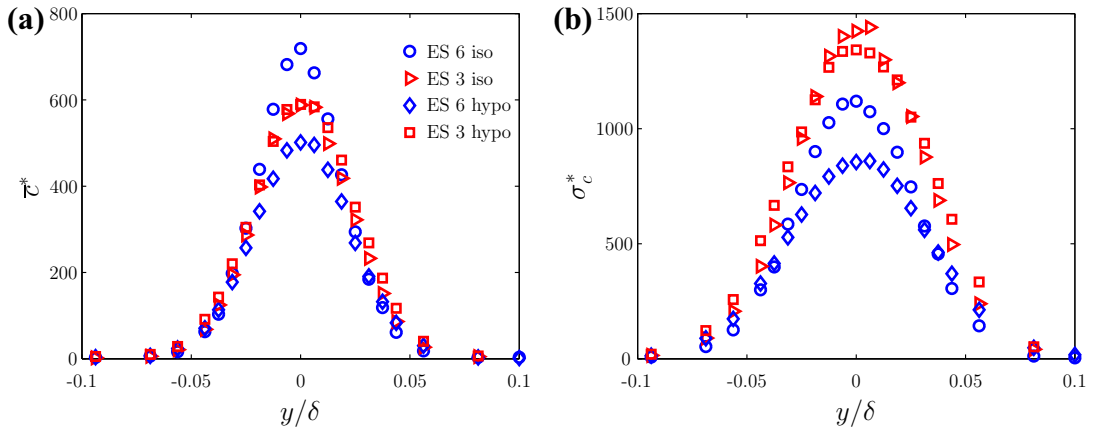

Fig. 11 Comparison between isokinetic and hypokinetic conditions: transversal profiles at $x/\delta = 0.3125$ of **a** mean concentration $\overline{c}^*$, and **b** standard deviation σ_c^*

5.2 Influence of the Emission Conditions

The evidence that most of the concentration variance is produced in a relatively limited region very close to the source emphasizes the need to analyze the effect on the concentration field of varying emission conditions (Sect. 5.1.2), which are here assumed to be fully governed by the parameter $u_s/\overline{u}_s$. The interest is focused on two emission conditions (see Sect. 3): $u_s/\overline{u}_s = 1$, i.e. isokinetic conditions, and $u_s/\overline{u}_s = 0.03$ (approximating the condition $u_s/\overline{u}_s \to 0$) referred to as hypokinetic conditions. Investigating the effect of a highly forced source condition, i.e. $u_s/\overline{u}_s \gg 1$, is conversely beyond the aim of this study.

Concentration profiles were measured close to the source, at stations $x/\delta = 0.3125$ and $x/\delta = 0.625$ (Fig. 11). Measurements show that the differences between the hypokinetic and isokinetic conditions for the $\sigma_0 = 3$ mm source are negligible at both distances. Conversely for the ES with $\sigma_0 = 6$ mm the emission conditions produce non-negligible differences in the concentration statistics at $x/\delta = 0.3125$ that are then no longer detectable at $x/\delta = 0.625$. We can therefore conclude that this effect extends over a distance $x < 80\sigma_0$, and is therefore significantly reduced compared to that induced by a variation in the source diameter.

For ES 6 mm, the hypokinetic emission produces a smaller mean concentration and standard deviation than the isokinetic emission. In a sense, we can say that generally the hypokinetic emission results in a reduced effective source, which produces therefore enhanced concentration fluctuations. In most of the studies on passive scalar dispersion in turbulent boundary layers, it is implicitly assumed that the particles emitted at the source take the statistics of the external velocity field almost instantaneously, so that there is no difference between Lagrangian statistics of the fluid particles injected at the source and those in the ambient fluid passing close to it. However it is worth noting that we do not have any information to identify which of the two conditions (isokinetic or hypokinetic) induce a concentration field that is closer to the one generated by these ideal source conditions. This is a feature that certainly deserves to be further analyzed, by comparing our experimental data with numerical results of computational fluid dynamics models or Lagrangian stochastic models obtained by varying the emission conditions at the source.

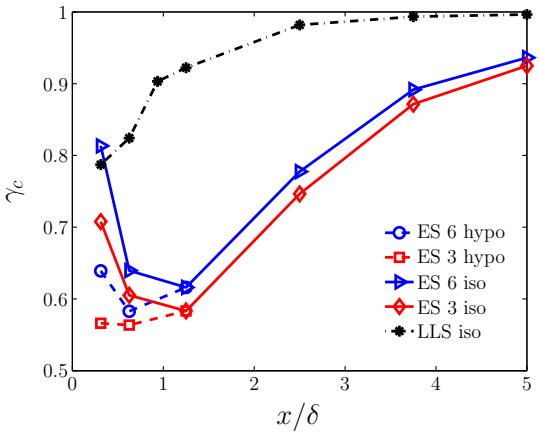

Fig. 12 Longitudinal profiles of the intermittency factor at the source height for different source conditions

5.3 Intermittency Factor

To further investigate the role of the large-scale meandering motion on the concentration fluctuation, we focus on the intermittency factor γ_c of the concentration signals. This is defined as the percentage of time for which the plume is experienced at a given point, i.e. the probability that at a position $\mathbf{x}$ and time t the concentration c is non-zero,

$$\gamma_c(\mathbf{x}, t) = \text{prob}\{c(\mathbf{x}, t) > 0\}. \tag{21}$$

A reliable determination of the intermittency depends on the fine-scale structure of turbulence, whose temporal and spatial resolutions are invariably accompanied by random instrumental noise, whose amplitude depends also on the setting of the gain with which the fluctuations of the measured signal are amplified. Given these limitations due to the instrumentation, in order to quantify γ_c we fixed a threshold value of non-dimensional concentration, referred to as Γ_t, so that

$$\gamma_c(\mathbf{x}, t) = \text{prob}\{c^*(\mathbf{x}, t) > \Gamma_t\}. \tag{22}$$

Since the need for this threshold is due to the measurement errors affecting the zero concentration values, Γ_t has to be a small constant value independent of the downwind distance. For all stations, $\Gamma_t = 1$ was chosen, an arbitrary value that allowed us to efficiently distinguish the moments when the plume is experienced by the probe and the moments of zero concentration.

Profiles of intermittency factor at the plume centreline are plotted in Fig. 12 and show that the emission conditions have an important influence on the intermittency. The channeling of the plume, produced by the isokinetic condition at the source, results in a reduced meandering and therefore in a lower intermittency of the signal (and γ_c values closer to unity). If the tracer is released hypokinetically, the plume is easily captured by the ambient eddies, which engulf the plume in a meandering motion resulting in a higher intermittency of the signal. This effect can be further amplified by the action of the unsteady wake of the source, whose effect extends up to several tens of source diameters (Nironi 2013). As already observed in Sect. 5.2, in both cases—hypokinetic and isokinetic conditions—the higher the source, the greater the influence of the emission velocity on the concentration field.

The ground-level emission is less intermittent than the elevated ones and γ_c attains unity as $x/\delta \geq 2.5$. It can be noted that, independently of the source configuration, the intermittency factor approaches unity when the plumes reach the ground and are efficiently mixed by the small-scale surface-generated turbulence that acts by suppressing concentration fluctuations.

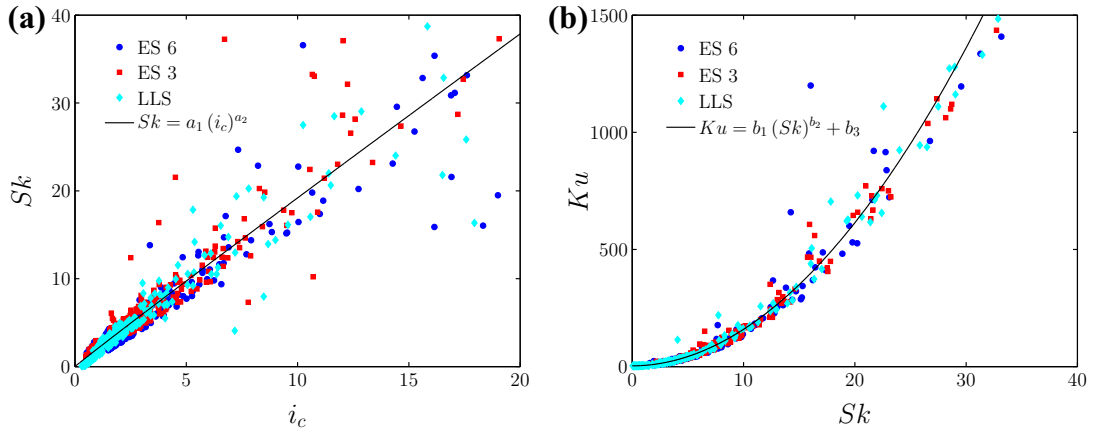

Fig. 13 **a** Skewness against intensity, **b** Kurtosis against skewness. The relations $Sk = a_1\,(i_c)^{a_2}$ and $Ku = b_1\,(Sk)^{b_2} + b_3$ are fitted to the data using least squares

5.4 Higher Order Moments and Concentration PDFs

With the aim of seeking a suitable model for the concentration PDF, and defining its dependence on the distance from the source and the emission conditions, following Mole and Clarke (1995), we began by verifying the consistency of our dataset with simple functional dependencies between moments of the concentration PDF of the form

$$Sk = a_1\,(i_c)^{a_2}, \tag{23}$$

$$Ku = b_1\,(Sk)^{b_2} + b_3, \tag{24}$$

where $i_c = \sigma_c/\overline{c}$ is the intensity of the concentration fluctuations, $Sk = \dfrac{m^{*3}_{3c}}{\sigma^{*3}_c}$ is the skewness, $Ku = \dfrac{m^{*4}_{4c}}{\sigma^{*4}_c}$ is the kurtosis and a_1, a_2, b_1, b_2, and b_3 are free parameters. These latter were determined by fitting Eqs. 23 and 24 to the data (Fig. 13). This preliminary analysis showed two main features: firstly, the values of the parameters did not show any clear dependence on the source dimension, elevation and emission velocity. Secondly, the values of the parameters provided by the best fit $a_1 = 2.01$, $a_2 = 0.98$, $b_1 = 1.67$, $b_2 = 1.97$, and $b_3 = 2.99$ were in excellent agreement with the relations $Sk = 2\,i_c$ and $Ku = 1.5\,Sk^2 + 3$ that correspond to a Gamma distribution of the form

$$p(\chi) = \frac{k^k}{\Gamma(k)}\chi^{k-1}\exp(-k\chi), \tag{25}$$

with $\Gamma(k)$ the Gamma function, $k = i_c^{-2}$ and $\chi \equiv c/\overline{c}$ (c being the sample space variable and $\overline{c}$ the mean value). These findings clearly support the existence of a universal function for the PDF of the concentration that can be suitably modelled by a family of one-parameter Gamma distributions (Villermaux and Duplat 2003; Duplat and Villermaux 2008; Yee and Skvortsov 2011).

PDFs measured on the plume centreline at various distances from the source location are plotted in Fig. 14, enlightening their link to the intensity of the concentration fluctuations i_c (Fig. 14a). The Gamma distribution (Eq. 25) is rather efficient in reproducing the changing in the shape of the PDF while increasing the distance from the source: from an exponential-like distribution in the near field, a log-normal-like distribution with short tail in the intermediate

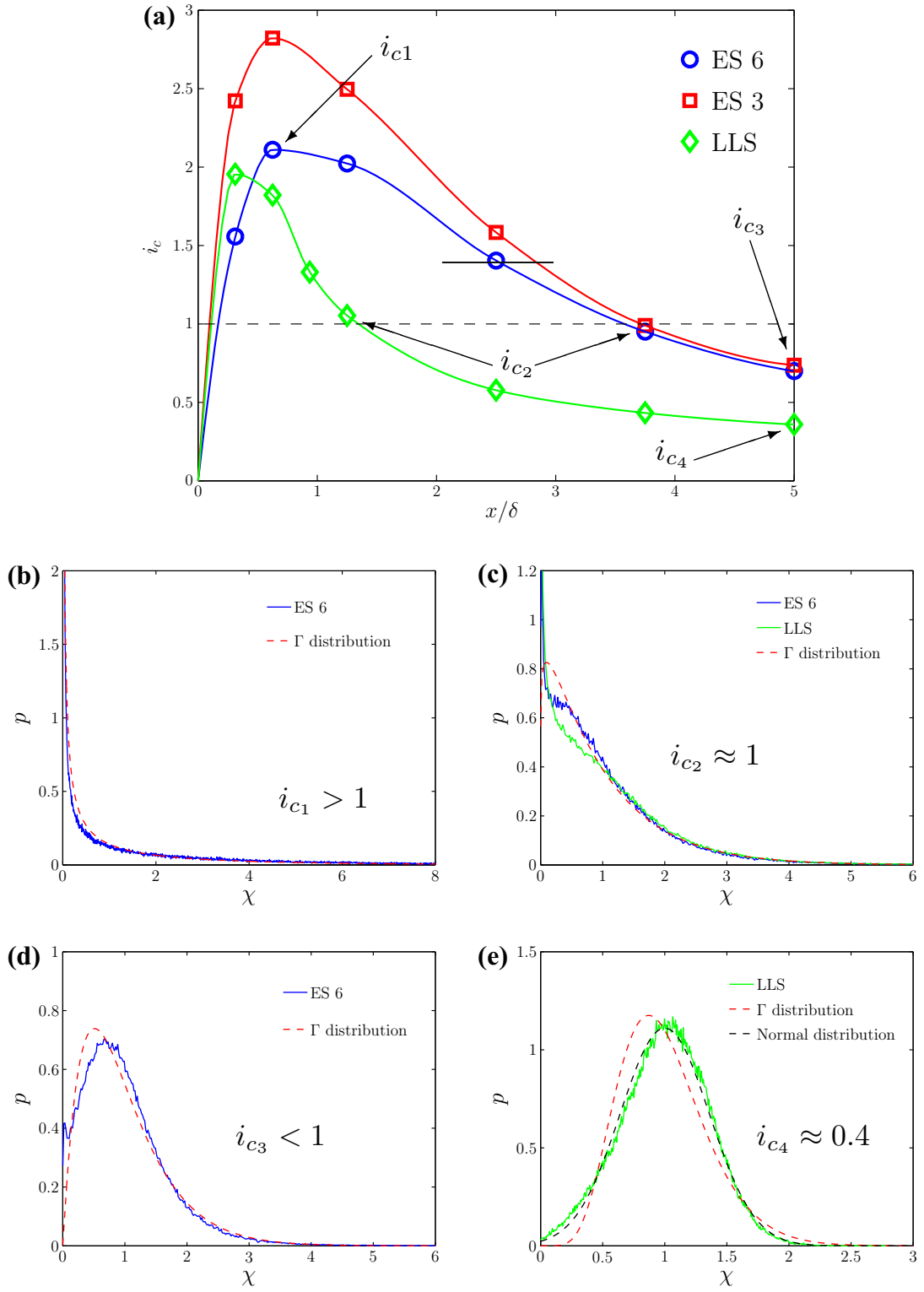

Fig. 14 Relation between the concentration fluctuation intensity i_c and the concentration PDF. Results are recorded on the plume centreline at a growing distance from the source for the three source configurations at isokinetic conditions: **a** i_c vs x/δ for ES and LLS cases. Concentration PDF p for **b** $i_c > 1$, **c** $i_c \approx 1$, **d** $i_c < 1$, **e** $i_c \approx 0.4$

field and a Gaussian-like distribution in the far field. It is worth noting that, mathematically, these transitions are fully regulated by the value of i_c only, and specifically to its value relative to unity. Physically, these transitions can be fully interpreted by an analysis of the intermittency factors γ_c.

In the near field, the plume exhibits large-scale fluctuations due to its meandering motions that result in high intermittency of the signals, i.e. low γ_c, and values of $i_c > 1$ (Fig. 14b). The maximal value of i_c, and its location with respect to the source, depend on h_s/δ and σ_0/δ. As the meandering motion is damped, due to the progressive growth of the instantaneous plume caused by relative dispersion, the intermittency is reduced (γ_c increases) and i_c decreases to reach unity (Fig. 14c), with a rate that is again significantly dependent on h_s/δ and σ_0/δ. From hereafter, meandering is suppressed and relative dispersion becomes the only mechanism controlling the turbulent transfer. The intermittency factor γ_c tends asymptotically to unity and i_c falls below one (Fig. 14d). In the very far field, as i_c tend to its asymptotic value $\approx$0.4, the concentration PDF tends to an invariant form, which approaches a clipped-Gaussian (Fig. 14e).

5.4.1 Third- and Fourth-Order Moments

In the light of the previous discussion on the form of the concentration PDF, we finally turn to the third and fourth moments of concentration. Transversal profiles of the third and fourth moments downwind from the source are presented in Fig. 15a, c, e, and in 16a, c, e for the transversal profiles, while the vertical profiles are shown in Figs. 15b, d, f, and in 16b, d, f. Third-order and fourth-order moments are shown to be very sensitive to both the source size and the source elevation. As observed for σ_c^*, the smaller source generates higher moments, due to the enhanced role of the meandering in the near field. Moving downwind, the difference between the concentration field generated by the two releases is progressively reduced (Figs. 15a, c, e, 16a, c, e) and consequently the profiles gradually approach one to the other and finally collapse at $x/\delta = 3.75$.

It is remarkable how a small difference in the source size, whose diameter varied by a factor of 2 (from 3 to 6 mm), is reflected in significant variations of higher-order moments of the concentration fluctuations, which persist up to a distance of about 3 m, i.e. in the range $500\sigma_0 < x < 1000\sigma_0$.

The source elevation is even more determinant in shaping the moment profiles. While profiles from the ES emission have a Gaussian shape, in the LLS plume the shape changes quickly in the downwind direction. At $x/\delta = 1.25$ the profiles are already characterized by a plateau at the plume centre. Further away from the source (from $x/\delta = 3.75$), as the values of both m_{3c}^* and m_{4c}^* become almost two orders of magnitude smaller than that in the near field, their profiles exhibit off-centreline peaks, showing how the intermittency is progressively reduced in the core of the plume, as the pollutant is well mixed. The third moment is the most affected by off-centreline peaks, which however appear also on m_{4c}^* profiles. Finally, we note how the plots for m_{3c}^* and m_{4c}^* show generally more scatter in the profiles compared to those of lower order moments. This is due to the undesired spikes recorded in the signals due to aerosol sampling, whose effect becomes evident as the order of the moments of the concentration PDF increases (Sect. 3.3).

Finally, we discuss the reliability of the estimates of higher order moments evaluated adopting the model provided by a simple Gamma distribution (Eq. 25) and using the experimental estimates of the concentration fluctuations i_c. Predictions of m_{3c}^* and m_{4c}^* as estimated from Eq. 25, i.e. $m_{3c\Gamma}^* = \left(\frac{2}{\sqrt{k}}\right)^{1/3} \sigma_c^*$ and $m_{4c\Gamma}^* = \left(\frac{6}{k} + 3\right)^{1/4} \sigma_c^*$, turn out to be very accurate

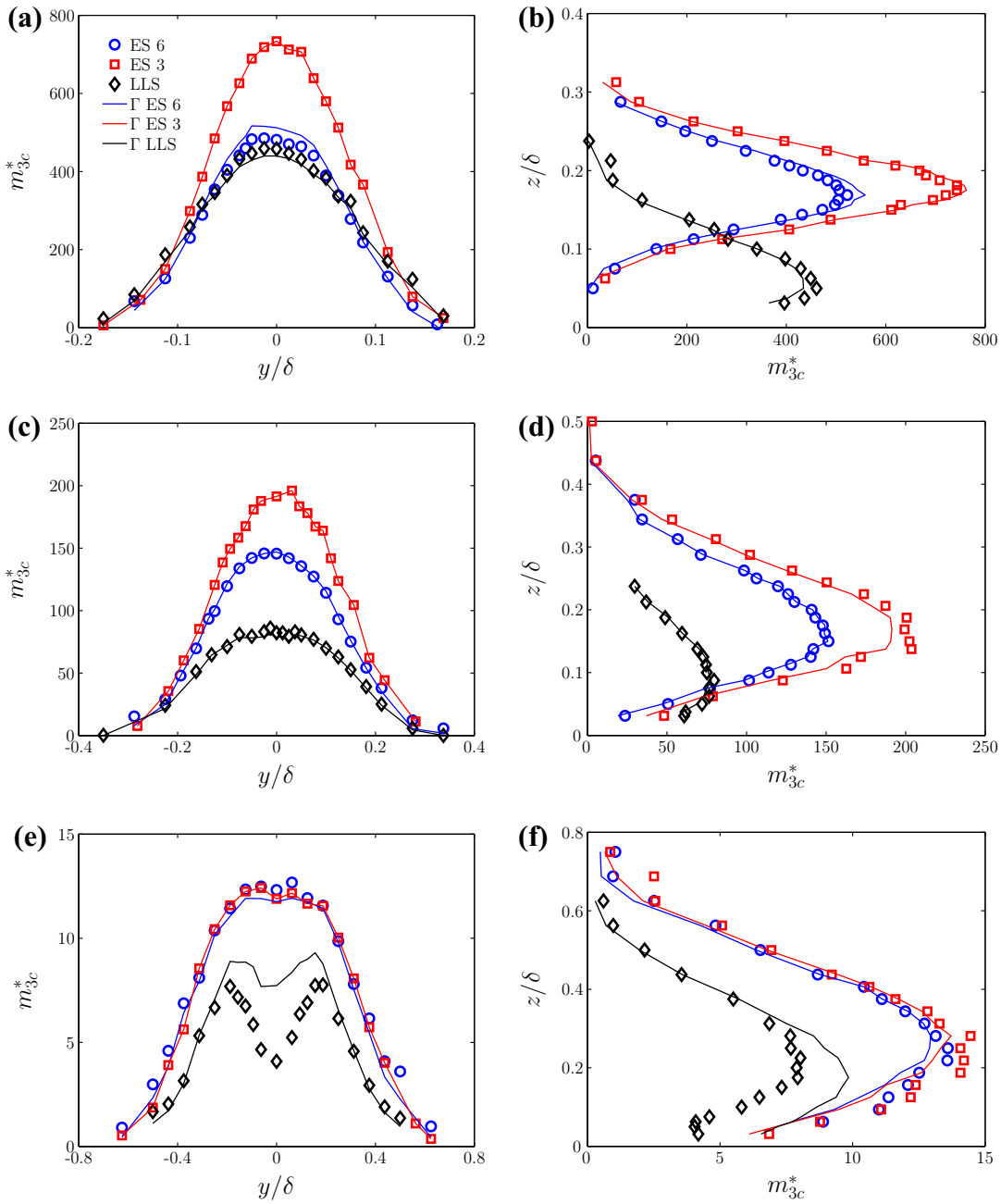

Fig. 15 Transversal profiles (at the source height) and vertical profiles (at the plume centre) of m^*_{3c} for the ES and LLS, at various distances downwind: **a** and **b** $x/\delta = 0.625$, **c** and **d** $x/\delta = 1.25$, **e** and **f** $x/\delta = 3.75$

close to the source (see Figs. 15a–d, 16a–d). Conversely, in the far field (Figs. 15e, f, 16e, f), we observe discrepancies between the Gamma distribution predictions and experiments. At the plume core, for the ES case, $m^*_{3c\Gamma}$ and $m^*_{4c\Gamma}$ tend to underestimate experimental data, especially the fourth-order moments, whereas the estimates of m^*_{3c} still present a good accuracy. These discrepancies are particularly evident in the far field for the LLS case, where the third-order and fourth-order moments exhibit off-centreline peaks and the Gamma distribution provides a substantial overestimate of the experimental data. A possible explanation of this lost of accuracy is that in the far field the concentration PDF (at the plume centreline) of the LLS relaxes towards a normal distribution (Fig. 14e) and then Eq. 25 provides solutions

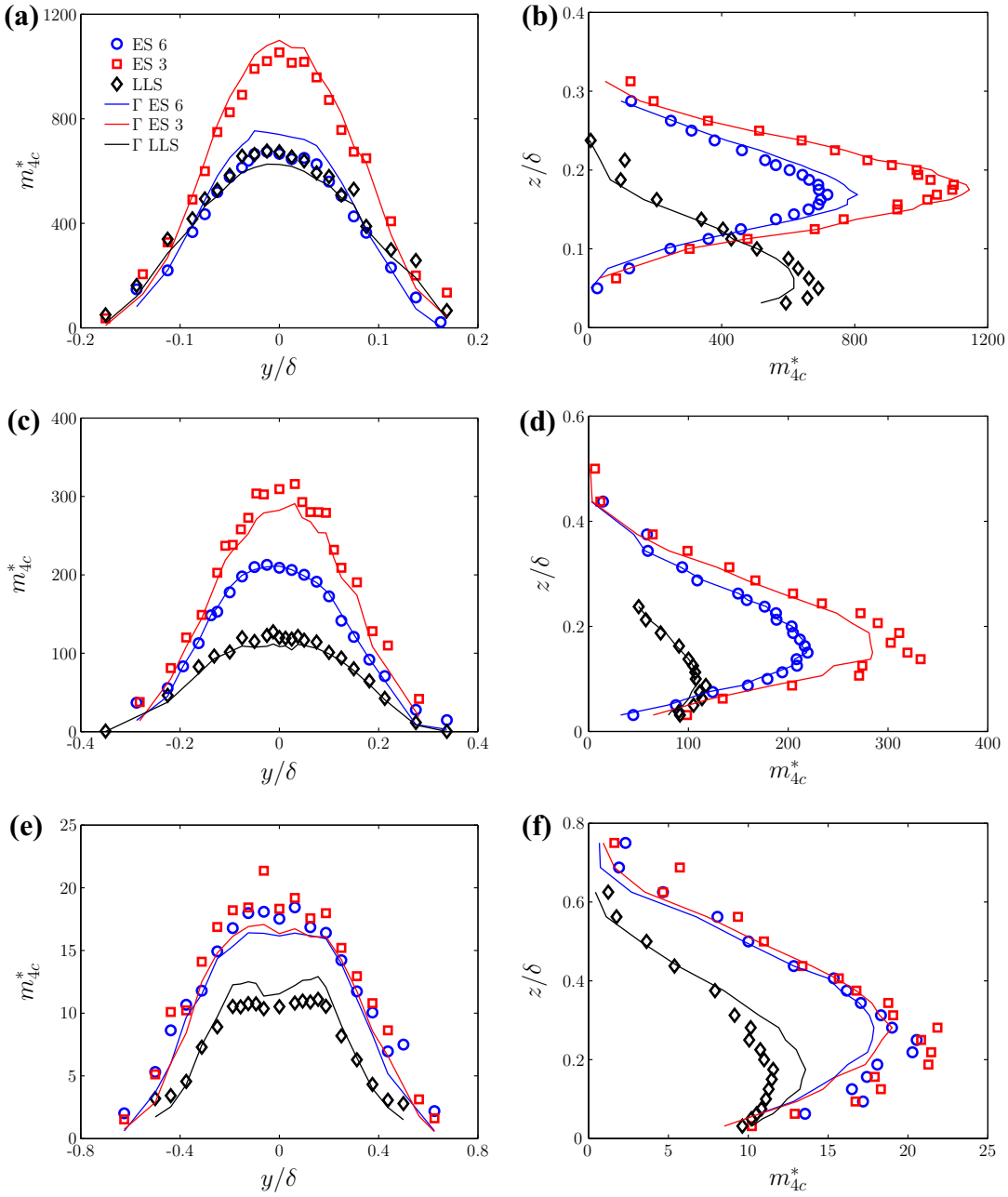

Fig. 16 Transversal profiles (at the source height) and vertical profiles (at the plume centre) of m^*_{4c} for the ES and LLS, at various distances downwind: **a** and **b** $x/\delta = 0.625$, **c** and **d** $x/\delta = 1.25$, **e** and **f** $x/\delta = 3.75$

that are less reliable. However, these comparisons clearly show that a simple Gamma PDF can be assumed as a suitable model to compute the high order moments in the whole domain.

6 Conclusions

We have investigated experimentally the dispersion of a passive scalar emitted within a turbulent boundary layer from a localized source with varying configurations. With the aim of extending the work of Fackrell and Robins (1982a) on concentration fluctuations, we

characterized the spatial evolution of the concentration statistics with a focus of the first four moments of the concentration PDF. The experimental results also include a detailed description of the structure of the turbulent boundary layer within which the dispersion process takes place, which is shown to be similar to that reproduced by Fackrell and Robins (1982a) in their experiments. The investigation of the velocity field is performed by analyzing the vertical profiles of one- and two-point velocity statistics. In particular, the latter allowed us to provide a direct estimate of the integral length scales of the flow. These were subsequently used to infer the characteristic integral time scale, which represents a key parameter for the modelling of atmospheric pollutant dispersion.

We discussed the influence of the source configuration on the dispersion by analyzing three main aspects: the source elevation, the source size and the gas emission velocity. Our results show that the source size and elevation have a major influence on the spatial distribution of the higher moments of the concentration PDF. This can be explained by an interaction of the plume during its initial stage of growth with the different scales of motion in the surrounding atmospheric flow. These effects are more and more evident as the moments of the PDF increase, and persist over a distance that is almost three orders of magnitude larger than the source size.

The production of turbulent fluctuations occurs in a region very close to the source, and is therefore likely to be highly influenced by the emission condition and the design of the source. The variation of the emission conditions at the source from isokinetic to hypokinetic can affect the concentration field over a distance of a few tens of source diameters, therefore lower than that in the case of a varying diameter. Decreasing the velocity of the emission results in a reduced effective source size, which implies an increased intermittency of the plume.

Our experimental data generally confirm the results of Fackrell and Robins (1982a) on the effects of source size and elevation on the concentration field. Considering an elevated source, the spatial distribution of the mean concentrations agrees very well with their data, whereas discrepancies are observed in the longitudinal profiles of the intensity of the concentration fluctuations. The reasons for these differences are not fully clear. It is suggested that these may be related to the influence of a slightly different source design on the plume dynamics in its initial phase of growth.

Finally, the experimental non-dimensional PDF is shown to be very well modelled by a Gamma distribution for any of the source configuration considered, irrespective of the source conditions. This implies that the higher order concentration moments can be fully expressed as a function of only one parameter, the intensity of the concentration fluctuation $i_c = \sigma_c/\overline{c}$.

Acknowledgments The authors would like to express their gratitude to D. Cane for his support in artworks and to O. Marsden for carefully reading the manuscript and providing a critical review of its content.

References

Amicarelli A, Salizzoni P, Leuzzi G, Monti P, Soulhac L, Cierco FX, Leboeuf F (2012) Sensitivity analysis of a concentration fluctuation model to dissipation rate estimates. Int J Environ Pollut 48:164–173

Andronopoulos S, Grigoriadis D, Robins A, Venetsanos A, Rafailidis S, Bartzis J (2002) Three-dimensional modeling of concentration fluctuations in complicated geometry. Environ Fluid Mech 1:415–440

Arya PS (1999) Air pollution meteorology and dispersion. Oxford University Press, UK, 310 pp

Bergametti G, Dutot AL, Buat-Ménard P, Losno R, Remoudaki E (1989) Seasonal variability of the elemental composition of atmospheric aerosol particles over the northwestern Mediterranean. Tellus 41B:353–361

Bewley GP, Chang K, Bodenschatz E (2012) On integral length scales in anisotropic turbulence. Phys Fluids 24:061702

Carlotti P, Drobinski P (2004) Length scales in wall-bounded high-Reynolds-number turbulence. J Fluid Mech 516:239–264
Cassiani M, Franzese P, Giostra U (2005a) A PDF micromixing model of dispersion for atmospheric flow. Part I: development of the model, application to homogeneous turbulence and neutral boundary layer. Atmos Environ 39:1457–1469
Cassiani M, Franzese P, Giostra U (2005b) A PDF micromixing model of dispersion for atmospheric flow. Part II: application to convective boundary layer. Atmos Environ 39:1471–1479
Chatwin PC, Sullivan PJ (1990) A simple and unifying physical interpretation of scalar fluctuations measurements from many turbulent shear flows. J Fluid Mech 212:533–556
Du S, Sawford BL, Wilson JD (1995) Estimation of the Kolmogorov constant for the Lagrangian structure function, using a second order Lagrangian model of grid turbulence. Phys Fluids 7:3083–3090
Duplat J, Villermaux E (2008) Mixing by random stirring in confined mixtures. J Fluid Mech 617:51–86
Durbin PA (1980) A stochastic model of two-particles dispersion and concentration fluctuations in homogeneous turbulence. J Fluid Mech 100:279–302
Fackrell JE (1980) A flame ionisation detector for measuring fluctuating concentration. J Phys E Sci Instrum 13:888–893
Fackrell JE, Robins AG (1982a) Concentration fluctuations and fluxes in plumes from point sources in a turbulent boundary layer. J Fluid Mech 117:1–26
Fackrell JE, Robins AG (1982b) The effects of source size on concentration fluctuations in plumes. Boundary-Layer Meteorol 22:335–350
Franzese P (2003) Lagrangian stochastic modeling of a fluctuating plume in the convective boundary layer. Atmos Environ 37:1691–1701
Frisch U (1995) Turbulence. Cambridge University Press, UK, 296 pp
Gifford F (1959) Statistical properties of a fluctuating plume dispersion model. Adv Geophys 6:117–137
Hall DJ, Emmott MA (1991) Avoiding aerosol sampling problems in fast response flame ionisation detectors. Exp Fluids 10:237–240
Hilderman T, Wilson DJ (2007) Predicting plume meandering and averaging time effects on mean an fluctuating concentrations in atmospheric dispersion simulated in a water channel. Boundary-Layer Meteorol 122:535–575
Hinze JO (1975) Turbulence. McGraw-Hill, New York, 790 pp
Jackson PS (1981) On the displacement height in the logarithmic velocity profile. J Fluid Mech 111:15–25
Jiménez J (2004) Turbulent flows over rough walls. Annu Rev Fluid Mech 36:173–196
Jorgensen FE (2002) How to measure turbulence with hot-wire anemometers—a practical guide. Technical report, Dantec Dynamics
Kaimal JC, Wyngaard JC, Izumi J, Coté OR (1972) Spectral characteristics of surface-layer turbulence. Q J R Meteorol Soc 98:563–589
Klein PM, Young DT (2011) Concentration fluctuations in a downtown urban area. Part I: analysis of Joint Urban 2003 full-scale fast-response measurements. Environ Fluid Mech 11:23–42
Klein PM, Leitl B, Schatzmann M (2011) Concentration fluctuations in a downtown urban area. Part II: analysis of Joint Urban 2003 wind tunnel measurements. Environ Fluid Mech 11:43–60
Krogstad PA, Antonia RA (1994) Structure of turbulent boundary layers on smooth and rough walls. J Fluid Mech 277:1–21
Leuzzi G, Amicarelli A, Monti P, Thomson DJ (2012) A 3D Lagrangian micromixing dispersion model LAGFLUM and its validation with a wind tunnel experiment. Atmos Environ 54:117–126
Lewis DM, Chatwin PC, Mole N (1997) Investigation of the collapse of the skewness and kurtosis exhibited in atmospheric dispersion data. Il Nuovo Cimento 20 C:385–398
Lien R, D'Asaro EA (2002) The Kolmogorov constant for the Lagrangian velocity spectrum structure function. Phys Fluids 14:4456–4459
Luhar AK, Hibberd MF, Borgas MS (2000) A skewed meandering plume model for concentration statistics in the convective boundary layer. Atmos Environ 34:3599–3616
Marro M, Nironi C, Salizzoni P, Soulhac L (2015) Dispersion of a passive scalar from a point source in a turbulent boundary layer. Part II: analytical modelling. Boundary-Layer Meteorol. doi:10.1007/s10546-015-0041-9
Milliez M, Carissimo B (2008) Computational fluid dynamical modelling of concentration fluctuations in an idealized urban area. Boundary-Layer Meteorol 127(2):241–259
Mole N, Clarke E (1995) Relationships between higher moments of concentration and of dose in turbulent dispersion. Boundary-Layer Meteorol 73:35–52
Nironi C (2013) Concentration fluctuations of a passive scalar in a turbulent boundary layer. PhD Thesis, Ecole Centrale de Lyon

Philips DA, Rossi R, Iaccarino G (2013) Large-eddy simulation of passive scalar dispersion in an urban-like canopy. J Fluid Mech 723:404–428
Pope SB (2000) Turbulent flows. Cambridge University Press, UK, 771 pp
Postma JV, Wilson DJ, Yee E (2011) Comparing two implementations of a micromixing model. Part I: wall shear-layer flows. Boundary-Layer Meteorol 140:207–224
Raupach M, Coppin P (1983) Turbulent dispersion from an elevated line source: measurements of wind concentration moments and budgets. J Fluid Mech 136:111–137
Raupach MR, Thom AS, Edwards I (1980) A wind-tunnel study of turbulent flow close to regularly arrayed rough surfaces. Boundary-Layer Meteorol 18:373–397
Rizza U, Mangia C, Carvalho JC, Anfossi D (2006) Estimation of the Lagrangian velocity structure function constant C_0 by large-eddy simulation. Boundary-Layer Meteorol 120:25–37
Salizzoni P, Soulhac L, Mejean P, Perkins R (2008) Influence of a two scale surface roughness on a turbulent boundary layer. Boundary-Layer Meterorol 127(1):97–110
Sawford B (2004) Micro-mixing modelling of scalar fluctuations for plumes in homogeneous turbulence. Flow Turbul Combust 72:133–160
Sawford B, Hunt JCR (1986) Effects of turbulence structure, molecular diffusion and source size on scalar fluctuations in homogeneous turbulence. J Fluid Mech 165:373–400
Sawford B, Stapountzis H (1986) Concentration fluctuations according to fluctuating plume models in one and two dimensions. Boundary-Layer Meteorol 37:89–105
Schopflocher TP, Sullivan PJ (2005) The relationship between skewness and kurtosis of a diffusing scalar. Boundary-Layer Meteorol 115:341–358
Sykes RI, Lewellen WS, Parker SF (1984) A turbulent-transport model for concentration fluctuations and fluxes. J Fluid Mech 139:193–218
Takimoto H, Inagaki A, Kanda M, Sato A, Michioka T (2013) Length-scale similarity of turbulent organised structures over surfaces with different roughness types. Boundary-Layer Meteorol 147:217–236
Taylor G (1921) Diffusion by continuous movements. Proc Lond Math Soc 20:196–211
Tennekes H (1982) Similarity relations, scaling laws and spectral dynamics. In: Niewstadt F, Van Dop H (eds) Atmospheric turbulence and air pollution modelling. D. Reidel Publishing Company, Dordrecht, pp 37–68
Tennekes H, Lumley JL (1972) A first course in turbulence. MIT Press, Cambridge, MA, 300 pp
Thom AS (1971) Momentum absorption by vegetation. Q J R Meteorol Soc 97:414–428
Tritton DJ (1988) Physical fluid dynamics. Oxford Science Publications, UK, 519 pp
Villermaux E, Duplat J (2003) Mixing as an aggregation process. Phys Rev Lett 91:184501
Vinkovic I, Aguirre C, Simoëns S (2006) Large-eddy simulation and Lagrangian stochastic modeling of passive scalar dispersion in a turbulent boundary layer. J Turbul 7:1–14
Xie Z, Hayden P, Voke P, Robins A (2004) Large-eddy simulation of dispersion: comparison between elevated and ground-level sources. J Turbul 5:1–16
Yee E (2009) Probability law of concentration in plumes dispersing in an urban area. Environ Fluid Mech 9:389–407
Yee E, Biltof CA (2004) Concentration fluctuation measurements in a plume dispersing through a regular array of obstacles. Boundary-Layer Meteorol 111:363–415
Yee E, Chan R (1997) A simple model for the probability density function of concentration fluctuations in atmospheric plumes. Atmos Environ 31:991–1002
Yee E, Skvortsov A (2011) Scalar fluctuations from a point source in a turbulent boundary layer. Phys Rev E 84:036306
Yee E, Wilson DJ (2000) A comparison of the detailed structure in dispersing tracer plumes measured in grid-generated turbulence with a meandering plume model incorporating internal fluctuations. Boundary-Layer Meteorol 94:253–296
Yee E, Chan R, Kosteniuk PR, Chandler GM, Biltoft CA, Bowers JF (1994) Incorporation of internal fluctuations in a meandering plume model of concentration fluctuations. Boundary-Layer Meteorol 67:11–39

7.2 Analytical modelling

Boundary-Layer Meteorol (2015) 156:447–469
DOI 10.1007/s10546-015-0041-9

ARTICLE

Dispersion of a Passive Scalar Fluctuating Plume in a Turbulent Boundary Layer. Part II: Analytical Modelling

Massimo Marro[1] · Chiara Nironi[1] · Pietro Salizzoni[1] · Lionel Soulhac[1]

Received: 20 December 2013 / Accepted: 11 May 2015 / Published online: 26 May 2015

Abstract We investigate the reliability of a meandering plume model in reproducing the passive scalar concentration statistics due to a continuous release in a turbulent boundary layer. More specifically, we aim to verify the physical consistency of the parametrizations adopted in the model through a systematic comparison with experimental data. In order to perform this verification, we take advantage of the velocity and concentration measurements presented in part I of the present study (Nironi et al., Boundary-Layer Meteorol, 2015) particularly concerning estimates of the Eulerian integral length scales and the higher order moments of the concentration probability density function. The study is completed by a sensitivity analysis in order to estimate the effects of the variations of the key parameter to the model results. In the light of these results, we discuss the benefits and shortcomings of this modelling approach and its suitability for operational purposes.

Keywords Atmospheric turbulence · Concentration · Fluctuating plume · Meandering · Pollutant dispersion · Probability density function · Relative dispersion

1 Introduction

Fluctuating plume dispersion models are conceived to estimate the concentration statistics of a pollutant dispersing within a turbulent flow. Compared to other modelling approaches, such as micro-mixing Lagrangian models (Sawford 2004; Cassiani et al. 2005; Leuzzi et al. 2012; Amicarelli et al. 2012; Cassiani 2013) and large-eddy simulations (Xie et al. 2004; Vinkovic et al. 2006), their relatively simple formulation makes them suitable for operational purposes.

✉ Pietro Salizzoni
pietro.salizzoni@ec-lyon.fr

[1] Laboratoire de Mécanique des Fluides et d'Acoustique, University of Lyon, CNRS UMR 5509 Ecole Centrale de Lyon, INSA Lyon, Université Claude Bernard, 36, avenue Guy de Collongue, 69134 Ecully, France

The basic principle of this modelling approach (Gifford 1959) is to split the total plume dispersion into two components: meandering and relative dispersion. The first mechanism describes the fluctuation of the plume centroid, whereas the relative dispersion drives the spreading of a plume element around its centre of mass. The two mechanisms can be treated as independent, as long as it is assumed that they are related to spatial scales separated by several orders of magnitude. As pointed out by Yee et al. (1994), and as discussed later, this hypothesis is strictly valid only close to the source or in the far field. In between there does not exist a clear spectral gap between the scales of motion contributing to the plume meandering and those associated with the relative dispersion. Despite this theoretical weakness, this modelling approach was shown to be quite robust in simulating the dispersion of a passive scalar in a variety of turbulent flows (Fackrell and Robins 1982; Sawford and Stapountzis 1986; Yee et al. 1994; Franzese 2003).

Adopting this assumption, the concentration probability density function (PDF), p, can be written as the convolution of the PDF of the location of the cloud instantaneous centroid, p_m, characterizing the large-scale random crosswind displacements of the centre of mass, and the PDF of the concentration in the meandering reference scheme (y_m, z_m), p_{cr},

$$p(c; x, y, z) = \int_0^\infty \int_{-\infty}^\infty p_{cr}(c; x, y, z, y_m, z_m)\, p_m(x, y_m, z_m) \mathrm{d}y_m \mathrm{d}z_m, \tag{1}$$

where c is the instantaneous concentration. Once p is known, the moments of the concentration can be computed as,

$$\overline{c^n}(x, y, z) = \int_0^\infty c^n\, p(c; x, y, z) \mathrm{d}c. \tag{2}$$

The practice of partitioning the concentration fluctuations depending on the their characteristic length scales was originally introduced by Gifford (1959). He proposed a model for dispersion in isotropic and homogeneous turbulence, neglecting the role of internal concentration fluctuations, so that p_{cr} was parametrized by the Dirac delta function δ_D,

$$p_{cr}(c; x, y, z, y_m, z_m) = \delta_D \left\{ c - \overline{c}_r(x, y, z, y_m, z_m) \right\}, \tag{3}$$

where $\overline{c}_r$ is the mean concentration relative to the instantaneous plume centroid. The assumption of negligible internal fluctuations is reliable for short times, so far as meandering is the mechanism governing the dispersion process. It becomes unrealistic in the far field, where the role of relative dispersion overcomes that of meandering.

This relatively simple model was shown to reliably predict the main features characterizing the near-field dynamics of a fluctuating plume emitted from an elevated source. Fackrell and Robins (1982) simulated the effect of a varying source size on the intensity of the concentration fluctuation in an anisotropic and non-homogeneous velocity field. According to their analysis, this can be attributed to the different role of the meandering motion, whose intensity increases as the source size decreases, since the range of scales of the turbulent motion, that are responsible for displacing the plume centre of mass, widens. The model is also able to distinguish between the different shapes that the concentration PDF assumes according to the type of source (Sawford and Stapountzis 1986), predicting a unimodal PDF for the point source and a bimodal PDF for the line source, in agreement with experimental observations.

The role of the relative in-plume fluctuations was firstly taken into account by Yee et al. (1994) who introduced the intensity of the relative concentration fluctuations i_{cr} as a new parameter, defined as the ratio between the standard deviation of the mean relative concen-

tration, σ_{cr}, and $\overline{c}_r$. The overall statistics of the relative dispersion were then parametrized by means of a Gamma distribution,

$$p_{cr}(c; x, y, z, y_m, z_m) = \frac{\lambda^\lambda}{\overline{c}_r \Gamma(\lambda)} \left(\frac{c}{\overline{c}_r}\right)^{\lambda-1} \exp\left(-\frac{\lambda c}{\overline{c}_r}\right), \tag{4}$$

where $\Gamma(\lambda)$ is the gamma function and $\lambda = 1/i_{cr}^2$. A one-dimensional formulation of the model was tested against in situ measurements of concentrations (Yee et al. 1994) at different heights above the ground within an atmospheric boundary layer over a uniform flat terrain. A two-dimensional formulation of the model for homogeneous and isotropic turbulence was tested by Yee and Wilson (2000) against water-plume measurements of the first four moments of the concentration PDF of a passive scalar dispersing in grid turbulence. In order to reliably model the anisotropy and the inhomogeneity of the velocity field within a turbulent boundary layer, several authors (Reynolds 2000; Luhar et al. 2000; Franzese 2003; Mortarini et al. 2009) have reconstructed the spatial evolution of the vertical component of the plume centroid PDF, p_{zm}, by means of stochastic Lagrangian models simulating the trajectories of the puff centre of mass. Cassiani and Giostra (2002) have also developed a generalized approach that allows p_{zm} to be computed by means of a mean concentration field, without the need for a Lagrangian particle model. All the above-mentioned models include a simple formulation of i_{cr} that is assumed to depend on the longitudinal coordinate only. More complex parametrizations of i_{cr} have been proposed only recently. Gailis et al. (2007) introduced a three-dimensional model of i_{cr} to predict the concentration PDF within a dispersion plume in a group of obstacles. This same parametrization was used by Ferrero et al. (2013) to compute the concentration statistics of two reactive chemical species within a convective boundary layer.

In this paper, we present a formulation of the fluctuating plume model (Sect. 2) and discuss the parametrizations that render the model suitable for simulating the dispersion process within a turbulent neutral boundary layer (Sect. 3). In particular, we aim to analyze the consistency of these parametrizations in the light of the experimental characterization of the velocity field performed by Nironi et al. (2015), especially concerning the estimates of the Eulerian integral length scales (Sect. 3.1). Subsequently, the focus is on i_{cr} (Sect. 3.2) that is modelled adopting two different parametrizations. Assuming $i_{cr} = i_{cr}(x)$ (Sect. 3.2.1), the formulation of the meandering model leads to an analytical solution for $p(c; x, y, z)$, whereas assuming $i_{cr} = i_{cr}(x, y, z)$ (Sect. 3.2.2) leads to a semi-analytical solution. Both formulations are compared to the experimental wind-tunnel results of Nironi et al. (2015), providing a unique dataset concerning the spatial distribution of the first four moments of the concentration PDF (Sect. 4). Finally we perform an error and sensitivity analysis of several key parameters (Sect. 5) to determine the robustness and accuracy of the model and discuss its advantages and shortcomings, as well as its suitability for operational purposes (Sect. 6).

2 Meandering Plume Model

We consider a source of diameter σ_0 located at coordinates $(0, y_s, z_s)$ within a turbulent boundary layer of depth δ. Following Yee and Wilson (2000) and Luhar et al. (2000) we assume the statistical independence of the plume meandering in the lateral and vertical directions, so that p_m can be expressed as the product of two components, p_{ym} and p_{zm},

$$p_m(x, y_m, z_m) = p_{ym}(x, y_m) p_{zm}(x, z_m). \tag{5}$$

We stress here that this assumption is not supported by any theoretical consideration, but is rather justified by the need for simplicity in the formulation of the model.

Since the velocity statistics are assumed to be homogeneous in the horizontal planes, the crosswind distribution of the centroid locations is Gaussian,

$$p_{ym}(x, y_m) = \frac{1}{\sqrt{2\pi}\sigma_{ym}} \exp\left(-\frac{(y_m - y_s)^2}{2\sigma_{ym}^2}\right), \tag{6}$$

where σ_{ym} is the centroid horizontal spread.

Conversely, p_{zm} requires a slightly more complex formulation in order to account for the effects of ground reflection and the non-homogeneity of the velocity statistics in the vertical direction. This is modelled by means of the following reflected Gaussian distribution (Arya 1999),

$$p_{zm}(x, z_m) = \frac{1}{\sqrt{2\pi}\sigma_{zm}} \left\{\exp\left[-\frac{(z_m - z_s)^2}{2\sigma_{zm}^2}\right] + \exp\left[-\frac{(z_m + z_s)^2}{2\sigma_{zm}^2}\right]\right\}, \tag{7}$$

where σ_{zm} is the vertical spread of the plume centroid. In the presence of one boundary, a reflected Gaussian ensures a constant mass flux $\int_0^\infty p_{zm} \mathrm{d}z_m = 1$ through any vertical section perpendicular to the wind direction, a constraint that is not satisfied by a simple Gaussian model far from the source, which gives

$$\frac{1}{\sqrt{2\pi}\sigma_{zm}} \int_0^\infty \exp\left(-\frac{(z_m - z_s)^2}{2\sigma_{zm}^2}\right) \mathrm{d}z_m = \frac{1}{2}\left(1 + \mathrm{erf}\left(\frac{z_s}{\sqrt{2}\sigma_{zm}}\right)\right) \leq 1. \tag{8}$$

Note that different atmospheric stability conditions can alter significantly the shape of p_{zm}. For a detailed discussion on this topic, see Luhar et al. (2000) and Franzese (2003).

Similarly, to account for the anisotropy of the relative dispersion, we parametrize the relative mean concentration $\overline{c}_r$ as

$$\overline{c}_r = \frac{M_q}{\overline{u}_m} p_{yr}(x, y, y_m)\, p_{zr}(x, z, z_m), \tag{9}$$

where M_q is the mass flow rate and $\overline{u}_m = \overline{u}(\overline{z}_m)$ is the mean cloud advection velocity. This parameter, as well as all other velocity statistics—mean velocity, velocity variances and turbulent kinetic energy (TKE) dissipation rate—used in the model, is evaluated at the plume centroid $\overline{z}_m(x)$ and therefore depends solely on the downwind distance from the source. The implications of this assumption on the results are discussed in Sect. 5.2. The functions p_{yr} and p_{zr} are the lateral and vertical distributions of the mean concentration around the plume centroid and are modelled as,

$$p_{yr} = \frac{1}{\sqrt{2\pi}\sigma_{yr}} \exp\left(-\frac{(y - y_m)^2}{2\sigma_{yr}^2}\right), \tag{10}$$

$$p_{zr} = \frac{1}{\sqrt{2\pi}\sigma_{zr}} \left\{\exp\left(-\frac{(z - z_m)^2}{2\sigma_{zr}^2}\right) + \exp\left(-\frac{(z + z_m)^2}{2\sigma_{zr}^2}\right)\right\}, \tag{11}$$

where σ_{yr} and σ_{zr} are the relative plume spreads around the plume's centre of mass in the horizontal and vertical directions, respectively.

Substituting Eqs. 4, 6, 7 and 9 into Eq. 2 and solving the integral in the variable c, we obtain the n-th concentration moment as function of the position in space (x, y, z),

$$\begin{aligned}
\overline{c^n}(x,y,z) &= \int_0^\infty p_{zm}\,\mathrm{d}z_m \int_{-\infty}^\infty p_{ym}\,\mathrm{d}y_m \int_0^\infty c^n\, p_{cr}(c;x,y,z,y_m,z_m)\,\mathrm{d}c \\
&= \int_0^\infty p_{zm}\,\mathrm{d}z_m \int_{-\infty}^\infty \frac{1}{\lambda^n}\frac{\Gamma(n+\lambda)}{\Gamma(\lambda)}\overline{c}_r^n\, p_{ym}\,\mathrm{d}y_m \\
&= \left(\frac{M_q}{2\pi\sigma_{yr}\sigma_{zr}\overline{u}_m}\right)^n \frac{1}{2\pi\sigma_{ym}\sigma_{zm}} \\
&\quad\times \int_{-\infty}^\infty \exp\left(-\frac{(y_m-y_s)^2}{2\sigma_{ym}^2}\right)\exp\left(-\frac{n\,(y-y_m)^2}{2\sigma_{yr}^2}\right)\mathrm{d}y_m \\
&\quad\times \int_0^\infty \frac{1}{\lambda^n}\frac{\Gamma(n+\lambda)}{\Gamma(\lambda)}\left\{\exp\left(-\frac{(z_m-z_s)^2}{2\sigma_{zm}^2}\right)+\exp\left(-\frac{(z_m+z_s)^2}{2\sigma_{zm}^2}\right)\right\} \\
&\quad\times \left\{\exp\left(-\frac{(z-z_m)^2}{2\sigma_{zr}^2}\right)+\exp\left(-\frac{(z+z_m)^2}{2\sigma_{zr}^2}\right)\right\}^n \mathrm{d}z_m. \qquad (12)
\end{aligned}$$

In Sect. 3.2 we provide analytical and semi-analytical solutions of Eq. 12, depending on the formulation of $\lambda = 1/i_{cr}^2$.

3 Set of Model Parameters

In order to have a complete formulation of the model, we need to parametrize σ_y, σ_{yr}, σ_{ym}, σ_z, σ_{zr}, σ_{zm}, and i_{cr}. To this end, we take advantage of the information provided by the experimental investigation of the velocity and concentration field presented in Nironi et al. (2015). The analysis is performed for the emissions released from three different sources of varying size σ_0/δ and elevation z_s/δ (see Table 1).

3.1 Parametrization of the Plume Spreads

The global plume spreads are related to the spread of the plume centroid and to the relative spread by the following relations (Gifford 1959),

$$\sigma_y^2 = \sigma_{ym}^2 + \sigma_{yr}^2, \qquad (13)$$

$$\sigma_z^2 = \sigma_{zm}^2 + \sigma_{zr}^2. \qquad (14)$$

There are therefore two independent plume spread parameters that have to be set. Following Luhar et al. (2000) and Franzese (2003) we model the global spreads σ_y and σ_z, the relative spreads σ_{yr} and σ_{zr}, and then obtain σ_{ym} and σ_{zm} by means of Eqs. 13 and 14.

Table 1 Diameter σ_0 and height z_s of the three sources

	σ_0/δ	z_s/δ
Elevated Source ES 3	0.00375	0.19
Elevated Source ES 6	0.0075	0.19
Low-Level Source LLS	0.00375	0.06

The global spreads are parametrized according to Taylor's statistical theory as Nironi et al. (2015),

$$\sigma_y^2 = \frac{\sigma_0^2}{6} + 2\sigma_v^2 T_{Lv}\left\{t - T_{Lv}\left[1 - \exp\left(-\frac{t}{T_{Lv}}\right)\right]\right\}, \tag{15}$$

$$\sigma_z^2 = \frac{\sigma_0^2}{6} + 2\sigma_w^2 T_{Lw}\left\{t - T_{Lw}\left[1 - \exp\left(-\frac{t}{T_{Lw}}\right)\right]\right\}, \tag{16}$$

where σ_v and σ_w are the standard deviations of the transverse and vertical velocity component, T_{Lv} and T_{Lw} are Lagrangian time scales, and $t = x/\overline{u}_m$ is the flight time. As is customary (Tennekes 1982), the Lagrangian time scales are parametrized as $T_{Lv} = \frac{2\sigma_v^2}{C_0\varepsilon}$ and $T_{Lw} = \frac{2\sigma_w^2}{C_0\varepsilon}$, where C_0 is the Kolmogorov constant assumed here equal to 4.5 (Nironi et al. 2015), and ε is the mean dissipation rate of the TKE.

The parametrization of the relative dispersion coefficients, σ_{yr} and σ_{zr}, has to satisfy two asymptotic conditions (for brevity we report only those of σ_{yr}, since the same conditions are imposed on σ_{zr}, see Franzese 2003; Franzese and Cassiani 2007),

$$t \to 0 \qquad \sigma_{yr}^2 = (C_r/6)\varepsilon\,(t_s + t)^3, \tag{17}$$

$$t \to \infty \qquad \sigma_{yr}^2 \to \sigma_y^2 = 2\sigma_v^2 T_{Lv} t, \tag{18}$$

where C_r is the Richardson–Obukhov constant and $t_s = \left[\sigma_0^2/(C_r\varepsilon)\right]^{1/3}$ represents the flight time needed by a plume emitted from a virtual point source to expand to the size σ_0.

Equation 17 follows from the Richardson–Obukhov law for a finite source size (Ott and Mann 2000; Franzese and Cassiani 2007) and models the cloud spreading as a function of the flight time t (Richardson 1926) and ε (Obukhov 1941). Equation 18 is the Taylor's limit for large dispersion time, which applies to σ_{yr} (and σ_{zr}) when the meandering process becomes negligible and the relative dispersion approaches the global dispersion. The objective is to define a suitable transition between the two asymptotic behaviours. To that purpose we adopt an approach similar to that proposed by Luhar et al. (2000) and Franzese (2003). In contrast to them, we introduce the time scales T_{my} and T_{mz}. These are needed in order to ensure that the transition from the inertial scaling to the diffusive asymptotic scaling is consistent with the main characteristics of the large-scale dynamics of the velocity field, presented in Nironi et al. (2015). The evolutions of σ_{yr}^2 and σ_{zr}^2 are then modelled as

$$\sigma_{yr}^2 = \frac{(C_r/6)\varepsilon\,(t_s + t)^3}{\left\{1 + \left[(C_r/6)\varepsilon t^2/\left(2\sigma_v^2 T_{Lv}\right)\right]^{2/5}\right\}^{5/2}} \exp\left[-\left(\frac{t}{T_{my}}\right)^2\right] + \sigma_y^2\left\{1 - \exp\left[-\left(\frac{t}{T_{my}}\right)^2\right]\right\}, \tag{19}$$

$$\sigma_{zr}^2 = \frac{(C_r/6)\varepsilon\,(t_s + t)^3}{\left\{1 + \left[(C_r/6)\varepsilon t^2/\left(2\sigma_w^2 T_{Lw}\right)\right]^{2/5}\right\}^{5/2}} \exp\left[-\left(\frac{t}{T_{mz}}\right)^2\right] + \sigma_z^2\left\{1 - \exp\left[-\left(\frac{t}{T_{mz}}\right)^2\right]\right\}, \tag{20}$$

so that the spatial evolutions of σ_{yr} and σ_{zr} are therefore a function of the parameters T_{my}, T_{mz} and C_r, whose setting is discussed in the following paragraphs.

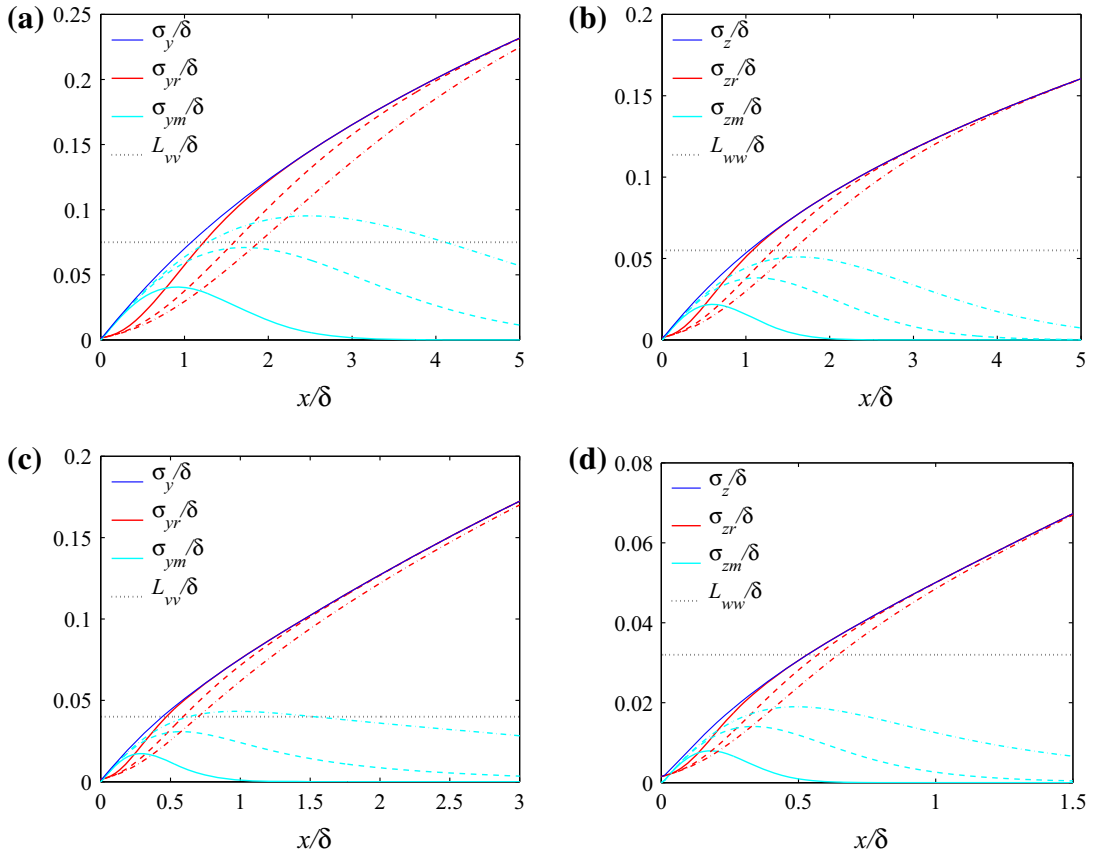

Fig. 1 Modelled transverse and vertical dispersion coefficients varying α_T ($C_0 = 4.5$ and $C_r = 0.8$): **a**, **b** ES 3 source; **c**, **d** LLS source. *Solid line* $\alpha_T = 1$, *dash line* $\alpha_T = 2$, *dash-dot line* $\alpha_T = 3$. The *black-dotted lines* represent reference values of the Eulerian integral length scales L_{vv} and L_{ww} at source height, as estimated by Nironi et al. (2015)

3.1.1 The Time Scales T_{my} and T_{mz}

The time scales T_{my} and T_{mz} can be thought of as thresholds beyond which relative dispersion becomes the prevalent mechanism. This occurs when the size of the relative plume exceeds that of the largest scale eddies ($\mathcal{L}$), so that the contribution of the TKE to the fluctuations of the cloud centroid becomes negligible. It is questionable if the quantity $\mathcal{L}$ refers to Lagrangian statistics, as proposed by Franzese and Cassiani (2007), or to Eulerian statistics. The latter are adopted here, since we dispose of the direct measurements of the Eulerian integral length scales L_{vv} and L_{ww} (Nironi et al. 2015).

Both T_{my} and T_{mz} are assumed to be proportional to the Lagrangian time scales, $T_{my} = \alpha_{Ty} T_{Lv}$ and $T_{mz} = \alpha_{Tz} T_{Lw}$. In order to define the value of the proportionality coefficients α_{Ty} and α_{Tz}, we analyze the evolution of σ_{yr} and σ_{zr}, as given by Eqs. 19 and 20, and we compare it with the experimental estimates of L_{vv} and L_{ww} evaluated at source height z_s. In doing that, we fix the value of the Richardson–Obukhov constant $C_r = 0.8$ (the sensitivity to C_r is discussed in Sect. 3.1.2). The evolution of σ_{yr} and σ_{zr}, as well as that of σ_{ym} and σ_{zm}, is plotted in Fig. 1 for varying values of $\alpha_{Ty} = \alpha_{Tz} = 1, 2, 3$. As expected, the plot shows that the behaviour of the dispersion coefficients depends on the source elevation. In particular the spreads due to the centre of mass, σ_{ym} and σ_{zm}, for the elevated source ES (Fig. 1a, b) are larger than those of the low-level source LLS (Fig. 1c, d). This can be explained

by two features. Firstly, in the lower part of the boundary layer the size of the most energetic eddies is smaller and, as a consequence, the effects on the dispersion due to the displacement of the plume centroid are significantly reduced. Secondly, the effects of the ground (Luhar et al. 2000; Franzese 2003) result in a more rapid damping of the plume meandering in the vertical direction (Fig. 1b, d) with respect to the transverse coordinate (Fig. 1a, c).

The aim here is to define α_{Ty} and α_{Tz} so that σ_{ym} and σ_{zm} do not exceed L_{vv} and L_{ww}, respectively, (Fig. 1) as σ_{yr} and σ_{zr} attain their asymptotic values. The choice of the most appropriate α_{Ty} and α_{Tz} is somehow arbitrary. In order to constrain the degree of freedom of the model in the parameter space, we impose $\alpha_{Ty} = \alpha_{Tz} = \alpha_T$, a condition that may not be appropriate for any source configurations (as a crosswind line source). Adopting these criteria yields $\alpha_T = 2$. It is worth noting that, in the present case study, the original formulation proposed by Luhar et al. (2000) and Franzese (2003), i.e. without the corrective terms involving T_{my} and T_{mz} in Eqs. 19 and 20, leads to a slower increase of σ_{yr} and σ_{zr} with the distance from the source, implying an unphysical growth of σ_{ym} and σ_{zm} to values exceeding the Eulerian scales. Finally, we point out that the characteristic length scales of the meandering and relative dispersion processes are well-separated only very close to the source and in the far field (where $\sigma_{my}, \sigma_{mz} \to 0$). However, as expected (Fig. 1), this hypothesis is not verified in an intermediate region that actually covers most of the investigated domain, both for the ES and LLS cases.

3.1.2 Richardson–Obukhov Constant C_r

Values of C_r are affected by a significant uncertainty. In homogeneous and isotropic turbulence, estimates obtained with direct numerical simulations are approximately in the range $0.4 < C_r < 0.8$ (Ishihara and Kaneda 2002; Boffetta and Sokolov 2002; Biferale et al. 2005), and in non-homogeneous and anisotropic turbulence the range is further widened. Franzese (2003) adopted $C_r = 1.4$ in a convective boundary layer whereas Mortarini et al. (2009) assumed $C_r = 0.06$ in a plant canopy.

In order to emphasize the influence on the model due to the Richardson–Obukhov constant variations, in Fig. 2 we plot $\frac{\sigma_{ym}}{\sigma_y}$, $\frac{\sigma_{zm}}{\sigma_z}$, $\frac{\sigma_{yr}}{\sigma_y}$, and $\frac{\sigma_{zr}}{\sigma_z}$ as a function of the downwind distance from the source, for values of C_r spanning a range consistent with the literature data, i.e.

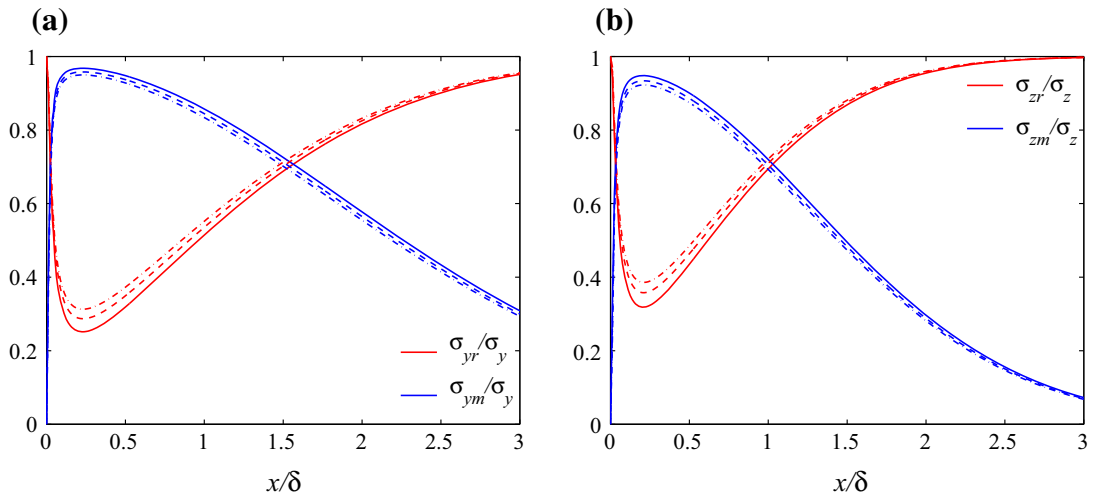

Fig. 2 **a** σ_{yr}/σ_y, σ_{ym}/σ_y, and **b** σ_{zr}/σ_z, σ_{zm}/σ_z vs x/δ for ES 3 varying $C_r = 0.4, 0.8, 1.2$ ($C_0 = 4.5$ and $\alpha_T = 2$); *solid line* $C_r = 0.4$, *dash line* $C_r = 0.8$, *dash-dot line* $C_r = 1.2$

$C_r = 0.4-1.2$. The effects of the variations of C_r are significantly reduced compared to those of α_T, plotted in Fig. 1. Nevertheless, the influence of C_r is non-negligible in an intermediate region (see Fig. 2), from $x/\delta \approx 0.2$ up to $x/\delta \approx 1.5$, within which it can appreciably affect the model results. According to Franzese and Cassiani (2007), the quantity C_r/C_0 should be fixed and equal to $1/11$. Since we adopted $C_0 = 4.5$ this leads to $C_r \approx 0.4$. However, for reasons that will be made clear in the next paragraph (Sect. 3.2), this value was not consistent with the formulation of the model for i_{cr}. We have therefore assumed $C_r = 0.8$ which implies a ratio $C_r/C_0 \approx 0.17$. Note however that this value is quite close to the theoretical value suggested by Franzese and Cassiani (2007) compared to those presented in previous studies (Franzese 2003 imposed $C_r/C_0 \approx 0.5$ and Mortarini et al. 2009 assumed $C_r/C_0 \approx 1/33$).

3.2 Parametrization of the Intensity of Relative Concentration Fluctuations

The determination of the spatial evolution of the intensity of relative concentration fluctuations i_{cr} is a key aspect in the formulation of the meandering models. The dependence of this parameter on the flow dynamics and emission conditions however has been rarely characterized either experimentally or numerically. As far as we know, the only attempt to measure this parameter is that of Gailis et al. (2007), who studied the dispersion of a passive scalar with optical measurement techniques within both a turbulent boundary layer and an obstacle array. Given this lack of information, most of the meandering plume models found in the literature (Luhar et al. 2000; Yee and Wilson 2000; Franzese 2003; Mortarini et al. 2009) adopt quite simple models for i_{cr}, which is generally assumed to be dependent on the x-coordinate only. This assumption however can significantly deteriorate the numerical results in the far field. As shown by Mortarini et al. (2009), to avoid this lack of accuracy of the model it is then necessary to impose an unphysical growth of i_{cr} for increasing distance from the source.

In what follows, we consider two different formulations of the model. In the first case we consider $i_{cr} = i_{cr}(x)$, in the second case $i_{cr} = i_{cr}(x, y, z)$. Both formulations are set in order to ensure the physical consistency of the model with respect to the evolution of the intensity of the concentration fluctuations, $i_c = \sigma_c/\overline{c}$, determined experimentally in the wind-tunnel experiments presented in Nironi et al. (2015).

3.2.1 1-D Model of i_{cr}

In the case of $i_{cr} = i_{cr}(x)$, Eq. 12 can be solved analytically, leading to

$$\begin{aligned}\overline{c^n}(x,y,z) = &\left(\frac{M_q}{2\pi\sigma_{yr}\sigma_{zr}\overline{u}_m}\right)^n \frac{\sigma_{yr}}{\left(n\sigma_{ym}^2+\sigma_{yr}^2\right)^{0.5}} \frac{\sigma_{zr}}{\left(n\sigma_{zm}^2+\sigma_{zr}^2\right)^{0.5}} \frac{1}{\lambda^n} \frac{\Gamma(n+\lambda)}{\Gamma(\lambda)} \\ &\times \exp\left[-\frac{n(y-y_s)^2}{2\left(n\sigma_{ym}^2+\sigma_{yr}^2\right)}\right] \sum_{k=0}^{n} \left\{ \binom{n}{k} \exp\left[-\frac{(n-k)(z-z_s)^2}{2(n\sigma_{zm}^2+\sigma_{zr}^2)}\right] \right. \\ &\left. \times \exp\left[-\frac{k(z+z_s)^2}{2(n\sigma_{zm}^2+\sigma_{zr}^2)}\right] \exp\left[-\frac{(2z)^2 k(n-k)}{2(n\sigma_{zm}^2+\sigma_{zr}^2)} \frac{\sigma_{zm}^2}{\sigma_{zr}^2}\right] \right\}, \end{aligned} \tag{21}$$

where $\binom{n}{k}$ is the binomial coefficient.

With some algebra, Eq. 21 can be rearranged in order to illustrate the relation between i_{cr} and i_c on the plume centreline ($y = y_s, z = z_s$),

$$i_{cr}^2 = \left(i_c^2 + 1\right) F_c - 1, \tag{22a}$$

$$\begin{aligned} F_c = & \frac{\sigma_{yr}\sqrt{2\sigma_{ym}^2 + \sigma_{yr}^2}}{\sigma_y^2} \frac{\sigma_{zr}\sqrt{2\sigma_{zm}^2 + \sigma_{zr}^2}}{\sigma_z^2} \\ & \times \left\{ 1 + 2\exp\left(-\frac{2(z_s)^2}{(2\sigma_{zm}^2 + \sigma_{zr}^2)}\right) \exp\left(-\frac{2(z_s)^2}{(2\sigma_{zm}^2 + \sigma_{zr}^2)} \frac{\sigma_{zm}^2}{\sigma_{zr}^2}\right) \right. \\ & \left. + \exp\left(-\frac{4(z_s)^2}{(2\sigma_{zm}^2 + \sigma_{zr}^2)}\right) \right\}^{-1} \left\{ 1 + \exp\left(-\frac{2(z_s)^2}{\sigma_z^2}\right) \right\}^2, \end{aligned} \tag{22b}$$

where the evolution of F_c is fully determined by the parametrization (Sect. 3.1) of the plume spreads (total, relative and centroid position). For all release conditions i_c is larger than i_{cr} close to the release point, where the meandering process is significant both for the ES and LLS cases. Moving away from the source, the relative dispersion becomes the prevalent mechanism and $i_{cr} \to i_c$.

As Eq. 22b clearly shows, the model of i_{cr} depends on the distribution of i_c, which therefore requires an independent estimate. To overcome this problem, Yee et al. (1994) and Yee and Wilson (2000) have set i_{cr} by fitting models of the form of Eq. 22b to the experimental estimates of i_c. Following this same approach, we then turn to the experimental values of $i_c(x, y_s, z_s)$ collected by Nironi et al. (2015). By substituting these data in Eq. 22b we determined i_{cr} at six different distances from the source. Since two asymptotic bounds have to be satisfied at source location ($x \to 0$) and in the very far field ($x \to \infty$), the following rational curve was used to fit the i_{cr} estimates,

$$i_{cr} \to 0 \qquad \text{at } \frac{x}{\delta} \to 0, \tag{23a}$$

$$i_{cr} \to i_c = \frac{\sigma_c}{\overline{c}} \neq 0 \qquad \text{at } \frac{x}{\delta} \to \infty, \tag{23b}$$

$$i_{cr} = x_{ad} \frac{p_1 x_{ad}^2 + p_2 x_{ad} + p_3}{x_{ad}^3 + q_1 x_{ad}^2 + q_2 x_{ad} + q_3}, \tag{23c}$$

where $x_{ad} = x/\delta$. The values of the parameters in Eq. 23c for the three cases considered are computed with the method of least-squares and are summarized in Table 2.

As discussed in Sect. 3.1.2, the values of i_{cr} close to the source depend significantly on the choice of C_r (with variations of order 30 %). In particular, for $C_r = 0.4$, we found unphysical negative values of i_{cr}. We have therefore excluded this value, even though it is supported by the theoretical analysis proposed by Franzese and Cassiani (2007), and adopted $C_r = 0.8$ instead.

Figure 3 shows a comparison at increasing distances from the source between the experimental values of i_c, measured on the plume centreline, and the values of i_{cr} computed through

Table 2 Coefficients used in Eq. 23c to calculate i_{cr}

	p_1	p_2	p_3	q_1	q_2	q_3
ES 3	0.35	−1.30	24.54	1.74	−0.58	9.95
ES 6	0.35	0.56	38.64	8.47	−8.70	25.18
LLS	0.35	−0.65	5.97	2.50	−0.55	1.20

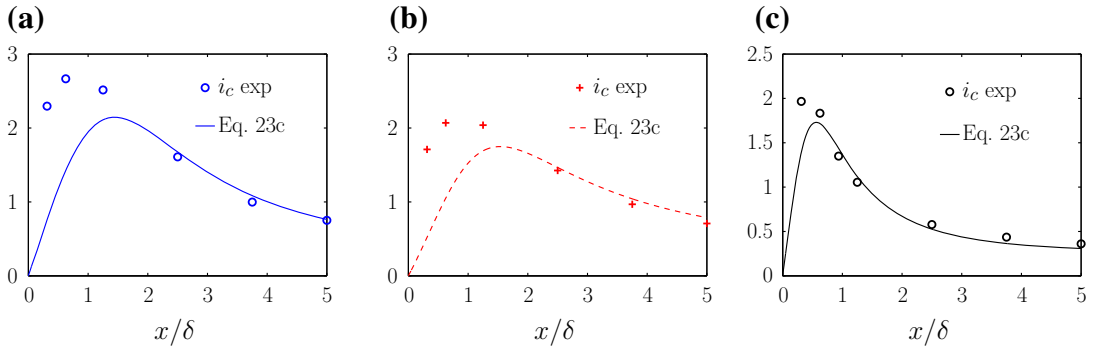

Fig. 3 Experimental values of i_c (*symbols*) and i_{cr} computed through Eq. 23c (*lines*) vs x/δ at the plume centreline: **a** ES 3, **b** ES 6, **c** LLS

Eq. 23c. In both ES and LLS cases, i_{cr} exhibits an initial growth and thereafter decreases monotonically to an asymptotic value, which is reached far from the source. As the meandering motion weakens, i_{cr} correctly approaches i_c. In the ES case the meandering influence disappears later ($x/\delta \approx 2$, Fig. 3a, b) in accordance with the model of σ_{ym} and σ_{zm} (Fig. 1). Conversely, in the LLS case the fluctuation of the plume centre of mass is damped very rapidly by the presence of the ground and $i_{cr} \to i_c$ at $x/\delta \approx 1$ (Fig. 3c). In both cases, the model leads to the same asymptotic value of the relative concentration fluctuations (at $x/\delta \to \infty$, $i_{cr} \to 0.35$).

It is worth mentioning that as $i_{cr} \to i_c$ the intermittency in the core of the plume is suppressed. Note that according to the analysis performed in Sect. 5.3 and Sect. 5.4 in Nironi et al. (2015), this actually takes place at distances ($x/\delta \approx 3.75$ for the ES) that are larger than those predicted by the present model ($x/\delta \approx 2.5$ for the ES, see Fig. 3a, b). In this sense, the model is not fully consistent with the experimental data in this intermediate region between the near and the far field.

As shown in Fig. 3, the model reproduces a dependence of i_{cr} on the source size and elevation. The dependence on z_s is due to the inhomogeneity of the velocity field, whereas the influence of σ_0 is not easily explained. According to this model, the increased intensity i_c observed for the smaller source size is due partially to the increased intensity of the meandering motion and partially to an increased intensity of the relative concentration fluctuations. It is questionable if this trend represents the real physics of the phenomenon or if it has to be attributed to a fictitious effect related to the formulation of the model. The answer to this question, however, can be given only through a direct estimate of i_{cr} by means of experiments or direct numerical simulations.

3.2.2 3-D Model of i_{cr}

By means of experimental measurements, Gailis et al. (2007) showed that the lateral and vertical profiles of i_{cr} exhibit large variations on the y–z plane. Based on these measurements, they proposed to parametrize i_{cr} as a function of the mean relative concentration $\overline{c}_r$,

$$i_{cr}^2(x, y, z) = [1 + i_{cr0}^2(x)] \left[\frac{\overline{c}_r(x, y, z)}{\overline{c}_r(x, y_m, z_m)} \right]^{-\zeta(x)} - 1, \tag{24}$$

where, for each transverse section corresponding to a given distance x, i_{cr0} is the minimum of i_{cr}, ζ is a shape parameter depending on the longitudinal coordinate and $\overline{c}_r(x, y_m, z_m)$ is the mean relative concentration evaluated at the instantaneous plume centroid. The same

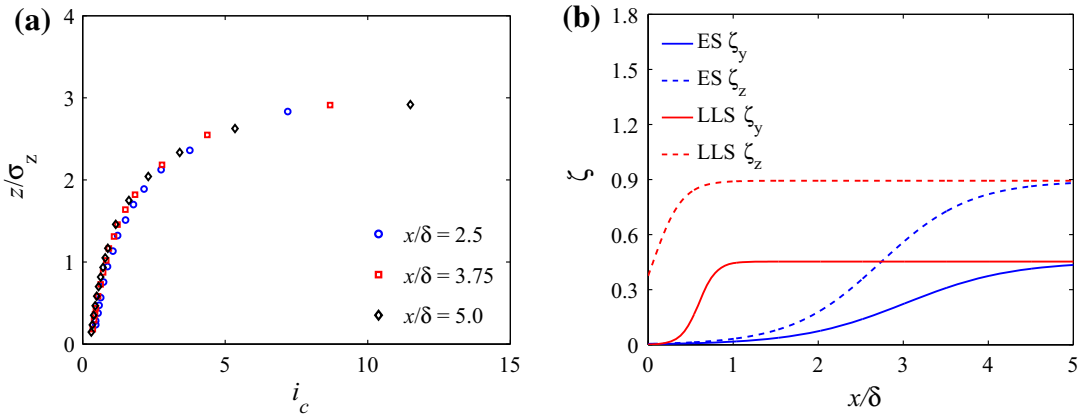

Fig. 4 **a** Self-similarity of the vertical profiles of i_c in the far field, experimental data for the LLS from Nironi et al. (2015); **b** shape parameters ζ_y and ζ_z vs x/δ

parametrization was assumed by Ferrero et al. (2013) in a convective boundary layer. We adopt here a similar formulation, which we slightly modify by introducing two shape parameters, ζ_y and ζ_z, to take into account the effects of anisotropy in the y and z directions,

$$\begin{aligned} i_{cr}^2 = (1 + i_{cr0}^2) &\left\{ \exp\left(-\frac{(y - y_m)^2}{2\sigma_{yr}^2} \right) \right\}^{-\zeta_y} \\ &\times \left\{ \exp\left(-\frac{(z - z_m)^2}{2\sigma_{zr}^2} \right) + \exp\left(-\frac{(z + z_m)^2}{2\sigma_{zr}^2} \right) \right\}^{-\zeta_z} \\ &\times \left\{ 1 + \exp\left(-\frac{(2z_m)^2}{2\sigma_{zr}^2} \right) \right\}^{\zeta_z} - 1, \end{aligned} \tag{25}$$

where the longitudinal evolution of i_{cr0} remains the same as that defined in the previous paragraph (Sect. 3.2.1).

The evolution of the shape parameters ζ_y and ζ_z with x has been modelled in order to ensure consistency with the main feature characterizing the plume relative dispersion. Close to the source the size of the cloud relative to the plume centroid, σ_{yr} and σ_{zr}, is smaller than the Eulerian integral length scale and mixing with the ambient air is due to eddies whose size ranges from the Kolmogorov scale to that of the cloud itself. We can then expect an efficient mixing within the core of the plume, leading to an almost uniform i_{cr} with respect to y and z directions. Conversely, in the far field σ_{yr} and σ_{zr} approach respectively σ_y and σ_z and exceed significantly the Eulerian integral length scale, so that mixing with ambient air is due to eddies smaller than the plume. The intermittency of the entrainment of ambient air within the plume produces high fluctuations of the relative concentration at the edges of the plume, that are progressively reduced approaching the core. In this case, i_{cr} depends on y- and z-coordinates and the form of its transverse and vertical profiles varies with downwind distance from the source and tends to a self-similar behaviour in the far field. This tendency can be reproduced by modelling the shape parameters with a sigmoid function, viz.

$$\zeta = \frac{\alpha_1}{\alpha_2 + \exp\left(-\alpha_3 \frac{x}{\delta}\right)}. \tag{26}$$

Close to the source location $i_{cr}(x) \approx i_{cr0}(x)$ and, therefore, ζ_y and ζ_z should assume values close to zero. The values of α_1 and α_2 have been set in order to fit the self-similar profile of i_c observed experimentally in the LLS case (see Fig. 4a) at large distance from the

Table 3 Sigmoid function coefficients

	LLS		ES	
	ζ_y	ζ_z	ζ_y	ζ_z
α_1	1.43×10^{-3}	0.65	3.58×10^{-3}	5.0×10^{-3}
α_2	3.16×10^{-3}	0.72	7.9×10^{-3}	5.6×10^{-3}
α_3	9.64	5.8	1.6	1.9

Table 4 a_j coefficients evaluated through Eq. 28 for the first four concentration moments

n	a_0	a_1	a_2	a_3
1	1			
2	0	1		
3	0	−1	2	
4	2	2	−7	6

source. The values of α_3 drive the transition between the asymptotic states corresponding to the near and far fields. The spatial extent of this transition is small for the LLS plume, since the profiles of i_c rapidly attain self-similarity, and larger for the ES plume. Therefore, moving away from the source, ζ_y and ζ_z increase and tend to different values, giving an i_{cr} that is shaped differently in the transverse and vertical directions. The values of the coefficients α_1, α_2 and α_3 adopted in our model are reported in Table 3 and the resulting downwind variations of ζ_y and ζ_z are plotted in Fig. 4b.

Substituting Eqs. 25 and 26 in Eq. 12, we obtain an analytical solution in y_m and an integral in z_m, that has to be solved numerically. The moments of the concentration are then given by the following relation,

$$\overline{c^n}(x,y,z) = \left(\frac{M_q}{2\pi\sigma_{yr}\sigma_{zr}\overline{u}_m}\right)^n \int_0^\infty \sum_{j=0}^{n-1} \left\{ a_j \left[(i_{cr0}^2+1)\left(1+\exp\left(-\frac{4z_m^2}{2\sigma_{zr}^2}\right)\right)^{\zeta_z} \times \left(\frac{1}{\sqrt{2\pi}\sigma_{zr}\, p_{zr}}\right)^{\zeta_z}\right]^j \frac{\sigma_{yr}}{\sqrt{(n-j\zeta_y)\sigma_{ym}^2+\sigma_{yr}^2}} \times \exp\left(-\frac{(n-j\zeta_y)(y-y_s)^2}{2((n-j\zeta_y)\sigma_{ym}^2+\sigma_{yr}^2)}\right)\right\} \left(\sqrt{2\pi}\sigma_{zr}\, p_{zr}\right)^n p_{zm}\, \mathrm{d}z_m \tag{27}$$

where a_j are the coefficients of the polynomial

$$P(x) = \sum_{j=0}^{n-1} a_j x^j = \prod_{k=1}^{n} [(n-k)x - (n-k-1)] \tag{28}$$

computable through Vieta's formulae. The values of the coefficients a_j for the first four concentration moments are reported in Table 4.

3.2.3 Asymptotic Behaviour

At large distance from the source ($x/\delta \to \infty$, $t/T_L \to \infty$) the relative dispersion becomes the only mechanism characterizing the dispersion process, so that,

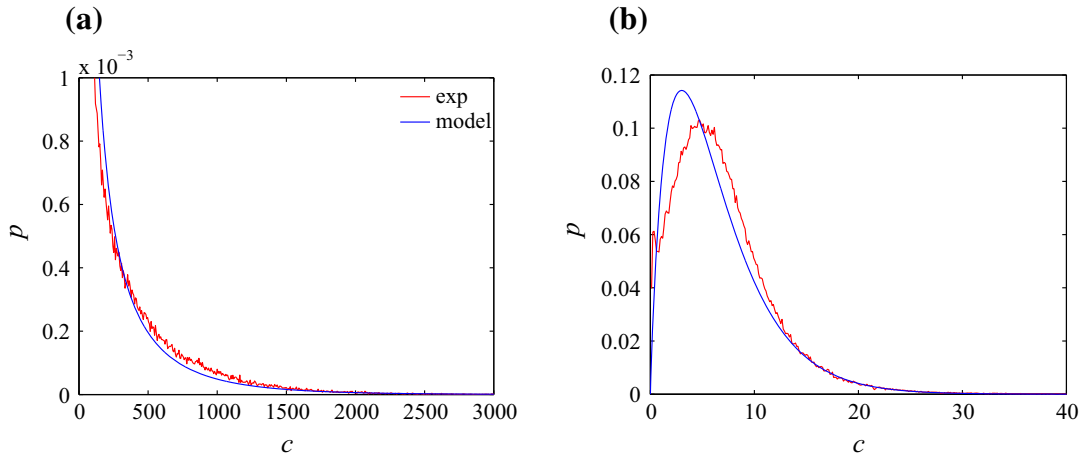

Fig. 5 Experimental and modelled PDF on the mean plume centreline varying with the distance from the source location for ES 6 at $y/\delta = 0$, $z/\delta = z_s/\delta$: **a** $x/\delta = 0.625$, **b** $x/\delta = 5.0$

$$i_{cr} \to i_c, \tag{29a}$$

$$\sigma_{ym} \to 0, \quad \sigma_{yr} \to \sigma_y, \tag{29b}$$

$$\sigma_{zm} \to 0, \quad \sigma_{zr} \to \sigma_z. \tag{29c}$$

In these conditions, the centroid PDF p_m tends to a Dirac delta distribution and the PDF of the global dispersion (p) is equal to the relative concentration PDF, that assumes the following formulation,

$$p_m \to \delta_D, \tag{30}$$

$$p_{cr} \to p = \frac{\lambda^\lambda}{\bar{c}\Gamma(\lambda)} \left(\frac{c}{\bar{c}}\right)^{\lambda-1} \exp\left(-\frac{\lambda c}{\bar{c}}\right) \tag{31}$$

with $\lambda = 1/i_{cr}^2 \to 1/i_c^2$.

This formulation of the model is in agreement with one of the main findings of the experimental investigation presented in Nironi et al. (2015), i.e. that the PDF of the concentration can be modelled with high accuracy by a Gamma distribution.

4 Comparison with Experimental Results

We finally test the agreement of the fluctuating plume model with the wind-tunnel measurements of the concentration statistics, carried out by Nironi et al. (2015). A first qualitative analysis concerns the form of the concentration PDF at the plume centreline, presented for both formulations of i_{cr} in Sect. 3.2. As an example, in Fig. 5 we report a comparison between the modelled and experimental PDFs at two distances from the source. Close to the source the meandering mechanism prevails (see Fig. 1) and the form of the PDF is similar to a negative exponential distribution (Fig. 5a). In the far field, the meandering becomes negligible with respect to the relative dispersion. The intermittency within the plume is damped, and the shape of the PDF is similar to a log-normal distribution with a short tail, as shown in Fig. 5b. In both cases the model captures the plume dynamics well and accurately reproduces the shape of the concentration PDF.

To perform a more accurate analysis of the model reliability and to quantify the errors in the predictions, we focus on the profiles of the first four moments around the mean, referred

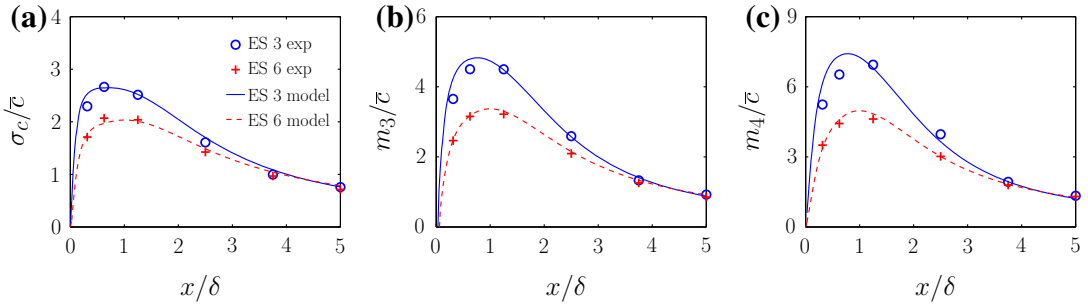

Fig. 6 ES case: concentration statistics vs x/δ at $y/\delta = 0$, $z/\delta = z_s/\delta$: **a** $\sigma_c/\overline{c}$, **b** $m_3/\overline{c}$, **c** $m_4/\overline{c}$

to as m_i, with $i = 1, 2, 3, 4$. These can be computed from Eq. 2 using the following relations (Monin and Yaglom 1971),

$$m_1 = \overline{c}, \tag{32a}$$

$$m_2 = \sigma_c^2 = \overline{c^2} - \overline{c}^2, \tag{32b}$$

$$m_3 = \overline{c^3} - 3\overline{c^2}\overline{c} + 2\overline{c}^3, \tag{32c}$$

$$m_4 = \overline{c^4} - 4\overline{c^3}\overline{c} + 6\overline{c^2}\overline{c}^2 - 3\overline{c}^4. \tag{32d}$$

In the analysis we apply the following normalization:

$$m_i^* = {m_i}^{1/i} \frac{u_\infty \delta^2}{M_q}, \tag{33}$$

where u_∞ is the velocity at the top of the boundary layer.

It is worth noting that in what follows (as well as in the analysis presented in Sect. 5), the computed values of the first two moments, the mean and the standard deviation, are actually the results of a best fit of the models given by Eq. 21 and Eq. 27 (with $n = 1$ and $n = 2$) to the experimental data, obtained by tuning the model parameters, as discussed in Sect. 3. A real comparison between model and experiments is therefore performed only for m_3^* and m_4^*, whose estimates can be considered as fully independent from the experimental observations.

4.1 Elevated Source

Firstly, we analyze the longitudinal profiles of the ratio between the values of the concentration statistics (σ_c, $m_3^{1/3}$, and $m_4^{1/4}$) and mean concentration $\overline{c}$ at source height, where the estimates of the two models of i_{cr} do not differ one from the other. As Fig. 6 shows, the model provides accurate estimates in the whole domain investigated here ($0 \leq x/\delta \leq 5$), for the two elevated sources considered. In particular, the model reproduces well the influence of the source size in the near field, that progressively vanishes as the meandering motion becomes less effective at displacing the plume centre of mass. The concentration statistics then tend to the same asymptotic values in the far field, independently of the source conditions.

A further analysis concerns the transverse profiles of the concentration statistics at source height. As an example we show in Fig. 7a, c, e, and g a comparison between experiments and model predictions at $x/\delta = 0.625$, $z/\delta = z_s/\delta$. At this distance from the source, the two formulations of the i_{cr} provide almost identical values since $i_{cr} = i_{cr0}$ in both cases. The varying source diameter does not affect the profiles of mean concentration (Fig. 7a), whereas it significantly influences the profiles of the higher order moments (Fig. 7c, e, g). The model results are in excellent agreement with the experimental observations.

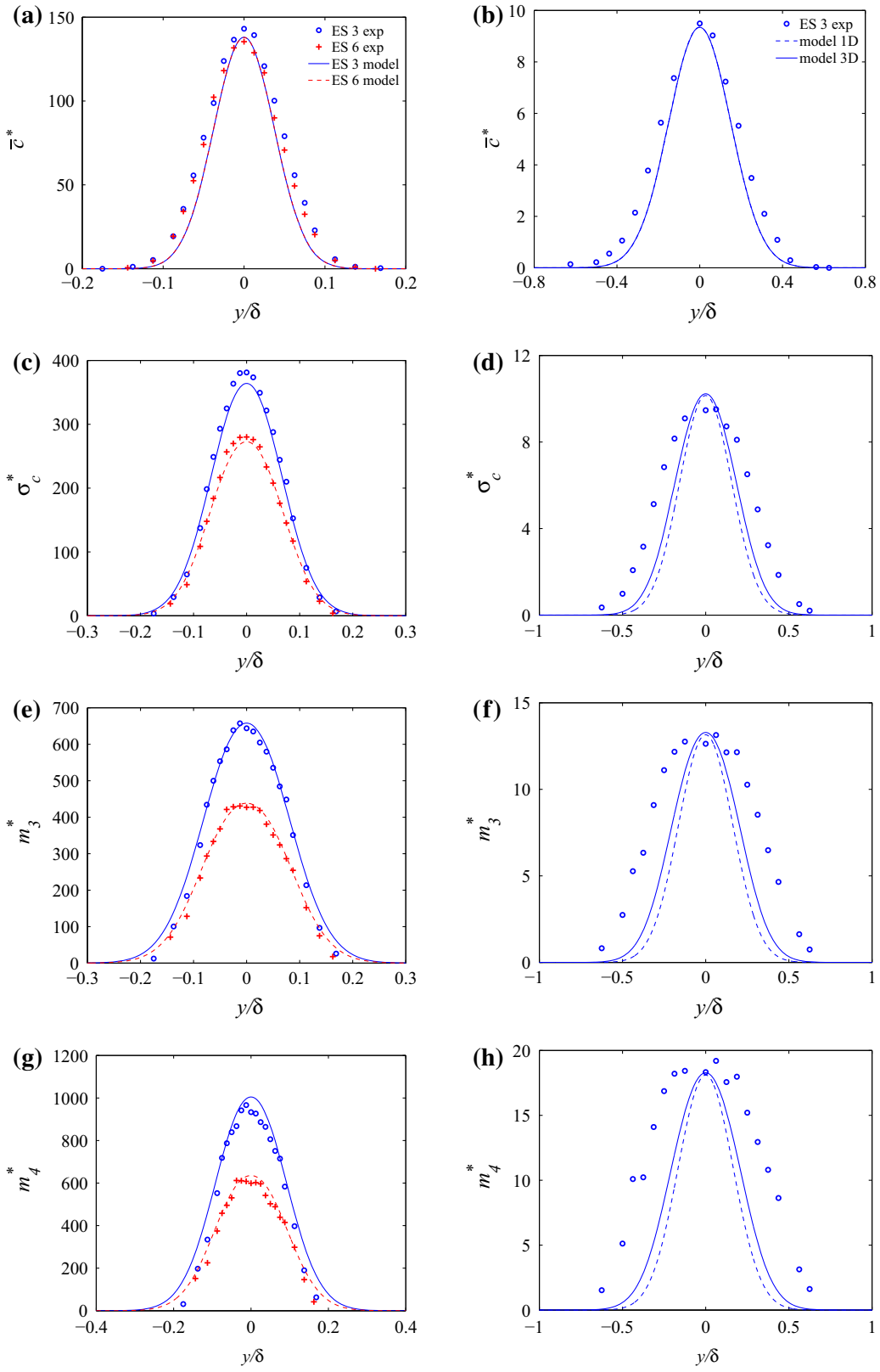

Fig. 7 ES case: comparison between experimental and modelled transverse profiles of the concentration statistics at source height and at $x/\delta = 0.625$: **a** $\overline{c}^*$, **c** σ_c^*, **e** m_3^*, **g** m_4^*, and at $x/\delta = 3.75$: **b** $\overline{c}^*$, **d** σ_c^*, **f** m_3^*, **h** m_4^*. *Blue circles* experimental values for ES 3, *red crosses* experimental values for ES 6, *blue solid line* and *red dash line* solutions provided by Eq. 27, *blue dash line* solutions provided by Eq. 21. Note that at $x/\delta = 0.625$ the differences between the solutions computed by means of Eq. 21 and Eq. 27 are negligible

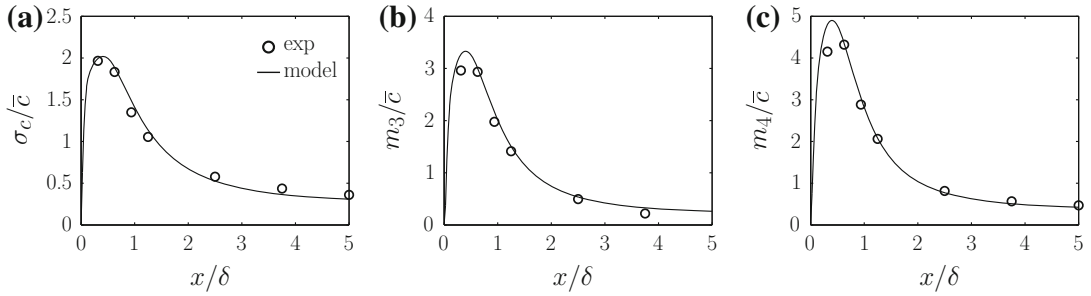

Fig. 8 LLS case: concentration statistics vs x/δ at $y/\delta = 0$, $z/\delta = z_s/\delta$: **a** $\sigma_c/\overline{c}$, **b** $m_3/\overline{c}$, **c** $m_4/\overline{c}$

As we proceed downwind from the source, the results show a slight deterioration, which is only partially corrected by adopting a 3-D model of i_{cr}. In Fig. 7b, d, f, and h we show a comparison between experimental and analytical results for the ES 3 emission, computed with both the 1-D and the 3-D models of i_{cr} (Eq. 25) at $z/\delta = z_s/\delta$ and $x/\delta = 3.75$, where the influence of the source size has become negligible. The model provides quite accurate estimates of the concentration statistics, even though the spreads of the simulated profiles of m_3^* and m_4^* are narrower than the experimental profile.

4.2 Low-Level Source

As for the ES case, the modelled profiles of the second-, third- and fourth-order moments of the concentration as function of the x-coordinate at $y = 0$ and $z = z_s$ (Fig. 8) present a fairly good agreement with the experimental data, both close to the source and in the far field.

Even in this case the predictions performed through 1-D and 3-D formulations of i_{cr} provide good results of the concentration statistics close to the source, given the ζ_y coefficient is next to zero up to $x/\delta \approx 0.5$ (see Fig. 4). This is shown in Fig. 9a, c, e, and g, where we have plotted the transverse profiles of the concentration statistics at the source height.

In the far field, the model with $i_{cr} = i_{cr}(x)$ is not able to reproduce the profiles of the concentration statistics, even qualitatively. As Fig. 9d, f, and h show, the model fails to reproduce the off-centreline peaks and the transverse profiles keep a Gaussian shape. In order to improve the model prediction it is then necessary to assume $i_{cr} = i_{cr}(x, y, z)$. The results of the model are however less accurate than in the ES case. In the far field, the model underestimates the mean concentration peak on the plume axis (Fig. 9b), due to the discrepancies between the modelled σ_y (Eq. 15) and its experimental values (Nironi et al. 2015). The transverse profiles of the higher order moments show the emergence of off-centreline peaks, that are particularly marked for the third order moment. The model captures these tendencies qualitatively but its quantitative predictions show significant discrepancies with the experimental data (Fig. 9d, f, h).

5 Error and Sensitivity Analysis

Finally, we evaluate the reliability and robustness of the fluctuating plume model by means of:

- estimates of its global accuracy, computed through a comparison between the measured and computed concentration statistics;
- a Monte-Carlo analysis providing the sensitivity of the solutions to variations of the key parameters.

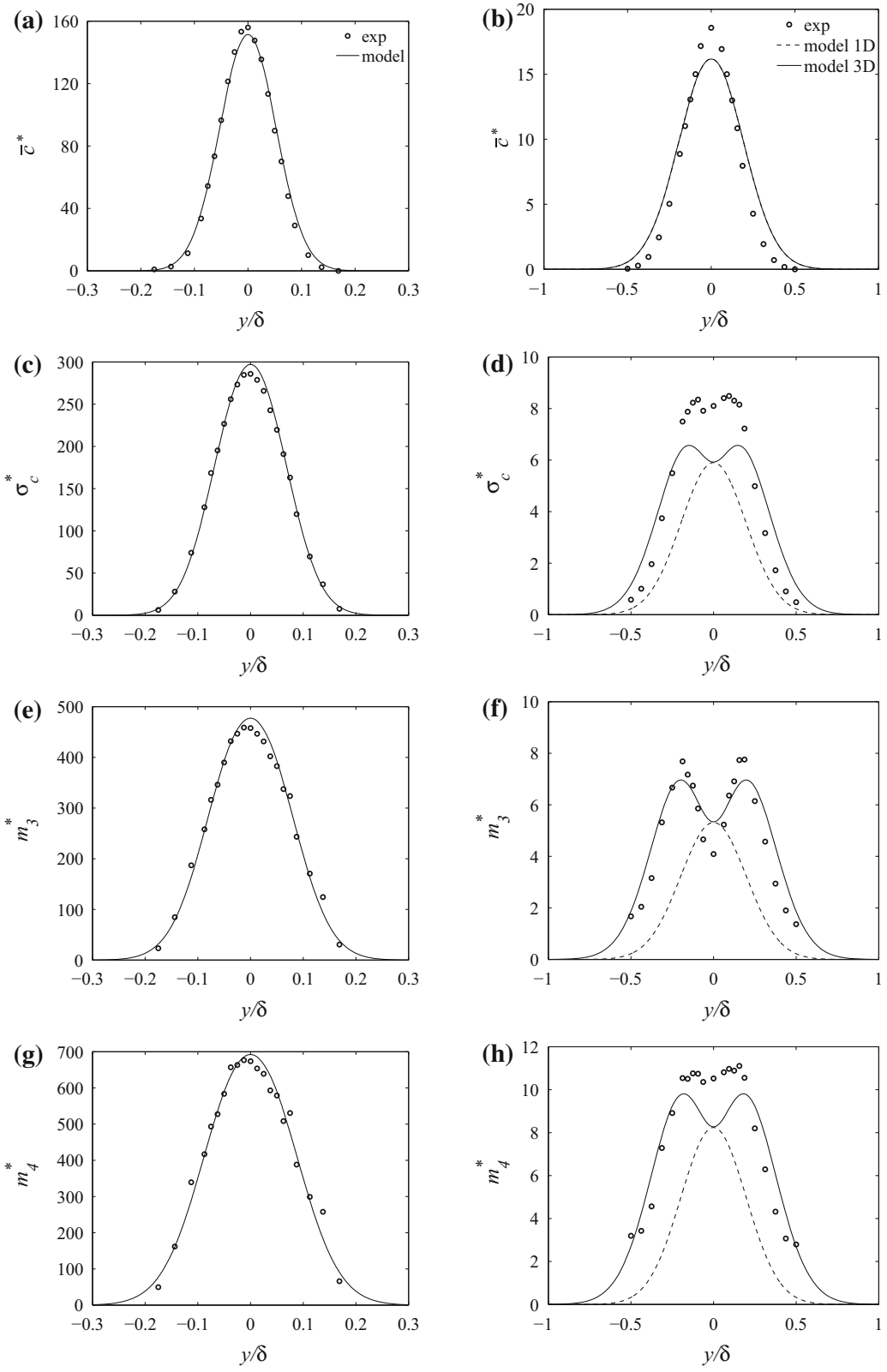

Fig. 9 LLS case: comparison between experimental and modelled transverse profiles of the concentration statistics at the source height and at $x/\delta = 0.625$: **a** $\overline{c}^*$, **c** σ_c^*, **e** m_3^*, **g** m_4^*, and at $x/\delta = 3.75$: **b** $\overline{c}^*$, **d** σ_c^*, **f** m_3^*, **h** m_4^*. *Circles* experimental values, *solid line* solutions provided by Eq. 27, *dash line* solutions provided by Eq. 21. Note that at $x/\delta = 0.625$ the differences between the solutions computed by means of Eq. 21 and Eq. 27 are negligible

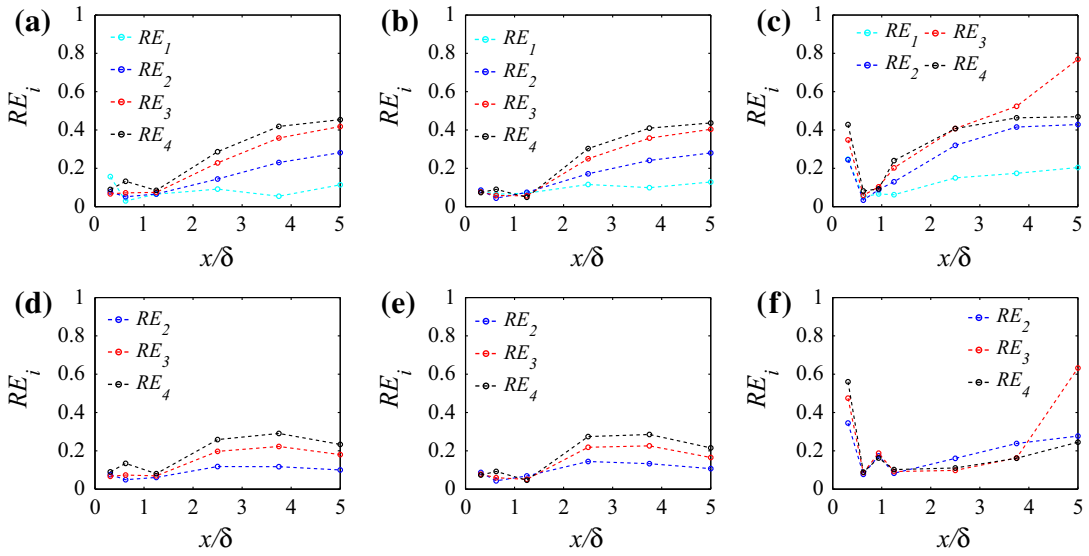

Fig. 10 Relative error of the transversal profiles vs x/δ for 1-D model of i_{cr}: **a** ES 3, **b** ES 6, **c** LLS; and 3-D model of i_{cr}: **d** ES 3, **e** ES 6, **f** LLS

5.1 Errors

To investigate the reliability of the model we need to quantify the gap between the measured, $(m_i^*)_{exp}$ and the computed $(m_i^*)_{mod}$ values of the moments of the concentration. To this end we define the relative error as

$$RE_i = \sqrt{\frac{\int \left[(m_i^*)_{mod} - (m_i^*)_{exp}\right]^2 \mathrm{d}s}{\int \left[(m_i^*)_{exp}\right]^2 \mathrm{d}s}}, \tag{34}$$

with $i = 1, 2, 3, 4$, $\mathrm{d}s = \mathrm{d}y, \mathrm{d}z$ and where i is the moment number.

The analysis is performed considering the cases of i_{cr} parametrized by the 1-D model (Eq. 23c) and the 3-D model (Eq. 25). Figure 10a–c show that the relative error associated to the mean concentration RE_1 takes low values across the whole domain. Conversely RE_2, RE_3 and RE_4 computed for 1-D i_{cr} model are bounded close to the release point, but they increase significantly away from it.

The relative errors evaluated for 3-D i_{cr} model are reported in Fig. 10d–f, where RE_1 is not plotted, since it does not depend on the formulation of i_{cr}. RE_i of the transversal profiles are bounded in all the cases, except for RE_3 in the LLS case (Fig. 10f). This is due to the particular shape of the experimental profile of m_3^* at $x = 5\delta$, that exhibits significant off-centreline peaks. As shown in Fig. 9f, the model reproduces this behaviour only qualitatively, but it fails in quantifying the centreline values of m_3^*.

In the light of this analysis, we can however conclude that, by adopting a suitable parametrization of i_{cr}, the model reproduces the statistics of the concentration field produced by a fluctuating plume with good accuracy.

5.2 Sensitivity Analysis

In order to discuss the reliability of the model for operational purposes, we analyze its sensitivity to several key parameters, whose evaluation is potentially affected by non-negligible errors. Our analysis focuses on two main features. Firstly, we discuss the uncertainties related

Table 5 Turbulent velocity field at $\overline{z}_m$ and z_s

	$\overline{u}$ (m s^{-1})	σ_v (m s^{-1})	σ_w (m s^{-1})	ε (m^2 s^{-3})
$\overline{z}_m = 0.14\delta$	3.2	0.28	0.23	0.18
$z_s = 0.06\delta$	2.6	0.29	0.22	0.38

to the reference value of the vertical coordinate at which are evaluated the velocity statistics used to compute the model parameters. Secondly, we analyze the errors induced by uncertainties in the parametrizations of i_{cr}.

In the results presented in Sect. 4, velocity statistics, i.e. $\overline{u}_m$, σ_v, σ_w and ε, were evaluated at the plume centroid $z = \overline{z}_m$, which varies with the distance from the source. A simpler approach consists of estimating these same quantities at a fixed reference height, generally the source elevation z_s. As an example, we show in Table 5 the differences of these velocity statistics in the far field ($x/\delta = 3.75$) for the LLS emission, as computed at z_s and $\overline{z}_m$ (in this case $\approx 2.5 z_s$). As shown in Table 5 the two parameters that exhibit higher variations are $\overline{u}_m$ and ε. Comparisons of the concentration statistics computed at $x/\delta = 3.75$ for the LLS case, and adopting these two different sets of input data, are plotted in Fig. 11a–c. Results clearly show that these variations in the input data affect significantly the model performances and produce differences in the standard deviation and the third- and fourth-order moments of the concentration exceeding 100 %.

As a second step, we investigate the sensitivity on the parametrization of i_{cr} (Eq. 23c). Since the spatial distribution of the concentration fluctuations downwind the source is highly influenced by the emission conditions (Nironi et al. 2015), i.e. source size and elevation, the determination of a suitable longitudinal profile of i_{cr} represents actually the main modelling challenge. To test the influence of uncertainties in the parametrization of i_{cr} we performed a Monte-Carlo simulation, assuming that the coefficients in Eq. 23c are normally distributed, with averages values given by the reference values reported in Table 2 and a standard deviation corresponding to 10 % of the average. These turn out to be a maximum close to the source (≈15 %) and a minimum far from it (≈10 %). The variations of the second-, third- and fourth-order moments are shown in Fig. 11d–f and attain a maximal value ≈20 %.

The same analysis was performed for the parameters ζ_y and ζ_z (see Eq. 25) characterizing the evolution of i_{cr} in the transversal and vertical directions. These were assumed to be normally distributed, with a standard deviation equal to 10 % of the mean values reported in Table 3. The resulting uncertainties in the vertical profiles of the high order concentration statistics at $x/\delta = 0.625$ for the LLS case are plotted in Fig. 11g–i. These show that variations of these parameters have little influence on σ_c^* (Fig. 11g) and m_3^* (Fig. 11h) whereas they can induce significant variations in the m_4^* profiles (Fig. 11i), especially at the plume edges.

6 Discussion and Conclusion

We have investigated the reliability of a meandering plume model to simulate the dispersion of a passive scalar emitted within a neutral turbulent boundary layer. Following most authors who presented a similar model (Sawford and Stapountzis 1986; Yee et al. 1994; Luhar et al. 2000; Cassiani and Giostra 2002; Franzese 2003), we base its formulation on two main assumptions. The first is that the dispersion of the plume centre of mass and that of the tracer particles around it are statistically independent. The second is that both dispersion processes

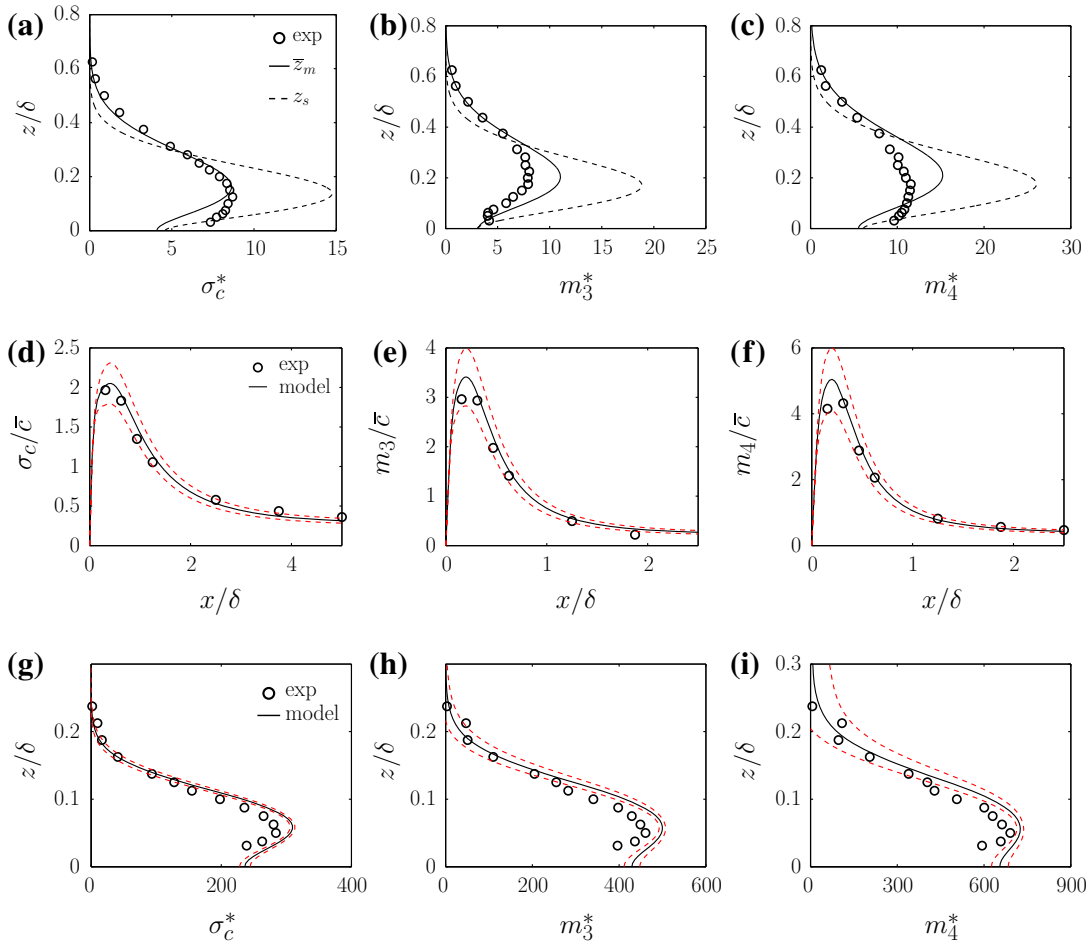

Fig. 11 Sensitivity analysis for the LLS case. Influence of the plume centroid on the vertical profiles of the concentration statistics, $x/\delta = 3.75$, $y = 0$: **a** σ_c^*, **b** m_3^*, **c** m_4^*; *circles* experiments; *solid line* model with $\overline{u}(\overline{z}_m)$, $\sigma_v(\overline{z}_m)$, $\sigma_w(\overline{z}_m)$, $\varepsilon(\overline{z}_m)$; *black dash line* model with $\overline{u}(z_s)$, $\sigma_v(z_s)$, $\sigma_w(z_s)$, $\varepsilon(z_s)$. Influence of an uncertainty of ± 10 % in the estimate of the coefficients of i_{cr} (Table 2) on the longitudinal profiles of the concentration statistics at $y/\delta = 0$, $z/\delta = z_s/\delta$: **d** $\sigma_c/\overline{c}$, **e** $m_3/\overline{c}$, **f** $m_4/\overline{c}$. Influence of an uncertainty of ± 10 % in the estimate of the coefficient ζ_z (Table 3) on the vertical profiles of the concentration statistics at $y/\delta = 0$, $x/\delta = 0.625$: **g** σ_c^*, **h** m_3^*, **i** m_4^*. The uncertainty is evaluated as the ratio between the standard deviation and the mean value and it is represented by *red dash lines*

are given by motions in the vertical and transversal plane that are decoupled one from the other. The first assumption is actually verified only close to the source and in the far field. The second cannot be strictly justified on some physical basis. It is rather adopted since it allows simplification of the model formulation.

A fluctuating plume model requires the setting of several parameters. According to our formulations, these are C_0 and C_r, the Kolmogorov and Richardson–Obukhov constants, respectively, α_T, required to evaluate the time scales T_{my} and T_{mz} characterizing the intensity of the meandering downwind the source, and the parameters needed to model the spatial evolution of the intensity of the relative concentration fluctuations i_{cr} in the longitudinal direction and in the transversal planes (α_1, α_2 and α_3). All these parameters were set by systematically comparing our model results to the experimental data presented in Nironi et al. (2015), in particular concerning the Eulerian integral length scales, the total plume spreads σ_y and σ_z and the spatial distribution of i_c. Furthermore, the information provided by this experimental dataset was used here to verify the consistency of the model formulation, as

well as of the procedure adopted to tune its parameters, with the main features characterizing the physics of the dispersion process.

We have then tested the performances of the model by comparing its solutions with experimental profiles of the higher-order moments of the concentration PDF (Nironi et al. 2015). The comparison shows that, despite the theoretical weakness of some of its basic assumptions, once properly set the governing parameters, the meandering model is able to predict the concentration statistics with a suitable accuracy and to simulate the effects due to the source size and elevation. In the near field, a good accuracy of the results could be achieved assuming a constant i_{cr} on the yz-planes. The good agreement between model simulations and experimental data persists even at larger distances from the source, where the assumption of the statistical independence of the meandering and the relative dispersion, as well as of the vertical and transversal motions, is far from being verified. Finally, in the far field, as the relative dispersion becomes the only relevant dispersion mechanism, the 1-D model results progressively deteriorate. To reliably reproduce profiles of the higher-order moments, the model requires a more complex formulation of i_{cr}, which takes account for its variability along the transverse and vertical directions.

In view of the application of the model for operational purposes, we have finally tested its sensitivity to the variations of several key parameters. The analysis shows that the model performances can be significantly affected by varying the reference values of the height from the ground at which the velocity statistics are estimated. Furthermore, the model is shown to exhibit also a strong sensitivity on the parametrization of i_{cr}, especially in the near field.

This sensitivity of the model to parametrization of i_{cr} represents, in our opinion, the main limitation for its use for operational purposes, since the spatial distribution of i_{cr} is strictly linked to that of i_c. As widely discussed in Nironi et al. (2015), the evolution of i_c is highly influenced by the conditions at the emissions. These include the source elevation and diameter and the emission velocity, as well as other features characterizing the source design that can affect the flow dynamics in the wake of the source, where most of the production of the concentration variance takes place. All these aspects influencing the plume dynamics in its initial phase of growth can not realistically be fully characterized when applying the model to atmospheric emissions. As a consequence, estimates of the higher-order concentration statistics in this near-field region can be affected by significant uncertainties.

Given these uncertainties of the model results in real case studies and in the light of the findings presented in Nironi et al. (2015), a last remark can be made. As long as the Gamma distribution was shown to reliably model the concentration PDF (independently of the emission conditions), it is actually questionable if, for operational purposes, the concentration statistics deserve to be computed by a meandering plume model, that requires several input parameters, rather than with more simple semi-empirical models. These should be formulated in order to provide solely estimates of $\overline{c}$ and i_c, the two independent quantities needed to fix the form of the Gamma distribution, which can be subsequently used to compute the higher-order moments.

References

Amicarelli A, Salizzoni P, Leuzzi G, Monti P, Soulhac L, Cierco FX, Leboeuf F (2012) Sensitivity analysis of a concentration fluctuation model to dissipation rate estimates. Int J Environ Pollut 48:164–173

Arya PS (1999) Air pollution meteorology and dispersion. Oxford University Press, Oxford, 310 pp

Biferale L, Boffetta G, Celani A, Devenish BJ, Lanotte A, Toschi F (2005) Lagrangian statistics of particle pairs in homogeneous isotropic turbulence. Phys Fluids 17:115101/1–115101/9

Boffetta G, Sokolov I (2002) Relative dispersion in fully developed turbulence: the Richardson's law and intermittency corrections. Phys Lett 88:094501/1–094501/4

Cassiani M (2013) The volumetric particle approach for concentration fluctuations and chemical reactions in Lagrangian particle and particle-grid models. Boundary-Layer Meterol 146:207–233

Cassiani M, Franzese P, Giostra U (2005) A PDF micromixing model of dispersion for atmospheric flow. Part I: Development of the model, application to homogeneous turbulence and neutral boundary layer. Atmos Environ 39:1457–1469

Cassiani M, Giostra U (2002) A simple and fast model to compute concentration moments in a convective boundary layer. Atmos Environ 36:4717–4724

Fackrell JE, Robins AG (1982) The effects of source size on concentration fluctuations in plumes. Boundary-Layer Meteorol 22:335–350

Ferrero E, Mortarini L, Alessandrini S, Lacagnina C (2013) Application of a bivariate gamma distribution for a chemically reacting plume in the atmosphere. Boundary-Layer Meteorol 147:123–137

Franzese P (2003) Lagrangian stochastic modeling of a fluctuating plume in the convective boundary layer. Atmos Environ 37:1691–1701

Franzese P, Cassiani M (2007) A statistical theory of turbulent relative dispersion. J Fluid Mech 571:391–417

Gailis RM, Hill A, Yee E, Hilderman T (2007) Extension of a fluctuating plume model of tracer dispersion to a sheared boundary layer and to a large array of obstacles. Boundary-Layer Meterol 607:577–607

Gifford F (1959) Statistical properties of a fluctuating plume dispersion model. Adv Geophys 6:117–137

Ishihara T, Kaneda Y (2002) Relative diffusion of a pair of fluid particles in the inertial subrange of turbulence. Phys Fluids 14:L69–L72

Leuzzi G, Amicarelli A, Monti P, Thomson DJ (2012) A 3D Lagrangian micromixing dispersion model LAGFLUM and its validation with a wind tunnel experiment. Atmos Environ 54:117–126

Luhar AK, Hibberd MF, Borgas MS (2000) A skewed meandering plume model for concentration statistics in the convective boundary layer. Atmos Environ 34:3599–3616

Monin AS, Yaglom AM (1971) Statistical fluid mechanics, vol 1. MIT Press, Cambridge, 769 pp

Mortarini L, Franzese P, Ferrero E (2009) A fluctuating plume model for concentration fluctuations in a plant canopy. Atmos Environ 43:921–927

Nironi C, Salizzoni P, Marro M, Mejan P, Grosjean N, Soulhac L (2015) Dispersion of a passive scalar fluctuating plume in a turbulent boundary layer. Part I: Velocity and concentration measurements. Boundary-Layer Meteorol

Obukhov AM (1941) On the distribution of energy in the spectrum of turbulent flow. Izv Akad Nauk USSR, Ser Geogr Geofiz 5:453–466

Ott S, Mann J (2000) An experimental investigation of the relative diffusion of particle pairs in three-dimensional turbulent flow. J Fluid Mech 422:207–223

Reynolds AM (2000) Representation of internal plume structure in Gifford's meandering plume model. Atmos Environ 34:2539–2545

Richardson LF (1926) Atmospheric diffusion shown on a distance-neighbour graph. Proc R Soc Lond 110:709–737

Sawford B (2004) Micro-mixing modelling of scalar fluctuations for plumes in homogeneous turbulence. Flow Turbul Combust 72:133–160

Sawford B, Stapountzis H (1986) Concentration fluctuations according to fluctuating plume models in one and two dimensions. Boundary-Layer Meteorol 37:89–105

Tennekes H (1982) Similarity relations, scaling laws and spectral dynamics. In: Niewstadt F, Van Dop H (eds) Atmospheric turbulence and air pollution modelling. D. Reidel Publishing Company, Dordrecht, pp 37–68

Vinkovic I, Aguirre C, Simoëns S (2006) Large-eddy simulation and Lagrangian stochastic modeling of passive scalar dispersion in a turbulent boundary layer. J Turbul 7:1–14

Xie Z, Hayden P, Voke PR, Robins AG (2004) Large-eddy simulations of dispersion: comparison between elevated and ground level sources. J Turbul 5:1–16

Yee E, Chan R, Kosteniuk PR, Chandler GM, Biltoft CA, Bowers JF (1994) Incorporation of internal fluctuations in a meandering plume model of concentration fluctuations. Boundary-Layer Meteorol 67:11–39

Yee E, Wilson DJ (2000) A comparison of the detailed structure in dispersing tracer plumes measured in grid-generated turbulence with a meandering plume model incorporating internal fluctuations. Boundary-Layer Meteorol 94:253–296

7.3 Stochastic modelling

Dispersion of a Passive Scalar Fluctuating Plume in a Turbulent Boundary Layer. Part III: Stochastic Modelling.

Massimo MARRO, Pietro SALIZZONI, Lionel SOULHAC
Laboratoire de Mécanique des Fluides et d'Acoustique, University of Lyon, CNRS UMR 5509 Ecole Centrale de Lyon , INSA Lyon, Université Claude Bernard, 36, avenue Guy de Collongue, 69134 Ecully, France.

Massimo CASSIANI
NILU - Norwegian Institute for Air Research, Kjeller, Norway

September 29, 2016

Abstract. A Lagrangian stochastic micromixing model is used to predict the concentration fluctuations of a continuous release in a neutral turbulent boundary layer. We present the computational algorithm that implements two different micromixing schemes and we verify its reliability with the experimental data. We discuss the influence of the source size on the concentration probability density function in the near and far-field and point out skills and shortcomings of the two schemes.

Keywords: Atmospheric boundary layer; concentration statistics; fluctuating plume; Lagrangian stochastic model.

1. Introduction

The impact assessment of risks related to the dispersion of flammable gases and toxic substances requires a reliable description of the concentration probability density function (PDF) and estimates of the higher order moments of the concentration. This can be achieved by means of Lagrangian stochastic micromixing models, which simulate the effects of molecular diffusivity on the mixing of a pollutant with ambient air. So far, this approach was used by several authors for varying flow configurations. Cassiani et al. (2005a) and Postma et al. (2011a) simulated the dispersion of a point source in the neutral boundary layer and compared the concentration fluctuation intensity with the experimental profiles provided by Fackrell and Robins (1982). Cassiani et al. (2005b) analysed the case of a convective boundary layer whereas (Postma et al., 2011b) focused on a neutrally stratified canopy flow. In all over mentioned studies, the analysis was however limited to the first two moments of the concentration PDF. To our knowledge, the only analysis extended up to the fourth moment is that of Sawford (2004) in homogeneous turbulence.

Here we take advantage of recent wind tunnel experiments (Nironi et al., 2015) and we evaluate the accuracy of a such a model in es-

timating the first four concentration moments in a fluctuating plume in neutral boundary layer. In doing so, we test two different schemes. One is usually referred to as Interaction by Exchange with the Conditional Mean (IECM) model, the other as Volumetric Particle Approach (VPA). Both models rely on a same macromixing scheme, formulated according to the Thomson's (1987) well-established well-mixing condition.

2. Model equations

The temporal evolution of the velocity and position X_i of an ensemble of independent fluid particles is governed by the following stochastic differential equations:

$$dU_i' = a_i(\mathbf{X}, \mathbf{U}', t)dt + b_{ij}(\mathbf{X}, \mathbf{U}', t)d\xi_j, \quad (1)$$

$$dX_i = (\langle u_i \rangle + U_i')dt, \quad (2)$$

where U_i' is the Lagrangian velocity fluctuation related to the Eulerian mean velocity $\langle u_i \rangle$, $d\xi_j$ is an incremental Wiener process (Gardiner, 1983) with zero mean and variance dt.

The deterministic acceleration term a_i is a function of the turbulent statistics and its simplest three-dimensional solution is given imposing the well-mixed condition (Thomson, 1987). This assumes that for a fixed temporal instant and a space position, if the particle distribution in the domain is homogeneous, each statistic of the particle velocity has to be equal to the statistic of Eulerian velocity of the fluid. As a consequence of that, the particles have the same dynamical properties of the fluid. For uncorrelated velocity components, the term a_i is defined by the following equation:

$$a_i = -\frac{U_i'}{T_{Li}} + \frac{1}{2}\frac{\partial \sigma_{ui}^2}{\partial x_i} + \frac{U_i'}{2\sigma_{ui}^2}\left(U_j \frac{\partial \sigma_{ui}^2}{\partial x_j}\right) \qquad \text{with} \qquad i = 1, 2, 3, \quad (3)$$

The stochastic diffusive term b_{ij} is defined from the Kolmogorov's hypotheses of self-similarity and local isotropy in the inertial subrange (Pope, 1987):

$$b_{ij} = \delta_{ij}\sqrt{C_0 \varepsilon}, \quad (4)$$

where δ_{ij} is the Kronecker delta. We recall that the Lagrangian integral time scales T_{Li} represent the autocorrelation coefficients of the Lagrangian velocity and they are expressed as a function of the velocity variances σ_{ui}^2, mean turbulent kinetic energy dissipation rate ε and

Lagrangian Kolmogorov constant C_0:

$$T_{Li} = \frac{2\sigma_{ui}^2}{C_0\varepsilon}. \tag{5}$$

2.1. Interaction by Exchange with the Conditional Mean (IECM) model

Eqs. 1 and 2 provide information about first-order statistics only. The simulation of the higher-order statistics of the concentration field requires the introduction of another Markovian state variable C representing the particle concentration:

$$\frac{dC}{dt} = \phi(C, \mathbf{X}, \mathbf{U}', t), \tag{6}$$

where the drift coefficient ϕ is responsible for the dissipation scalar variance. This approach aims in suitably modelling the evolution of PDF concentration in composition space accounting for the effects of the molecular diffusivity (Pope, 1998). In other words, the modelling of ϕ requires that the concentration field is homogenised by mixing towards the mean values. One of the most sophisticated models used to reproduce the main features of the concentration PDF is the IECM model that assumes the following parametrization (Sawford, 2004, Cassiani et al., 2005a, Postma et al., 2011a):

$$\frac{dC}{dt} = -\frac{C - \langle C|\mathbf{X}, \mathbf{U}\rangle}{\tau_m}, \tag{7}$$

where $\langle C|\mathbf{X}, \mathbf{U}\rangle$ is the mean scalar concentration conditioned on the local position and velocity. The parameter τ_m represents the time scale of the local mixing, which is driven by relative dispersion (Cassiani et al., 2005a). The time scale τ_m is then expressed as a function of local velocity variance, mean turbulent kinetic energy dissipation rate, source size, and particle flight time. The IECM model simulates explicitly the micromixing process as given by a mass exchange between polluted fluid particles and 'clean' particles of ambient air.

2.2. Volumetric Particle Approach

The Volumetric Particle Approach (VPA) was developed by Cassiani (2013) in order to compute the first two moments of the concentration (mean and variance) without taking into account the background particles. That causes a substantial simplification in the representation of the phenomenon allowing one to obtain a considerable saving in the

computational resources. In this approach we associate the fictitious volume V_p to the plume particles and we simulate the micromixing as a change in V_p. In particular, the dissipation of scalar fluctuations is related to a sort of dilution of the marked particles. To define the volume V_p we introduce the mass of tracer m_p carried by a particle. For a non-reactive scalar this mass is conserved ($dm_p/dt = 0$) and V_p is defined as the ratio $V_p = m_p/C$. The temporal evolution of the volume V_p is described by the following equation:

$$V_p(t + dt) = V_p(t)\frac{C(t)}{C(t + dt)} \tag{8}$$

whereas the concentration C can be modelled through Eq. 7.

The computation of the mean concentration $\langle C\rangle_c$ requires the spatial discretisation of the computational domain and it depends on the global mass M_c in each space element

$$\langle C\rangle_c = \frac{M_c}{V_c} = \frac{1}{V_c}\sum_{i=1}^{N_c} m_{p_i} = \sum_{i=1}^{N_c} C_i\frac{V_{p_i}}{V_c} \tag{9}$$

where N_c is the particle number held in the generic cell.

The term V_{p_i}/V_c is the probability that the particle i takes the concentration C_i. With this assumption the second-order moment $\langle C^2\rangle_c$ can be estimated in analogy to Eq. 9:

$$\langle C^2\rangle_c = \frac{M_c}{V_c} = \frac{1}{V_c}\sum_{i=1}^{N_c} m_{p_i} = \sum_{i=1}^{N_c} C_i^2\frac{V_{p_i}}{V_c} \tag{10}$$

In what follows, for the mean concentration $\overline{c}$ and variance σ_c^2 we assume this notation:

$$\overline{c} \;= \langle C\rangle_c \tag{11}$$

$$\sigma_c^2 \;= \langle C^2\rangle_c - \langle C\rangle_c^2. \tag{12}$$

It is worth noting that the VPA model provides satisfactory results for the second-order statistics (Cassiani, 2013) but it is not able to reproduce the evolution of the PDF concentration. Despite this shortcoming inherent to the model formulation, one of the main results presented in Nironi et al. (2015) is that concentration PDF can be described with good accuracy by a Gamma distribution univocally defined by $\overline{c}$ and σ_c^2:

$$p(\chi) = \frac{k^k}{\Gamma(k)}\chi^{k-1}\exp(-k\chi) \tag{13}$$

where $\Gamma(k)$ is the Gamma function, $k = i_c^{-2} = (\sigma_c/\overline{c})^{-2}$ and $\chi \equiv c/\overline{c}$ (c being the sample space variable). This implies that the higher order statistics can be easily computed with Eqs. 9 and 10 to obtain $\overline{c}$ and σ_c, and assuming a Gamma distribution.

3. Model parameters

The coupling between the Lagrangian stochastic model (Eqs. 1 and 2) and the micromixing model (Eq. 7) is performed by the numerical code SLAM, Safety Lagrangian Atmospheric Model (Vendel et al., 2011).

The micromixing time and conditional mean concentrations are estimated during a pre-processing step, computing the trajectories of a small ensemble of particles released at the source location.

3.1. IECM model

The molecular diffusivity effects on the concentration fluctuations are considered by simulating the influence of the background particles. This strategy allows us to obtain a multitude of concentration values and, therefore, suitable approximations of the concentration PDFs.

The numerical simulations are performed following the approach of Cassiani et al. (2007). At the initial time-step a set of particles is uniformly distributed in the whole computational domain and each particle moves in accordance with the Eqs. 1 and 2. During this motion the particle concentration changes (Eq.7) assuming a large variety of values that allows the high order statistics to be computed . In order to increase the solution accuracy, a time-averaging is performed. A suitable choice of the boundary conditions allows us to correctly reproduce the dispersion of the passive scalar and to keep constant the number of particles during the simulations:

- top, the particle velocity and position are perfectly reflected and the concentration is absorbed;
- ground, the particles are elastically reflected and they conserve their concentration;
- inflow/outflow, periodic conditions are applied to the particle position and the absorption of the concentration is imposed;
- source, the influence of the source is taken into account by marking the near-source particles with a normally distributed scalar

concentration C_{src}:

$$C_{src} = \frac{Q}{2\pi\sigma_0^2\langle u_x\rangle}\exp\left(-\frac{r^2}{2\sigma_0^2}\right) \tag{14}$$

where Q is the source mass-flow, $\langle u_x\rangle$ is the longitudinal Eulerian mean velocity at the source location (x_s, y_s, z_s), σ_0 is the source size and $r^2 = (y-y_s)^2 + (z-z_s)^2$ is the distance from the particle to the source in yz-plane.

It is worth noting that, the perfect reflection of the particles is able to ensure the well-mixed condition (Thomson, 1987) if the turbulence is Gaussian and homogeneous, but no reflection scheme satisfies the well-mixed condition where the PDF for the normal velocity is asymmetric or locally inhomogeneous (Wilson and Flesch, 1993, Wilson and Sawford, 1996). However, according to Wilson and Flesch (1993), the perfect reflection is acceptable in bounded Gaussian inhomogeneous turbulence, e.g., neutral surface layer.

Such micromixing model requires the tuning of some free parameters in order to get a suitable accuracy in the solutions (Postma et al., 2011a): the Kolmogorov constant C_0, that influences the Lagrangian integral time-scales, the Richardson-Obukhov constant C_r and the micro-mixing constant μ_t, that affect the micromixing time, and the initial source distribution σ_0, that depends on the source diameter d_s. It is worth noting that this approach requires a large amount of computational resources due to the elevated number of particles.

The numerical experiments concerned a preliminary study of the influence of the discretisation parameters. We performed some simulations on a uniform grid, varying the cell dimensions and the time-step length, and we verified that the solutions were affected by neither the time-step length nor the space discretization (Figure 1a). The same analysis was carried out on the influence of number of the velocity classes used in the definition of the conditional mean concentration. Figure 1b shows that 3 classes for each velocity components are sufficient in order to have a suitable accuracy. Table I summarizes the parameter values adopted in the simulations in order to have a satisfactory agreement with the experimental measures.

Table I. Free parameter values adopted in the simulations.

C_0	σ_0	C_r	μ_t	Velocity classes
4.5	$2d_s$	0.3	0.6	$3\times3\times3$

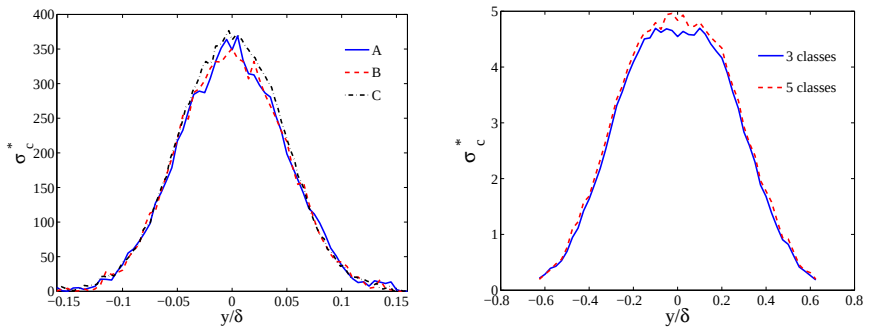

a) space and time discretisation b) velocity classes

Figure 1. Non-dimensional standard deviation of the concentration σ_c^* vs. y/δ at the source height. (a): $x/\delta = 0.625$, (A) $\Delta t = 1.0e-3$ s, $\Delta x = 0.02$ m, $\Delta y = \Delta z = 5.0e-3$ m; (B) $\Delta t = 5.0e-4$ s, $\Delta x = 0.02$ m, $\Delta y = \Delta z = 5.0e-3$ m; (C) $\Delta t = 1.0e-3$ s, $\Delta x = 0.01$ m, $\Delta y = \Delta z = 3.0e-3$ m; (b) $x/\delta = 5.0$

3.2. VPA model

As shown in Cassiani (2013), the VPA model is able to provide accurate solutions by implementing the Interaction by Exchange with the Mean (IEM) model (Pope, 2000), that corresponds to Eq. 7 with a unique class:

$$\frac{dC}{dt} = -\frac{C - \langle C(\mathbf{X})\rangle}{\tau_m}. \tag{15}$$

where $\langle C(\mathbf{X})\rangle$ is the mean concentration in the space domain. The source is approximated by a cylindrical top-hat distribution with size $\sqrt{8}\sigma_0$:

$$C_{src} = \frac{Q}{\frac{\pi}{4}(8\sigma_0^2)\langle u_x\rangle} \tag{16}$$

The value of C_0 and C_r are the same for IECM model, whereas the micromixing constant μ_t is equal to 0.35. The difference between μ_t in the IECM and VPA models was previously discussed in Cassiani (2013).

4. Results

The ability of the Lagrangian stochastic micromixing model SLAM to estimate the concentration fluctuations was investigated. In the numerical experiments we simulated the dispersion of a fluctuating plume produced by a continuous release from two point sources in the neutral boundary layer and we compared the numerical results with the wind

tunnel measurements presented in Nironi et al. (2015). We investigate the concentration plume releases by two elevated sources ($z_s/\delta = 0.19$) of different diameters d_s:

- ES 3: $d_s = 0.00375\delta$,
- ES 6: $d_s = 0.0075\delta$.

The main features of the velocity field imposed in the simulations are also presented in Nironi et al. (2015).

4.1. Profiles of concentration statistics

In order to test the reliability of the model, we computed the mean concentration $\overline{c}$ and 2^{nd}, 3^{rd} and 4^{th} moments around the mean and we compared them with the corresponding experimental values after a suitable normalization:

$$m_i^* = \left[\frac{1}{N_c} \sum_{p=1}^{N_c} (C_p - \overline{c})^i \right]^{1/i} \frac{u_\infty \delta^2}{Q} \qquad i = 2,\, 3,\, 4 \tag{17}$$

where u_∞ is the velocity at the boundary layer height, N_c is the number of particles in a control volume and C_p is the particle concentration. For the sake of simplicity in the figures we replace m_2^* with σ_c^*.

4.1.1. *IECM model*

The experimental data show that the differences in the source diameter do not affect the mean concentration, whereas they influence the higher order moments (Fackrell and Robins, 1982, Nironi et al., 2015). This influence is significant in the near-field (Figures 2 and 3) and it gradually becomes negligible for increasing distances from the source (Figure 4).

In the near-field (Figures 2 and 3) the model is able to reproduce the influence of the source size on the concentration fluctuations showing a good agreement with the experimental values; in particular, Figures 2b-d and Figures 3b-d show that the differences in the concentration PDFs due to the source diameter are correctly simulated.

In the far-field ($x \sim 500 - 1000 d_s$) the model slightly overestimates the experimental values, but it is able to suitably simulates the negligibility of the source size on the computed standard deviation (Figures 4a and 4b). On the contrary, some discrepancies occur on the higher order moments: the numerical solutions overestimate the experimental results and some differences due to the source diameter persist (Figures 4c and 4d).

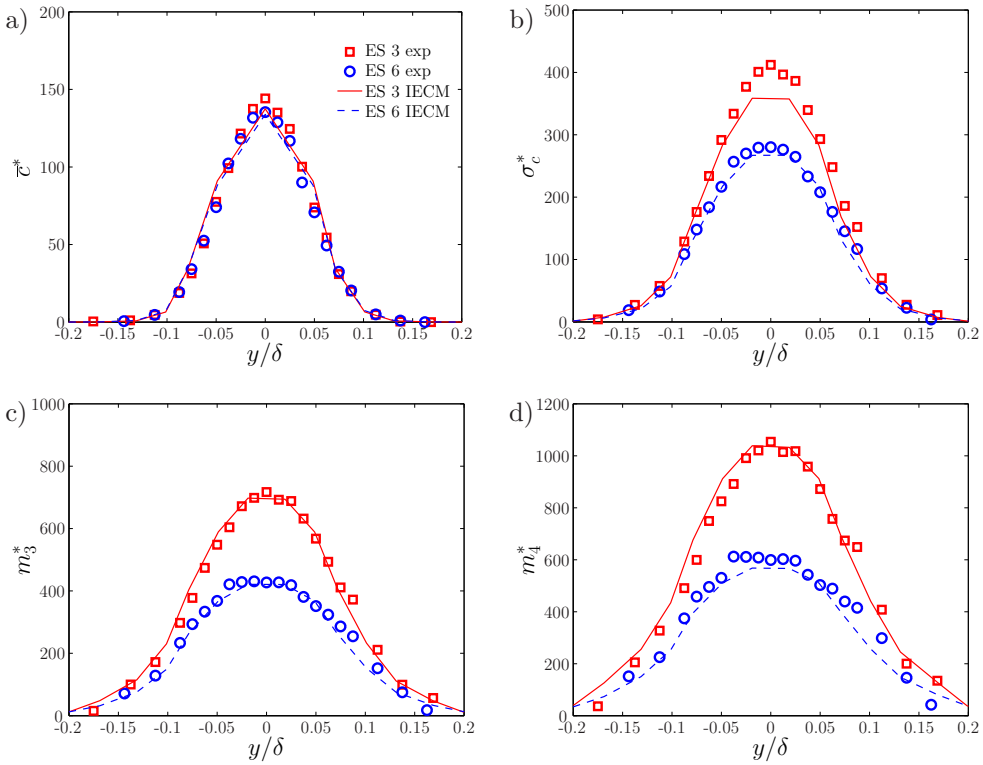

Figure 2. ES case: concentration statistics vs y/δ at $x/\delta = 0.625$, $z/\delta = z_s/\delta$: a) $\overline{c}^*$, b) σ_c^*, c) m_3^*, d) m_4^*.

The longitudinal evolutions at the height source z_s and $y = 0$ of the fluctuation intensity $i_c = \sigma_c/\overline{c}$, skewness Sk and kurtosis Ku of concentration show the shortcomings of the model. In fact, the agreement between experimental and numerical profiles of i_c is satisfactory in all the domain (Figure 5a), whereas the computed Sk and Ku globally overestimate the experimental values (Figures 5b and c) and in the far-field the influence of the source size is still significant.

Note that at $x/\delta = 5$ the experimental concentration PDF has not yet assumed a Gaussian shape since $Sk \simeq 2$ and $Ku \simeq 16$. We recall that a Normal distribution is characterized by $Sk = 0$ and $Ku = 3$.

4.1.2. *VPA model*

The VPA model allows the estimate of the spatial distribution of the first two moments of the concentration PDF, i.e. $\overline{c}^*$ and σ_c^*, only. Higher order moments will be computed assuming that the PDF is modelled as a Gamma distribution, whose form is fully determined by $\overline{c}^*$ and σ_c^*.

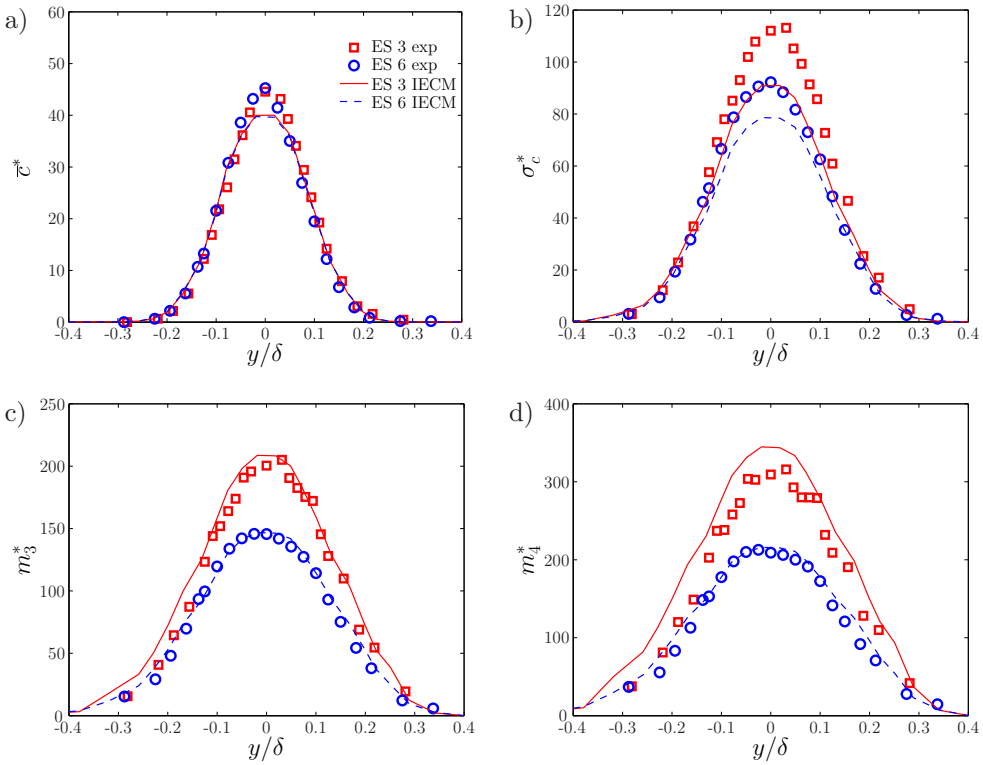

Figure 3. ES case: concentration statistics vs y/δ at $x/\delta = 1.25$, $z/\delta = z_s/\delta$: a) $\overline{c}^*$, b) σ_c^*, c) m_3^*, d) m_4^*.

The relation for the 3^{rd} and 4^{th} order moments are therefore given by:

$$m_3^* = (2i_c)^{1/3}\,\sigma_c^* \tag{18}$$

$$m_4^* = \left(6i_c^2 + 3\right)^{1/4}\,\sigma_c^* \tag{19}$$

Figure 6 shows that in the near field, i.e. $x/\delta = 0.625$, the VPA model associated with the Gamma distribution correctly simulates all the moments of the concentration for the small source, whereas the experimental values of the ES 6 source are quite overestimated, especially on the plume axis. However, the differences between the ES 3 and ES 6 sources are partially reproduced. Moving away from the source, $x/\delta = 1.25$ the model tends instead in slightly underestimating values of all moments of ES 3 source, whereas the agreement with the ES 6 source is very good (Figure 7). At this location the model fails to reproduce the differences due to the source sizes as shown in the experiments. The VPA formulation seems to produce a smoothing effect on the concentration fluctuations induced by the meandering

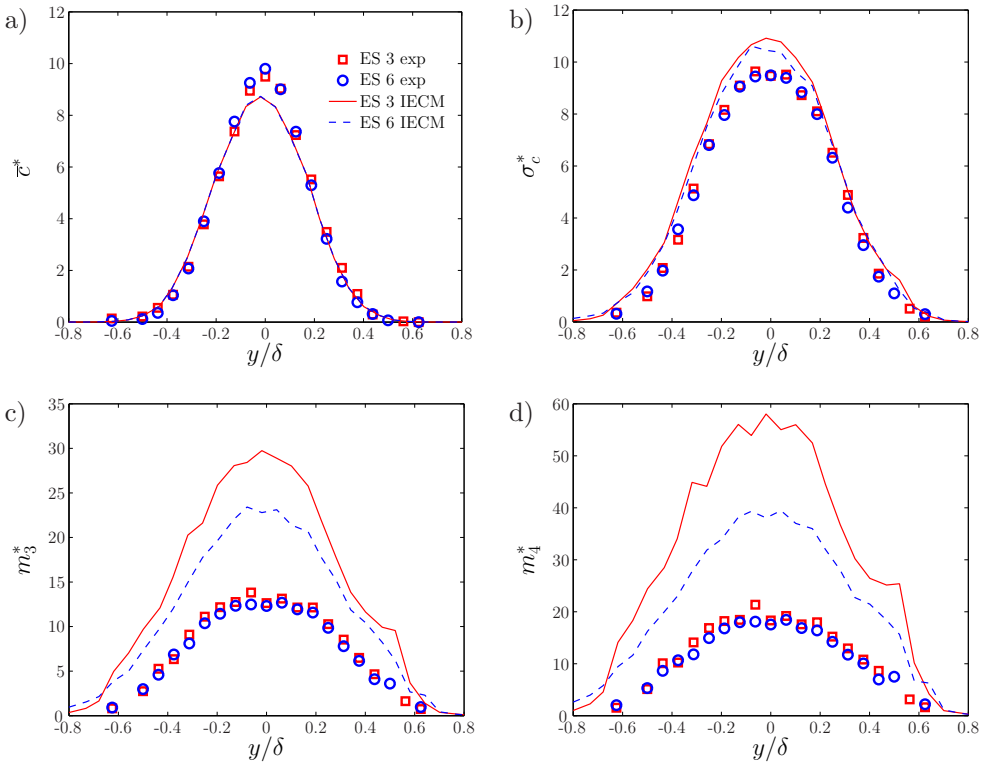

Figure 4. ES case: concentration statistics vs y/δ at $x/\delta = 3.75$, $z/\delta = z_s/\delta$: a) $\overline{c}^*$, b) σ_c^*, c) m_3^*, d) m_4^*.

mechanism that results in reducing too quickly the differences due to the source diameter. In the far-field, i.e. at $x/\delta = 3.75$, the model reproduces accurately the profiles of all moments, with a general tendency in slightly underestimating their values (Figures 8). Here VPA model is able to make negligible the effects of the source size on the higher order moments as shown in the experimental data. Comparing longitudinal profiles along the plume axis provided by the IECM and VPA model (Figures 5 and 9) we observe that the latter can actually reliably reproduce the tendencies registered in the experiments for the intensity of the concentration fluctuations i_c, as well as for the skewness Sk and the kurtosis Ku.

4.2. One-point concentration PDF

In order to look inside the micromixing model and its possible shortcomings, we report some plots of the concentration PDFs evaluated at $y = 0$ and $z = z_s$ at varying distances from the release point. The

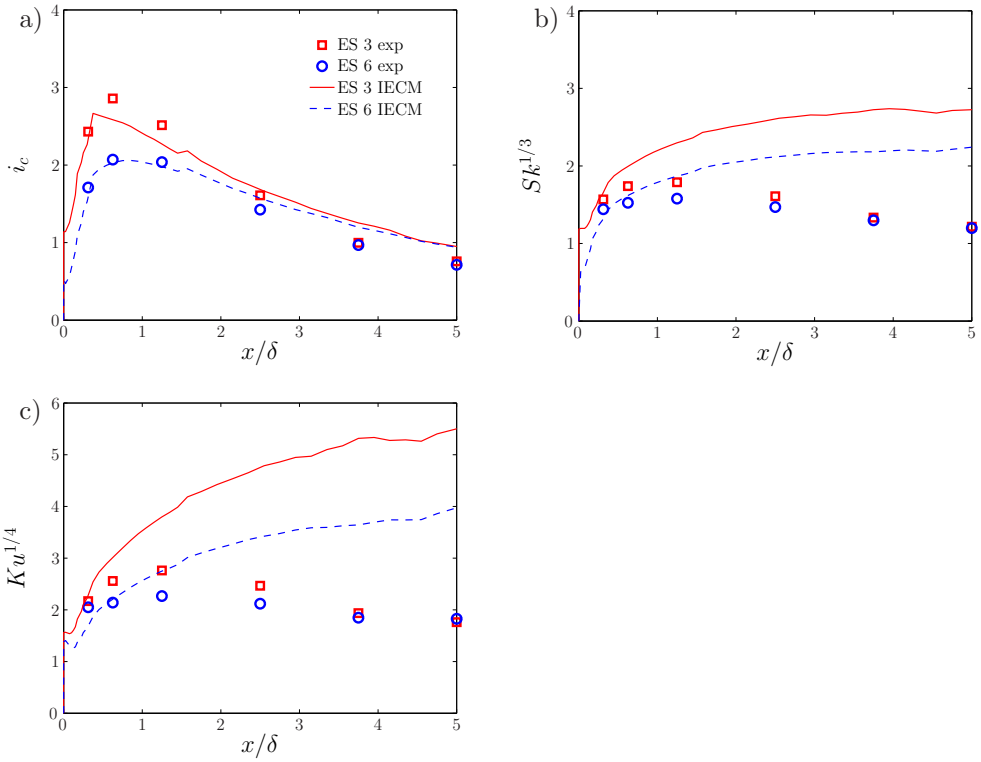

Figure 5. High order statistics of concentration vs x/δ: a) i_c, b) Sk, c) Ku.

PDFs are non-dimensionalised with the local mean concentration (see Eq. 13) and plotted in logarithmic scale in order to highlight also the effect of the small concentration values.

4.2.1. *IECM model*

For the numerical solutions, we obtained the PDFs by collecting a large number of particles passing through some small volume elements. In order to verify the reliability of the Gamma distribution to describe the concentration PDF, we also plot the Eq. 13 parametrized with the experimental values of i_c. Figure 10 shows the comparison between the experimental and computed PDF in the near-field at $x/\delta = 0.625$. We observe that the shape of PDFs estimated by the experimental and numerical data is very similar and it approaches a Gamma distribution, both in ES 3 (Figures 10a and 11a) and ES 6 cases (Figures 10b and 11b). At $x/\delta = 1.25$ the agreement between experiments and simulations worsen (Figure 11) and the PDFs obtained with IECM model exhibit a shape quite different from the Gamma distribution, underes-

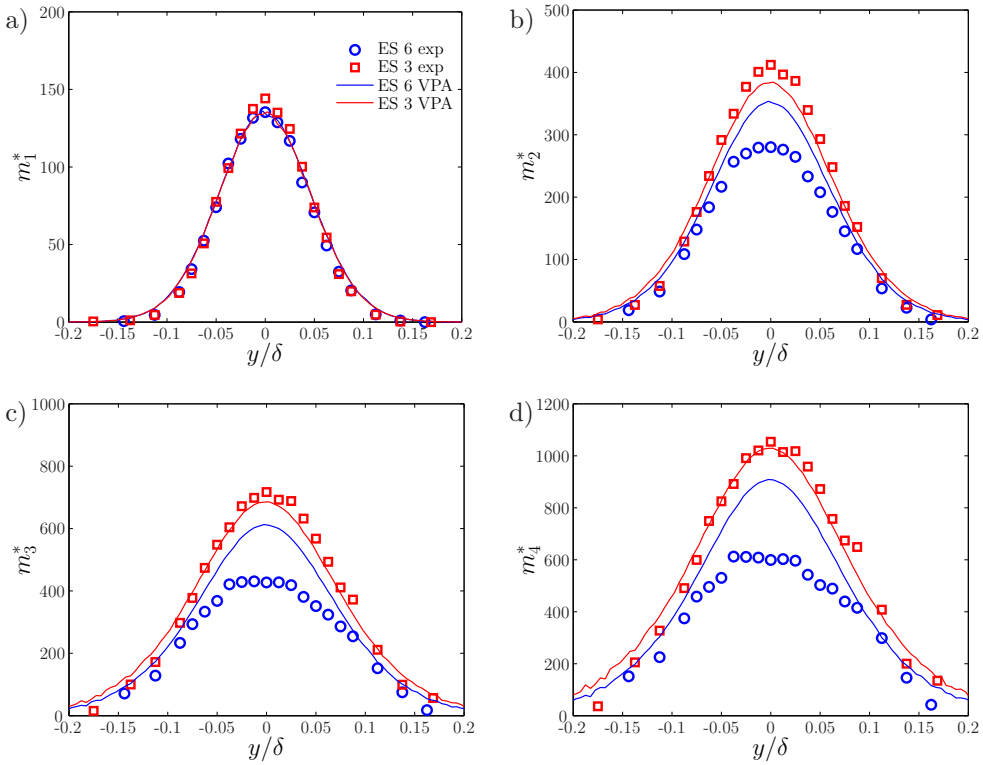

Figure 6. ES case: concentration statistics vs y/δ at $x/\delta = 0.625$, $z/\delta = z_s/\delta$: a) $\overline{c}^*$, b) σ_c^*, c) m_3^*, d) m_4^*.

timating the intermediate values of concentration and overestimating the small ones. Nevertheless the agreement between the global profiles is quite satisfactory (Figure 3).

Increasing the distance from the source location, Gamma distribution approximates the experimental PDF again, whereas the differences with the IECM results become substantial. In particular, the modelled PDFs significantly underestimate the occurrence of weak concentration values. This is clearly shown in Figure 12 where we compare experimental and numerical PDFS for the ES 6 case at $x/\delta = 3.75$ and 5.0.

4.2.2. *VPA model*

One-point PDF for the VPA model are computed through Eq. 13, using as parameters $\overline{c}^*$ and σ^* obtained by Eqs. 9 and 10. In the near-field at $x/\delta = 0.625$ we observe a general good agreement between numerical and experimental estimates for the ES 3 source (Figure 13a), whereas the ES 6 case presents some significant differences in the large and

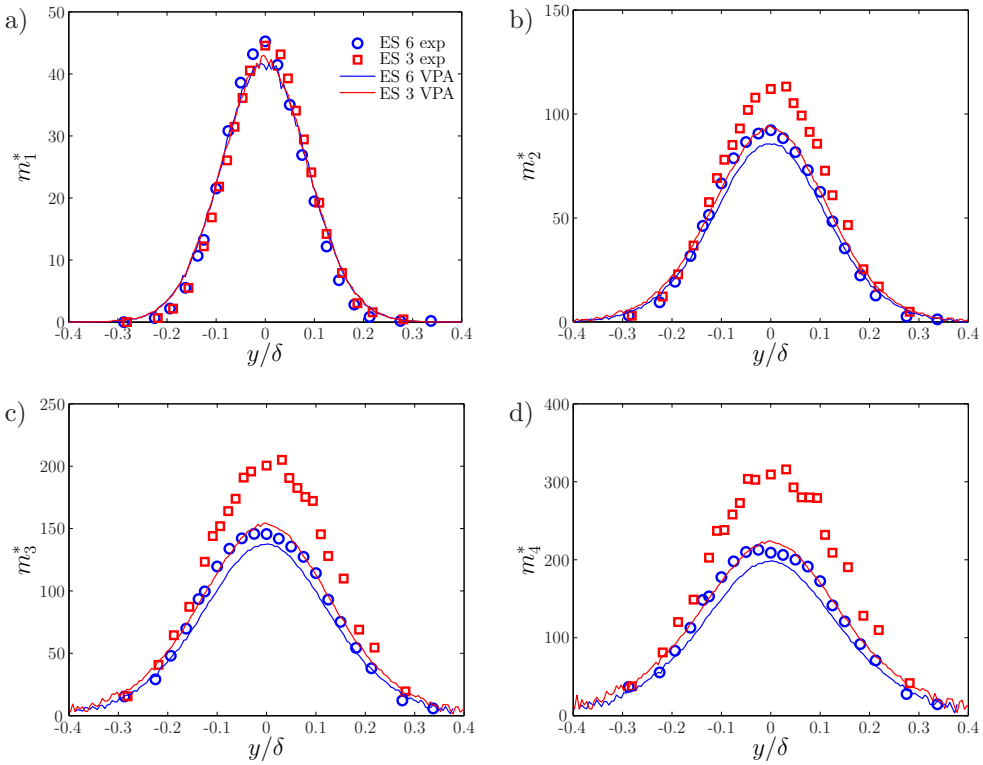

Figure 7. ES case: concentration statistics vs y/δ at $x/\delta = 1.25$, $z/\delta = z_s/\delta$: a) $\overline{c}^*$, b) σ_c^*, c) m_3^*, d) m_4^*.

intermediate scales (Figure 13b) that cause the overestimate of the higher concentration moments as shown in Figure 6 for the global profiles.

Increasing the distance at $x/\delta = 1.25$ the numerical PDF of the ES 3 source (Figure 14a) is globally displaced towards smaller values with respect to the experimental one. That results in an underestimate of the profiles of the concentration higher moments as reported in Figure 7. On the contrary, Figure 14b shows that the model reproduces with very good accuracy the experimental values for the ES 6 case.

In the far-field we observe a general good agreement between numerical and experimental estimates (Figure 15). Some differences between concern lower values, where experimental data generally show PDFs with higher levels of concentration.

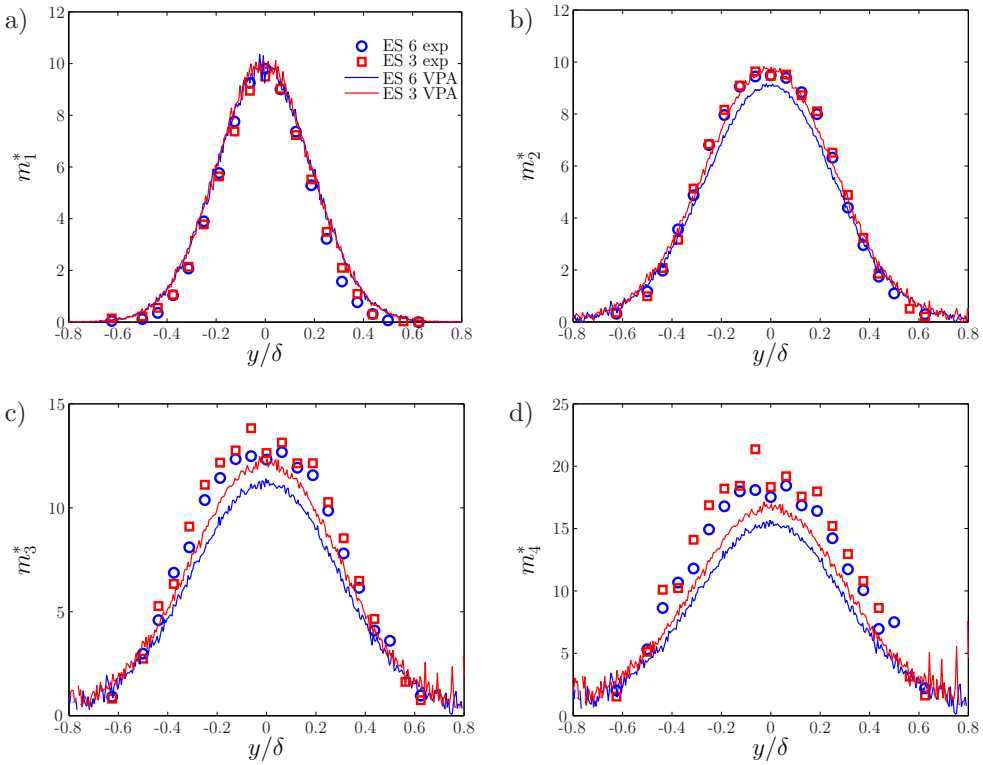

Figure 8. ES case: concentration statistics vs y/δ at $x/\delta = 3.75$, $z/\delta = z_s/\delta$: a) $\overline{c}^*$, b) σ_c^*, c) m_3^*, d) m_4^*.

4.2.3. *Effect of the source size*

We have studied the influence of the source size on the concentration PDF directly. Figure 16a shows that in the near-field at $x/\delta = 0.625$ σ_0 affects the tails of experimental PDF: the probability of large values of concentration is larger for the smaller source, whereas the probability of weak values increases for ES 6 case. The effect of σ_0 on the IECM numerical PDFs is less clear: the probability at the tails is very similar for ES 3 and ES 6 and some differences occur for the intermediate values (Figure 16b). The PDFs computed by the VPA model show that the probability of large values is larger for ES 3 case, although the differences between the two sources are less evident that for the experimental PDFs (Figure 16c).

In the far-field, the influence of the source size on the experimental data disappears and the two PDFs are quite superimposed (Figure 17a). Conversely, some discrepancies persist on the IECM results, as observed previously in §4.1. In particular, ES 6 presents a slightly

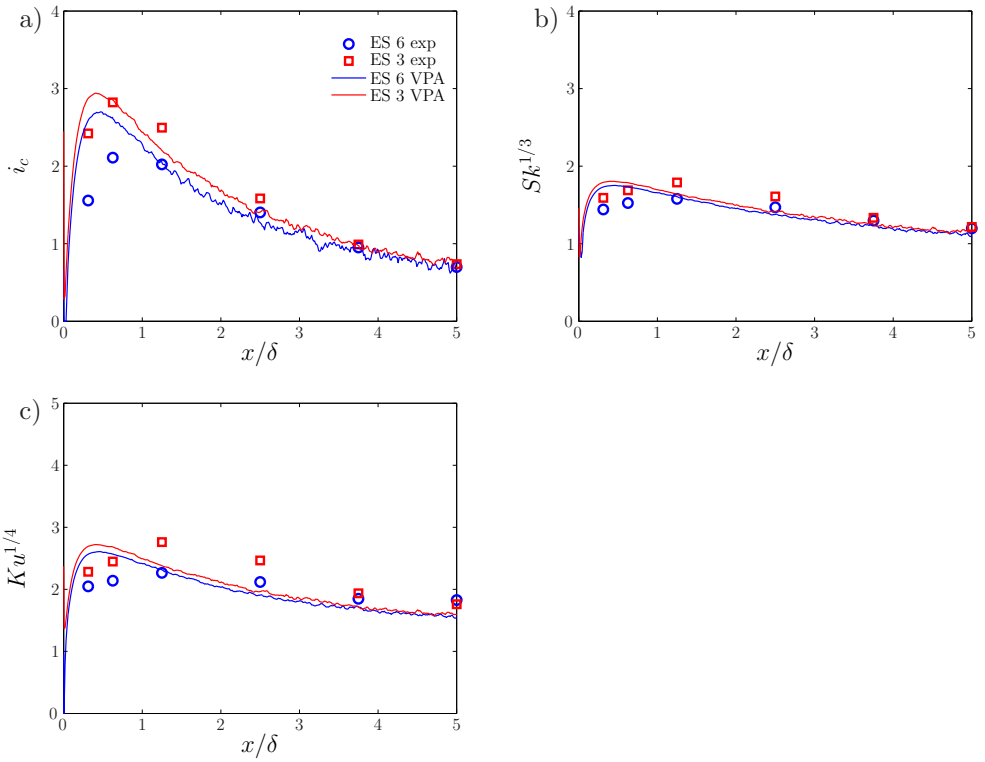

Figure 9. High order statistics of concentration vs x/δ: a) i_c, b) Sk, c) Ku.

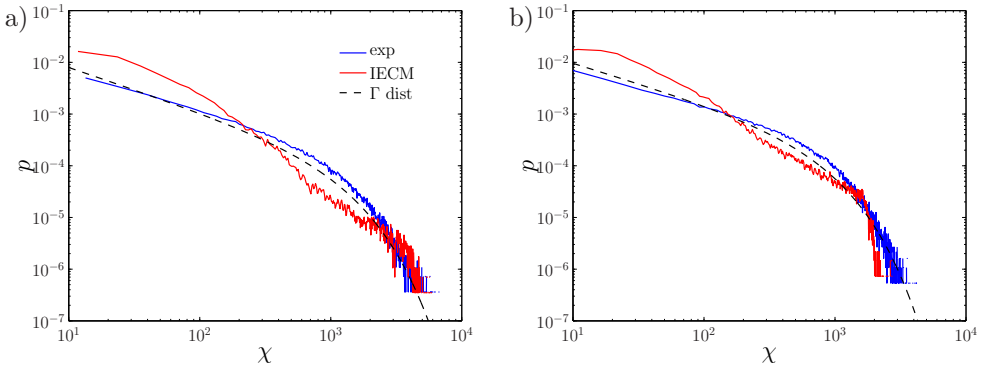

Figure 10. concentration PDF at $x/\delta = 0.625$, $y = 0$, $z/\delta = z_s/\delta$. a) ES 3, b) ES 6.

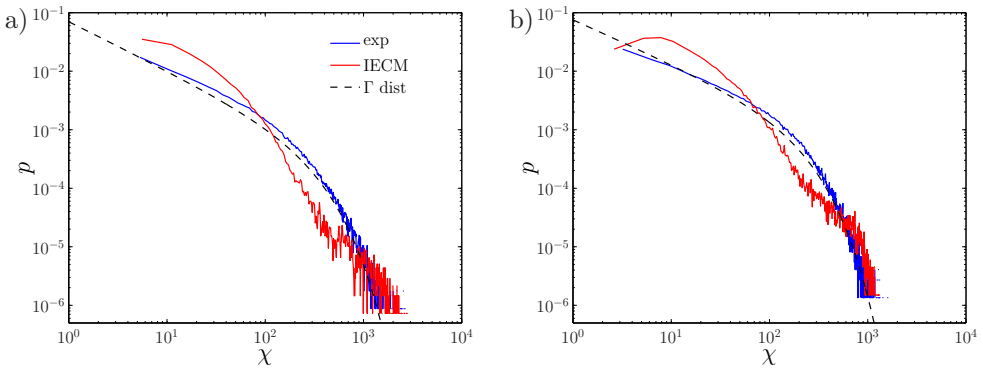

Figure 11. concentration PDF at $x/\delta = 1.25$, $y = 0$, $z/\delta = z_s/\delta$. a) ES 3, b) ES 6.

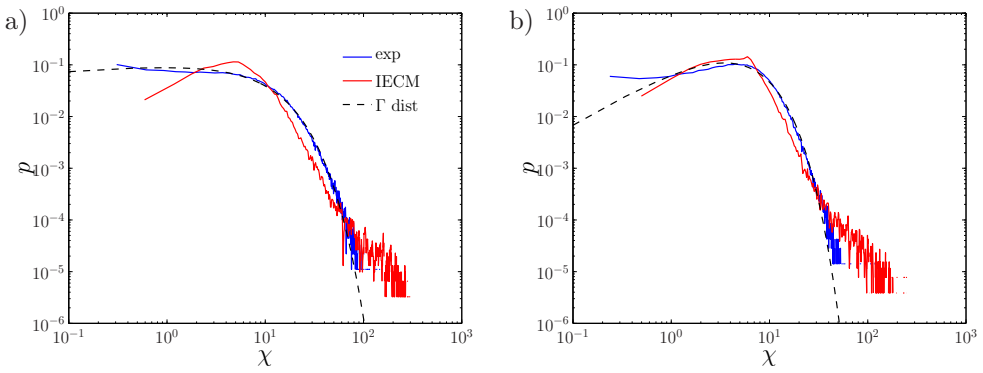

Figure 12. concentration PDF of ES 6 in the far-field at $y = 0$, $z/\delta = z_s/\delta$: a) $x/\delta = 3.75$, b) $x/\delta = 5.0$.

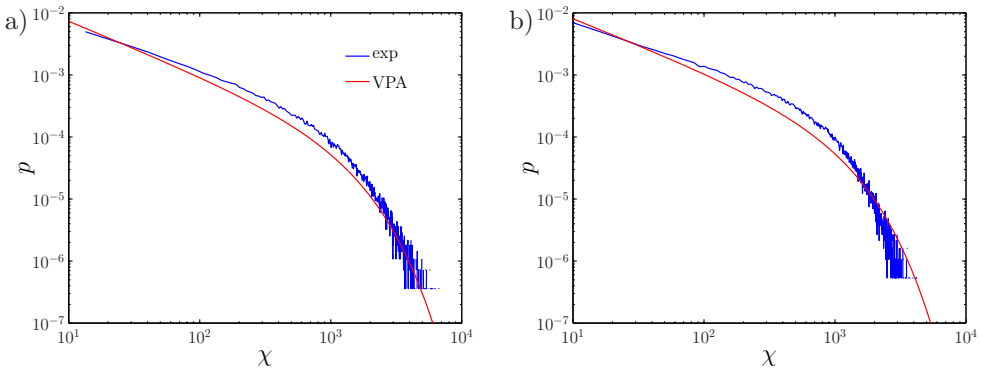

Figure 13. concentration PDF at $x/\delta = 0.625$, $y = 0$, $z/\delta = z_s/\delta$. a) ES 3, b) ES 6.

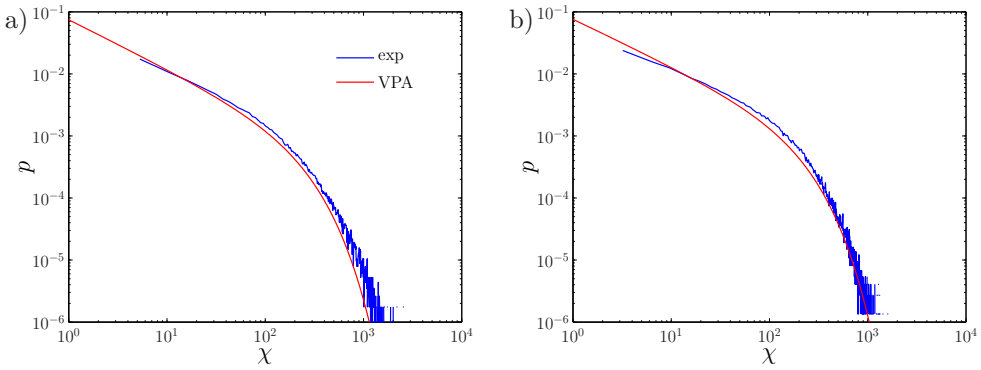

Figure 14. concentration PDF at $x/\delta = 1.25$, $y = 0$, $z/\delta = z_s/\delta$. a) ES 3, b) ES 6.

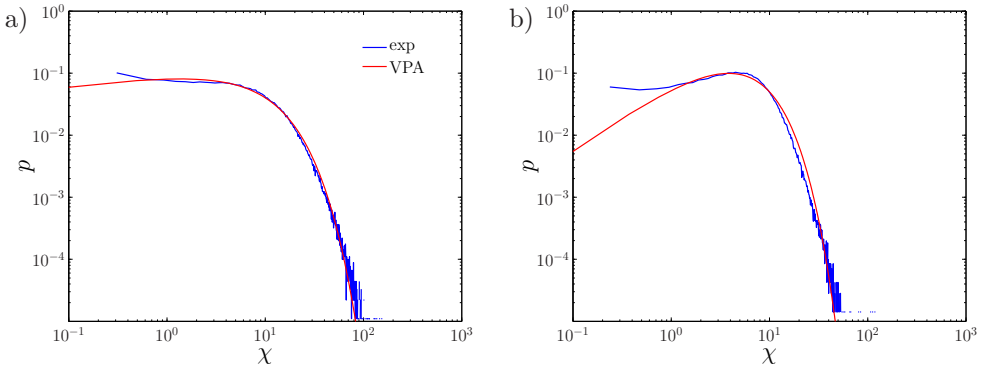

Figure 15. concentration PDF of ES 6 in the far-field at $y = 0$, $z/\delta = z_s/\delta$: a) $x/\delta = 3.75$, b) $x/\delta = 5.0$.

larger probability for the high values of concentration, whereas the tail corresponding to the low values assumes a larger probability for ES 3 (Figure 17b). The VPA model provides solutions that exhibit the correct behaviour in the far-field, i.e. the influence of the source size becomes negligible, as shown in Figure 17c. The small differences that persist in the lower values do not significantly affect the global profiles of the higher concentration moments (see Figure 8).

5. Discussion and Conclusions

We have tested two formulations of the micromixing model, the Interaction with Exchange with the Conditional Mean (IECM) and the Volume Particle Approach (VPA). These were implemented in a Lagrangian stochastic model (named SLAM) and we investigated their ability in

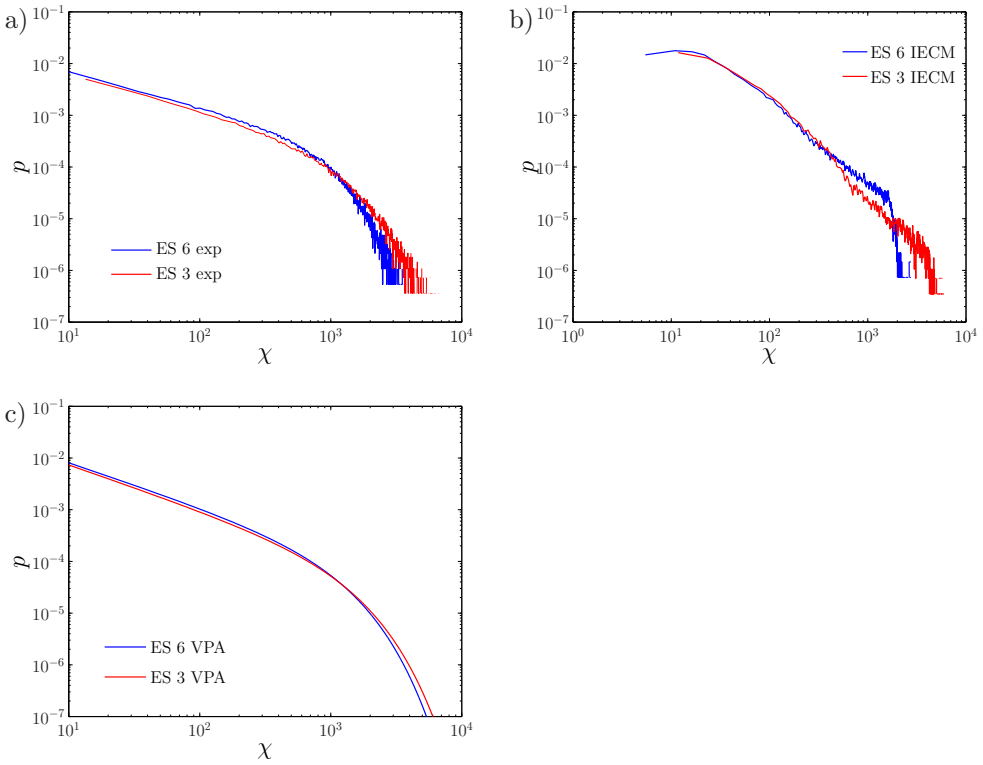

Figure 16. concentration PDF at $x/\delta = 0.625$, $y = 0$, $z/\delta = z_s/\delta$: a) experiment, b) IECM model, c) VPA model.

estimating the statistics of the concentration of a passive scalar emitted within a turbulent boundary layer. We simulated the dispersion of a fluctuating plume produced by a continuous release from two point sources of different diameter and we compared the numerical results with the experimental data-set reported in Nironi et al. (2015). The numerical solutions show that the IECM model is able to correctly simulate the concentration statistics in the near-field, reproducing the source size effects on the high order moments. In the far-field the numerical and experimental values of the mean and standard deviation of the concentration are in good agreement. Concerning the third and fourth moments, the IECM results in the far-field ($x \geq 3\delta$) show two main differences when compared to the experimental data. Firstly, the IECM model clearly tends to overestimate the third and fourth moments. Secondly, numerical profiles of the third and fourth moments are shown to be still sensitive to the size of the source. This is not the case in the experiments, where the influence of the source is no more

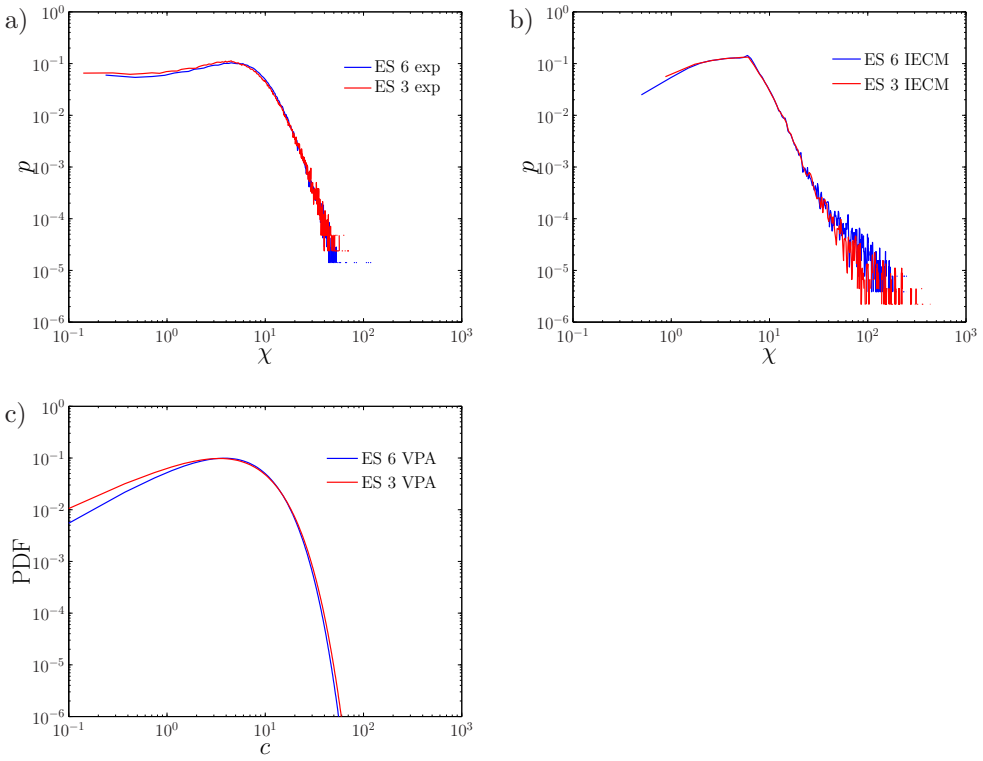

Figure 17. concentration PDF at $x/\delta = 5.0$, $y = 0$, $z/\delta = z_s/\delta$: a) experiment, b) IECM model, c) VPA model.

detectable as $x \geq 3\delta$. This behaviour can be reasonably attributed to the tendency of the IECM model in underestimating the occurrence of concentration values that are lower than the mean where the mean concentration gradients are weak (Cassiani et al., 2005a).

These limitations of the IECM model can be conveniently avoided by assuming that the concentration PDF corresponds to a Gamma distribution, as suggested by Nironi et al. (2015). In this case all higher concentration moments can be directly computed when disposing of estimates of the mean and of the standard deviation of the concentration. The semi-empirical approach is shown here to provide reliable estimates of third and fourth order moment both in the near and in the the far-field.

In this study we have further shown that the values of the mean and of the standard deviation of the concentration can be also accurately computed with a VPA model. The main advantages of this latter model, compared to the IECM model, are the low computational costs. The

VPA model requires a number of particles which is significantly smaller to those needed in a IECM model, and therefore a smaller request of RAM and CPU time. This feature makes the VPA model suited for the simulation of dispersion phenomena for operational purposes and in complex geometries.

References

Cassiani, M.: 2013, 'The volumetric particle approach for concentration fluctuations and chemical reactions in Lagrangian particle and particle-grid models'. *Boundary-Layer Meteorol* **146**, 207–233.

Cassiani, M., P. Franzese, and U. Giostra: 2005a, 'A PDF micromixing model of dispersion for atmospheric flow. Part I: development of the model, application to homogeneous turbulence and neutral boundary layer'. *Atmos Environ* **39**, 1457–1469.

Cassiani, M., P. Franzese, and U. Giostra: 2005b, 'A PDF micromixing model of dispersion for atmospheric flow. Part II: application to convective boundary layer'. *Atmos Environ* **39**, 1471–1479.

Cassiani, M., A. Radicchi, J. D. Albertson, and U. Giostra: 2007, 'An efficient algorithm for scalar PDF modelling in incompressible turbulent flows; numerical analysis with evaluation of IEM and IECM micro-mixing models'. *J Comput Phys* **223**, 519–550.

Fackrell, J. E. and A. G. Robins: 1982, 'The effects of source size on concentration fluctuations in plumes'. *Boundary-Layer Meteorol* **22**, 335–350.

Gardiner, C. W.: 1983, *Handbook of stochastic methods for physics chemistry and the natural sciences*. Springer, Berlin.

Nironi, C., P. Salizzoni, P. Mejan, N. Grosjean, M. Marro, and L. Soulhac: 2015, 'Dispersion of a passive scalar from a point source in a turbulent boundary layer. Part I: Velocity measurements'. *Boundary-Layer Meteorol* **156**, 415–446.

Pope, S. B.: 1987, 'Consistency conditions for random-walk models of turbulent dispersion'. *Phys Fluids* **30 (8)**, 23742379.

Pope, S. B.: 1998, 'The vanishing effect of molecular diffusivity on turbulent dispersion: implications for turbulent mixing and the scalar flux'. *J Fluid Mech* **359**, 299–312.

Pope, S. B.: 2000, *Turbulent flows*. Cambridge University Press.

Postma, J. V., D. J. Wilson, and E. Yee: 2011a, 'Comparing two implementations of a micromixing model. Part I: wall shear-layer flows'. *Boundary-Layer Meteorol* **140**, 207–224.

Postma, J. V., D. J. Wilson, and E. Yee: 2011b, 'Comparing two implementations of a micromixing model. Part II: canopy flow.'. *Boundary-Layer Meteorol* **140**, 225–241.

Sawford, B.: 2004, 'Micro-mixing modelling of scalar fluctuations for plumes in homogeneous turbulence'. *Flow Turbul Combust* **72**, 133–160.

Thomson, D. J.: 1987, 'Criteria for the selection of the stochastic models of particle trajectories in turbulent flows.'. *J Fluid Mech* **180**, 529–556.

Vendel, F., L. Soulhac, P. Mejean, L. Donnat, and O. Duclaux: 2011, 'Validation of the safety Lagrangian atmospheric model (SLAM) against a wind tunnel experiment over an industrial complex area'. In: *14th Conference on Harmonisation within Atmospheric Dispersion Modelling for Regulatory Purposes*.

Wilson, D. J. and T. K. Flesch: 1993, 'Flow boundaries in random-flight dispersion models: enforcing the well-mixed condition'. *J Appl Meteorol* **32**, 1695–1707.
Wilson, D. J. and B. L. Sawford: 1996, 'Review of Lagrangian stochastic models for trajectories in the turbulent atmosphere'. *Boundary-Layer Meteorol* **78**, 191–210.

Chapter 8

Free and confined buoyant flows

There are a large number of flow configurations involving releases of buoyant pollutant which are of major interest for environmental applications. Here our focus is on localised releases of buoyant flows both in open and enclosed spaces. Examples are given by fire plumes in the atmosphere (fig. 8a), the leakage of hydrogen from a pipe (fig. 8b) or the propagation of smoke within a ventilated tunnel.

In all these cases the buoyant releases evolve as a rising column of fluid, driven by the buoyancy and/or the momentum imposed at the source. These flows are usually referred to as a *plume* or a *jet*, depending on the predominance of buoyancy or momentum on the flow dynamics. For safety and environmental problems, a key issue is that of determining the rate at which the plume dilutes in ambient air.

Turbulent plumes can be described, without loss of generality, by integral models with a small number of constant coefficients. An example of such a coefficient is the classic entrainment coefficient, usually referred to as α, that relates the strength of the flow that is induced by a plume to the characteristic velocity scale of the plume at a given height (Taylor, 1945). Following the classic work of Priestley & Ball (1955) and Morton *et al.* (1956), integral models of turbulent plumes have provided physical insights and a robust means of predicting bulk flow properties in applications ranging from natural ventilation (Linden, 1999) to geophysics (Woods, 2010). Integral models are useful from an operational and theoretical viewpoint because they focus one's attention on dominant balances.

The importance of turbulent jets and plumes in practical problems and as a canonical turbulent flow has inspired many experiments over the last 50 years (see e.g. List, 1982, and references therein) and, more recently, numerical simulations (e.g. Plourde *et al.*, 2008; Craske & van Reeuwijk, 2016). However, in spite of the vast quantity of data that has been collected, several leading-order questions remain open. What determines the rate at which a plume entrains fluid from its surroundings? How does entrainment relate to the small-scale behaviour of turbulence? What determines the relative rate of spread of the velocity and buoyancy profile in a turbulent plume?

To answer these questions we take advantage of laboratory experiments (sect. 8.1) and direct numerical simulations (sect. 8.2) of buoyant releases characterised by their source conditions, given by the balance between the fluxes of volume, momentum and buoyancy, and identified by a plume Richardson number Γ_0.

Following the approach originally taken by Priestley & Ball (1955), and subsequently resurrected by Kaminski *et al.* (2005), we investigate herein the relationship between turbulent entrainment and the mean-flow energetics of plumes. The key ingredient of these studies was to absorb the continuity constraint into simultaneous equations for the momentum and the mean kinetic energy of the flow. Direct numerical simulations and experiments indicate that turbulent entrainment depends on the plume Richardson number, and that this mean-flow contribution is distinct from that associated with the production of turbulence kinetic energy.

This work on turbulent buoyant releases provides interesting insight into the advantages and the shortcomings of experimnetal and numerical methods to investigate these flows. The design of the

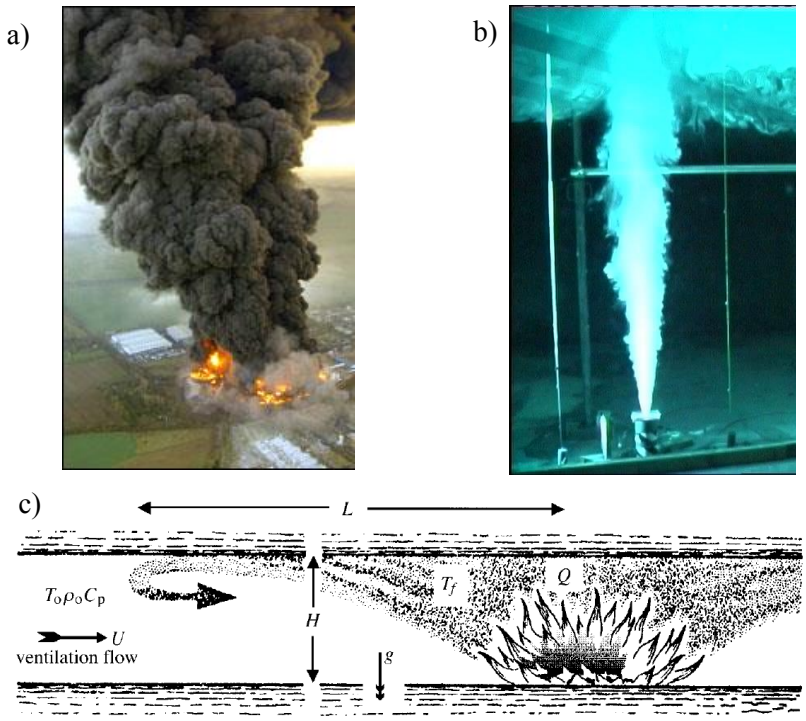

Figure 8.1: Examples of buoyant releases within free atmosphere and confined spaces. a) smoke propagation in the Buncefield fire (11 December 2005 at the Hertfordshire Oil Storage Terminal); b) hydrogen release from a pipe; c) sketch of the smoke propagation in a ventilated tunnel.

experimental apparatus needed is not trivial to conceive, since it requires the production of buoyant plumes in large spaces, i.e. over domains in which the evolution of the plume is i) sheltered by external pressure and velocity perturbations and ii) not influenced by the presence of the wall bounding the domain. Handling these boundary conditions in laboratory experiments is very difficult. These difficulties are likely to be the cause of the discrepancies observed in the experimental estimates of some key plume parameters presented in the literature, namely the entrainment coefficient and the turbulent Prandtl number. In these conditions the use of Direct Numerical Simulations (DNS), at Reynolds number that exceed 5000, becomes evidently a very attractive option. Setting the same boundary conditions in DNS is much easier (although not trivial). Furthermore, the use of DNS has two more relevant advantages compared to experiments: i) they provide information on flow parameters that would be extremely difficult to measure experimentally (e.g. pressure); and ii) they provide information over a whole volume of fluid, which is extremely useful when estimating bulk flow parameters (such as the entrainment coefficient).

Finally, in sect. 8.3 we present an interesting application of integral plume models to predict key elements of the flow dynamics within an enclosed space. Namely, we are interested in the intensity of the ventilation that has to be imposed within a tunnel in order to control the propagation of a buoyant flow release within it (see fig. 8c). Combining laboratory experiments with a mathematical model, based on integral plume models, allows us to enlighten new features about the dynamics of non-Boussinesq releases, i.e. characterised by large density differences between the buoyant and the ambient flow. Our experiments show that buoyancy-driven releases are predicted to behave as point sources of pure buoyancy, independently of their radius and of the density of the emitted fluid. This implies that the so-called non-Boussinesq effects have no major influence on the flow dynamics as far as gravitational effects take over those related to inertia. It is worth noting that, from a practical point of view, both features support the use of simplified mathematical models for the simulation of these flows, and define the ventilation systems for the management and the mitigation of accidental risks related to the releases of toxic and flammable fluids in enclosed spaces.

Bibliography

Craske, John & van Reeuwijk, Maarten 2016 Generalised unsteady plume theory. *Journal of Fluid Mechanics* **792**, 1013–1052.

Kaminski, E., Tait, S. & Carazzo, G. 2005 Turbulent entrainment in jets with arbitrary buoyancy. *Journal of Fluid Mechanics* **526**, 361–376.

Linden, P. F. 1999 The fluid mechanics of natural ventilation. *Annual Review of Fluid Mechanics* **31** (1), 201–238.

List, E. J. 1982 Turbulent jets and plumes. *Annual Review of Fluid Mechanics* **14** (1), 189–212.

Morton, B. R., Taylor, G. I. & Turner, J. S. 1956 Turbulent gravitational convection from maintained and instantaneous sources. *Proceedings of the Royal Society of London. Series A. Mathematical and Physical Sciences* **234** (1196), 1–23.

Plourde, F., Pham, M. V., Kim, S. D. & Balachandar, S. 2008 Direct numerical simulations of a rapidly expanding thermal plume: structure and entrainment interaction. *Journal of Fluid Mechanics* **604**, 99–123.

Priestley, C. H. B. & Ball, F. K. 1955 Continuous convection from an isolated source of heat. *Quarterly Journal of the Royal Meteorological Society* **81** (348), 144–157.

van Reeuwijk, M. & Craske, J. 2015 Energy-consistent entrainment relations for jets and plumes. *Journal of Fluid Mechanics* **782**, 333–355.

Taylor, G. I. 1945 Dynamics of a mass of hot gas rising in air. *Technical Report*. U.S. Atomic Energy Commission. Los Alamos National Laboratory Research Library. Report 236.

Woods, A. W. 2010 Turbulent plumes in nature. *Annual Review of Fluid Mechanics* **42** (1), 391–412.

8.1 Dynamical variability of axisymmetric buoyant plumes

J. Fluid Mech. (2015), *vol.* 765, *pp.* 576–611.
doi:10.1017/jfm.2014.694

Dynamical variability of axisymmetric buoyant plumes

A. Ezzamel[1,2], P. Salizzoni[2,†] and G. R. Hunt[3]

[1]Department of Civil and Environmental Engineering, Imperial College London, Imperial College Road, London SW7 2AZ, UK

[2]Laboratoire de Mécanique des Fluides et d'Acoustique, University of Lyon, CNRS UMR 5509 Ecole Centrale de Lyon, INSA Lyon, Université Claude Bernard, 36, avenue Guy de Collongue, 69134 Ecully, France

[3]Department of Engineering, University of Cambridge, Cambridge CB2 1PZ, UK

(Received 8 January 2014; revised 7 October 2014; accepted 28 November 2014; first published online 26 January 2015)

We present experimental measurements conducted on freely propagating, turbulent, steady thermal air plumes. Three plumes are studied with differing source conditions, ranging from jet-like, momentum flux dominated releases, to pure plume releases, characterised by a balance between the momentum, volume and buoyancy fluxes at the source. Velocity measurements from near the source to a height of tens of source diameters were made using particle image velocimetry (PIV), providing a high spatial resolution. Temperatures were measured with thermocouples. From these measurements, we investigate the vertical development of the plume fluxes and radial profiles of the mean velocity and temperature. These allow us to analyse the local self-preserving characteristics of the mean flow and to estimate the dependence with height of the plume Richardson number Γ. In addition, we analyse the similarity of one-point and two-point second-order velocity statistics, and we discuss the role of Γ on the vertical development of the bulk dynamical parameters of the plume, namely, the turbulent viscosity, the turbulent Prandtl number and the entrainment coefficient α_G. Comparison with previous experimental results and with estimates of the entrainment coefficient based on the mean kinetic energy budget allow us to conclude on the influence of Γ on the entrainment process and to explain possible physical reasons for the high scatter in estimates of α_G in the literature.

Key words: plumes/thermals, turbulent convection, turbulent mixing

1. Introduction

Axisymmetric turbulent forced plumes produced by horizontal, circular sources of constant buoyancy, momentum and volume fluxes have been the subject of considerable research over the last 70 years or so. Zel'dovich (1937), Priestley & Ball (1955) and Morton, Taylor & Turner (1956) developed the classic plume model assuming a conceptual point source of buoyancy flux alone, complete dynamical self-similarity, fully developed turbulence, small density differences and

† Email address for correspondence: pietro.salizzoni@ec-lyon.fr

negligible diffusion and radiation. The backbone of this theory has remained virtually unchanged since. The validation of this theory has been comprehensive and has essentially fallen into two categories: the first through widespread application where the bulk flow of plumes occurring over a range of different scales, in the natural and built environments, and in industry, are of interest; and the second through predominantly experimental campaigns focusing on the details of the internal flow. Although relatively few in number, the latter have provided a quantification of some of the key dynamical quantities, such as the entrainment coefficient, the mean to turbulent ratio of the vertical fluxes and of the radial spread of the buoyancy and velocity profiles. These quantities are however characterised by a non-negligible scatter, with differences that can exceed 20–25 % (Linden 2000). Despite this scatter, the classic plume solutions provide a robust and reliable model for buoyant plumes in geophysical and industrial contexts and have been extended to account for stratified environments (Batchelor 1954; Caulfield & Woods 1998; Kaye & Scase 2011), non-constant source strengths (Scase *et al.* 2006), negative buoyancy (Baines, Turner & Campbell 1990; Carazzo, Kaminski & Tait 2008; Burridge & Hunt 2012; Mehaddi, Vauquelin & Candelier 2012), chemical reactions (Zhou 2002; Campbell & Cardoso 2010; Ülpre, Eames & Greig 2013) and their non-Boussinesq counterparts (Rooney & Linden 1996; Carlotti & Hunt 2005). For further reading on the development of plume theory, review papers by List (1982), Kaye (2008), Woods (2010) and Hunt & van den Bremer (2011) are recommended as is the text of Linden (2000).

More generally, we can assert that the dynamical properties of buoyant jets in their asymptotic states of 'pure jet' and 'pure plume' are nowadays widely identified in the literature. Much less is known about the variability characterising the dynamics of buoyant releases in what may be regarded as the 'transition' states between these asymptotic states, for example as the buoyancy flux of a highly forced plume is systematically increased. Assuming a fully turbulent Boussinesq plume, with negligible influence of diffusive phenomena, developing in an unstratified quiescent ambient fluid, the flow dynamics can be shown to depend on a single non-dimensional parameter: the plume Richardson number Γ. This may be evaluated at any height z above the source (at $z = 0$) based on the local volume, momentum and buoyancy fluxes (Hunt & Kaye 2001) as

$$\Gamma(z) = \frac{5}{2^{7/2}\pi^{1/2}\alpha_{ref}} \frac{Q(z)^2 B(z)}{M(z)^{5/2}} \tag{1.1}$$

where α_{ref} denotes the reference value of the entrainment coefficient for Gaussian profiles and the mean fluxes of volume Q, specific momentum M and specific buoyancy B are defined as

$$\left.\begin{aligned} Q(z) &= 2\pi \int_0^\infty w(r, z) r \mathrm{d}r \\ M(z) &= 2\pi \int_0^\infty w^2(r, z) r \mathrm{d}r \\ B(z) &= 2\pi \int_0^\infty w(r, z) g'(r, z) r \mathrm{d}r, \end{aligned}\right\} \tag{1.2}$$

where w is the Reynolds-averaged vertical velocity, r denotes the radial coordinate of the axisymmetric plume (figure 1) and $g' = g((\rho_e - \rho)/\rho_e)$ denotes the Reynolds-averaged buoyancy (g is the gravitational acceleration) of the plume fluid, of density $\rho(r, z)$, relative to a fixed representative density ρ_e of the ambient.

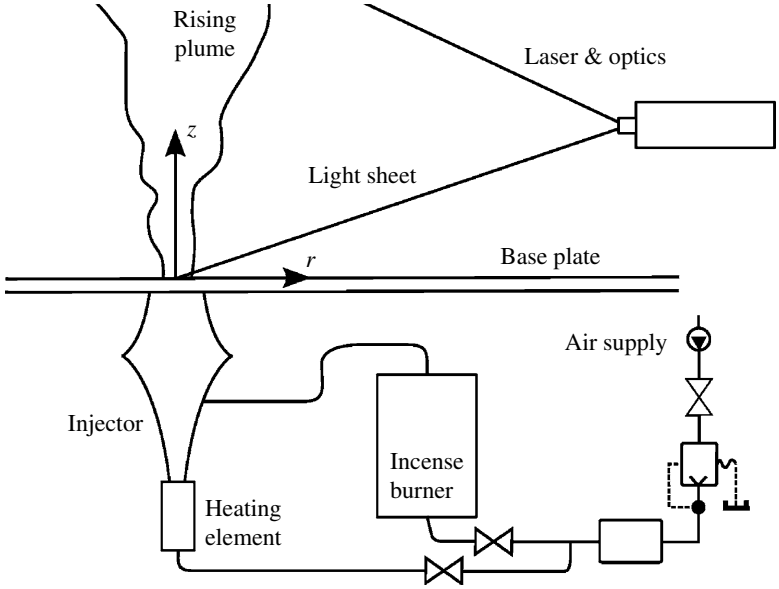

FIGURE 1. Schematic of the experimental set-up for PIV on thermal air plumes with the coordinate system (r, z) employed herein.

It is worth mentioning that when the plume density is significantly lower than that of the ambient, such that the conditions are non-Boussinesq (Rooney & Linden 1996; Carlotti & Hunt 2005; van den Bremer & Hunt 2010), the ratio ρ/ρ_e has to be considered as a second non-dimensional parameter on which the flow dynamics depend.

The dependence of the plume dynamics on Γ and on ρ/ρ_e has rarely been investigated experimentally and represents nowadays a major research axis in this field. In order to focus on this variability, and primarily on the role of Γ, benefitting from advancement in visualisation and data acquisition techniques, we have performed experiments on steady, thermal air plumes injected into a nominally quiescent, unstratified laboratory enclosure at differing source Richardson number. The remainder of this paper is structured as follows. We begin by reviewing the major findings of previous experimental works on buoyant plumes in order to motivate a further experimental investigation. The experimental set-up and plume source conditions investigated are outlined in § 2. Radial profiles of time-averaged velocities derived from particle image velocimetry (PIV) velocity and thermocouple temperature measurements are examined in § 3. From the high spatial resolution of the PIV measurements, we investigate the turbulent intensities, the turbulent momentum transfer and the spatial structure of the turbulent flow (§ 4). Finally, in § 5 we present different estimates of the entrainment coefficient that allow us to conclude on the influence of Γ on the entrainment process.

1.1. *Previous experimental results*

In early experimental work, Ricou & Spalding (1961) injected air radially inwards towards buoyant jets enclosed by a porous cylinder until they measured a zero pressure drop across the cylinder. This satisfied what they called the 'entrainment appetite' of the flow and, as a result, they determined the entrainment coefficient for buoyant gas jets of varying densities. Although the releases were buoyant, the forcing at source

was such that the flows were relatively jet-like over the region of interest. The major contribution of their work was to establish a dependence of the entrainment coefficient on the ratio ρ_0/ρ_e of the injected fluid density ($\rho_0 = \rho(z = 0)$) to the ambient fluid density; the subscript '0' is used throughout to denote the value of quantities at the source.

George, Alpert & Tamanini (1977) investigated the buoyant plume and made concurrent temperature and velocity measurements using two-wire probes. The plumes were neither Boussinesq nor fully turbulent at the source. They found that the velocity profiles were Gaussian and approximately 10 % wider than their buoyancy counterparts. Their measurements of the fluctuating flow components show that these were still developing at heights exceeding 20 source radii, yet also tend towards Gaussian profiles. The entrainment coefficient in the far field was estimated as $\alpha_G = 0.108$ (throughout the paper we always refer to Gaussian entrainment coefficients, a factor $\sqrt{2}$ lower than the top-hat equivalent in classic plume theory). Finally, George *et al.* (1977) estimated that the turbulent fluxes of momentum, i.e. related to the standard deviation of the vertical velocity σ_w^2, and of buoyancy, i.e. related to the correlation of vertical velocity and temperature $\overline{\tilde{w}\tilde{T}}$, are responsible for 8 and 15 % of the overall fluxes, respectively. The same experimental apparatus was used by Shabbir & George (1994), who conducted simultaneous velocity and temperature measurements by means of a set of hot-wire and cold-wire probes. In this case, the experimental facility was completed by a rack of thermocouples to monitor the ambient air stratification and by concentric screens placed around the source to prevent horizontal plume drift: the latter may have inadvertently influenced plume entrainment. Source Reynolds numbers were slightly higher than those attained by George *et al.* (1977), but not high enough to produce fully turbulent plumes at the source. The study extended the George *et al.* (1977) analysis to third-order moments of the velocity components, of the temperature and of their correlations. A relatively poor fit of the mean vertical velocity data to a Gaussian curve is presented. Given this poor fit of the key first statistical moment of the data, the validity of the computation of second and third moments is questionable. Nevertheless, good agreement is achieved between the measurements of the vertical fluxes and the power-law relationships predicted by the classic plume model. Both George *et al.* (1977) and Shabbir & George (1994) focus on the region where the flow reaches the truly plume-like asymptotic condition, i.e. $\Gamma = 1$, and do not provide any information on the transition region, as the flow adjusts from either jet-like ($\Gamma \ll 1$) or highly lazy ($\Gamma \gg 1$) states at its source.

A first systematic investigation of buoyant jets examining the role of the plume Richardson number at the source was performed by Papanicolaou & List (1988). They used laser-Doppler anemometry (LDA) combined with laser-induced fluorescence (LIF) to simultaneously measure velocities and concentrations in saline plumes at frequencies of up to 50 Hz over a vertical extent of 80 cm ($\approx$40–100b_0, where b_0 is the source radius) from an orifice measuring 0.75–2.0 cm in diameter. The spatial resolution of their measurements was an order of magnitude lower than that reported herein and their velocity data was acquired at points rather than over a plane. However, the simultaneous measurement of salinity and velocity signals enabled correlation of the two, and thereby one of the few published estimates of the turbulent buoyancy flux in plumes: of approximately 16 % of the mean buoyancy flux. The source Richardson number varied from jet-like to plume-like buoyant releases. Papanicolaou & List (1988) found that the forced plume examined behaved in a jet-like manner for $z/L_M < 1$, a plume-like manner for $z/L_M > 5$ and a smooth vertical transition

between the two regimes occurred over $1 < z/L_M < 5$, $L_M = \mathscr{C} \cdot M_0^{3/4}/B_0^{1/2}$ denoting a characteristic length known as the 'jet length' (with $\mathscr{C} = (5/9\alpha_{ref})^{1/2}(2/\pi)^{1/4}$). The vertical extent of these regions agrees well with the theoretical prediction of Morton (1959). Their measurements showed that the radial profiles of the statistics of density and velocity within jet-like and plume-like releases do not differ significantly from each other. Furthermore, these profiles do not show any significant discrepancy with the LDA measurements on isothermal jets performed by Hussein, Capp & George (1994). The noteworthy differences observed were related to the transport of buoyancy produced turbulence, with almost twice the flux in pure plumes as in jet-like releases. Other major differences concerned the ratio of length scales

$$\varphi = b_{g'}/b_w \tag{1.3}$$

between the spread of buoyancy $b_{g'}$ and velocity b_w profiles that took an average value of $\varphi = 1.19$ in plume-like releases and $\varphi = 1.33$ in jet-like releases, thereby contradicting the findings of George, Alpert & Tamanini (1977). Finally, the entrainment coefficient α_G was found to be equal to $\alpha_j = 0.0545$ in pure jets and $\alpha_p = 0.0875$ in pure plumes. The investigation of the dependence of φ and α_G with the plume Richardson number, however, was beyond the scope of their study.

Only relatively recently have plume dynamics been investigated with PIV thereby allowing for higher spatial resolution of the velocity measurements than earlier techniques. Wang & Law (2002) performed simultaneous velocity and density measurements with PIV and planar laser-induced fluorescence (PLIF). They performed experiments over a large number of saline plumes that were all highly forced at the source, i.e. $\Gamma_0 \ll 1$. As far as we are aware, this is the first experimental study reporting the variability of φ and α_G with the local Richardson number. Wang & Law (2002) found a general trend of a decreasing φ with increasing Richardson number, whereas α_G was shown to increase with the Richardson number. Both features will be widely discussed throughout the present paper. More recently Pham, Plourde & Kim (2005) focused on the dynamics of a thermal plume generated by a heated plate maintained at a constant temperature $T_0 = 400\,^{\circ}\mathrm{C}$. Pham *et al.* (2005) provided a detailed description of the three-dimensional structure of the velocity field by means of stereoscopic PIV, but did not report any temperature or density measurement. From their PIV measurements they directly measured the entrainment coefficient and compared it with estimates provided by classic indirect methods. However, the lack of temperature data prevented them from linking the values of the entrainment coefficient to the variation of Γ.

This overview of previous studies highlights the general lack of knowledge on the behaviour of a buoyant plume in the transition state characterised by a local variation of the plume Richardson number. This lack of knowledge motivates our work, which aims to shed light on the dynamical variability of buoyant plumes. To this end we performed experiments on plumes with highly contrasting conditions at the source, characterised by values of Γ_0 varying over three orders of magnitude.

2. Experimental set-up and parameters

We measured velocities and temperatures using PIV and thermocouples, respectively, in thermal air plumes in a windowless, thermally insulated enclosure.

The experimental set-up is shown in figure 1. Air was fed from a compressor to a mass flow-rate meter, where the mass flux was monitored and controlled by an electronic feedback system. A small fraction of the air ($\approx 5\,\%$ by volume) passed

via a chamber where it was seeded with incense particles. The seeded air rejoined the unseeded air immediately upstream of the heating element. The heated air then passed through a diverging–converging section, over a turbulence grid and finally through a diaphragm opening. Air temperature was monitored continuously at the diaphragm to ensure steady source conditions. The ambient air was seeded using a stage smoke generator, which filled the whole enclosure with approximately spherical 1 μm polyethylene glycol particles. Over a 10 min period, the release of smoke spread to fill the enclosure uniformly. When the ambient air motion induced by the initial jet of smoke dissipated, acquisition of data could begin. Approximately one smoke injection per hour seeded the ambient sufficiently. Seeding both plume and ambient air was necessary in order to obtain proper velocity statistics, statistics which would otherwise be biased when solely seeding the plume.

Temperature measurements were made with a horizontal rake of thermocouples spaced at 10 mm intervals. The uncertainty associated with these measurements was estimated as ± 0.5 K. The rake was sequentially displaced vertically at increments of 10 mm, from $z = 12$ to $z = 512$ mm. Temperatures were measured for 3 min at 10 Hz.

We acquired and processed PIV data using LaVision's DaVis 7.2 software. Circular interrogation areas with a 50 % overlap were employed, resulting in a spatial resolution of 0.7 mm. To achieve this resolution, the measurement plane was split into various fields of view with 3000 image pairs acquired sequentially for each field. In order to record sufficiently large particle images to allow for PIV processing at 16×16 pixels and to minimise peak-locking, we split the acquisition into 8 adjacent fields of view measuring approximately 150 mm (horizontal) $\times$ 100 mm (vertical) with a 15 mm vertical overlap between successive fields to ensure continuity of data. The camera could not be moved further than 1.5 m from the laser plane to prevent peak-locking from becoming significant. Subpixel accuracy of the processing algorithm was thus maintained. Measurements on plumes at a spatial resolution of less than 1 mm have seldom been undertaken and those presented herein represent a resource for numerical practitioners, experimentalists and theoreticians alike. Velocity measurements were made at a frequency of 4 Hz, and the duration of each acquisition was 12.5 min. Dynamic statistics were obtained from the 3000 instantaneous measurements.

In order to compare the spatial and temporal resolutions of our measurements with characteristic (turbulent) time and length scales of the flows, estimates of a typical length scale ℓ and velocity scale υ, the former approximately equal to the plume radius and the latter to the standard deviation of the vertical velocities, were computed. In the flows analysed here, ℓ varied from a minimum of approximately 10 mm in the near field of release J to a maximum of 75 mm in the far field of release P (see table 1), whereas υ is of the order 1 m s^{-1} in release J and 0.1 m s^{-1} in release P. From these we obtained typical time scales $\tau \sim \ell/\upsilon$ of the order 10^{-2} s for release J and 10^{-1} s for release P. The temporal resolution of the PIV and thermocouple measurements are therefore slightly larger than τ and insufficient to allow the computation of turbulent velocity and temperature spectra. The spatial resolution of the PIV measurements is at least one order of magnitude lower than ℓ allowing for a detailed description of the velocity field structure. Conversely, for thermocouple measurements the spatial resolution is coarser and approaches ℓ in the near field of release J.

The injected air velocity was kept as high as practicable in order to maximise the Reynolds number and reduce the influence of background disturbances. A nozzle was

Release	b_0 (cm)	T_0 (K)	g_0' (cm s^{-2})	Q_0 (cm^3 s^{-1})	M_0 (cm^4 s^{-2})	B_0 (cm^4 s^{-3})	L_M (cm)	Γ_0	Re_0	z_B (cm)	$\frac{z_{max}}{b_0}$	$\frac{z_{max}}{L_M}$
J	0.5	381	0.0232	0.54×10^3	3.7×10^5	1.3×10^5	98	0.001	7700	15	132	0.8
F	1.5	381	0.0232	1.49×10^3	3.1×10^5	3.46×10^5	47	0.034	2600	15	44	1.8
P	2.5	391	0.0252	1.01×10^3	5.6×10^4	2.65×10^5	15	0.96	1100	13	26	5.5

TABLE 1. The three source conditions of the releases investigated giving the plume Richardson number $\Gamma_0 = \{0.001, 0.034, 0.96\}$; note that the value $\alpha_{ref} = 0.1$ has been assumed when calculating Γ_0 from (1.1). The source buoyancy is $g_0' = g(\Delta T_0/T_0)$. Here J refers to jet-like, F to forced plume and P to pure plume. We use z_B to denote the non-Boussinesq length scale (2.1), $L_M = \mathscr{C} \cdot M_0^{3/4}/B_0^{1/2}$ to denote the jet-length, with $\mathscr{C} = (5/9\alpha_{ref})^{1/2}(2/\pi)^{1/4}$. The final two columns report, respectively, the limiting measurement heights, z_{max}, scaled on the source radius, b_0, and on the jet length, L_M.

selected with a maximum radius of 2.5 cm. With the 2 kW coiled heating element, a maximum temperature difference of $\Delta T_0 = T_0 - T_e \approx 90$–$100$ K (T_e is the ambient air temperature) was possible and this enabled us to achieve a relatively high source buoyancy flux at the lower velocities we considered. Table 1 summarises the three different releases studied, where the letters J, F and P refer to jet-like, forced and pure plume releases, respectively. Measurements were made over a vertical extent ranging from 1 to 70 cm above the source. The corresponding non-dimensional heights are listed in the final two columns of table 1.

For our set-up, the Reynolds number at the source ($Re_0 = (w_0 b_0)/\nu$, w_0 denoting the velocity at the source and ν the air kinematic viscosity) decreases with increasing Γ_0. The higher source Richardson number (table 1) of the pure plume required relatively low flow velocities so that $Re_0 \approx 1000$, implying that the near-source flow field is not fully turbulent (we return to this in § 3). The temperature at the source reached 393 K, producing flow conditions that are nominally beyond the limits of the Boussinesq approximation. Woods (1997) suggested a length scale over which non-Boussinesq effects are significant as

$$z_B = \frac{5}{3}\left(\frac{B_0^2}{20\alpha_{ref}^4 g^3}\right)^{1/5}. \tag{2.1}$$

An estimate of this length scale for our experiments leads to $z_B \sim 15$ cm. A non-negligible part of the domain could therefore be affected by non-Boussinesq effects on the flow dynamics.

The experimental apparatus was conceived to produce buoyant turbulent plumes within an unstratified quiescent environment. We however observed two main features inducing non-negligible departures from these ideal conditions. The first concerned the diffusion of heat along the horizontal rigid wooden base plate within which the nozzle was mounted (figure 1). Heat transferred from this plate (at $z = 0$) resulted in a region, of approximately 5 % of the vertical extent of the domain, where the ambient air temperatures could not be considered to be uniform. Figure 2 shows the mean temperatures in the ambient measured over the course of the three experiments using a rack of thermocouples. From these we estimate the temperature gradient to be 1 K cm^{-1} over a layer approximately 3 cm thick immediately above the plate. The second concerned the ambient air which was not perfectly still. Background air motion was unavoidable for a number of reasons: the release induces a flow

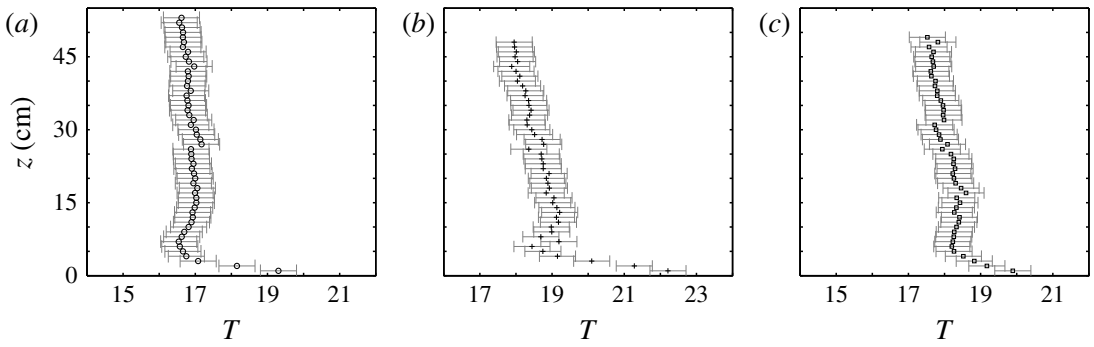

FIGURE 2. Vertical profiles of ambient temperature T (degrees centigrade) registered in experiments for releases (*a*) J, (*b*) F and (*c*) P.

Symbol	○	●	□	△	▷	◁	∗	+	×	▽	◇	■	●
J	9.0	16.1	23.2	30.2	37.3	44.4	51.5	58.5	65.6	72.7	79.8	86.8	93.9
F	3.0	5.4	7.8	10.2	12.5	14.9	17.3	19.7	22.0	24.5	26.8	29.2	31.6
P	1.8	3.2	4.6	6.0	7.4	8.8	10.2	11.6	13.0	14.4	15.8	17.2	18.6

TABLE 2. Non-dimensional profile heights $z_b = z/b_0$ plotted in figures 3, 4, 9, 10 and 15.

within the confines of the test room as it was necessary to seed the environment with smoke. Mean air velocities in the background, as estimated by PIV measurements, never exceeded 10 % (for releases J and F this percentage was far lower) of the mean centreline plume velocity w_m and the standard deviation of this fluctuation about this mean was always less than $0.1w_m$: equivalent to an actual velocity of 7 cm s^{-1}. These intensities of background motion are directly comparable with those in previous plume studies.

3. Mean flow and temperature field

First, we focus on the evolution of mean velocity and buoyancy (temperature). We examine the radial evolution of the vertical component of the mean velocity and of the mean temperature. Whilst over 800 velocity profiles were gathered for each release, plotting all of the data collected was unhelpful in explaining the trends; for this reason each plot shows 13 radial profiles equally spaced in height and spanning the entire vertical extent of each experiment. See table 2 for heights and symbols used in these plots. Mean temperature profiles are given at these same distances from the source. We discuss the reliability of the assumption of Gaussian profiles (§§ 3.1 and 3.2), profiles which allow us to readily identify characteristic scales for the plume width, velocity and buoyancy with height. The analysis of the variation with height of these local scales (§§ 3.3.1 and 3.3.2) provides first evidence of the dynamical behaviour of the three releases. To discuss this further, we compute the vertical evolution of the plume Richardson number $\Gamma(z)$ by integrating the radial profiles of mean vertical velocity and temperature (§ 3.3.3). Finally, we discuss the implication of self-similarity of radial profiles in light of the concept of 'local self-similarity' proposed by George *et al.* (1977).

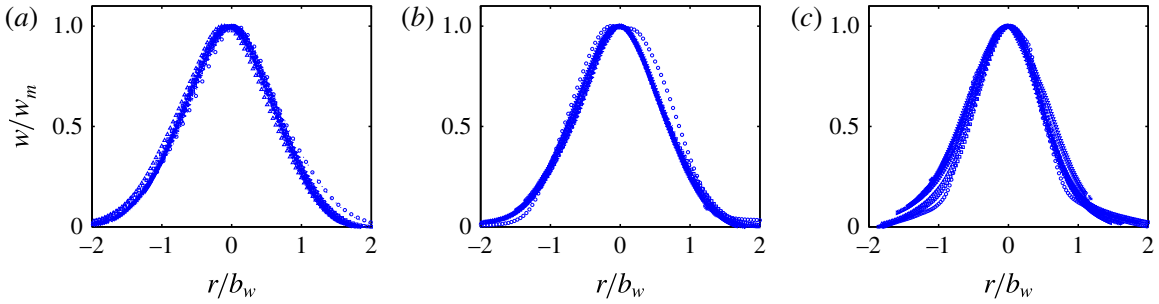

FIGURE 3. (Colour online) Non-dimensionalised radial profiles of time-averaged vertical velocity in releases (*a*) J (profiles plotted in the range $9 < z/b_0 < 94$); (*b*) F (profiles plotted in the range $3 < z/b_0 < 32$); and (*c*) P (profiles plotted in the range $2 < z/b_0 < 19$).

3.1. *Radial profiles of mean vertical velocity*

From each profile of the measured averaged vertical velocity, $w(r, z)$, a Gaussian profile centred on $r = 0$ was fitted to the data. The form of each profile

$$\frac{w(r, z)}{w_m(z)} = \exp\left\{\frac{-r^2}{b_w^2(z)}\right\}, \tag{3.1}$$

is determined by b_w, which we define to be the plume width and by w_m, the mean vertical centreline velocity, which, in a quiescent environment, corresponds to the maximum mean velocity. Due to background air motion and camera positioning uncertainties (estimated to be ± 2 mm horizontally) the maximum mean velocity did not always perfectly coincide with the axis ($r = 0$) of the experiment. When this was the case, the maximum value of $w(r)$ was recorded and the radial coordinate system locally translated so that $w_m(z) = w(0, z)$, so as not to introduce errors in the determination of the plume radius and the bulk quantities. These adjustments were never more than ± 3 mm.

Figure 3 shows non-dimensionalised radial profiles of mean vertical velocity. Figure 3(*a*,*b*) shows that the mean vertical velocity for plumes J and F exhibit a clear self-similarity and collapse tightly on to a Gaussian curve. Examination of figure 3(*c*) reveals a slightly increased scatter for plume P, compared to cases J and F. The reasons are twofold. Given the intermediate source Reynolds number, $Re_0 \approx 10^3$, in plume P (table 1), self-similarity of even the mean flow field is not to be expected in the near-source region. Moreover, the profiles for release P were at lower non-dimensional distances above the source (see table 1), where the flow was still influenced by the source profile. However, we verified that the Gaussian function provided a very good fit to the data, with $R^2 \geqslant 0.95$, for $z/b_0 > 5$.

3.2. *Buoyancy profiles*

The radial profiles of buoyancy are now examined. Figure 4 shows that, albeit with non-negligible scatter, the buoyancy profiles exhibit approximate self-similarity at all heights and in all experiments, even close to the source. The near-source behaviour noted in the velocity profiles is not observed, probably due to the cooling from the injector walls which resulted in a more pronounced parabolic shape of the outlet profiles. An identical curve-fitting procedure was used as that described in the

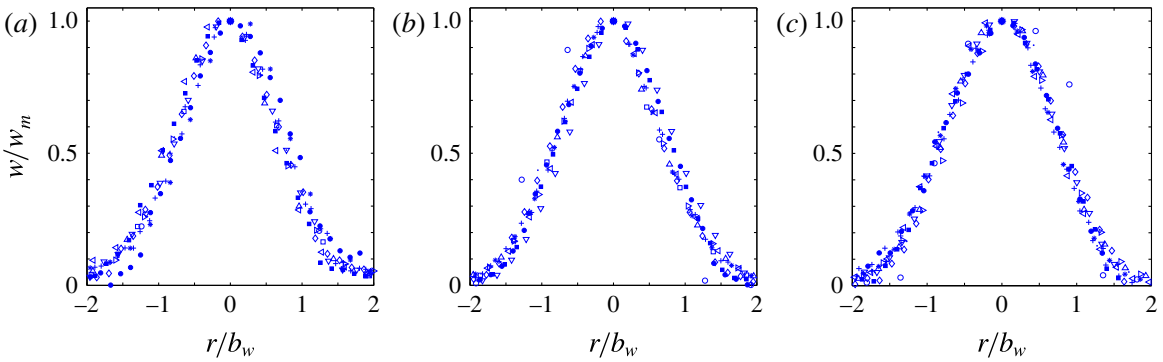

FIGURE 4. (Colour online) Non-dimensionalised profiles of buoyancy g'/g'_m for releases (*a*) J, (*b*) F and (*c*) P plotted over the same vertical extent as in figure 3.

previous section, with a fit of the form

$$\frac{g'(r,z)}{g'_m(z)} = \exp\left\{\frac{-r^2}{b^2_{g'}(z)}\right\}. \tag{3.2}$$

The characteristic length scale is now the standard deviation of the Gaussian buoyancy profiles, denoted $b_{g'}$, and the characteristic buoyancy scale is the maximum centreline buoyancy, g'_m. The goodness of the fit with a Gaussian function is lower than for the velocity profiles, with $R^2 \geqslant 0.95$ for releases J and F, and $R^2 \geqslant 0.9$ for release P.

3.3. *Vertical evolution of plume dynamics*

In order to unravel the dynamical evolution with height of the releases considered, we plot the vertical evolution of the centreline velocity and buoyancy, the plume radii and the local Richardson number $\Gamma(z)$.

To allow for direct comparisons between the different releases and the experimental data of others, the dynamic quantities are scaled on their source values and all lengths on the source radius, b_0.

3.3.1. *Radial growth from velocity and temperature profiles*

Figure 5 shows how the normalised plume radius b_w/b_0 evolves with height. From this we observe that all three releases tend to spread linearly with height in the far field, but at different rates.

While in both forced releases, J and F, the radius grows monotonically from very close to the source, albeit in a less-than-linear fashion, release P exhibits a different behaviour. The pure plume P appears to be straight-sided over a vertical distance of approximately $5b_0$, indicating that entrainment is substantially reduced in this section.

In the same figure we show the vertical evolution of the radius $b_{g'}$ as estimated from the temperature profiles; $b_{g'}$ equals or exceeds b_w for all releases and at all heights. This suggests that the radial turbulent transfer of heat is more effective than that of momentum. A further discussion on the physical implications of this feature is provided in § 4.3.

It is worth noting that the estimates of $b_{g'}$, as shown in figure 5, are characterised by a non-negligible scatter: scatter that becomes increasingly visible from release J to release P, as we 'zoom in' the spatial resolution (note the difference in the vertical axis scale in figure 5*a–c*). We attribute this scatter to the experimental uncertainties

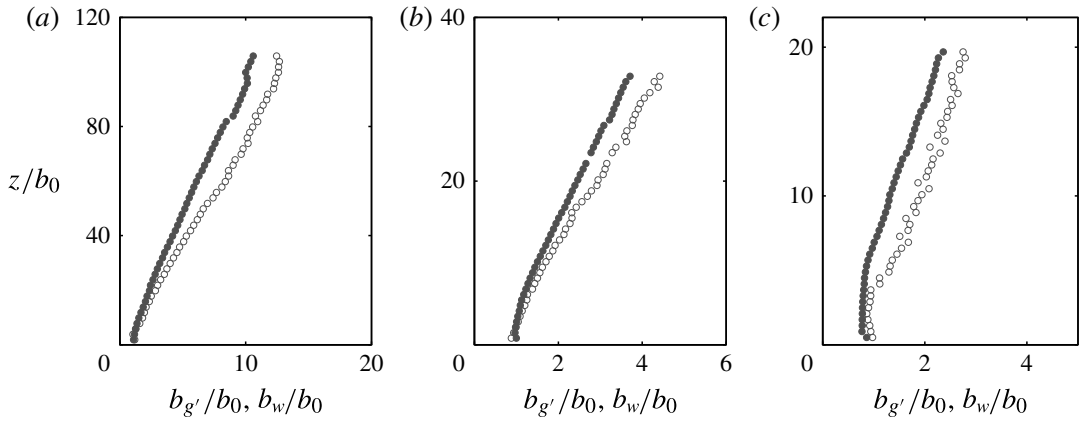

FIGURE 5. Comparison of normalised widths of velocity profiles b_w/b_0 and buoyancy profiles $b_{g'}/b_0$ with height z/b_0 for releases (*a*) J, (*b*) F and (*c*) P. Filled circles denote b_w/b_0, hollow circles denote $b_{g'}/b_0$.

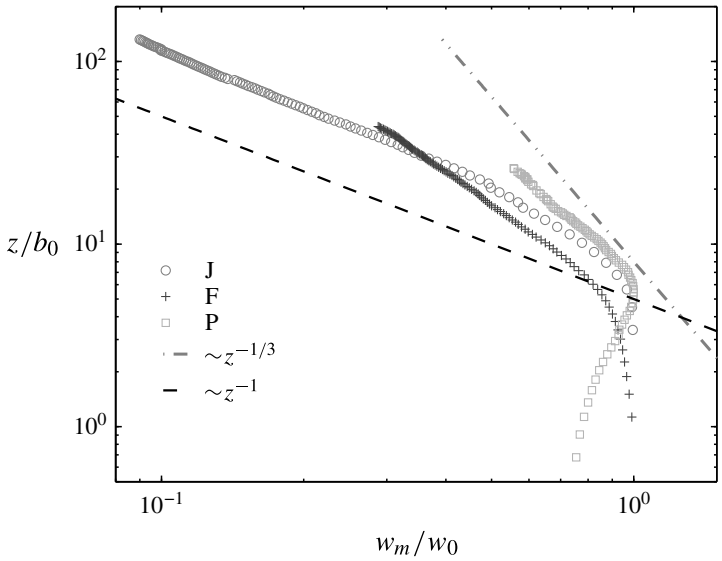

FIGURE 6. Vertical dependency of normalised centreline velocity w_m/w_0 for the three releases J, F, P with the pure jet, $\sim(z/b_0)^{-1}$, and pure plume, $\sim(z/b_0)^{-1/3}$, power laws.

in temperature measurement which lead to a variability in the estimates of $b_{g'}$ of approximately $\pm 5\,\%$. The uncertainty related to b_w was approximately $\pm 2.5\,\%$.

3.3.2. *Centreline vertical velocity and buoyancy*

We plot in figures 6 and 7 the vertical variations of centreline vertical velocity and centreline buoyancy, showing as a reference their theoretical pure-plume and pure-jet dependencies, that is $w_j/w_0 \sim (z/b_0)^{-1}$ and $g'_j/g'_{m0} \sim (z/b_0)^{-1}$ in pure jets (Fischer *et al.* 1979) and $w_p/w_0 \sim (z/b_0)^{-1/3}$ and $g'_p/g'_{m0} \sim (z/b_0)^{-5/3}$ in pure plumes (Morton *et al.* 1956).

Figures 6 and 7 highlight a substantial variation in the nature of the velocity decay with height for the three releases (in figure 6, data for plume P has been shifted to the left for ease of comparison). Release J, the most jet-like, closely follows the $\sim(z/b_0)^{-1}$ trend (dashed line) for both w_m/w_0 and g'_m/g'_{m0}: the latter for sufficiently large z/b_0.

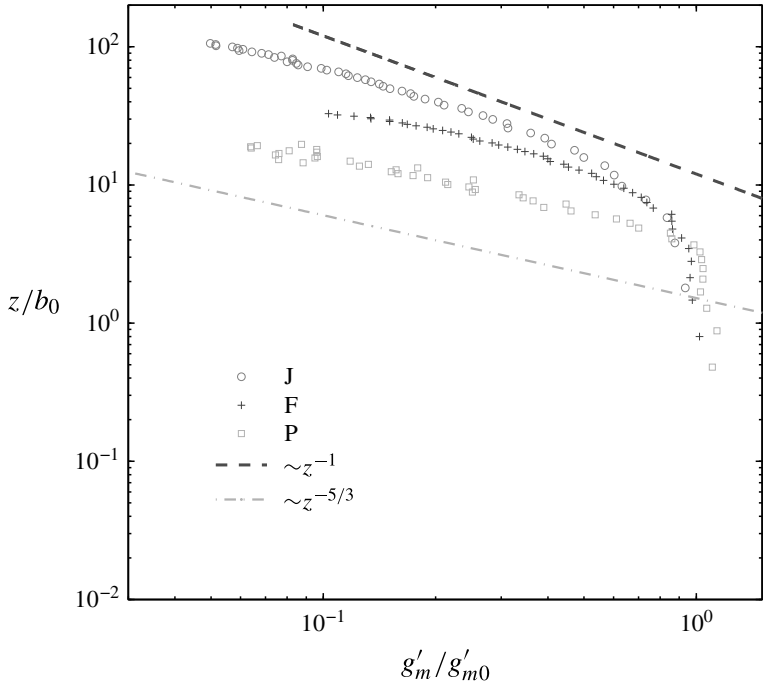

FIGURE 7. Vertical dependency of normalised centreline buoyancy g'_m/g'_{m0} for the three releases J, F, P, with the pure plume, $\sim(z^{-5/3})$, and pure jet, $\sim(z^{-1})$, dependencies.

This data indicates that heat is little more than a passive scalar quantity in this flow and the source momentum flux completely dominates that induced by the action of the buoyancy force. This is unsurprising as $z_{max} \approx L_M/3$, so the entire experiment is well within one jet-length of the source.

In release F, fluid decelerates and dilutes at a rate intermediate to the pure jet and pure plume. Even at a non-dimensional height of $z/b_0 \approx 40$, the behaviour shows no appreciable tendency to approach the $w_m/w_0 \sim (z/b_0)^{-1/3}$ and $g'_m/g'_{m0} \sim (z/b_0)^{-5/3}$ behaviour (dot–dashed line). Experiment F reaches a height of $z_{max} \approx 2L_M$ and is therefore entirely within the five jet lengths over which the flow is expected to exhibit a smooth transition between the near-field jet-like and the far-field plume-like asymptotic states (Morton 1959; Papanicolaou & List 1988).

As expected, release P exhibits a vertical behaviour that is fully consistent with the scaling laws of a purely buoyancy-driven plume, with a deceleration of the form $w_m/w_0 \sim (z/b_0)^{-1/3}$ and a dilution of buoyancy $g'_p/g'_{m0} \sim (z/b_0)^{-5/3}$.

It is worth noting that figures 6 and 7 show that close to the source, i.e. for $z/b_0 \leqslant 5$, all releases dilute and decelerate slowly, suggesting the presence of a non-turbulent core that, in turn, may be related to a reduced entrainment rate of ambient air. This tendency is particularly evident in release P. As figure 6 shows, the centreline velocity increases in release P by up to 20 % over the interval $0 \lesssim z/b_0 \lesssim 5$; this is a similar height range to that required for the velocity profiles to exhibit approximate self-similarity. The near-source acceleration is likely to be due to the relatively low Reynolds number in the near-source zone which implies a suppression of entrainment into the plume. In this condition, the unmixed fluid released accelerates due to its buoyancy. This acceleration persists until the flow becomes sufficiently turbulent to entrain at a rate consistent with a fully developed turbulent plume, with a radial momentum transfer that acts to reduce the centreline velocity.

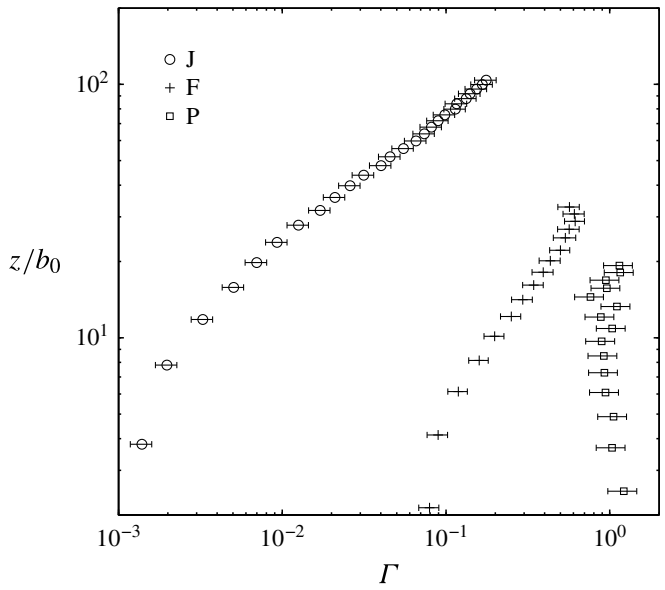

FIGURE 8. Vertical dependency of plume Richardson number Γ.

This simple analysis of the vertical variation of w_m and g'_m clearly shows that the dilution rate with increasing distance from the source varies significantly between the three cases considered. Therefore, behind an apparent similarity of the radial profiles of mean velocity and mean buoyancy, the flows develop with different dynamical behaviours which results in the entrainment of ambient air at different rates.

3.3.3. *Plume Richardson number*

An estimate of the plume Richardson number, $\Gamma(z)$ from (1.1), is essential in order to physically interpret the different behaviour of the three releases.

The plume Richardson number could be estimated at all heights by means of the mean vertical fluxes of volume, momentum and buoyancy. These fluxes were explicitly computed by means of the integrals (1.2), fitting the experimental data with the Gaussian profiles presented in §§ 3.1 and 3.2 and assuming rotational symmetry. Figure 8 shows this estimate for Γ. Error bars of amplitude 15 %, are associated primarily with uncertainty in the estimates of $b_{g'}$ and b_w (§ 3.3.1).

Encouragingly, the values of Γ near to the source closely match those in table 1, indicating that the source Richardson numbers achieved were very similar to those intended.

As has been customary, in this section we begin with an assessment of releases J and F; both low Richardson number, high Reynolds number flows at source. As expected, for both, Γ tends towards unity, release F at an increased rate compared to J as the theoretical models predict (Hunt & Kaye 2001).

The behaviour of $\Gamma(z)$ in plume P for small z/b_0 may appear surprising, since the Richardson number slightly 'overshoots' unity for $z/b_0 \leqslant 5$ – i.e. Γ first increases above unity and then decreases to unity with height. A similar behaviour can be observed in the numerical simulation performed by Devenish, Rooney & Thomson (2010). However, in our case, the 'overshoot' has to be attributed to a numerical artefact associated with the significant errors in the interpolation of the near-source velocity profiles with a Gaussian curve, and has therefore no physical significance.

Figure 8 clearly captures the variability of the dynamical state of the three releases examined. It is worth noting that, although there is considerable dynamical variability, the mean radial profiles previously examined showed a self-similar profile over the majority of the rise height. This then provides a clear example of what George (1989) defines as a 'local self-preserving flow', i.e. a flow that appears to scale with local quantities even though the equations of motion do not admit self-similar solutions, since any solution should account for the variability of Γ. However, as is evident in the analysis of the vertical variation of the centreline velocity and centreline buoyancy, behind this local self-similarity the plumes develop different dynamical behaviour with height that results, notably, in a different mixing rate with the ambient.

4. Turbulence

The aim here is to use turbulent statistics of the velocity data to illuminate the discussion that follows in § 5, particularly with regards to the (non-constant) entrainment coefficient.

4.1. *Turbulence intensities*

Figure 9 contains plots showing non-dimensionalised radial profiles of second-order moments of the velocity statistics, namely the vertical and radial turbulence intensities, $I_w = \sigma_w/w_m$ and $I_u = \sigma_u/w_m$ (where σ_w and σ_u are the root mean squares (r.m.s.) of the vertical and radial velocity), respectively. Heights of the radial profiles and symbols used in these plots are the same as those used for the mean velocities, as specified in table 2.

For release J, the turbulence intensity (figure 9*a*,*b*) exhibits a very good collapse on to a single curve with the exception of the four lowermost profiles. Neither these near-source profiles, nor those further from the source, are approximately Gaussian in contrast to the suggestion of Papanicolaou & List (1988). Rather, the maximum turbulence intensities are approximately constant within the range $|r/b_w| < 1$ (at $I_u = 0.2$ and $I_w = 0.25$). As the other experimental results demonstrate in due course, these turbulence intensity profiles are consistent for the three release conditions in the developed flow field and, what is more, they are consistent with previous data (Hussein *et al.* 1994; Shabbir & George 1994; Wang & Law 2002).

Figure 9(*c*,*d*) reveal that the lowermost turbulence intensity profiles for release F differ significantly from the developed profiles. A core of reduced turbulent intensities centred on the plume axis is clearly identifiable, becoming less pronounced with height. This appears to correspond to the zone of flow establishment, where the shear layer which develops on the plume perimeter has not fully penetrated into the plume interior. The fully developed turbulence intensity profiles approximately match those in release J. For F and J, the peak values of I_w and I_u show good agreement with the experimental results for non-buoyant jets of Hussein *et al.* (1994), namely $I_w \simeq 0.27$ and $I_u \simeq 0.22$, Shabbir & George (1994), namely $I_w \simeq 0.32$ and $I_u \simeq 0.19$, and Wang & Law (2002), namely $I_w \simeq 0.3$ and $I_u \simeq 0.2$. This confirms one major finding of the previous results; even though the increased buoyancy within the plume enhances local turbulence production, the excess of turbulent kinetic energy (t.k.e.) $\propto I^2$ appears to be fully scalable with the local variables w_m and b_w. In other words, the intensity of the t.k.e. and its spatial distribution within the plume appear to be independent of the processes that are responsible for its generation, i.e. related to inertial instabilities or thermal stratification. The concept of local self similarity can therefore also be extended to the t.k.e. levels within the release.

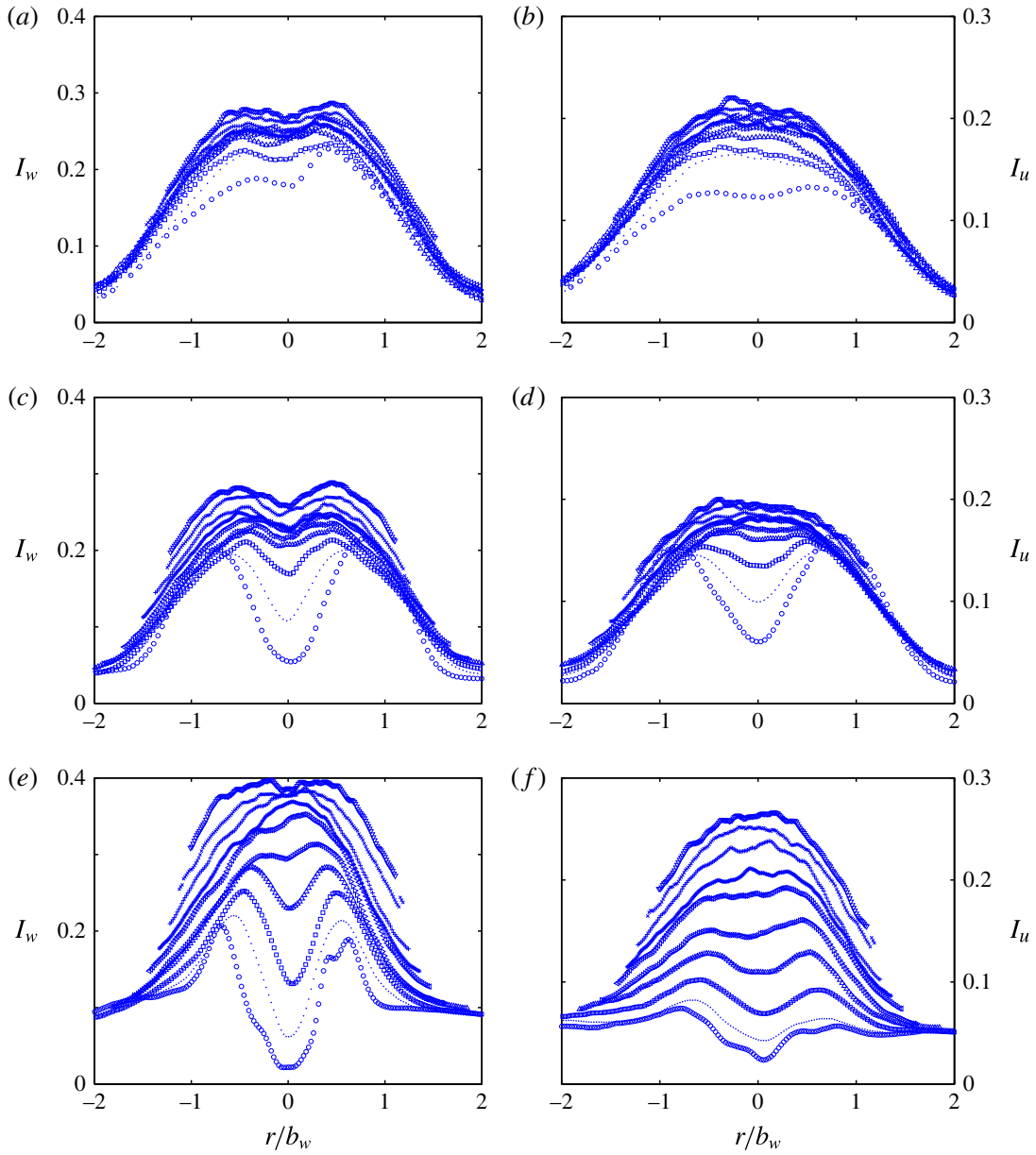

FIGURE 9. (Colour online) Non-dimensionalised radial profiles of the normalised r.m.s. vertical I_w and radial I_u velocities: (*a*,*b*) release J (profiles plotted in the range $9 < z/b_0 < 94$); (*c*,*d*) release F (profiles plotted in the range $3 < z/b_0 < 32$); (*e*,*f*) release P (profiles plotted in the range $2 < z/b_0 < 19$).

For release P, plots 9(*e*,*f*) show that for small z/b_0 the turbulent intensities are as low as 5 % inside the plume, indicating a quasi-laminar flow. The core of reduced turbulent intensity persists over approximately 5 source diameters and is noticeable in plots of both I_w and I_u. The maximum turbulence intensity is slightly increased in magnitude compared with the previous, more forced cases. However, this could be reasonably attributed to the higher scatter in the data and to the role of ambient turbulence (due to an ambient that is not perfectly quiescent) which increases as the velocities in the plume are reduced. Similar features can be observed in the measurements, obtained with the same measurement technique, of Wang & Law (2002). Their radial profiles of both I_w and I_u exhibit a similar scatter, and a similar

tendency to approach a value of approximately 0.1 (i.e. non-zero) beyond the plume borders.

A final remark concerns the fetch needed by the second-order velocity statistics to become (locally) self-similar. The analysis of the radial profiles of I_u and I_w suggest that self-similarity is attained between $30 < z/b_0 < 35$ for release J, $10 < z/b_0 < 15$ for F and $5 < z/b_0 < 10$ for P. This observation is in agreement with the idea that the higher the value of Γ at the source, the more rapid is the transition toward an asymptotic state of plume equilibrium. However, given the non-identical nozzle geometry for the three releases and their different source Reynolds numbers, these relationships between Γ_0 and the fetch required to attain self-similarity cannot be considered to be general values.

4.2. *Radial turbulent transfer of momentum and buoyancy*

4.2.1. *Reynolds stress and turbulent viscosity*

Figure 10(*a*) shows radial profiles of the Reynolds stress $\overline{\tilde{u}\tilde{w}}$ ($\tilde{u}$ is the fluctuation of the radial velocity) for the jet-like, high-source-Reynolds-number release J. Evidently, the Reynolds stress profiles tend towards a single profile at sufficiently high elevation. The form of the Reynolds stress profile is qualitatively very similar to that published in the numerical work of Zhou (2001) and with the measurements of Hussein *et al.* (1994) in isothermal jets, with a maximum stress value of approximately $|\overline{\tilde{u}\tilde{w}}/w_m^2| \simeq 0.025$. Examination of figure 10(*c*) for release F leads to the same broad observations as those above. As in release J, the Reynolds stresses for release F tend toward a single profile and show profiles very similar to those in figure 10(*a*). These observations are in very good agreement with the findings of Wang & Law (2002).

For the nominally pure plume release P, near to the source the Reynolds stresses (figure 10*e*) are negligible and approximately constant across the plume. However, with increasing distance from the source, the profiles begin to converge towards a self-similar profile which is similar in form to release F.

The high spatial resolution of the velocity statistics gathered allows us to achieve an experimental estimate of the turbulent viscosity, usually defined as

$$\nu_T(r, z) = -\overline{\tilde{u}\tilde{w}}(r, z) \Big/ \left(\frac{\partial w(r, z)}{\partial r} \right). \tag{4.1}$$

This quantity provides potentially important information concerning both the turbulence dynamics and the momentum transfer within the plume. The curves for the corresponding non-dimensional turbulent viscosity $\widehat{\nu_T} = \nu_T/(w_m b_w)$ are shown in figure 10. Near the plume axis, the small Reynolds stress is divided by a small velocity gradient which explains why the turbulent viscosity peaks here. In the two releases characterised by high Reynolds number, namely J and F, the radial profiles of $\widehat{\nu_T}$ (figure 10*b*,*d*), although scattered, tend towards a single profile at sufficiently high elevations that is similar to that identified by Hussein *et al.* (1994) for non-buoyant jets. This confirms that the momentum transfer within the releases is almost unaffected by buoyancy, as are the t.k.e. levels (see § 4.1), in the sense that any variation can be fully rescaled on local quantities leading to the same local self-similar curves.

It is questionable whether the values of $\widehat{\nu_T}$ in release P (figure 10*f*) genuinely exceed those of the other plumes. Non-dimensional profiles are far from collapsing on to a single curve (and the data is affected by significant scatter) which indicates the varying dynamical nature of the plume with height. Despite this, several profiles show a qualitative tendency that is very similar to that observed for releases J and F.

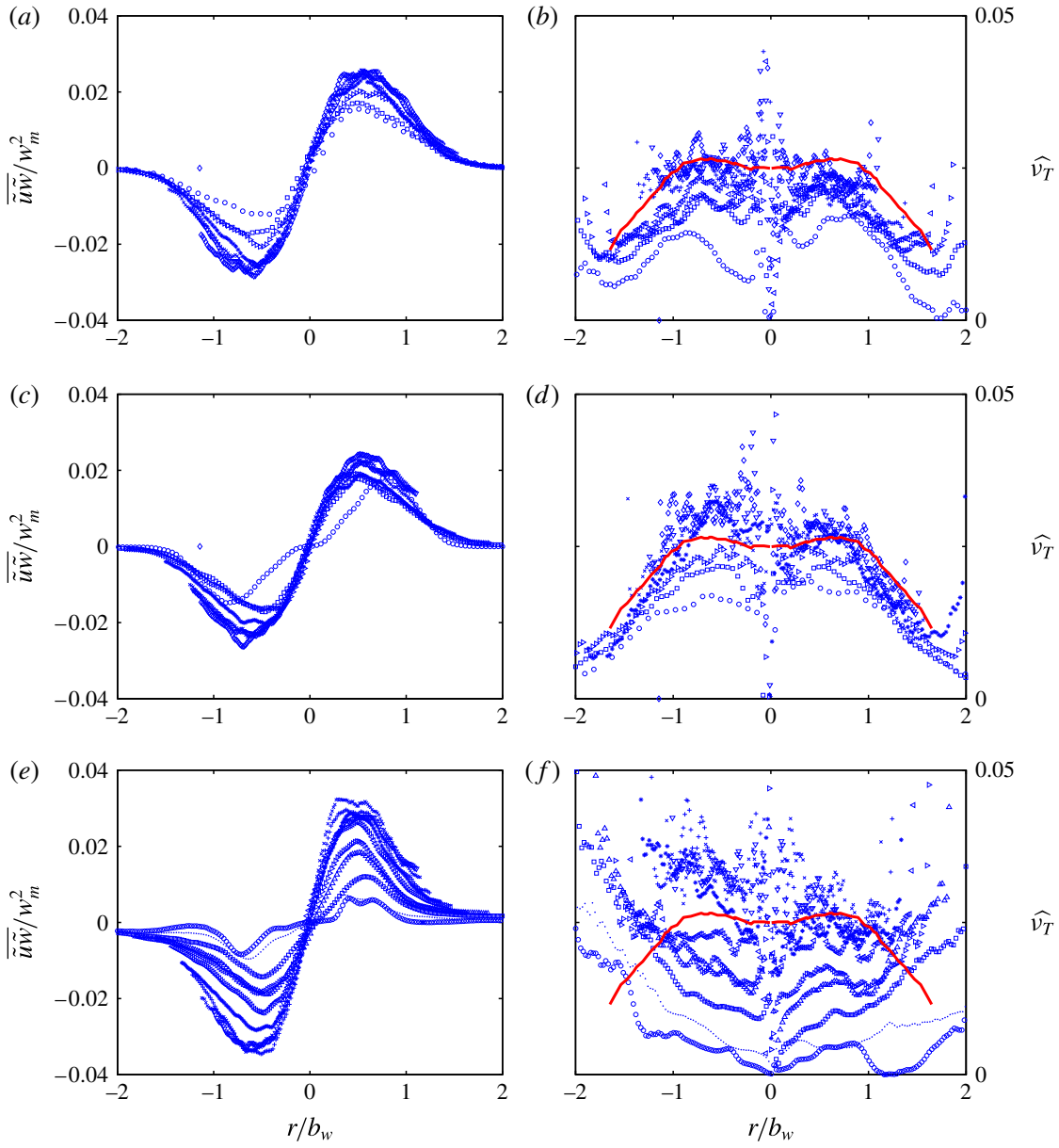

FIGURE 10. (Colour online) Radial profiles of non-dimensional Reynolds stress (*a*,*c*,*e*) and non-dimensional turbulent viscosity $\widehat{\nu_T} = \nu_T/(w_m b_w)$ (*b*,*d*,*f*) for (*a*,*b*) release J (profiles plotted in the range $9 < z/b_0 < 94$), (*c*,*d*) release F (profiles plotted for $3 < z/b_0 < 32$) and (*e*,*f*) release P (profiles plotted for $2 < z/b_0 < 19$). The continuous (red online) line represents the fit of the experimental data of Hussein *et al.* (1994) in a non-buoyant jet.

We can therefore conclude that evidently there is no one-to-one dependence of $\widehat{\nu_T}$ on Γ, i.e. that the increased role played by buoyancy in the dynamics as Γ increases does not necessarily result in a more effective turbulent radial transfer of momentum as is consistent with an increase in $\widehat{\nu_T}$. Just as for the other turbulent quantities examined, variations in the turbulent viscosity can be completely rescaled by local quantities confirming the 'local' self-similar behaviour.

To unravel the influence of Γ on the radial turbulent transfer of momentum it is instructive to examine the vertical evolution of a non-dimensional bulk turbulent

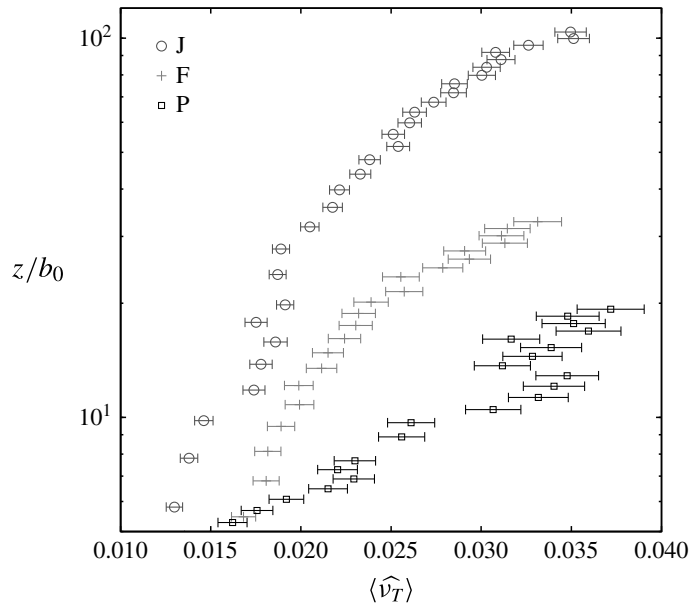

FIGURE 11. Vertical evolution of the non-dimensional bulk turbulent viscosity $\langle\widehat{\nu_T}\rangle$ for releases J, F and P.

viscosity $\langle\widehat{\nu_T}\rangle$, representing a spatial average of $\widehat{\nu_T}$ over the plume section. Values of $\langle\widehat{\nu_T}\rangle$ were estimated as those giving the best agreement on fitting the $\overline{\tilde{u}\tilde{w}}$ profiles with a function of the form

$$\mathscr{F}(r, z) = 2\langle\widehat{\nu_T}\rangle \frac{r^2}{b_w^2} \exp \frac{r^2}{b_w^2} \tag{4.2}$$

i.e. assuming the Gaussian form of the velocity profile (3.1). The vertical evolution of $\langle\widehat{\nu_T}\rangle$ plotted in figure 11 sheds light on the influence of a varying Γ on the plume dynamics. Despite a non-negligible uncertainty in the estimate of $\langle\widehat{\nu_T}\rangle$, which is reflected in error bars of 10–25 %, figure 11 depicts a clear tendency in its vertical evolution for the three releases considered. The quantity $\langle\widehat{\nu_T}\rangle$ evolves with height up to a far-field value of approximately 0.035 in all three cases, as could also be inferred by examining figure 10(*b*,*d*,*f*). It is however evident that the enhanced role of buoyancy in the plume dynamics accelerates significantly this evolution. As a result, for release J, $\langle\widehat{\nu_T}\rangle$ requires a distance of almost 100 radii to attain its far-field value. By contrast, for release P the evolution to the far-field value occurs over a fetch of approximately $10b_0$. As discussed in § 5, this feature plays a major role in the way the different releases entrain ambient air.

4.3. *Turbulent Prandtl number*

An experimental estimate of the radial turbulent transfer of heat (or mass) requires simultaneous measurement of velocity and temperature (or solute concentration c) in order to assess the radial variability of the correlation between fluctuations of temperature $\tilde{T}$ (or concentration $\tilde{c}$) and radial velocity. Just as for the momentum transfer, the adoption of a gradient closure model of the form (4.1), leads to an estimate of a turbulent diffusivity of heat (or mass) D_T, and therefore to the turbulent

Prandtl (or Schmidt) number $Pr_T = \nu_T/D_T$, that characterises the relative effectiveness of the two transport phenomena.

This kind of simultaneous measurement has seldom been undertaken and represents a major challenge in the experimental investigation of buoyant plumes. Shabbir & George (1994) performed these measurements in air plumes with hot-wire anemometry. Despite the remarkable experimental effort however, the radial profiles of $\overline{\tilde{u}\tilde{T}}$ presented in their study were affected by a considerable scatter, showing the limitations of wire anemometry in evaluating the variation of $\overline{\tilde{u}\tilde{T}}$ for varying dynamical plume conditions. Far smoother profiles were obtained by means of optical techniques in saline plumes by Papanicolaou & List (1988) and Wang & Law (2002). Both papers report profiles of $\overline{\tilde{u}\tilde{w}}$ and $\overline{\tilde{u}\tilde{c}}$ in jets and plumes with similar results. Far-field profiles of $\overline{\tilde{u}\tilde{w}}/w_m^2$ were insensitive to enhanced buoyancy, whereas $\overline{\tilde{u}\tilde{c}}/w_m c_m$ showed a clear tendency to be higher in plumes compared with jets. Papanicolaou & List (1988) found that $\overline{\tilde{u}\tilde{c}}/w_m c_m \simeq 0.12$ in jets and $\simeq 0.25$ in plumes, whereas Wang & Law (2002) found $\overline{\tilde{u}\tilde{c}}/w_m c_m \simeq 0.15$–$0.2$ in jets and $\simeq 0.25$–0.3 in plumes. Both studies indicate a general tendency of Pr_T to decrease as Γ increases.

Given the difficulty associated with the direct estimation of Pr_T, several authors could only infer its spatial average (over the plume section) by estimating the ratio $\varphi = b_{g'}/b_w$ between the local spread of the buoyancy and velocity profiles. Assuming Gaussian profiles, the (spatially averaged) turbulent Prandtl number can be estimated as

$$\langle Pr_T \rangle = \varphi^{-2}, \quad \varphi = \frac{b_{g'}}{b_w}. \tag{4.3}$$

It is worth noting that the values for φ in the open literature show a high variability. For example, Papanicolaou & List (1988) find $\varphi = 1.19$ in nominally pure plumes. Their estimates are consistent with their direct measurements of the radial turbulent fluxes of momentum and mass, and indicate that the spread of buoyancy exceeds that of the velocity owing to turbulence radially transferring buoyancy more effectively than momentum. However, experiments of other researchers on buoyancy-dominated plumes, including George *et al.* (1977) and Nakagome & Hirata (1977), led to the contradictory conclusion that $\varphi < 1$. This unexplained contradiction in the experimental results is particularly evident in the study of Wang & Law (2002). Their measurements indicate that φ decreases with increasing Γ, from a value of approximately 1.25 for a pure jet close to the source, toward unity for a pure plume in the far field. We stress here that this decrease is in contrast to the results of Papanicolaou & List (1988) and with Wang & Law's own experimental results, results that showed a tendency for $\overline{\tilde{u}\tilde{c}}/w_m c_m$ to increase with Γ.

The ratio φ, as a function of the normalised distance from the source, obtained from the estimates of $b_{g'}$ ($\pm 5\,\%$) and b_w ($\pm 2.5\,\%$) (see § 3.3.1 for details) is plotted in figure 12. A cursory examination clearly shows that the width of the error bars on φ are of the same order as its variation over the plume's vertical extent. This feature highlights a striking difference between the vertical evolution of φ (and Pr_T) and that of $\langle \widehat{\nu_T} \rangle$ (see figure 11) and Γ (see figure 8); while the trends in $\langle \widehat{\nu_T} \rangle$ and Γ are clear, the precise trend in φ is less clear.

Beyond this general uncertainty one could argue that there is a tendency in releases J and F for φ to increase with height. For release P the values of φ are higher although it is difficult to discern a clear trend. In all three cases, φ tends to a far-field value slightly higher than 1.2, which corresponds to $\langle Pr_T \rangle = 1/1.2^2 \simeq 0.7$: a result that

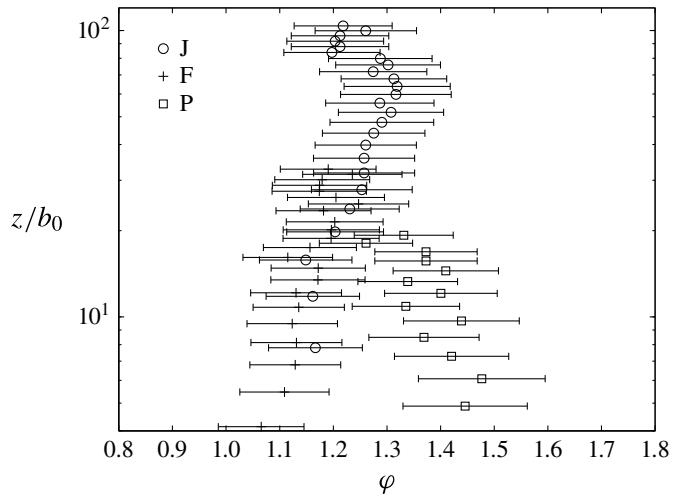

FIGURE 12. Vertical evolution of $\varphi = b_{g'}/b_w$ for releases J, F and P.

supports the findings of Papanicolaou & List (1988) and Panchapakesan & Lumley (1993) who found $\varphi \approx 1.2$ for pure plumes.

Kaminski, Tait & Carazzo (2005) suggested that the considerable discrepancy reported in the literature in the values of φ could be explained by the distance from the source at which profiles were measured. They noticed that researchers who obtained $\varphi < 1$ acquired data close to the source ($z/b_0 \sim 10$), whereas measurements further away ($z/b_0 \sim 100$) resulted in $\varphi > 1$. Kaminski *et al.* (2005) plotted the parameter $A = (2/3)(\varphi^2 + 1)$ against z/b_0, which varied from approximately $A = 1.1$ for $z/b_0 \leqslant 10$ to approximately $A = 1.9$ for $z/b_0 \simeq 100$. This led them to conclude that φ increases slowly with height, with typical values of $\varphi < 1$ in the near field and $\varphi \simeq 1.36$ ($\langle Pr_T \rangle \simeq 0.56$) in the far field. They referred to this evolution in the value of φ as 'similarity drift'.

Our data plotted in figure 12 partially supports their assertion. For releases J and F, φ shows a tendency to increase with z/b_0 to attain slightly higher values compared with those reviewed by Kaminski *et al.* (2005). In contrast, the data for release P suggests a tendency of φ to decrease with height, a tendency that is not consistent with 'similarity drift'. As already mentioned, a similar anomalous (with respect to the 'similarity drift' model) decrease of φ can be observed in the data of Wang & Law (2002). In the present case however, it is worth noting that this tendency is captured only over a limited vertical range from the source, since $z_{max}/b_0 = 19$ for plume P, and is inconclusive given the significant amplitude of the error bars. We therefore conclude that our data agrees partially with the concept of 'similarity drift' and that the non-negligible uncertainty in the estimates of φ does not bring to an end this controversy.

However, our experimental results highlight two important features that concern the nature of this 'drift'. These warrant discussion as they could help in explaining the wide spread of the literature data. First, whilst at the outset it may have been tempting to examine the variation of φ with Γ, we cannot identify any clear one-to-one relationship between them, and therefore between Pr_T and Γ (or indeed between $\langle \widehat{\nu_T} \rangle$ and Γ). Second, for two of the releases we observed a tendency of φ to increase. These aspects suggest that the evolution of $\langle \widehat{\nu_T} \rangle$ and φ is similar. From the nozzle the flow develops seeking its equilibrium state, with a near-field evolution whose rapidity is influenced by Γ. Therefore, at a given distance from the source, a forced

plume can exhibit varying φ depending on its Γ_0 (just as it can exhibit different $\langle\widehat{v_T}\rangle$), which explains the variety of values presented in the literature.

There is another reason that can potentially explain this variability. In their analysis, Kaminski *et al.* (2005) refer to data from 9 different experimental data sets; 5 of these refer to measurements taken between 10 and 30 radii from the source. It is well known from the literature data, and as discussed in §§ 4 and 4.2.1, that in this region intermediate to near field and to far field, the flow has not necessarily reached conditions for self-similarity. The region of the 'drift' is therefore, at least partially, a region within which the flow retains some memory of its source state. We cannot then exclude that the observed variability of φ is due to the influence of the source conditions (conditions that cannot be perfectly controlled by the experimentalist) on the subsequent evolution of the flow dynamics. It is customary to refer to the source condition as given by steady and self-similar radial profiles of velocity and temperature (or concentration), so that we can fully characterise the release by the governing parameters: Γ_0, Re_0 and T_0/T_e. The actual source flow conditions reproduced in an experiment (or in a numerical simulation) may, however, exhibit non-negligible departures from these idealised reference conditions. This can be due, for example, to a different form of the velocity and temperature profiles, to non-null intensities of the turbulent fluctuations or of the Reynolds stress. Thus, for identical values of Γ_0, Re_0 and T_0/T_e (defined by means of spatially averaged quantities), we can then have a variety of source conditions; these can exert their influence over a distance of several source diameters (see figure 8), along which the release evolves toward a condition of dynamical equilibrium and may exhibit a high variability of the local Γ. We stress that, if the uncertainties associated with the conditions imposed at the source do indeed have a significant influence on the near-field plume behaviour, it would be unclear how to dissociate them from the dependence of flow variables, such as φ (or α_G), on the local variation of Γ (or Re).

4.4. *Turbulence structure*

To provide further information on the turbulence dynamics we investigated its spatial structure by computing two-point velocity correlations throughout the domain. We focus here on the two-point correlation functions R_{uu} and R_{ww} of the vertical and radial velocity components, defined as

$$R_{uu}(\boldsymbol{x}_0, \boldsymbol{s}) = \frac{\overline{\tilde{u}(\boldsymbol{x}_0)\tilde{u}(\boldsymbol{x}_0+\boldsymbol{s})}}{\sigma_u^2(\boldsymbol{x}_0)} \tag{4.4}$$

$$R_{ww}(\boldsymbol{x}_0, \boldsymbol{s}) = \frac{\overline{\tilde{w}(\boldsymbol{x}_0)\tilde{w}(\boldsymbol{x}_0+\boldsymbol{s})}}{\sigma_w^2(\boldsymbol{x}_0)} \tag{4.5}$$

where $\boldsymbol{x}_0$ is any point in the domain, $\boldsymbol{s}$ is a displacement relative to $\boldsymbol{x}_0$ and the ensemble averaging is performed over the 3000 instantaneous velocity field measurements.

The integral over $\boldsymbol{s}$ of the functions (4.4) and (4.5) gives a length scale, referred to as an Eulerian integral length scale, which is representative of the maximal distance over which the velocities are correlated and, thus, provides an indication of the scale of an eddy. As an example we have plotted, in figures 13 and 14, isolines of R_{uu} and R_{ww} for releases F and P, computed on the centreline at the same non-dimensional distance from the source ($z/b_0 = 15$). Two main features are shown. First, a clear anisotropy of the turbulent field is evident with vertical velocity correlations that are

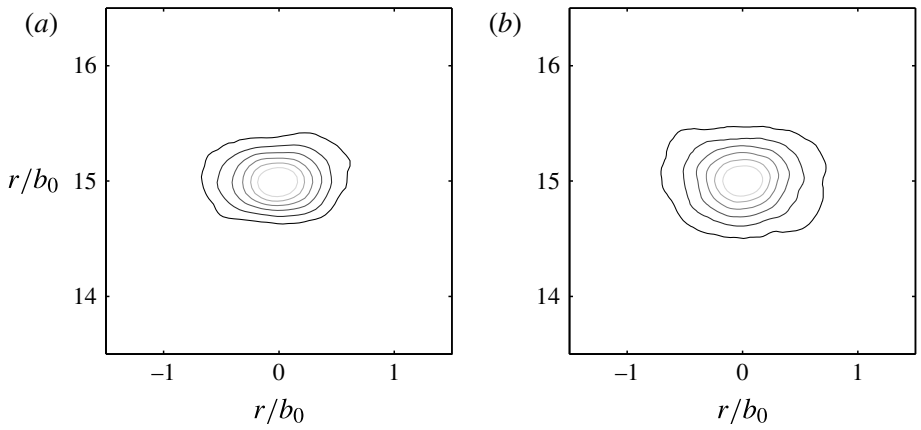

FIGURE 13. Correlation coefficient $R_{uu} = (\overline{\tilde{u}(x_0)\tilde{u}(x_0 + \boldsymbol{r})})/\sigma_u^2$ computed on the centreline at $z/b_0 = 15$ for release: (*a*) F and (*b*) P. Isolines vary from 0.8 for the inner contour to 0.3 for the outer.

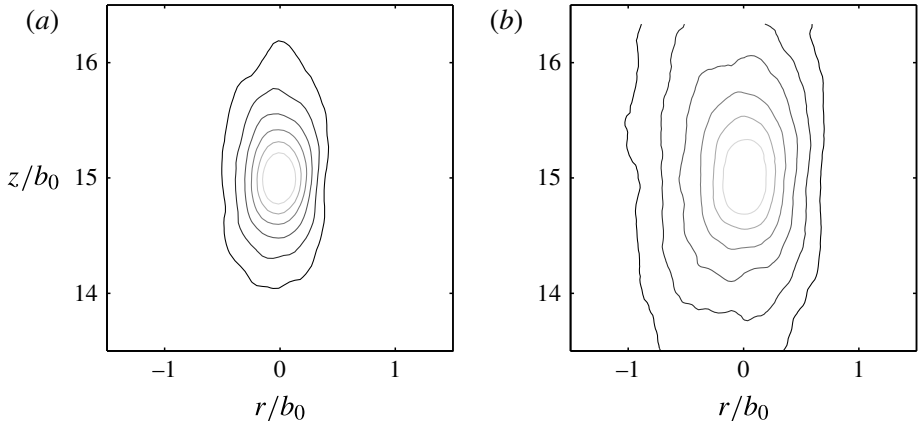

FIGURE 14. Correlation coefficient $R_{ww} = (\overline{\tilde{w}(x_0)\tilde{w}(x_0 + \boldsymbol{r})})/\sigma_w^2$ computed on the centreline at $z/b_0 = 15$ for release: (*a*) F and (*b*) P. Isolines vary from 0.8 for the inner contour to 0.3 for the outer.

considerably larger than their horizontal counterparts and with higher correlations. Second, the correlations for release P are higher than for release F. The influence of buoyancy in marginally widening (figure 13) and in elongating (figure 14) the eddy structure is immediately evident.

In order to quantify these differences and investigate the spatial variation of the Eulerian integral length scales we have attempted to estimate typical correlation distances over the whole domain. To that end, we have assumed that the two-point correlation functions can be modelled as an exponential function. Accordingly, we fitted the vertical and horizontal sections of R_{uu} and R_{ww} with functions of the form

$$f(r) = \exp\{-r/\mathscr{L}_{uu}\} \tag{4.6}$$

$$f(z) = \exp\{-z/\mathscr{L}_{ww}\}. \tag{4.7}$$

Values of the parameters $\mathscr{L}_{uu}$ and $\mathscr{L}_{ww}$, fitting this exponential curve to the data, provide a measure of a radial and a vertical integral length scale, respectively. The

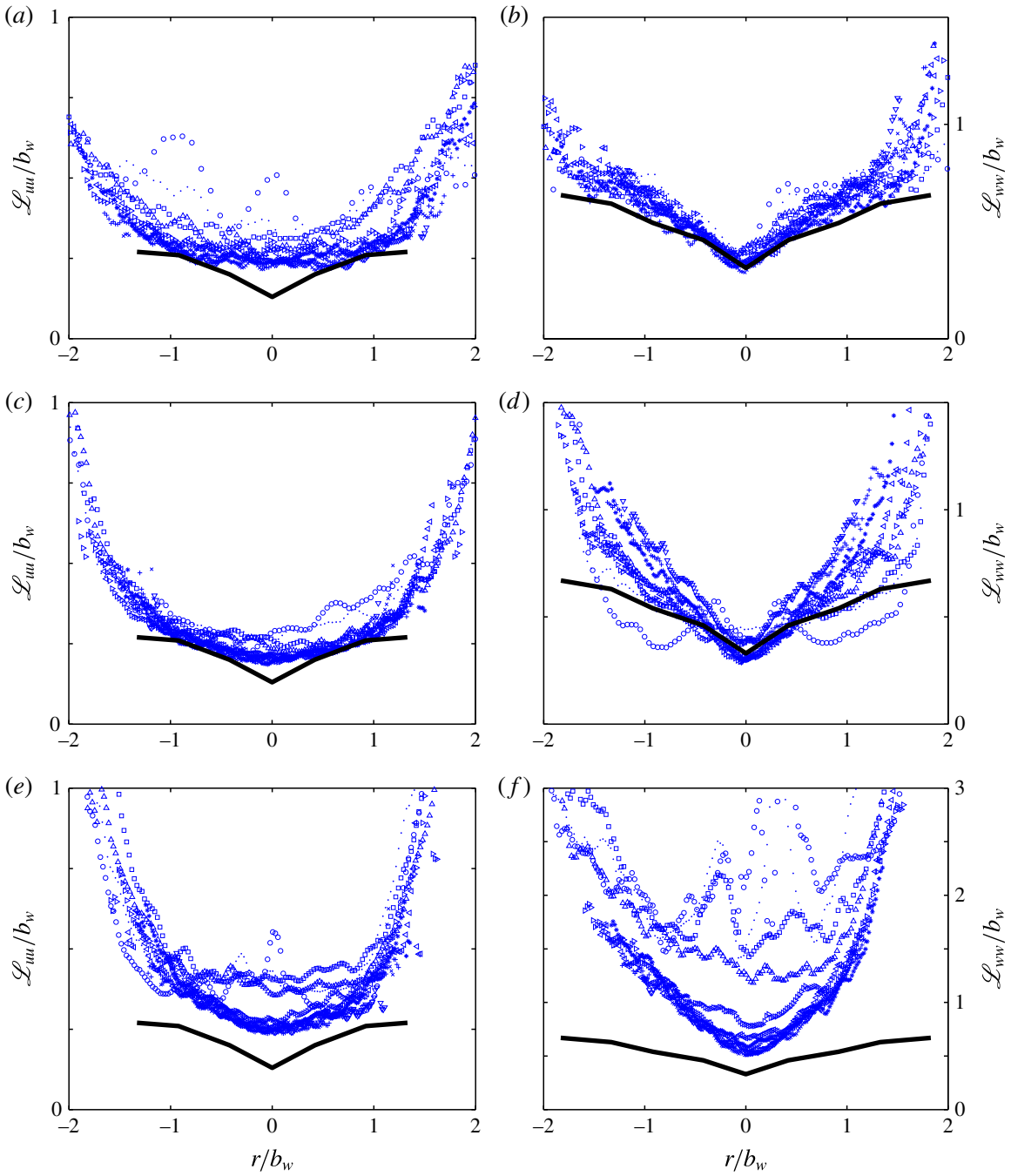

FIGURE 15. (Colour online) Radial profiles of the integral length scales, horizontal scale $\mathscr{L}_{uu}$ and vertical scale $\mathscr{L}_{ww}$, non-dimensionalised on plume width, b_w, for (a,b) release J (profiles plotted in range $9 < z/b_0 < 94$), (c,d) release F (profiles plotted in range $3 < z/b_0 < 32$) and (e,f) release P (profiles plotted in range $2 < z/b_0 < 19$). The continuous line indicates the experimental estimates by Wygnanski & Fiedler (1969) for a non-buoyant jet.

resulting non-dimensional integral length scale profiles are shown in figure 15 and are compared with the results of Wygnanski & Fiedler (1969) for non-buoyant releases.

This data highlights the anisotropy of the large-scale turbulent motion, as the vertical length scale, $\mathscr{L}_{ww}$, is 1–3 times larger than the radial scale $\mathscr{L}_{uu}$. Results bolster the findings of § 3 showing that approximate self-similarity of the profiles is

achieved for each of the three release conditions. The local self-similar behaviour, however, differs slightly from release J to release F, and markedly from release P. Data for J and F agrees well with Wygnanski & Fiedler's (1969) measurements of non-buoyant plumes showing, once again, that the effect of an excess of buoyancy on the plume dynamics can be fully re-scaled by local quantities, thereby indicating a local self-similarity of the flow, characterising even the local turbulence structure. The only difference that can be observed between releases J and F is the slightly higher values of non-dimensional $\mathscr{L}_{ww}$ towards the perimeter of release F. Conversely, a clear departure from this self-similar behaviour can be observed for plume P, which is also characterised by higher values of both $\mathscr{L}_{uu}$ and $\mathscr{L}_{ww}$ compared with the others. This departure from self-similarity can be reasonably attributed to two features. First, to the vorticity production by the baroclinic torque, whose effect is enhanced for higher Γ. This produces a coalescence of vortices that extends, both laterally and vertically, the larger eddies within the plume. Second, the higher values of $\mathscr{L}_{uu}$ observed for higher Γ can be also attributed to the meandering that characterises the morphology of release P: meandering that was hardly detectable in releases J and F.

5. Entrainment coefficient

Finally, we focus on the rate of entrainment. Our aim is twofold. First, we aim to quantify the apparent differential entrainment coefficient evidenced by the vertical profiles of centreline buoyancy examined in § 3.3.2. Second, in light of the analysis of the flow structure performed so far, we aim to shed light on the dynamical causes of this variation.

The entrainment coefficient $\alpha_G = u_e/w_m$ is defined as the ratio of two velocities, the entrainment velocity u_e and the mean centreline vertical velocity, and represents the simplest way to close the volume flux conservation equation:

$$\frac{\mathrm{d}Q}{\mathrm{d}z} = 2\pi b_w u_e = 2\pi b_w \alpha_G w_m. \tag{5.1}$$

Although widely and successfully applied to many problems of practical interest (Turner 1986), this form of turbulence closure that attempts to capture the turbulent process, by which ambient fluid is entrained across the shear layers forming the plume boundary and into the plume, is nonetheless a rather crude model of a complex physical phenomenon. Many researchers have attempted to infer the entrainment coefficient from experimental observations (Turner 1986) as it is central to plume theory. A major problem in the experimental estimates of α_G reported in the literature, for both jets and plumes, is the consistent scatter in the data. A comprehensive review of the estimates of the entrainment coefficient provided by previous authors is presented by Linden (2000) and by Carazzo, Kaminski & Tait (2006). For Gaussian profiles, the entrainment coefficient is in the range $0.045 < \alpha_j < 0.056$ in pure momentum-dominated jets and $0.07 < \alpha_p < 0.11$ in pure buoyancy-dominated plumes (Carazzo *et al.* 2006). Whilst this variability remains only partially explained it can, in part, be attributed to different conditions at the source, the nozzle geometry, or to the different experimental techniques deployed. In addition to this uncertainty, however, we can expect that buoyant plumes produce different entrainment rates according to their local dynamical condition. Assuming fully-turbulent plumes with relatively low density differences, we may therefore expect the dynamics of the entrainment process to depend on the plume Richardson number Γ. Previous authors have tried to define the functional dependence of α_G on Γ, or to equivalent non-dimensional parameters

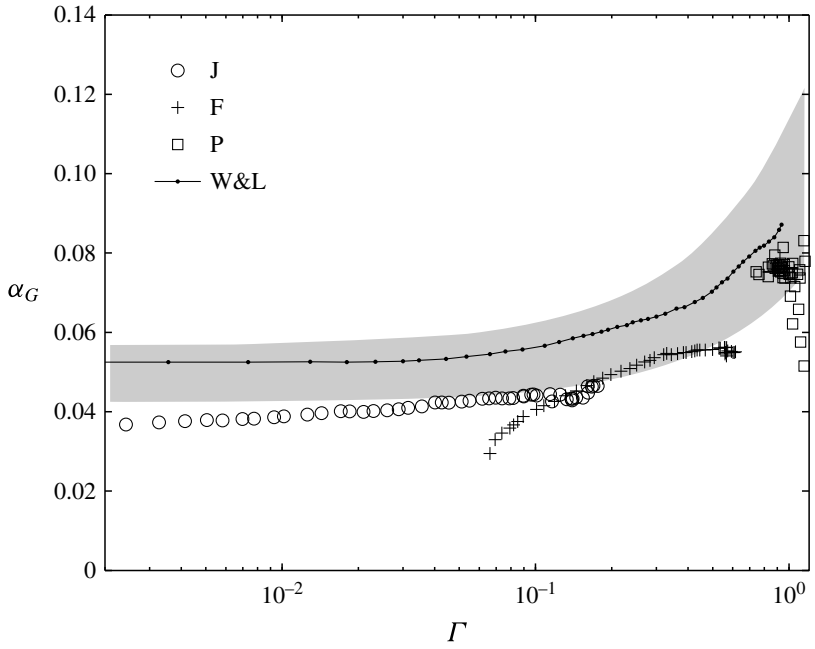

FIGURE 16. Entrainment coefficient α_G plotted against local plume Richardson number Γ. Experimental data of the present study refers to release J (○), F (+) and P (□). The grey shaded area represents estimates based on the Priestley & Ball model (5.2) assuming an upper and lower bound provided by maximal and minimal entrainment values for jets and plumes from the literature data (see the text). Experimental data from Wang & Law (2002) is referred to as W&L.

(the Froude number). Among these, we cite the semi-empirical model derived from the theoretical analysis of Priestley & Ball (1955)

$$\alpha_G(\Gamma) = \alpha_j + (\alpha_p - \alpha_j)\Gamma, \tag{5.2}$$

which assumes a linear variation between two asymptotic values (determined experimentally) for a pure jet α_j and a pure plume α_p. Then 50 years later Kaminski *et al.* (2005), following Priestley & Ball (1955), proposed a formulation of the entrainment coefficient based on a mean kinetic energy budget, and that includes explicitly the direct contribution of the variation of Γ on α_G.

The entrainment coefficient is computed herein from the PIV velocity estimates of the mean vertical volume flux $Q(z)$. To avoid scatter in the data due to spatial discretisation, prior to determining its derivative, the volume flux variation with height was fitted by means of a sixth-order polynomial, and thereafter α_G estimated from (5.1). Results are shown in figure 16, where we plot the entrainment coefficient for the three releases as a function of Γ. We have excluded only the data of release P for $z/b_0 \leqslant 5$, data that was highly affected by the non-fully turbulent condition of the flow, as widely discussed in §§ 3.3.1, 3.3.3 and 4.

Results are compared with the model of Priestley & Ball (1955) discussed above and with experimental results reported by Wang & Law (2002). To the best of the authors' knowledge, Wang & Law (2002) provide the only experimental estimate of the entrainment coefficient as a function of the local Richardson number in the literature. The data of Wang & Law (2002) was originally plotted against a non-dimensional parameter, denoted here as Fr, which is related to the plume

Richardson number via $\Gamma = Fr^2(5/(2^{7/2}\sqrt{\pi}\alpha_{ref}))$. Wang & Law (2002) estimated Fr, taking also into account the turbulent fluxes of buoyancy and momentum, which are neglected in (1.1). Since the turbulent fluxes constitute approximately 20 % of the total buoyancy flux and 10 % of the total momentum flux, neglecting these leads to overestimates of Γ of approximately 5 %. The outcome of the Priestley & Ball (1955) model is plotted assuming the two limits for both asymptotic values of α_G identified by Carazzo *et al.* (2006), i.e. $\alpha_j = 0.045$ and $\alpha_j = 0.056$ for $\Gamma \to 0$, and $\alpha_p = 0.07$ and $\alpha_p = 0.11$ for $\Gamma \to 1$.

As a general remark we note that our estimates show a clear tendency for α_G to increase with Γ. For the condition of a 'highly forced plume', $\Gamma \to 0$, our α_G tends to be slightly lower than that in the literature for jets. For increasing Γ, our results show generally good agreement with the lower bound defined by the semi-empirical model of Priestley & Ball (1955). Across the whole range of forced plume conditions $0 < \Gamma < 1$, our estimates are systematically lower than those provided by Wang & Law (2002). This discrepancy is significantly reduced for pure plume conditions. In addition, our estimates show good agreement with the other literature on pure plumes, in particular the PIV estimates by Pham *et al.* (2005) within a thermal plume rising above a heated plate.

To help explain the differences between our estimates of α_G and the estimates of Wang & Law (2002), as well as the differences in α_G in our own data at a given value of Γ (i.e. for releases J and F for $0.06 < \Gamma < 0.2$) we turn to the expression developed by Kaminski *et al.* (2005) for the entrainment coefficient. Following recent developments proposed by Craske & van Reeuwijk (2014) for the analysis of unsteady jets, we adopt a formulation that makes no assumption about the slenderness of the flow. In particular, this allows us to quantify the behaviour of the entrainment in the very near field, where the usual assumption of 'thin plume' (negligible vertical gradients of second-order statistics compared with radial gradients) does not necessarily hold. Assuming that the radial profiles of velocity and buoyancy are well approximated by a Gaussian, even close to the source (as we verified in §§ 3.1 and 3.2), and adopting a simple gradient-law closure to model the Reynolds stress, the entrainment coefficient can be expressed as

$$\alpha_G = (2\varphi^2 - 1)\frac{2\alpha_{ref}}{5}\Gamma + \frac{3}{2}\langle\widehat{v_T}\rangle + \alpha_{nf} - \alpha_m \tag{5.3}$$

where

$$\alpha_{nf} = 3b_w I_7 - 2b_w \frac{\mathrm{d}I_6}{\mathrm{d}z}, \tag{5.4}$$

$$\alpha_m = 2b_w I_6 \frac{\mathrm{d}}{\mathrm{d}z}\ln\left(b_w^2 w_m^2\right), \tag{5.5}$$

and where I_6 and I_7 are related to integrals of radial profiles of second-order velocity statistics. Details on the derivation of (5.3) are provided in the appendix A.

The formulation of the entrainment coefficient (5.3) helps to clarify the role of the different terms in the entrainment process and their physical meaning. The first term $(2\varphi^2 - 1)(2\alpha_{ref}/5)\Gamma$ reflects the effect of the radial gradient of hydrostatic pressure, induced by the presence of a column of warm air, in drawing ambient air into the plume. This term is therefore related to the mean radial velocity field. The second term $(3/2)\langle\widehat{v_T}\rangle$ is directly linked to the local production of t.k.e. by inertial instabilities (Kaminski *et al.* 2005), i.e. to the product of Reynolds stress and mean vertical velocity radial gradient. It is therefore related to the fluctuating component of the velocity field. The remaining two terms, originally neglected by

Kaminski *et al.* (2005), are both related to the t.k.e. production and to the vertical mean kinetic energy transfer (and thereby related to the vertical gradient of the first- and second-order velocity statistics). The term α_{nf} tends to zero in the far field, as the second-order velocity statistics attain self-similarity and therefore plays a role only in the very near field. The term α_m tends to zero in the far field only in pure jets, $\Gamma = 0$, as the mean momentum flux maintains a constant value. Its contribution however is non-null for buoyant releases. It is instructive to evaluate the magnitude of α_m in the case of a nominal pure plume, i.e. $\Gamma \approx 1$. Considering simple scaling relations for a pure plume, i.e. $b_w^2 w_m^2 \propto z^{4/3}$ and $b_w \propto (6/5)\alpha_{ref} z$, and estimating the integral $I_6 \simeq 0.05$ from our experimental data, we can estimate $\alpha_m \simeq 1.6 \times 10^{-2}$, which represents a contribution of approximately 10 % to the total entrainment.

As pointed out in appendix A, it is worth noting that, under the assumption of Gaussian radial profiles of mean vertical velocity and temperature, the contribution to α_G given by the 'drift term' and pointed out by Kaminski *et al.* (2005) vanishes, even in the case of a varying φ.

A systematic comparison of estimates of the entrainment coefficient obtained from (5.1) with those from (5.3) offers a means to explain the variability of $\alpha_G = \alpha_G(\Gamma)$ shown in figure 16.

First, we analyse the Wang & Law (2002) data. Their estimates of α_G are obtained for releases with $0.01 < \Gamma_0 < 0.1$ and in the range $60 < z/b_0 < 110$. In contrast to us, Wang & Law (2002) focus on the far-field region, i.e. where $\langle \widehat{\nu_T} \rangle$ is expected to have reached its asymptotic value, and where the second-order statistics have clearly already attained a condition of self-similarity, so that the contribution of the term α_{nf} is null. An examination of their Reynolds stress and mean velocity vertical profiles suggests $\langle \widehat{\nu_T} \rangle \simeq 0.35$, which leads to values of the parameter $C = (3/2)\langle \widehat{\nu_T} \rangle (\varphi^2 + 1)$ (see appendix A) in the range $0.12 < C < 0.14$ (Kaminski *et al.* 2005). This value of $\langle \widehat{\nu_T} \rangle$ corresponds approximately to the same value as observed in the far field of all three releases examined here (see figure 11). Over a similar range of distances from the source Wang & Law (2002) data exhibits a decrease of φ, from a near-field value of 1.25 down to 1.05 in the far field. As a first approximation, we neglect the contribution of α_m in (5.3), and estimate the entrainment coefficient as

$$\alpha_G \simeq (2\varphi^2 - 1)\frac{2\alpha_{ref}}{5}\Gamma + \frac{3}{2}\langle \widehat{\nu_T} \rangle. \tag{5.6}$$

On imposing $\langle \widehat{\nu_T} \rangle = 0.35$ we plot α_G from (5.6) for $\varphi = 1.05$, 1.15 and 1.25. As is clear from figure 17, the tendency of $\alpha_G = \alpha_G(\Gamma)$ from Wang & Law (2002) can be fully reproduced by (5.6) with $\varphi = 1.05$. For $\Gamma \geqslant 10^{-1}$ we note that entrainment responds sensitively to φ, with variation of φ less than 10 % inducing considerable variation in α_G. As a consequence of this sensitivity, the actual variation of φ with height in the Wang & Law (2002) experiments, that we have here neglected, is likely to alter the close agreement seen. However, a detailed estimate of all terms in (5.3) for the Wang & Law releases is clearly beyond the scope of the present study and requires further information on the velocity statistics, specifically those related to the term α_m. Our aim here is only to demonstrate that the estimates of α_G provided by Wang & Law (2002) are consistent with the plume dynamics in the far field, where both φ and $\langle \widehat{\nu_T} \rangle$ have reached their asymptotic values: values that closely match their experimental estimates.

Second, we focus on our three releases J, F and P. The measurements gathered during our experimental campaign allow for a direct estimate of all terms comprising

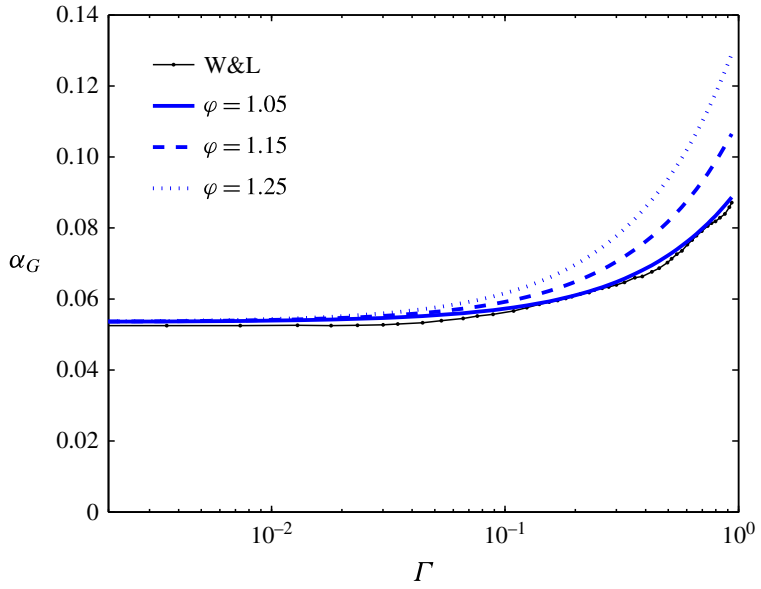

FIGURE 17. (Colour online) Entrainment coefficient α_G plotted against local plume Richardson number Γ. Experimental data from Wang & Law (2002) and estimates of the formulation of Kaminski *et al.* (2005) given by (5.6) for a fixed $\langle\widehat{\nu_T}\rangle = 0.035$ and three different values of φ (see text).

α_G in (5.3). However, an estimate of the terms in α_{nf}, involving vertical derivatives of second-order velocity statistics, is characterised by a large uncertainty due to an insufficient number of sampled velocity fields. Accurate estimates of these terms would require a number of samples of at least an order of magnitude larger. For these reasons, in estimating α_G by means of (5.3), we consider as a first approximation, $\alpha_{nf} = 0$ which we expect to lead to underestimations of α_G in the near field.

Since release P exhibits almost no variation of Γ, the evolution of the estimates of α_G provided by (5.1) and (5.3) shown in figure 18 is plotted against z/b_0, rather than against Γ. Estimates from (5.3) are shown for all three releases with 20 % error bars, evaluated taking into account the uncertainties related to Γ (figure 8), $\langle\widehat{\nu_T}\rangle$ (figure 11) and φ (figure 12).

For releases J and F, estimates from (5.3) tend to systematically underestimate those from (5.1) in the near field. This can be explained by the neglected contribution of α_{nf}. Even in the case of plume P, the two estimates of α_G differ significantly in the near field. This difference can primarily be attributed to the non-fully turbulent condition of the plume for $z/b_0 < 5$, conditions that invalidate the formulation of (5.3). Discrepancies in the near-field region can also be attributed to the two features discussed in § 2, i.e. eventual non-Boussinesq effects and the thermal stratification of the ambient very close to the source (in a region that extends up to $z/b_0 \sim 6$ for release J, $z/b_0 \sim 2$ for F and $z/b_0 \sim 2$ for P). Both features are not accounted for in the formulation of (5.3). However, despite the non-negligible extent of the error bars, we observe a relatively good agreement between the two estimates for releases J, F and P. This allows us to interpret the physical variation of α_G with z/b_0 as given by the variations with z/b_0 of the terms on the right-hand side (r.h.s.) of (5.3) and to shed light on the role of Γ in the intensity of the entrainment of ambient air. Focusing on the first two terms on the r.h.s. of (5.3), terms that represent the highest contribution to the total entrainment, we may assert that the role of Γ is twofold: directly through term $(2\varphi^2 - 1)(2\alpha_{ref}/5)\Gamma$ and indirectly through the vertical evolution of $\langle\widehat{\nu_T}\rangle$.

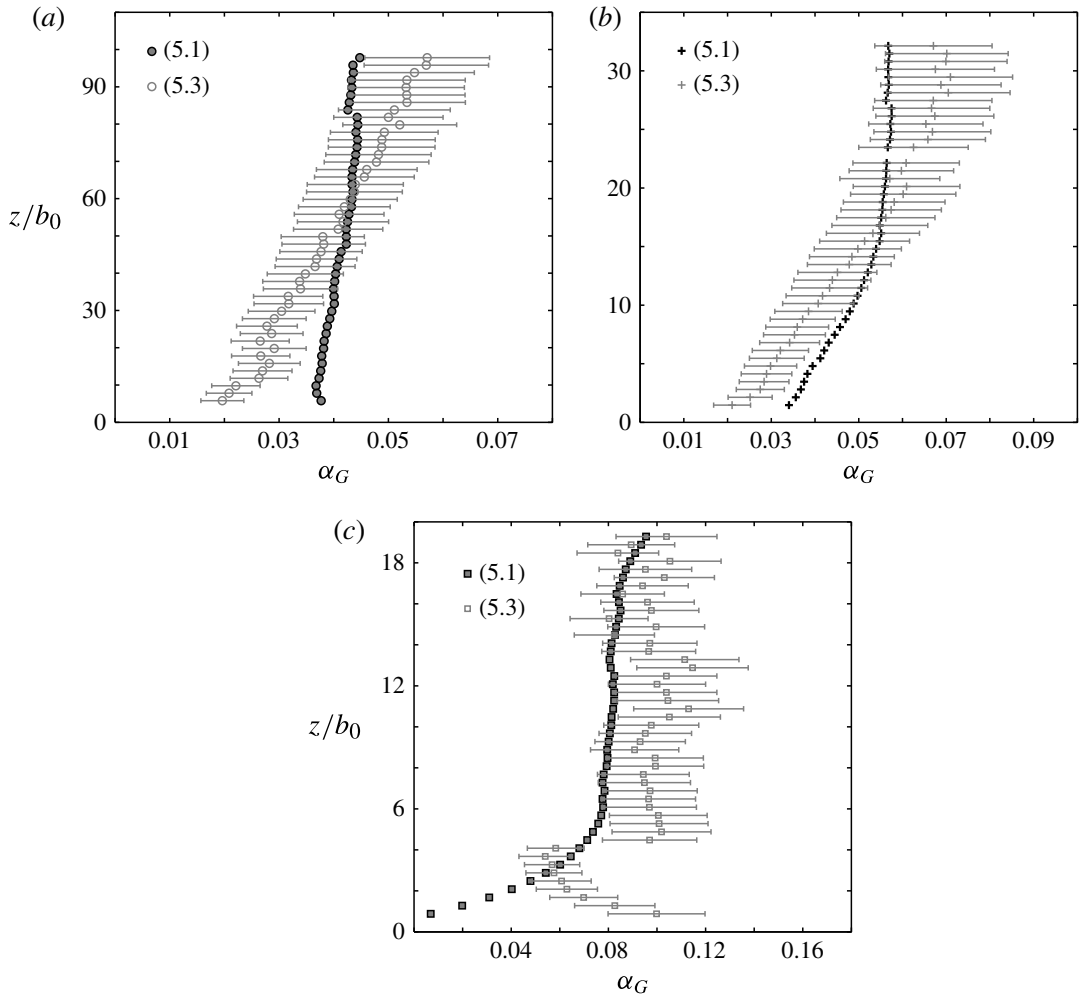

FIGURE 18. Variation of entrainment coefficient as a function of distance from source. Comparison of entrainment coefficient estimated from the volume flux balance equation (5.1) and from the formulation (5.3) for releases (*a*) J, (*b*) F and (*c*) P.

The relatively low values of α_G in the near field of releases J and F can then be fully explained by the corresponding low values of $\langle\widehat{\nu_T}\rangle$ (figure 11). Moving away from the source, $\Gamma \to 1$ and the contribution of $\langle\widehat{\nu_T}\rangle$ to α_G increases (at a rate that depends on Γ) as does the direct contribution of the term including Γ. As widely discussed in § 4, a buoyant release can exhibit different $\langle\widehat{\nu_T}\rangle$ and φ for a given Γ, depending on the release conditions and distance from the source. This explains why, in general, a plume can exhibit a different value of α_G for the same local Γ and provides, in this particular case, a robust justification for the differences observed between our estimates of α_G and those reported by Wang & Law (2002). This feature is also likely to explain the high variability of values of the entrainment coefficient reported in the literature.

6. Summary of findings

We have presented a highly resolved set of velocity and temperature measurements carried out on three turbulent plumes of source Richardson number (1.1) in the range $10^{-2} < \Gamma_0 < 1$. These measurements have been used to assess local dynamical self-similarity, to confirm the evolution of key dynamic quantities, to investigate the large

scale structure of the flow and the variability of the rate of entrainment with height from the source.

Despite a variable local dynamical condition, characterised by a varying plume Richardson number Γ, the radial profiles of the mean and of the r.m.s. of the velocity components can be rescaled on local quantities, namely the mean centerline velocity w_m and the mean plume radius b_w, to yield self-similar profiles for the flow variables for a wide range of distances from the source. This local self-similarity applies also to the mean temperature (buoyancy) profiles and to the turbulent viscosity $\widehat{\nu_T}$, showing that even the increased radial turbulent momentum transfer induced by an excess of buoyancy can be fully rescaled by local quantities. Even the Eulerian length scales $\mathscr{L}_{uu}$ and $\mathscr{L}_{ww}$ appear to rescale locally when normalised with the plume radius. In contrast to the other flow variables however, the local self-similar function describing the spatial evolution of the Eulerian length scales differs significantly depending on Γ.

The influence of Γ on the turbulence dynamics within each release was studied by focusing on the evolution of radial profiles of second-order velocity statistics and estimating bulk quantities, including the spatially averaged turbulent viscosity $\langle\widehat{\nu_T}\rangle$ and $\varphi = b_{g'}/b_w$ which is directly linked to the spatially averaged turbulent Prandtl number. Summarising, our results show that:

(*a*) the higher the value of Γ, the lower is the fetch required for second-order statistics to attain local self-similarity;

(*b*) the higher the value of Γ, the more rapid the rate of increase of $\langle\widehat{\nu_T}\rangle$ toward its asymptotic value;

(*c*) the influence of Γ on φ is likely to be similar to the influence of Γ on $\langle\widehat{\nu_T}\rangle$, but this effect is difficult to unequivocally confirm, given the vertical variation of φ exhibited by a buoyant release is comparable with the uncertainty associated with its experimental estimate;

(*d*) neither $\langle\widehat{\nu_T}\rangle$ nor φ do not show a one-to-one dependence with Γ, since their magnitude depends, at least in a region of flow transition, also on the distance from the source.

The study culminated with an analysis of the influence of Γ on the rate of entrainment of ambient air as quantified by the entrainment coefficient α_G. Two distinct experimental estimates of α_G were obtained. The first by estimating the vertical variation of the volume flux. The second adopting a formulation of α_G similar to that originally proposed by Kaminski *et al.* (2005), and that makes explicit the role of the main non-dimensional parameters governing the dynamics of the plume, i.e. Γ, $\langle\widehat{\nu_T}\rangle$ and φ. In this way we could fully explain the observed variations of α_G in the three releases studied as well as in the existing literature data, depending on Γ and on the distance from the source.

Our analysis shows that it is not possible to identify a one-to-one dependence of α_G on Γ, since its variations are due also to changes in $\langle\widehat{\nu_T}\rangle$ and φ, whose magnitude, for a given Γ depends on the distances from the source and the value of Γ at the source.

Acknowledgements

We would like to express our gratitude to C. Nicot and N. Grosjean who contributed their laboratory expertise. Also our thanks go to the EPSRC for their financial support through the doctoral training scheme at Imperial College London and Bourse

Ministérielle at LMFA for financing the work in Lyon. G.R.H. would like to thank the CNRS for funding his visiting position at the Ecole Centrale de Lyon. P.S. would like to thank M. Marro for invaluable help in data processing and C. Cancelli, M. van Reeuwijk, M. Creyssels and S. Vaux for fruitful discussions.

Appendix A

Following the analysis undertaken by Craske & van Reeuwijk (2014) on unsteady jets, we present an extension of the model of Kaminski *et al.* (2005). For clarity, the notation will be kept as similar as possible to that adopted by Kaminski *et al.* (2005). We begin by writing the steady balance equations for mass, momentum and buoyancy in cylindrical coordinates under the Boussinesq approximation and assuming negligible viscous effects:

$$\left.\begin{aligned} \frac{\partial rw}{\partial r}+\frac{\partial ru}{\partial r}&=0,\\ \frac{\partial}{\partial z}(rw^2)+\frac{\partial}{\partial r}(ruw)&=rg'-\frac{\partial}{\partial r}(r\overline{\tilde{u}\tilde{w}})-\frac{1}{\rho_e}\frac{\partial}{\partial z}(pr)-\frac{\partial}{\partial z}(\sigma_w^2 r),\\ \frac{\partial}{\partial z}(rwg'+r\overline{\tilde{w}\tilde{g}'})+\frac{\partial}{\partial r}(rug'+r\overline{\tilde{u}\tilde{g}'})&=0, \end{aligned}\right\} \tag{A 1}$$

where p represents the difference from hydrostatic pressure $p_e=\rho_e gz$. In contrast to Kaminski *et al.* (2005), equation (A 1) includes the vertical derivatives of σ_w^2 and pressure. Since the pressure distribution is difficult to measure, its vertical gradient is usually modelled as (Hussein *et al.* 1994; Shabbir & George 1994; Wang & Law 2002)

$$-\frac{\partial p}{\rho_e\partial z}\approx\frac{\partial(\sigma_u^2+\sigma_v^2)}{2\partial z}\approx\frac{\partial\sigma_u^2}{\partial z}, \tag{A 2}$$

where σ_v denotes the standard deviation of the azimuthal velocity component.

By combining mass and momentum balances, we can write the mean kinetic energy balance as

$$\frac{\partial}{\partial z}\left(\frac{1}{2}rw^3\right)+\frac{\partial}{\partial r}\left(\frac{1}{2}ruw^2\right)=rwg'-w\frac{\partial}{\partial r}\left(r\overline{\tilde{u}\tilde{w}}\right)-w\frac{\partial}{\partial z}\left(\sigma_w^2-\sigma_u^2\right)r. \tag{A 3}$$

The balance equations (A 1) can be integrated over r, from 0 to ∞, assuming as boundary conditions that $\lim_{r\to\infty} ruw=\lim_{r\to\infty} r\overline{\tilde{u}\tilde{w}}=\lim_{r\to\infty} rug'=\lim_{r\to\infty} r\overline{\tilde{u}\tilde{g}'}=0$, so that

$$\left.\begin{aligned} \frac{\mathrm{d}}{\mathrm{d}z}\int_0^\infty rw\mathrm{d}r&=-\left[ru\right]_0^\infty,\\ \frac{\mathrm{d}}{\mathrm{d}z}\int_0^\infty rw^2\mathrm{d}r&=\int_0^\infty rg'\mathrm{d}r-\frac{\mathrm{d}}{\mathrm{d}z}\int_0^\infty\left(\sigma_w^2-\sigma_u^2\right)r\mathrm{d}r,\\ \frac{\mathrm{d}}{\mathrm{d}z}\int_0^\infty(rwg'+r\overline{\tilde{w}\tilde{g}'})\mathrm{d}r&=0,\\ \frac{\mathrm{d}}{\mathrm{d}z}\int_0^\infty\frac{1}{2}rw^3\mathrm{d}r&=\int_0^\infty rwg'\mathrm{d}r+\int_0^\infty r\overline{\tilde{u}\tilde{w}}\frac{\partial w}{\partial r}\mathrm{d}r-\int_0^\infty rw\frac{\partial}{\partial z}\left(\sigma_w^2-\sigma_u^2\right)\mathrm{d}r. \end{aligned}\right\} \tag{A 4}$$

As in Kaminski *et al.* (2005), the mean and variance of the vertical velocity, the mean buoyancy and the Reynolds stress are expressed by shape functions:

$$\left.\begin{aligned} w(r,z) &= w_m(z) f(r,z), \\ g'(r,z) &= g'_m(z) h(r,z), \\ \widetilde{\tilde{u}\tilde{w}} &= -\tfrac{1}{2} w_m(z)^2 j(r,z), \\ \sigma_w^2 - \sigma_u^2 &= \tfrac{1}{2} w_m^2 l(r,z). \end{aligned}\right\} \tag{A 5}$$

With reference to (4.2) in § 4.2.1 we note that, for Gaussian profiles, $j(r,z) = 2\mathscr{F}(r,z)$. These shape functions allow the computation of the integrals in (A 4) without making any assumption regarding the similarity of the profiles,

$$\left.\begin{aligned} I_0 &= \int_0^\infty r^* f(r^*,z)\mathrm{d}r^*, \\ I_1 &= \int_0^\infty r^* f(r^*,z) h(r^*,z)\mathrm{d}r^*, \\ I_2 &= \int_0^\infty r^* h(r^*,z)\mathrm{d}r^*, \\ I_3 &= \int_0^\infty r^* f(r^*,z)^2\mathrm{d}r^*, \\ I_4 &= \int_0^\infty r^* f(r^*,z)^3\mathrm{d}r^*, \\ I_5 &= \int_0^\infty r^* j(r^*,z)\frac{\partial f}{\partial r^*}\mathrm{d}r^*, \\ I_6 &= \int_0^\infty r^* l(r^*,z)\mathrm{d}r^*, \\ I_7 &= \int_0^\infty \left(2l\frac{\mathrm{d}}{\mathrm{d}z}\ln w_m + \frac{\partial l}{\partial z}\right) f(r^*,z) r^* \mathrm{d}r^*, \end{aligned}\right\} \tag{A 6}$$

where $r^* = r/b_m$, with b_m denoting a generic radius scale.

Top-hat variables are defined according to the following relations

$$\left.\begin{aligned} R^2 W^2 &= \int_0^\infty r w^2 \mathrm{d}r, \\ R^2 G' &= \int_0^\infty r g' \mathrm{d}r, \\ R^2 W G' &= \int_0^\infty r w g' \mathrm{d}r, \\ R^2 \Sigma_q^2 &= \int_0^\infty (\sigma_w^2 - \sigma_u^2) r \mathrm{d}r. \end{aligned}\right\} \tag{A 7}$$

With the integrals (A 7), introducing the usual entrainment assumption in the volume balance equation (A 4)

$$-[ru]_0^\infty = \alpha_G b_m w_m, \tag{A 8}$$

and neglecting the vertical turbulent transfer of buoyancy (i.e. $\overline{\tilde{w}\tilde{g}'}$), the system (A 4) can be rewritten in top-hat equation form as

$$\left.\begin{aligned} \frac{\mathrm{d}}{\mathrm{d}z}R^2W &= 2RW\alpha_t, \\ \frac{\mathrm{d}}{\mathrm{d}z}R^2W^2 &= R^2G' - \frac{\mathrm{d}}{\mathrm{d}z}R^2\Sigma_q^2, \\ \frac{\mathrm{d}}{\mathrm{d}z}R^2WG' &= 0, \\ \frac{\mathrm{d}}{\mathrm{d}z}R^2W^3 &= \frac{2}{A}R^2WG' - R^2W^3\frac{\mathrm{d}\ln A}{\mathrm{d}z} - W^3R(C+RD), \end{aligned}\right\} \tag{A 9}$$

where the relations between 'top-hat' variables and the real variables are

$$\left.\begin{aligned} R &= \frac{I_3^{1/2}I_2}{I_1}b_m, \\ W &= \frac{I_1}{I_2}w_m, \\ G' &= \frac{I_1^2}{I_2I_3}g'_m, \\ \Sigma_q^2 &= \frac{1}{2}\frac{I_1^2I_6}{I_2^2I_3}w_m^2, \end{aligned}\right\} \tag{A 10}$$

where

$$\left.\begin{aligned} A &= \frac{I_2I_4}{I_1I_3}, \\ C &= \frac{I_2I_3^{1/2}I_5}{I_1I_4}, \\ D &= \frac{I_7}{I_4}, \end{aligned}\right\} \tag{A 11}$$

and where the top-hat entrainment coefficient α_t in (A 9) is related to the Gaussian coefficient α_G in (A 8) by

$$\alpha_t = \left[\frac{\alpha_G}{2}\frac{I_3^{1/2}I_2}{I_1I_0} - \frac{R}{2}\frac{\mathrm{d}}{\mathrm{d}z}\ln\frac{I_1I_0}{I_3I_2}\right]. \tag{A 12}$$

It is worth noting that the relation between the 'top-hat' entrainment coefficient α_t and α_G is not simply given by a proportionality coefficient, i.e. $\sqrt{2}$, as in the classic top-hat formulations of the plume equations (Morton *et al.* 1956). This is due to the fact that the definitions of the top-hat variables in (A 7) differ from those of Morton *et al.* (1956).

With some algebra, the top-hat momentum and mean kinetic energy balance can be manipulated in order to conveniently express the continuity equation as

$$\frac{\mathrm{d}}{\mathrm{d}z}R^2W = 2RW\left[\underbrace{Ri\left(1-\frac{1}{A}\right) + \frac{1}{2}R\frac{\mathrm{d}\ln A}{\mathrm{d}z} + \frac{1}{2}C + \frac{1}{2}RD - \frac{1}{RW^2}\frac{\mathrm{d}}{\mathrm{d}z}\left(\Sigma_q^2R^2\right)}_{\alpha_t}\right], \tag{A 13}$$

where the term within the square brackets is equal to the entrainment coefficient α_t in (A 9) and $Ri \equiv (RG')/W^2$ represents a bulk Richardson number. The volume flux balance (A 13) provides a formulation for α_t that allows for its direct estimate from first- and second-order velocity statistics.

We now assume local self-similarity of the first-order velocity statistics (but not of second-order statistics) and adopt Gaussian profiles of velocity and buoyancy of the form $f = \mathrm{e}^{-r*^2}$ and $h = \mathrm{e}^{-(r*^2/\varphi^2)}$, with $r* = r/b_w$. Furthermore, we model the Reynolds stress by a gradient law of the form $j = \langle\widehat{\nu_T}\rangle(\partial f/\partial r^*)$. The integrals in (A 6) then reduce to $I_0 = 1/2$, $I_1 = \varphi^2/(2(\varphi^2+1))$, $I_2 = \varphi^2/2$, $I_3 = 1/4$, $I_4 = 1/6$, $I_5 = \langle\widehat{\nu_T}\rangle/2$, so that the relations in (A 10), (A 11) can be written

$$\left.\begin{aligned} R &= \tfrac{1}{2}(\varphi^2+1)b_w, \\ W &= \frac{w_m}{\varphi^2+1}, \\ G' &= \frac{2\varphi^2}{(\varphi^2+1)^2}g'_m, \\ \Sigma_q^2 &= \frac{2}{(\varphi^2+1)^2}I_6 w_m^2, \\ A &= \tfrac{2}{3}(\varphi^2+1), \\ C &= \tfrac{3}{2}\langle\widehat{\nu_T}\rangle(\varphi^2+1), \\ D &= 6I_7 \end{aligned}\right\} \tag{A 14}$$

and the Richardson number Ri in (A 13) can be expressed as

$$Ri \equiv \frac{b_w g'_m}{w_m^2}\varphi^2(\varphi^2+1) = \frac{2\alpha_{ref}}{5}(\varphi^2+1)^2\Gamma. \tag{A 15}$$

From (A 12), the relation linking the entrainment coefficients α_G and α_t then reduces to

$$\alpha_G = \frac{2}{\varphi^2+1}\alpha_t - \frac{b_w}{2}\frac{\mathrm{d}}{\mathrm{d}z}\ln(\varphi^2+1). \tag{A 16}$$

By combining (A 13)–(A 16) we finally obtain an expression for the Gaussian entrainment coefficient as a function of the first- and second-order velocity statistics

$$\alpha_G = (2\varphi^2-1)\frac{2\alpha_{ref}}{5}\Gamma + \frac{3}{2}\langle\widehat{\nu_T}\rangle + 3b_w I_7 - \frac{2}{b_w w_m^2}\frac{\mathrm{d}}{\mathrm{d}z}\left(I_6 b_w^2 w_m^2\right). \tag{A 17}$$

Note that, assuming Gaussian radial profiles of mean vertical velocity and buoyancy, even with a variable φ, the 'drift' term $(R(\mathrm{d}\ln A/\mathrm{d}z))/2$ in (A 13) vanishes when converting α_t in α_G. The last term can be expressed as

$$\frac{2b_w}{b_w^2 w_m^2}\frac{\mathrm{d}}{\mathrm{d}z}\left(I_6 b_w^2 w_m^2\right) = 2b_w\frac{\mathrm{d}I_6}{\mathrm{d}z} + 2b_w I_6\frac{\mathrm{d}}{\mathrm{d}z}\ln\left(b_w^2 w_m^2\right), \tag{A 18}$$

so that (A 17) can be finally written as

$$\alpha_G = (2\varphi^2-1)\frac{2\alpha_{ref}}{5}\Gamma + \frac{3}{2}\langle\widehat{\nu_T}\rangle + \alpha_{nf} - \alpha_m, \tag{A 19}$$

with

$$\alpha_{nf} = 3b_w I_7 - 2b_w \frac{\mathrm{d}I_6}{\mathrm{d}z}, \tag{A 20}$$

and

$$\alpha_m = 2b_w I_6 \frac{\mathrm{d}}{\mathrm{d}z} \ln\left(b_w^2 w_m^2\right). \tag{A 21}$$

REFERENCES

BAINES, W. D., TURNER, J. S. & CAMPBELL, I. H. 1990 Turbulent fountains in an open chamber. *J. Fluid Mech.* **212**, 557–592.

BATCHELOR, G. K. 1954 Heat convection and buoyancy effects in fluids. *Q. J. R. Meteorol. Soc.* **80**, 339–358.

BURRIDGE, H. C. & HUNT, G. R. 2012 The rise heights of low-and high-Froude-number turbulent axisymmetric fountains. *J. Fluid Mech.* **691**, 392–416.

CAMPBELL, A. N. & CARDOSO, S. S. S. 2010 Turbulent plumes with internal generation of buoyancy by chemical reaction. *J. Fluid Mech.* **655**, 122–151.

CARAZZO, G., KAMINSKI, E. & TAIT, S. 2006 The route to self-similarity in turbulent jets and plumes. *J. Fluid Mech.* **547**, 137–148.

CARAZZO, G., KAMINSKI, E. & TAIT, S. 2008 On the dynamics of volcanic columns: a comparison of field data with a new model of negatively buoyant jets. *J. Volcanol. Geotherm. Res.* **178**, 94–103.

CARLOTTI, P. & HUNT, G. R. 2005 Analytical solutions for turbulent non-Boussinesq plumes. *J. Fluid Mech.* **538**, 343–359.

CAULFIELD, C. P. & WOODS, A. W. 1998 Turbulent gravitational convection from a point source in a non-uniformly stratified environment. *J. Fluid Mech.* **360**, 229–248.

CRASKE, J. & VAN REEUWIJK, M. 2014 Energy dispersion in turbulent jets. Part 1: direct simulation of steady and unsteady jets. *J. Fluid Mech.* accepted for publication.

DEVENISH, B. J., ROONEY, G. G. & THOMSON, D. J. 2010 Large-eddy simulation of a buoyant plume in uniform and stably stratified environments. *J. Fluid Mech.* **652**, 75–103.

FISCHER, H. B., LIST, E. J., KOH, R. C. Y., IMBERGER, J. & BROOKS, N. H. 1979 *Mixing in Inland and Coastal Waters*. Academic.

GEORGE, W. K. 1989 The self-preservation of turbulent flows and its relation to initial condition and coherent structures. In *Recent Advances in Turbulence* (ed. R. E. A. Arndt & W. K. George). Springer.

GEORGE, W. K., ALPERT, R. & TAMANINI, F. 1977 Turbulence measurements in an axisymmetric buoyant plume. *Intl J. Heat Mass Transfer* **20** (11), 1145–1154.

HUNT, G. R. & KAYE, N. B. 2001 Virtual origin correction for lazy turbulent plumes. *J. Fluid Mech.* **435**, 377–396.

HUNT, G. R. & VAN DEN BREMER, T. S. 2011 Classical plume theory: 1937–2010 and beyond. *IMA J. Appl. Maths* **76** (3), 424–448.

HUSSEIN, J., CAPP, S. P. & GEORGE, W. K. 1994 Velocity measurements in a high-Reynolds-number, momentum-conserving, axisymmetric, turbulent jet. *J. Fluid Mech.* **258** (1), 31–75.

KAMINSKI, E., TAIT, S. & CARAZZO, G. 2005 Turbulent entrainment in jets with arbitrary buoyancy. *J. Fluid Mech.* **526**, 361–376.

KAYE, N. B. 2008 Turbulent plumes in stratified environments: a review of recent work. *Atmos.-Ocean* **46** (4), 433–441.

KAYE, N. B. & SCASE, M. M. 2011 Straight-sided solutions to classical and modified plume equations. *J. Fluid Mech.* **680**, 564–573.

LINDEN, P. F. 2000 Convection in the environment. In *Perspectives in Fluid Dynamics* (ed. G. K. Batchelor, H. K. Moffatt & M. G. Worster), pp. 289–345. Cambridge University Press.

LIST, E. J. 1982 Turbulent jets and plumes. *Annu. Rev. Fluid Mech.* **14**, 189–212.

MEHADDI, R., VAUQUELIN, O. & CANDELIER, F. 2012 Analytical solutions for turbulent Boussinesq fountains in a linearly stratified environment. *J. Fluid Mech.* **691**, 487–497.

MORTON, B. R. 1959 Forced plumes. *J. Fluid Mech.* **5**, 151–163.

MORTON, B. R., TAYLOR, G. I. & TURNER, J. S. 1956 Turbulent gravitational convection from maintained and instantaneous sources. *Proc. R. Soc. Lond.* A **234**, 1–23.

NAKAGOME, H. & HIRATA, M. 1977 The structure of turbulent diffusion in an axisymmetric turbulent plume. In *Proceedings 1976 ICHMT Seminar on Turbulent Buoyant Convection*, pp. 361–372. Hemisphere.

PANCHAPAKESAN, N. R. & LUMLEY, J. L. 1993 Turbulence measurements in axisymmetric jets of air and helium. Part 2. Helium jet. *J. Fluid Mech.* **246** (-1), 225–247.

PAPANICOLAOU, P. N. & LIST, E. J. 1988 Investigations of round vertical turbulent buoyant jets. *J. Fluid Mech.* **195**, 341–391.

PHAM, M. V., PLOURDE, F. & KIM, S. D. 2005 Three-dimensional characterization of a pure thermal plume. *Trans. ASME J. Heat Transfer* **127**, 624–636.

PRIESTLEY, C. H. B. & BALL, F. K. 1955 Continuous convection from an isolated source of heat. *Q. J. R. Meteorol. Soc.* **81** (348), 144–157.

RICOU, F. P. & SPALDING, D. B. 1961 Measurements of entrainment by axisymmetrical turbulent jets. *J. Fluid Mech.* **11**, 21–32.

ROONEY, G. G. & LINDEN, P. F. 1996 Similarity considerations for non-Boussinesq plumes in an unstratfied environment. *J. Fluid Mech.* **318**, 237–250.

SCASE, M. M., CAULFIELD, C. P., DALZIEL, S. B. & HUNT, J. C. R. 2006 Time dependent plumes and jets with decreasing source strength. *J. Fluid Mech.* **563**, 443–461.

SHABBIR, A. & GEORGE, W. K. 1994 Experiments in a round turbulent buoyant plume. *J. Fluid Mech.* **275**, 1–32.

TURNER, J. S. 1986 Turbulent entrainment: the development of the entrainment assumption, and its application to geophysical flows. *J. Fluid Mech.* **173**, 431–471.

ÜLPRE, H., EAMES, I. & GREIG, A. 2013 Turbulent acidic jets and plumes injected into an alkaline environment. *J. Fluid Mech.* **743**, 253–274.

VAN DEN BREMER, T. S. & HUNT, G. R. 2010 Universal solutions for Boussinesq and non-Boussinesq plumes. *J. Fluid Mech.* **644**, 165–192.

WANG, H. & LAW, A. W.-K. 2002 Second-order integral model for round turbulent jet. *J. Fluid Mech.* **459**, 397–428.

WOODS, A. W. 1997 A note on non-Boussinesq plumes in an incompressible stratified environment. *J. Fluid Mech.* **345**, 347–356.

WOODS, A. W. 2010 Turbulent plumes in nature. *Annu. Rev. Fluid Mech.* **42** (1), 391–412.

WYGNANSKI, I. & FIEDLER, H. E. 1969 Some measurements in the self-preserving jet. *J. Fluid Mech.* **38**, 577–612.

ZEL'DOVICH, Y. B. 1937 The asymptotic laws of freely-ascending convective flows. *Zh. Eksp. Teor. Fiz.* **7**, 1463–1465.

ZHOU, X. 2001 Large-eddy simulation of a turbulent forced plume. *Eur. J. Mech. (*B*/Fluids)* **20** (2), 233–254.

ZHOU, X. 2002 Vortex dynamics in spatio-temporal development of reacting plumes. *Combust. Flame* **129** (1–2), 11–29.

8.2 Turbulent transport and entrainment in jets and plumes: a DNS study

PHYSICAL REVIEW FLUIDS **1**, 074301 (2016)

Turbulent transport and entrainment in jets and plumes: A DNS study

Maarten van Reeuwijk*
Department of Civil and Environmental Engineering, Imperial College London, London SW7 2AZ, United Kingdom

Pietro Salizzoni
Laboratoire de Mécanique des Fluides et d'Acoustique, University of Lyon, CNRS UMR No. 5509, Ecole Centrale de Lyon, INSA Lyon, Université Claude Bernard, 36 Avenue Guy de Collongue, 69134 Ecully, France

Gary R. Hunt
Department of Engineering, University of Cambridge, Cambridge CB2 1PZ, United Kingdom

John Craske
Department of Civil and Environmental Engineering, Imperial College London, London SW7 2AZ, United Kingdom
(Received 31 March 2016; published 7 November 2016)

We present a direct numerical simulation (DNS) data set for a statistically axisymmetric turbulent jet, plume, and forced plume in a domain of size $40r_0 \times 40r_0 \times 60r_0$, where r_0 is the source diameter. The data set supports the validity of the Priestley-Ball entrainment model in unstratified environments (excluding the region near the source) [Priestley and Ball, Q. J. R. Meteor. Soc. **81**, 144 (1955)], which is corroborated further by the Wang-Law and Ezzamel *et al.* experimental data sets [Wang and Law, J. Fluid Mech. **459**, 397 (2002); Ezzamel *et al.*, *ibid.* **765**, 576 (2015)], the latter being corrected for a small but influential coflow that affected the statistics. We show that the second-order turbulence statistics in the core region of the jet and the plume are practically indistinguishable from each other, although there are significant differences near the plume edge. The DNS data indicate that the turbulent Prandtl number is about 0.7 for both jets and plumes. For plumes, this value is a result of the difference in the ratio of the radial turbulent transport of radial momentum and buoyancy. For jets, however, the value originates from a different spread of the buoyancy and velocity profiles, in spite of the fact that the ratio of radial turbulent transport terms is approximately unity. The DNS data do not show any evidence of similarity drift associated with gradual variations in the ratio of buoyancy profile to velocity profile widths.

DOI: 10.1103/PhysRevFluids.1.074301

I. INTRODUCTION

The mixing of buoyant fluid releases with the surrounding fluid is of primary concern for a wide number of industrial and environmental turbulent flows, spanning the ascending motions of thermals in the atmosphere, the rise and fall of volcanic eruption columns, the release of airborne pollutants, or the propagation of smoke in free or enclosed spaces [1]. Much attention has therefore been paid to the turbulence dynamics of buoyant releases in a multiplicity of flow configurations. One of the most studied flows among these, commonly referred to as a plume, is the free-shear flow arising from a localized source of buoyancy. Since the pioneering work of Zel'dovich [2], Priestley and Ball [3], and Morton *et al.* [4], plumes have been the subject of several theoretical [5], experimental [6–9], and

*m.vanreeuwijk@imperial.ac.uk; civilsfluids@imperial.ac.uk

numerical [10,11] investigations and are well documented in a number of review articles [12–14]. In this context, the well-known turbulent jet can be regarded as a plume without buoyancy and provides a reference state for understanding how buoyancy modifies the behavior of these free-shear flows.

Jets and plumes are canonical examples of flows that evolve in a self-similar fashion [14]: Sufficiently far from the source, a rescaling of the radial coordinate and dependent variables by a characteristic local width r_m, velocity w_m, and buoyancy b_m results in a collapse of the data onto a single curve. The velocity and buoyancy profiles are well represented by a Gaussian form [12] and self-similarity allows power laws, relating the scales r_m, w_m, and b_m to the streamwise (vertical direction opposing the gravitational vector) z coordinate [4], to be deduced. Due to the presence of buoyancy, the z dependence of plumes is markedly different from that of jets, yet in other respects, as discussed in this paper, these flows are broadly alike.

There are several ways to determine the characteristic scales r_m, w_m, and b_m. A popular experimental method is to capitalize on the Gaussian shape of the velocity and buoyancy profiles and associate r_m with the standard deviation of the Gaussian and w_m and b_m with the maximum velocity and buoyancy, respectively. A method that does not rely directly on the assumption of a Gaussian shape is to determine local scales based on integral quantities of the flow:

$$r_m \equiv \frac{Q}{M^{1/2}}, \quad w_m \equiv \frac{M}{Q}, \quad b_m \equiv \frac{B}{r_m^2}, \tag{1}$$

where the integral volume flux Q, specific momentum flux M, and buoyancy B are defined as

$$Q \equiv 2\int_0^\infty \overline{w} r dr, \quad M \equiv 2\int_0^\infty \overline{w}^2 r dr, \quad B \equiv 2\int_0^\infty \overline{b} r dr. \tag{2}$$

Here $\overline{w}$ is the average (ensemble or time) streamwise velocity, $b = g(\rho_e - \rho)/\rho_e$ is the fluid buoyancy and $\overline{b}$ its average value, g is the modulus of the gravitational acceleration, and ρ_e is the density of the environment. Here Q, M, and B are scaled, rather than actual, integral fluxes due to a factor π that is not present in their definitions; this is common practice as it simplifies the resulting analytical expressions [15].

It should be noted that the definition of b_m, in Eq. (1) is nonstandard as it is usually expressed in terms of the buoyancy flux

$$F \equiv 2\int_0^\infty \overline{w}\overline{b} r dr, \tag{3}$$

as $b_m = F/Q = F/w_m r_m^2$. While this is a perfectly reasonable definition, it implicitly assumes averaging over a radius associated with the buoyancy profile that, in general, will not be exactly equal to r_m. With a single length scale r_m as defined in Eq. (1), it follows that $F = \theta_m w_m r_m^2 b_m$, where θ_m is a dimensionless profile coefficient (see also Sec. III C); thus the definition of b_m in terms of F, in the current framework, is $b_m = F/\theta_m Q$. The profile coefficient θ_m, which is intimately related to the ratio of the widths of the buoyancy and velocity profiles (see Sec. III C), plays an important role in longitudinal mixing in jets [16], and is purportedly responsible for the large scatter in measurements of plume entrainment [17].

The dilution of jets and plumes can be quantified by integrating the continuity equation over the radial direction, which results in

$$\frac{1}{r_m}\frac{dQ}{d\zeta} = -2[ru]_\infty. \tag{4}$$

Here $\zeta \equiv \int_0^z r_m^{-1} dz'$ is a dimensionless vertical coordinate and $[ru]_\infty$ is a net volume flux into the jet or plume per unit height. The entrainment assumption [4,18–20] links the radial volume flux to internal jet or plume properties via

$$-[ru]_\infty = \alpha r_m w_m, \tag{5}$$

where α is the entrainment coefficient. Substitution of (5) into (4) and rearranging results in

$$\alpha = \frac{1}{2Q}\frac{dQ}{d\zeta}. \tag{6}$$

Thus, the entrainment coefficient can be interpreted as (half) the relative increase in volume flux over a typical jet or plume radius r_m. This relation also clearly establishes that α is a measure of dilution: the higher its value, the more fluid will be mixed into the jet or plume per (vertical) unit r_m.

Typical ranges of values for α in jets and plumes are, respectively [21], $0.065 < \alpha_j < 0.084$ and $0.10 < \alpha_p < 0.16$, which, in spite of the scatter, strongly suggests that $\alpha_p > \alpha_j$. Using the observation that the spreading rates dr_m/dz of jets and plumes are approximately equal [12,22] and the well-known far-field solutions $r_m = 2\alpha_j z$ and $r_m = \frac{6}{5}\alpha_p z$ for jets [23] and plumes [4], respectively, it follows directly that

$$\alpha_p \approx \tfrac{5}{3}\alpha_j. \tag{7}$$

By applying the relation above to the observed range of values of α_j, we obtain $0.108 < 5\alpha_j/3 < 0.133$, which is in reasonably good agreement with the available data for α_p.

The fact that the spreading rates of jets and plumes are practically identical is intimately linked with the turbulence production in the interior. Indeed, by considering balance equations for the kinetic energy of the mean flow in jets and plumes [17,24–26], the spreading rate can be directly linked to the turbulence production inside the plume. For a self-similar Gaussian plume, ignoring turbulence and pressure effects and assuming $\theta_m = 1$, it follows that [26]

$$\frac{dr_m}{dz} = -\frac{3}{4}\delta_m, \tag{8}$$

where

$$\delta_m = \frac{4}{w_m^3 r_m}\int_0^\infty \overline{u'w'}\frac{d\overline{w}}{dr} r\,dr \tag{9}$$

is a dimensionless profile coefficient associated with the integral of turbulence production due to shear. This quantity is generally negative as it signifies the energy transfer from the mean to the turbulence. Hence, under the realistic assumptions leading to (8), it follows that δ_m is solely responsible for the plume spread and identical spreading rates imply identical values for δ_m. Direct estimations, either using flow measurements or with high-fidelity simulations, confirm that the value of δ_m for jets and plumes is indeed nearly identical [26].

Using the equation for mean kinetic energy, it is possible to derive entrainment relations that fundamentally link α to the production of turbulence kinetic energy, the Richardson number, and shape effects. For a self-similar Gaussian plume with $\theta_m = 1$, ignoring turbulence and pressure effects [24], the entrainment relation is [26]

$$\alpha = -\tfrac{3}{8}\delta_m + \tfrac{1}{4}\mathrm{Ri}, \tag{10}$$

where the Richardson number Ri, defined as

$$\mathrm{Ri} = \frac{b_m r_m}{w_m^2} = \frac{BQ}{M^{3/2}}, \tag{11}$$

characterizes the significance of buoyancy compared with inertia. An important implication of the fact that δ_m does not differ between jets and plumes is that (10) shows that the difference in α is caused purely by the influence of mean buoyancy via Ri. By using the observation that δ_m is a constant, (10) can be rewritten as [26]

$$\alpha = \alpha_j + (\alpha_p - \alpha_j)\Gamma, \tag{12}$$

which is commonly referred to as the Priestley-Ball entrainment model [3,24]. Here $\Gamma = \mathrm{Ri}/\mathrm{Ri}_p$ is the flux balance parameter, where $\mathrm{Ri}_p = 8\alpha_p\beta_g/5$ is the Richardson number for a pure plume [26]

and β_g is a profile coefficient associated with the total momentum flux (see Sec. III C for its definition). The condition $\Gamma = 1$ represents a stable equilibrium (with respect to perturbations in Γ), a condition referred to as that of a pure plume. The other equilibrium condition is given by $\Gamma = 0$, i.e., that of a pure jet, which is a condition that is unstable to the addition of an arbitrarily small amount of buoyancy [15]. For forced plumes, which have an excess of momentum (relative to pure plume conditions) at the source [5], $0 < \Gamma < 1$, whereas $\Gamma > 1$ for lazy plumes, which have a deficit of momentum [15]. Previous experimental studies observed that (12) accurately describes the behavior of jets, plumes, and forced plumes [9,25].

If the magnitude of the dimensionless turbulence production δ_m is approximately equal in jets and plumes, one is led to ask what this implies about the radial transport of scalar quantities in the flow. The turbulent Prandtl number

$$\mathrm{Pr}_T = \frac{\nu_T}{D_T}, \tag{13}$$

where ν_T and D_T are the eddy viscosity and eddy diffusivity, respectively, quantifies the effectiveness with which the flow mixes momentum compared with buoyancy or mass and is a useful quantity in this regard. The consensus is that $\mathrm{Pr}_T = 0.7$ in axisymmetric jets and plumes [27], which suggests that turbulence transports buoyancy or mass more efficiently than momentum [28] in both cases. However, the underlying physics and their implications for entrainment and for the relative widths of the scalar profile compared with the velocity profile are not understood. For jets there is good agreement between investigators that suggests the scalar field is wider than the velocity field [6,9,23,27]. For plumes, however, as discussed in Ref. [29] and elsewhere, there is significant uncertainty: some studies reveal that the velocity field is wider than the buoyancy field [8,27,30], others reveal that it is narrower [6,23,25,31]; several results imply that the velocity and scalar profiles have roughly the same width [9,32] and some imply that the relative width varies with height [17]. The present paper seeks to untangle the confusion regarding the relationship between Pr_T and the widths of the scalar and velocity profiles by supplementing the available experimental data with precise information from direct numerical simulation (DNS).

Herein, we follow the approach of Ezzamel *et al.* [25] by performing a side-by-side comparison of turbulent jets, plumes, and the intermediate case of a forced plume, but using DNS rather than laboratory experiments. With DNS it is relatively straightforward to prescribe boundary conditions consistent with the analytical solutions and furthermore, DNS provides access to all variables, including pressure, at Kolmogorov-scale resolutions. In Sec. II the simulation details are presented. Integral flow statistics, such as the evolution of $\Gamma(z)$, are presented in Sec. III A and the deduced entrainment coefficient α is shown to follow closely the Priestley-Ball entrainment model (12). Self-similarity of the first- and second-order statistics is discussed in Sec. III B, which includes an analysis of the invariants of the anisotropy tensor. Profile coefficients, which represent the relative contribution of various physical processes relative to the characteristic scales, are presented in Sec. III C and these are used to decompose the entrainment coefficient into its individual components in Sec. III D. Section III E discusses the radial turbulent transport of streamwise momentum and buoyancy, as quantified by the eddy viscosity ν_T and diffusivity D_T. The turbulent Prandtl number will be decomposed and it is shown that even though jets and plumes share a very similar value for Pr_T, the underlying reason in each case is different. Concluding remarks are made in Sec. IV.

II. SIMULATION DETAILS

We simulate axisymmetric jets and plumes driven by an isolated source of steady specific momentum flux M_0, volume flux Q_0, and buoyancy flux F_0. The source is approximately circular and located at the center of the base of a cuboidal domain of size $40^2 \times 60$ source radii r_0. The fluid motion is governed by the incompressible Navier-Stokes equations under the Boussinesq approximation, which we solve numerically using $1280^2 \times 1920$ computational cells over a uniform Cartesian grid. The code for the DNS employs a spatial discretization of fourth-order accuracy that

TABLE I. Simulation details. The entrainment coefficient α and virtual origin z_v are determined directly from r_m (see Fig. 1). The constants a_w and a_b are prefactors of the mixing lengths of velocity and buoyancy, respectively [Eq. (25)], and $\langle \mathrm{Pr}_T \rangle$ is the typical turbulent Prandtl number [Eq. (13)].

Simulation	$N_x N_y N_z$	$L_x L_y L_z / r_0^3$	Re_0	Γ_0	t_{run}/τ_0	α	z_v/r_0	a_w	a_b	$\langle \mathrm{Pr}_T \rangle$
J	$1280^2 \times 1920$	$40^2 \times 60$	5000	0	400	0.067	−3.66	0.12	0.14	0.72
F	$1280^2 \times 1920$	$40^2 \times 60$	5000	≈0.03	480	varies	varies			
P	$1280^2 \times 1920$	$40^2 \times 60$	1667	∞	480	0.105	−3.90	0.13	0.15	0.68

conserves volume, momentum, and energy, and integration in time is performed using a third-order Adams-Bashforth scheme (further details can be found in Ref. [33]). On the vertical and top faces of the domain we impose open boundary conditions. These allow fluid to enter and leave the domain in a manner that is consistent with flow in an unconfined domain [34]. We initiate the turbulence by applying uncorrelated perturbations of 1% to the velocities in the first cell above the source.

To simulate the jet J we impose a constant uniform vertical velocity w_0 at the source. Consequently, a constant scalar flux can be maintained by imposing a Dirichlet boundary condition $b = b_0$ on a given scalar quantity b at the source. For the jet simulation J, this scalar quantity is passive, i.e., its presence does not imply a source term in the momentum equation. In the forced plume simulation F, for which b corresponds to buoyancy, the Dirichlet boundary condition on b at the source results in a positive buoyancy flux F_0. The source conditions used in the simulation of plume P correspond to $w_0 = 0$ and a specified positive integral buoyancy flux F_0; in practice, the buoyancy flux F_0 is a diffusive flux resulting from a Neumann condition on the buoyancy at the source. Therefore, the plume simulation P is infinitely lazy at the source ($\Gamma_0 \equiv 5F_0 Q_0^2/8\alpha_p M_0^{5/2} = \infty$) although, over a relatively short distance, plume P becomes pure. Based on the analysis of Hunt and Kaye [15], in which a constant entrainment coefficient model is assumed, the rate of decrease of the local Richardson number immediately above a highly lazy plume source scales as

$$\left.\frac{d\Gamma}{d\zeta}\right|_{\zeta=0} \propto -\Gamma_0^{9/5}. \tag{14}$$

Thus, the vertical distance required to approach pure-plume behavior reduces to zero as the laziness of the source increases, i.e., as $\Gamma_0 \to \infty$. As a consequence, our plume arising from the heated disk boundary condition, which represents the limit of an infinitely lazy plume source, is expected to establish pure-plume behavior immediately above the source and as such to closely mimic a true pure-plume source. For jet J and forced plume F we define the source Reynolds number $\mathrm{Re}_0 \equiv 2M_0^{1/2}/\nu$ and for plume P, $\mathrm{Re}_0 \equiv 2F_0^{1/3} r_0^{2/3}/\nu$. The calculated values of Re_0, in addition to further details of the simulations, can be found in Table I.

Statistics were acquired from each simulation over a duration that is large in comparison with the typical turnover time. For jet J and forced plume F, the turnover time based on the source conditions is $\tau_0 \equiv r_0^2/M_0^{1/2}$. For plume P, $\tau_0 \equiv r_0^{4/3}/F_0^{1/3}$. Prior to obtaining statistics we ensure that transient effects arising from initial conditions are imperceptible in the leading-order statistics. Statistics were gathered over the time period shown in Table I.

Azimuthally averaged data were obtained by partitioning the domain into concentric cylindrical cells and averaging over all cells lying within a given shell. To compute integrals over lateral slices of the jet (for the definition of these integrals see Sec. III C), we define the upper limit of integration r_d according to $\overline{w}(r_d,z,t) = 0.02\,\overline{w}(0,z,t)$.

Detailed validation of the jet and plume simulations was performed in previous work [35,36] for simulations at identical Re_0. The results presented below are for a larger domain and are obtained with even higher resolutions. A detailed validation will thus not be repeated here; agreement with existing data will be pointed out in the text and, where appropriate, included in the figures.

TABLE II. Asymptotic far-field solutions of jets and plumes including turbulence and pressure effects. In the expressions above, M_0 and F_0 are the mean specific momentum and buoyancy fluxes far away from the source.

Quantity	Jet	Plume
Γ	0	1
Ri	0	$8\alpha_p\beta_g/5$
r_m	$2\alpha_j z$	$\frac{6}{5}\alpha_p z$
w_m	$\frac{M_0^{1/2}}{2\alpha_j} z^{-1}$	$\frac{5}{6\alpha_p}\left(\frac{9}{10}\frac{\alpha_p}{\theta_m\beta_g}F_0\right)^{1/3} z^{-1/3}$
b_m	$\frac{F_0}{2\alpha_j\theta_m} M_0^{-1/2} z^{-1}$	$\frac{5F_0}{6\alpha_p\theta_m}\left(\frac{9}{10}\frac{\alpha_p}{\beta_g\theta_m}F_0\right)^{-1/3} z^{-5/3}$

III. RESULTS

A. Integral flow statistics

From an integral perspective, the plume dynamics are fully determined by the evolution of the characteristic radius r_m, velocity w_m, and buoyancy b_m. For the limiting cases of a pure jet ($\Gamma = 0$) and of a pure plume ($\Gamma = 1$), the scaling of these parameters with the distance from the source takes the form of a power law, which can be derived from the plume equations [4]. Recently [26], these solutions were extended to account for turbulence and pressure effects via the profile coefficient β_g and for differences in the widths of velocity and buoyancy profiles via the coefficient θ_m (Table II). The profile coefficients β_g and θ_m will be defined rigorously in Sec. III C. The streamwise evolution of r_m is shown in Fig. 1(a), confirming the almost identical linear spreading rate for the three simulations considered. Figures 1(b)–1(d) show that the jet and plume both exhibit the expected power-law scaling. The forced plume transitions from a near-field jetlike scaling to a far-field plumelike scaling.

As visible in Fig. 1(a), the outflow boundary condition appears to affect the statistics in the upper part of the domain. This is caused by subtle modification of the mean flow near the outflow boundary, presumably because of slight pressure gradients [34]. These small disturbances affect the integral quantities Q, M, and F via the thresholding technique (which is based on $\overline{w}$; see Sec. II). Hereafter, all considerations on the dynamics of the flow will therefore be based on the analysis of the flow statistics for $z/r_0 < 50$.

For the two limiting cases J and P, the plume radius $r_m(z)$ is fitted in the far field ($20 < z/r_m < 50$) to the analytical solutions $r_m = a\alpha(z - z_v)$, where z_v is the virtual origin [29] and $a = 2$ for jets and $a = 6/5$ for plumes (see Table II). We obtain $\alpha_j = 0.067$ and $\alpha_p = 0.105$, values that agree well with the literature and provide evidence of enhanced dilution within a plume compared to a jet.

A flux balance parameter $\Gamma(z)$ that takes into account turbulence, pressure effects, and differences in profile widths is defined as [26]

$$\Gamma = \frac{5FQ^2}{8\alpha_p\beta_g\theta_m M^{5/2}} \tag{15}$$

and its variation with height is shown for the three simulations in Fig. 2(a). For simulation J, Γ is identically zero for all values of z. For simulation P, $\Gamma \approx 1$ except for a rapid variation in the very near field $z/r_0 < 5$. It is worth noting that for simulation P, the turning points of Γ in the near field are not compatible with classical solutions of the plume equations [15] and have to be attributed to the near-field variations of the profile coefficients (Sec. III C). For forced plume simulation F, Γ evolves approximately linearly towards its equilibrium state $\Gamma = 1$, a condition that is however not attained at the upper limit of the simulated domain.

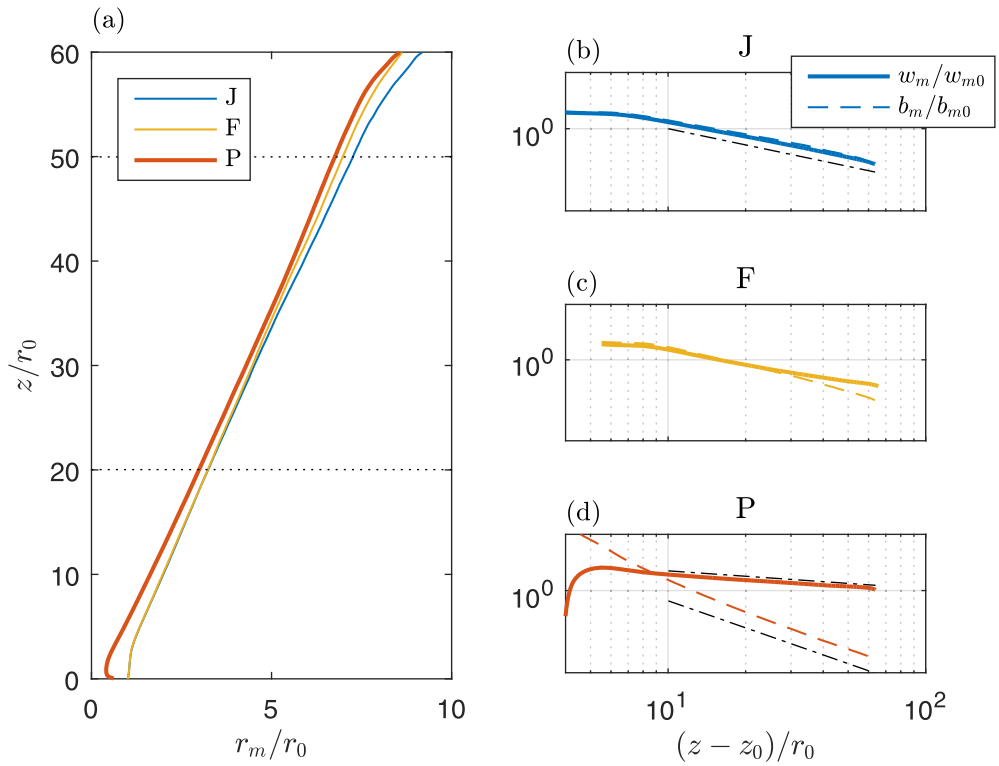

FIG. 1. Variation of the characteristic plume quantities with height z for simulations J, F, and P: (a) $r_m(z)$, (b) b_m and w_m for J release, (c) b_m and w_m for F release, and (d) b_m and w_m for P release. Dash-dotted lines in (b)–(d) show asymptotic power-law scaling (Table II).

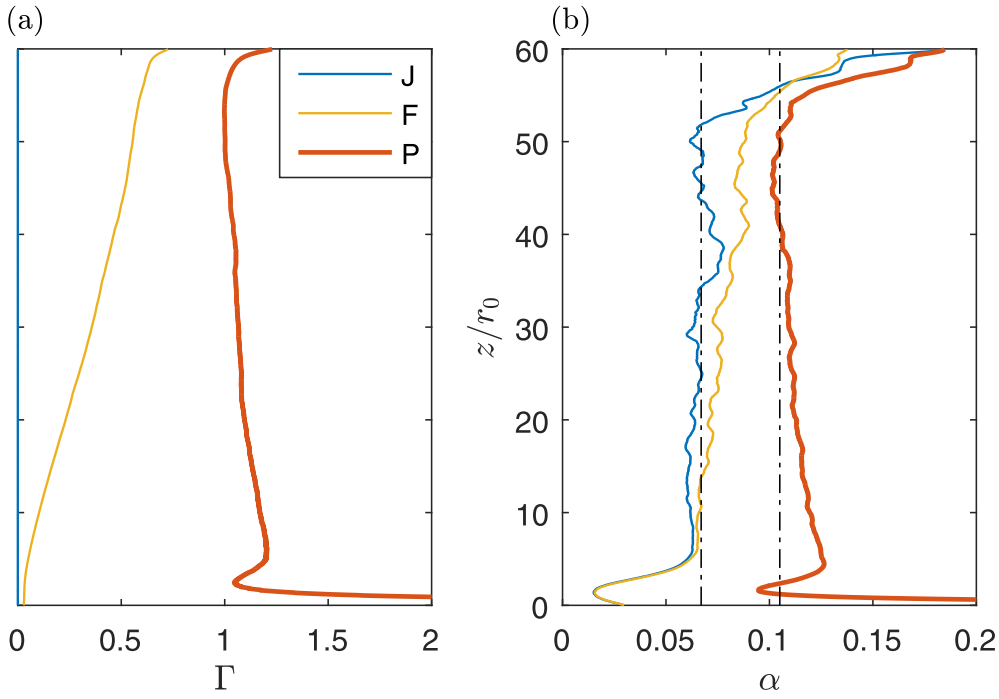

FIG. 2. Vertical evolution for the simulations J, F, and P of (a) the flux balance parameter Γ and (b) the entrainment coefficient α computed from (6).

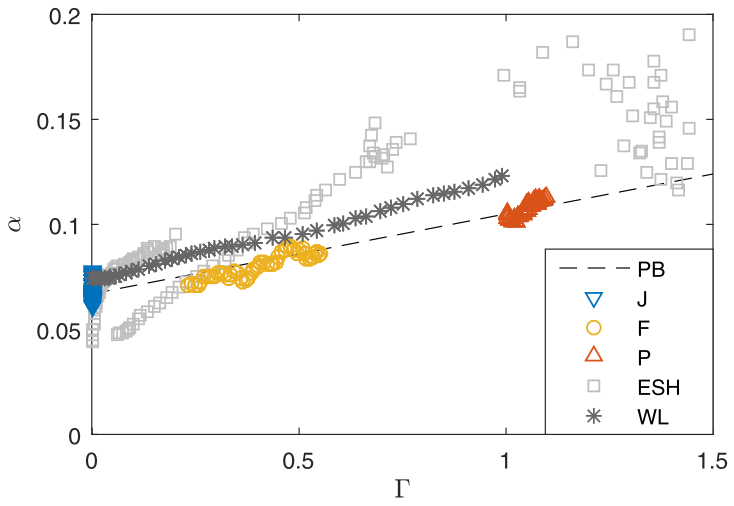

FIG. 3. Entrainment coefficient α as a function of Γ over the interval $20 < z/r_0 < 50$ for simulations J, F, and P, confirming the good agreement with the PB [3] entrainment model. The WL [9] and ESH [25] data are also shown.

The variation of the entrainment coefficient α with the vertical coordinate z, as determined from (6), is plotted in Fig. 2(b). Here Q was filtered to smooth out occasional small step changes in its value caused by the thresholding, which would otherwise result in unphysical spikes in $dQ/d\zeta$ and $\alpha(z)$. The values of α_j and α_p (Table I) inferred from r_m are displayed with the dash-dotted lines and are in good agreement with the far-field values for the jet and the plume, respectively. The entrainment in the pure jet shows a high variability in the near field but rapidly attains the constant value α_j, within no more than five source radii. The entrainment coefficient for simulations J and F are almost the same in the near field. However, with increasing distance from the source, the entrainment coefficient in the forced plume simulation F shows a clear increasing trend. For the pure plume, the entrainment coefficient is very large in the near field ($z/r_0 < 5$) and then attains an approximately constant value, which is in close agreement with the far-field estimate $\alpha_p = 0.105$ obtained from r_m. These results are in agreement with previous experimental investigations [9,25] and show a clear tendency of the entrainment coefficient to increase with increasing Γ.

By plotting the computed values of α as a function of Γ, it is possible to test directly the appropriateness of the Priestley-Ball (PB) [3] entrainment model (12) (see Fig. 3). Shown in the same plot is the experimental data from Wang and Law [9] and the recent measurements from Ezzamel *et al.* [25]. The latter has been reprocessed in the Appendix to better represent the coflow in the ambient, which significantly influences the entrainment statistics. The new ambient-flow correction shows much better agreement between the volume-flux-based estimate of α and that obtained from the entrainment relation, although the data do not display the constant value of α that one would expect from self-similarity in the far field for the jet and plume experiments.

As is evident from Fig. 3, all data sets show a dependence on Γ. The current DNS data set and the Wang-Law (WL) data convincingly demonstrate the linear dependence on Γ of the Priestley-Ball entrainment model (12) for unstratified environments in the self-similar regime. However, the figure also exposes the variability in what may be regarded as the limiting (or end member) entrainment coefficients; the values one would choose for α_j and α_p in Eq. (12) would be slightly different for the WL and current data sets. The dashed line shows the PB entrainment model using the values of α_j and α_p presented in Table I and good agreement with the DNS data can be observed. The Ezzamel-Salizzoni-Hunt (ESH) data confirm the appropriateness of the PB model qualitatively, but despite the ambient-flow correction (Appendix) the data remain noisy. The linear dependence of α on Γ implies that δ_m is practically identical in jets and plumes, as argued in the Introduction. The entrainment coefficient will be decomposed into its various parts in Sec. III D.

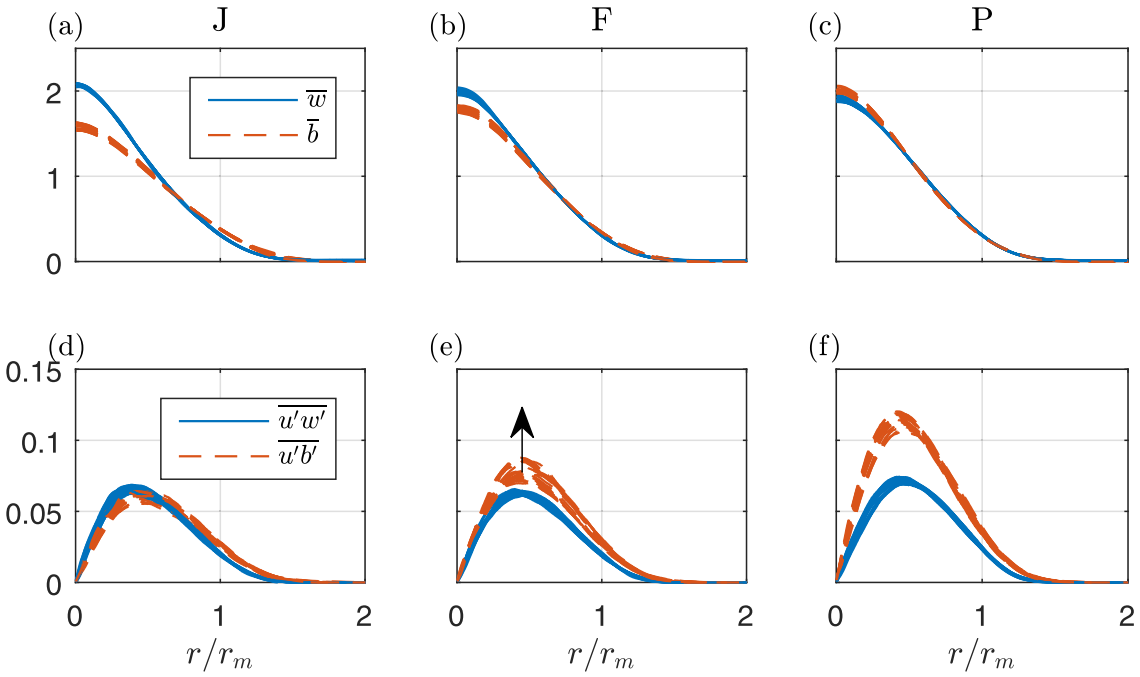

FIG. 4. Self-similarity profiles of $\overline{w}$, $\overline{b}$, $\overline{u'w'}$, and $\overline{u'b'}$ over the interval $20 < z/r_0 < 50$ for (a) and (d) jet simulation, (b) and (e) forced plume simulation, and (c) and (f) pure plume simulation.

B. Self-similarity

Shown in Fig. 4 are the mean velocity $\overline{w}$, buoyancy $\overline{b}$, radial turbulent momentum flux $\overline{u'w'}$, and turbulent buoyancy flux $\overline{u'b'}$ over the vertical interval $20 < z/r_0 < 50$. As is customary, all variables are presented in dimensionless form, normalized by the local value of r_m, b_m, and w_m. In line with our expectations, for all three simulations the mean vertical velocity $\overline{w}$ collapses onto a single profile that closely resembles a Gaussian profile.

The radial profiles of mean buoyancy $\overline{b}$ also exhibit a clear Gaussian-like dependence on the radial coordinate. However, the centerline values and spread differ for the three simulations. Profiles for velocity and buoyancy almost coincide for plumes [Fig. 4(c)], whereas for the forced plume and the jet, the buoyancy profiles have a slightly larger spread (as further quantified by the profile coefficient θ_m associated with mean scalar transport; see Sec. III C). As the integral under the dimensionless curves is unity by construction, a wider profile will reduce the centerline value of $\overline{b}/b_m$, particularly since small changes far from the centerline contribute significantly to the integral due to the conical geometry.

The profile of the turbulent radial momentum flux $\overline{u'w'}$ is practically identical for the jet, forced plume, and pure plume [Figs. 4(d)–4(f)], which is consistent with the notion of the profile coefficient associated with the production of turbulence kinetic energy δ_m being insensitive to Γ. However, the normalized radial turbulent buoyancy flux shows large variations in amplitude. For the jet simulations, the profiles of $\overline{u'w'}$ and $\overline{u'b'}$ are practically identical. For the plume simulation, $\overline{u'b'}$ is about 60% larger in amplitude than $\overline{u'w'}$. The profile of $\overline{u'b'}$ for the forced plume transitions smoothly from the jet profile to the plume profile as Γ tends to unity, as indicated by the arrow in Fig. 4(e); this is in contrast to Fig. 4(f), where no systematic variation with height is present.

The normalized mean radial velocity $\overline{u}$ is shown in Fig. 5(a). Contrary to the mean vertical velocity $\overline{w}$ profiles, the shape of $\overline{u}$ differs significantly between the jet, forced plume, and pure plume. For the jet, $\overline{u}$ increases from a value of zero (imposed by the radial symmetry of the flow), reaches a peak at $r/r_m \approx 0.5$, then decreases, becomes negative with a minimum at $r/r_m \approx 1.4$, and then decays approximately inversely proportional to the radius due to the fact that the flow varies very slowly

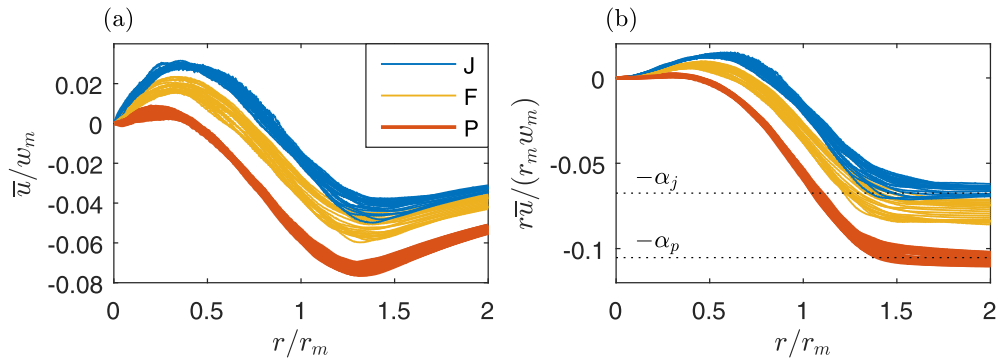

FIG. 5. (a) Self-similar profiles for mean radial velocity $\overline{u}$ and (b) normalized mean radial specific volume flux. The dotted lines indicates the values of α_j and α_p in Table I.

with z. For the plume, the maximum in $\overline{u}$ is significantly smaller, implying a reduction in the mean outward radial transport in a plume. The normalized specific radial volume flux $r\overline{u}/r_m w_m$, shown in Fig. 5(b) for all three simulations, tends to a constant value outside the plume for $r/r_m > 1.5$. By rearranging Eq. (5), it clear that the constant value is equal to the entrainment coefficient α. The

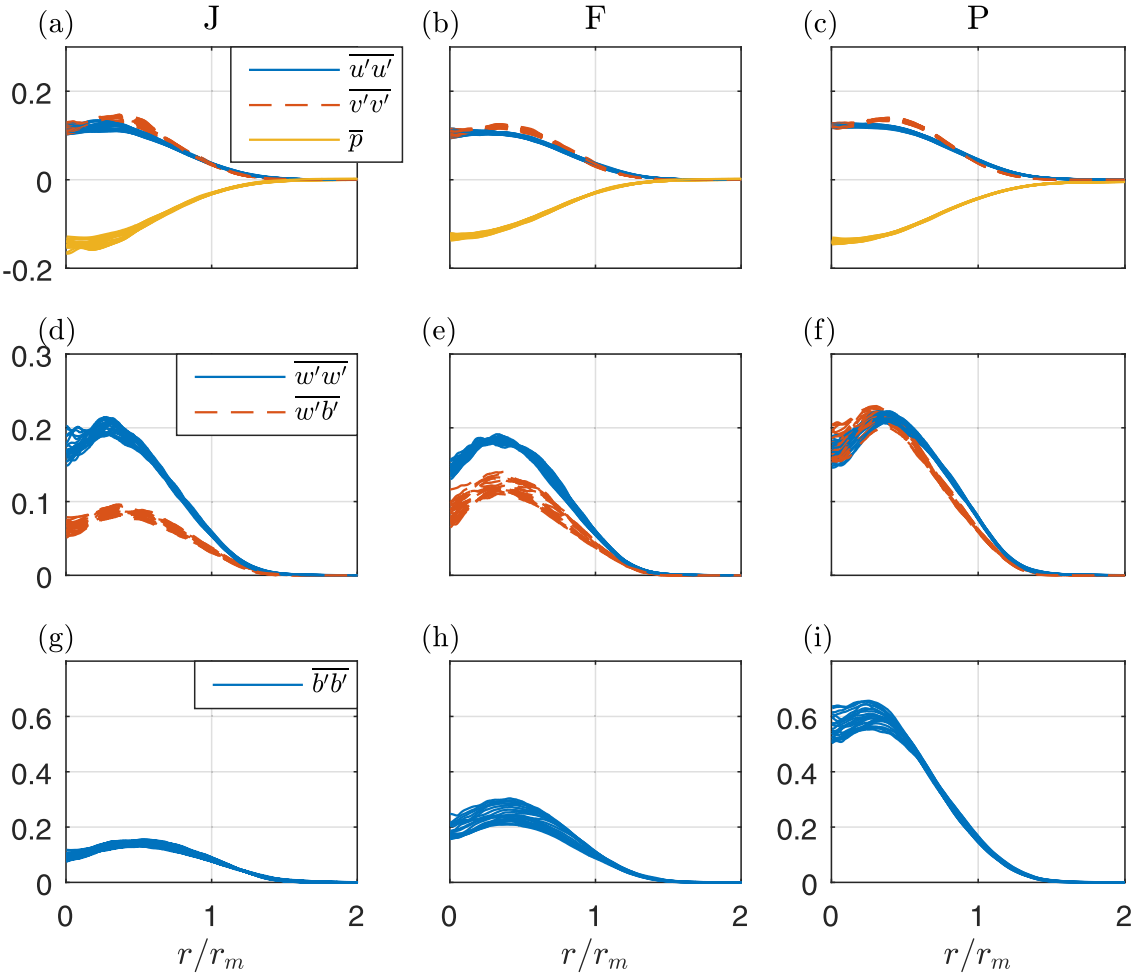

FIG. 6. Self-similarity profiles of second-order quantities and pressure. All quantities are normalized.

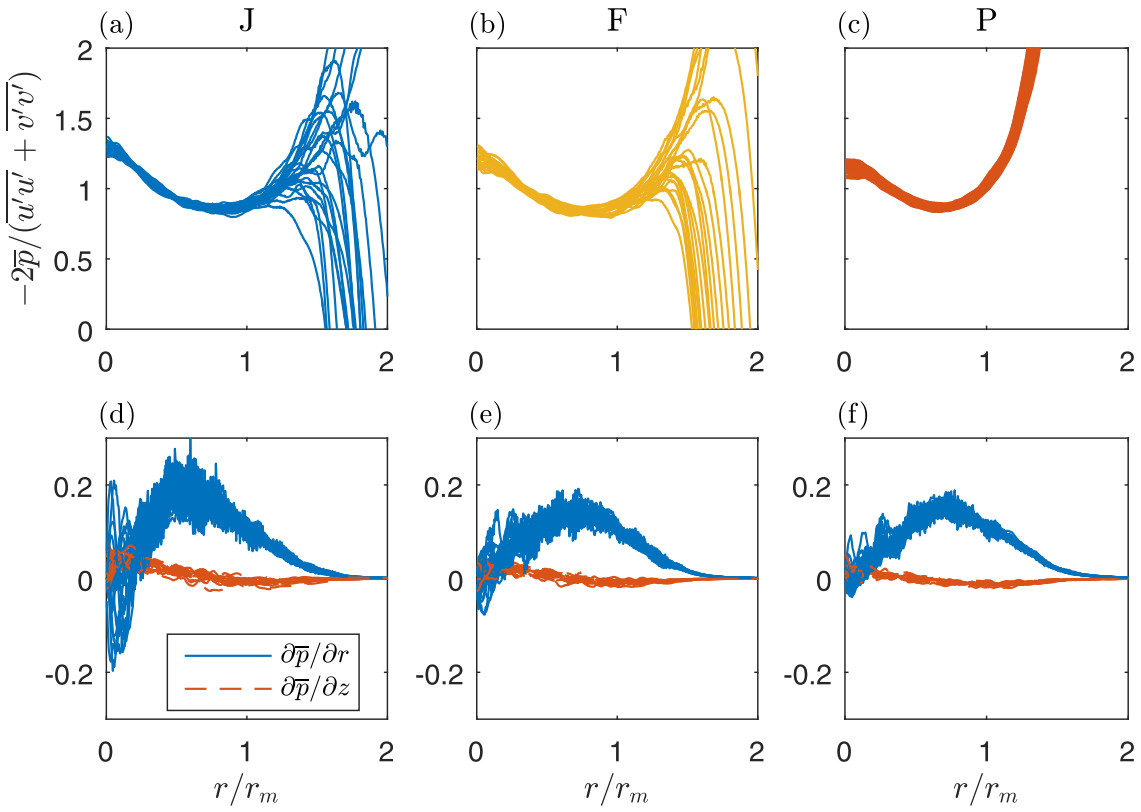

FIG. 7. (a)–(c) Ratio of mean pressure $\overline{p}$ and $-(\overline{u'u'}+\overline{v'v'})/2$ and (d)–(f) horizontal and vertical pressure gradients for (a) and (d) simulation J, (b) and (e) simulation F, and (c) and (f) simulation P.

dashed lines in Fig. 5(b) are the values of α in Table I; excellent agreement is shown with the values deduced from r_m.

The turbulent components $\overline{u'u'}$ and $\overline{v'v'}$, shown as a function of r/r_m in Figs. 6(a)–6(c), are self-similar and practically identical. Furthermore, their dependence on Γ is negligible, providing further confirmation that the turbulence inside plumes and jets is similar, at least in terms of the second-order statistics. The mean pressure $\overline{p}$ is extremely difficult to measure in laboratory experiments and is usually approximated by [9,25,37] $\overline{p} \approx -(\overline{u'u'}+\overline{v'v'})/2$. The quantity $\overline{p}$ is readily available in DNS and it is clear from Figs. 6(a)–6(c) that it correlates well with $-(\overline{u'u'}+\overline{v'v'})/2$, although upon closer inspection (Fig. 7) it becomes evident that $-(\overline{u'u'}+\overline{v'v'})/2$ underestimates $\overline{p}$ by 30% in the core of the flow, while it overestimates $\overline{p}$ by about 10% near $r/r_m = 1$. Thus, the DNS data demonstrate that $\overline{p} = -(\overline{u'u'}+\overline{v'v'})/2$ within, say, 20% (see [37] for a detailed explanation of the various sources of error). Like the gradient of all quantities in a slender turbulent boundary layer, the gradient of pressure in the radial direction is expected to be larger than in the vertical direction by a factor proportional to the spreading rate of the flow. The DNS data confirm that this is the case [Figs. 7(d)–7(f)].

Figures 6(d)–6(f) show the streamwise turbulent momentum and buoyancy flux. While the vertical turbulent momentum flux is more or less identical for cases J, F, and P, the buoyancy profile differs significantly between the three subplots. Clearly, an increase in the value of Γ increases the vertical turbulent buoyancy flux, as well as the radial buoyancy flux [Figs. 4(d)–4(f)]. A similar trend is observable in the turbulence buoyancy variance [Figs. 6(g)–6(i)]. Note that given a sufficient vertical extent of the domain, we expect both $\overline{w'b'}$ and $\overline{b'b'}$ for simulation F to increase to levels observed in simulation P.

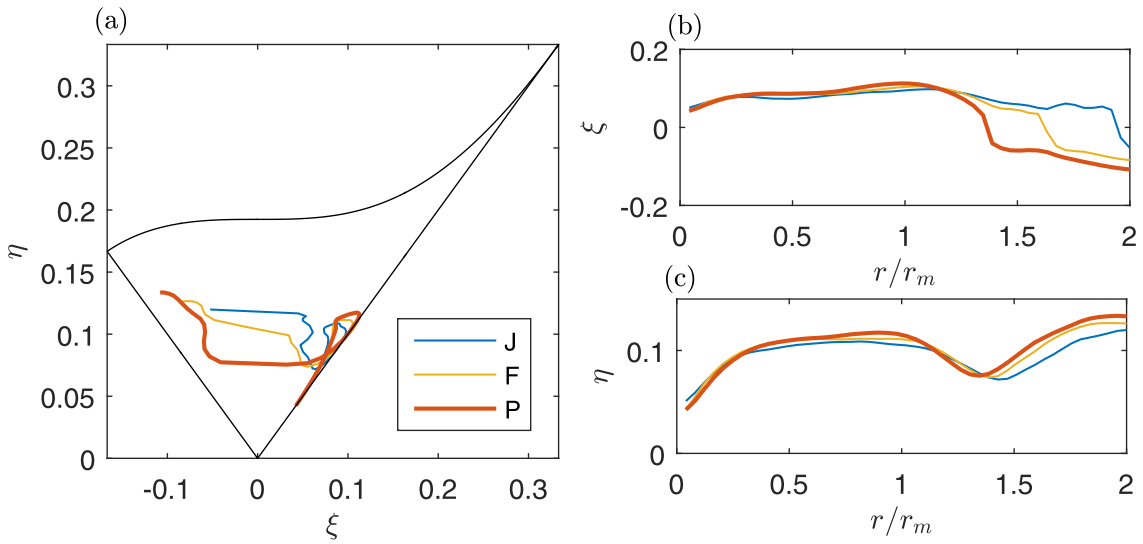

FIG. 8. Invariants of the anisotropy tensor (16) for the jet, forced plume, and plume. (a) Plot in ξ-η space, together with the Lumley triangle. (b) Dependence of ξ on r/r_m. (c) Dependence of η on r/r_m.

To provide further evidence of the similarity of the turbulence statistics in plumes and jets it is instructive to calculate the invariants of the anisotropy tensor [38]

$$b_{ij} = \frac{\overline{u_i' u_j'}}{2e} - \frac{1}{3}\delta_{ij}, \tag{16}$$

where $e = \frac{1}{2}\overline{u_i' u_i'}$ is the turbulence kinetic energy and δ_{ij} is the Kronecker delta. As the turbulence is incompressible, one invariant of $\mathbf{b}$ is zero and the other two, denoted ξ and η, are defined via $\mathrm{Tr}(\mathbf{b}^2) \equiv 6\xi^2$ and $\mathrm{Tr}(\mathbf{b}^3) \equiv 6\eta^3$, where Tr denotes the tensor trace. The invariants of $\mathbf{b}$ cannot take any value; realizable flows are confined to a region of the ξ-η space commonly known as the Lumley triangle [38].

The invariants are calculated as follows. The second-order statistics shown in Figs. 4 and 6 are averaged over the range $20 < z/r_m < 50$, after which ξ and η are calculated as a function of r/r_m. Figures 8(b) and 8(c) show, respectively, the profiles of invariants η and ξ as a function of r/r_m. It is evident that the profiles for J, F, and P are nearly indistinguishable for $r/r_m < 1.5$, providing further evidence that turbulence in jets and plumes is similar. In the ξ-η plane [Fig. 8(a)], the data are close to the $\xi = \eta$ line, which is indicative of axisymmetric turbulence with one large eigenvalue, i.e., rodlike turbulence. Interestingly, at the edge of the jet or plume, ξ changes very rapidly from positive to negative. For plumes, the crossover appears to happen closer to the centerline than for the jet. Thus, near the plume edge, the average picture of the turbulence resembles axisymmetric turbulence with one small eigenvalue, i.e., disklike turbulence. These observations are in agreement with the laboratory experiments of Hussein *et al.* [37], which were presented in terms of the (ξ,η) invariants in [39].

Consideration of the vertical gradient $\partial\overline{w}/\partial z$ provides a possible explanation for why the point at which turbulence changes from being dominated by one component (the core region) to two components (the edge of the flow) differs in jets compared with plumes. Noting that $w_m \sim z^{-1}$ in jets, whereas $w_m \sim z^{-1/3}$ in plumes, the point at which $\partial\overline{w}/\partial z = 0$ occurs at larger values of r/r_m in jets than it does in plumes. Likening the flow with a diverging (core region, $\partial\overline{w}/\partial z < 0$) or converging (edge region, $\partial\overline{w}/\partial z > 0$) nozzle, one would therefore expect the point of transition between one-component and two-component regimes, respectively, to be affected by differences in the point at which $\partial\overline{w}/\partial z$ changes sign.

C. Profile coefficients

Profile coefficients encapsulate integrated information about the mean and turbulent fluxes of momentum, buoyancy, mean kinetic, and turbulence production. In classical integral descriptions of the plume equations [4], the profile coefficients are generally assumed to be either unity or zero. However, preserving information about profile shapes is crucial in the description of unsteady jets and plumes [35,36,40] and is also the key to decomposing entrainment into its various processes. The profile coefficients for the fluxes of momentum β, buoyancy θ, and mean kinetic energy γ, as well as the dimensionless turbulence production δ are given by, respectively,

$$\begin{aligned}
&\beta_m \equiv \frac{M}{w_m^2 r_m^2} \equiv 1, && \beta_f \equiv \frac{2}{w_m^2 r_m^2}\int_0^\infty \overline{w'^2} r dr, && \beta_p \equiv \frac{2}{w_m^2 r_m^2}\int_0^\infty \overline{p} r dr,\\
&\gamma_m \equiv \frac{2}{w_m^3 r_m^2}\int_0^\infty \overline{w}^3 r dr, && \gamma_f \equiv \frac{4}{w_m^3 r_m^2}\int_0^\infty \overline{w}\,\overline{w'^2} r dr, && \gamma_p \equiv \frac{4}{w_m^3 r_m^2}\int_0^\infty \overline{wp} r dr,\\
&\delta_m \equiv \frac{4}{w_m^3 r_m}\int_0^\infty \overline{w'u'}\frac{\partial \overline{w}}{\partial r} r dr, && \delta_f \equiv \frac{4}{w_m^3 r_m}\int_0^\infty \overline{w'^2}\frac{\partial \overline{w}}{\partial z} r dr, && \delta_p \equiv \frac{4}{w_m^3 r_m}\int_0^\infty \overline{p}\frac{\partial \overline{w}}{\partial z} r dr,\\
&\theta_m \equiv \frac{F}{w_m b_m r_m^2}, && \theta_f \equiv \frac{2}{w_m b_m r_m^2}\int_0^\infty \overline{w'b'} r dr. &&
\end{aligned} \tag{17}$$

The total momentum flux is given by $\beta_g M$, where $\beta_g = \beta_m + \beta_f + \beta_p$. Similarly, θ_g is associated with the total buoyancy flux, γ_g with the total energy flux, and δ_g with the total turbulence production (including pressure redistribution). Profile coefficients β and θ show up naturally upon radial integration of the Reynolds-averaged volume, vertical momentum, and buoyancy equations of a high-Reynolds-number flow in a neutral environment [26]

$$\frac{1}{Q}\frac{dQ}{d\zeta} = 2\alpha, \tag{18a}$$

$$\frac{1}{M}\frac{d}{d\zeta}(\beta_g M) = \mathrm{Ri}, \tag{18b}$$

$$\frac{1}{F}\frac{d}{d\zeta}\left(\frac{\theta_g}{\theta_m}F\right) = 0. \tag{18c}$$

These equations reduce to the classical plume equations [4] on setting $\beta_g = 1$ and $\theta_g = \theta_m = 1$. Furthermore, we note that $\mathrm{Ri} = 0$ by definition for the jet, implying that the evolution of F and M are uncoupled (and that F in that case corresponds to a passive scalar flux). Similarly, γ and δ emerge naturally from integration of the mean kinetic energy equation

$$\frac{Q}{M^2}\frac{d}{d\zeta}\left(\gamma_g \frac{M^2}{Q}\right) = \delta_g + 2\theta_m \mathrm{Ri}. \tag{19}$$

Figure 9 shows the profile coefficients as a function of z. The coefficients associated with the mean flow, β_m, γ_m, δ_m, and θ_m, are shown in Figs. 9(a)–9(c). There are large variations in the profile coefficients in the near field, which are due to changes in the velocity and buoyancy profiles as the jet or plume develops; indeed, the largest changes occur over a small region $z/r_0 < 5$, for the plume even closer to the source ($z/r_0 < 3$). However, for larger z/r_0 the coefficients become constant, which is consistent with self-similarity.

The average values of the profile coefficients over the interval $20 < z/r_0 < 50$ are presented in Table III. The dimensionless buoyancy flux θ_m is less than unity for the jet, implying that the spread of the buoyancy field exceeds the spread of the velocity field. This can be shown by assuming a

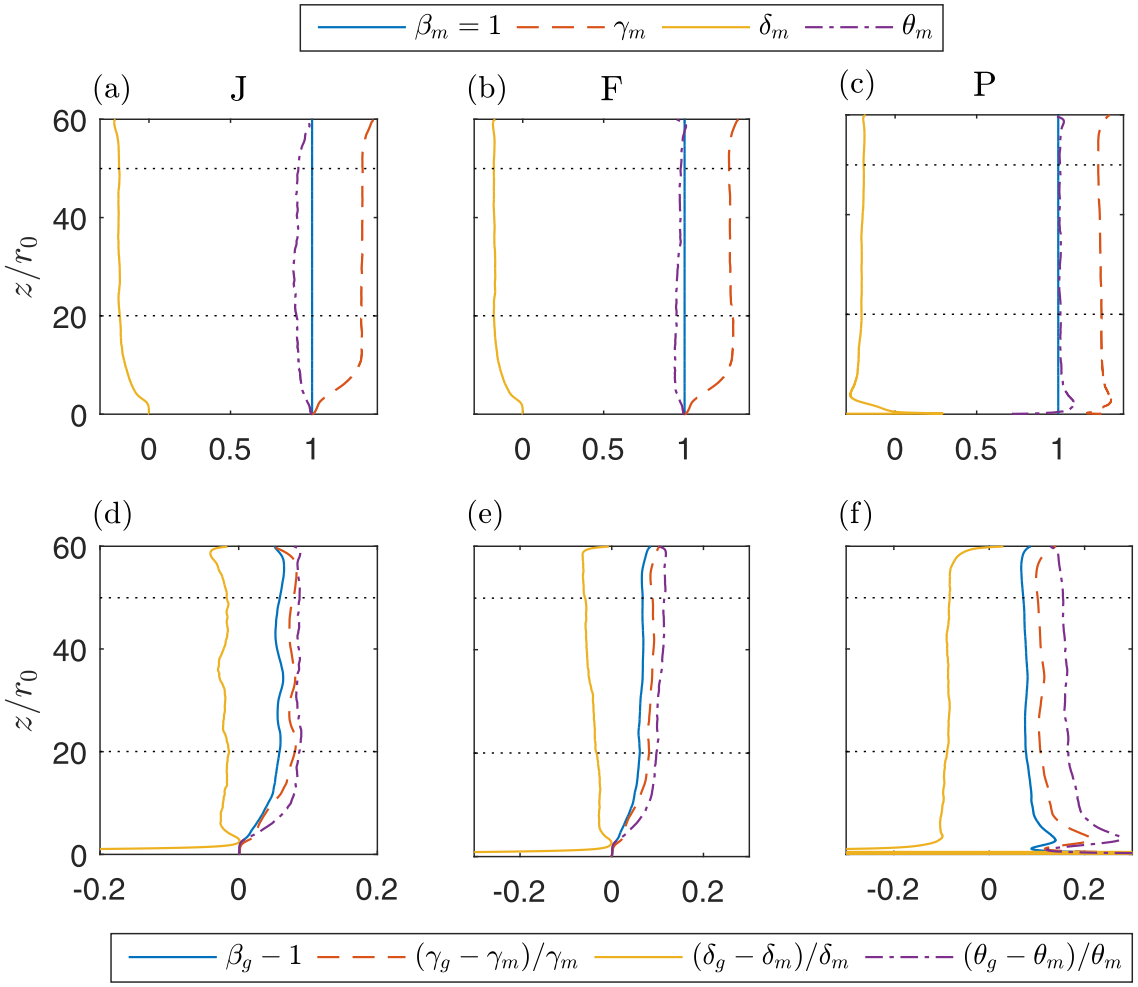

FIG. 9. (a)–(c) Mean profile coefficients and (d)–(f) relative contribution of turbulence and pressure to the dimensionless coefficients for (a) and (d) simulation J, (b) and (e) simulation F, and (c) and (f) simulation P. The dashed lines indicate the averaging interval $20 < z/r_0 < 50$ used for the profile coefficients displayed in Table III.

Gaussian form for the velocity and buoyancy profiles

$$\overline{w} = 2w_m \exp\left(-2\frac{r^2}{r_m^2}\right), \quad \overline{b} = 2\frac{b_m}{\varphi^2}\exp\left(-2\frac{r^2}{\varphi^2 r_m^2}\right), \tag{20}$$

where φr_m is the characteristic width of the buoyancy profile and φ is the ratio of the buoyancy to velocity radii. These profiles are consistent with the definitions $\beta_m = 1$ and $B = b_m r_m^2$ and evaluation of the profile coefficient for the mean energy flux results in $\gamma_m = 4/3$. The buoyancy flux is given by $F = 2\int_0^\infty \overline{w}\overline{b}rdr = \frac{2}{\varphi^2+1} w_m b_m r_m^2$. By substituting this expression into the definition of profile coefficient θ_m (17), it directly follows that

$$\theta_m = \frac{2}{\varphi^2 + 1}. \tag{21}$$

For the plume, $\theta_m \approx 1$, implying that $\varphi \approx 1$ also. The value of θ_m for the forced plume tends to become closer to unity with increasing z. The dimensionless turbulence production δ_m shows differences of the order of 10% between the jet and the plume (see also Table III), which is too small to explain the observed differences in α (see Sec. III D).

TABLE III. Average profile coefficients over the interval $20 < z/r_0 < 50$.

Coefficient	J	F	P
β_f	0.151	0.149	0.183
β_u	0.095	0.088	0.106
β_v	0.102	0.095	0.110
β_p	−0.093	−0.084	−0.107
β_g	1.058	1.065	1.076
γ_m	1.306	1.282	1.256
γ_f	0.276	0.267	0.319
γ_p	−0.175	−0.156	−0.183
γ_g	1.406	1.393	1.391
δ_m	−0.184	−0.175	−0.201
δ_f	0.006	0.016	0.038
δ_p	−0.002	−0.008	−0.021
δ_g	−0.180	−0.167	−0.184
θ_m	0.901	0.964	1.011
θ_f	0.078	0.103	0.162
θ_g	0.979	1.067	1.172

Figures 9(d)–9(f) show the relative contribution of turbulence and pressure terms to the total, which are neglected in classical plume theory. Gradual changes can be observed in the far field that are caused by the fact that the second-order statistics require a greater vertical distance to become fully self-similar than the first-order statistics. Indeed, Wang and Law [9] observed that full self-similarity of the turbulence statistics did not occur before $z/r_0 \approx 100$, which is nearly twice the vertical extent of our domain. However, it is clear that, in general, the influence of turbulence and pressure is less than 10% of the mean value, which partially explains why plume theory provides such robust predictions for plume behavior. The largest deviations between mean and total are found in θ, the dimensionless buoyancy flux, which for plumes is as high as 20%, consistent with the literature [32,41]. Here we would like to point out that θ_f is a source of systematic error in laboratory experiments where the (total) buoyancy flux is usually determined *a priori* [(nozzle volume flux)×(buoyancy)]. However, plume theory only considers means and the mean buoyancy flux is about 20% less than the total buoyancy flux. Indeed, we find good agreement of the DNS data with the classical solutions of plume theory only by explicitly calculating the mean buoyancy flux.

D. Decomposing the entrainment coefficient

As shown by van Reeuwijk and Craske [26], taking (6) as a definition of α and using (19) and (18b), α can be decomposed as

$$\alpha = \underbrace{-\frac{\delta_g}{2\gamma_g}}_{\alpha_{\text{prod}}} + \underbrace{\left(\frac{1}{\beta_g} - \frac{\theta_m}{\gamma_g}\right)\text{Ri}}_{\alpha_{\text{Ri}}} + \underbrace{\frac{d}{d\zeta}\left(\log\frac{\gamma_g^{1/2}}{\beta_g}\right)}_{\alpha_{\text{shape}}}. \tag{22}$$

The entrainment relation (22) quantifies the contribution to α of turbulence production α_{prod}, mean buoyancy α_{Ri}, and changes in profile shape α_{shape}. The vertical evolution of the individual contributions to α, the direct estimate of α using (6), and the estimate of α using r_m (Table I) are plotted in Fig. 10. The three estimates of α are in good agreement with each other, demonstrating the consistency of the data with the underlying integral equations. The analysis of data from the plume literature carried out by van Reeuwijk and Craske [26] highlighted that δ_m, and thus α_{prod},

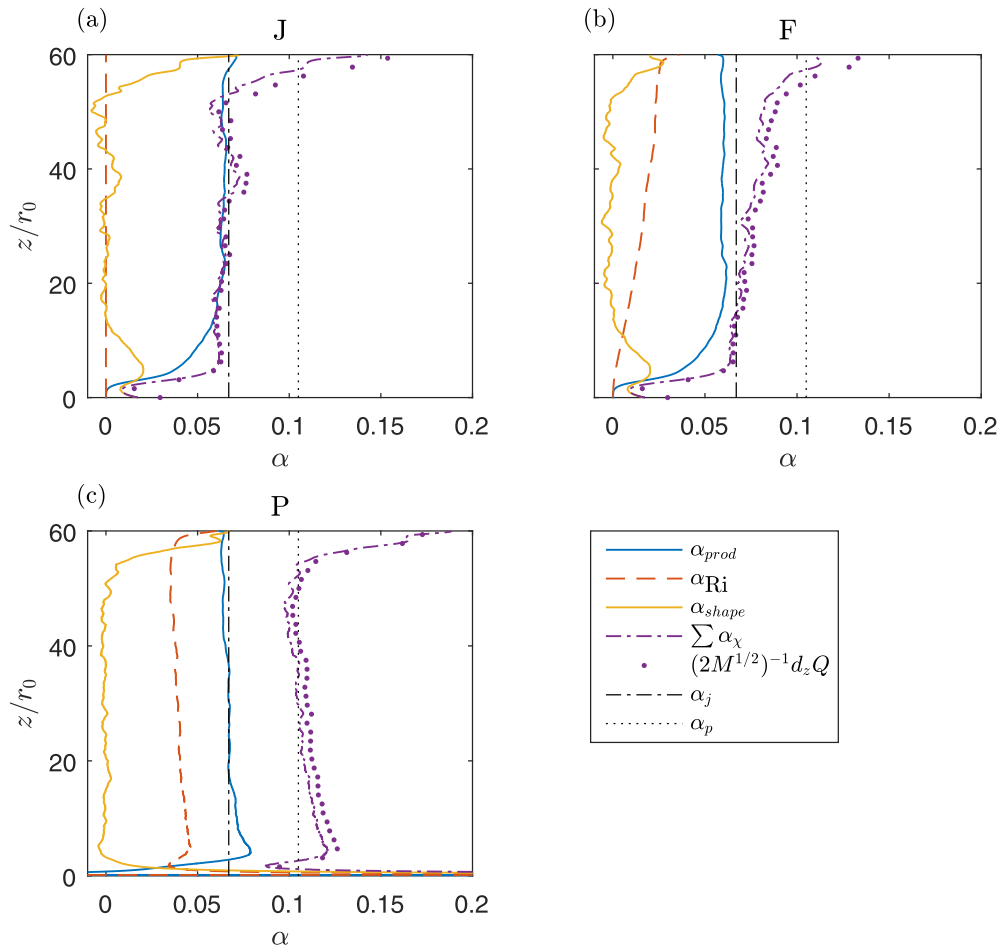

FIG. 10. Evolution of the contribution to entrainment due to turbulent kinetic energy production α_{prod}, buoyancy α_{Ri} and departure from self-similarity α_{shape}, as a function of z. Note that in the legend, $\sum \alpha_\chi = \alpha_{\mathrm{prod}} + \alpha_{\mathrm{Ri}} + \alpha_{\mathrm{shape}}$.

was approximately identical in jets and plumes. This is convincingly confirmed in Fig. 10(c), as α_{prod} matches closely with the value of α_j inferred from the jet data. For the forced plume, α_{prod} is slightly lower than α_j but remains in good agreement. The mean-flow contribution of buoyancy to α is constant for simulation P and has a magnitude of $2\alpha_j/3$. For simulation F, α_{Ri} can be observed to increase with height.

The term α_{shape} will only be nonzero when the profiles of first- and second-order statistics change in shape, i.e., when the profiles are not self-similar. Non-self-similar behavior is dominant in the near field, where the flow transitions to turbulence and the mean profiles attain their Gaussian shapes. The near-field region, within which α_{shape} is different from zero, extends up to about 15 source diameters for the jet and the forced jet and only for about 5 source diameters for the plume.

Next we explore the concept of similarity drift, which pertains to a possible variation in z of the ratio of buoyancy to velocity profile width $\varphi(z)$. The concept of similarity drift can be traced back to Kaminski *et al.* [17], who derived an entrainment relation that contains a term of the form

$$\alpha_e = \cdots + \frac{1}{2} R \frac{d}{dz} \log A, \tag{23}$$

where R is a typical radius, $A = \gamma_m/\theta_m = \gamma_m(1+\varphi^2)/2$, and α_e is an entrainment coefficient that is related [26], but not identical to α [α_e uses nonstandard characteristic scales in Ref. [17], implying that the α_{shape} in the entrainment relation in terms of α (22) is independent of θ]. Hence, (23)

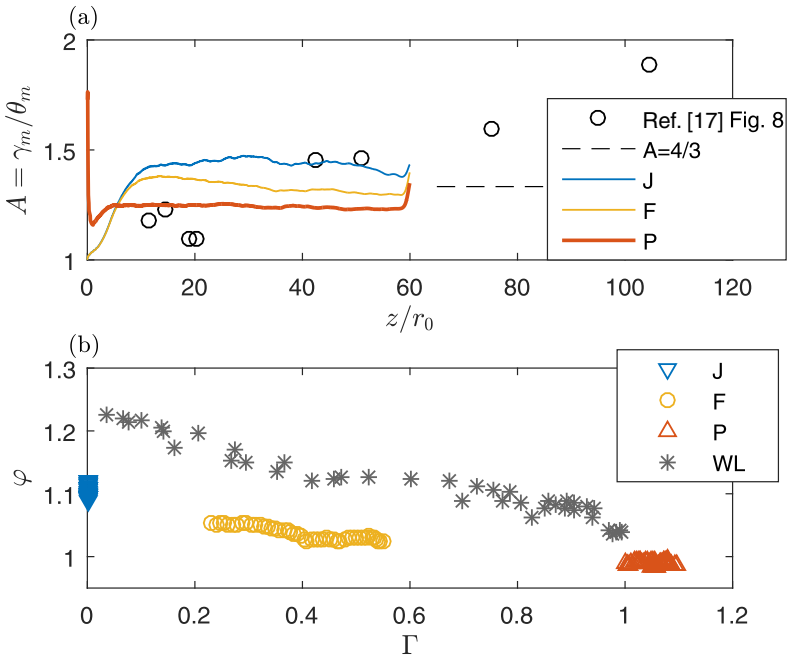

FIG. 11. Exploration of similarity drift for (a) $A = \gamma_m/\theta_m$ as a function of z/r_0 and (b) φ as a function of Γ.

indicates that changes in A, e.g., because of a drift $\varphi = \varphi(z)$, will have a nonzero contribution to α_e. In Ref. [17] the value A was calculated for published data, which, despite significant scatter, showed an increasing trend of A with the distance from the source.

Figure 11(a) shows the experimental data collected from Fig. 8 in Ref. [17] together with the DNS data set discussed in this article. Unlike the experimental data, the DNS data do not imply that A varies as a function of z. Indeed, it is unclear what physical mechanism could be responsible for producing similarity drift. Full self-similarity of the process results from an asymptotically small dependence on the source conditions and ambient conditions that scale in the same way as the local behavior of the plume. We therefore suggest that the similarity drift observed in experiments is caused by the absence of an ideal undisturbed, unbounded ambient environment (including confinement effects), or a persistent dependence of the process on source conditions.

The DNS and WL data suggest a relation between φ and Γ [see Fig. 11(b)]. As for Fig. 3, the DNS and WL data show that φ is a decreasing function of Γ, tending to $\varphi \approx 1$ at $\Gamma = 1$. The Γ dependence is more pronounced for the WL data than the DNS data, the reason for which is unclear.

E. Turbulent transport

The turbulent radial transport of streamwise momentum $\overline{u'w'}$ and buoyancy $\overline{u'b'}$ are crucial in determining the profile shape and entrainment behavior of jets and plumes. These quantities can be related to the mean fields using the gradient diffusion hypothesis, i.e.,

$$\overline{u'w'} = -\nu_T \frac{\partial \overline{w}}{\partial r}, \quad \overline{u'b'} = -D_T \frac{\partial \overline{b}}{\partial r}. \tag{24}$$

These quantities were computed using $\nu_T/w_m r_m = -f_{uw}/f_w'$ and $D_T/w_m r_m = -f_{ub}/f_b'$, where the similarity functions f_χ are the averages of those presented in Fig. 4 and the prime denotes differentiation with respect to η. The results are shown in Figs. 12(a) and 12(b) for the jet and plume, respectively. The radial distributions of ν_T and D_T have a similar shape, with D_T systematically higher than ν_T for both the jet and the plume. The values for ν_T and D_T are slightly higher for the plume than for the jet.

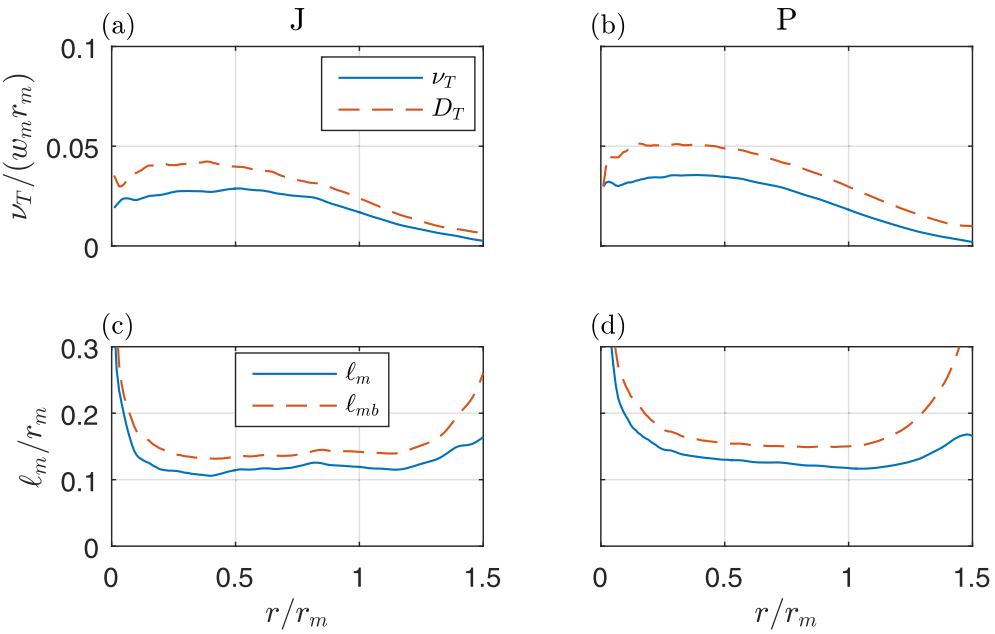

FIG. 12. Radial profiles of ν_T and D_T for (a) the jet and (b) the pure plume. Radial mixing length radial profiles for (c) the jet and (d) the pure plume.

The profiles for ν_T and D_T show substantial variations over the interval $0 < r/r_m < 1$. A Prandtl mixing length model [42] with mixing lengths for momentum and buoyancy of the form $\ell_m = a_w r_m$ and $\ell_{mb} = a_b r_m$, resulting in

$$\frac{\nu_T}{w_m r_m} = a_w^2 |f_w'|, \quad \frac{D_T}{w_m r_m} = a_b^2 |f_w'|, \tag{25}$$

provides values of $\ell_m/r_m \equiv a_w$ and $\ell_{mb}/r_m \equiv a_b$ that are roughly constant in the core region [Figs. 12(c) and 12(d)]. Very close to the centerline, the mixing length becomes very large because $|f_w'|$ and $|f_b'|$ tend to zero. For $r/r_m > 1$, the mixing length concept does not work well, which we attribute to intermittency effects associated with the plume edge. The typical values for a_w and a_b over the region $0.3 < r/r_m < 1.0$ are presented in Table I. Estimates of the mixing length show remarkable agreement with the experimental results recently presented by Ezzamel *et al.* [25], who estimated the Eulerian integral length scale of the two-point velocity statistics (their Fig. 15). In particular, note that the measurements revealed almost constant values of the Eulerian integral length in the core of the plume, for both jets and plumes.

The turbulent Prandtl number Pr_T is a quantity of great relevance because of its extensive use in turbulence modeling. By substituting (24) into (13), one obtains

$$\mathrm{Pr}_T = \frac{\nu_T}{D_T} = \frac{f_{uw}}{f_{ub}} \frac{f_b'}{f_w'}. \tag{26}$$

Thus, Pr_T can be thought of as the product of two ratios: (i) the ratio of the radial turbulent fluxes f_{uw}/f_{ub} and (ii) the ratio of gradients of the mean buoyancy and velocity f_b'/f_w'. The turbulent Prandtl number, plotted in Fig. 13, is almost constant over the entire cross section with values in the range 0.6–0.8. The average value $\langle \mathrm{Pr}_T \rangle$ over the interval $0.3 < r/r_m < 1.0$ is 0.72 for the jet simulation and 0.67 for the plume simulation (see also Table I). Thus, the estimates of $\langle \mathrm{Pr}_T \rangle$ are remarkably close, despite the effect of buoyancy on the plume's behavior. Shown in Fig. 13(b) is the ratio f_b'/f_w'. For the plume, the ratio is approximately unity, but for the jet it is significantly lower due to the fact that $\theta_m < 1$ and thus $\varphi > 1$. The ratio f_{uw}/f_{ub}, shown in Fig. 13(c), is approximately

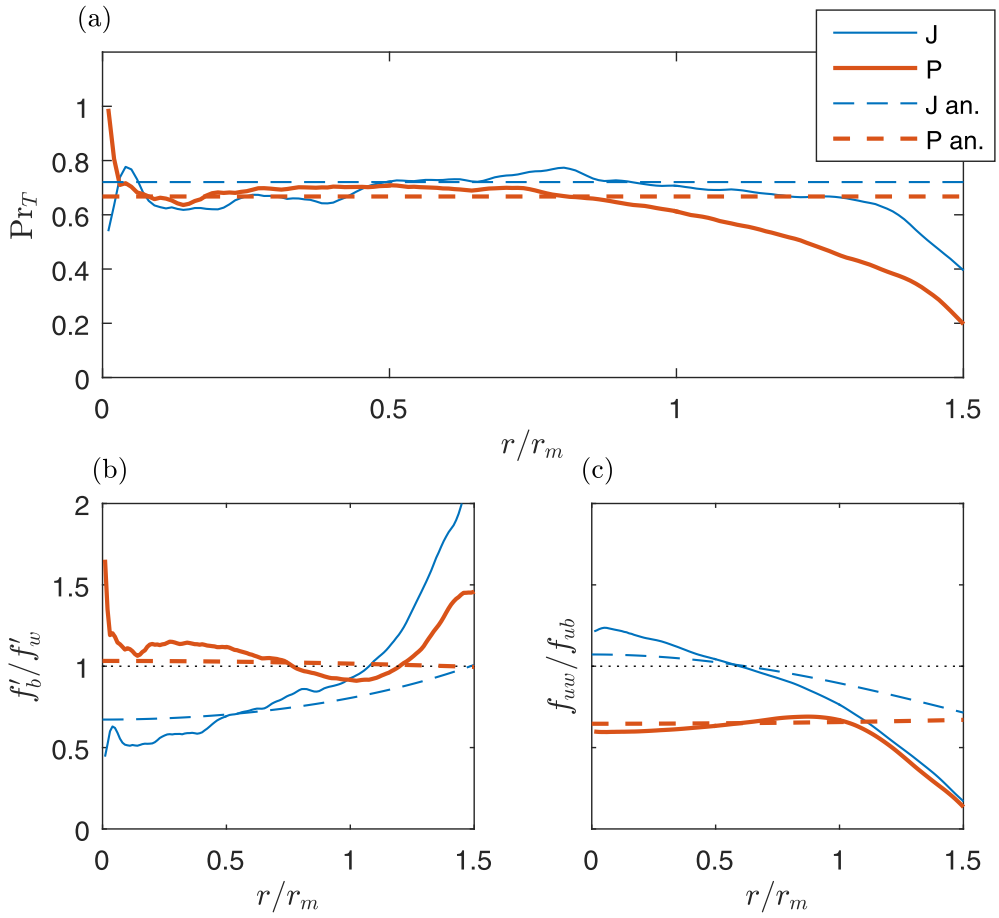

FIG. 13. Radial profiles of (a) the turbulent Prandtl number Pr_T, (b) the ratio of the similarity functions f_b'/f_w', and (c) f_{uw}/f_{ub} (see the text). The solid lines show the DNS data and the dashed lines the analytical predictions (27).

constant for the plume with a value of about 0.6. For the jet, f_{uw}/f_{ub} decreases slowly with an average value of about 1.

Thus, although Pr_T is very similar for plumes and jets, the reason is different: for jets it is caused primarily by f_b'/f_w', which is associated with the ratio of widths φ, and for the plume primarily by the turbulent flux ratio f_{uw}/f_{ub} (see also Fig. 4). This can be made explicit by evaluating the ratios [by substituting the Gaussian profiles for $f_w = \overline{w}/w_m$ and $f_b = \overline{b}/b_m$ (20)] into (24) and (25), resulting in

$$\frac{f_b'}{f_w'} = \frac{1}{\varphi^4}\exp\left(-\frac{\varphi^2-1}{\varphi^2}\frac{r^2}{r_m^2}\right), \quad \frac{f_{uw}}{f_{ub}} = \varphi^4\frac{a_w^2}{a_b^2}\exp\left(\frac{\varphi^2-1}{\varphi^2}\frac{r^2}{r_m^2}\right), \tag{27}$$

noting that $(\varphi^2-1)/\varphi^2 = (2-2\theta_m)/(2-\theta_m)$. The product of these two terms evaluates to $\langle \mathrm{Pr}_T \rangle = a_w^2/a_b^2$, consistent with (25). Equation (27) shows that the amplitude of the ratio f_b'/f_w' is solely determined by the value of φ. The amplitude of the ratio f_{uw}/f_{ub} is determined both by φ and the ratio of mixing lengths a_w/a_b. The theoretical predictions of (27), using parameter values for a_w and a_b from Table I and θ_m from Table III, are plotted in Fig. 13 with dashed lines. The results agree quite well in the interval $0 < r/r_m < 1$, in terms of both the amplitude and the trend. Near the plume edge, it is clear that the mixing lengths and Gaussian distributions do not describe the behavior.

Previous authors [25] have suggested that a spatially averaged (over the radial plume section) turbulent Prandtl number $\langle \mathrm{Pr}_T \rangle$ can be inferred from the ratio of the plume radii r_m and r_b, estimated through a Gaussian fit of the radial profiles of mean vertical velocity and buoyancy, respectively. For jets this approach is valid because, to leading order, the scalar field and the vertical velocity field essentially obey the same similarity equations, which state that radial mixing must balance the divergence in the vertical flux. As noted previously [43], the ratio of r_m and r_b can be obtained via the substitution of Gaussian profiles into the similarity equations. Evaluation of the resulting balance on the centerline of the flow allows one to relate D_T to r_b and ν_T to r_m. Equivalently, one can view the problem in a moving frame of reference, in which $z^2 \propto t$, and apply the classical relation for diffusion, which predicts that $r_b \propto \sqrt{t D_T}$ and $r_m \propto \sqrt{t \nu_T}$. Both approaches result in $\langle \mathrm{Pr}_T \rangle = \varphi^{-2}$. For jets, we observe that $\varphi \approx 1.1$ and therefore would expect $\langle \mathrm{Pr}_T \rangle \approx 0.8$, which is reasonably consistent with Fig. 13(a). In the case of plumes, however, the analysis described above is not appropriate, unless one accounts for the additional term arising from buoyancy in the governing momentum equation. Indeed, our results indicate values of $\langle \mathrm{Pr}_T \rangle$ that are systematically lower than unity in plumes [see, e.g., Fig. 13(a)], in spite of the fact that $\varphi \approx 1$.

IV. CONCLUSION

The dynamics and transport properties of a turbulent pure jet, a pure plume, and a forced plume were examined using high-fidelity direct numerical simulations. The motivation for this work, the numerical analog of the experimental study by Ezzamel *et al.* [25], was specifically to shed light on the physical processes linking turbulent transport and entrainment.

The detailed spatial resolution of the DNS allowed the effectiveness of turbulent transport to be quantified, e.g., via turbulent diffusion coefficients and the dilution of fluid in the plume or jet with the ambient. For the forced plume, within which the flow dynamically adjusts towards a pure-plume behavior asymptotically with height, of particular relevance was the vertical variation of the entrainment coefficient α, numerous models having been proposed to capture this variation. Our results support the Priestley-Ball [3] entrainment model (12) and show that, beyond a near-source region (specifically for $z/r_0 \gtrsim 20$), the entrainment coefficient is a function only of the local Richardson number.

By decomposing α [see (22)] into contributions due to turbulence production, to buoyancy, and to shape effects, we show that the production of turbulence due to shear (as represented by the dimensionless quantity δ_m) is practically identical for jets and for plumes, which is indeed the assumption underlying (12). Moreover, since the *turbulent* component of entrainment has been shown to be unaltered by buoyancy [26], this confirms that α is larger for plumes than for jets due to entrainment associated with *mean* flow processes.

The fact that the production of turbulence due to shear takes approximately the same value for jets and plumes suggests that their turbulence structure is quite similar, despite the absence of buoyancy in a jet. The second-order statistics $\overline{u'u'}$, $\overline{v'v'}$, and $\overline{w'w'}$ indeed suggest that the turbulence levels are very similar. The invariance of the turbulence anisotropy tensor confirms that turbulence in the core region of a jet or plume is practically indistinguishable. There is, however, evidence of clear distinctions between the structure of a jet and a plume. For example, while there is a transition from rodlike to disklike turbulence moving radially outward from the centerline, this transition occurs closer to the centerline in a plume; these distinctions are believed to be linked with vertical velocity gradients $\partial \overline{w}/\partial z$. Further differences between jets and plumes exist in the second-order scalar statistics, such as $\overline{w'b'}$ and $\overline{b'b'}$. Analysis of the budgets for these quantities would indicate how such differences can exist between flows whose dynamics are similar and would therefore make a valuable contribution to an overall understanding of turbulence in free-shear flows.

In agreement with existing measurements, the turbulent Prandtl number is found to be almost identical for jets and plumes, taking a value of $\langle \mathrm{Pr}_T \rangle = 0.7$. However, by writing this quantity as the ratio of turbulent fluxes and radial gradients of mean quantities, it becomes evident that for jets, the

value of $\langle \mathrm{Pr}_T \rangle$ can be attributed to differences in the ratio of velocity to buoyancy profile widths φ, whereas for plumes, the value of $\langle \mathrm{Pr}_T \rangle$ is associated with the ratio of the turbulent radial transport of buoyancy and streamwise momentum.

The DNS data do not support the notion of similarity drift and we conjecture that the observed variations in profile widths between experiments are possibly a result of confinement or other deviations from ideal boundary conditions.

ACKNOWLEDGMENTS

We acknowledge the UK Turbulence Consortium (Grant No. EP/L000261/1) and an Engineering and Physical Sciences Research Council (EPSRC) ARCHER Leadership Grant for providing the computational resources required to carry out the computations. In addition, J.C. gratefully acknowledges funding from the EPSRC Doctoral Prize under Grant No. EP/M507878/1. P.S. gratefully acknowledges the support of Cambridge University's Engineering Department and Peterhouse College. Supporting data for this article are available on request.

APPENDIX: AMBIENT-FLOW CORRECTION OF THE ESH DATA

The purpose of this Appendix is twofold: (i) to correct the ESH data [25] for vertical variation in the ambient flow and (ii) to present the experimental data in terms of the notation used in this paper. A significant part of the ESH work was associated with the analysis of $\alpha(z)$. The z dependence of α was determined in two ways: (i) via volume conservation (6) and (ii) via the entrainment relation (22) considering mean contributions and self-similarity only, assuming Gaussian profiles ($\gamma_m = 4/3$):

$$\alpha = -\tfrac{3}{8}\delta_m + \left(1 - \tfrac{3}{4}\theta_m\right)\mathrm{Ri}. \tag{A1}$$

In Ref. [25] this relation was presented in terms of the relative plume width $\varphi = \sqrt{2/\theta_m - 1}$, the effective eddy viscosity $\langle \hat{v}_T \rangle = -\delta_m/8\sqrt{2}$, and the flux balance parameter $\Gamma = 5\mathrm{Ri}/8\alpha_p$ (note that $\beta_g = 1$ as only means are considered), i.e., as

$$\alpha_G = 3\langle \hat{v}_T \rangle + (2\varphi^2 - 1)\frac{2\alpha_{pG}\theta_m}{5}\Gamma. \tag{A2}$$

Here $\alpha_G = \alpha/\sqrt{2}$ is the Gaussian entrainment coefficient and $\alpha_{pG} = \alpha_p/\sqrt{2}$ the Gaussian entrainment coefficient for a pure plume. The prefactor for $\langle \hat{v}_T \rangle$ is a factor 2 larger than reported in Ref. [25]. Furthermore, the factor θ_m in the buoyancy contribution was not present in Ref. [25]; this is caused by the inclusion of β_g and θ_m in the flux balance parameter Γ (15). Indeed, denoting the classical flux balance parameter [5] by $\Gamma^* = 5FQ^2/8\alpha_p M^{5/2}$, we have $\Gamma^* = \beta_g\theta_m\Gamma$.

As discussed in Ref. [25], the measurements revealed a small but significant flow in the ambient, caused by (i) the diffusion of heat from the warm-air plume source along the horizontal rigid wooden base plate within which the plume nozzle was mounted, giving rise to vertical convective motion, and (ii) the seeding of the ambient with a stage smoke generator. Indeed, the background mean motion, whose vertical velocity we denote by Δw, was clearly captured by particle image velocimetry (PIV) fields when measuring velocities away from the plume perimeter in the lower regions of the domain, a region where the plume width was significantly smaller than the lateral extent of the PIV field. Measurements indicated $\Delta w \approx 0.15\ \mathrm{ms}^{-1}$ close to the source (whose radius is denoted r_0) for the jetlike, the forced, and the pure-plume experiments, referred to as J, F, and P, respectively. However, at larger vertical distances above the source, the size of the PIV field did not permit measurement of the (now significantly wider) plume or the ambient far beyond the plume perimeter. In Ref. [25] it was therefore assumed that the background motion was uniform throughout the domain; hence $\Delta w = 0.15\,\mathrm{ms}^{-1}$ was subtracted from the mean vertical velocities before fitting the radial profiles

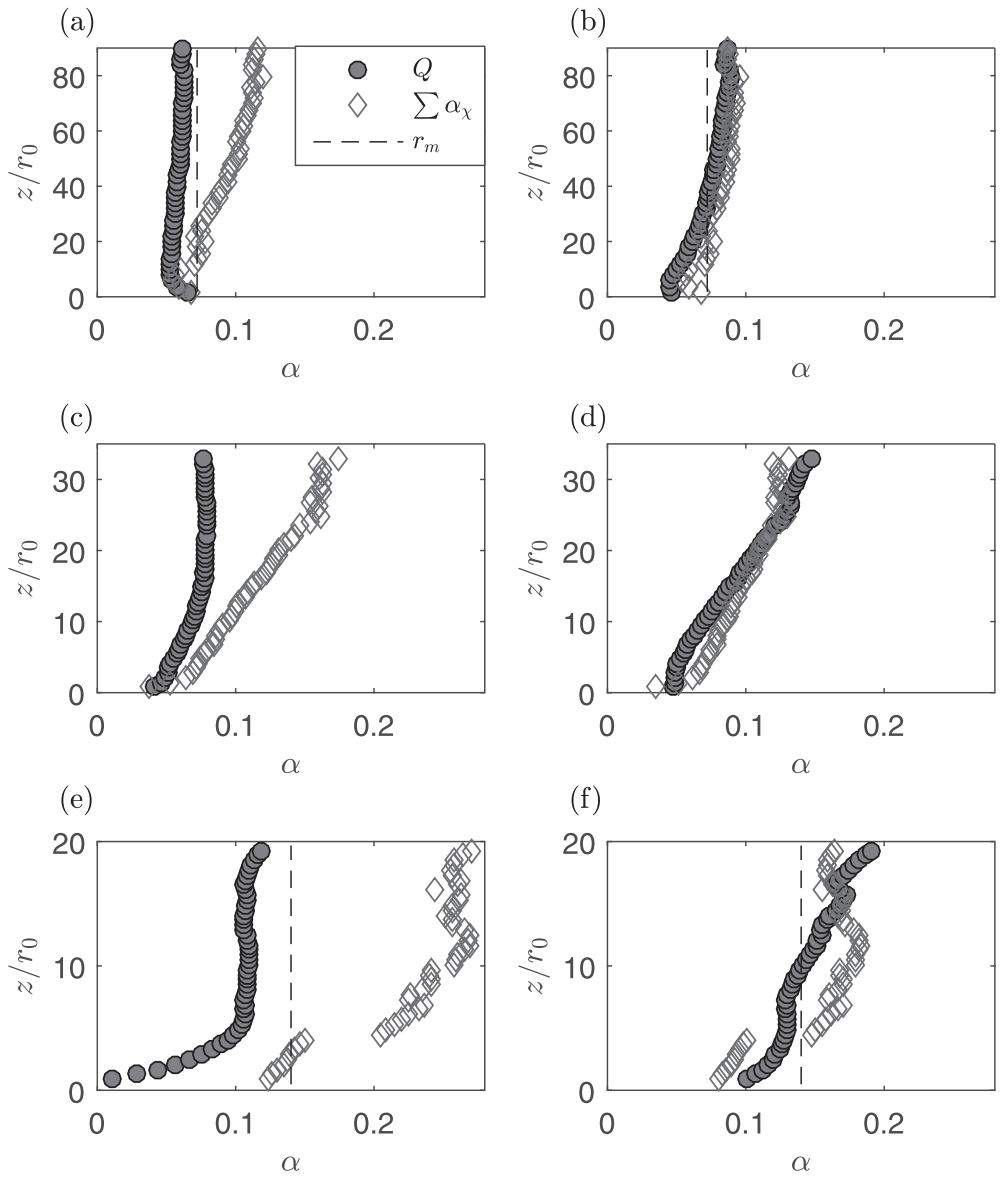

FIG. 14. Variation of entrainment coefficient as a function of distance above the source. Comparison of entrainment coefficient estimated from r_m, the volume flux balance (6), and from the entrainment relation (A2) for (a) and (b) J, (c) and (d) F, and (e) and (f) P with (a), (c), and (e) $\Delta w = 0.15$ ms^{-1} and (b), (d), and (f) $\Delta w = 0.15(z/z_0)^{-1/3}$ ms^{-1}.

with a Gaussian curve of the form

$$\frac{\overline{w}(r,z)}{w_g(z)} = \exp\left(\frac{-r^2}{r_g^2(z)}\right), \tag{A3}$$

where $w_g = 2w_m$ denotes the plume centerline velocity and $r_g = r_m/\sqrt{2}$ the Gaussian plume radius.

Figures 14(a), 14(c), and 14(e) show the J, F, and P estimates for α from [25] in the current notation. Indicated with the dashed line in Figs. 14(a) and 14(c) is an estimate for α inferred from $r_m(z)$ (using the relations for r_m in Table II). All three estimates of α should formally provide the same value for α. For the DNS data, this is clearly the case (Fig. 10), but experiments are much more difficult to control, particularly the boundary conditions. The measurement data show a

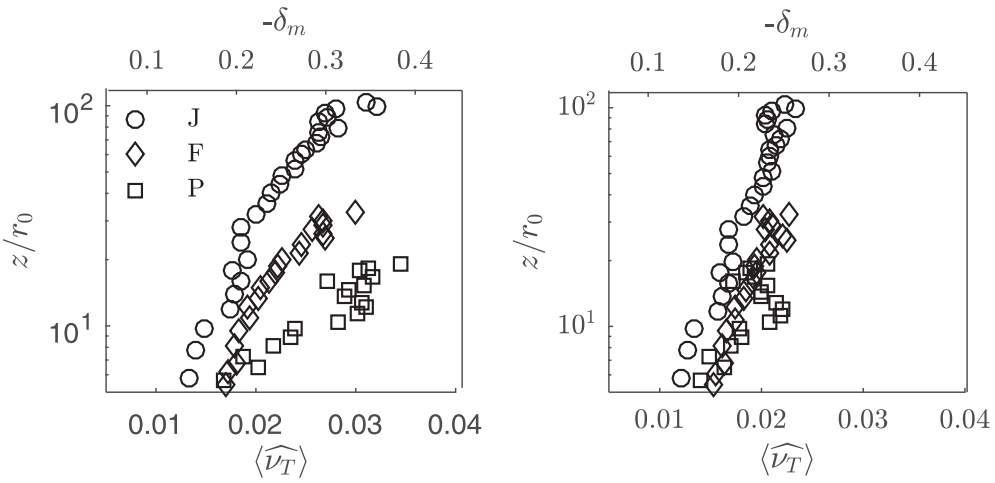

FIG. 15. Vertical evolution of δ_m for J, F, and P with (a) $\Delta w = 0.15$ ms^{-1} and (b) $\Delta w = 0.15(z/z_0)^{-1/3}$ ms^{-1}.

large discrepancy between the Q-based estimate for α and the one obtained from the entrainment relation (A2). This difference points to a mismatch in either the momentum balance or the mean kinetic energy balance, which can be traced back to the background flow in the ambient.

In what follows we show that the differences between our estimates for α can be significantly reduced by using a background motion whose magnitude is progressively reduced with distance from the source. As a consequence of the convection above the base plate, the plumes studied developed in a weak background velocity field that we would expect to scale as $\Delta w \sim z^{-1/3}$, i.e., the plume effectively developed within a weaker plume rising from the base plate. By applying a background correction of the form $\Delta w = 0.15(z/z_0)^{-1/3}$, where z_0 is the distance from the plate where the ambient vertical velocity was 0.15 m/s, the three estimates of α exhibit an improved agreement, as shown in Figs. 14(b), 14(d), 14(f); all estimates are in reasonably good agreement with each other.

The method by which δ_m has been calculated for the entrainment relation data (A2) is performed differently than in Ref. [25]. Indeed, upon close inspection of the experimental radial profiles of the Reynolds stress $\overline{u'w'}$, in Ref. [25] the gradient diffusion hypothesis led to a systematic overestimation of δ_m. As in Ref. [25], the $\overline{u'w'}$ profile is fitted to a function of the form

$$\frac{\overline{u'w'}}{w_g^2} = 2\langle\hat{\nu}_T\rangle\frac{r}{r_g}\exp\left(-\frac{r^2}{r_g^2}\right), \tag{A4}$$

which follows from the substituting the Gaussian velocity profile (A3) into the gradient-diffusion hypothesis (24) using a constant (in r) eddy viscosity $\langle\nu_T\rangle = w_g r_g\langle\hat{\nu}_T\rangle$. However, we now consider r_g as a free parameter [not necessarily fixed by the value provided by the fit of (A3)] and calculate $\langle\hat{\nu}_T\rangle$ based on the value of r_g for which the least-squares error between the measurements and (A4) is minimized.

By substituting (A3) and (A4) into the definition for δ_m, it immediately follows that $\delta_m = -8\sqrt{2}\langle\hat{\nu}_T\rangle$; the corrected values for both $\langle\hat{\nu}_T\rangle$ and δ_m are shown in Fig. 15(b). For all three releases, the values for δ_m are now reasonably consistent, although there is a clear increasing trend with z that is not consistent with fully self-similar behavior (in which case δ_m is expected to be constant). Nevertheless, the data are much more consistent than the original ambient-flow correction estimate shown in Fig. 15(a). The data shown in Figs. 14(b), 14(d), 14(f), and 15(b) were used to provide the input to Table 3 in Ref. [26].

[1] J. C. R. Hunt, Industrial and environmental fluid mechanics, Annu. Rev. Fluid Mech. **23**, 1 (1991).
[2] Y. Zel'dovich, The asymptotic laws of freely-ascending convective flows, Zh. Eksp. Teor. Fiz. **7**, 1463 (1937).
[3] C. Priestley and F. K. Ball, Continuous convection from an isolated source of heat, Q. J. R. Meteor. Soc. **81**, 144 (1955).
[4] B. R. Morton, G. I. Taylor, and J. S. Turner, Turbulent gravitational convection from maintained and instantaneous sources, Proc. R. Soc. London Ser. A **234**, 1 (1956).
[5] B. R. Morton, Forced plumes, J. Fluid Mech. **5**, 151 (1959).
[6] P. N. Papanicolaou and E. J. List, Investigations of round vertical turbulent buoyant jets, J. Fluid Mech. **195**, 341 (1988).
[7] N. R. Panchapakesan and J. L. Lumley, Turbulence measurements in axisymmetric jets of air and helium. Part 1. Air jet, J. Fluid Mech. **246**, 197 (1993).
[8] A. Shabbir and W. K. George, Experiments in a round turbulent buoyant plume, J. Fluid Mech. **275**, 1 (1994).
[9] H. Wang and A. W.-K. Law, Second-order integral model for a round turbulent buoyant jet, J. Fluid Mech. **459**, 397 (2002).
[10] M. V. Pham, F. Plourde, and K. S. Doan, Direct and large-eddy simulations of a pure thermal plume, Phys. Fluids **19**, 125103 (2007).
[11] F. Plourde, M. V. Pham, S. D. Kim, and S. Balachandar, Direct numerical simulations of a rapidly expanding thermal plume: Structure and entrainment interaction, J. Fluid Mech. **604**, 99 (2008).
[12] E. List, Turbulent jets and plumes, Annu. Rev. Fluid Mech. **14**, 189 (1982).
[13] A. W. Woods, Turbulent plumes in nature, Annu. Rev. Fluid Mech. **42**, 391 (2010).
[14] G. R. Hunt and T. S. van den Bremer, Classical plume theory: 1937–2010 and beyond, IMA J. Appl. Math. **76**, 424 (2011).
[15] G. R. Hunt and N. B. Kaye, Lazy plumes, J. Fluid Mech. **533**, 329 (2005).
[16] J. Craske, A. Debugne, and M. van Reeuwijk, Shear-flow dispersion in turbulent jets, J. Fluid Mech. **781**, 28 (2015).
[17] E. Kaminski, S. Tait, and G. Carazzo, Turbulent entrainment in jets with arbitrary buoyancy, J. Fluid Mech. **526**, 361 (2005).
[18] G. I. Taylor, Dynamics of a mass of hot gas rising in air, US Atomic Energy Commission, Los Alamos National Laboratory Report No. 236, 1945 (unpublished).
[19] G. K. Batchelor, Heat convection and buoyancy effects in fluids, Q. J. R. Meteor. Soc. **80**, 339 (1954).
[20] J. Turner, Turbulent entrainment: the development of the entrainment assumption, and its application to geophysical flows, J. Fluid Mech. **173**, 431 (1986).
[21] G. Carazzo, E. Kaminski, and S. Tait, The route to self-similarity in turbulent jets and plumes, J. Fluid Mech. **547**, 137 (2006).
[22] E. J. List and J. Imberger, Turbulent entrainment in buoyant jets and plumes, J. Hydraul. Div. ASCE **99**, 1461 (1973).
[23] H. B. Fischer, E. J. List, R. C. Koh, J. Imberger, and N. H. Brooks, *Mixing in Inland and Coastal Waters* (Academic Press, New York, 1979).
[24] D. G. Fox, Forced plume in a stratified fluid, J. Geophys. Res. **75**, 6818 (1970).
[25] A. Ezzamel, P. Salizzoni, and G. R. Hunt, Dynamical variability of axisymmetric buoyant plumes, J. Fluid Mech. **765**, 576 (2015).
[26] M. van Reeuwijk and J. Craske, Energy-consistent entrainment relations for jets and plumes, J. Fluid Mech. **782**, 333 (2015).
[27] C. Chen and W. Rodi, *Vertical Turbulent Buoyant Jets—A Review of Experimental Data* (Pergamon, Oxford, 1980).
[28] L. P. Chua and R. A. Antonia, Turbulent Prandtl number in a circular jet, Int. J. Heat Mass Transf. **33**, 331 (1990).
[29] G. R. Hunt and N. B. Kaye, Virtual origin correction for lazy turbulent plumes, J. Fluid Mech. **435**, 377 (2001).

[30] W. K. George, R. Alpert, and F. Tamanini, Turbulence measurements in an axisymmetric buoyant plume, Int. J. Heat Mass Transf. **20**, 1145 (1977).
[31] H. Rouse, C. S. Yih, and H. W. Humphreys, Gravitational convection from a boundary source, Tellus **4**, 201 (1952).
[32] B. J. Devenish, G. G. Rooney, and D. J. Thomson, Large-eddy simulation of a buoyant plume in uniform and stably stratified environments, J. Fluid Mech. **652**, 75 (2010).
[33] J. Craske and M. van Reeuwijk, Energy dispersion in turbulent jets. Part 1. Direct simulation of steady and unsteady jets, J. Fluid Mech. **763**, 500 (2015).
[34] J. Craske and M. van Reeuwijk, Robust and accurate open boundary conditions for incompressible turbulent jets and plumes, Comput. Fluids **86**, 284 (2013).
[35] J. Craske and M. van Reeuwijk, Energy dispersion in turbulent jets. Part 2. A robust model for unsteady jets, J. Fluid Mech. **763**, 538 (2015).
[36] J. Craske and M. van Reeuwijk, Generalised unsteady plume theory, J. Fluid Mech. **792**, 1013 (2016).
[37] J. H. Hussein, S. P. Capp, and W. K. George, Velocity measurements in a high-Reynolds-number, momentum conserving, axisymetric jet, J. Fluid Mech. **258**, 31 (1994).
[38] S. B. Pope, *Turbulent Flows* (Cambridge University Press, Cambridge, 2000).
[39] F. Kuznik, G. Rusaouen, and J. Brau, Experimental study of turbulent structures in a non isothermal horizontal jet issuing from a round nozzle distanced from a wall, Int. J. Ventil. **10**, 277 (2011).
[40] M. Woodhouse, J. Phillips, and A. Hogg, Unsteady turbulent buoyant plumes, J. Fluid Mech. **794**, 595 (2016).
[41] P. F. Linden, in *Perspectives in Fluid Dynamics: A Collective Introduction to Current Research*, edited by G. K. Batchelor, H. K. Moffatt, and M. G. Worster (Cambridge University Press, Cambridge, 2003), Chap. 8, p. 289.
[42] H. Schlichting, *Boundary Layer Theory* (McGraw-Hill, New York, 1960).
[43] J. Chen and E. J. List, *Proceedings of the 1976 ICHMT Seminar on Turbulent Buoyant Convection* (unpublished), p. 171.

8.3 The control of releases of buoyant fluid in a ventilated tunnel

The control of releases of buoyant fluid in ventilated tunnels

Lei Jiang [1] , Mathieu Creyssels [1] and Pietro Salizzoni[1]†

[1]Laboratoire de Mécanique des Fluides et d'Acoustique, University of Lyon, CNRS UMR 5509 Ecole Centrale de Lyon, INSA Lyon, Université Claude Bernard, 36, avenue Guy de Collongue, 69134 Ecully, France

(Received xx; revised xx; accepted xx)

The release of buoyant harmful gases within enclosed spaces, such as tunnels and corridors, may engender specific industrial and transportation risks. For safety, a simple ventilation strategy of these spaces is to impose a flow, whose velocity is defined as 'critical', that confines the front of harmful buoyant gases downwind of the source of emission. Determining the intensity of the critical velocity as a function of the geometrical and dynamical conditions at the source is a basic fluid mechanics problem which has yet to be elucidated; this problem involve issues on the dynamics of non-Boussinesq releases, relating to large differences between the densities of the buoyant and the ambient fluid. To investigate this problem, we have performed experiments in a reduced-scale tunnel. Experimental results enlighten i) the existence of two flow regimes, depending on the plume Richardson number at the source Γ_i, one for momentum-driven releases, $\Gamma_i \ll 1$ and one for buoyancy-driven releases, $\Gamma_i \gg 1$; ii) a transition between the two occurring in the range $10^{-2} < \Gamma_i < 1$, and iii) the presence of relevant non-Boussinesq effects only for momentum-driven releases. All these tendencies can be conveniently predicted by means of a simple model of a top-hat plume in a crossflow, which also helps in clarifying the effect of the source radius. Asymptotic solutions of the model reveal interesting behaviours in the limits $\Gamma_i \to 0$ and $\Gamma_i \to \infty$. Notably, buoyancy-driven releases, i.e. with $\Gamma_i \to \infty$, are predicted to behave as point sources of pure buoyancy, independently of their radius and of the density of the emitted fluid. Experiments reveal that this behaviour is actually observed for any release with $\Gamma_i < 1$. This finding supports the adoption of simplified models to simulate buoyancy-driven releases in ventilated confined spaces.

Key words: buoyant plumes, non-Boussinessq releases, entrainment.

1. Introduction

The study of the release of a buoyant fluid within a layer of ambient fluid confined vertically (Jirka & Harleman 1979) and laterally (Barnett 1993) is of major interest in industrial and environmental flows (Hunt 1991). Here we investigate the dynamics of a release of buoyant fluid discharged within a tunnel (Barnett 1993) and subjected to a forced mechanical ventilation. A peculiar aspect of these flows (see figure 1) is the appearance of a back-layer of buoyant fluid, which forms after impingement of the release at the confinement surface (or at the ground), and whose front, driven by a pressure gradient, can move forward against the ventilation (depending on its intensity). The focus is on the control of the propagation of this buoyant front by means of the forced tunnel ventilation. This issue is directly linked to industrial and transportation safety problems related to the dispersion of harmful gases in confined spaces. Examples

† Email address for correspondence: pietro.salizzoni@ec-lyon.fr

(a) (b)

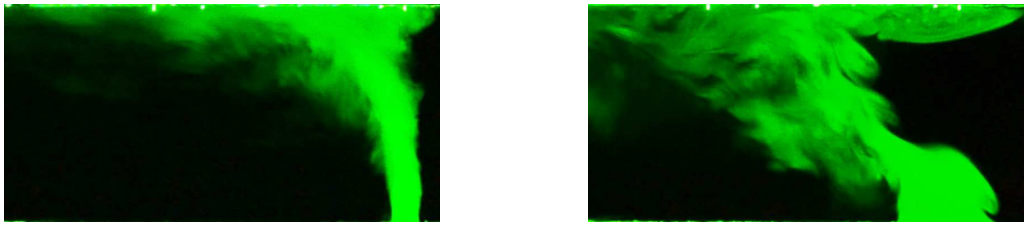

FIGURE 1. Flow visualisations of the buoyant release subjected to a critical ventilation velocity (from right to left): (a) forced release $\Gamma_i < 1$, (b) lazy release $\Gamma_i > 1$.

include the leakage of high pressure natural gas from pipelines, the accidental releases of hydrogen or hydrogen sulfide, and the propagation of smoke from fires in road and rail tunnels as well as on underground escalators (Hunt 1991). This problem has been notably addressed to assess the safety of twin-bore road tunnels (Grant *et al.* 1998), where the ventilation velocity, which blows all the smoke downstream, allowing the users to evacuate by the entrance, is usually referred to as the 'critical velocity'.

These practical implications are therefore related to a fundamental problem, that of defining the intensity of the 'critical' ventilation velocity depending on the geometrical and dynamical conditions at the source. To investigate this problem, we consider a horizontal and infinitely long tunnel of height H and width W within which is continuously released a fluid of density ρ_i, lighter than the ambient fluid ρ_0, with physical properties (molecular diffusivity D_m, viscosity ν) identical to those of the ambient air. The release issues from a source of radius b_i, with a velocity w_i and is placed at the centre of the tunnel. The critical velocity V_c can then be expressed as a function of nine dimensional parameters, namely:

$$V_c = f(w_i, \rho_i, \rho_0, \nu, D_m, g, b_i, W, H), \tag{1.1}$$

where g is the module of the gravitational acceleration. According to Vashy-Buckingham theorem, the non-dimensional critical velocity can be expressed as a function of six non-dimensional parameters:

$$\frac{V_c}{w_i} = f(\Gamma_i, Re_i, \mathrm{Sc}, \frac{\rho_i}{\rho_0}, \frac{b_i}{H}, \frac{W}{H}), \tag{1.2}$$

where $Re_i = 2w_i b_i/\nu$ is the source Reynolds number, $\mathrm{Sc} = D_m/\nu$ is the Schmidt number, and $\Gamma_i = \dfrac{5}{8\alpha_0}\dfrac{\eta_i g b_i}{w_i^2}$ is the plume Richardson number, with $\eta_i = (\rho_0 - \rho_i)/\rho_0$ and $\alpha_0 = 0.127$ (a reference value for the 'top-hat' entrainment coefficient for a pure plume). The latter is a parameter that allows for a classification of buoyant releases in momentum-driven forced plumes ($\Gamma < 1$), and buoyancy-driven pure ($\Gamma = 1$) and lazy ($\Gamma > 1$) plumes (Hunt & Kaye 2005). In the case of negligible diffusive effects (high Re), a fixed tunnel geometry and a fixed Sc, (1.2) reduces to:

$$\frac{V_c}{w_i} = f(\Gamma_i, \frac{\rho_i}{\rho_0}, \frac{b_i}{H}). \tag{1.3}$$

In what follows we explore the dynamics of these buoyant releases by investigating the functional dependence expressed by (1.3). Our aim is to extend and complete the analysis previously presented by Le Clanche *et al.* (2014), mainly focusing on buoyancy-dominated releases, and investigate (1.3) for a wide range of dynamical conditions at the source, spanning from almost pure jets ($\Gamma \ll 1$) to highly lazy plumes ($\Gamma \gg 1$). To that end we have performed experiments within a reduced-scale model and interpreted the

results by means of a simple model of a plume in a crossflow. Our focus will be mainly on the role of Γ_i and on that of the density ratio ρ_i/ρ_0, the key non-dimensional parameter used to evaluate dynamical effects referred to as 'non-Boussinesq' (Ricou & Spalding 1961; Rooney & Linden 1996) whose influence has still not been fully elucidated.

2. Experiments

Experiments were performed in a reduced-scale model (figure 2) of length $L = 8.9\,\mathrm{m}$, width $W = 0.36\,\mathrm{m}$ and height $H = 0.185\,\mathrm{m}$. The side walls are made of toughened glass which permit visualisation of the flow. The releases of buoyant fluid are mixtures of air and helium, whose flow rates were controlled independently and measured by two flowmeters. To visualise the flow, the buoyant mixture is seeded with nebulised oil and lit with a laser sheet emitted by a lens installed at the inlet of the tunnel. Note that the mass of oil added to seed the buoyant release is a tiny fraction of the total mass injected at the source and thus does not affect the density of the mixture. The longitudinal ventilation is imposed by a fan at the end of the tunnel. The flow rate within the tunnel is measured by means of a hot-wire anemometer placed within a Venturi tube at the inlet, providing a spatially averaged velocity over the tunnel section in the range $0.11 \leqslant V_c \leqslant 1.15\,\mathrm{m\,s^{-1}}$.

The velocity at the source is instead $0.17 \leqslant w_i \leqslant 11\,\mathrm{m\,s^{-1}}$, producing a buoyancy flux at the injection:

$$B_i = \pi b_i^2 w_i g \eta_i \tag{2.1}$$

in the range $1 \cdot 10^{-3} \leqslant B_i \leqslant 6.3 \cdot 10^{-2}\ \mathrm{m^4\,s^{-3}}$. Experimental results were obtained by varying values of the three control parameters, spanning the ranges $0.004 < \Gamma_i < 24$, $0.25 < \rho_i/\rho_0 < 0.92$, and $0.068 \leqslant b_i/H \leqslant 0.270$ (source diameters measured 0.1, 0.075, 0.05, 0.035, 0.025 m). Note, however, that results could not be produced for any possible combination of the control parameters in these ranges of values. Experimental conditions were constrained by the Reynolds number, that had to be kept sufficiently high to avoid viscous effects, and by the power of the fan used to produce the longitudinal ventilation. These limitations did not allow us to produce releases with $\Gamma_i > 2$ with 'small' radii (i.e. $b_i/H < 0.15$) and highly-forced ($\Gamma_i < 1$) non-Boussinesq ($\rho_i/\rho_0 < 0.15$) releases with 'large' radii (i.e. $b_i/H > 0.3$). The Reynolds number varied in the range $700 < Re_i < 11100$. Note that Re_i generally decreased with increasing Γ_i, with $2500 < Re_i < 11000$ for $\Gamma_i < 0.5$, $1000 < Re_i < 6000$ for $0.5 < \Gamma_i < 1$ and $700 < Re_i < 2000$ for $\Gamma_i > 1$. All pure and lazy releases therefore exceeded the critical value $Re_{cr} = 600$, indicated by Arya & Lape (1990) as a threshold ensuring negligible viscous effects on buoyant releases in a crossflow.

In the tunnel safety literature (Grant *et al.* 1998) the critical velocity is generally defined as that which prevents the back-layer flow from moving upward beyond the source. Its experimental evaluation by means of flow visualisations is somehow simple, since it solely requires, once the source conditions are fixed, an adjustment to the fan power to assess the position of the back-layer front at the up-wind border of the source. This protocol inevitably involves a number of experimental uncertainties in determining the position of the front. To estimate these uncertainties we performed 20 independent iterations of the same experiment, for a reduced number of experimental conditions. For each of these conditions, the uncertainty was then quantified as half of the difference between the minimum and maximum value of V_c. This never exceeded $\pm 10\%$, which was therefore assumed to be the reference value of the experimental uncertainty.

While performing the experiments, it was immediately evident that the critical ventilation condition was related to very different morphologies of the rising column of

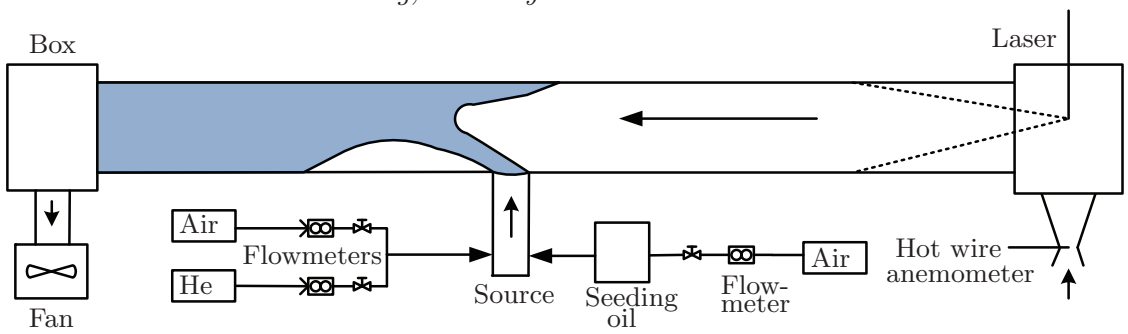

FIGURE 2. Schematic of the experimental set-up.

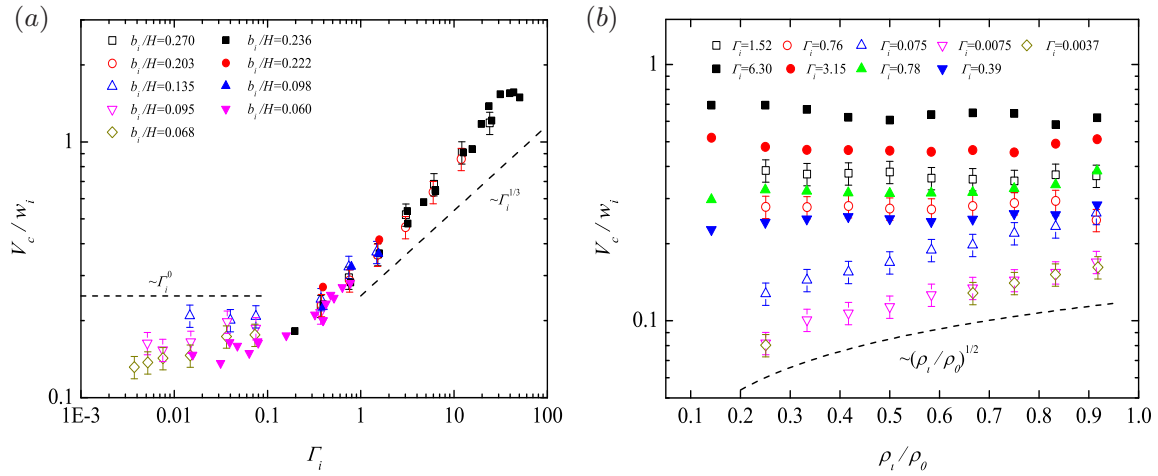

FIGURE 3. Non-dimensional critical velocity as a function of (a) the plume Richardson number Γ_i and (b) the density ratio ρ_i/ρ_0. Hollow points indicate data from the present study and solid points data from Le Clanche *et al.* (2014). In (b), the radius is $b_i/H = 0.068$ for $\Gamma_i = 0.0037$ and $\Gamma_i = 0.0075$, $b_i/H = 0.135$ for $\Gamma_i = 0.075$, $b_i/H = 0.203$ for $\Gamma_i = 0.76$, and $b_i/H = 0.270$ for $\Gamma_i = 1.52$.

buoyant fluid, depending on the value of the Richardson number Γ_i (see figure 1). Forced momentum-driven releases $\Gamma_i < 0.1$ resulted in an almost vertical jet impinging on the ceiling immediately downstream of the source position and producing a small (compared to the tunnel height) recirculating bubble immediately upstream of the impinging region (figure 1a). The injection of buoyancy-dominated releases ($\Gamma_i \geqslant 0.1$) resulted instead in a bent-over plume which actually appeared as the result of the intermittent rise of blobs of fluid, shaped by large-scale instabilities (figure 1b). Compared with the previous case, the (time-averaged) position of the impinging point was moved downstream and a back-flow appeared in the form of an elongated layer extending up to the upwind source end.

To analyse the dependence of V_c/w_i in the parameter space given by (1.3) we performed a different series of experiments. In each of these, we conveniently changed the values of the control parameters at the source, i.e. w_i, b_i, and ρ_i, in order to vary one of the three, i.e. Γ_i, b_i/H, ρ_i/ρ_0, non-dimensional parameters whilst keeping the other two fixed.

Results are shown in figure 3 and are compared to those obtained by Le Clanche *et al.* (2014) in a reduced-scale model with aspect ratio $H/W = 0.5$, slightly different from that of the reduced model used here, and equipped with different instrumentation. Figure 3a shows the dependence of the non-dimensional critical velocity on the Richardson number Γ_i, for varying radii b_i/H and a fixed density ratio $\rho_i/\rho_0 = 0.7$. Figure 3b shows the influence of the density ratio ρ_i/ρ_0 on a series of releases with fixed Γ_i, each of which

has the same radius b_i/H. Note that to ensure a turbulent release, larger radii had to be adopted for larger Γ_i. As previously mentioned, the constraints of $Re_i > 700$ significantly limited exploration of the effect of a varying radius at large Γ_i, whereas the constraint on highly forced releases was mainly limited by the power of the fan producing the tunnel ventilation.

Experimental results on slightly forced to lazy releases, i.e. $\Gamma_i > 0.1$, agree well with previous data obtained by Le Clanche *et al.* (2014) (2014) and therefore confirm their main findings, namely that the non-dimensional critical velocity i) does not show any clear dependence on the density ratio ρ_i/ρ_0, whereas ii) it clearly exhibits a dependence on the plume Richardson number of the form $\propto \Gamma_i^{1/3}$.

Extending the investigation to $\Gamma_i < 0.1$ reveals further interesting features. Firstly, we observe a weakening of the dependence of the non-dimensional critical velocity on Γ_i as this falls below 0.1. This feature is in agreement with the phenomenological observation of the two distinct flow regimes previously discussed and represented in figure 1. This weakening of the dependence on Γ_i is also in accordance with the prediction given by the simple dimensional argument, which indicates $V_c/w_i \sim const$ for $\Gamma_i \to 0$ (for any fixed pair b_i/H and ρ_i/ρ_0). The critical velocity exhibits non-negligible dependence on b_i/H as $\Gamma_i \to 0$ (see figure 3a), whereas any influence of b_i/H seems to diminish for $\Gamma_i > 1$. As already mentioned however, the investigation on the role of b_i/H for large Γ_i was limited by the constraints imposed by the experimental set-up. Data on highly forced releases also reveals a clear dependence of the critical velocity on the density ratio. Namely, V_c/w_i exhibits a dependence of the form $(\rho_i/\rho_0)^{1/2}$, which implies a significant reduction as the flow attains non-Boussinesq conditions. It is worth noting that this effect, which could not be observed in the data set of Le Clanche *et al.* (2014), is only observed in momentum-driven flows and becomes undetectable as $\Gamma_i > 0.1$. This suggests that, as far as the critical velocity is concerned, non-Boussinesq effects have a significant dynamical effect only in the case of forced momentum-driven releases, and become negligible as buoyancy begins to act on the flow dynamics.

Summarising, results show that for almost pure and lazy releases, i.e. $\Gamma_i \geqslant 1$, the non-dimensional critical velocity is mainly dependent on Γ_i, whereas the dependence on ρ_i/ρ_0 seems to fade out. In other words, the release seems to lose information about its source conditions, notably concerning its density, while keeping only that related to the ratio of the amount of the fluxes (volume, buoyancy and momentum) that were herein imposed. This can be physically interpreted as the effect of the intermittency in the rising of volumes of buoyant fluid and to enhanced mixing in the very near field of the source.

To gain further insight into the functional dependence (1.3) we have compared the experimental results with those provided by a simple mathematical model of a bent-over plume in a crossflow.

3. Model

Following the well-established approach initiated by Morton *et al.* (1956), we represent the rising column of buoyant fluid as a 'top hat' plume. The effect of the tunnel ventilation is taken into account by a drag force exerted by the crossflow on the plume itself. The balance equations for mass, vertical momentum, density difference and horizontal

momentum can be written as

$$\begin{cases} \dfrac{\mathrm{d}}{\mathrm{d}y}(\rho w b^2) = 2\rho_0 u_e b, & (3.1a) \\ \dfrac{\mathrm{d}}{\mathrm{d}y}(\rho w^2 b^2) = (\rho_0 - \rho) g b^2, & (3.1b) \\ \dfrac{\mathrm{d}}{\mathrm{d}y}\left[(\rho_0 - \rho) w b^2\right] = 0, & (3.1c) \\ \dfrac{\mathrm{d}}{\mathrm{d}y}(\rho u w b^2) = C_x \sqrt{\rho\rho_0}(V-u)^2 b/\pi, & (3.1d) \end{cases}$$

where b is the characteristic plume radius, w and u are its vertical and longitudinal velocities, respectively, $u_e = \alpha w$ is the entrainment velocity, ρ is the plume density, V is the ventilation velocity, and C_x is a drag coefficient. In order to limit the number of free parameters we assume $C_x = 1$. The drag in $(3.1d)$ is proportional to $\sqrt{\rho\rho_0}$, which expresses the weighting role of the local density on the force exerted by the ventilation flow. Boundary conditions imposed at the source are $b(0) = b_i$, $w(0) = w_i$, $u(0) = 0$, and $\rho(0) = \rho_i$. The entrainment coefficient α is assumed to be of the form $\alpha = \alpha_0(\rho/\rho_0)^{1/2}$ as is customary when dealing with non-Boussinesq releases (Rooney & Linden 1996; Van Den Bremer & Hunt 2010).

The system of equations $(3.1a)-(3.1d)$ represents a highly simplified model of the dynamics of the buoyant fluid release and of its interaction with the ventilation flow. The model does not take into account pressure gradients and turbulent fluxes, whose roles are not necessarily negligible when considering the flow developing within a few source radii (Ezzamel *et al.* 2015; Craske & van Reeuwijk 2015), as is the case in the present study. Furthermore, the model $(3.1a)-(3.1d)$, as it is conceived, is of course unable to simulate any effect of the flow induced by the presence of the ceiling and of the side walls. It is therefore worth remembering that adopting such a model is only motivated by the aim of capturing the main bulk phenomena governing the interaction between the two flows, rather than giving a detailed description of it.

The critical ventilation condition can be imposed by assuming that the plume longitudinal momentum flux is balanced at the ceiling height ($y = H$) by the entrained momentum flux: $\pi b^2 \rho u^2(H, V_c) = \varphi^2 \pi b^2 \rho_0 u_e^2(H, V_c)$. The parameter φ, which is expected to be of order 1, is the only free parameter of the model to be determined by fitting the experimental measurements. In other words, at the critical velocity condition, the dynamical pressure imposed by the plume (ρu^2) is balanced by that associated with the entrainment air flux ($\rho_0 u_e^2$). Using $\alpha = \alpha_0(\rho/\rho_0)^{1/2}$, the critical velocity condition is reached when the ratio between the longitudinal and the vertical velocities of the release reach a critical value at the ceiling height:

$$\frac{u(H, V_c)}{w(H, V_c)} = \alpha_0 \varphi. \tag{3.2}$$

In its mathematical formulation, the problem is therefore that of controlling the trajectory of the plume's centre of mass as it moves vertically and of its impingement point at the ceiling (see figure 4*a*). Note that, given the different regimes observed in the flow visualisations (figure 1), the parameter φ cannot be considered as a constant, but must be dependent on the dynamical condition of the buoyant release at the ceiling height, which is represented by the value of the plume Richardson number at that height $\Gamma_H = \Gamma(H)$.

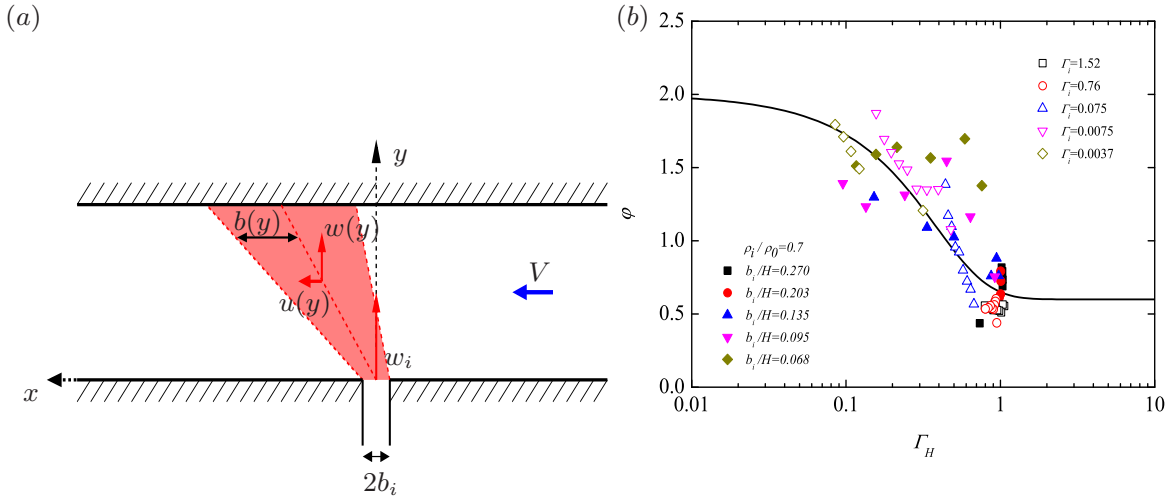

FIGURE 4. (*a*) Sketch of the plume in a ventilated tunnel. (*b*) φ as a function of Γ_H, experiments (symbols) and fitting function $\varphi = 2 - 1.4\ \tanh(2\Gamma_H)$.

3.1. *Numerical solution*

In order to determine the dependence $\varphi = \varphi(\Gamma_H)$ we have considered φ as a free parameter and retained, for each case, the value providing the best agreement between experimental and numerical results. These values, as a function of Γ_H, are plotted in figure 4*b*, which shows three main features. First, as expected the value of φ is effectively of order 1, and in the range $0.6 < \varphi < 2$. Second, according to the plume equations (3.1*a*)-(3.1*c*), almost all releases attain the ceiling height H with a local value of the plume Richardson number in the range $0.1 < \Gamma_H \leqslant 1$. Third, values of φ providing the best fit show a clear tendency in decreasing as $\Gamma_H \to 1^-$.

Our flow visualisations (figure 1) clearly show that the morphologies of the buoyant releases can be divided into two distinct regimes for $\Gamma_H < 0.1$ and for $\Gamma_H > 1$. Visualisations suggest that, within these two regimes, the trajectory of the plume's centre of mass, the position of the impinging point at the ceiling, as well as other flow features, do not exhibit any detectable difference with variation of the three control parameters (1.3), so that the flows can be considered as similar. Given these similarity conditions, we can therefore assume that φ is constant for both $\Gamma_H < 0.1$ and for $\Gamma_H > 1$, matching the values of the asymptotic conditions $\Gamma_H \to 0$ and $\Gamma_H \to \infty$, respectively. In order to combine the two asymptotic conditions and fit the data in the range $0.1 < \Gamma_H < 1$, we adopt a function of the form: $\varphi = 2 - 1.4\ \tanh(2\Gamma_H)$.

Comparisons between experimental and numerical results obtained by imposing this form of $\varphi(\Gamma_H)$ are presented in figure 5, which shows that, once φ is set, the model (3.1*a*)−(3.1*d*) is, in general, in good agreement with the experiments and helps in depicting the main trends of the flow dynamics. Firstly, the model predicts the existence of two asymptotic flow regimes, for forced $\Gamma_i \to 0$ and lazy $\Gamma_i \to \infty$ releases. In the first regime $V_c/w_i \propto const.$, whereas in the second $V_c/w_i \propto \Gamma_i^{1/3}$. The transition between the two regimes occurs for $0.01 < \Gamma_i < 1$ and depends upon the source radius. Namely, the transition takes place for lower values of Γ_i, as the ratio b_i/H decreases, i.e. as the non-dimensional distance from source to ceiling increases. In this transition region the solution exhibits a minimum, which is difficult to depict in the experimental results.

In accordance with what was observed in the experiments, the model predicts a greater influence of the source radius for the forced releases than for the lazy releases. The model reproduces well the trend in V_c/w_i induced by a varying density ratio and fixed Γ_i (figure

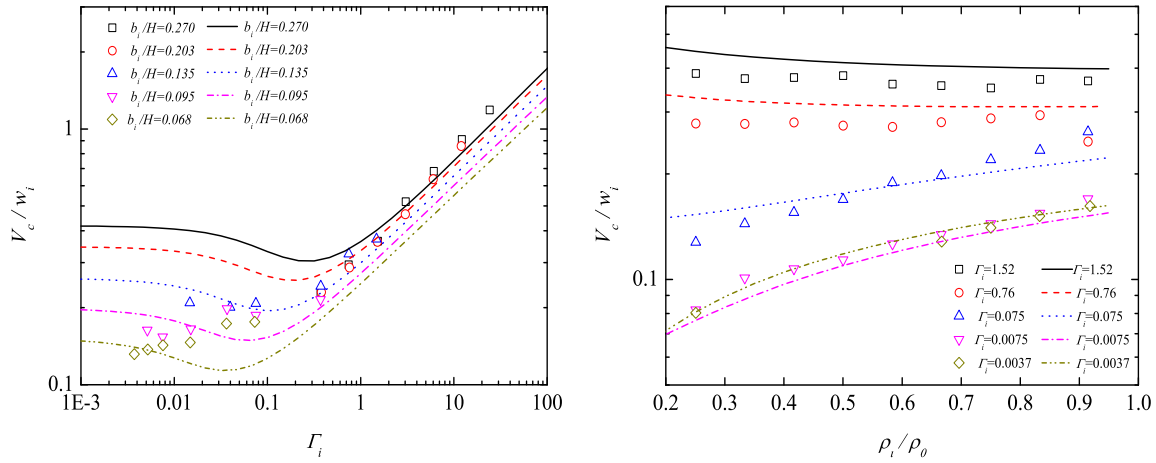

FIGURE 5. Non-dimensional critical velocity as a function of a) plume Richardson number Γ_i and b) density ratio ρ_i/ρ_0: comparison between numerical solution and experimental data.

5b); the critical velocity is not sensitive to variations of ρ_i/ρ_0 for slightly forced, pure and lazy releases, whereas it shows significant reductions with decreasing ρ_i/ρ_0 for highly forced releases, i.e. $\Gamma_i < 0.1$. This confirms that the influence of non-Boussinesq effects is confined to momentum-driven releases. Finally, note that the agreement between model and experiments suggests that the side-walls of the tunnel do not play any major role in the dynamics of the buoyant plume, which therefore behaves as a release in a (laterally) unbounded domain.

3.2. *Analytical solution*

Adopting an entrainment coefficient of the form $\alpha = \alpha_0(\rho/\rho_0)^{1/2}$, the system of equations (3.1a)−(3.1d) can be rewritten as (Rooney & Linden 1996)

$$\begin{cases} \dfrac{\mathrm{d}}{\mathrm{d}y}(w\beta^2) = 2\alpha_0\beta w, & (3.3a) \\ \dfrac{\mathrm{d}}{\mathrm{d}y}(w^2\beta^2) = \widetilde{\eta} g \beta^2, & (3.3b) \\ \dfrac{\mathrm{d}}{\mathrm{d}y}(\widetilde{\eta} w \beta^2) = 0, & (3.3c) \\ \dfrac{\mathrm{d}}{\mathrm{d}y}(uw\beta^2) = C_x(V-u)^2\beta/\pi, & (3.3d) \end{cases}$$

where $\beta = (\rho/\rho_0)^{1/2} b$ is a modified plume radius and $\widetilde{\eta} = (\rho_0 - \rho)/\rho$ is a modified density deficit.

Following previous authors (Hunt & Kaye 2005; Michaux & Vauquelin 2008; Van Den Bremer & Hunt 2010), we can obtain an analytical solution of the system (3.3a)−(3.3c), based on the solution of a freely propagating plume in an unstratified

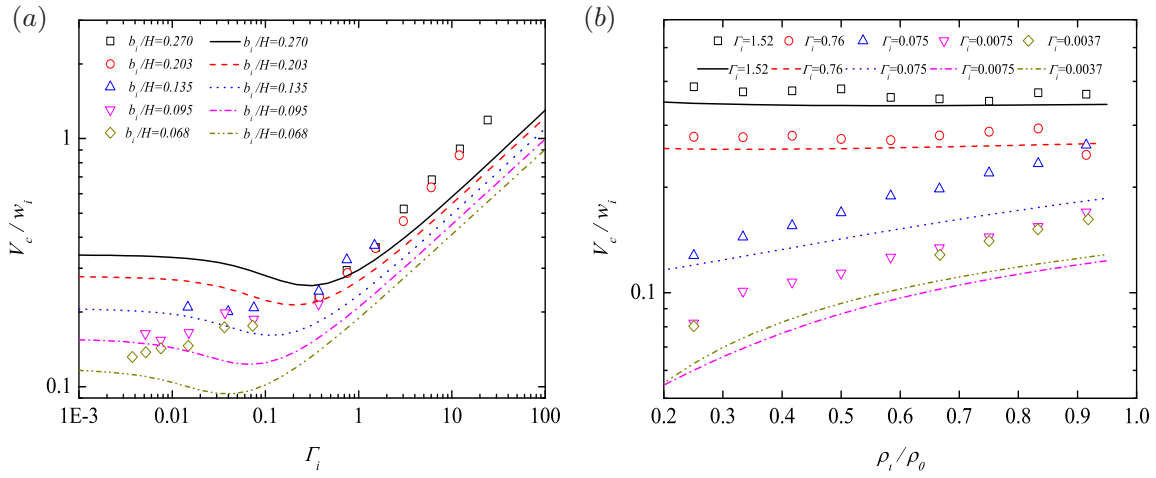

FIGURE 6. Analytical solution of (3.9) for the effect of Γ_i (a) and density ratio (b).

atmosphere, namely:

$$\begin{cases} \dfrac{\beta}{\beta_i} = \left(\dfrac{\widetilde{\Gamma}}{\widetilde{\Gamma}_i}\right)^{1/2} \left(\dfrac{1-\widetilde{\Gamma}_i}{1-\widetilde{\Gamma}}\right)^{3/10}, \\ \dfrac{w}{w_i} = \left(\dfrac{\widetilde{\Gamma}_i}{\widetilde{\Gamma}}\right)^{1/2} \left(\dfrac{1-\widetilde{\Gamma}}{1-\widetilde{\Gamma}_i}\right)^{1/10}, \\ \dfrac{\widetilde{\eta}}{\widetilde{\eta}_i} = \left(\dfrac{\widetilde{\Gamma}_i}{\widetilde{\Gamma}}\right)^{1/2} \left(\dfrac{1-\widetilde{\Gamma}}{1-\widetilde{\Gamma}_i}\right)^{1/2}, \end{cases} \tag{3.4}$$

where $\widetilde{\Gamma} = \dfrac{5g}{8\alpha_0}\dfrac{\widetilde{\eta}\beta}{w^2}$ is a modified plume Richardson number which changes with height and can be computed as

$$\begin{cases} \dfrac{\mathrm{d}\widetilde{\Gamma}}{\mathrm{d}y} = \dfrac{1}{\Lambda_i}\widetilde{\Gamma}^{1/2}(1-\widetilde{\Gamma})^{13/10} \quad \text{for } \widetilde{\Gamma} < 1, \\ \dfrac{\mathrm{d}\widetilde{\Gamma}}{\mathrm{d}y} = -\dfrac{1}{\Lambda_i}\widetilde{\Gamma}^{1/2}(\widetilde{\Gamma}-1)^{13/10} \quad \text{for } \widetilde{\Gamma} > 1, \end{cases} \tag{3.5}$$

with $\Lambda_i = \dfrac{\beta_i}{4\alpha_0}\dfrac{|\widetilde{\Gamma}_i - 1|^{3/10}}{\widetilde{\Gamma}_i^{1/2}}$ is a characteristic length imposed by the conditions at the source. From (3.5) we obtain $\dfrac{y}{\Lambda_i} = F(\widetilde{\Gamma}) - F(\widetilde{\Gamma}_i)$, where the function F is

$$F(X) = \begin{cases} 2X^{1/2} \quad \text{for } X \to 0, \\ \dfrac{10}{3}[(1-X)^{-3/10} - 1] \quad \text{for } X \to 1^-, \\ \dfrac{10}{3}(X-1)^{-3/10} \quad \text{for } X \to 1^+, \\ \dfrac{5}{4}X^{-4/5} \quad \text{for } X \to \infty. \end{cases} \tag{3.6}$$

The analytical solution can then be obtained assuming that the tunnel ventilation is much larger than the longitudinal velocity of the plume, i.e. $V \gg u$, so that (3.3d)

reduces to

$$\frac{\mathrm{d}}{\mathrm{d}y}(uw\beta^2) = C_x V^2 \beta/\pi. \tag{3.7}$$

By combining (3.7) with (3.4) we obtain a relationship between u and w, which is valid for both forced $\widetilde{\Gamma}_i < 1$ and lazy plumes $\widetilde{\Gamma}_i > 1$ (for brevity, we skip the solution for a pure plume, i.e. $\widetilde{\Gamma}_i = 1$):

$$\frac{u}{w} = \frac{5C_x}{12\pi\alpha_0\widetilde{\Gamma}_i}\left(\frac{1-\widetilde{\Gamma}}{1-\widetilde{\Gamma}_i}\right)^{\frac{2}{5}}\left[\left(\frac{1-\widetilde{\Gamma}}{1-\widetilde{\Gamma}_i}\right)^{-\frac{3}{5}} - 1\right]\left(\frac{V}{w_i}\right)^2. \tag{3.8}$$

Imposing the condition (3.2) *i.e.* $u/w = \varphi\alpha_0$ at the ceiling height ($y = H$), we can therefore compute the critical velocity as

$$\frac{V_c}{w_i} = 2\alpha_0\left(\frac{3\varphi\pi}{5C_x}\right)^{\frac{1}{2}}\widetilde{\Gamma}_i^{\frac{1}{2}}\left(\frac{1-\widetilde{\Gamma}_H}{1-\widetilde{\Gamma}_i}\right)^{\frac{1}{10}}\left[1-\left(\frac{1-\widetilde{\Gamma}_H}{1-\widetilde{\Gamma}_i}\right)^{\frac{3}{5}}\right]^{-\frac{1}{2}}, \tag{3.9}$$

where $\widetilde{\Gamma}_H = \widetilde{\Gamma}(y = H)$ is obtained by solving (3.5). The analytical solution (3.9) is plotted in figure 6 against experimental data. The general trends of the solution are very similar to those observed for the numerical solution. The assumption $V \gg u$ implies larger discrepancies between model and experiments for both forced $\Gamma_i \ll 1$ and lazy $\Gamma_i \gg 1$ releases. In the case of almost pure releases the differences between the analytical (3.9) and the numerical solution are less evident.

3.3. *Asymptotic behaviours*

To gain an insight into the main physical aspects enlightened by the experiments it is instructive to investigate the solutions of the system of equations (3.3) in the limits of highly forced and lazy releases, respectively. We initially focus on the general case (3.3) and examine subsequently the case of a tunnel ventilation much larger than the longitudinal velocity of the plume.

Forced releases, $\Gamma_i \to 0$

The main findings of plume theory (Van Den Bremer & Hunt 2010) indicate that the lower the value of Γ_i, the larger the distance needed to attain pure plume conditions, i.e. $\Gamma = 1$. Based on this, and given the relatively short distance between source and ceiling, we assume here that highly forced releases, i.e. $\widetilde{\Gamma}_i \to 0$, impinge the ceiling with an identical balance of fluxes, i.e. $\widetilde{\Gamma}(y = H) \to 0$. With this assumption, making use of (3.6), we obtain: $\widetilde{\Gamma} = \left(1 + \frac{2\alpha_0 y}{\beta_i}\right)^2 \widetilde{\Gamma}_i$. Thus, (3.3*a*)-(3.3*c*) can be approximated as

$$\frac{\beta}{\beta_i} = \frac{w_i}{w} = \frac{\eta_i}{\eta} = 1 + \frac{2\alpha_0 y}{\beta_i} = \widehat{y}_F. \tag{3.10}$$

Using (3.10) we can rewrite the horizontal momentum equation (3.3*d*) as

$$\frac{\mathrm{d}\widehat{u}_F}{\mathrm{d}\widehat{V}_F} = \frac{C_x}{2\alpha_0\pi\widehat{V}_F}(\widehat{V}_F - \widehat{u}_F)^2, \tag{3.11}$$

where $\widehat{V}_F = \frac{V}{w_i}\widehat{y}_F$ and $\widehat{u}_F = \frac{u}{w_i}\widehat{y}_F$.

According to the model, the critical ventilation condition is fixed by (3.2) or, in a non-dimensional form: $\widehat{u}_F(H) = \widehat{u}_{c,F} = \alpha_0\,\varphi_F$, where $\varphi_F = 2$ is the value of φ for highly forced releases. Equation (3.11) can be solved numerically giving $\widehat{u}_F$ as a function of $\widehat{V}_F$

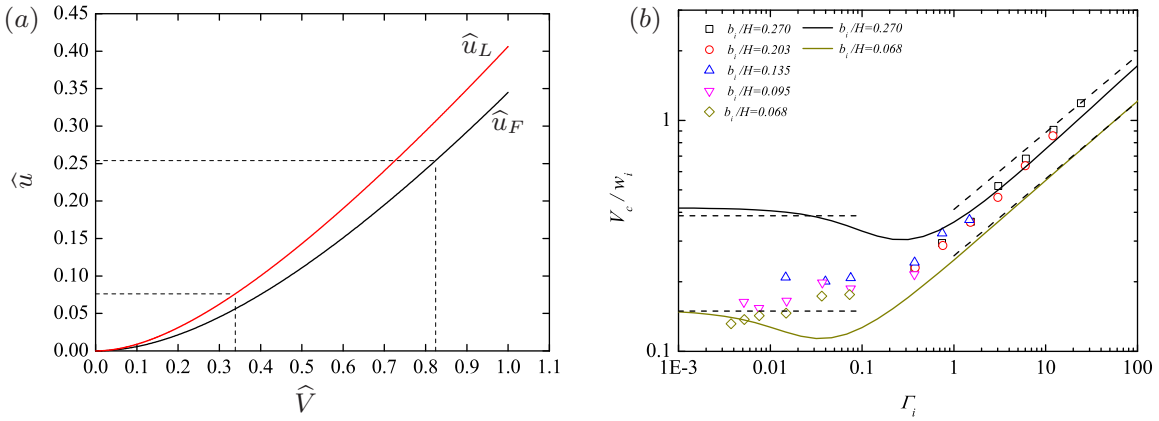

FIGURE 7. (*a*) Non-dimensional longitudinal velocity as a function of non-dimensional ventilation velocity for forced (solid line) and lazy (dashed line) releases. (*b*) Solid lines: numerical solution of (3.1*a*)−(3.1*d*); dashed lines: asymptotic solution of (3.17).

(see figure 7*a*) and at the critical ventilation condition, $\widehat{u}_{c,F} = 0.254$ and $\widehat{V}_{c,F} = 0.824$. For highly forced releases we therefore finally obtain:

$$\frac{V_c}{w_i} = \frac{\widehat{V}_{c,F}}{1 + \frac{2\alpha_0 H}{\beta_i}}. \tag{3.12}$$

Lazy releases, $\Gamma_i \to \infty$

In comparison to forced plumes (Van Den Bremer & Hunt 2010), lazy plumes rapidly attain the condition of a pure plume ($\widetilde{\Gamma} \to 1^+$) as $\widetilde{\Gamma}$ decreases quickly with distance from the source (see also figure 4*b*). We therefore assume that for $\widetilde{\Gamma}_i > 1$, the release impinges the ceiling in the condition $\widetilde{\Gamma}(y = H) \to 1$. With this assumption, making use of (3.6), we obtain: $\frac{y}{\Lambda_i} = \frac{10}{3}(\widetilde{\Gamma}_y - 1)^{-\frac{3}{10}} - \frac{5}{4}\widetilde{\Gamma}_i^{-\frac{4}{3}}$, which implies that

$$(\widetilde{\Gamma} - 1)^{-\frac{3}{10}}\, \widetilde{\Gamma}_i^{-\frac{1}{5}} = \frac{6\alpha y}{5\beta_i} = \widehat{y}_L. \tag{3.13}$$

Thus, (3.3*a*)-(3.3*c*) can be approximated as

$$\begin{cases} \beta/\beta_i = \widehat{y}_L, \\ w/w_i = \widetilde{\Gamma}_i^{\frac{1}{3}} \widehat{y}_L^{-\frac{1}{3}}, \\ \widetilde{\eta}/\widetilde{\eta}_i = \widetilde{\Gamma}_i^{-\frac{1}{3}} \widehat{y}_L^{-\frac{5}{3}}. \end{cases} \tag{3.14}$$

The horizontal momentum equation (3.3*d*) then gives

$$\widehat{V}_L \frac{\mathrm{d}\widehat{u}_L}{\mathrm{d}\widehat{V}_L} + 4\widehat{u}_L = \frac{5C_x}{2\alpha_0 \pi}(\widehat{V}_L - \widehat{u}_L)^2, \tag{3.15}$$

where $\widehat{V}_L = \frac{V}{w_i}\left(\frac{\widehat{y}_L}{\widetilde{\Gamma}_i}\right)^{\frac{1}{3}}$ and $\widehat{u}_L = \frac{u}{w_i}\left(\frac{\widehat{y}_L}{\widetilde{\Gamma}_i}\right)^{\frac{1}{3}}$. (3.15) can be solved numerically giving $\widehat{u}_L$ as a function of $\widehat{V}_L$ and at the critical ventilation condition, $\widehat{u}_L(H) = \widehat{u}_{c,L} = \alpha_0\, \varphi_L$, where $\varphi_L = 0.6$, giving $\widehat{u}_{c,L} = 0.076$ and $\widehat{V}_{c,L} = 0.339$ (figure 7*a*). Finally, for highly lazy releases:

$$\frac{V_c}{w_i} = \widehat{V}_{c,L}\left(\frac{5}{6\alpha_0}\frac{\beta_i}{H}\widetilde{\Gamma}_i\right)^{\frac{1}{3}}. \tag{3.16}$$

Summarising, the asymptotic conditions can be expressed in the form:

$$\frac{V_c}{w_i} = \begin{cases} \dfrac{\widehat{V}_{c,F}}{1+\frac{2\alpha_0 H}{b_i}\left(\frac{\rho_0}{\rho_i}\right)^{\frac{1}{2}}} & \text{for } \Gamma_i \to 0, \\ \widehat{V}_{c,L}\left(\dfrac{5}{6\alpha_0}\dfrac{b_i}{H}\Gamma_i\right)^{\frac{1}{3}} & \text{for } \Gamma_i \to \infty. \end{cases} \tag{3.17}$$

Figure 7(b) shows a comparison between (3.17) and the numerical solution of (3.1a)−(3.1d). For simplicity, only two source radii are shown.

A similar result can also be obtained in the case of $u \ll V_c$. Making use of (3.6) the limits of the analytical solution (3.9) become:

$$\frac{V_c}{w_i} = \begin{cases} \dfrac{\tilde{V}_{c,F}}{\left\{\left[1+\frac{2\alpha_0 H}{b_i}\left(\frac{\rho_0}{\rho_i}\right)^{\frac{1}{2}}\right]^2 - 1\right\}^{\frac{1}{2}}} & \text{for } \Gamma_i \to 0 \\ \tilde{V}_{c,L}\left(\dfrac{5}{6\alpha_0}\dfrac{b_i}{H}\Gamma_i\right)^{\frac{1}{3}} & \text{for } \Gamma_i \to \infty \end{cases} \tag{3.18}$$

where $\tilde{V}_{c,F} = 2\alpha_0\sqrt{\frac{\varphi_F \pi}{C_x}} = 0.637$ and $\tilde{V}_{c,L} = 2\alpha_0\sqrt{\frac{\varphi_L \pi}{C_x}}\sqrt{\frac{3}{5}} = 0.270$.

For lazy releases, (3.18) is identical to (3.17); the constant $\widehat{V}_{c,L} = 0.339$ is just replaced by $\tilde{V}_{c,L} = 0.270$. For forced releases, (3.18) converges to (3.17) when the height of the tunnel is much larger than the radius of the source ($H/b_i \to \infty$); the constant $\widehat{V}_{c,F} = 0.824$ is then replaced by $\tilde{V}_{c,F} = 0.637$.

According to (3.17) and (3.18), for $\Gamma_i \to 0$, the critical velocity becomes independent of Γ_i and depends instead only on the source radius b_i/H and the square root of the density ratio. Most importantly, for $\Gamma_i \to \infty$, the critical velocity becomes independent of the density ratio and depends on the cubic roots of Γ_i and b_i/H. Very interestingly, (3.17) and (3.18) therefore capture the role of non-Boussinesq effects, i.e. related to ρ_i/ρ_0 in both regimes, and confirm the dependence on $\Gamma_i^{1/3}$ suggested by the trend observed experimentally.

Finally, it is to note that, for $\Gamma_i \to \infty$, expressing Γ_i as a function of the buoyancy flux B_i (2.1), both w_i and b_i vanish in (3.17) and (3.18), which therefore can be rewritten in the form of a constant critical Froude number $\widehat{\mathrm{Fr}}_c$, as:

$$\Gamma_i \to \infty \quad V_c\left(\frac{H}{B_i}\right)^{\frac{1}{3}} = \widehat{\mathrm{Fr}}_c \tag{3.19}$$

with $\widehat{\mathrm{Fr}}_c = \left(\frac{25}{48\pi\alpha_0^2}\right)^{\frac{1}{3}} \widehat{V}_{c,L}$. Similarly, (3.18) gives a constant critical Froude number $\tilde{\mathrm{Fr}}_c = \left(\frac{15\pi}{4}\right)^{\frac{1}{6}}\left(\frac{\varphi_L}{C_x}\right)^{\frac{1}{2}} \alpha_0^{\frac{1}{3}} \tilde{V}_{c,L}$.

Equation (3.19) expresses that, for highly lazy plumes, the dynamical similarity conditions of the flow are reduced to one non-dimensional parameter only. In other words, the governing flow parameters in (1.1) (for negligible viscous effects and fixed tunnel geometry) could be simply rewritten as $V_c = f(B_i, H)$. The conditions imposed at the source can therefore be fully expressed by the buoyancy flux B_i only, without any need to provide information on its radius b_i and density ρ_i. As shown in figure 8, this similarity condition of a constant Fr_c, predicted by the model in the limit $\Gamma_i \to \infty$ actually holds

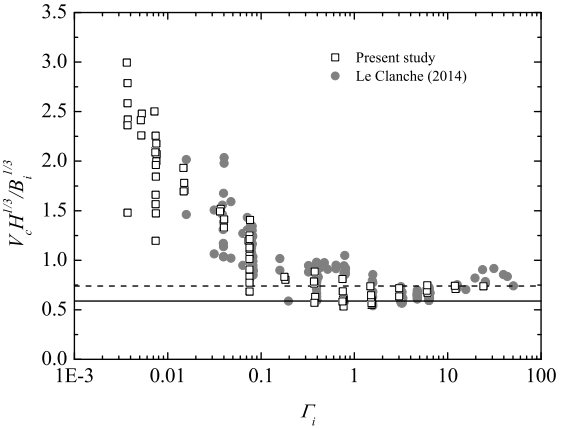

FIGURE 8. Critical Froude number $\mathrm{Fr}_c = V_c \left(\frac{H}{B_i}\right)^{\frac{1}{3}}$, as a function of Γ_i: experimental results (squares) and data from Le Clanche *et al.* (2014) (plain circles). Also shown: the critical Froude number $\widehat{\mathrm{Fr}}_c$ obtained from (3.17) (dashed horizontal line) and from (3.18) (solid horizontal line).

for $\Gamma_i \geqslant 1$. This finding suggests that the dynamics of plume-like releases in ventilated tunnels can reliably be modelled as Boussinesq releases of pure buoyancy emitted by a point source, neglecting any non-Boussinesq effect arising at low values of the ratio ρ_i/ρ_0.

4. Conclusions

We have investigated the dynamics of a release of buoyant fluid discharged from a circular source placed at the centre of a longitudinally ventilated tunnel. In particular, we focused on the dependence of the so-called 'critical ventilation velocity' V_c, that allows the buoyant fluid to be confined downwind of the release point, on varying conditions at the source: the injection velocity w_i, density ρ_i and radius b_i. By assuming negligible diffusive effects, and a tunnel with a fixed aspect ratio (between height and width), the non-dimensional critical velocity V_c/w_i has been shown to depend on three non-dimensional groups: the plume Richardson number Γ_i, the non-dimensional source radius b_i/H and the density ratio ρ_i/ρ_0. This latter parameter is particularly relevant in order to investigate dynamical effects known as non-Boussinesq, i.e. related to large density differences between buoyant and ambient fluid, whose influence is still not fully elucidated in the case of highly buoyant releases, i.e. large Γ_i.

To investigate these dependencies, we performed experiments in a reduced-scale tunnel, where buoyant releases were produced with a mixture of helium and air. Experiments have shown the following main features:

- the dependence of V_c/w_i on Γ_i reveals the existence of two flow regimes, one for $\Gamma_i \ll 1$ and one for $\Gamma_i \gg 1$;
- the transition between the two regimes occurs in the range $10^{-2} < \Gamma_i < 1$;
- V_c/w_i does not show any dependence on the density ratio as $\Gamma_i > 0.1$, whereas for lower Γ_i the dependence is of the form $(\rho_i/\rho_0)^{1/2}$; and
- in the range of source radii investigated, V_c/w_i seems to be more sensitive to b_i/H for forced releases, i.e. $\Gamma_i < 1$, rather than for lazy releases $\Gamma_i > 1$.

To obtain further insight into the dynamics of these flows we interpreted the experiments by comparing their results to a numerical and analytical solution of a simple model of a plume in a crossflow, which was formulated following the well-established approach by Morton *et al.* (1956). Despite its simplicity, the model is able to capture all the main

trends identified by the experiments, namely the existence of two flow regimes, depending on Γ_i, and the rise of non-Boussinesq effects for highly forced releases only, $\Gamma_i < 0.1$. Furthermore, the model helps in elucidating the role of the source radius on b_i/H on the flow dynamics.

Finally, asymptotic solutions of the model, in the limits $\Gamma_i \to 0$ and $\Gamma_i \to \infty$, reveal key aspects of the dynamics of these releases. For forced releases, i.e. $\Gamma_i \to 0$, the critical velocity is a function of b_i/H and ρ_i/ρ_0, only. Concerning this latter parameter, V_c/w_i is shown to depend on $(\rho_i/\rho_0)^{1/2}$, although it does not fully rescale on it. For lazy releases, i.e. $\Gamma_i \to \infty$, asymptotic solutions show that V_c/w_i rescales on $\Gamma_i^{1/3}$ and $(b_i/H)^{1/3}$. Notably, this dependence implies that $V_c \propto (B_i/H)^{1/3}$, i.e. that the critical velocity actually depends only on the buoyancy flux at the source B_i, irrespective of its radius, velocity and density. The good agreement of our experimental data set with this simple scaling has two major theoretical implications:

- for pure and lazy releases, the release can be represented as a point source of pure buoyancy, for any source conditions; and
- the so-called non-Boussinesq effects have no major influence on the flow dynamics as far as gravitational effects take over those related to inertia.

It is worth noting that, from a practical point of view, both features support the use of simplified mathematical models for the simulation of these flows, and define the ventilation systems for the management and the mitigation of accidental risks related to the releases of toxic and flammable fluids in enclosed spaces.

Acknowledgements

Lei Jiang is sponsored by the China Scholarship Council.

REFERENCES

Arya, S.P.S. & Lape, J.F. jr. 1990 A comparative study of the different criteria for the physical modelling of buoyant plume rise in a neutral atmosphere. *Atmos. Environ.* **24**, 289–295.

Barnett, S. J. 1993 A vertical buoyant jet with high momentum in a long ventilated tunnel. *J. Fluid Mech.* **252**, 279–300.

Craske, J. & van Reeuwijk, M. 2015 Energy dispersion in turbulent jets. part 1: Direct simulation of steady and unsteady jets. *J. Fluid Mech.* **763**, 500–537.

Ezzamel, A., Salizzoni, P. & Hunt, G. R. 2015 Dynamical variability of axisymmetric buoyant plumes. *J. Fluid Mech.* **765**, 576–611.

Grant, G. B., Jagger, S. F. & Lea, C. J. 1998 Fires in tunnels. *Phil. Trans. R. Soc. London A* **356**, 2873–2906.

Hunt, G. R. & Kaye, N. B. 2005 Lazy plumes. *J. Fluid Mech.* **533**, 329–338.

Hunt, J. C. R. 1991 Industrial and environmental fluid mechanics. *Annu. Rev. Fluid Mech.* **23**, 1–41.

Jirka, G. H. & Harleman, D. R. F. 1979 Stability and mixing of a vertical plane buoyant jet in confined depth. *J. Fluid Mech.* **94** (02), 275–304.

Le Clanche, J., Salizzoni, P., Creyssels, M., Mehaddi, R., Candelier, F. & Vauquelin, O. 2014 Aerodynamics of buoyant releases within a longitudinally ventilated tunnel. *Exp. Therm Fluid Sci.* **57**, 121–127.

Michaux, G. & Vauquelin, O. 2008 Solutions for turbulent buoyant plumes rising from circular sources. *Phys. Fluids* **20**, 066601.

Morton, B. R., Taylor, G. I. & Turner, J. S. 1956 Turbulent gravitational convection from maintained and instantaneous sources. *Proc. Roy. Soc. London A* **234**, 1–23.

Ricou, F. P. & Spalding, D. B. 1961 Measurements of entrainment by axisymmetrical turbulent jets. *J. Fluid Mech.* **11**, 21–32.

Rooney, G. G. & Linden, P. F. 1996 Similarity considerations for non-Boussinesq plumes in an unstratified environment. *J. Fluid Mech.* **318**, 237–250.

Van Den Bremer, T. S. & Hunt, G. R. 2010 Universal solutions for Boussinesq and non-Boussinesq plumes. *J. Fluid Mech.* **644**, 165–192.

Chapter 9

Direct and inverse modelling of pollutant dispersion in the built environment

This work relies on a long-term research activity conducted at the LMFA and devoted to the modelling of pollutant dispersion in urban areas. The aim of this research was to develop an operational model for the assessment of chronic urban pollution that could fulfill two main requirements:

- to use low computational resources, compared to traditional Computational Fluid Dynamics codes, in order to run simulations of a large number of scenarios over large domains, i.e. up to 30×30 Km, and over long time period, i.e. one year (or more); and
- to provide reliable time-averaged concentration values with a high spatial resolution, at the street scale.

The model, named SIRANE (Soulhac *et al.*, 2011), adopts a simplified representation of the urban geometry (fig. 9.1a-b) and is based on the parameterisations of the main phenomena that drive the pollutant transfer in urban areas. SIRANE assumes a decoupling of the domain into two parts: the urban canopy and the overlying boundary layer. Flow and dispersion in the canopy are simulated by means of a so-called *street-network* model, whereas in the overlying boundary layer the flow is modelled according to the Monin-Obukhov similarity theory and dispersion by means of a Gaussian plume model (fig. 9.1c). In the street network approach the urban canopy is represented as a series of boxes (fig. 9.1d), connected one to the other through nodes (fig. 9.1e), modelling street intersections. In the network, it is assumed that dispersion is governed by only three bulk exchange phenomena, namely: pollutant retention in street canyons due to the recirculating patterns of flow within them, their channelling along the street axes and their transfer of pollutants at street intersection. These phenomena are regulated by three parameters:

- the advective velocity along the street axes (Soulhac *et al.*, 2008);
- wind horizontal fluctuations at street intersections (Soulhac *et al.*, 2009); and
- the mass transfer velocity between the street canyon and the atmosphere (Salizzoni *et al.*, 2009; Soulhac *et al.*, 2013).

As is customary for pollutant dispersion models, SIRANE simulates the unsteadiness of meteorological conditions and of emission intensity with a quasi-steady approach, assuming steady conditions over hourly time steps. These can be subsequently used to compute long-term concentration statistics (fig. 9.2).

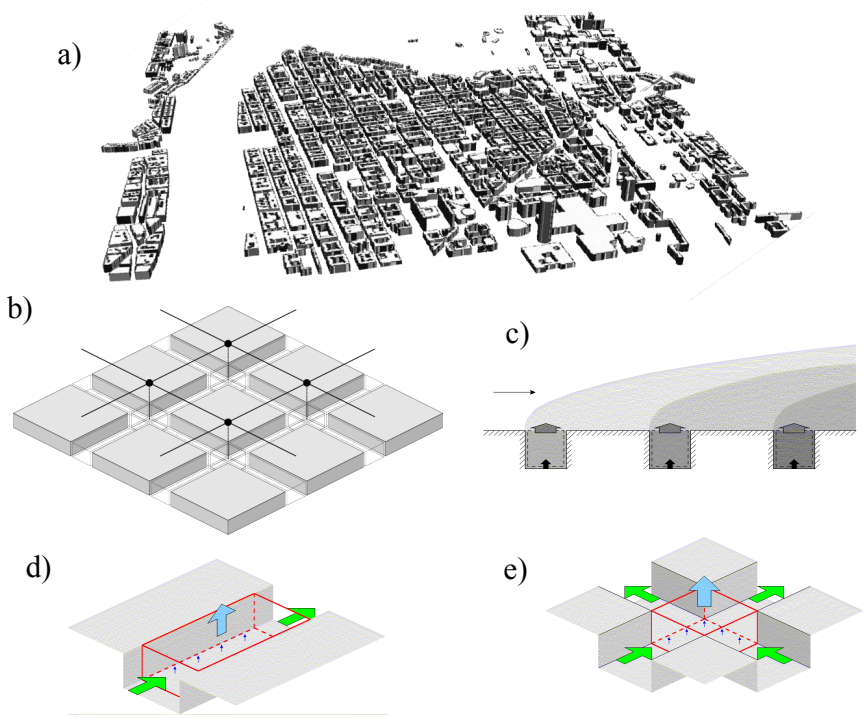

Figure 9.1: a) real urban geometry, an example of a district in Lyon; b) street network geometry; c) turbulent exchanges at street intersections; d) pollutant dispersion over roof level; e) mass balance within a street canyon.

This approach has been recently extended in order to develop an operational model for accidental hazards. The aim is then to simulate unsteady pollutant releases, i.e. whose source strength intensity varies over a timescale which is much shorter than that associated with the variation of meteorological conditions. The purpose is to simulate the evolution of a puff of pollutant emitted by impulsive releases of harmful gases in a built environment, as a consequence of an uncontrolled leakage within an industrial site or a deliberate release, due to a terrorist act, within a densely populated urban area.

In what follows (chapter 9.1) we present the principle of the parameterisation implemented in this approach, as well as of a detailed validation against wind tunnel experiments. This new formulation the model presents two main differences compared to SIRANE:

- dispersion above roof level is based on a puff model, including the effect of wind shear on dispersion; and
- the size of the boxes composing the network are now smaller that the size of a street canyon and their volume is not fixed in time.

The performance of the model is analysed by a detailed comparison with wind tunnel experiments. These experiments concern the dispersion of steady and unsteady pollutant releases within and above obstacle arrays with varying geometrical configurations, representing different topologies of idealised urban districts. Results enlighten notably the effect of wind shear on the longitudinal dispersion of the pollutant puffs. The good agreement with experimental data provides further evidence of the reliability of the street-network approach in simulating pollutant dispersion within dense urban areas.

Note that, in its actual formulation, the model, named SIRANERISK, predicts the evolution of an ensemble-averaged pollutant cloud, only. Its use for the assessment of accidental risk will therefore require the inclusion of a new module for the estimate of the statistics of the concentration fluctuations around this average value. Nevertheless, as we discuss in sect. 9.2, in its actual formulation (predicting the evolution of an ensemble-averaged time-averaged signal), SIRANERISK can be conveniently used as a 'direct model' of an inversion algorithm to estimate the mass of release ejected by the impulsive

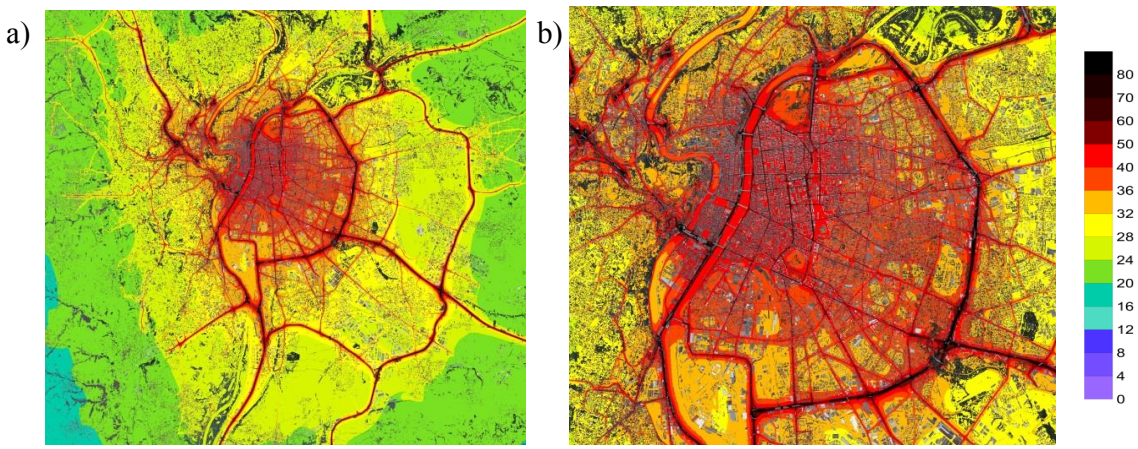

Figure 9.2: Examples of results provided by SIRANE: yearly-averaged NO_2 concentrations ($\mu g \cdot m^{-3}$).

source, which is assumed to be unknown both in the case of an industrial accident and of a terrorist attack. Notably, we show that this sort of inverse model is also reliable when using information provided by high-frequency concentration signals, characterised by fluctuations that, in principle, the direct model is not able to treat. To that purpose however, the inverse algorithm, which is essentially based on least squares method, requires the incorporation of a specific module, known as Tikhonov regularisation, to deal with the unsteadiness and irregularity of the signal. This allows filtering of the signal mitigating the effect of fluctuations on the inverse model prediction errors, while keeping the information needed to provide a reliable estimate of the total amount of mass emitted at the source.

The originality of this study is twofold. Firstly, the inversion is performed using high-frequency fluctuating, i.e. turbulent, concentration signals. Secondly, the inverse algorithm is applied to a dispersion process within a dense urban canopy, at the district scale, and a street network model, SIRANERISK, is adopted.

As shown by comparison with experimental results, the model allows us to estimate the order of magnitude of the mass of pollutant ejected, information that is more than useful when assessing the risks related to accidental pollutant releases in a built environment. These results strongly support the use of such a modelling approach for operational purposes and for the management of risks due to accidental pollutant releases in a built environment.

Bibliography

Salizzoni, P., Soulhac, L., and Mejean, P. 2009. Street canyon ventilation and atmospheric turbulence. *Atmospheric Environment*, **43**, 5056–5067.

Soulhac, L., Perkins, R. J., and Salizzoni, P. 2008. Flow in a street canyon for any external wind direction. *Boundary-Layer Meteorology*, **126**, 365–388.

Soulhac, L., Garbero, V., Salizzoni, P., Mejean, P., and Perkins, R. 2009. Flow and Dispersion in Street Intersections. *Atmospheric Environment*, **43**, 2981–2996.

Soulhac, L., Salizzoni, P., Cierco, F.-X., and Perkins, R.J. 2011. The model SIRANE for atmospheric urban pollutant dispersion; part I, presentation of the model. *Atmospheric Environment*, **45**, 7379–7395.

Soulhac, L., Salizzoni, P., Mejean, P., and Perkins, R.J. 2013. Parametric laws to model urban pollutant dispersion within a street network approach. *Atmospheric Environment*, **67**, 229–241.

9.1 SIRANERISK: modelling dispersion of steady and unsteady pollutant releases in the urban canopy

Atmospheric Environment 140 (2016) 242–260

Contents lists available at ScienceDirect

Atmospheric Environment

journal homepage: www.elsevier.com/locate/atmosenv

SIRANERISK: Modelling dispersion of steady and unsteady pollutant releases in the urban canopy

L. Soulhac [a], G. Lamaison [a], F.-X. Cierco [b], N. Ben Salem [c], P. Salizzoni [a, *], P. Mejean [a], P. Armand [d], L. Patryl [d]

[a] Laboratoire de Mécanique des Fluides et d'Acoustique, UMR CNRS 5509 University of Lyon, Ecole Centrale de Lyon, INSA Lyon, Université Claude Bernard Lyon I, 36, avenue Guy de Collongue, 69134 Ecully, France
[b] Compagnie Nationale du Rhône, Engineering Department, River Systems and Climate Hazards Division, 2, rue André Bonin, 69004 Lyon, France
[c] Air Rhône-Alpes, 3 allée des Sorbiers, 69500 Bron, France
[d] CEA, DAM, DIF, F-91297 Arpajon, France

HIGHLIGHTS

- SIRANERISK is a new operational dispersion model for unsteady releases of pollutant within a built environment.
- The model is validated against wind tunnel experiments.
- SIRANERISK is a reliable tool to estimate effects of accidental releases of harmful pollutant.

GRAPHICAL ABSTRACT

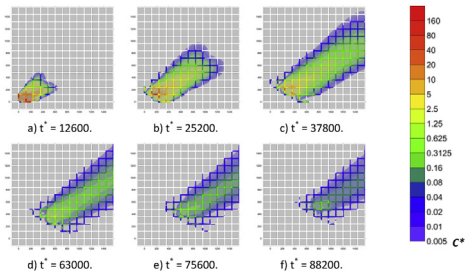

ARTICLE INFO

Article history:
Received 24 December 2015
Received in revised form
19 April 2016
Accepted 20 April 2016
Available online 4 June 2016

Keywords:
Accidental releases
Model validation
Turbulent dispersion
Urban boundary layer
Wind tunnel experiments

ABSTRACT

SIRANERISK is an operational model for the simulation of the dispersion of unsteady atmospheric releases of pollutant within and above an urban area. SIRANERISK is built on the same principles as the SIRANE model, and couples a street network model for the pollutant transfers within the urban canopy with a Gaussian puff model for the transfers above it. The performance of the model are here analysed by a detailed comparisons with wind-tunnel experiments. These experiments concern the dispersion of steady and unsteady pollutant releases within and above obstacle arrays with varying geometrical configurations, representing different topologies of idealised urban districts. The overall good agreement between numerical and experimental data demonstrates the reliability of SIRANERISK as an operational tool for the assessment of risk analysis and for the management of crises due to the accidental release of harmful airborne pollutants within a built environment.

1. Introduction

The release of toxic, flammable or explosive substances in the atmosphere is a major risk related to the occurrence of an accident or a terrorist act within an industrial site or a densely populated urban area. In both of these cases, the release of harmful pollutant is likely to be characterised by an unsteadiness of the source strength (short-duration release). In this case, the typical time scale related to the release is short compared to the characteristic time scale related to the advection (or to the turbulent diffusion) of the puff in

* Corresponding author.
E-mail address: pietro.salizzoni@ec-lyon.fr (P. Salizzoni).

http://dx.doi.org/10.1016/j.atmosenv.2016.04.027
1352-2310/

the atmosphere. The evaluation of the consequences of the accidental releases in the surrounding areas requires estimating the temporal and spatial evolution of the pollutant concentration of the harmful substances, which determines the toxic effects on health or the risk of explosion. This is essential both for the risk assessment analysis and the crisis management. It is therefore necessary to model the atmospheric dispersion of the pollutants within a densely built environment, characterised by a complex geometry of the domain within which the dispersion process takes place.

Computational Fluid Dynamics (CFD) is widely recognized as the most suitable numerical tool to model the atmospheric dispersion of pollutant within a complex built environment (Blocken, 2015), as it permits simulation of the effects of the wide range of spatial scales characterizing geometry of the industrial sites and urban areas and influencing the dispersion process. However, CFD codes still require excessive computational resources when adopted as operational tools for crisis management in case of accidental (or deliberate) releases of harmful pollutants.

The need for a reduction of the computational costs led so far to the development of different modelling strategies (Di Sabatino et al., 2013). One approach is that provided by the so-called CFD-based fast response models. The computation of the velocity field is achieved by means of diagnostic models, based on a mass-consistent approach, or prognostic models, based on averaged (spatially or over time) formulations of the Navier-Stokes equations closed with simple algebraic models. Dispersion is simulated with an Eulerian or a Lagrangian approach. The most well-known models in this category are QUIC-URB (Brown et al., 2009) and MSS-Spray (Moussafir et al., 2004; Tinarelli et al., 2007) along with the principles first proposed by Röckle (1990).

An alternative approach relies in developing dispersion models based on a simplified description of the flow and dispersion and on the parameterisation of the main mechanisms driving pollutant dispersion within and above the urban canopy. Examples of this approach are given by ADMS-Urban (Carruthers et al., 2000) or SIRANE (Soulhac et al., 2011), which are both conceived to simulate steady releases. Among these 'simplified' dispersion models, as far as we are aware, the only one aiming at simulating the dispersion of unsteady releases within a built environment is the Urban Dispersion Model (UDM). This is basically an unsteady Gaussian puff model which is coupled with some empirically-derived formulae simulating the effects of building wakes on pollutant dispersion (Brook et al., 2003).

The aim of this paper is to present a new operational model for the atmospheric dispersion of airborne pollutant emitted by an unsteady source within a built environment. The model, named SIRANERISK, is built on the same principles as the SIRANE model and is based on the parameterisation of the main phenomena driving pollutant dispersion within and above an urban area, namely: dispersion over roof level, advection along street axes, dispersion at street intersections and vertical exchanges between street canyons and overlying atmosphere. Compared to SIRANE, the model has been modified in order to treat unsteady releases (§2). To give an overview of the model results, we present graphically in the abstract the time evolution of the simulated non-dimensional ensemble averaged concentration field induced by an impulsive pollutant emission within an idealised dense urban canopy (the same used in the experiments performed for the model validation and presented in the next sections). The figure shows the longitudinal and transversal spreading of the puff within the canopy, driven by the advective mass fluxes along the canyon axes and the transfers at the street intersections. The limited vertical mass exchange from the canopy to the atmosphere is made evident by the retention of pollutant within the streets that persists for time that exceeds a typical advective time scale of the puff. This kind of simulations on an idealised urban district requires only few minutes when run on a standard laptop. Concerning a real scenario case, the application of the parallel version of SIRANERISK on the whole city of Paris requires between 5 and 10 min (depending on the frequency at which concentration field are produced as a model output).

The model is validated against wind-tunnel experiments (§3) of passive scalar dispersion within and above idealised city districts, involving both steady and unsteady releases. A systematic comparison between experimental and numerical results allows us to discuss the advantages and the limitations of model (§4) and to draw some conclusions and perspectives to the model development (§5).

2. From SIRANE to SIRANERISK

SIRANERISK is an operational atmospheric dispersion model that is able to simulate the dispersion of an unsteady airborne pollutant release within and above the urban canopy. Based on the street-network approach (Belcher et al., 2015; Soulhac et al., 2013, 2011), SIRANERISK is built on the same principles as the model SIRANE and assumes a decoupling of the domain in two parts, the external boundary layer flow and the urban canopy (Soulhac et al., 2011). Mass transfer phenomena within the two sub-domains and between them are modelled by means of parametric relations, and namely:

- The pollutant dispersion above roof level (Soulhac et al., 2011);
- The advective transfer along the street axes (Soulhac et al., 2008);
- The transfer at street intersections (Soulhac et al., 2009);
- The trapping of the pollutant within the street canyons due to the recirculating motion within them and the exchange with the overlying boundary-layer flow (Soulhac et al., 2013).

Since the details of each of these parameterisations have been already presented in the papers cited above, in what follows we provide a very concise presentation of the basic modelling principle implemented in the model. For further details on the adopted parameterisation and the model structure the reader is referred to (Soulhac et al., 2011) and (Ben Salem et al., 2015). In order to simulate the dispersion of unsteady releases, the model presents two main differences compared to SIRANE:

- The dispersion above roof height is simulated by means of a Gaussian puff model (§2.1) that includes a module for the effects of wind shear on the longitudinal puff spread;
- The mass balance is computed over control volumes that can be smaller than that of a street canyon (§2.2) and whose size can be variable with time.

2.1. Flow and dispersion above the urban canopy

The velocity field above the urban canopy is modelled as an atmospheric boundary layer over a rough surface which has reached a dynamical equilibrium condition. Therefore the flow is assumed to be homogeneous in the horizontal plane so that the velocity statistics depend on the vertical coordinate only, and can suitably be modelled by means of similarity profiles. The temporal evolution of the pollutant concentration field induced by an instantaneous release (at $t = 0$) of a mass M of pollutant from a point source (of coordinates x_0, y_0, z_0) is simulated by a generalised Gaussian puff model of the form

$$C = \frac{Q}{(2\pi)^{3/2}\sqrt{det(\Sigma)}} exp\left(-\frac{1}{2}\Delta^2\right) \quad (1)$$

where $\Delta^2 = (\mathbf{x}-\mathbf{x}_c)^T \times \mathbf{\Sigma}^{-1} \times (\mathbf{x}-\mathbf{x}_c)$ is the Mahalanobis distance (an iso-Mahalanobis distance curve corresponds to an iso-concentration line), $\boldsymbol{x}$ is the receptor position,

$$\boldsymbol{x}_c(t) = \iiint \boldsymbol{x}\bar{c}(\boldsymbol{x},t)d\boldsymbol{x} \quad (2)$$

is the position of the puff centre of mass and

$$\sum(t) = \begin{pmatrix} \sigma_x^2 & \sigma_{xy} & \sigma_{xz} \\ \sigma_{xy} & \sigma_y^2 & \sigma_{yz} \\ \sigma_{xz} & \sigma_{yz} & \sigma_z^2 \end{pmatrix} \text{ with } \sigma_{ij}(t) = \iiint (\boldsymbol{x}_i - \boldsymbol{x}_{c_i})\cdot(\boldsymbol{x}_j - \boldsymbol{x}_{c_j})\bar{c}(\boldsymbol{x},t)d\boldsymbol{x} \quad (3)$$

is the variance-covariance matrix. The flight time is computed as $t = x/U_p$, being U_p the speed of the puff centre of mass. Note that, by considering the variation of the height of the centre of mass as a function of time, it is then possible to take into account the effect of the flow inhomogeneity on the dispersion process. The terms of the variance-covariance matrix are expressed as follows:

$$\left.\frac{d\sigma_{ij}}{dt}\right|_{tot} = \left.\frac{d\sigma_{ij}}{dt}\right|_{turb} + \left.\frac{d\sigma_{ij}}{dt}\right|_{shear} \quad (4)$$

where the first term denotes the plume spread due to turbulent fluctuations, and the second term models the effects of the mean wind shear. As customary, the first term is modelled as

$$\left.\frac{d\sigma_{ij}}{dt}\right|_{turb} = \begin{cases} 2\sigma_{u,i}^2 T_{L,i}\left[1-\exp(-t/T_{L,i})\right] & \text{if} \quad i=j \\ 0 \quad \text{if} \quad i\neq j \end{cases} \quad (5)$$

where Lagrangian time scales are estimated as $T_{L,u_i} = \frac{2\sigma_{u_i}^2}{C_0\varepsilon}$ [16], with $C_0 = 4.5$ the Kolmogorov constant and $\varepsilon = \frac{u_*^3}{\kappa(z-d)}$ the turbulent kinetic energy dissipation rate ($\kappa = 0.4$ is the Von Karman constant, d is the displacement height, and u_* is the friction velocity of the overlying boundary layer flow, see §3.1). According to (Sykes and Henn, 1995), the shear contribution is modelled in the form:

$$\left.\frac{d\sigma_{ij}}{dt}\right|_{shear} = \sigma_{ik}\frac{\partial\overline{u}_j}{\partial x_k} + \sigma_{jk}\frac{\partial\overline{u}_i}{\partial x_k} \quad (6)$$

2.2. Flow and dispersion within the urban canopy

As in the SIRANE model, the district is considered as a network of connected streets, each of them characterised by its width W, height H and length L (Fig. 1a). The mass balance within each single street is then computed as follows (Fig. 1b):

$$\frac{d(HWLC_{street})}{dt} = Q_s + Q_{in} - Q_{out} - Q_{turb} \quad (7)$$

where Q_s is the pollutant mass rate emitted within the box, Q_{in} is the pollutant flux entering the street at its upstream section, Q_{out} is the pollutant flux flowing out of the street at its downstream section and Q_{turb} is the canopy/atmosphere vertical pollutant flux. The longitudinal and lateral spread of the pollutant puff within the urban canopy will be the result of the mass transfers, as modelled by (7), from one box to another. In what follows, we provide a brief description on how the fluxes Q_{turb},Q_{in} and Q_{out} in (7) are parameterised in the SIRANERISK model, based upon the principles of the SIRANE model.

The street-atmosphere vertical transfer in (7) is computed as:

$$Q_{turb} = u_d(C_{street} - C_{ext})WL \quad (8)$$

where u_d is a bulk exchange velocity (Barlow et al., 2004; Narita, 2007; Salizzoni et al., 2009a) whose intensity is assumed to be proportional to the friction velocity of the external atmospheric flow (see (Salizzoni et al., 2009a; Soulhac et al., 2013, 2011). As a default value, in SIRANERISK it is assumed that $u_d = 0.27u_*$ (Ben Salem et al., 2015). This latter relation was obtained by a theoretical model of the turbulent fluxes across a two dimensional shear-layer, whose details can be found in Soulhac et al. (2013). The vertical mass-transfer is modelled as solely due to the turbulent transfer, neglecting any contribution of the vertical mean velocity component. As recently shown by Buccolieri et al. (2015), this may lead to under predict the intensity of Q_{turb} in case of large wind incidence angles (with respect to the street axis) and in case of street aspect ratios H/W < 1.

The pollutant flux Q_{in} entering the street is computed by means of a specific model for pollutant transfer at street intersections as (Soulhac et al., 2009)

$$Q_{in,j} = \sum_i \overline{P_{ij}}\ C_{street,i} \quad (9)$$

where $\overline{P_{ij}}(\varphi)$, the air flux entering the downwind street j, is modelled as

$$\overline{P_{ij}}(\varphi) = \int_{\varphi_0-3\sigma_\varphi}^{\varphi_0+3\sigma_\varphi} f(\varphi^*-\varphi)P_{ij}(\varphi^*)d\varphi^* \quad (10)$$

with $P_{ij}(\varphi^*)$ the advective flux from street i to street j (computed by means of the algorithm presented in (Soulhac et al., 2009)), and with the wind direction φ^*, a random variable given by a Gaussian probability density function of the form:

$$f(\varphi^*-\varphi) = \frac{1}{\sigma_\varphi\sqrt{2\pi}}\exp\left(-\frac{1}{2}\frac{(\varphi^*-\varphi)^2}{\sigma_\varphi^2}\right) \quad (11)$$

where φ and σ_φ are the mean value and the standard deviation, respectively. The value of σ_φ depends on the meteorological conditions and on the geometry of the intersection. For operational purposes in SIRANE, it is usually assumed σ_φ as given by the ratio between the standard deviation of transversal velocity and the mean longitudinal velocity (Soulhac et al., 2012), both estimated as roof height, i.e. $\sigma_\varphi = \frac{\sigma_v(H)}{U(H)}$. In the present case we have $\sigma_\varphi = 12°$ (Ben Salem et al., 2015).

The downstream flux Q_{out} is equal to $HWU_{street}C_{street}$, where U_{street} and C_{street} are an advective velocity and concentration within the street, that in SIRANE are assumed both to be uniform over the whole street volume. The velocity U_{street} is computed with the analytical model developed by Soulhac et al. (2008) for the flow within a street which is inclined at an angle φ with the direction of the external wind:

$$U_{street} = u_*\cdot\cos(\varphi)\cdot h\left(\frac{H}{W},\frac{z_{0,build}}{W}\right)\cdot f(\varphi) \quad (12)$$

where $h\left(\frac{H}{W},\frac{z_{0,build}}{W}\right)$ is the reference value for an infinite street with an axis parallel to the external wind direction ($z_{0,build}$ represents the roughness of the street canyon walls) and $f(\varphi)$ is an empirical correction function (Garbero et al., 2010) to take account of the dynamical effects induced by the vortices with a vertical axis close

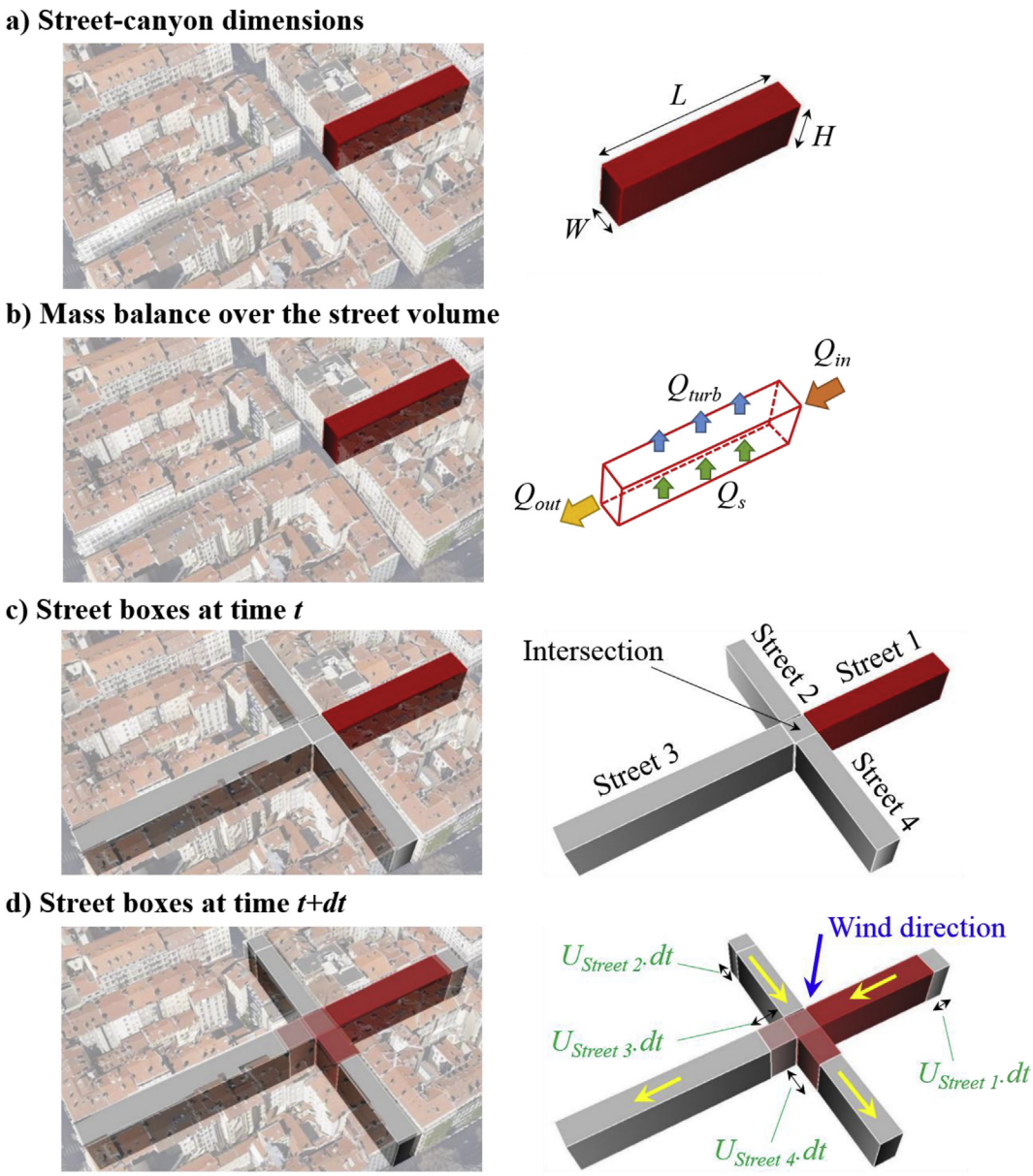

Fig. 1. Transport processes within the canopy: a) Street canyon dimensions, b) Mass balance over the street volume, c) and d) Advection transport along the streets, with the creation of Lagrangian boxes which move along each street.

to the street intersections.

It is worth noting that, in the case of unsteady advection-diffusion of the concentration, the SIRANE parameterisation for Q_{out} will generate an instantaneous longitudinal advective transfer within a single street (from the upwind to the downwind intersection), and therefore introduce a numerical diffusion in the simulations, leading to an over prediction of the longitudinal spreading of the pollutant plume as a function of time. To avoid this spurious effect and properly model the unsteadiness of the transfer of a pollutant puff within the urban canopy, we have implemented in SIRANERISK an algorithm of "Lagrangian moving boxes" that discretises the street canyon volume in several boxes, moving along each street according to its mean advective velocity U_{street}. This Lagrangian scheme prevents the effect of a longitudinal numerical diffusion and ensures a lower computation time compared to a CFD like Eulerian approach, which would require a high resolution mesh. As shown in Fig. 1c and d, this discretisation evolves for each time step, since the boxes are created at the street upwind section and are evacuated at the street downwind section.

3. Wind tunnel experiments

The experiments were performed in the recirculating wind tunnel of the Ecole Centrale de Lyon, having a test section measuring 14 m long, 2.5 m high and 3.7 m wide. The passive scalar dispersion took place in three flow configurations (Fig. 2) simulating neutral atmospheric boundary layers developing over different obstacle arrays. These were obtained by combining the effect of spires (Irwin, 1981) of varying height placed at the beginning of the test section and roughness elements of different size H (and spacing). In all studied cases, the obstacle arrays simulating urban blocks covered the entire working section in order to avoid the development of an internal boundary layer due to roughness changes.

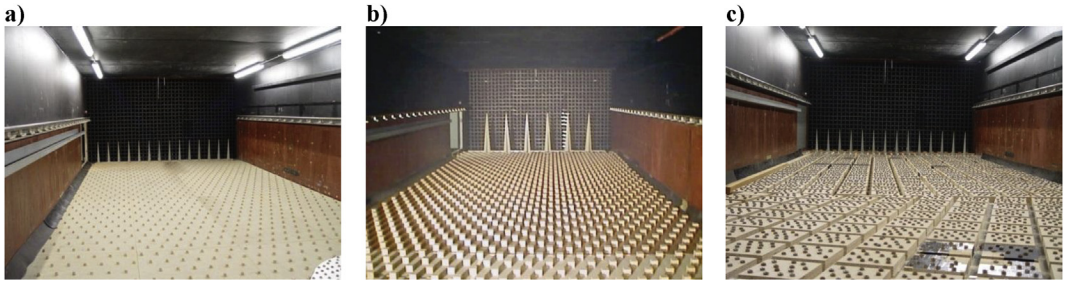

Fig. 2. Experimental set-up for the a) R20, b) R50 and c) B50 configurations.

In the first configuration, referred to as R20 (Fig. 2), the height of the vortex generators was equal to 50 cm and the floor was covered by a staggered array of cubes of size 20 mm, spaced of 17 cm longitudinally and 13 cm laterally. This flow configuration is identical to that analysed by Nironi et al. (2015) in order to study the dynamics of a fluctuating plume within a turbulent boundary layer. In the second configuration, referred to as R50, the height of the vortex generators was equal to 100 cm and the cubes were 50 mm high and spaced (longitudinally and laterally) by a distance of 50 mm.

The configuration B50 (Fig. 2) is the same as that studied by Garbero et al. (2010) and represents an idealised urban district, made up of an array of equal-height (H = 50 mm) squared base ($L = 5H$) obstacles, separated by a distance H. The obstacles were covered by nuts in order to simulate the effects of smaller scale roughness elements (Salizzoni et al., 2008, 2009b). The simulated urban district was overlain by a neutrally stratified boundary whose depth δ was approximately 0.8 m, generated by a row of 0.5 m high spires. The free-stream velocity U_∞ at the top of the boundary layer was equal to 5 m·s^{-1}. Differently from the two others configurations, experiments in the B50 configuration were performed for varying angles of the incident wind according to the district orientation.

Geometrical details on the configurations, including the values of the planar λ_P and frontal area index λ_F (computed according to the definition of Grimmond and Oke (1999)), and the relative main flow parameters are given in Table 1.

In all the three cases, the source was placed at a distance of about 10δ from the beginning of the test section, where the boundary layer flow had already reached an equilibrium condition. The source height for both the R20 and R50 configurations was larger than the obstacle height and equal to $H_r = 25$ mm for R20 and H_r = 60 mm for R50. Conversely, for the B50 configuration, H_r = 25 mm ($H/2$), and was therefore lower than the obstacle height. In this latter case the source was placed at a street intersection within the array (see Garbero et al., 2010).

3.1. Velocity field

The velocity field above the obstacle arrays was investigated by means of hot-wire anemometer with an X-probe. For each measurement point, we registered 5 min signals with a frequency of 5000 Hz. Details on the probe calibration are provided in (Nironi et al., 2015). Vertical profiles of the first and second-order moments of the velocity are plotted in Fig. 3. The mean velocity profiles in the lower part of the boundary layer are well fitted (Fig. 3a) by a logarithmic law of the form:

$$U(z) = \frac{u_*}{\kappa}\ln\left(\frac{z-d}{z_0}\right) \tag{13}$$

where z_0 is the roughens length.

We have estimated the friction velocity as $u_* = \sqrt{-\overline{u'w'}}$ by averaging the $\overline{u'w'}$ data in the lower part of the flow field (Fig. 3b) where the Reynolds stresses vary only slightly with respect to their average value. The two other parameters, z_0 and d, are then estimated through the best fit of the mean velocity profile with the logarithmic law (13), assuming the computed value of u_*. Conversely, the mean longitudinal velocity throughout the whole boundary layer is suitably modelled with a power-law of the form (Ben Salem et al., 2015):

$$\frac{U}{U_\infty} = \eta^n, \tag{14}$$

where $\eta = (z\text{-}d)/(\delta\text{-}d)$ is the normalised vertical coordinate and where the values of the exponent n depend on the wall roughness (see Table 1).

Fig. 3-b-c shows that the profiles of the second-order velocity statistics registered in the three configurations, when rescaled on u_*, can be expressed as invariant functions of $\eta = (z\text{-}d)/(\delta\text{-}d)$, which proves that the three flow configurations are dynamically similar. Namely, the profiles of the standard deviations (Fig. 3-c) of the fluctuating velocities are well fitted by the following 3rd order polynomials:

$$\sigma_u = 2.44u_*\left(1 + 0.68\eta + 0.67\eta^2 - 0.67\eta^3\right), \tag{15a}$$

$$\sigma_v = 1.66u_*\left(1 - 0.15\eta - 0.120\eta^2 - 0.38\eta^3\right), \tag{15b}$$

$$\sigma_w = 1.2u_*\left(1 + 0.96\eta - 2\eta^2 + 0.4\eta^3\right), \tag{15c}$$

Note that, as shown by Garbero et al. (2010) and Ben Salem et al.

Table 1
Parameters of the obstacle array and of the overlying boundary layer flows for the three configurations studied (boundary layer height δ, friction velocity u_*, source height H_r, roughness length z_0, displacement height d, obstacle height H, planar λ_P and frontal area index λ_F exponent n of the power-law, see (14)).

Config.	δ (m)	u_* (m·s^{-1})	H_r (m)	z_0 (m)	d (m)	H(m)	λ_P	λ_F (0°)	n
R20	0.8	0.18	$2.5\cdot10^{-2}$	10^{-4}	$7\cdot10^{-3}$	$2\cdot10^{-2}$	0.018	0.018	0.25
R50	1.2	0.24	$6\cdot10^{-2}$	$1.14\cdot10^{-3}$	$3.8\cdot10^{-2}$	$5\cdot10^{-2}$	0.25	0.25	0.29
B50	0.8	0.22	2.5 ·10-2	$1.32\cdot10^{-4}$	$5\cdot10^{-2}$	$5\cdot10^{-2}$	0.69	0.14	0.27

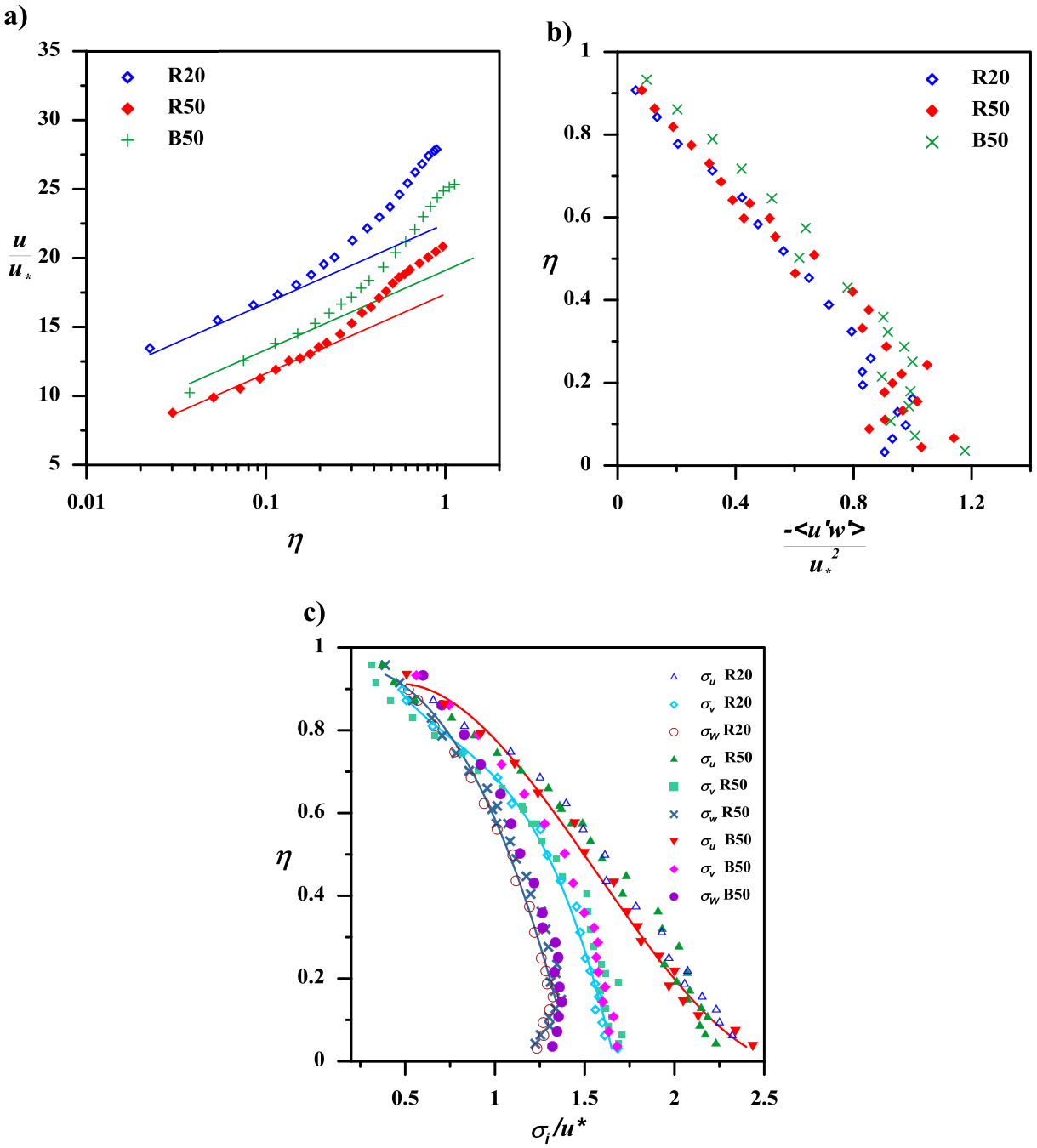

Fig. 3. Experimental characterisation of the turbulent boundary layer above the idealised urban canopy. (a) Vertical profiles of the mean longitudinal velocity: symbols represent experimental data whereas lines refer to the logarithmic profiles (13). (b) Vertical profiles of the non-dimensional Reynolds stress (c) Vertical profiles of the standard deviation of the three velocity component: symbols represent experimental data whereas lines refer to 3rd order polynomials given by (15a), (15b) and (15c).

(2015), for the B50 configuration the flow field above the obstacle array was not sensitive to variations of the wind directions. This feature is directly related to the nature of the skimming flow regime developing above the simulated urban canopy (Salizzoni et al., 2008; Ben Salem et al., 2015).

3.2. Passive scalar dispersion

The passive scalar dispersion experiments consisted in the simulation of steady and unsteady releases of ethane (C_2H_6) from a point source placed at varying height (Table 1), within the simulated neutral atmospheric boundary layer flow. The source was composed of a curved tube with a circular section, having an 8 mm external diameter and a 6 mm internal diameter. In the unsteady experiments, the release was produced by a piston expelling a mass M of pure ethane, corresponding to a volume of 28.4 cm^3. This source configuration is a compromise between different constraints, namely to have a source i) small enough not to filter out the effects of meandering on the puff dispersion and ii) large enough not to generate an excessive outlet velocity.

The ejection lasted of 0.17 s (Fig. 4a), simulating an impulsive release. The duration of this release was chosen so as to emit a mass of ethane sufficiently large to allow for its detection at a distance of 4 m from the source but not as high as to produce excessive flow

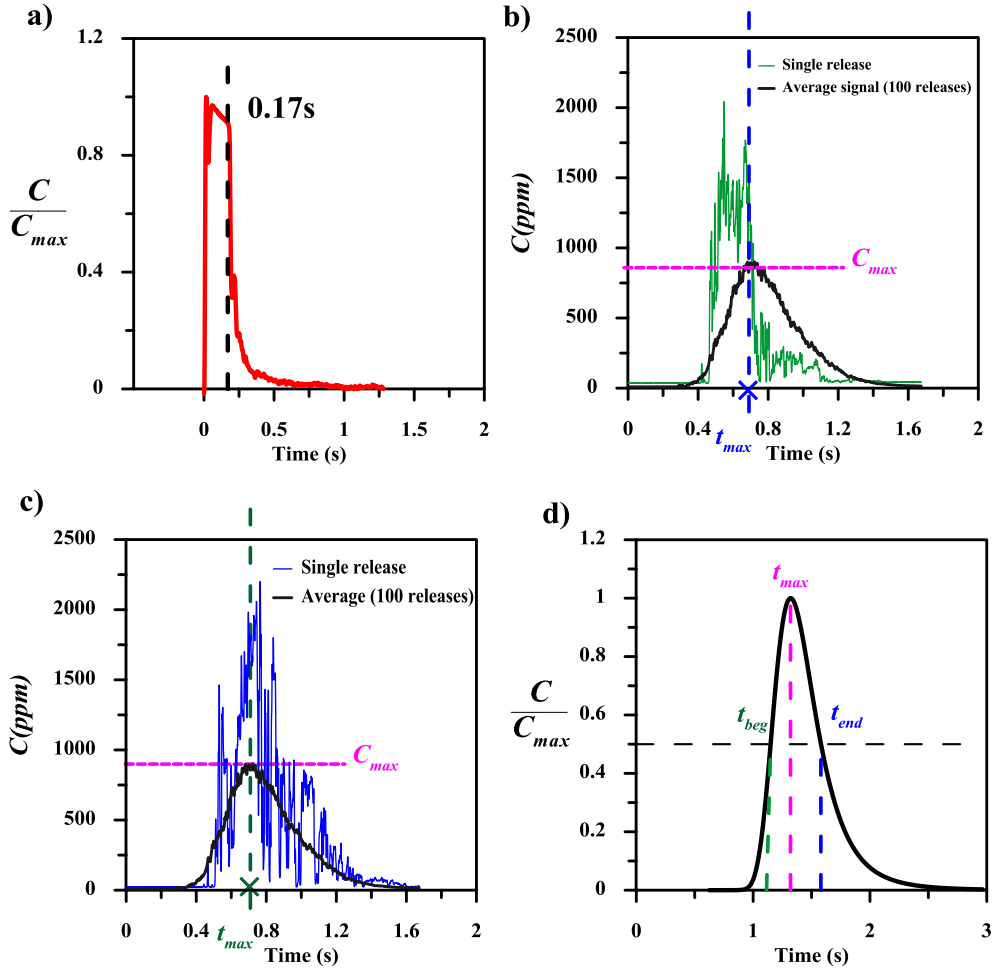

Fig. 4. a) Concentration signal registered at the source during the emission. b) and c) Temporal evolution of the concentrations down-wind the source: comparisons between signals registered during a single realisation of the experiment at $x^* = 2.5$, $y^* = 0$ and $z^* = 0.031$ (see text) and the ensemble averaged signals (computed over 100 realisations). (d) Definition of characteristic puff advective time t_{max} and characteristic time of the longitudinal puff spread (t_{end}−t_{beg}).

perturbation close to the release point. Velocity at the source was 5.9 m s^{-1}. Using a simple analytical model for a co-flowing jet (Blevins, 1984), the relative velocity difference between the passive scalar release and the surrounding flow was estimated to be of approximately 26% at 25 cm from the source, 13% at 50 cm and 6.5% at 1 m.

Passive scalar concentrations were measured by means of a Flame Ionisation Detector, with a sampling frequency of 400 Hz (Nironi et al., 2015). For steady releases, signals were recorded over 2 min. For unsteady releases, in order to achieve a reliable statistical description of the time-dependent concentration field induced by the pollutant releases, experiments were repeated 100 times for each measurement point. This allowed us to estimate an ensemble average time-dependent concentration, for each measurement location. We show in Fig. 4-b-c two comparisons between single concentration signal (as a function of time) and average over 100 of these signals, measured for the R20 configuration at $x^* = 2.5$, $y^* = 0$ and $z^* = 0.031$ (distances are made dimensionless using the boundary layer δ height as a length scale). As Fig. 4-b-c show, the fluctuation levels compared to the ensemble average can be extremely different from one realisation to another. The time-dependent ensemble averages were used as a benchmark to validate the results provided by the model. In particular, the model validation was based on the comparisons of three parameters (Fig. 4-c-d): i) the maximal value of the ensemble averaged concentration, referred to as $C_{\max}$ (Fig. 4-b), ii) a characteristic advection time, referred to as $t^*_{\max}$, and iii) a time lapse representative of the longitudinal spreading, referred to as $(t^*_{end} - t^*_{beg})$.

For the R20 and R50 configurations, in which the source is higher than the obstacle height, experiments were performed for a single wind direction and both steady and unsteady measurements were located at the source height, i.e. above the obstacle array. For the B50 configuration, in which the source is placed within the obstacle array, experiments were performed for varying wind directions and concentration signals were measured within ($z/H = 1/2$) and above ($z/H = 2$) the urban canopy. Note that the results for steady releases in the B50 configuration are those of (Garbero et al., 2010), who performed experiments for four different wind directions: $\varphi = 2.5°$; $\varphi = 10°$; $\varphi = 25°$; $\varphi = 45°$. In this same experimental set-up, we have performed a new series of experiments to simulate the dispersion of impulsive pollutant releases, for two different wind directions only, i.e. $\varphi = 30°$ and $\varphi = 45°$.

4. Results

We verify the reliability of the SIRANERISK model by comparing its results to those provided by wind tunnel experiments. Firstly (§ 4.1), we analyse the dispersion within a turbulent boundary layer over varying roughness walls, i.e. in the R20 and R50 configurations. In this case, the focus will be mainly on the effects of

longitudinal shear on the dispersion of unsteady releases.

Secondly (§ 4.2), we analyse the dispersion within and above a dense urban canopy, i.e. the B50 configuration. For this configuration, we initially evaluate the dispersion of steady releases (§ 4.2.1) discussing the performances of the SIRANERISK model compared to those of the SIRANE model. Subsequently, we focus on the ability of SIRANERISK in predicting ensemble averaged concentrations of unsteady releases (§ 4.2.2), and namely on the level of the concentration peaks, their arrival time at a given receptor and their longitudinal spread.

4.1. Configuration R20 and R50 – dispersion above sparse city districts

In the R20 and R50 configurations, the source emits above the obstacles placed on the ground, in a region of the flow where the mean shear rate is maximal. In simulating this dispersion process, we do not explicitly represent the obstacle array, whose effect on the flow is therefore taken into account as a distributed drag acting on the overlying boundary layer. Therefore to run the simulations, we only use the module for the dispersion above the urban canopy presented in §2.1. This requires to set the vertical profile of the mean longitudinal velocity, given here by (14) (with varying values of the n exponent given in Table 1), and of the standard deviation of the three velocity components, computed by means of (15a), (15b) and (15c), adopting the corresponding values of the friction velocity u_* (Table 1). These data are used to compute the spreading (4) of the puff and displacement of its centre of mass. In what follows, our analysis mainly focuses on the modelling of the wind shear effect, i.e. the terms, on the passive scalar dispersion.

The spatial evolution of the mean concentration field downwind from a steady source of pollutant is a problem that has been extensively studied in the literature (e.g. Fackrell and Robins, 1982). Therefore, for brevity, we do not show here the results for these cases. These were essentially used to perform preliminary comparisons to check the accordance of our Gaussian-puff model with the experimental data. The only thing we want to point out is that, in case of steady releases, the concentration results computed activating and deactivating the contribution of the wind shear, i.e. (6), are very similar, showing that, as pointed out by previous authors (e.g. Chatwin, 1968), this effect has almost no influence on the lateral and vertical spread of a steady plume.

We focus instead on the case of unsteady puff releases. These have equally received a considerable attention over the years, since the pioneering theoretical work of (Chatwin, 1968). Experiment on puff-like releases have been however more rarely presented in the literature, due to the higher complexity of the set-up and measurement techniques required to perform these experiments (Yee, 1998).

We show in Fig. 5 the evolution of the non-dimensional concentration for configurations R20 and R50 as a function of the non-dimensional time $t^* = \frac{tU_\infty}{\delta}$, registered at five different transversal positions and for different distances from the source. The comparison between experimental and numerical results show that the time-dependent concentration signals modeled by activating the shear model are quite different from those calculated without it (Fig. 5).

As Fig. 6-a shows, the maximum concentrations calculated by the Gaussian puff model including the effect of shear reproduces well the experimental results whereas neglecting this effect leads to systematically overestimating the maximal concentration and underestimating the longitudinal puff spreading. The comparison with experiments shows that the model reproduces accurately the characteristic longitudinal spread of the mean puff in both configurations R20 and R50 (Fig. 6-b) when the effect of shear is properly taken into account. However (see Fig. 6-c), the time of occurrence of peaks of the ensemble averaged signals can be also reliably predicted by a conventional Gaussian puff model. This can be explained by the fact that the centre of mass of the puff moves at the same speed in both models, and is therefore not affected by the role of shear. In other words, the shear acts in modifying the longitudinal puff spread and, therefore, its structure around its centre of mass, but does not alter the velocity at which the centre of mass moves downstream. All these features confirm experimental findings presented in previous experimental studies, e.g. (Yee, 1998), and support the theoretical analysis originally developed by Chatwin (1968).

This highlights the reliability of the parameterisation of wind shear (4) included in the generalised Gaussian model (1) in reproducing the physics of the dispersion of a short-duration release of a passive scalar in the atmospheric boundary layer. The wind shear induces a dilution of the pollutants within the plume associated with the increased longitudinal dimension of the puff. Indeed, for the same amount of mass released into the atmosphere, the modelling of the stretching of the puff is crucial in correctly predict the decrease of concentration levels downwind the source. Therefore this effect is generally taken into account in Gaussian puff dispersion models (Hunt, 1982; McHugh et al., 1997).

4.2. Configuration B50 – dispersion within a dense city district

In the case B50, the model for flow and dispersion above the canopy is similar to that adopted for R20 and R50 (with different values of u_* and n). Differently from the two aforementioned cases, the urban canopy is explicitly modelled by means of the street network module (§ 2.2). This requires three parameters to be set: the empirically-derived corrective function $f(\varphi)$ for the computation of the mean advective velocity U_{street}, the intensity of the velocity fluctuation σ_φ to compute mass exchanges at street intersections, and the non-dimensional canopy-atmosphere exchange velocity u_d/u_*. The function $f(\varphi)$ is determined as (see Ben Salem et al. (2015))

$$\begin{cases} f(\varphi) = 1 + a\dfrac{\varphi}{\pi}\left(\dfrac{\varphi}{\pi} - b\right) & \text{for } 0 \le \varphi \le \dfrac{\pi}{2} \\ f(\varphi) = f(\pi - \varphi) = f(-\varphi) & \text{for } \varphi \notin \left[0, \dfrac{\pi}{2}\right] \end{cases} \tag{16}$$

with $a = 6.4$ and $b = 0.5$. The value of exchange parameters σ_φ and u_d/u_*, for the four wind directions considered are given in Table 2. These parameters are not the reference values currently adopted in the SIRANE model, i.e. $\sigma_\varphi = \frac{\sigma_v(H)}{U(H)} = 12°$ and $u_d/u_* = 0.27$, but are the ones providing the best agreement between the SIRANE model and the experimental results in the analysis performed by Ben Salem et al. (2015).

The interpretation of the physical causes inducing the variability of σ_φ and u_d/u_* with φ shown in Table 2 has been extensively discussed in Ben Salem et al. (2015) and is beyond the scope of the present analysis. This will instead focus on the effects of a finer spatial discretisation of the domain within the canopy. It is however to note that, in general, adopting the reference value $\sigma_\varphi = \frac{\sigma_v(H)}{U(H)} = 12°$ and $u_d/u_* = 0.27$ deteriorates only slightly the model performances (Ben Salem et al., 2015) since they alter significantly the values of the statistical indices used to evaluate the model, according to the criteria proposed by Chang and Hanna (2004) (see § 4.2.1).

4.2.1. Steady releases

We begin by analysing the results for the case of steady releases. SIRANERISK results are systematically compared to the

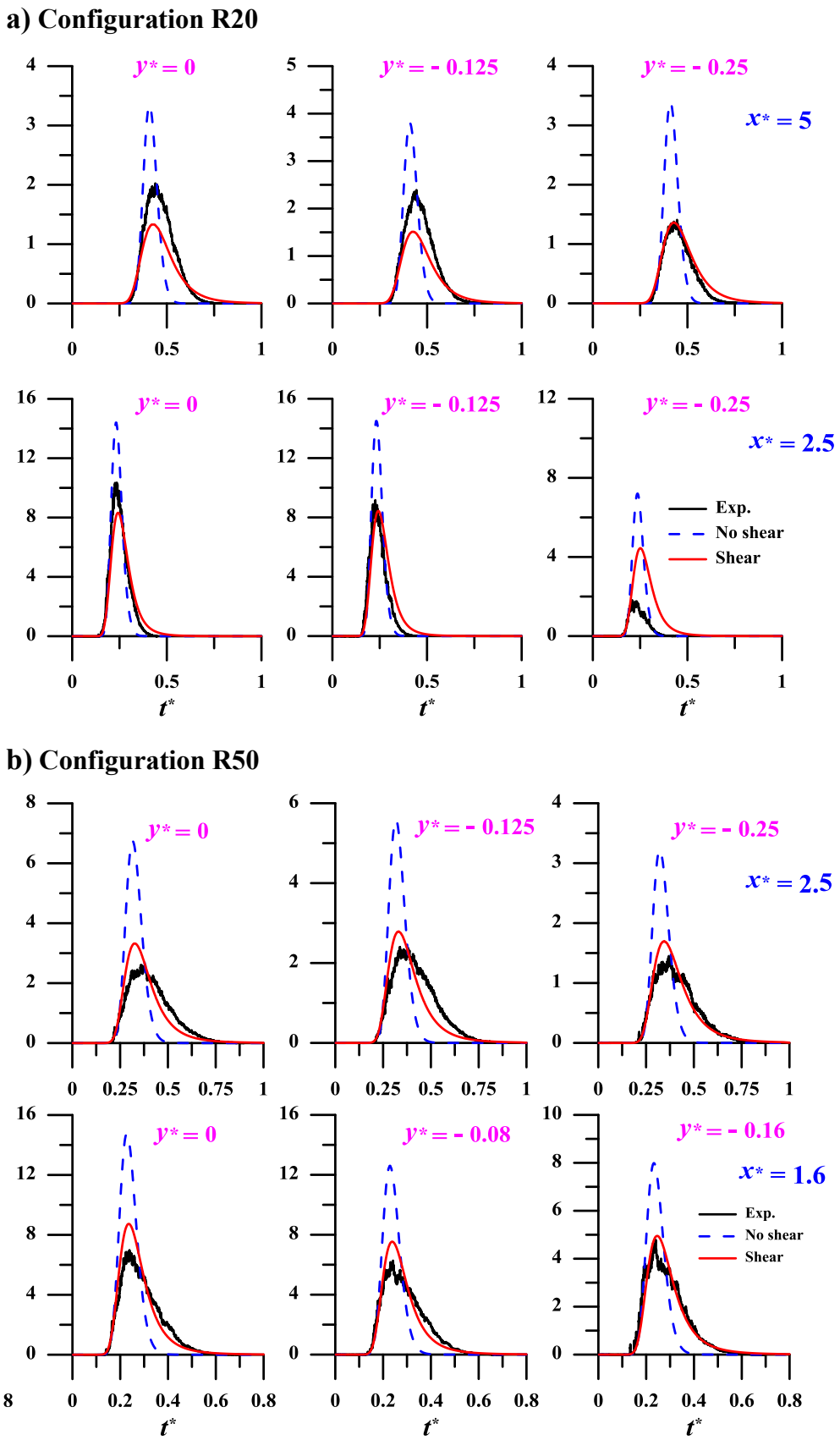

Fig. 5. Time dependent ensemble averaged concentration in the a) R20 and b) R50 configurations. Evolution of the non-dimensional concentration $C^* = C\delta^3/M$ at receptors placed at varying distances from the source $x^* = \frac{x}{\delta}$ as a function of the non-dimensional time $t^* = \frac{tU_\infty}{\delta}$. Comparison between experimental signals (black) and SIRANERISK prediction obtained with (red) and without (blue) the effect of wind shear. (For interpretation of the references to colour in this figure legend, the reader is referred to the web version of this article.)

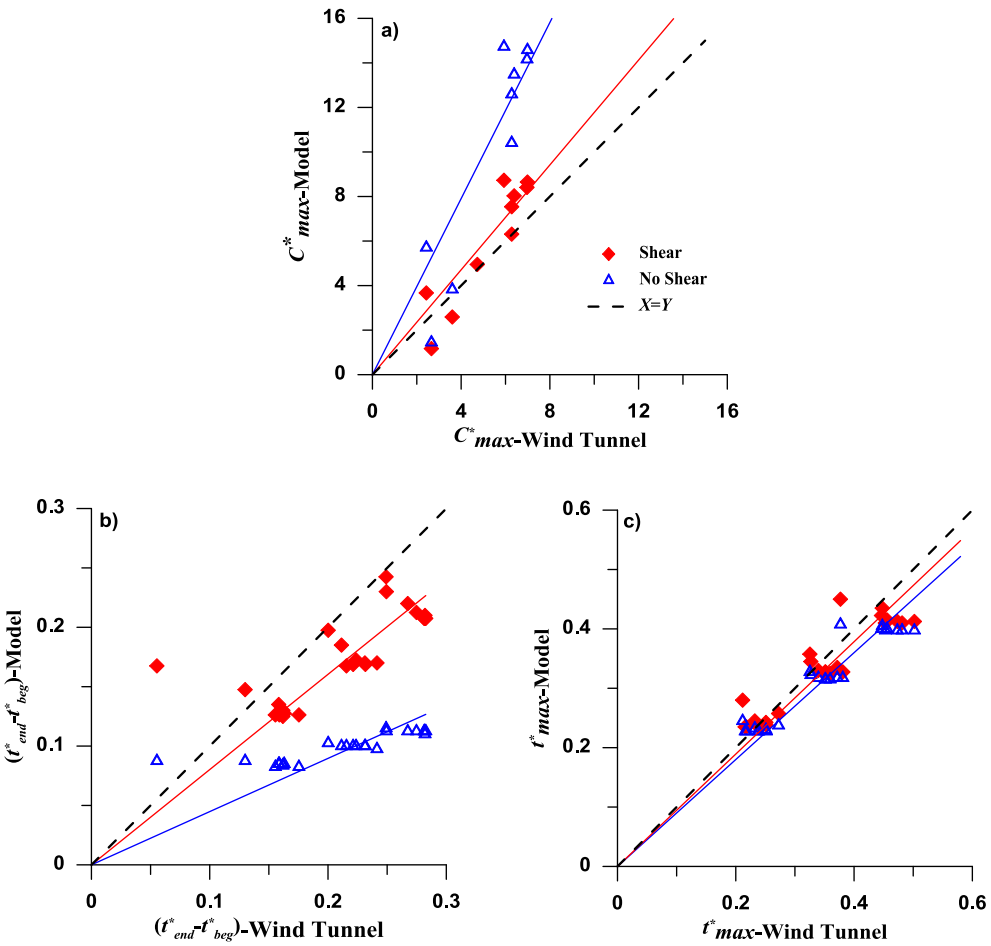

Fig. 6. Scatter plots comparing results provided by the experiments and SIRANERISK simulations without (blue triangles) and with (red diamonds) the effect of shear for configurations R20 and R50. (a) Maximal ensemble-averaged concentrations, (b) longitudinal puff spreading and (c) averaged advection times. (For interpretation of the references to colour in this figure legend, the reader is referred to the web version of this article.)

Table 2
Values of the exchange parameters σ_φ and u_d/u_* adopted in the simulations for the configuration B50.

	$\varphi = 2.5°$	$\varphi = 10°$	$\varphi = 25°$	$\varphi = 45°$
σ_φ	15°	15°	30°	30°
u_d/u_*	0.3	0.35	0.25	0.55

experimental data and to the results provided by SIRANE, presented by Ben Salem et al. (2015). The aim of this analysis is to examine the influence of the finer discretisation of the domain within the canopy adopted by SIRANERISK in which the lengths of the boxes are smaller than that of the streets, compared to that adopted by SIRANE which models each street as a single box (§ 2.2). Therefore we do not focus on the accuracy of the model parameterisations, a subject that has been widely discussed by Ben Salem et al. (2015).

In order to quantify the agreement between the simulations and the experiments, we take into account four statistical parameters, as is customary in the recent literature (Chang and Hanna, 2004), which help in quantifying the differences observed between C_p^*, the non-dimensional averaged concentration predicted by SIRANE, and C_m^*, the one measured in the experiments (the concentrations for steady releases are made dimensionless by dividing them by $\Delta C = Q/(U_\infty \delta^2)$). These are the correlation coefficient R, the fractional bias FB, the normal mean square error $NMSE$, defined as,

$$R = \frac{\overline{\left(C_p^* - \overline{C_p^*}\right)\left(C_m^* - \overline{C_m^*}\right)}}{\sqrt{\overline{\left(C_p^* - \overline{C_p^*}\right)^2}\,\overline{\left(C_m^* - \overline{C_m^*}\right)^2}}} \tag{17}$$

$$FB = \frac{\overline{C_p^*} - \overline{C_m^*}}{\frac{1}{2}\left(\overline{C_p^*} + \overline{C_m^*}\right)}, \tag{18}$$

$$NMSE = \frac{\overline{\left(C_p^* - C_m^*\right)^2}}{\overline{C_p^*}\;\overline{C_m^*}}, \tag{19}$$

and the fraction of observations within a factor 2 of Prediction (FAC2), defined as the fraction of data having the properties $0.5 \leq \overline{C_p^*}/\overline{C_m^*} \leq 2$, respectively. The statistical indices are computed in two ways: considering all the data above and within the canopy, and considering the data within the canopy only. The comparison between the three datasets is presented in Figs. 7–10, for the four wind directions considered. A summary of the model performances, compared to those of SIRANE, is given in Table 3.

For $\varphi = 2.5°$ (Fig. 7-a,b,c,d), SIRANERISK results are almost identical to those computed by SIRANE (see Fig. 7 and Table 3). The

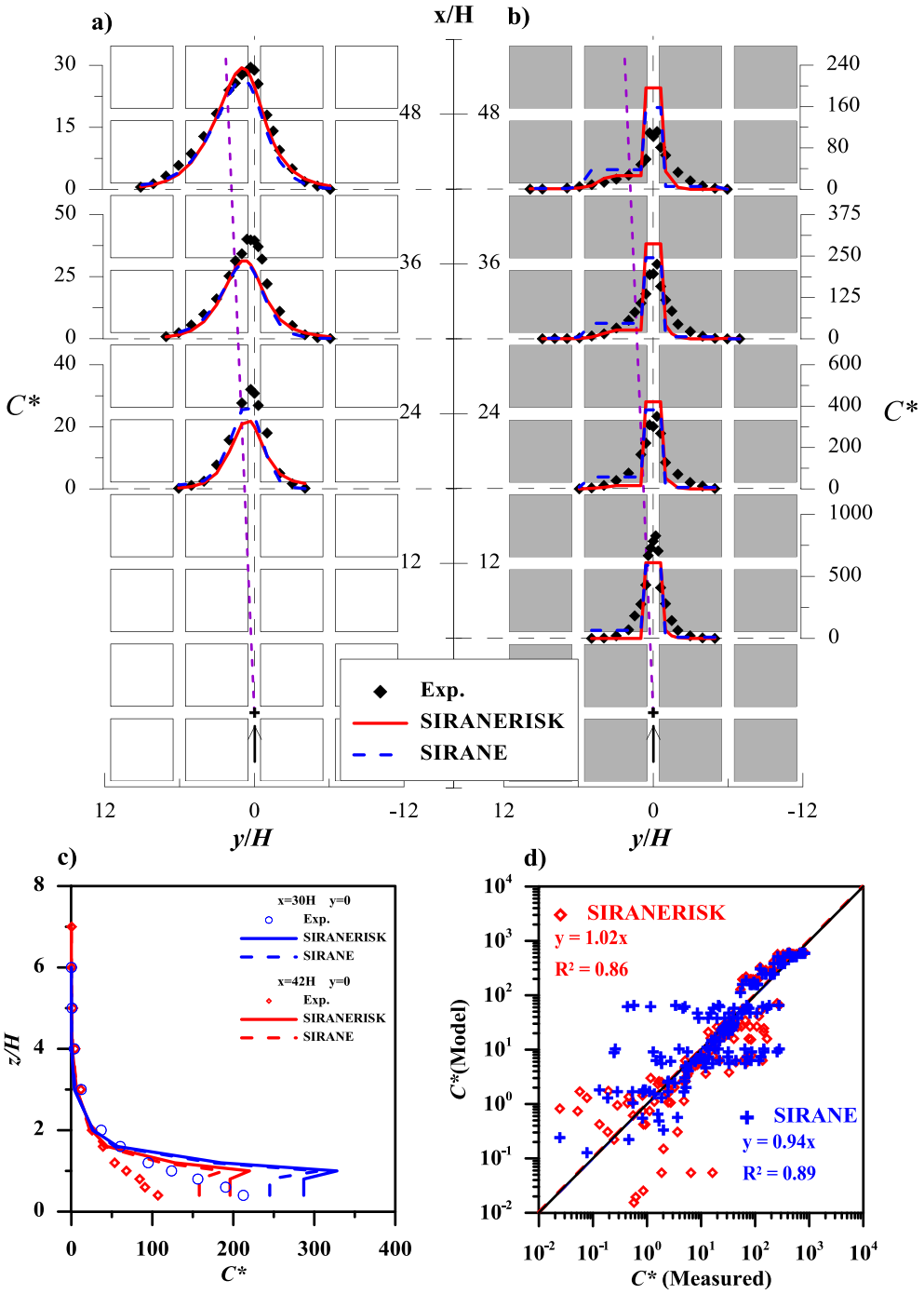

Fig. 7. Steady plume behaviour throughout the array for $\varphi = 2.5°$. Comparison between experimental data (black diamonds) at varying distance from the source position (+) with numerical results of the SIRANERISK model (red line) and SIRANE model (blue dashed line) above the canopy (z = 2H) (**a**) and (**b**) within it (z = H/2). (**c**) Comparison between the experimental vertical profiles (points) and the numerical results (lines) at different heights. (**d**) Scatter plots comparing the concentrations predicted by SIRANERISK and SIRANE with the all wind tunnel data. (For interpretation of the references to colour in this figure legend, the reader is referred to the web version of this article.)

model generally reproduces well the concentration distribution within and above the canopy. As already enlightened by Ben Salem et al. (2015), the main limitation of the model for these low angle configurations is its inability in predicting the turbulent mass fluxes directed towards the transversal streets (Fig. 7-b). It is of note that this limitation persists in SIRANERISK, i.e. even when adopting a finer discretisation of the domain within the canopy.

Transversal profiles above the canopy (Fig. 7-a) are almost indistinguishable. The only differences between the two models can be detected at the farthest downstream sections, where SIRANERISK tends to predict higher concentrations (Fig. 7-b,c). However, the overall comparison of the experimental results with the two models shows that the slope of the regression line (Fig. 7d) and the relative R^2 coefficient for the SIRANE and SIRANERISK results are very close one to the other.

The case $\varphi = 10°$ (Fig. 8-a,b,c,d) is the only configuration within which SIRANERISK seems to effectively benefit from a finer spatial discretisation within the canopy. Even though the concentrations

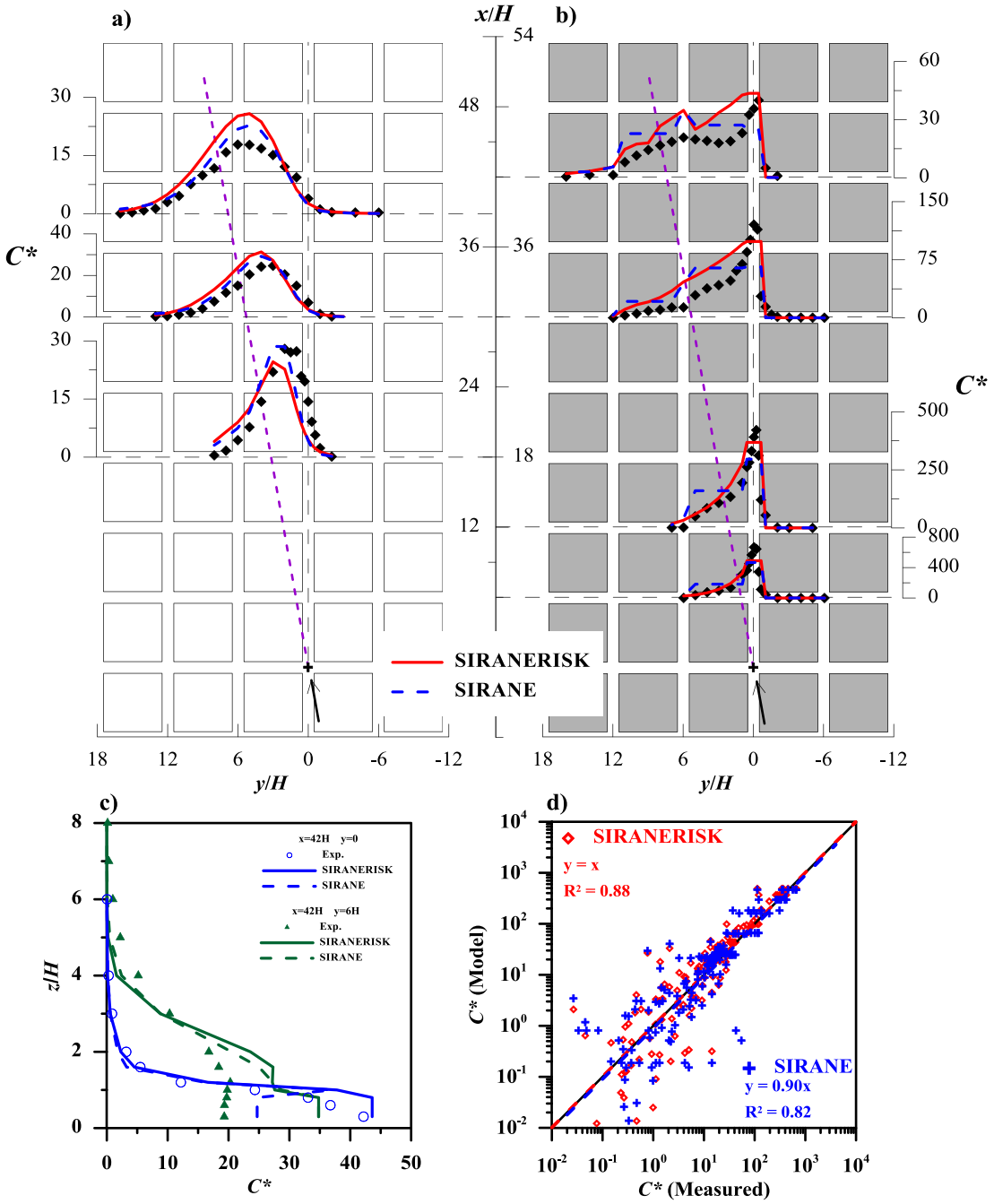

Fig. 8. As in Fig. 7 for $\varphi = 10°$.

above the canopy (Fig. 8-a,c) are very similar to those computed by SIRANE (and in a general good agreement with experimental data), the two models show significant differences in predicting concentration levels within the canopy. This is evident in particular by analyzing the concentration profiles along the transversal street. Differently from SIRANE that computes a unique spatially averaged concentration within each street, SIRANERISK is able to reproduce the high pollutant gradients within the transversal street, especially close to the source. However, note that this ability of SIRANERISK does not necessarily results in better performances of the model, compared to SIRANE, as estimated by the values of the statistical indices (see Table 3).

In the configuration $\varphi = 25°$ and $\varphi = 45°$, the results (Figs. 9 and 10) provided by SIRANERISK differ very slightly from those of SIRANE, and are in a general good agreement with the experimental data. This shows that the finer spatial discretisation adopted by SIRANERISK has almost no effect on the results both within (Figs. 9-b and 10-b) and above the canopy (Figs. 9-a and 10-a and Figs. 9-c and 10-c). In these configurations, the concentration field within the canopy is effectively characterised by almost constant levels within the street and abrupt variations at street intersections (Figs. 9b and 10b). A description of the concentration field at the street scale is therefore sufficient to capture this kind of variability within the canopy.

4.2.2. *Unsteady releases*

Finally, we analyse the performances of SIRANERISK in simulating the dispersion of unsteady releases within a dense urban

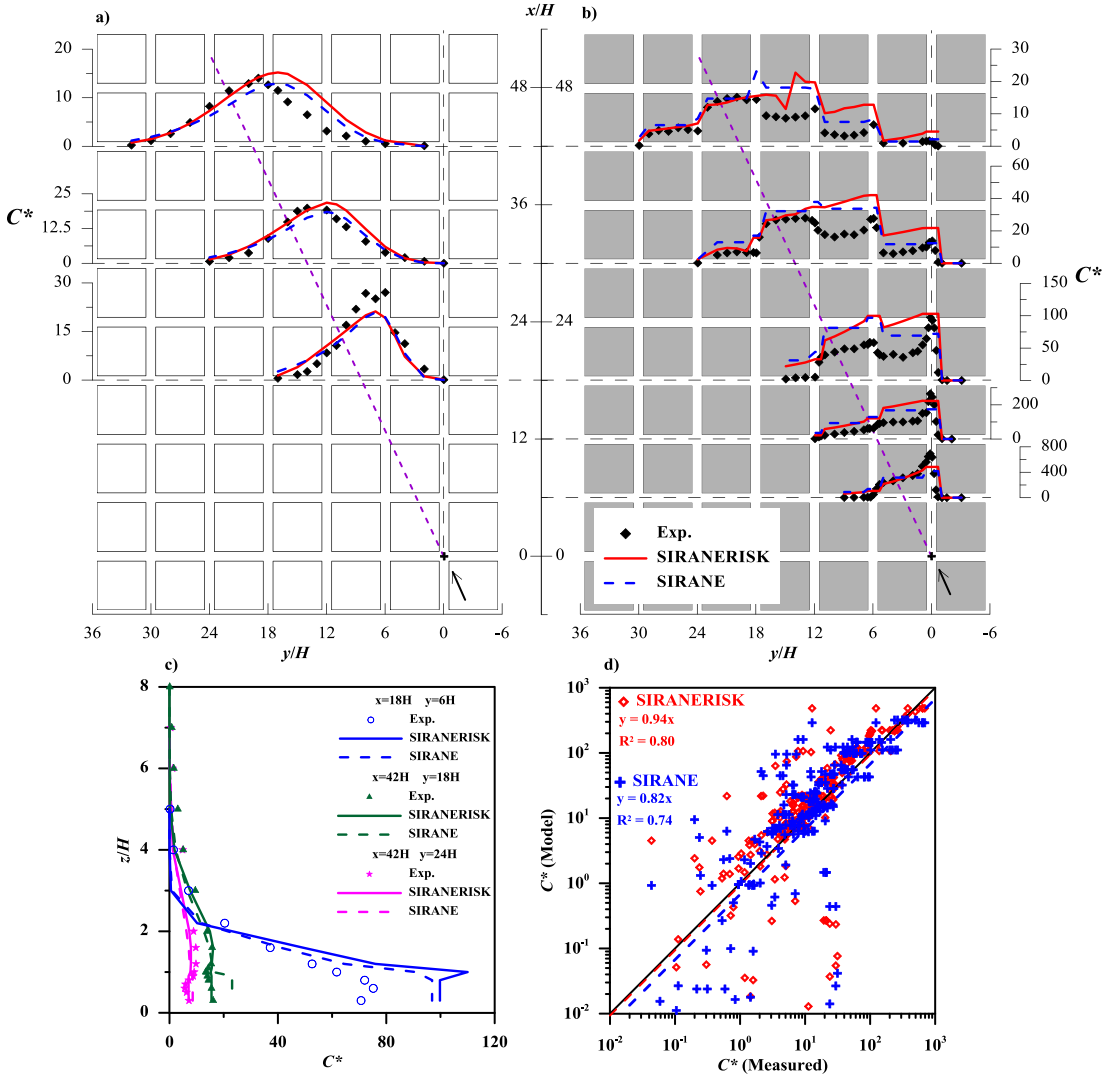

Fig. 9. As in Fig. 7 for $\varphi = 25°$.

canopy. Numerical results are compared to the experimental results obtained for two wind directions: $\varphi = 25°$ and $\varphi = 45°$. The location of the measurements points for these experiments is shown in Fig. 11.

A direct comparison between measured and simulated non-dimensional concentration for different locations downwind of the source within and above the urban canopy is presented in Figs. 12 and 13. Unlike the previous cases presented, concentrations are made dimensionless adopting the obstacle height H (and not the boundary layer height δ) as a length scale. The model predictions for the dense city district case (Fig. 13) look very different from those obtained for the boundary layer flow (Fig. 5). The simulated time dependent concentrations exhibit significant fluctuations, especially within the canopy (Fig. 13a). These are the results of several puffs passing through the position where these signals are recorded. The puffs reach this position travelling along different trajectories, within and above the canopy, and can therefore be characterised by concentration levels that can be very different. Their superposition can therefore produce concentration signals characterised by abrupt variations.

Results indicate that the model provides generally better agreement with the experimental results above the canopy than within it. For $\varphi = 25°$ (Fig. 12), the concentration signals above the canopy show a remarkable agreement with the experiments. The main differences between the two can be observed for the receptors located at the right border of the plume and can be reasonably attributed to a slight error in the evaluation of the wind direction (Ben Salem et al., 2015), where the experimental estimate was affected by an uncertainty of ±2.5° (Garbero et al., 2010). Results for $\varphi = 45°$ are slightly less accurate than for the $\varphi = 25°$ case. However, the model reproduces well the arrival time of the pollutant front, and the subsequent reduction of the concentration levels as a function of time (Fig. 14).

Within the canopy, results show that SIRANERISK is generally able to reproduce qualitatively the time evolution of the ensemble averaged concentration. For given receptors, and for both wind directions, the agreement with the experiment is excellent. This is the case for the receptors placed closed to the axis of the ensemble averaged plume centerline, whose orientation is very close to the wind direction. Larger discrepancies between experiments and numerical results can be conversely observed at receptors located at the lateral plume borders.

Despite these local differences between experimental and numerical results, an overall analysis of the dataset (see the scatter

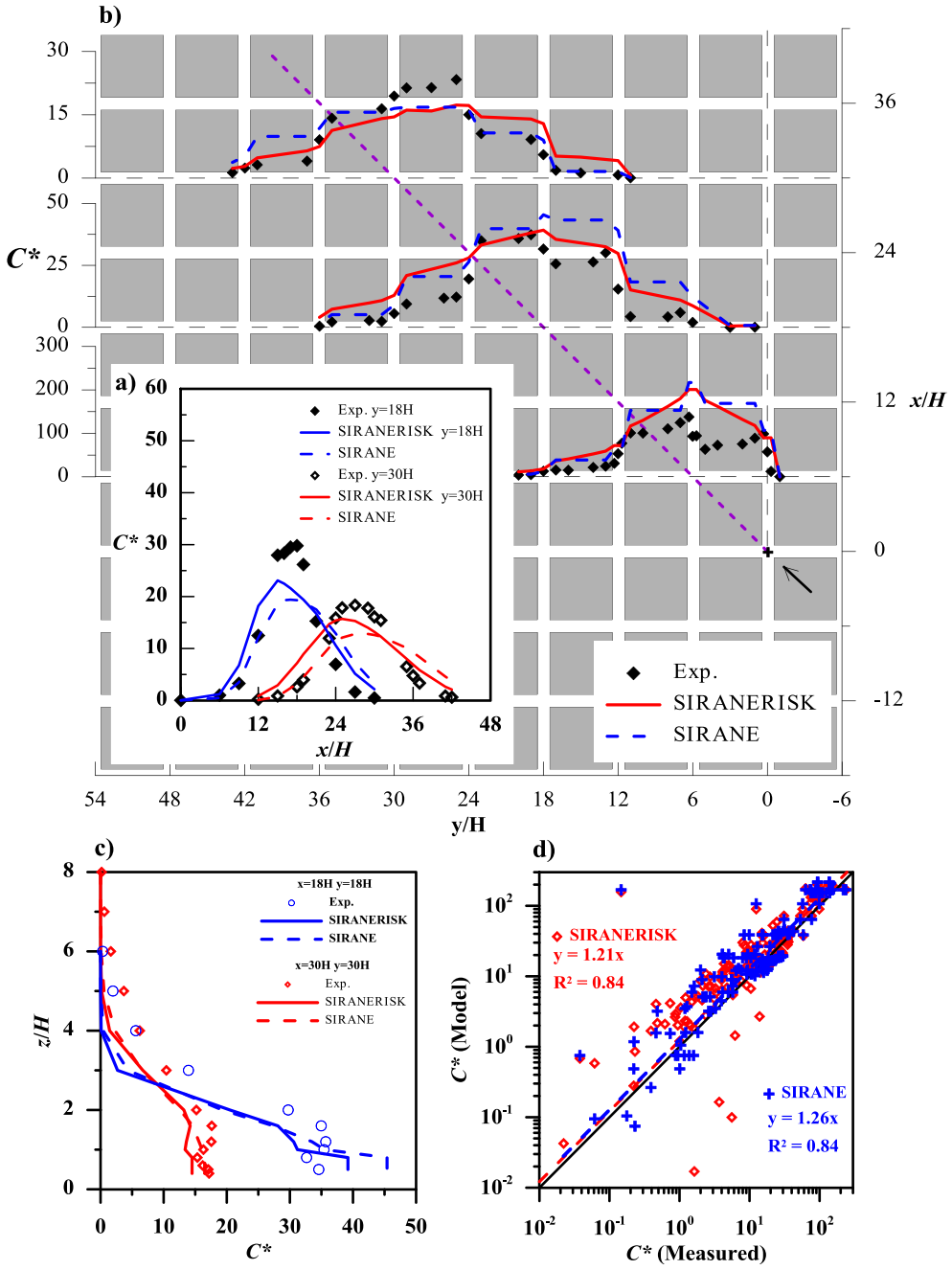

Fig. 10. As in Fig. 7 for $\varphi = 45°$.

Table 3
Model performances for the four wind directions: statistical indices refer to all data, i.e. within (at $z/H = 0.5$) and above (at $z/H = 2$) the canopy, and to data within (at $z/H = 0.5$) the canopy only. Values of the indices exceeding the Chang and Hanna (2004) threshold are in bold.

		$\varphi = 2.5°$		$\varphi = 10°$		$\varphi = 25°$		$\varphi = 45°$	
		SIRANERISK	SIRANE	SIRANERISK	SIRANE	SIRANERISK	SIRANE	SIRANERISK	SIRANE
All data	*R*	0.93	0.91	0.94	0.91	0.89	0.87	0.92	0.92
	FB	0.05	0.02	0.17	0.11	0.27	0.24	0.30	**0.34**
	NMSE	0.18	0.17	0.14	0.16	0.25	0.25	0.31	0.45
	FAC2	0.55	0.60	0.58	0.63	0.53	0.60	0.63	0.70
Canopy data	*R*	0.93	0.91	0.91	0.89	0.86	0.84	0.91	0.93
	FB	−0.01	−0.06	0.17	0.13	0.30	0.17	**0.38**	**0.43**
	NMSE	0.16	0.18	0.14	0.18	0.25	0.30	0.32	0.47
	FAC2	**0.40**	0.53	0.56	0.58	**0.46**	0.54	0.63	0.68

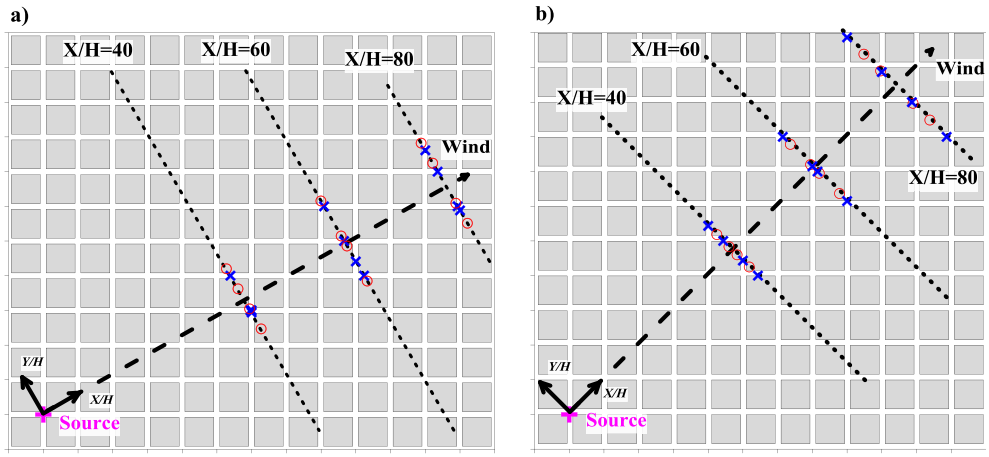

Fig. 11. Locations of the measurement points for the unsteady release experiments, within (blue crosses) and above (red circles) the urban canopy for the two wind directions: (a) $\varphi = 25°$ and (b) $\varphi = 45°$. (For interpretation of the references to colour in this figure legend, the reader is referred to the web version of this article.)

plots presented in Fig. 14) shows that the model is able to reliably simulate the arrival time of the pollutant puff and has a tendency in overestimating the maximal concentration registered at a given location. This can be reasonably attributed to an underestimation of the longitudinal puff spreading due to the velocity shear inside the canopy, which is not taken into account in the model. As originally shown by Taylor (1953) in the case of a pipe flow, the velocity shear generates a significant longitudinal spreading which controls the concentration dilution in the pipe. Similarly, the velocity shear observed within a flow developing within a street canyon (Soulhac et al., 2008) can significantly affect the dilution of pollutant concentration. However, these effects of shear are not included in the parameterisation implemented in the canopy-module of SIRANERISK. This feature can explain the overestimate of the maximum concentration simulated by SIRANERISK.

5. Conclusions

The aim of this study was to present the SIRANERISK model and to evaluate its performances against wind-tunnel measurements of steady and unsteady pollutant releases within an idealised urban district. SIRANERISK is built on the same principles as the model SIRANE and adopts specific parameterisation to simulate flow and dispersion in a densely built environment, i.e. in areas characterised by densely packed groups of buildings and characterised by two main features: i) the spacing between the buildings (the street width) generally do not exceed the building height, therefore producing flow patterns that are commonly referred to as 'street canyon flows' and ii) the width of the building blocks exceeds that of the streets separating them, so that the flow developing in the streets is somehow decoupled from that in the intersections. In these urban geometries, referred to as 'street networks' (Belcher et al., 2015; Soulhac et al., 2011) the main phenomena driving flow and dispersion are (Soulhac et al., 2011) the dispersion above roof level, the mean advection along the street axes, the dispersion at street intersections and the vertical exchanges between canopy and atmosphere. Unlike SIRANE, SIRANERISK is able to simulate the unsteadiness of the transfer within and above the canopy. For that purpose, SIRANERISK presents two main differences compared to SIRANE:

- Concerning the dispersion in a boundary layer flow, it integrates the effect of wind shear on the spreading of the pollutant puff;
- Concerning the dispersion in the urban canopy, it adopts a finer discretisation of the street networks, by means of a model of moving boxes.

In order to evaluate the performance of the model, we have compared its results to wind tunnel experiments of passive scalar dispersion within and over different obstacle arrays. Two of these, referred to as R20 and R50 configurations, were devoted to the simulation within a turbulent boundary layer above a rough surface, representing a sparse city district. The other, referred to as B50, was devoted to the simulation of the dispersion within a dense city district.

Firstly, we have analysed the dispersion of steady and unsteady releases of a passive scalar within a turbulent boundary layer, focusing on the role of the vertical shear of the mean longitudinal velocity in the dispersion of steady plumes and unsteady puffs. Results confirm main findings of previous theoretical (Chatwin, 1968) and experimental (Yee, 1998) analyses. These show that the effect of shear is almost negligible on the mean concentration field produced by steady releases. Conversely, its effect is significant in the case of instantaneous releases. Comparisons with experimental data show that the model reproduces accurately the arrival time of the concentration peaks at any downstream location, as well as the spatial distribution of the concentration within the puff as it travels downstream.

Secondly, we have analysed the case of dispersion within a dense urban canopy. For steady state releases, the results of SIRANERISK are very similar to those of SIRANE both within and above the canopy. In other words, the model does not really benefit from a finer discretisation of the domain within the canopy. Even though SIRANERISK, unlike SIRANE, is able to reproduce concentration gradients within a single street, its performances are not boosted by this skill. This result suggests that, for operational purposes, the simulation of steady releases with a street network approach does not require to discretise the domain at a scale smaller than the street scale. Considering the case of impulsive releases within the urban canopy, SIRANERISK is shown to simulate reliably the time evolution of concentration signals obtained by the ensemble average of 100 realisations of the same release. In a general way, the model tends to capture very well the arrival time of the concentration peak for all considered receptors. However, the value of the maximal (ensemble averaged) concentration is generally slightly overestimated by the model, which can be attributed to an underestimation of the longitudinal dispersion of the pollutant puff

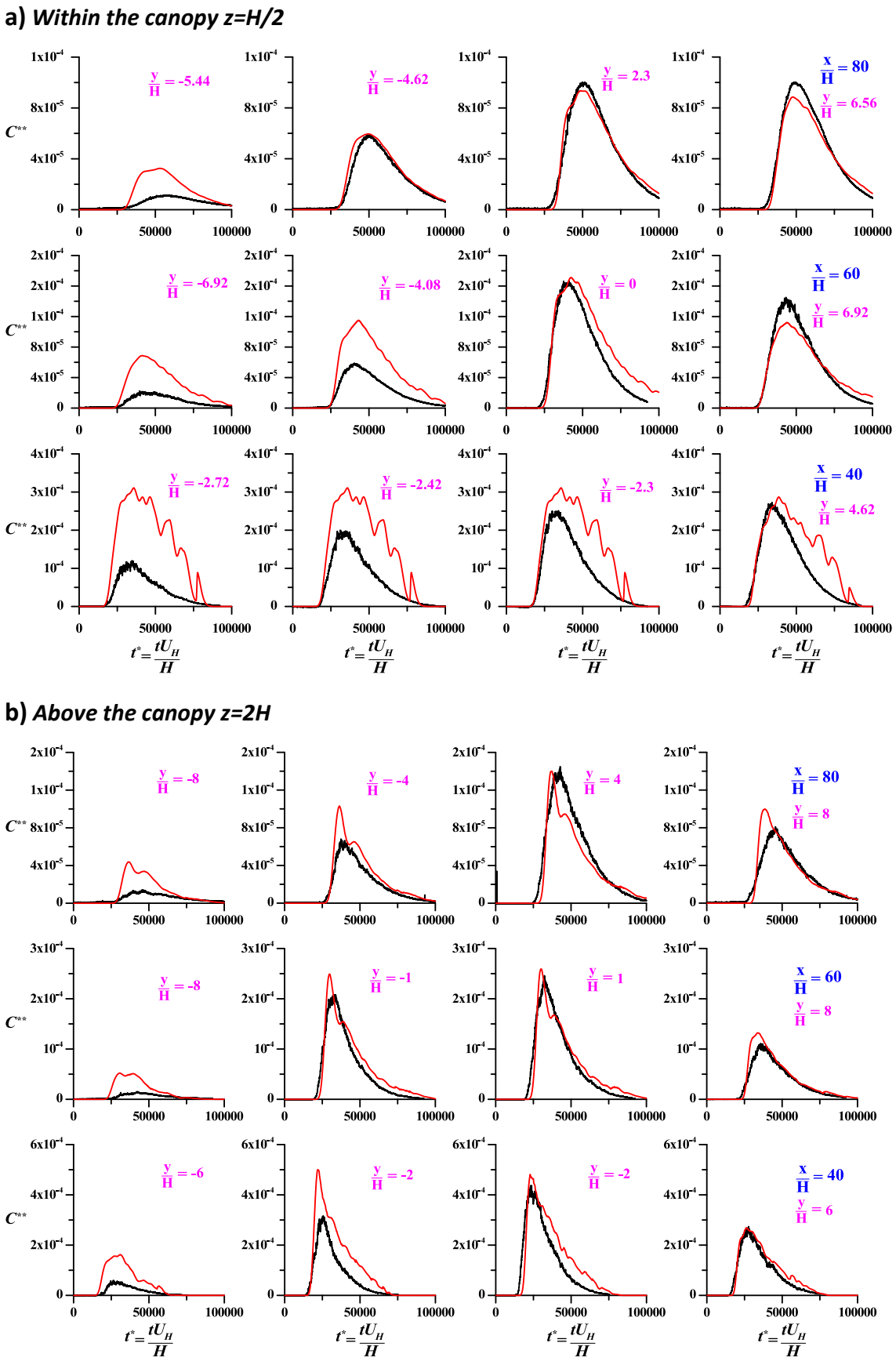

Fig. 12. Results for $\varphi = 25°$ at a) $z = H/2$ and b) $z = 2H$. Temporal evolution of the non-dimensional concentration $C^* = CH^3/M$ at different positions downwind the source. Comparison between wind-tunnel experiments (back) and the SIRANERISK model (red).

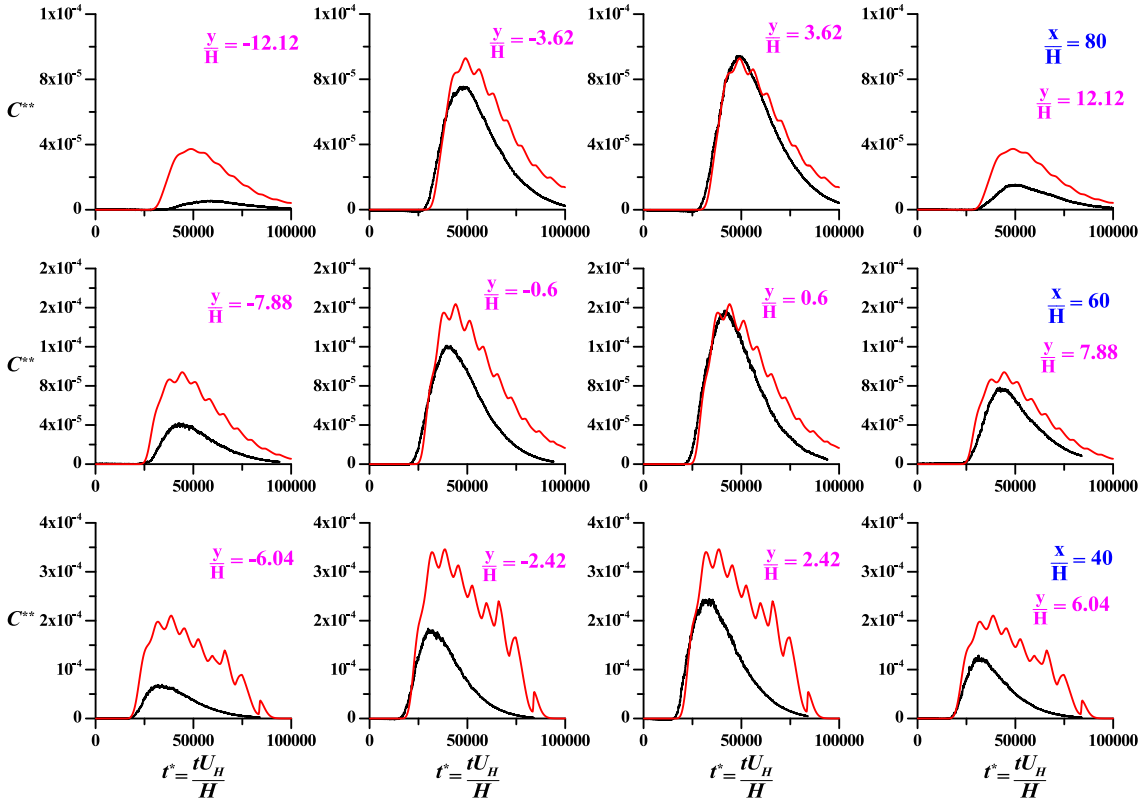

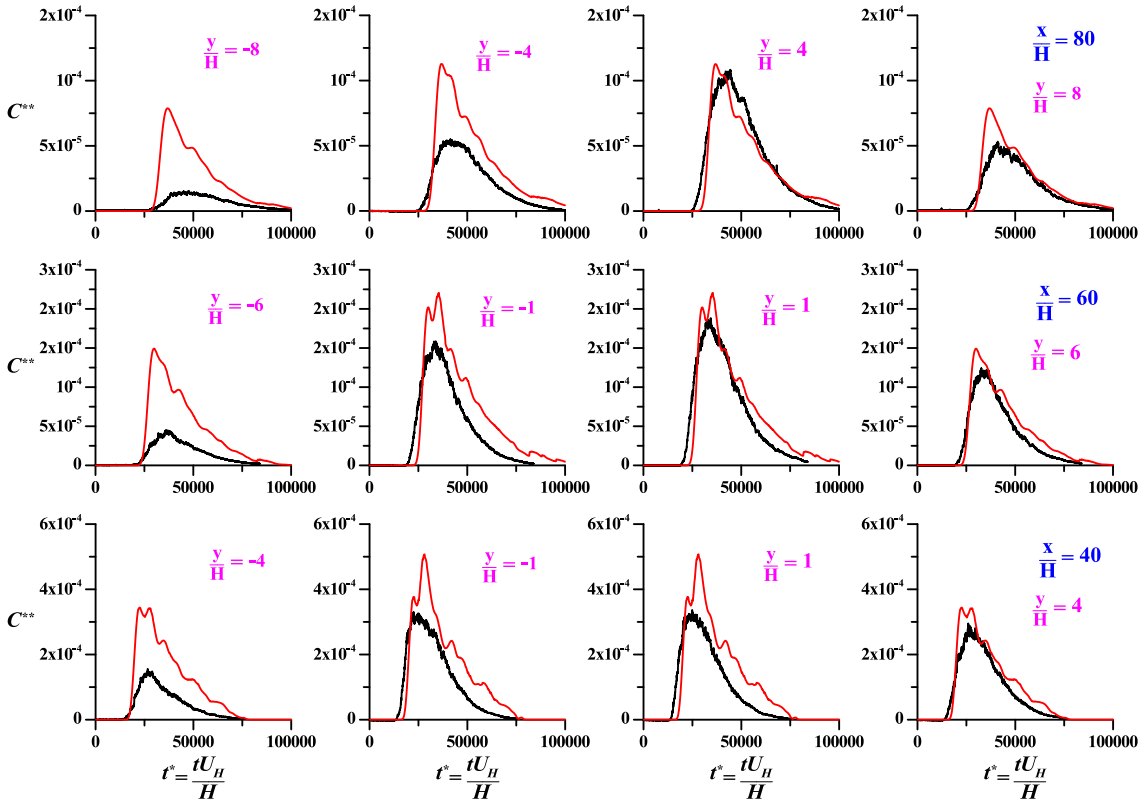

Fig. 13. As in Fig. 12 for $\varphi = 45°$.

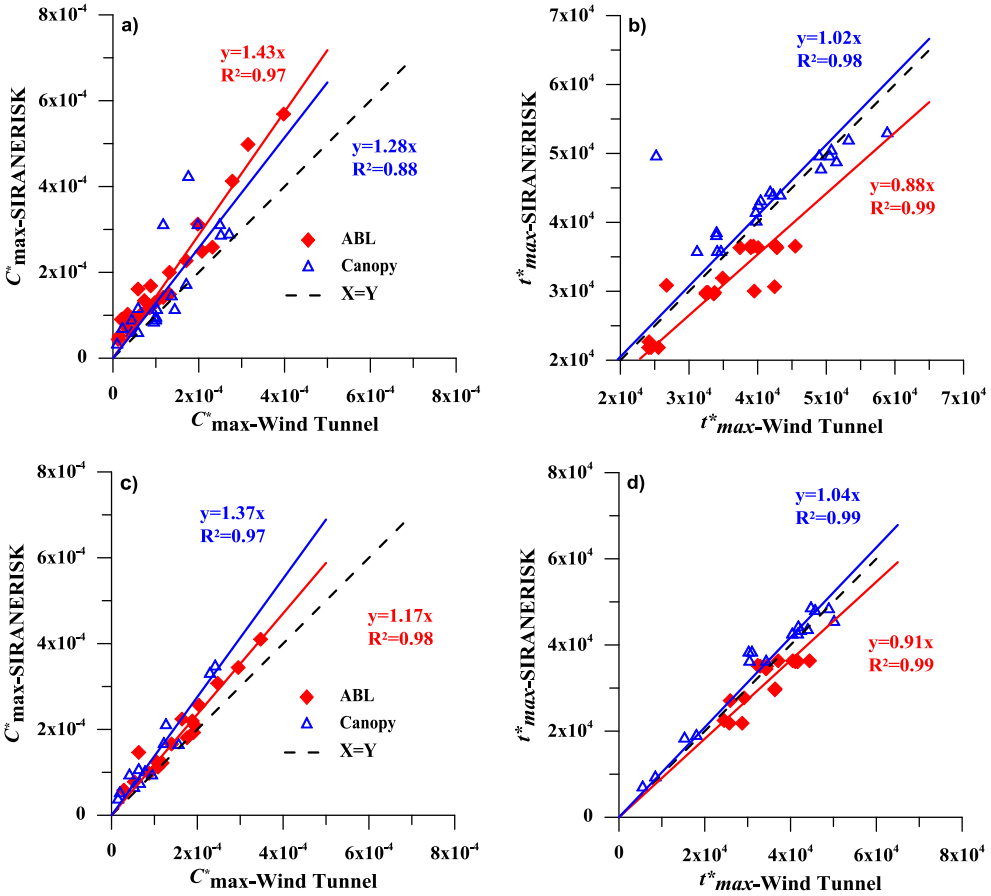

Fig. 14. Scatter plots comparing results provided by the experiments and SIRANERISK simulations within (blue triangles) and above (red diamonds) the urban canopy for $\varphi = 25°$ (a) maximal ensemble-averaged concentrations and (b) averaged advection times, and for $\varphi = 45°$ (c) maximal ensemble-averaged concentrations and (d) averaged advection times. (For interpretation of the references to colour in this figure legend, the reader is referred to the web version of this article.)

within the canopy.

These results demonstrate that the SIRANERISK model is a suitable operational tool for risk analysis and crisis management in case of accidental or deliberate releases of harmful pollutants in the urban atmosphere. Further research work is planned in order to include a parameterisation for the concentration fluctuations (Cierco et al., 2012) within the puff and to model the effects of buoyancy in order to simulate the dispersion of light and dense releases (Marro et al., 2014).

Acknowledgements

This study was supported by the Region Rhône-Alpes and the ANR (Estimair project ANR-13-MONU-0001).

Appendix A. Supplementary data

Supplementary data related to this article can be found at http://dx.doi.org/10.1016/j.atmosenv.2016.04.027.

References

Barlow, J.F., Harman, I.N., Belcher, S.E., 2004. Scalar fluxes from urban street canyons. Part I: laboratory simulation. Bound. Layer. Meteorol. 113, 369–385.
Belcher, S.E., Coceal, O., Goulart, E.V., Rudd, A.C., Robins, A.G., 2015. Processes controlling atmospheric dispersion through city centres. J. Fluid Mech. 763, 51–81.
Ben Salem, N., Garbero, V., Salizzoni, P., Lamaison, G., Soulhac, L., 2015. Modelling pollutant dispersion in a street network. Bound. Layer. Meteorol. 155, 157–187.
Blevins, R.D., 1984. Applied Fluid Dynamics Handbook. Van Nostrand Reinhold Company.
Blocken, B., 2015. Computational fluid dynamics for urban physics: importance, scales, possibilities, limitations and ten tips and tricks towards accurate and reliable simulations. Build. Environ. Fifty Year Anniv. Build. Environ. 91, 219–245.
Brook, D.R., Felton, N.V., Clem, C.M., Strickland, D.C.H., Griffiths, I.H., Kingdon, R.D., Hall, D.J., Hargrave, J.M., 2003. Validation of the urban dispersion model (UDM). Int. J. Environ. Pollut. 20, 11–21.
Brown, M., Gowardhan, A., Nelson, M., Williams, M., Pardyjak, E., 2009. Evaluation of the QUIC wind and dispersion models using the Joint Urban 2003 Field Experiment dataset. In: AMS 8th Symposium in Urban Environment, Phoenix, AZ, p. 16.
Buccolieri, R., Salizzoni, P., Soulhac, L., Garbero, V., Di Sabatino, S., 2015. The breathability of compact cities. Urban Clim. 13, 73–93.
Carruthers, D.J., Edmunds, H.A., Lester, A.E., McHugh, C.A., Singles, R.J., 2000. Use and validation of ADMS-urban in contrasting urban and industrial locations. Int. J. Environ. Pollut. 14, 364–374.
Chang, J., Hanna, S.R., 2004. Air quality model performance evaluation. Meteorol. Atmos. Phys. 87, 167–196.
Chatwin, P.C., 1968. The dispersion of a puff of passive contaminant in the constant stress region. Q. J. R. Meteorol. Soc. 94, 350–360.
Cierco, F.-X., Soulhac, L., Salizzoni, P., Méjean, P., Lamaison, G., Armand, P., 2012. Modelling concentration fluctuations for operational purposes. Int. J. Environ. Pollut. 48, 18–86.
Di Sabatino, S., Buccolieri, R., Salizzoni, P., 2013. Recent advancements in numerical modelling of flow and dispersion in urban areas: a short review. Int. J. Environ. Pollut. 172.
Fackrell, J.E., Robins, A.G., 1982. Concentration fluctuations and fluxes in plumes from point sources in a turbulent boundary layer. J. Fluid Mech. 117, 1–26.
Garbero, V., Salizzoni, P., Soulhac, L., 2010. Experimental study of pollutant dispersion within a network of streets. Bound. Layer. Meteorol. 136, 457–487.
Grimmond, C.S.B., Oke, T.R., 1999. Aerodynamic properties of urban areas derived from analysis of surface form. J. Appl. Meteorol. 38 (9), 1262–1292.
Hunt, J.C.R., 1982. Diffusion in the stable boundary layer. In: Nieuwstadt, F.T.M., Dop, H. van (Eds.), Atmospheric Turbulence and Air Pollution Modelling,

Atmospheric Sciences Library. Springer, Netherlands, pp. 231–274.
Irwin, H.P.A.H., 1981. The design of spires for wind simulation. J. Wind Eng. Ind. Aerodyn. 7, 361–366.
Marro, M., Salizzoni, P., Cierco, F.X., Korsakissok, I., Danzi, E., Soulhac, L., 2014. Plume rise and spread in buoyant releases from elevated sources in the lower atmosphere. Environ. Fluid Mech. 14, 201–219.
McHugh, C.A., Carruthers, D.J., Edmunds, H.A., 1997. ADMS-urban: an air quality management system for traffic, domestic and industrial pollution. Int. J. Environ. Pollut. 8, 666–674.
Moussafir, J., Oldrini, O., Tinarelli, G., Sontowski, J., Dougherty, C., 2004. A new operational approach to deal with dispersion around obstacles: the MSS (Micro- Swift-Spray) software suite. In: Proc. 9th Int. Conf. On Harmonisation within Atmospheric Dispersion Modelling for Regulatory Purposes, 2, pp. 114–118.
Narita, K., 2007. Experimental study of the transfer velocity for urban surfaces with a water evaporation method. Bound. Layer. Meteorol. 122, 293–320.
Nironi, C., Salizzoni, P., Marro, M., Mejean, P., Grosjean, N., Soulhac, L., 2015. Dispersion of a passive scalar fluctuating plume in a turbulent boundary layer. Part I: velocity and concentration measurements. Bound. Layer. Meteorol. 156, 415–446.
Röckle, R., 1990. Bestimmung der stomungsverhaltnisse im Bereich Komplexer Bebauugsstrukturen. Ph.D. Thesis. Vom Fachbereich Mechanik, der Technischen Hochschule Darmstadt, Germany.
Salizzoni, P., Soulhac, L., Mejean, P., Perkins, R.J., 2008. Influence of a two-scale surface roughness on a neutral turbulent boundary layer. Bound. Layer. Meteorol. 127, 97–110.
Salizzoni, P., Soulhac, L., Mejean, P., 2009a. Street canyon ventilation and atmospheric turbulence. Atmos. Environ. 43 (32), 5056–5067.
Salizzoni, P., Van Liefferinge, R., Soulhac, L., Mejean, P., Perkins, R.J., 2009b. Influence of wall roughness on the dispersion of a passive scalar in a turbulent boundary layer. Atmos. Environ. 43, 734–748.
Soulhac, L., Perkins, R.J., Salizzoni, P., 2008. Flow in a street canyon for any external wind direction. Bound. Layer. Meteorol. 126, 365–388.
Soulhac, L., Garbero, V., Salizzoni, P., Mejean, P., Perkins, R.J., 2009. Flow and dispersion in street intersections. Atmos. Environ. 43, 2981–2996.
Soulhac, L., Salizzoni, P., Cierco, F.-X., Perkins, R.J., 2011. The model SIRANE for atmospheric urban pollutant dispersion; part I, presentation of the model. Atmos. Environ. 45, 7379–7395.
Soulhac, L., Salizzoni, P., Mejean, P., Didier, D., Rios, I., 2012. The model SIRANE for atmospheric urban pollutant dispersion; Part II, validation of the model on a real case study. Atmos. Environ. 49, 320–337.
Soulhac, L., Salizzoni, P., Mejean, P., Perkins, R.J., 2013. Parametric laws to model urban pollutant dispersion with a street network approach. Atmos. Environ. 67, 229–241.
Sykes, R.I., Henn, D.S., 1995. Representation of velocity gradient effects in a Gaussian puff model. J. Appl. Meteorol. 34, 2715–2723.
Taylor, G.I., 1953. Dispersion of a soluble matter in solvent flowing slowly through a tube. Proc. R. Soc. 219, 186–203.
Tinarelli, G., Brusasca, G., Oldrini, O., Anfossi, D., Castelli, S.T., Moussafir, J., 2007. Micro-swift-spray (MSS): a new modelling system for the simulation of dispersion at microscale. General description and validation. In: Borrego, C., Norman, A.-L. (Eds.), Air Pollution Modeling and its Application XVII. Springer, US, pp. 449–458.
Yee, E., 1998. Turbulent diffusion of instantaneous clouds in the atmospheric surface layer: measurements and comparison with Lagrangian similarity theory. Phys. Lett. A 242, 51–62.

9.2 Inverse atmospheric dispersion modelling to estimate the source strength of accidental pollutant releases in the built environment from turbulent concentration signals

Atmospheric Environment 148 (2017) 266–281

Contents lists available at ScienceDirect

Atmospheric Environment

journal homepage: www.elsevier.com/locate/atmosenv

Estimating accidental pollutant releases in the built environment from turbulent concentration signals

N. Ben Salem [a, *], P. Salizzoni [b], L. Soulhac [b]

[a] ATMO Auvergne Rhône-Alpes, 3 allée des Sorbiers, 69500 Bron, France
[b] Laboratoire de Mécanique des Fluides et d'Acoustique, UMR CNRS 5509 Université de Lyon, Ecole Centrale de Lyon, INSA Lyon, Université Claude Bernard Lyon I, 36, Avenue Guy de Collongue, 69134 Ecully, France

HIGHLIGHTS

- We present an inverse model for accidental pollutant releases in a built environment.
- The model are tested against wind tunnel experiments.
- Results support the use of the model as operational tool for risk assessment.

ARTICLE INFO

Article history:
Received 5 July 2016
Received in revised form
21 October 2016
Accepted 29 October 2016
Available online 31 October 2016

Keywords:
Inverse model
Accidental release
Turbulent dispersion
Urban dispersion model
Concentration fluctuations

ABSTRACT

We present an inverse atmospheric model to estimate the mass flow rate of an impulsive source of pollutant, whose position is known, from concentration signals registered at receptors placed downwind of the source. The originality of this study is twofold. Firstly, the inversion is performed using high-frequency fluctuating, i.e. turbulent, concentration signals. Secondly, the inverse algorithm is applied to a dispersion process within a dense urban canopy, at the district scale, and a street network model, SIRANERISK, is adopted. The model, which is tested against wind tunnel experiments, simulates the dispersion of short-duration releases of pollutant in different typologies of idealised urban geometries. Results allow us to discuss the reliability of the inverse model as an operational tool for crisis management and the risk assessments related to the accidental release of toxic and flammable substances.

1. Introduction

In cases of accidental atmospheric releases of harmful substances in an urban area or on an industrial site, gathering information about the mass of pollutant ejected is essential in order to:

- manage the crisis situation (shortly after the accident),
- assess the impact on the environment and human health (at later times).

For these purposes, inverse dispersion models are extremely useful tools as they comprise a direct atmospheric model and an inverse algorithm, whose coupling allows the position and strength (eventually as a function of time) of a source of pollutant to be reconstructed from the concentrations measured at receptors placed downwind of the source.

Managing risks and crises due to accidental pollutant releases has become an important issue, due to the occurrence of major industrial and nuclear accidents in the last decades (Fukushima in 2011 (Winiarek et al., 2012; Chai et al., 2015; Lin et al., 2015), AZF in 2001 in Toulouse (Taveau, 2010), Algeciras in 1998 and Chernobyl in 1986 (Quélo et al., 2007)) and an increased concern over terrorist attacks in densely populated urban areas.

Despite the relevance of these problems, as far as we are aware, there have been relatively few studies (e.g. Brereton and Johnson, 2012; Keats et al., 2007), which consider inverse modelling within urban and industrial environments. However, among the studies conducted on this subject we find Bady (2013), Chow et al. (2008), and Lien et al. (2006) who coupled inverse algorithms with Computational Fluid Dynamics (CFD) codes and Khlaifi et al. (2009), Krysta et al. (2006), Lushi and Stockie (2010), and Rudd et al. (2012)

* Corresponding author. ATMO Auvergne Rhône-Alpes, 3 allée des Sorbiers, 69500 Bron, France.
E-mail address: nbensalem@atmo-aura.fr (N. Ben Salem).

http://dx.doi.org/10.1016/j.atmosenv.2016.10.050
1352-2310/

who instead used simple Gaussian models. Note that both direct modelling approaches, i.e. CFD and Gaussian models, present major limitations in an operational context. CFD codes require long calculation times, which are not compatible with the short timescales imposed by a crisis situation. On the other hand, the results of Gaussian models are affected by significant errors due to the oversimplification of the representation of the velocity field and of the dispersion process in complex geometries.

An example of a source term identification study in a built environment based on an operational model is that of Glascoe et al. (2006), who used the UDM model (Urban Dispersion Model) with a stochastic sampling algorithm (MCMC) and the Bayesian approach. The study enlightened the limitations of an operational Gaussian model in identifying the source position, due to its inability to correctly simulate the main phenomena driving pollutant dispersion in an obstacle array (Joint Urban 2003 campaign), simulating an urban canopy. Similar conclusions were also drawn by Rudd et al. (2012) when working with data from wind tunnel experiments. They argued that the adoption of a direct model able to account explicitly for the local urban geometry (as street network models do), instead of a simple Gaussian model, would help in improving the accuracy of the inverse model.

In the case of a terrorist attack as well as in some industrial accident, the duration of the release, referred to hereafter as T_E, is likely to be much shorter than the typical timescales associated with the advection of a puff of pollutant in the surrounding atmosphere. In such 'short duration' releases, it is particularly difficult to obtain information about the evolution of the pollutant flow rate at the source and/or the total amount of pollutant released during the accident by means of an inverse model. Direct operational dispersion models (have to) rely on a statistical description of the dispersion process and therefore provide only 'time-averaged' or 'ensemble-averaged' values of concentrations. However, in the case of a short duration (accidental) release, the concept of 'ensemble average' is no longer pertinent, since we actually deal with a single realisation of the dispersion process. The only available information is (at best) a highly fluctuating, i.e. turbulent, concentration signal registered by one (or more) monitoring station(s) placed downwind of the source. It is therefore not clear what the reliability of the results of the inverse model would be in these circumstances.

To investigate these features, we have developed herein an inverse model to estimate the mass flow rate of an impulsive release within a built environment, that uses as input data a highly fluctuating turbulent concentration signal, registered at fixed receptors downwind of the release.

The model is here tested on 'short-duration' releases occurring in two flow configurations: a rough wall boundary layer, simulating a sparse urban city district, and a densely packed group of obstacles, simulating a dense city district. Both configurations are studied by means of wind tunnel experiments, presented in Section 2. In Section 3 we present the direct model (Soulhac et al., 2016), SIRANERISK, which is an operational dispersion model conceived to simulate the dispersion of unsteady pollutant releases within the urban canopy.

In Section 4 we provide details on the inverse algorithm, which is a particular case of a data assimilation method (Bocquet, 2010; Jeong et al., 2005). It is essentially a least-squares method, used to minimise the difference between concentrations measured at a receptor and predicted by the dispersion model. Similar methods have been widely applied, since the 1960s, to geophysical and meteorological problems (Backus and Gilbert, 1967; Kanasewich and Chiu, 1985; Lewis et al., 2006; Lewis and Derber, 1985; Richardson and Zandt, 2009), and more recently to pollutant dispersion problems for source identification (Issartel et al., 2012; Jeong et al., 2005; Krysta et al., 2006; Lushi and Stockie, 2010; Roussel et al., 2000; Sharan et al., 2012; Rudd et al., 2012; Singh et al., 2013). The least-squares approach is herein coupled with a regularization method to deal with the high level of fluctuation in the input data.

Finally (Section 5), we analyse the ability of the inverse model to estimate the mass flow rate at the source. The analysis is performed using both instantaneous signals and ensemble-averaged concentrations. By statistically evaluating the errors of the predictions obtained using these two types of signal, we finally discuss the reliability of the inverse model for operational purposes. The analysis presented here is characterised by two features that are worth emphasising. Firstly, data from only one receptor were used in each case, whereas in real applications there would probably be data from several detectors. Secondly, the detector positions are well chosen, i.e they are in the central region of the dispersing clouds. This avoids the issue of zero concentrations (noise) being returned in individual realisation from towards the edge of the clouds.

2. Wind tunnel experiments

Experiments, whose results have been recently presented by Soulhac et al. (2016), were performed in the wind tunnel of the Laboratoire de Mécanique des Fluides et d'Acoustique of the Ecole Centrale de Lyon. These consisted of producing impulsive releases of a passive scalar (ethane) in configurations simulating idealised urban geometries, reproduced at approximately a 1:400 scale.

The reference wind speed in the wind tunnel, the free-stream velocity $U_\infty = 5\ m{\cdot}s^{-1}$ at the top of the boundary layer, is assumed to be the same as that at the full scale. The release lasted $T_E = 0.17$ s in the wind tunnel, which therefore corresponds to about 68 s (Fig. 2a) at full scale (multiplied by a factor of 400).

The focus here is on only two of the three configurations presented by Soulhac et al. (2016): the R20 configuration that simulates a sparse city district, and the B50 configuration that simulates a dense urban district (see Fig. 1b). In both cases, the urban districts were overlain by a turbulent boundary layer of depth $\delta = 0.8$ m, generated by a row of spires (Irwin, 1981) 0.5 m high placed at the beginning of the test section.

In the R20 configuration, the floor was covered by a staggered array of cubes of side 20 mm, spaced 17 cm longitudinally and 13 cm laterally. The B50 configuration comprised an array of equal-height ($H = 50$ mm) square-based ($L = 5H$) obstacles, covered by nuts, and separated by a distance H. Among the experimental data set presented by Soulhac et al. (2016), for the B50 configuration, we refer here to measurements performed within the canopy at a height $z = H/2$ and for a wind direction $\varphi = 45°$, only.

In both the R20 and B50 configurations, the free-stream velocity U_∞ at the top of the boundary layer was equal to $5\ m{\cdot}s^{-1}$ and the source was placed at a distance of about 10δ from the beginning of the test section, where the boundary layer flow had already reached an equilibrium condition. The source height for the R20 configuration was larger than the obstacle height and equal to $H_r = 25$ mm. For the B50 configuration, the source height was lower than the obstacle height, $Hr = 25$ mm (H/2). In this latter case the source was placed at a street intersection within the array (see Garbero et al., 2010).

Time-dependent signals of passive scalar concentrations were measured downwind of the source at fixed positions by means of a Flame Ionisation Detector, with a sampling frequency of 400 Hz (Nironi et al., 2015).

In order to achieve a reliable statistical description of the time-dependent concentration field induced by the pollutant releases,

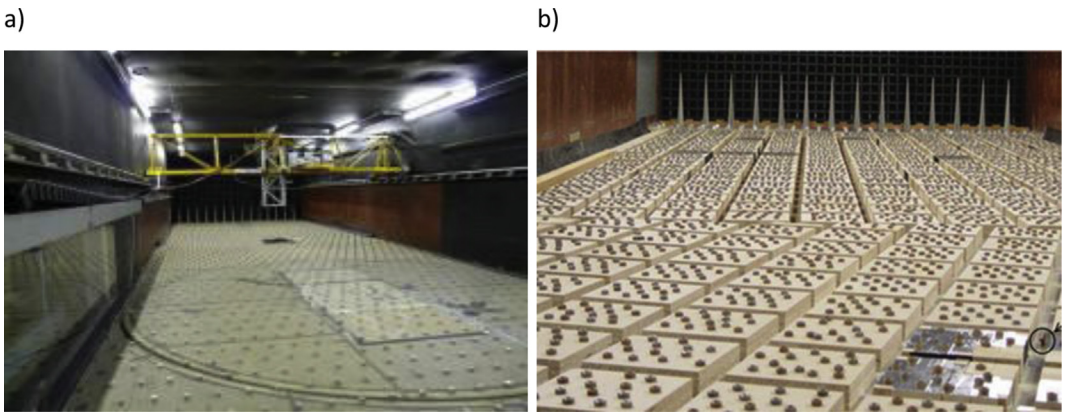

Fig. 1. Overview of the two configurations, a) configuration R20: releases within a turbulent boundary layer over a rough surface; b) configuration B50: releases within an idealised urban neighbourhood district overlain by a turbulent boundary layer.

experiments were repeated 100 times for each measurement point. This allowed us to estimate an ensemble-averaged time-dependent concentration for each measurement location. The time-dependent ensemble averages were used as a benchmark to validate the results provided by the direct model (see Section 3) and to identify parameters characterising the ensemble-averaged puff (Fig. 2b), namely: i) the maximal value of the ensemble-averaged concentration, referred to as $C_{\max}$; ii) a characteristic advection time, referred to as $t_{\max}$ and iii) a time lapse representative of the longitudinal spreading, referred to as $t_{end} - t_{beg}$ (note that the identification of $t_{\max}$ and $t_{end} - t_{beg}$ from these signal actually requires a travel time that greatly exceeds the emission duration, which implies that the receptors are placed beyond a certain fetch downstream).

We show in Fig. 2 comparisons between single concentration signals (as a function of time) and the ensemble average (over 100 realisations), measured for the R20 configuration at R2 (Fig. 2c and d) and for the B50 configuration at B1 (Fig. 2e and f).

To improve readability of the experimental results, signals are plotted with two distinct abscissa: one referring to a real time and the other to a non-dimensional time. Note that normalisation of time, as well as that of concentration and distance, is obtained by adopting different scales for the two configurations: δ and U_∞ for the R20 configuration and H and U_H (the mean longitudinal velocity at the roof height) for the B50 configuration. We therefore have $C^* = C\delta^3/M$, $\mathbf{x}^* = \frac{\mathbf{x}}{\delta}$, and $t^* = \frac{tU_\infty}{\delta}$ for R20 and $C^* = CH^3/M$, $\mathbf{x}^* = \frac{\mathbf{x}}{H}$ and $t^* = \frac{tU_H}{H}$ for B50. Note that, for a fixed amount of mass emitted, real-scale concentrations have to be rescaled by a factor δ^{-3}(or H^{-3}) with respect to those registered in the wind tunnel.

It is worth noting that the signals registered in configuration R20, especially those close to the source, show a higher intermittency than those registered in the B50 configuration (see Fig. 2c–f). This intermittency is due to the influence of the large-scale velocity fluctuations on the passive scalar dispersion (Gifford, 1959; Fackrell and Robins, 1982; Nironi et al., 2015; Marro et al., 2015). The large-scale vortices displace the pollutant puff as a whole, producing a phenomenon known as meandering (Gifford, 1959) and resulting in concentration signals characterised by abrupt variations from zero to the maximal value. In a general way, this phenomenon is reduced for increasing distances from the source, as the size of the pollutant puff is increased due to the effects of relative dispersion. When the size of the pollutant puff attains (or exceeds) the dimensions of the larger vortices, the meandering motion is suppressed and so is the intermittency of the concentration signals registered at a fixed receptor. Within a group of densely-packed obstacles, as for the street network considered herein (configuration B50), the distance between the obstacles limits the size of the larger vortices compared to those that would be present over a boundary layer flow (R20 configuration). For this reason, the presence of the obstacles inhibits the meandering motion, which explains the lower intermittency observed in the signals registered in configuration B50, compared to those registered in configuration R20.

Note that the reduction of meandering within a group of obstacle is occurring only within densely packed obstacle array, i.e. in the so called skimming flow regime, where the flow within the street canyons is actually decouples from that in the overlying external flow. When the distances between the obstacles is increased and the flow within the streets interacts more with that above, i.e. in the wake interference regime, the behavior of the plume within the array can be very different, leading to an intensification of the meandering motion on the horizontal plane. In these configurations (Hoydysh and Dabberdt, 1994; Robins et al., 2002) the flow becomes very sensitive to the wind direction relative to the street intersections (Soulhac et al., 2009), so that even small asymmetries in the configuration could lead to very different dispersion patterns (Hoydysh and Dabberdt, 1994; Robins et al., 2002).

3. The SIRANERISK model

SIRANERISK (Soulhac et al., 2016) is an operational model for the simulation of the atmospheric dispersion of unsteady pollutant releases within a built environment. SIRANERISK adopts the same parameterisations implemented in the model SIRANE (Soulhac et al., 2011), namely: the turbulent transfer between the canopy and the overlying boundary layer (Salizzoni et al., 2009; Soulhac et al., 2013), the channelling along the street axes (Soulhac et al., 2008) and the turbulent exchanges at street intersections (Soulhac et al., 2009). In the boundary layer above the urban canopy, the flow is modelled by means of the Monin-Obukhov similarity theory and dispersion by means of a Gaussian puff model.

To deal with unsteady releases, the model presents two main differences compared to SIRANE: i) the dispersion above roof height is simulated by means of a Gaussian puff model, and ii) the mass balances within the street network are computed over control volumes that are smaller than those of a street canyon and whose size can be varied with time.

Here, we briefly present some of the results concerning the validation of the model on a limited number of receptors, whose positions are specified in Fig. 3, and which will be subsequently used to discuss the performance of the inverse model. For an exhaustive discussion the reader is referred to Soulhac et al. (2016).

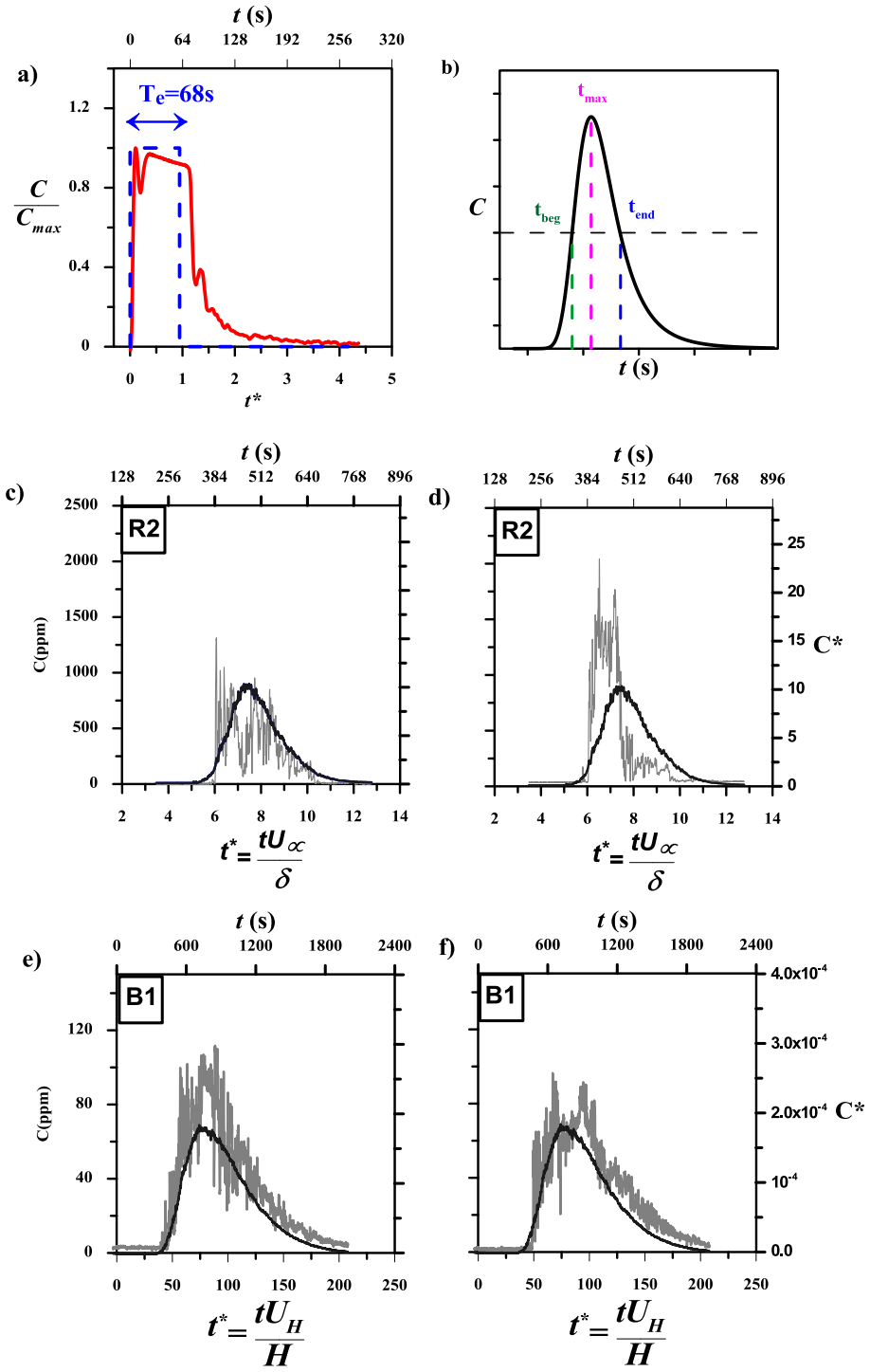

Fig. 2. a) time-dependent concentration signal registered at the source during a release in the R20 configuration; b) definition of characteristic puff advective time t_{max} and characteristic time of the longitudinal puff spread ($t_{end} - t_{beg}$). Time-evolution of the concentration signals registered downwind of the source: comparison between turbulent signals and ensemble-averaged signals; c) and d) examples of measurements for the R20 configuration; e) and f) examples of measurements for the B50 configuration.

We show in Fig. 4 and Fig. 5 the comparison of the concentration signals numerically simulated by SIRANERISK and the experimental results, i.e. the ensemble average of 100 realisations of the same release in the wind tunnel (Soulhac et al., 2016).

As discussed in detail in Soulhac et al. (2016), for the R20 configuration (boundary layer over a rough wall), SIRANERISK reliably predicts the arrival time of the concentration peaks at any downstream location. The model is less accurate in estimating the peak values of the concertation signal and the spatial distribution of the concentration within the puff as it travels downstream (Fig. 4). For the B50 configuration (dense urban canopy), SIRANERISK results are less accurate and show higher discrepancies with the experimental data (compared to the R20 configuration). Note also that within the canopy the simulated time dependent concentrations exhibit significant fluctuations. These are the product of the discretisation in time of the advection of pollutant puffs along the

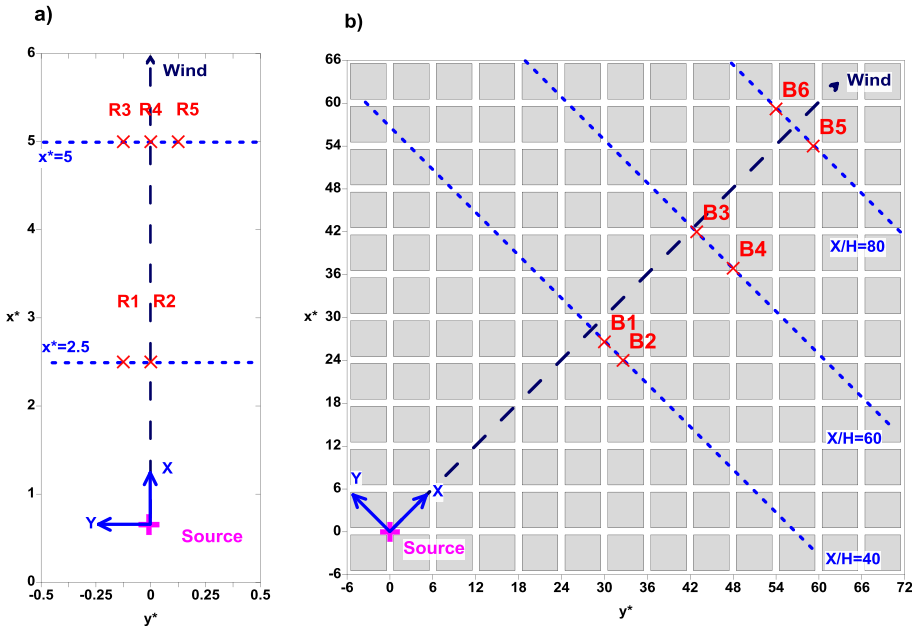

Fig. 3. Positions of the source and of the receptors (red) used in the inversion for both experimental configurations R20 (a) and B50 (b). (For interpretation of the references to colour in this figure legend, the reader is referred to the web version of this article.)

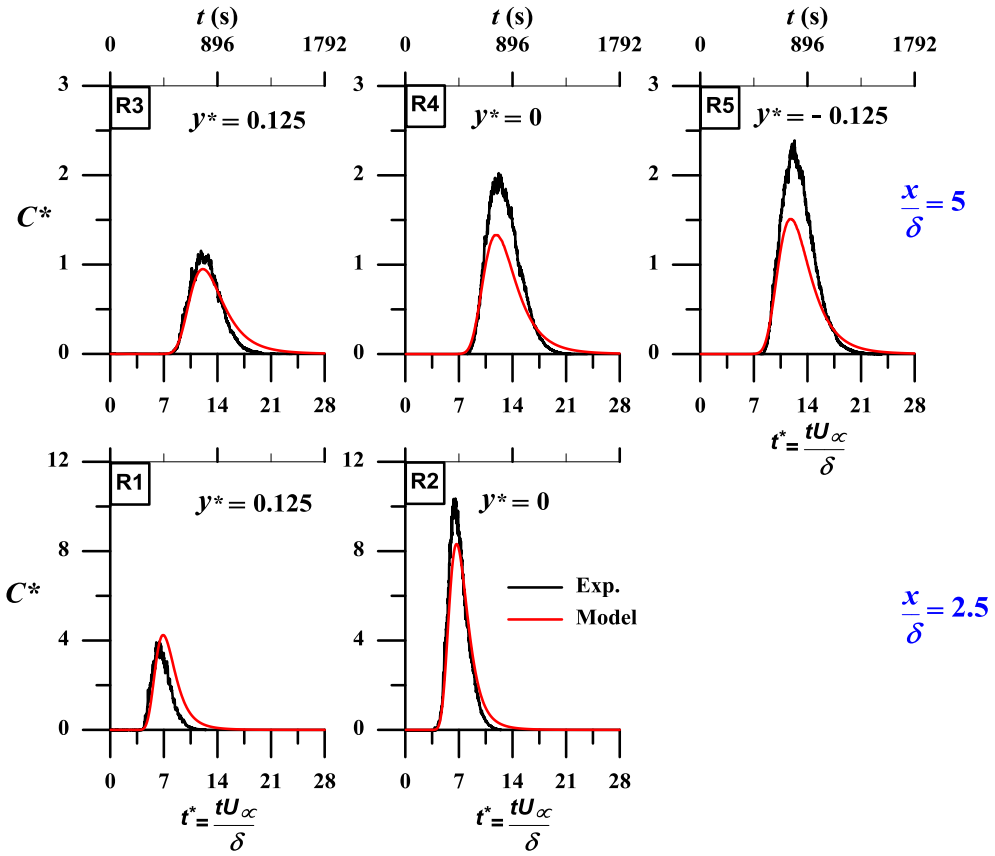

Fig. 4. Comparison between experimental (black) and SIRANERISK predictions (red) for dispersion for configuration R20 (rough boundary layer): evolution of the non-dimensional concentration C* at different receptors as a function of non-dimensional time t^* and real time t. Concentrations C* and time t^* are made dimensionless on adopting δ as a length scale and U_∞ as a velocity scale. (For interpretation of the references to colour in this figure legend, the reader is referred to the web version of this article.)

network of street.

In this latter case, the model tends to capture well the arrival time of the concentration peaks for all receptors (Fig. 5). However, the value of the maximal (ensemble-averaged) concentration is generally slightly overestimated by the model. This is likely to be due to an underestimation of the longitudinal dispersion of the

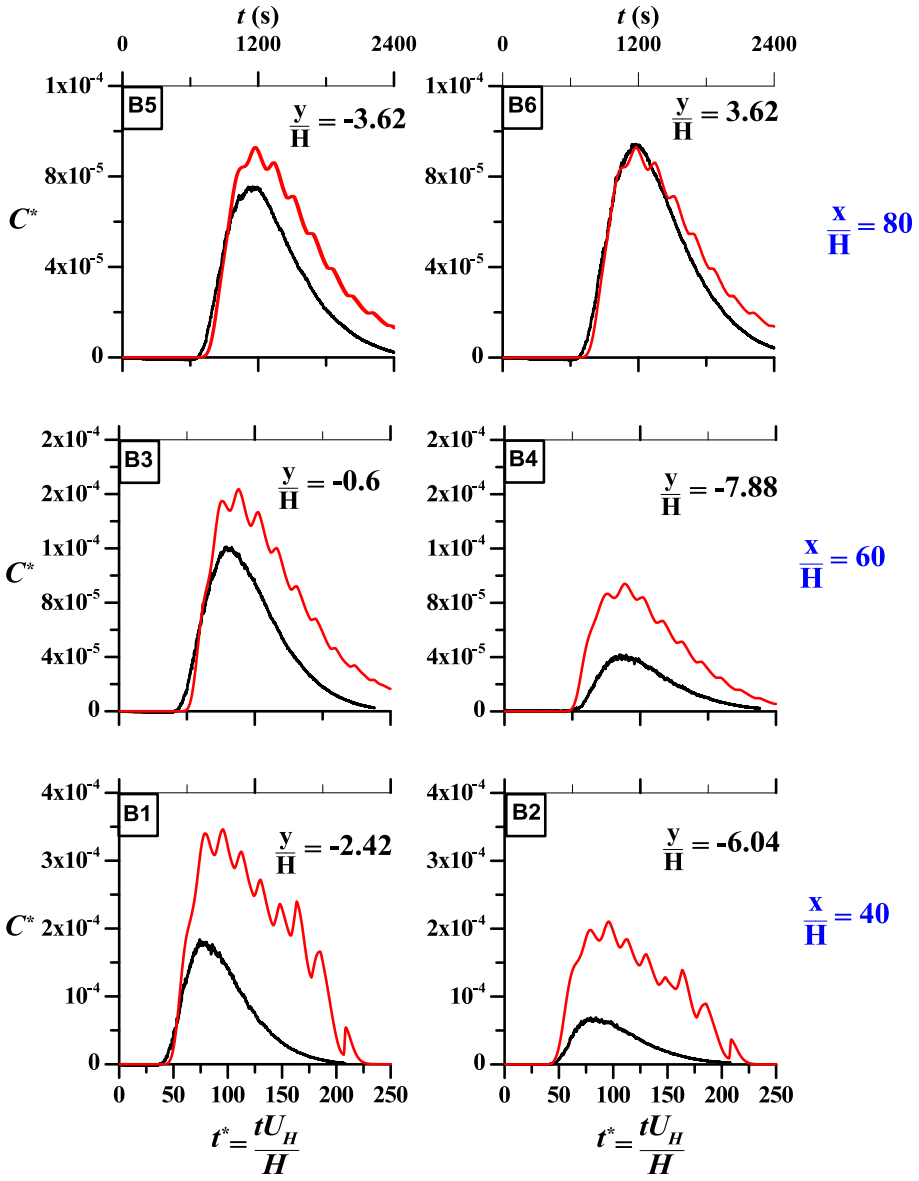

Fig. 5. As for Fig. 4 for configuration B50. Concentrations C*, time t* and distance x* are made dimensionless on adopting H as a length scale and U_H as a velocity scale.

pollutant puff within the canopy (Soulhac et al., 2016). In particular, results for the receptors closest to the source, i.e. B1 and B2, show differences between numerical and experimental results that exceed 100%.

4. Inverse method

The formulation of the inverse algorithm takes advantage of the linearity linking the flow rate emitted at the source Q and the passive scalar concentrations C^{obs} measured at a given receptor. Considering multiple sources and receptors, and assuming steady state conditions, in its general formulation the problem leads to a system of m equations and n unknowns:

$$C^{obs}(m) = ATC(m,n) \times Q(n) \quad (1)$$

where the Atmospheric Transfer Coefficient ATC (m, n) is the mathematical operator that models the physical mechanisms that are responsible for the dilution of the pollutant concentration in the atmosphere, and that characterise the contribution of each of the n sources Q on the concentrations C^{obs} measured at each of the m receptors.

Here we use (1) in order to estimate C^{obs} measured at m different time steps at a single receptor and emitted by a single source, at n different time steps. In this unsteady formulation of the problem and in order to run the inverse algorithm, we need to set four different timescales:

i) the time T_S over which the signal at the source is reconstructed;
ii) the time T_R over which the signal at the receptor is registered;
iii) the time step T_c fixing the sampling frequency $f_c = 1/T_c$ of the signal registered at the receptor; and
iv) the time step T_q fixing the frequency $f_q = 1/T_q$ at which the flow rate at the source is reconstructed.

The $n = T_s/T_q$ unknowns are therefore the values of Q at the n

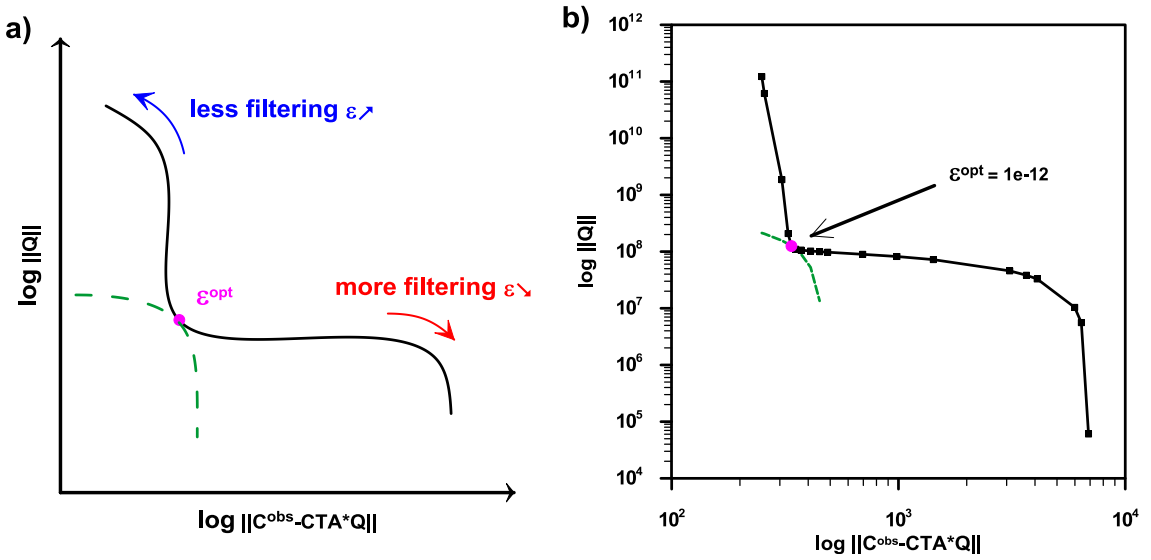

Fig. 6. Estimate of the optimal value of the regularization parameter ε. a) typical plots of the L-curve method; b) example of L-curve for inversions performed with a signal registered at a fixed receptor in the B50 configuration.

different time steps, reconstructed by means of $m = T_R/T_c$ observations, sampled from the concentration signal registered at a given receptor. Note that, once T_c is defined, then the average number of the representative observations on one single signal, can be roughly estimated as

$$m_{obs} = \frac{t_{end} - t_{beg}}{T_c} \tag{2}$$

where the difference $t_{end} - t_{beg}$ is a measure of the longitudinal time spread of the ensemble-averaged puff (see Fig. 2b).

Each column in (1) therefore contains the contribution of the emission at a single time step on all m time steps at the receptor. Each row contains information about the contribution of the emissions occurring at all n time steps on a single time step at the receptor.

Note that, since our objective here is confined to estimate the amount of the total mass ejected, and not the full reconstruction of the emission as a function of time, we do not impose any constraint concerning the positivity of the flow rate at the source.

4.1. Tikhonov regularization

In real case scenarios, where a series of input data can be affected by large uncertainties or lack of data for significant time delays, inverse problems are often mathematically ill-posed. It is well known (Enting, 2002) that when the problem is ill-conditioned, small uncertainties in the input data (or in the model parameters) can induce large errors in the estimate of the source conditions. For this reason, least-squares algorithms are often coupled with other optimization methods, such as quasi-Newton (Krysta et al., 2006; Rudd et al., 2012), conjugate gradient or Levenberg-Marquard methods (Cortés et al., 2009; Naveen et al., 2010; Pujol, 2007).

To minimise these uncertainties, we use here the Tikhonov regularization method (Tikhonov and Arsenin, 1977), which has been chosen because of its reliability (Skaggs and Kabala, 1995), despite its implementation being more complex than that of other similar methods such as the stabilisation techniques (Lattes and Lions, 1969).

The Tikhonov regularization method is based on the minimisation of a cost function of the form:

$$J = \left\| C^{obs} - CTA \times Q \right\|^2_{\mathbb{R}^{n_C}} + \varepsilon^2 \Gamma(Q) \tag{3}$$

where ε is the regularization parameter and $\Gamma(Q)$ is the penalization term, which is often expressed in a quadratic form as:

$$\Gamma(Q) = \left\| D \times (Q - Q_{priori}) \right\|^2 \tag{4}$$

with Q_{priori} the *a priori* solution, imposed as a constraint, and D the regularization operator, whose determination has been the object of several studies (Bruneau et al., 1991; Cullum, 1979; Neumaier, 1998). Following Bocquet (2010), we assume hereafter that the operator D is equal to the identity matrix. Note that (3) assumes that all observations are of equal value, since these will be here all collected by a same receptor. Conversely, when dealing with observation obtained from a variety of receptors it may be suitable to introduce weighting factors for different sets of data (Rudd et al., 2012; Abida and Bocquet, 2009).

The value of the function J in (3) varies between that provided by a least-squares method, when ε is very small, and the *a priori* solution, when ε is very large. The *a priori* information Q_{priori} is often unavailable in a real case scenario of accidental releases. In these cases, according to Davoine and Bocquet (2007) and Winiarek et al. (2012), it is therefore convenient to discard Q_{priori} from the formulation of the cost function, i.e. to set $Q_{priori} = 0$, which then reduces to:

$$J = \left\| C^{obs} - CTA \times Q \right\|^2_{\mathbb{R}^{n_C}} + \varepsilon^2 \|Q\|^2_{\mathbb{R}^{n_C}}. \tag{5}$$

Note that imposing $Q_{priori} = 0$ is likely to lead the inversion algorithm in generally underestimating the value of Q, rather than in overestimating it.

The minimum of (5) is computed by imposing:

$$\nabla J = -2\left[CTA^t \times C^{obs} - \left(CTA^t \times CTA + 2\varepsilon^2 I \right) \times Q \right] = 0 \tag{6}$$

which implies that the optimal solution is equal to:

$$Q = \left(CTA^t \times CTA + \varepsilon^2 I\right)^{-1} \times CTA^t \times C^{obs}. \quad (7)$$

Note that the solution depends on the regularization parameter ε, whose value has to be determined by imposing a balance between the two terms of the cost function (5).

In recent years, several authors proposed methods to determine the optimal value of ε (Calvetti et al., 2004, 2000; Chamorro-Servent et al., 2011; Engl and Grever, 1994; Hansen, 2000; Krawczyk-Stando and Rudnicki, 2007; Zhu et al., 2011). These can be essentially divided into two groups (Bouman, 1998): a posteriori methods and heuristic methods. We adopt herein a heuristic method based on the L-curve approach (Calvetti et al., 2000; Hansen, 2000, 1992; Hansen and O'Leary, 1993; Zhu et al., 2011) that has been widely used for inverse problems related to atmospheric pollutant dispersion (Davoine and Bocquet, 2007; Krysta et al., 2008; Winiarek et al., 2012).

This method allows the regularization parameter to be determined from the L-shaped curve (Fig. 6) that expresses, in logarithmic scale, the evolution of the error $\|Q\|$ due to the regularization as a function of the noise intensity of the signal $\left\|C^{obs} - CTA \times Q\right\|$. Hansen and O'Leary (1993) and Hansen (2000, 1992) showed that the optimal value ε^{opt} ensures a good balance between the effects of regularization errors due to the noise of the signal, i.e. it minimizes both $\|Q\|$ and $\left\|C^{obs} - CTA \times Q\right\|$. The optimal value ε^{opt} can be determined by drawing the -1 slope line and tangent to the curve (green dashed curve in Fig. 6a). In this study, this approach has been implemented numerically by reconstructing the L-curve with different values of $\varepsilon > 0$. As an example, we show in Fig. 6b the L-curve plot of one of the receptors studied.

Note that adding the regularization term $\varepsilon^2 \|Q\|^2_{\mathbb{R}^{n_C}}$ in the formulation of the problem has two main implications in its mathematical solution:

i) it dampens the effect of the fluctuations in the signal;
ii) it provide a further mathematical constrain to the solution of the problem. This implies that, once fixed ε^{opt}, (6) has a unique solution even in the case in which the number of unknowns of the problem exceeds the number of observation, a case in which the least-square problem would lead to infinite solutions.

To enlighten the importance of a regularization method, we present some preliminary results, with and without its inclusion in the inverse algorithm. Results refer to the inversion of i) a synthetic concentration signal, i.e. provided by the direct model, representing an ensemble average over an infinite number of realisations, and ii) an ensemble-averaged signal, i.e. obtained averaging the 100 signals registered, at a fixed receptor, during the passive scalar release experiments.

A comparison between the evolution of the flow rate at the source computed by the inverse model and the actual flow rate is presented in Fig. 7a and b for the synthetic and the ensemble-averaged signal, respectively. Despite some fluctuations, whose amplitude is about 10% of the intensity of the signal, the flow rate computed from the synthetic signal is accurate (Fig. 7a). Conversely, the solution of the inverse model applied to the ensemble-averaged signal (Fig. 7b) exhibits fluctuations whose amplitude can attain 1000% of the average value of the signal. Note that the level of the fluctuations of this experimental ensemble-averaged signal is significantly damped compared to that of a turbulent signal registered during one single realisation of the dispersion process (see Fig. 2c–f). This example therefore provides clear evidence of the high sensitivity of the least squares solution to fluctuations in the input signals, even when these are tiny compared to the turbulent fluctuations registered within a single realisation of the dispersion process (see Fig. 3c–e): a small amplitude noise prevents the least squares method providing insight on the flow rate at the source. This shows the need for a regularization method to mitigate the effects of noise and improve the quality of the results.

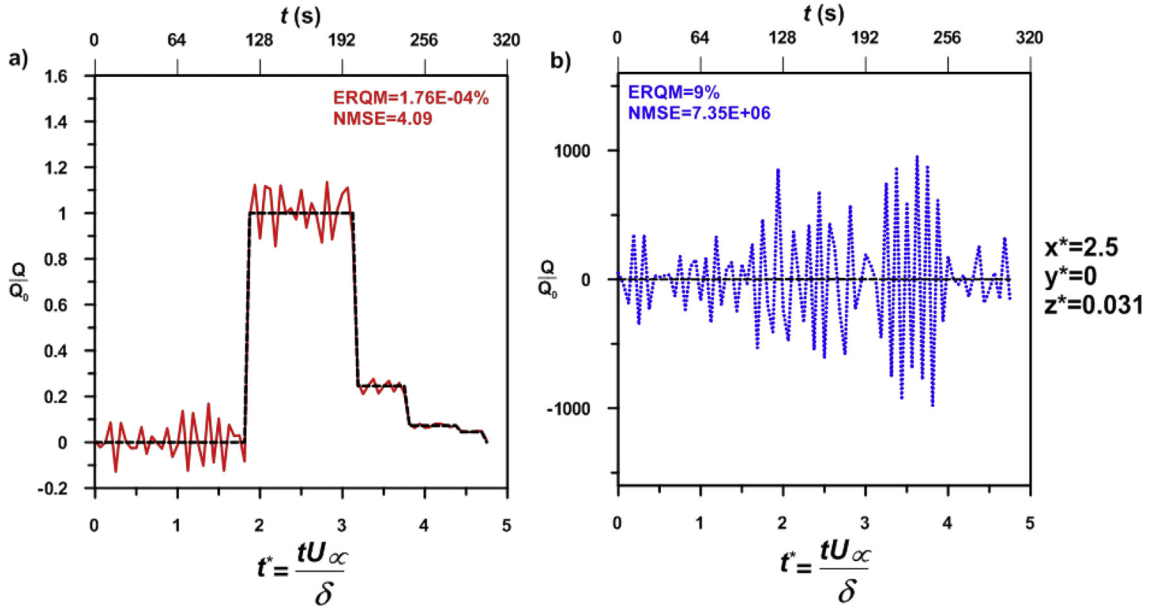

Fig. 7. Results of the inversion based on a simple least squares method, i.e. without using a regularization method, applied to a) synthetic observations provided by the SIRANERISK model (red) and b) an averaged signal computed from 100 realisations of the dispersion process registered in the wind tunnel experiments (blue). Results are compared to the actual emission flow rate (black dashed line). Signals refer to the R20 configurations, receptor R2. (For interpretation of the references to colour in this figure legend, the reader is referred to the web version of this article.)

5. Results

We test the reliability of the inverse model to estimate the mass flow arte at the source, using concentration signals registered at different receptors, whose positions are indicated in Fig. 6. For each receptor, we apply the inverse algorithm for each signal registered during each of the 100 releases. We also apply the inverse algorithm to the ensemble-averaged signals. As reference settings we also adopt $T_q = 4s$ and $T_c = 5s$. Sensitivity to varying T_q and T_c will be examined in Section 5.3. Values of T_S and T_R are assumed to be much larger than the emission time T_E (see Fig. 2a) and of the typical puff advection time, respectively.

Before going into the details of the results of the two configurations, we present an example (Fig. 8) of the inverse algorithm applied to the ensemble-averaged concentration signal and to the 100 turbulent signals for the receptor R2 (see Fig. 3). In Fig. 8 we plot the evolution of the flow rate $q_{est}(t)$, normalized by the real flow rate $q_{true}(t)$, predicted by inverting the ensemble-averaged signal (red), the average (blue), and the minimal and the maximal values (grey) of the 100 flow rates predicted by inverting the single realisations. The plot shows three main features:

- the inversion of the ensemble-averaged signal is very similar to the mean of the signals obtained inverting the turbulent signals;
- the maximal error in the prediction of the flow rate from a turbulent signal is of order 100%;
- the flow rate value is not bounded at zero, since we have not imposed a positivity constraint in the problem formulation.

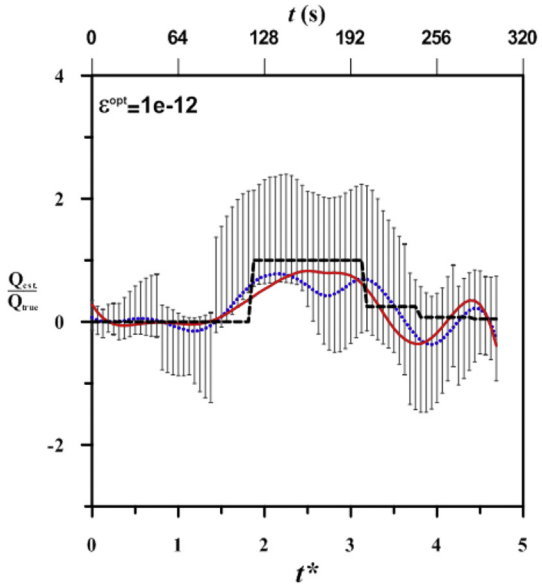

Fig. 8. Time evolution of the (non-dimensional) flow rate at the source. Comparison between the actual flow rate (black dashed line), the flow rate provided by the ensemble-averaged signal (red continuous line) and the average of the results of the instantaneous signals (blue dotted line). The error bars are delimited, at each time step, by the maximal and the minimal value of the flow rate among the 100 values obtained by inverting the 100 turbulent signals. (For interpretation of the references to colour in this figure legend, the reader is referred to the web version of this article.)

To quantify the error in the predictions of the inverse model we adopt two statistical indices to estimate a 'local' and a 'global' error. The 'local' error is quantified by the Normalized Mean Square Error (NMSE):

$$NMSE = \left[\frac{\frac{1}{n}\sum_{t_i=1}^{n}\left(q_{true}^{t_i} - q_{est.}^{t_i}\right)^2}{\frac{1}{n}\sum_{t_i=1}^{n}\left(q_{true}^{t_i}\right)\frac{1}{n}\sum_{t_i=1}^{n}\left(q_{est.}^{t_i}\right)} \right], \tag{8}$$

and reflects the uncertainties in the form of the reconstructed signals representing the time evolution of the emission at the source.

The 'global' error, referred herein as the Relative Error on the Quantity of Mass (ERQM), is computed as:

$$ERQM = \frac{\left(\left(\int_{t_0}^{t_f} q_{true}^{t_i} \times \Delta t - \int_{t_0}^{t_f} q_{est.}^{t_i} \times \Delta t\right) \times 100\right)}{\int_{t_0}^{t_f} q_{true}^{t_i} \times \Delta t} \tag{9}$$

and reflects the uncertainty in the estimate of the total mass of pollutant released.

In the literature (Chang and Hanna, 2004), it is generally assumed that for a direct dispersion model to perform well, it requires values of the local error NMSE $\leq$ 4. We adopt herein the same reference for the inverse model and we fix a reference value of 0.5 for the ERQM.

5.1. R20 configuration – dispersion above sparse city districts

We show in Fig. 9 the probability density function (PDF) of the global (ERQM) and local (NMSE) errors, respectively, obtained from 100 source flow rates computed by the model. In the graphs we also plot the average error (computed by averaging the errors of each of the 100 realisations) and the errors of the inversion of the ensemble-averaged signal.

The results show that the algorithm generally provides satisfactory information on the total mass of pollutant released. Indeed, the ERQM is always lower than 100%, a result that reflects the tendency of the inversion algorithm in underestimating Q, rather than overestimating it (see Section 4). The PDFs of the ERQM are generally positively skewed, except for R5, whose form is less defined compared to that of the other receptors. The ERQM of the ensemble-averaged signal is always lower than the mean of the ERQM of the turbulent signals, the former being always close to 20% and the latter close to 40%.

The NMSE (i.e. the uncertainty on the form of the signals) is generally acceptable. Its PDFs are also positively skewed, with almost 60% of the values of NMSE $\leq$1. This is probably reliant on the receptors being in the 'core' of the dispersing plume, therefore always intercepting it over the time the signals are recorded.

Results for varying lateral positions of the receptors (the direction Y) show that the overall trends of the PDF are similar at R1 and R2 (at $x^* = 2.5$) and at R3, R4 and R5 (at $X^* = 5$). For two receptors whose positions are symmetrical with respect to the wind direction axis, the results provided by the ensemble averages are almost identical (R3 and R5), whereas this is not the case for results obtained inverting the time-averaged concentration signals.

When analysing the PDFs of the NMSE it appears that the quality of the results is improved when inverting the signal registered far from the source. The PDF of the NMSE is considerably improved (but not that of the ERQM), i.e. shifted towards lower values, for R3, R4 and R5, compared to that of R1 and R2. Note that these differences cannot be attributed to the performance of the direct model. As shown in Fig. 4, the best agreement between the model and the experimental results is actually observed in the near field, i.e. at R1 and R2, whereas results in the far field, especially at R4 and R5, are characterised by larger discrepancies between the two. In other words, when reconstructing the form of the source flow rate, the

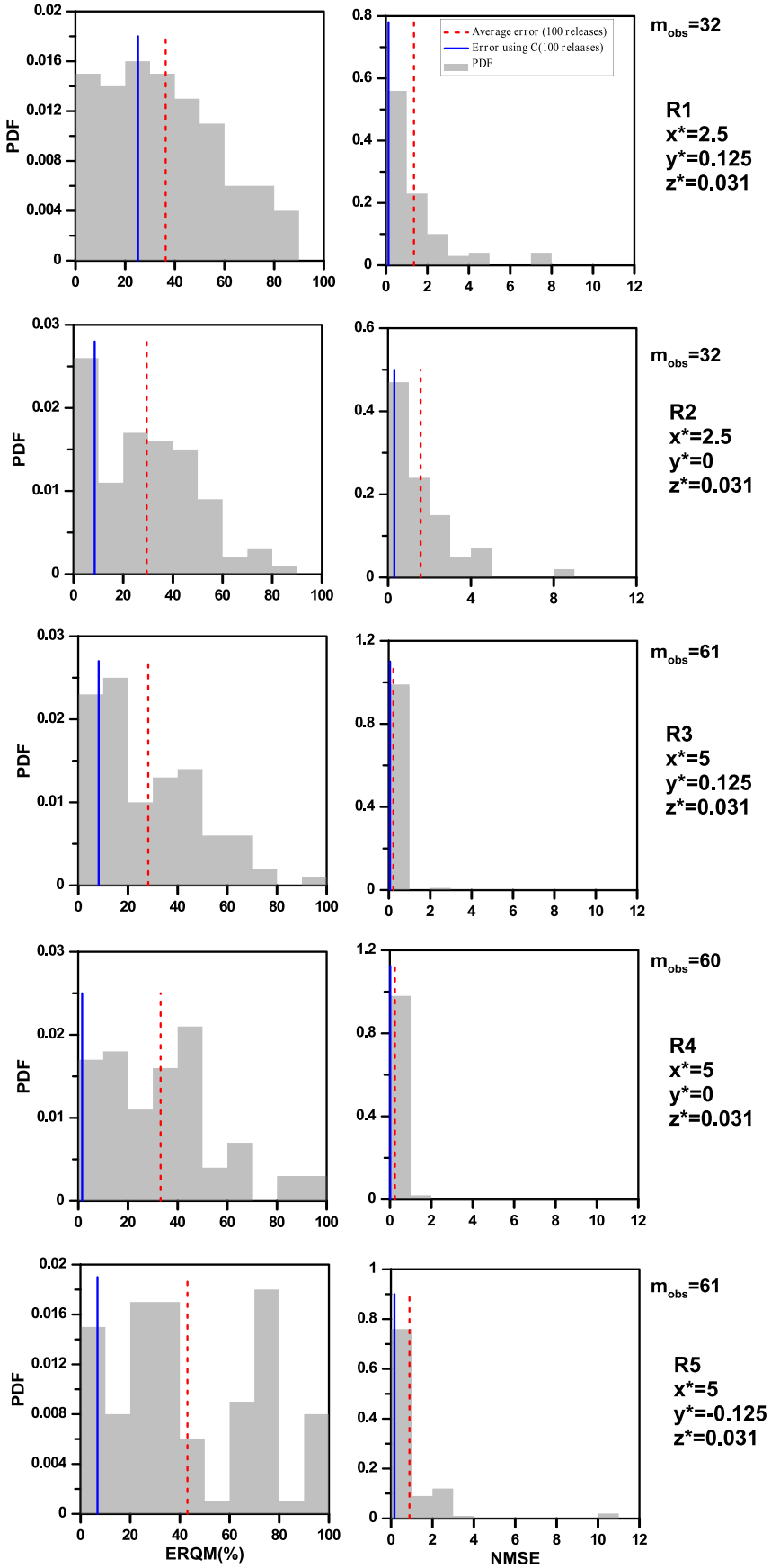

Fig. 9. PDF of the global (ERQM) and local (NMSE) error in the inverse model predictions for the R20 configuration. The red dotted line indicates the average error of the inversion of the turbulent signals and the continuous blue line indicates the error obtained by inverting the ensemble-averaged signal. (For interpretation of the references to colour in this figure legend, the reader is referred to the web version of this article.)

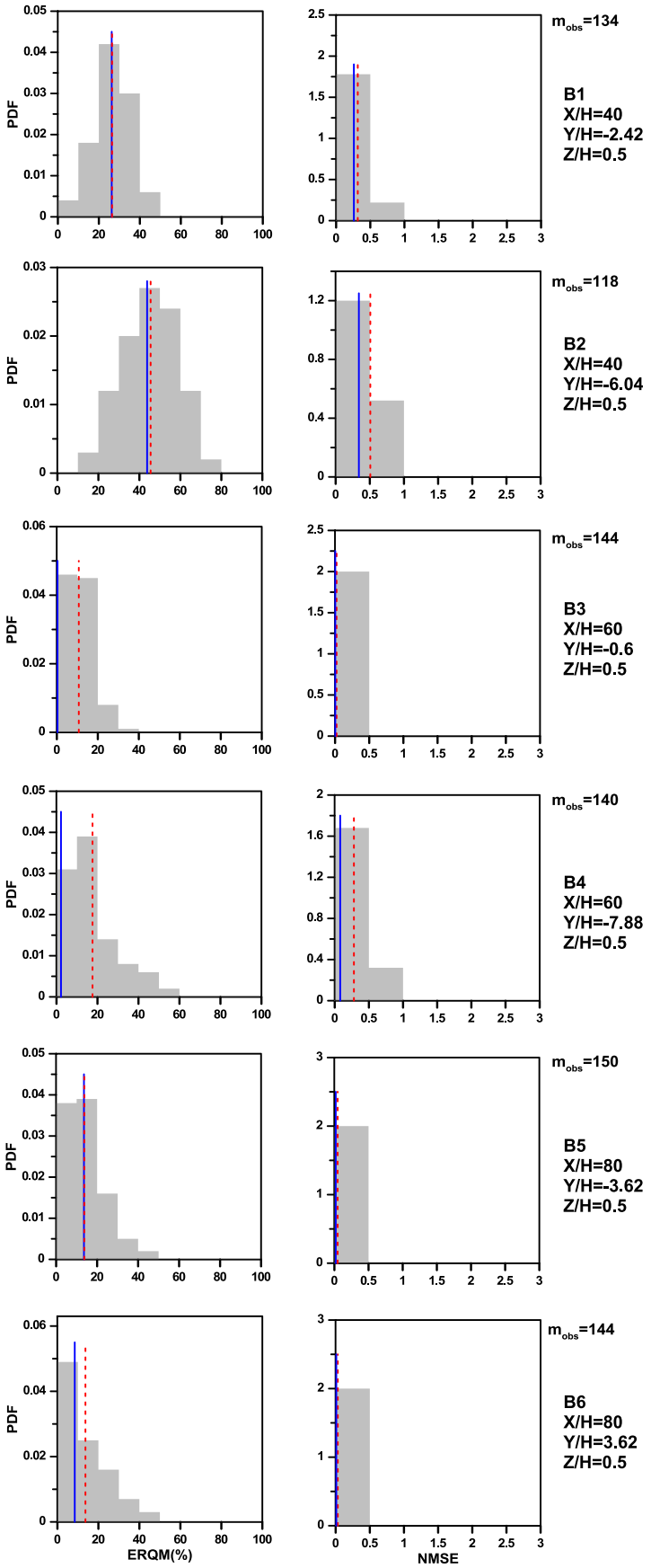

Fig. 10. As for Fig. 9, for the configuration B50.

inverse model provides better results for the receptors at which the direct model is shown to provide less accurate results. The reason for the improved accuracy of the prediction of the source flow rate by the inverse model can be reasonably attributed to the lower intermittency, which characterises the turbulent concentration signals registered away from the source, where the meandering motion is less effective.

5.2. B50 configuration - dispersion within a dense city district

Results for the B50 configuration, i.e. the idealised urban district, are given in Fig. 10, where we show the PDFs of the ERQM and NMSE provided by the sample of 100 results obtained by the corresponding turbulent concentration signals.

The first aspect to note is the significant improvement in the results compared to the R20 configuration. Except for the ERQM of B2, both the PDFs of the ERQM and of the NMSE of the B50 receptors are characterised by lower values compared to their analogues in the R20 configuration. In particular it is impressive how the NMSE values are reduced compared to the previous case analysed. Notably, the NMSE PDFs in Fig. 10 are all characterised by values ≤ 1 (with most of them ≤ 0.5).

The worst results are observed in the near field, i.e. at receptors B1 and B2, where the predictions of the direct model actually show significant discrepancies with the experimental results (see Fig. 5). This is particularly evident when analysing the PDFs of the ERQM. Differently from those of the other receptors, which are clearly positively skewed, the PDFs of the ERQM for B1 and B2 are normally distributed, with mean values that are larger than those for receptors B3–B6.

However, when analysing the accuracy in the prediction of the form of the signal at the source, i.e. the NMSE, the results are also surprisingly good for the receptors B1 and B2 (compared to their analogues in configuration R20, i.e. at receptors R1 and R2). Even in this case, the reasons for this higher accuracy can be reasonably attributed to the lower intermittency of the concentration signals registered in the B50 configuration, compared to the R20 configuration (see Fig. 2). This result highlights a major aspect of the performance of the inverse model. Its reliability in reconstructing the source flow rate is actually only partially related to the accuracy of the direct model, which, it is worth remembering, is only able to predict the ensemble-averaged concentration signal. Conversely, its ability to estimate the source flow rate is greatly affected by the intermittency of the signal.

5.3. Sensitivity tests

Finally, we test the sensitivity of the results to varying timescales T_c and T_q, i.e. to the frequency of the signals reconstructed at the source $f_q = \frac{1}{T_q}$ and the sampling frequency of the receptor $f_c = \frac{1}{T_c}$. In particular, we focus on the influence of the ratio between the two, i.e.

$$\tau = \frac{T_c}{T_q} = \frac{f_q}{f_c} \tag{10}$$

for different values of the ratio T_q/T_E. The analysis, which is performed with signals registered at a fixed receptor (R2, see Fig. 3) allows us to evaluate the effect on the accuracy of the prediction induced by the limited sampling frequency of the in-situ instruments.

We show in Fig. 11, results for $\frac{T_q}{T_E} = \frac{4}{68}$ and two different $\tau = \frac{T_c}{T_q}$. Note that PDFs for $\tau = 1.25$ are the same as those presented in Fig. 9

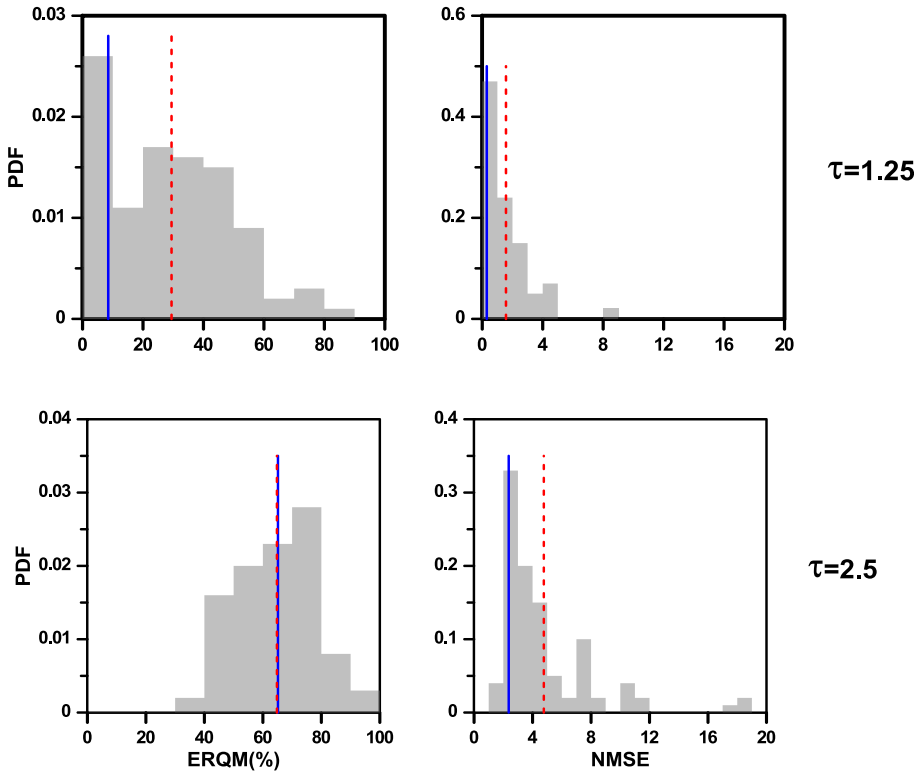

Fig. 11. PDF of the local (NMSE) and global (ERQM) errors in the predictions of the total mass ejected, from the signal registered at the R2 receptor (R20 configuration), with Tq = 4s. The red dotted line indicates the average of the errors of the turbulent signal, and the continuous blue line indicates the error provided by the ensemble-averaged signal. (For interpretation of the references to colour in this figure legend, the reader is referred to the web version of this article.)

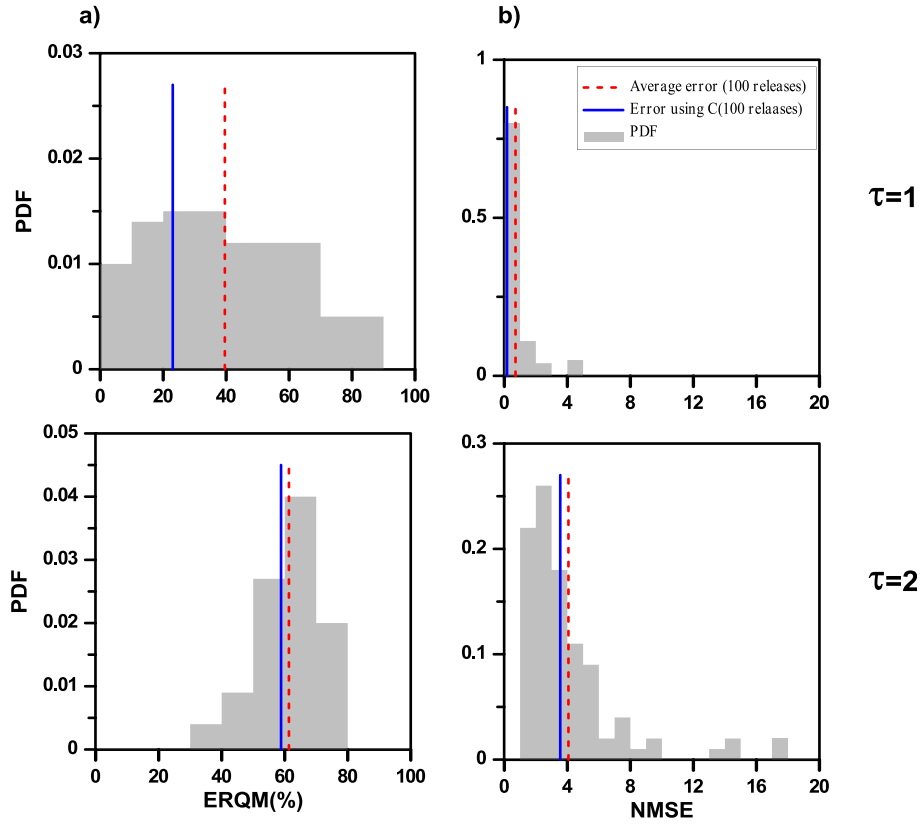

Fig. 12. As for Fig. 11, with Tq = 2s.

(second row). This latter result is compared to the case $\tau = 2.5$, i.e. of a halved sampling frequency at the receptor. Halving the sampling frequency leads to a significant deterioration in the results. The relative errors of the total mass do not exceed 100%, but their mean is almost doubled (by approximately 70%) and their values are all larger than 40%. Also, the values of the NMSE are all shifted toward larger values and their mean becomes larger than the threshold of 4, with peaks of almost 20.

A very similar behavior is observed for both a reduced 2/68 (Fig. 12) and an increased 20/68 (Fig. 13) ratio $\frac{T_q}{T_E}$. In both cases we compare results for $\tau = 1$ and $\tau = 2$. Note that this latter value can be considered as a threshold to adequately describe the temporal variations of the source strength according to the Shannon-Nyquist sampling theorem, which prescribes a minimal sampling frequency $f_c > 2/T_S$.

Plots in Fig. 12a are very similar to those in Fig. 11a, showing that reducing the ratio $\frac{T_q}{T_E}$ by a factor of two has little effect on the quality of the data, as long as T_q is significantly smaller than T_E. Conversely, as T_q approaches T_E, both local and global errors show a general trend to increase, even for low τ (Figs. 12 and 13).

In all cases analysed, we observe that the quality of the results deteriorates as $\tau \geq 2$, i.e. as the frequency of the reconstructed flow rate becomes larger than twice the sampling frequency of the concentration signal. In this case (see Figs. 11a and 12a), most of the global errors (ERQM) exceed 50%, and the local errors (NMSE) exceed the threshold value of 4.

Results for the ensemble-averaged signals (continuous blue line) are generally (much) better than those for the mean of the results obtained inverting the instantaneous signals (dotted red line). However, for $\tau \geq 2$, the error associated with the ensemble-averaged signals gradually approaches that of the mean of the error obtained by inverting the turbulent signals.

In a general way, and as expected, we can therefore conclude that the quality of the results deteriorates when reducing T_q and increasing T_c. We can however note that the effect of filtering the input data, i.e. increasing τ, is reduced when considering the global error (ERQM) rather than the local error (NMSE).

Reducing T_q (for a fixed T_c) leads to a deterioration in the results because of the limitations of the method in solving problems with a number of unknowns that exceed the input data, i.e. $n \gg m$. Increasing T_c (for a fixed T_q) leads to a deterioration in the results since it implies a reduction in the number of representative observations m_{obs} of the concentration signals used to reconstruct the flow rates, implying a loss of information for use in the reconstruction of the flow rate.

As shown in Fig. 14, the reduction of m_{obs} has a direct impact on both statistical indices ERQM and NMSE. For the same number of observations, the reliability of the algorithm deteriorates as T_q decreases (and therefore f_q increases). However, this tendency varies significantly for varying m_{obs}. Even though the trend of ERQM and NMSE as a function of m_{obs} is very similar in the different cases analysed, we cannot define a threshold value of m_{obs}, which ensures good quality results for any T_q. Nevertheless, in the case here considered, for $m_{obs} = 32$ results are satisfactory (Fig. 14b), according to both the values of the global, i.e. ERQM, and the local error, i.e. NMSE.

6. Discussion and conclusions

We have presented the results of inverse atmospheric dispersion modelling of unsteady pollutant emissions. The objective was to evaluate the ability of the inverse algorithm to estimate the mass

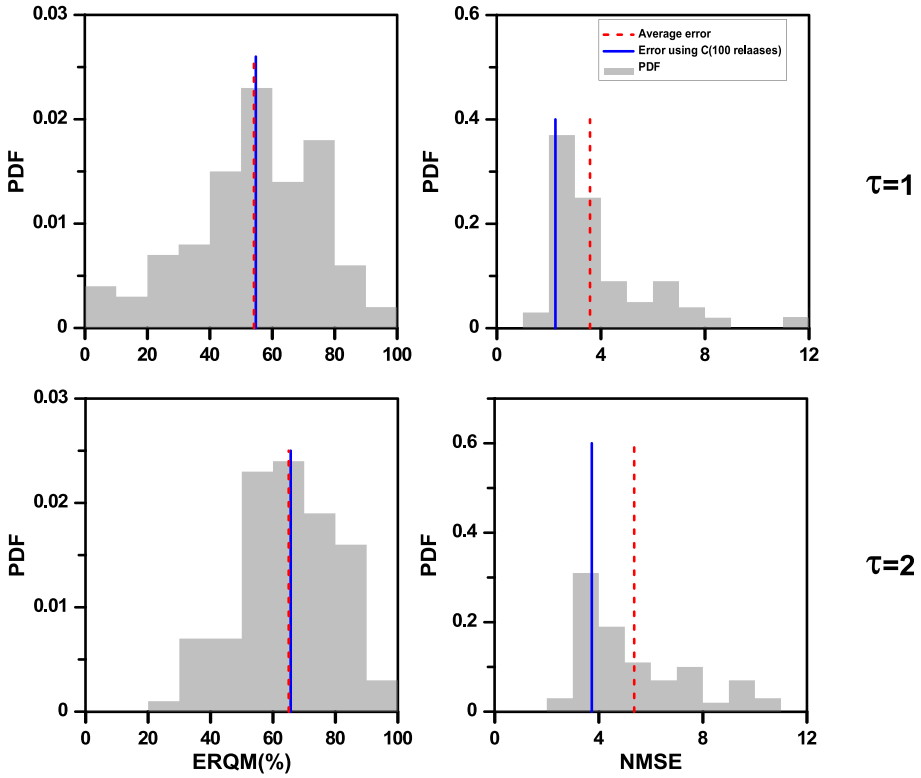

Fig. 13. As for Fig. 11, with Tq = 20s.

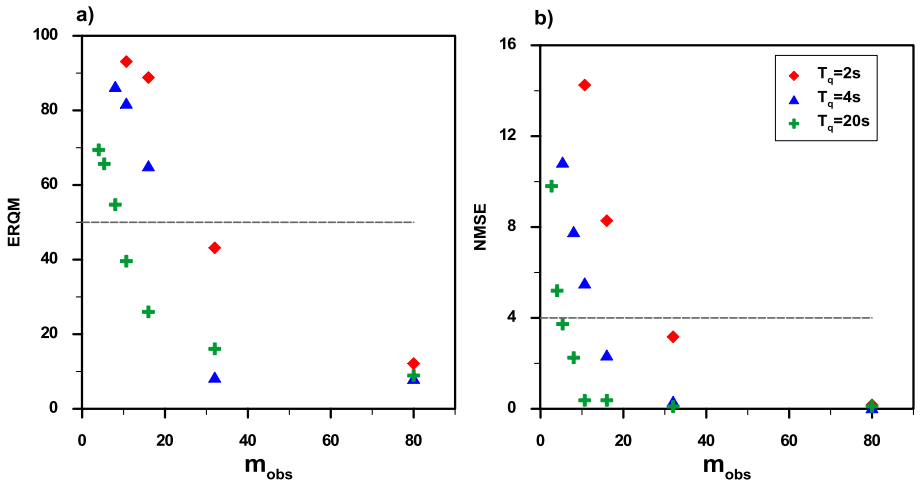

Fig. 14. Changes in ERQM (a) and NMSE (b) obtained by inverting the ensemble averages based on the number of representative observations in the concentration signals.

flow rate of an impulsive source of pollutant from turbulent concentration signals, measured in wind tunnel experiments, above a sparse city district (configuration R20) and within a dense urban canopy (configuration B50). The turbulent signals were inverted by adopting a least squares algorithm coupled with the Tikhonov regularization method.

The inverse model was applied using as input data the turbulent concentration signals registered at a fixed receptor and the corresponding ensemble-averaged signals (averaged over 100 realisations), and adopting as a direct model, SIRANERISK, which simulated the dispersion of unsteady releases with a street network approach. The comparison of the results obtained using these two types of input data provides useful insight into the reliability of an inverse algorithm in real case scenarios, when the algorithm is applied to turbulent signals using atmospheric dispersion models based on the concept of ensemble average. We have evaluated the performance of the model by means of two statistical indices, referred to as NMSE and ERQM, estimating a local and a global error, respectively.

We have shown that the inverse model is generally able to estimate the mass released with a global error, i.e. ERQM that does not exceed 100% in both configurations studied. This means that the model allows us to estimate the order of magnitude of the mass of pollutant ejected, information that is more than useful when assessing the risks related to accidental pollutant releases in a built environment. Note that this conclusion is based on the hypothesis

of disposing of data from a from a single well-positioned sensor, i.e. positioned in the core of the plume and returning concertation signals that are not just noise. In real case scenarios this would imply disposing of a network of sensor designed to ensure that at least one is well positioned in the gas cloud.

Concerning the prediction of the time-evolution of the source flow rate, the performance of the inverse model seems to be more sensitive to the level of intermittency and/or the intensity of fluctuation of the turbulent signals rather than to the accuracy of the direct model. Namely, according to the PDFs of the NMSE, the performance of the model was shown to be better for signals registered within a dense urban canopy (B50) than for signals registered over a rough surface (R20), even though the predictions of the direct model were generally better for the latter configuration rather than for the former. Notably, in the dense urban canopy configuration (B50), the NMSE values are shown to be lower than 1, with a global error on the total mass of generally lower than 50%. These results strongly support the use of such a modelling approach for operational purposes and for the management of risks due to accidental pollutant releases in a built environment.

Finally, we tested the sensitivity of the inverse method to the sampling frequency f_c of the registered concentration signal used as an input, and of the frequency f_q at which the variation of the flow rate at the source was reconstructed. These showed a deterioration in the reliability of the algorithm for decreasing f_c and increasing f_q. Reducing f_c can indeed significantly reduce the number of representative observations used in the inversion and therefore result in a lack of information for use in the inversion. These features provide important information on the sampling cut-off frequencies of the instruments adopted to build the monitoring network.

Acknowledgements

This study was supported by the Rhône-Alpes Region.

References

Abida, R., Bocquet, M., 2009. Targeting of observations for accidental atmospheric release monitoring. Atmos. Environ. 43, 6312–6327.
Backus, G.E., Gilbert, J.F., 1967. Numerical applications of a formalism for geophysical inverse problems. Geophys. J. Int. 13, 247–276.
Bady, M., 2013. Fundamentals of direct inverse CFD modeling to detect air pollution sources in urban areas. Comput. Water Energy Environ. Eng. 02, 31–42.
Bocquet, M., 2010. Modélisation inverse des sources de pollution atmosphérique accidentelle : progrès récents. Pollut. Atmos. Numero Spec. 151–160.
Bouman, J., 1998. Quality of Regularization Methods. Delft University Press, Delft.
Brereton, C.A., Johnson, M.R., 2012. Identifying sources of fugitive emissions in industrial facilities using trajectory statistical methods. Atmos. Environ. 51, 46–55.
Bruneau, J.M., Blanc-Feraud, L., Barlaud, M., 1991. Opérateurs de régularisation en restauration d'image : Calculs et comparaisons.
Calvetti, D., Morigi, S., Reichel, L., Sgallari, F., 2000. Tikhonov regularization and the L-curve for large discrete ill-posed problems. J. Comput. Appl. Math. 123, 423–446.
Calvetti, D., Reichel, L., Shuibi, A., 2004. L-curve and curvature bounds for Tikhonov regularization. Numer. Algorithms 35, 301–314.
Chai, T., Draxler, R., Stein, A., 2015. Source term estimation using air concentration measurements and a Lagrangian dispersion model – experiments with pseudo and real cesium-137 observations from the Fukushima nuclear accident. Atmos. Environ. 106, 241–251.
Chamorro-Servent, J., Aguirre, J., Ripoll, J., Vaquero, J.J., Desco, M., 2011. Feasibility of U-curve method to select the regularization parameter for fluorescence diffuse optical tomography in phantom and small animal studies. Opt. Express 19, 11490–11506.
Chang, J., Hanna, S.R., 2004. Air quality model performance evaluation. Meteorol. Atmos. Phys. 87, 167–196.
Chow, F.K., Kosović, B., Chan, S., 2008. Source inversion for contaminant plume dispersion in urban environments using building-resolving simulations. J. Appl. Meteorol. Climatol. 47, 1553–1572.
Cortés, O., Urquiza, G., Hernández, J.A., 2009. Inverse heat transfer using levenberg-marquardt and particle swarm optimization methods for heat source estimation. Appl. Mech. Mater 15, 35–40.
Cullum, J., 1979. The effective choice of the smoothing norm in regularization. Math. Comput. 33, 149–170.
Davoine, X., Bocquet, M., 2007. Inverse modelling-based reconstruction of the Chernobyl source term available for long-range transport. Atmos. Chem. Phys. 7, 1549–1564.
Engl, H.W., Grever, W., 1994. Using the L-curve for determining optimal regularization parameters. Numer. Math. 1, 25–31.
Enting, I.G., 2002. Inverse Problems in Atmospheric Constituent Transport. Cambridge University Press, Cambridge; New York.
Fackrell, J.E., Robins, A.G., 1982. The effects of source size on concentration fluctuations in plumes. Boundary-Layer Meteorol. 22, 335–350.
Garbero, V., Salizzoni, P., Soulhac, L., 2010. Experimental study of pollutant dispersion within a network of streets. Bound.-Layer Meteorol. 136, 457–487.
Gifford, F., 1959. Statistical properties of a fluctuating plume dispersion model. Adv. Geophys. 6, 117–137.
Glascoe, L., Neuman, S., Kosović, B., Dyer, K., Hanley, W., Nitao, J., 2006. Event reconstruction for atmospheric releases employing urban puff model UDM with stochastic inversion methodology. In: 86th AMS Annual Meeting.
Hansen, P.C., 1992. Analysis of discrete ill-posed problems by means of the L-curve. SIAM Rev. 34, 561–580.
Hansen, P.C., 2000. The L-curve and its use in the numerical treatment of inverse problems. In: Johnston, P. (Ed.), In Computational Inverse Problems in Electrocardiology. Advances in Computational Bioengineering. WIT Press, pp. 119–142.
Hansen, P.C., O'Leary, D.P., 1993. The use of the L-curve in the regularization of discrete ill-posed problems. SIAM J. Sci. Comput. 14, 1487–1503.
Hoydysh, W.G., Dabberdt, W.F., 1994. Concentration fields at urban intersections: fluid modeling studies. Atmos. Environ. 28, 1849–1860.
Irwin, H.P.A.H., 1981. The design of spires for wind simulation. J. Wind Eng. Ind. Aerodyn. 7, 361–366.
Issartel, J.-P., Sharan, M., Singh, S.K., 2012. Identification of a point of release by use of optimally weighted least squares. Pure Appl. Geophys. 169, 467–482.
Jeong, H.-J., Kim, E.-H., Suh, K.-S., Hwang, W.-T., Han, M.-H., Lee, H.-K., 2005. Determination of the source rate released into the environment from a nuclear power plant. Radiat. Prot. Dosim. 113, 308–313.
Kanasewich, E.R., Chiu, S.K., 1985. Least-squares inversion of spatial seismic refraction data. Bull. Seismol. Soc. Am. 75, 865–880.
Keats, A., Yee, E., Lien, F.-S., 2007. Bayesian inference for source determination with applications to a complex urban environment. Atmos. Environ. 41, 465–479.
Khlaifi, A., Ionescu, A., Candau, Y., 2009. Pollution source identification using a coupled diffusion model with a genetic algorithm. Math. Comput. Simul. 79, 3500–3510.
Krawczyk-Stando, D., Rudnicki, M., 2007. Regularization parameter selection in discrete ill-posed problems - the use of the U-Curve. Appl. Math. Comput. Sci. 17, 157–164.
Krysta, M., Bocquet, M., Sportisse, B., Isnard, O., 2006. Data assimilation for short-range dispersion of radionuclides: an application to wind tunnel data. Atmos. Environ. 40, 7267–7279.
Krysta, M., Bocquet, M., Brandt, J., 2008. Probing ETEX-II data set with inverse modelling. Atmos. Chem. Phys. 8, 3963–3971.
Lattes, R., Lions, J.L., 1969. The method of quasi-reversibility; applications to partial differential equations, by R. Lattes and J.-L. Lions. Translated from the French ed. and edited by Richard Bellman, Modern analytic and computational methods in science and mathematics ;; 18. American Elsevier Pub. Co, New York.
Lewis, J.M., Derber, J.C., 1985. The use of adjoint equations to solve a variational adjustment problem with advective constraints. Tellus A 37, 309–322.
Lewis, J.M., Lakshmivarahan, S., Dhall, S., 2006. Dynamic Data Assimilation: a Least Squares Approach. Cambridge University Press.
Lien, F.S., Yee, E., Ji, H., Keats, A., Hsieh, K.J., 2006. Application of CFD to security science: progress on the development of a high-fidelity numerical model for hazard prediction and assessment in the urban environment. CFD Soc. Can. Bull. 17, 9–16.
Lin, W., Chen, L., Yu, W., Ma, H., Zeng, Z., Lin, J., Zeng, S., 2015. Radioactivity impacts of the fukushima nuclear accident on the atmosphere. Atmos. Environ. 102, 311–322.
Lushi, E., Stockie, J.M., 2010. An inverse Gaussian plume approach for estimating atmospheric pollutant emissions from multiple point sources. Atmos. Environ. 44, 1097–1107.
Marro, M., Nironi, C., Salizzoni, P., 2015. Soulhac, Dispersion of a passive scalar fluctuating plume in a turbulent boundary layer. Part II: analytical modelling. Boundary-Layer Meteorol. 156, 447–469.
Naveen, M., Jayaraman, S., Ramanath, V., Chaudhuri, S., 2010. Modified Levenberg marquardt algorithm for inverse problems. In: Deb, K., Bhattacharya, A., Chakraborti, N., Chakroborty, P., Das, S., Dutta, J., Gupta, S.K., Jain, A., Aggarwal, V., Branke, J., Louis, S.J., Tan, K.C. (Eds.), Simulated Evolution and Learning, Lecture Notes in Computer Science. Springer Berlin Heidelberg, pp. 623–632.
Neumaier, A., 1998. Solving ill-conditioned and singular linear systems: a tutorial on regularization. SIAM Rev. 40, 636–666.
Nironi, C., Salizzoni, P., Marro, M., Mejean, P., Grosjean, N., Soulhac, L., 2015. Dispersion of a passive scalar fluctuating plume in a turbulent boundary layer. Part I: velocity and concentration measurements. Bound.-Layer Meteorol. 156, 415–446.
Pujol, J., 2007. The solution of nonlinear inverse problems and the Levenberg-Marquardt method. Geophysics 72, W1–W16.
Quélo, D., Krysta, M., Bocquet, M., Isnard, O., Minier, Y., Sportisse, B., 2007.

Validation of the Polyphemus platform on the ETEX, Chernobyl and Algeciras cases. Atmos. Environ. 41, 5300–5315.
Richardson, R.M., Zandt, G., 2009. Inverse Problems in Geophysics (No. GEOS 567). University of Arizona. Tuson, Arizona 85721.
Robins, A., Savory, E., Scaperdas, A., Grigoriadis, D., 2002. Spatial variability and source-receptor relations at a street intersection. Water Air Soil Pollut. Focus 2, 381–393.
Roussel, G., Delmaire, G., Ternisien, E., Lherbier, R., 2000. Separation problem of industrial particles emissions using a stationary scattering model. Environ. Model. Softw. 15, 653–661.
Rudd, A.C., Robins, A.G., Lepley, J.J., Belcher, S.E., 2012. An inverse method for determining source characteristics for emergency response applications. Bound.-Layer Meteorol. 144, 1–20.
Salizzoni, P., Soulhac, L., Mejean, P., 2009. Street canyon ventilation and atmospheric turbulence. Atmos. Environ. 5056–5067.
Sharan, M., Singh, S.K., Issartel, J.P., 2012. Least square data assimilation for identification of the point source emissions. Pure Appl. Geophys. 169, 483–497.
Singh, S.K., Sharan, M., Issartel, J.-P., 2013. Inverse modelling for identification of multiple-point releases from atmospheric concentration measurements. Bound.-Layer Meteorol. 146, 277–295.
Skaggs, T.H., Kabala, Z.J., 1995. Recovering the history of a groundwater contaminant plume: method of quasi-reversibility. Water Resour. Res. 31, 2669–2673.
Soulhac, L., Perkins, R.J., Salizzoni, P., 2008. Flow in a street canyon for any external wind direction. Boundary-Layer Meteorol. 126, 365–388.
Soulhac, L., Garbero, V., Salizzoni, P., Mejean, P., Perkins, R.J., 2009. Flow and dispersion in street intersections. Atmos. Environ. 43, 2981–2996.
Soulhac, L., Salizzoni, P., Cierco, F.-X., Perkins, R., 2011. The model SIRANE for atmospheric urban pollutant dispersion; part I, presentation of the model. Atmos. Environ. 45, 7379–7395.
Soulhac, L., Salizzoni, P., Mejean, P., Perkins, R.J., 2013. Parametric laws to model urban pollutant dispersion with a street network approach. Atmos. Environ. 67, 229–241.
Soulhac, L., Lamaison, G., Cierco, F.-X., Ben Salem, N., Salizzoni, P., Mejan, P., Armand, P., Patryl, L., 2016. SIRANERISK: modelling dispersion of steady and unsteady pollutant releases in the urban canopy. Atmos. Environ. 140.
Taveau, J., 2010. Risk assessment and land-use planning regulations in France following the AZF disaster. J. Loss Prev. Process Ind. 23, 813–823.
Tikhonov, A.N., Arsenin, V.Y., 1977. In: Solutions of Ill-posed Problems., Translation Edition. Halsted Press Book, Washington, DC.
Winiarek, V., Bocquet, M., Saunier, O., Mathieu, A., 2012. Estimation of errors in the inverse modeling of accidental release of atmospheric pollutant: application to the reconstruction of the cesium-137 and iodine-131 source terms from the Fukushima Daiichi power plant. J. Geophys. Res. Atmos. 117, D18118.
Zhu, Y., Sun, L., Xu, H., 2011. L-curve based Tikhonov's regularization method for determining relaxation modulus from creep test. J. Appl. Mech. 78, 031002.

Chapter 10

Conclusions and perspectives

The research activities leading to the results presented in the previous chapters constitute a body of work which provide the foundations for further ongoing research work. In what follows, we draw some preliminary conclusions and outline the main perspectives of these activities.

Despite the increasing power of computers, that open the field to highly resolved (in space and time) numerical simulations, experiments on turbulent dispersion remain very attractive when dealing with flows at high Reynolds number and bounded by solid rough walls, or flows developing within groups of obstacles. Results presented herein highlight the importance of handling 'classic' experimental techniques for the investigations of these flows, such as Particle Image Velocimetry, hot-wire (HWA) and Laser-Doppler Anemometry (LDA) for velocity measurements and of a Flame Ionisation Detector (FID) for concentration measurements. These kinds of techniques give direct information on turbulent fluxes of mass and momentum, with a significant spectral resolution, therefore providing essential information for the formulation of turbulent closure models for numerical schemes.

Interesting perspectives in the exploitation of these techniques are given by combining the FID system with HWA or LDA, to obtain direct information on the mass scalar fluxes $\overline{u_i c}$. Although not new, this approach has been rarely used to date. An example of results provided by this approach is given in fig. 10, and concerns the dispersion of a passive scalar in a turbulent boundary layer. In the near future we plan to adopt this same technique to study atmospheric dispersion of dense gases[1], in a project funded by Air Liquide.

New perspectives on experimental research are today given by the development of visualisation techniques, such as stereographic and holographic PIV, which will allow access to a description of the flow over a full three-dimensional domain. Major advances in the study of turbulent dispersion require, however, the development of new techniques to fill a main lack in experimental data, that of Lagrangian flow statistics. We may expect that recent progress on nano-technologies would provide new perspectives for their conception and exploitation.

At the same time, the increase in the computer power makes numerical simulations more and more attractive. As discussed in chapter 8, Direct Numerical Simulations of turbulent unbounded flows, such as jets and plumes, can be already considered as more reliable than experiments for the investigation of the basic mechanisms driving dispersion in these flows. The use of Large Eddy Simulations (LES) is more controversial. The impossibility of discerning the influence of the sub-grid model on the results is a major limitation for its use in fundamental studies. Conversely, LES simulations are today an extremely powerful tool for the simulation of flows in complex geometries, such as urban canopies and buildings. They provide a major contribution for the formulation of operational models, as they provide information that is extremely difficult to obtain experimentally (such as the turbulent fluxes

[1]These can be easily simulated in wind tunnel experiments by injecting mixtures of carbon dioxide and air. The small differences of molecular diffusivity in air of carbon monoxide and ethane allow the latter to be used as a tracer gas, whose concentration, measured with a FID, provide information to estimate the local fluid density.

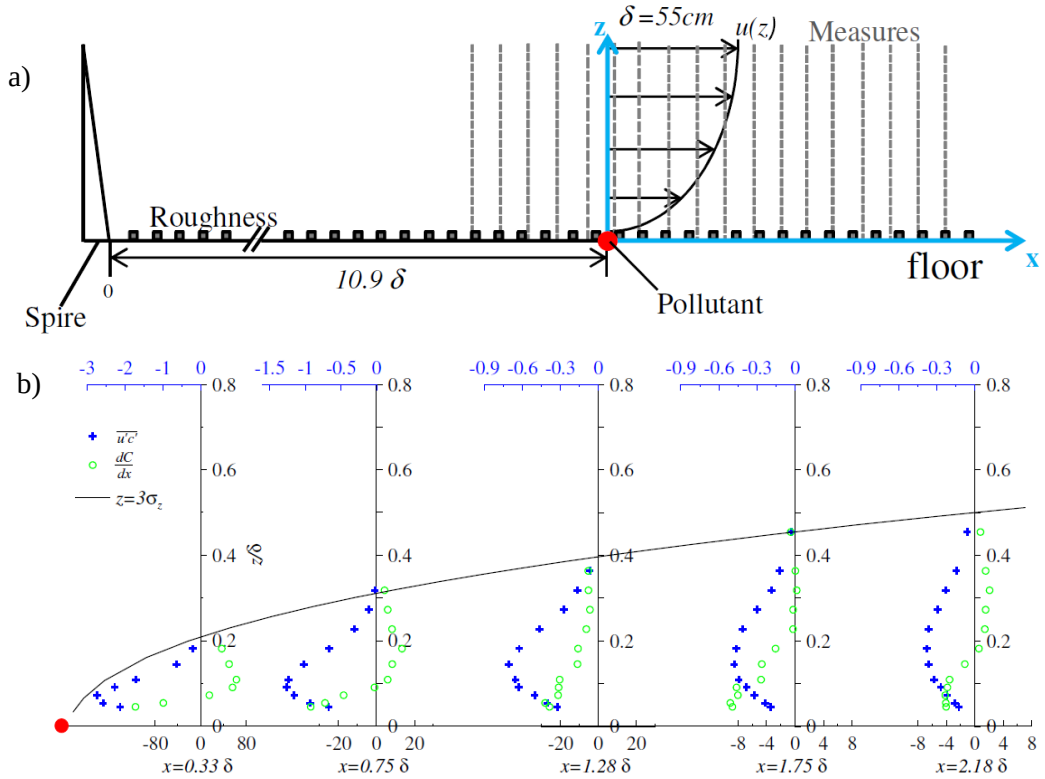

Figure 10.1: Dispersion of a passive scalar released from a line ground-level source in a turbulent boundary layer: examples of results (PhD of H. Gamel, 2015) combining FID and LDA probes. a) Wind tunnel set-up. b) Vertical profiles of longitudinal mass fluxes and mean concentration gradients enlightening the counter-gradient scalar transport.

of mass and heat).

Highly resolved numerical simulations and new experimental techniques will enable us to obtain more and more spatial and temporal details on the structure of turbulent flows. On the other hand, there is an increasing need to use dispersion models to estimate the impacts of air pollution over large domains and long periods. This need opens interesting perspectives in constructing multi-disciplinary research studies.

Current preoccupations with the impact of air pollution on health will inevitably lead to increasing demand for coupling dispersion and air quality modelling with epidemiological studies, and my current research with the Cancer and Environment group of the Centre Léon Bérard in Lyon gives a first indication of what might be possible. These project, named GEO3N and XENAIR, aim at estimating the impact of different kind of pollutants on breast cancer, and use the SIRANE model, developed at the LMFA, as a predictive tool to quantify scores of exposure to air pollution (see fig. 10).

Such studies will also inevitably require an evaluation of the economic costs of air pollution and possible remedial measures, making it necessary to integrate economic modelling into these multi-disciplinary modelling systems. The collaboration already established through the Masters RISE with researchers specialised in the economic aspects of environmental risk should prove invaluable in developing this aspect. Finally, sensor technology and internet connectivity is developing at such a rate that one can envisage that, in the near future, individuals will begin to act as real-time sensors, feeding pollution data into real-time air-quality models. This is already happening, to a limited extent, in some cities, though smart phone applications, and IBM has already expressed an interest in funding some pilot studies of large-scale distributed monitoring systems in the environment.

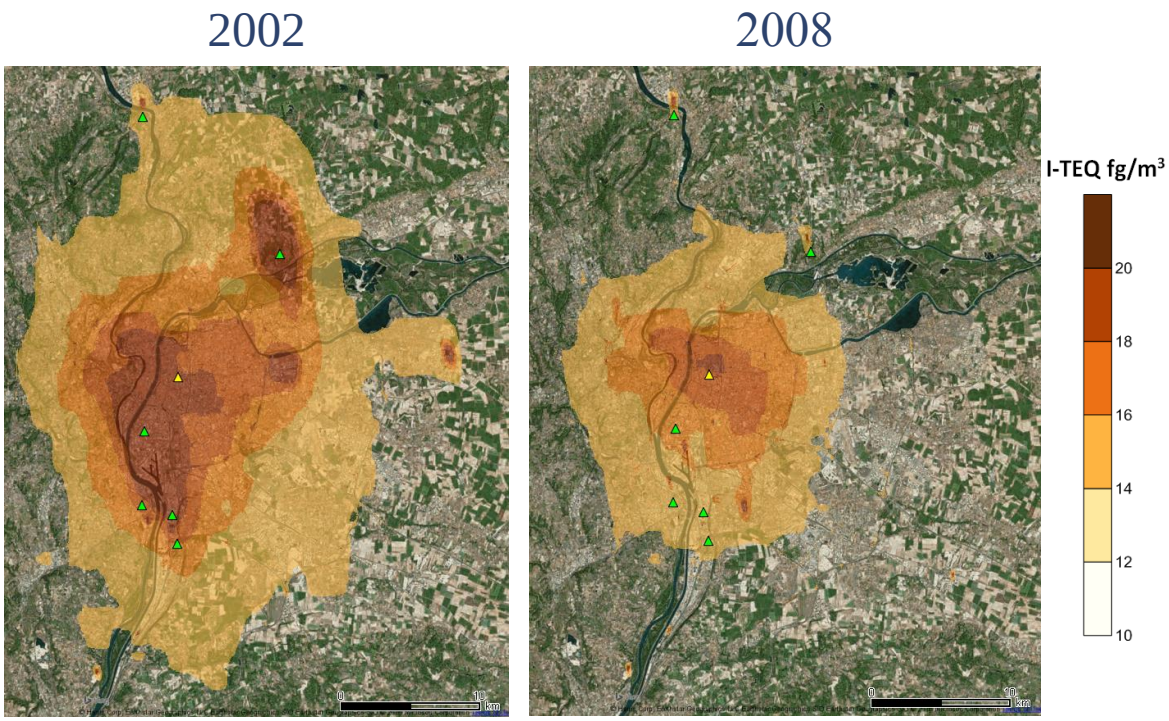

Figure 10.2: Ground level annual mean average dioxin concentration over the city of Lyon, simulated with the SIRANE model. Results of the GEO3N project in collaboration with the Centre Léon Bérard (PhD of T. Coudon).